Sectional Buckling of Built-up Cold-Formed Steel Columns

by

Mandana Abbasi

B.Sc., M.Sc.

A thesis submitted to fulfil requirements for the degree of

DOCTOR OF PHILOSOPHY

School of Civil Engineering, Faculty of Engineering

The University of Sydney

2022

STATEMENT OF ORIGINALITY

This is to certify that, to the best of my knowledge, the content of this thesis is my own work. This thesis has not been submitted for any degree or other purposes.

I certify that the intellectual content of this thesis is the product of my own work and that all the assistance received in preparing this thesis and sources have been acknowledged.

Mandana Abbasi

ABSTRACT

Cold-formed steel (CFS) sections are characterised by their high strength-to-weight ratio resulting in extensive applications that range from sheeted wall systems to low-rise frames. The manufacturing process of CFS and the introduction of built-up sections permit the optimisation of their geometry for enhanced capacity, which can further extend CFS applications. However, the presence of discrete fasteners can influence the behaviour of built-up members, including their buckling modes and associated capacities. This research investigates the sectional buckling of built-up CFS columns through a series of experimental tests and detailed finite element (FE) analyses. A comprehensive nonlinear FE model was developed by appropriately accounting for material and geometric nonlinearities, imperfections, restraint conditions, and constraints due to discrete fasteners and contact between component elements. The numerical model was shown to yield predictions in excellent agreement with experimental observations and utilised to perform extensive parametric studies on the influence of cross-section geometry and fastener spacing. A novel application of the Compound Strip Method to the elastic stability analysis of built-up members with discrete fasteners was also established to serve as a simple yet accurate analytical tool for practical design purposes. The reliability of the effective width method and the Direct Strength Method (DSM) for the design of built-up columns was assessed in the context of the Australian and North American provisions. The current DSM equations for local and distortional buckling capacities were rationally modified for conformal reliability in terms of the relative number of restrained components undergoing the sectional buckling mode of interest and the fastener spacing ratio normalised to the associated critical buckling half-wavelength. The proposed adjustments provided consistent predictions for different cross-section and fastener configurations.

ACKNOWLEDGEMENTS

AUTHORSHIP ATTRIBUTION STATEMENT

This thesis contains materials published in a peer-reviewed journal and presented at an international conference as follows:

- M. Abbasi, M. Khezri and K. J. R. Rasmussen and B. W. Schafer (2018), "Elastic buckling analysis of cold-formed steel built-up sections with discrete fasteners using the compound strip method." *Thin-Walled Structures*, 124, pp.58-71, and

- M. Abbasi, M. Khezri and K. J. R. Rasmussen (2017), "On extending the direct strength method to the design of cold-formed steel built-up columns." *ce/papers: Proceedings of Eurosteel 2017*, 1(2-3), pp.1600-1608,

for which I co-designed the study with the co-authors, analysed the data and wrote the drafts of the manuscripts. These materials are distributed through Chapter 2 and Chapter 3. I also acknowledge that the main program for the finite strip analysis utilised in these publications was developed by Dr Mani Khezri, and I contributed to implementing the compound strip analysis module in the existing code.

TABLE OF CONTENTS

LIST OF FIGURES

LIST OF TABLES

Chapter 1 INTRODUCTION

1.1 BACKGROUND

Cold-formed steel (CFS) sections are extensively used in the low-rise construction industry, ranging from residential houses to industrial buildings. In recent years, the desire for extending their applicability range to mid-rise construction and the demand for sections with higher capacities have created a new trend in the application of CFS by connecting several single sections to form built-up cross-sections using typical fasteners such as screws and bolts. The presence of discrete fasteners influences the overall behaviour of the members and changes the encountered buckling modes and associated capacities. The safe, practical application of these members requires reliable design equations and efficient analysis tools that can accurately incorporate the effects of discrete fasteners. This founded the basis for an Australian Research Council Discovery project on built-up cold-formed steel structures to undertake thorough experimental and numerical investigations of the global and sectional buckling of built-up CFS columns and beams and provide a scientific basis for the design and optimisation of this new generation of structural sections. This thesis constitutes one of its major components and is specifically concerned with the local and distortional buckling of built-up columns.

1.2 STATEMENT OF THE PROBLEM

This study is mainly concerned with the sectional buckling of open built-up sections under uniform compression, including experimental and numerical investigations. In addition, it comprises an extensive parametric study to investigate the influence of various design parameters, assess the reliability of current design equations, and propose adjustments to achieve efficient provisions that conform to the target reliability expectations.

1.3   RESEARCH OBJECTIVES

This research investigates the sectional buckling of built-up CFS columns and their complex behaviour to provide a foundation for the structurally reliable analysis and design of these members. The main objectives of this study can thus be summarised as follows:

- Implementation of a semi-analytical finite strip method with the incorporation of discrete fasteners for the efficient evaluation of the elastic buckling load of built-up members for design purposes, especially when using the direct strength design method,

- Establishment of a detailed finite element modelling approach within the framework of the ABAQUS software to accurately evaluate the complex behaviour of built-up CFS members and capture their inelastic response up to ultimate capacity and beyond,

- Experimental study on the local and distortional buckling of built-up CFS sections subjected to pure compression to facilitate validation of the proposed numerical method while providing valuable insights into the influence of critical parameters such as the buckling mode, cross-section geometry and fasteners spacing,

- Performing extensive parametric studies of various design parameters, including section geometry and fastener configurations, to observe their impacts and assist with the reliability assessment of currently available standard design equations, and

- Reliability assessment of current standardised methods for the design of built-up CFS members with discrete fasteners and proposing enhancements of these while conforming to the reliability expectations of the Australian and North American standards.

1.4   METHODOLOGY

This research is undertaken by a detailed numerical study and supported by an experimental investigation. The former comprises the Compound Strip Method (CSM) for the efficient elastic buckling analysis of built-up members accounting for partial composite actions due to

discrete fasteners and a detailed finite element inelastic analysis of built-up CFS columns up to and beyond their collapse load within the framework of ABAQUS software. Based on preliminarily numerical simulations, a set of laboratory experiments featuring local and distortional buckling are designed and conducted on a selection of built-up cross-sections featuring two, three and four component sections with various fastener configurations. The experiments provide insights into the problem while validating the proposed numerical finite element and finite strip methodologies.

Following that, a comprehensive set of parametric studies is designed and performed using nonlinear finite element simulations on a range of open sections with various section dimensions, built-up section geometry and slenderness ratios to acquire strength curves corresponding to sections failing in different buckling modes. Lastly, the current standardised methods for the limit state design of CFS members are compared in terms of applicability to built-up members and tested for reliability to account for the uncertainties in material properties, geometry and modelling. Finally, adjustments to existing direct strength design equations are proposed to incorporate the strength enhancement produced by discrete fasteners while meeting the expected minimum level of target reliability in the North American and Australian design specifications.

1.5   STRUCTURE OF DISSERTATION

The main components of this thesis are presented in seven chapters, where a summary of their contents and structure are given here. The next chapter delivers a comprehensive literature review summarising the most relevant research to this project. The current state-of-the-art research in the field of built-up cold-formed steel members with detailed coverage of the topics related to the main objectives of this study are summarised in individual sub-sections. This includes observed behaviour, failure modes, elastic buckling analysis, experimental investigation, numerical and parametric studies, available design methods and reliability assessment intending to identify the research gaps and the genesis of the research problem investigated in this thesis.

Chapter 3 describes the implementation of the Compound Strip Method (CSM) as a practical extension of the conventional Finite Strip Method (FSM) for the efficient elastic buckling analysis of built-up sections with any desired cross-sectional composition and fastener configuration. The proposed framework provides a useful numerical tool for undertaking extensive parametric studies and facilitates the structural design of built-up sections using the Direct Strength Method (DSM). In Section 3.2, the semi-analytical FSM is briefly reviewed, and then the formulation of connection elements with adjustable stiffness properties and their incorporation into the finite strip formulation is illustrated in detail. A series of numerical examples are presented in Section 3.3 to show the robustness and versatility of the CSM for the elastic buckling analysis of various built-up CFS sections, and the chapter concludes with a summary of outcomes in Section 3.4.

The experimental investigation of the local and distortional buckling of cold-formed steel built-up sections subjected to pure compression, as one of the major components of this study, is described in Chapter 4, which is written in terms of the key steps taken in chronological order. It commences with the procedure undertaken to design the geometry of test sections in Section 4.2, followed by the initial preparation of test specimens as explained in Section 4.3. Some standard coupon tests for evaluating the material properties of flat and corner segments are illustrated in Section 4.4. The procedures for measuring material and geometric imperfections are discussed in Sections 4.5 and 4.6, respectively. Section 4.7 describes the setup and execution of the compression tests and presents the test data in graphical and tabulated forms. Finally, an in-depth discussion of the obtained results and observed behaviour is provided in Section 4.8.

Chapter 5 describes the comprehensive finite element (FE) study undertaken in this research for the nonlinear analysis of cold-formed steel built-up columns within the framework of ABAQUS software. To this end, different components of the FE model are explained in Section 5.2 with relevant theoretical background, and comparisons are made on the available options with justifications of those chosen for this study. The accuracy and performance of the numerical simulations are validated in Section 5.3 against the results of experimental tests. The

verified and calibrated FE models are then utilised in Section 5.4 as the basis for performing extensive parametric studies of the effect of various influencing design parameters on the ultimate strength of built-up columns such as cross-section dimensions, built-up section configuration and fastener spacing.

Chapter 6 is concerned with the suitability of current standardised design methods for the structural design of cold-formed steel members and any adjustments if required. The most commonly used methods in international standards, i.e., the effective width and direct strength methods, are briefly reviewed in Section 6.2. The applicability of these two methods to the sectional buckling of built-up sections is preliminarily examined in Section 6.3 by comparison against the experimental test data of this study. The basics of the first-order reliability analysis and its applicability to CFS members are explained in Section 6.4, followed by a detailed reliability assessment based on the results of the extensive parametric studies described in Section 6.4.1.3. This aims to identify the strength and weaknesses of each design method and their associated target reliability index to evaluate local and distortional buckling capacities of built-up members and their interactions. Adjustments are then proposed in Section 6.5 to the current direct strength equations to enhance the ultimate capacity predictions for built-up CFS columns to accurately account for the influence of discrete fasteners while meeting the implicit reliability index requirements in the Australian and North American design provisions.

1.6 PUBLICATIONS

Alongside this dissertation, the main outcomes of this research have been shared in the following journal and conference papers, some of which have already appeared or been presented, whereas the remainders are in their final preparation stages for journal submission:

1.6.1   Conference papers

▪ M. Abbasi, M. Khezri and K. J. R. Rasmussen, 2017. 07.13: On extending the direct strength method to the design of cold-formed steel built-up columns. ce/papers: Proceedings of Eurosteel 2017, 1(2-3), pp.1600-1608.

▪ M. Khezri, M. Abbasi and K. J. R. Rasmussen, 2017. 07.20: Application of the compound strip method in buckling analysis of cold-formed steel built-up sections. ce/papers: Proceedings of Eurosteel 2017, 1(2-3), pp.1667-1676.

1.6.2   Journal publications

▪ M. Khezri, M. Abbasi and K. J. R. Rasmussen, 2017. A combined meshfree/finite strip method for analysis of plates with perforations and cracks. *Thin-Walled Structures*, 111, pp.113-125.

▪ M. Abbasi, M. Khezri, K. J. R. Rasmussen and B. W. Schafer, 2018. Elastic buckling analysis of cold-formed steel built-up sections with discrete fasteners using the compound strip method. *Thin-Walled Structures*, 124, pp.58-71.

▪ M. Abbasi, K. J. R. Rasmussen, M. Khezri and B. W. Schafer, 2022. Experimental investigation of the sectional buckling of built-up cold-formed steel columns. *Journal of Structural Engineering* (Submitted).

▪ M. Abbasi, K. J. R. Rasmussen, M. Khezri and B. W. Schafer, 2022. Computational modelling of built-up cold-formed steel columns. *Engineering Structures* (To be submitted).

▪ M. Abbasi, K. J. R. Rasmussen, M. Khezri and B. W. Schafer, 2022. Design rules for the sectional buckling of built-up cold-formed steel members in compression. *Journal of Structural Engineering* (To be submitted).

Chapter 2   LITERATURE REVIEW

2.1   INTRODUCTION

Cold-Formed Steel (CFS) sections have versatile applications in the building industry due to their high strength-to-weight ratio and compatibility with other construction materials. These applications span from simple roof-sheeting to low-rise building frames. The demand for sections with higher capacities has seen a substantial increase to expand the applicability range to mid-rise construction, which can be achieved by connecting multiple component sections to form a "built-up" cross-section. Over the past two decades, extensive research has been dedicated to providing a better understanding of built-up section behaviour, including numerical investigations and experimental studies. This chapter reviews some key research on the buckling behaviour of CFS single and built-up members and some of the existing methods of analysis and design.

2.1.1   Material and manufacturing

Cold-formed steel is named after its cold rolling manufacturing process, which is different from conventional hot forming. This key variation in manufacturing causes substantial differences in stress-strain behaviour and residual stresses of these sections compared to widely-used hot-rolled sections. CFS flat sheets are produced conventionally from carbon steel or stainless steel, characterised by a minimum chromium content of 10-12% that can form a protective surface layer of chromium oxide for effective corrosion protection when needed. CFS sections are then made by bending flat steel sheets at ambient temperatures into desired shapes to enhance the capacity. Roll forming and brake pressing are the two main methods of cold forming [1]. Cold rolling refers to the gradual formation of strips through consecutive pairs of rolls, the number of which depends on the complexity of geometry, thickness, and strength grade. This gradual formation can minimise longitudinal distortion or the spring-back effect.

Several advantages can be attributed to the cold rolling process, such as finely finished surfaces, uniform cross-sections with lower tolerances, and a much higher production capacity. On the contrary, brake pressing involves mechanical deformation of flat strips using a machine pressing tool, which is limited to geometries and lengths that fit between the punch and die set. Thereby, cold rolling is preferred for longer sections and mass production, which with computer-controlled rolling lines can produce highly complex shapes even with perforation accurately [2].

2.1.2 *Features and applications*

The high strength-to-weight ratio is considered the main feature of cold-formed steel sections resulting in light structural members, bringing substantial savings on material billing, transport and erection. The cold-formed thin-walled sections were historically used in applications mainly outside the building industry (e.g. aeronautics and mechanical engineering), where lightness was of prime importance. Its use in the building industry was limited to profiled sheeting and non-structural elements. However, enhancements in strength and manufacturing process alongside developments in research and design standards have led to its broader use in the building industry, ranging from roof and wall systems (see Figure 2-1) to low-rise residential buildings or industrial portal frames.

(a)   (b)

Figure 2-1: Examples of cold-formed steel applications: (a) wall-framing and (b) roof truss [3]

The morphology and manufacturing nature of CFS elements permits the cross-sectional geometry optimisation to obtain innovative and efficient new structural solutions. Together with the option of forming built-up sections using simple connections (e.g. screws, bolts and spot welds), this feature can result in almost endless possibilities for extending CFS applications to suit structural, architectural and construction needs. For example, built-up CFS members can be used as the primary structural members in mid-rise residential buildings and mid-span portal frames. Nevertheless, current construction methods and design guidelines are mostly limited to single-section members, highlighting the need for a further research base in the field of built-up sections as the fast-growing next generation of CFS structural members.

Despite the aforementioned favourable features of CFS sections and their extensive potential applications, one may highlight the fact that CFS members are more susceptible to instabilities, geometric imperfections and structural vibrations due to their slender nature and lightness, which must be adequately investigated and properly accounted in analysis and design.

2.2 THE BEHAVIOUR OF COLD-FORMED STEEL

2.2.1 Constitutive relationship

The overall behaviour of CFS members is governed by either yielding or buckling, where the former is mainly an issue in compact short columns, and the latter is more likely to dominate due to the high compactness ratio of CFS sections [4]. Carbon steel typically shows a generic elastic-plastic behaviour, containing four stages of linear elastic, sharp yielding, hardening, and softening. In contrast, stainless steel usually shows a gradual yielding behaviour with an indistinct yield point. The well-known Ramberg-Osgood stress-strain curve [5] for materials with plastic work hardening and a smooth elastic-plastic transition is commonly considered for mathematical representation of the inelastic behaviour, where the nominal yield point is characterised by a nominal offset line (i.e. typically 0.2% offset strain).

2.2.2   Plasticity and yield function

Assuming similar capacities in tension and compression, the yield initiation of steel can be captured by either the von Mises yield criterion for isotropic metals or the Hill criterion [6] as an extension of the von Mises criterion for orthotropic materials. However, a general anisotropy in compressive and tensile strengths can only be considered by adopting a more advanced yield criterion such as the Hosford [7] or the modified Hill [8] criteria. This consideration can assist in capturing the so-called "Bauschinger effect" under cyclic loading. As far as the incremental progression of plasticity is concerned, an associated flow rule is typically considered for ductile alloy materials.

2.2.3   Hardening

Once the yield initiation is established, the expected hardening behaviour may be taken into account by assuming an isotropic, a kinematic or generally a mixed-type hardening rule. According to experimental results of [9], the stress-strain behaviour of cold-formed steel may be simplified by an initially linear behaviour followed by a gradual yielding, which can be idealised as an elastoplastic material model with a simple von Mises yield criterion and isotropic strain hardening rule.

2.2.4   Imperfections

Like any other manufactured structure, CFS structures may have initial imperfections that can be categorised into material and geometric imperfections. The former can include the variation and inhomogeneity of the material properties within the member, while the latter stands for any difference between the nominal geometry of the section and the measured dimensions of the member in reality [10].

Due to manufacturing and fabricating processes, material imperfections such as residual stresses are induced in cold-formed sections. The coiling-uncoiling process mainly creates residual stresses and strains in the longitudinal direction, depending on the radius of the coils.

In contrast, the roll forming process mainly introduces additional residual stresses and strains in the transverse direction and at the corners [11]. The through-thickness residual stresses of a thin plate are typically decomposed into the membrane and bending stress components with a commonly assumed linear variation [12]. The experimental studies [12, 13] showed that the residual membrane stresses induced by brake pressing are relatively small and can be generally ignored in numerical modelling. The overall impact of the residual stresses and strains on the strength predictions may also be negligible due to the beneficial and detrimental effects of each parameter [14]. Contrarily, it has been well demonstrated that the geometrical imperfections may significantly influence the expected behaviour and failure modes of CFS members [12]. The manufacturing process may introduce different types of geometric imperfections (e.g. camber, twist or waviness) in a cold-formed steel member, while shipping, storage and construction processes may cause localised imperfections in the form of dents or holes.

The global geometric imperfections include bow (G1), camber (G2), and twist (G3) of the member as per Figure 2-2(a)-(c). The overall flexural imperfections are typically considered as the scaled version of the associated buckling mode shape with a predefined amplitude in terms of span/length, e.g. L/1000 as maximum [15, 16] or L/1500 as average [17]. On the other hand, the sectional imperfections are commonly considered as a portion of the element thickness with distribution based on relevant local (L) and/or distortional (D) buckling mode shapes, see Figure 2-2(d), (e). The amplitude of sectional imperfections is either derived analytically or back-calculated from experimental measurements [12, 17-19]. Lastly, the overall imperfection field can be approximated by a classical superposition approach of eigenmode imperfections [12, 19] or a multi-dimensional spectral representation of imperfections as random fields [20]. An effective combination of these two approaches was also proposed and validated by Zeinoddini and Schafer [17] as a 1D modal spectral approach, which aimed to preserve the favourable feature of each method. Among these approaches, the modal imperfection decomposition method has been used extensively in the literature, as explained in Section 2.4.2.1, and successfully incorporated into the codes of practice [15, 16].
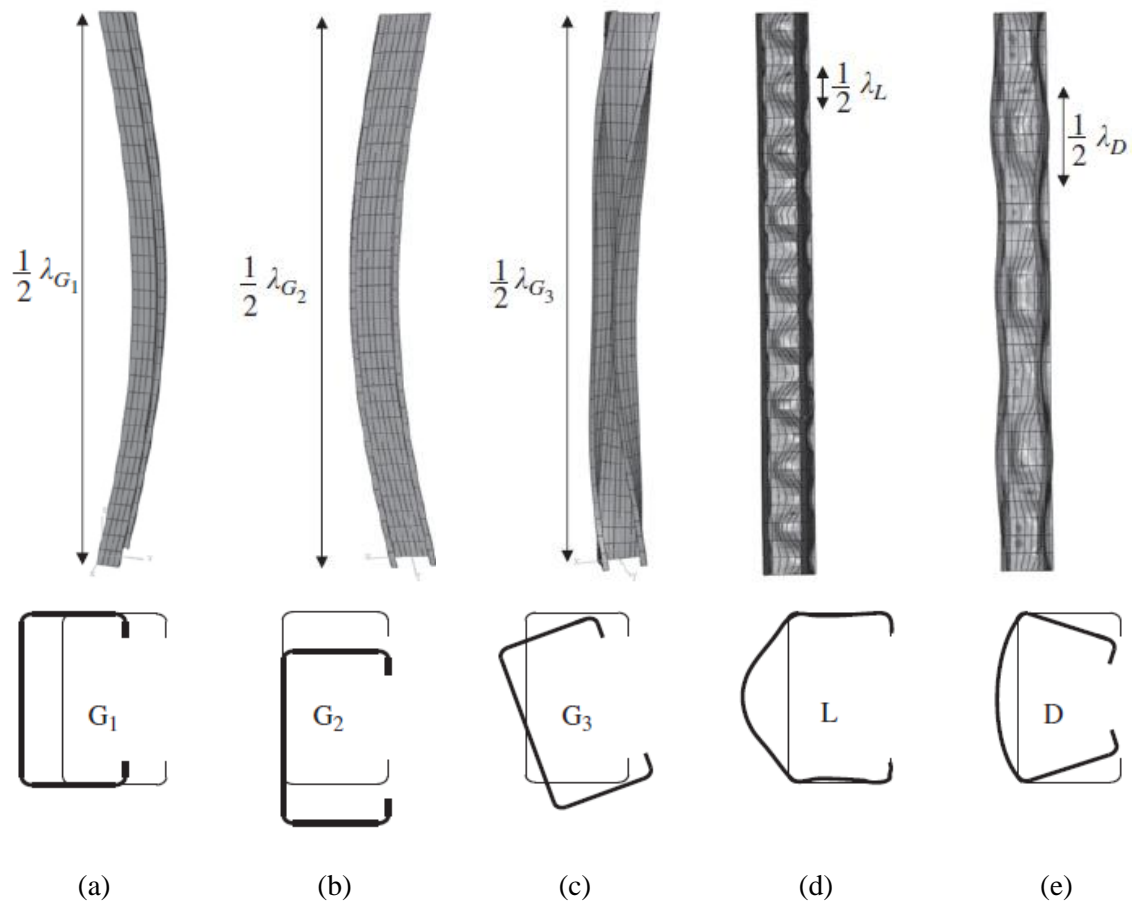
Figure 2-2: Typical member and sectional imperfections used in the traditional modal superposition approach [17]: (a) Bow – G1, (b) Camber – G2, (c) Twist – G3, (d) Local – L, (e) Distortional – D.

2.2.5   Plastic mechanisms

Despite the overwhelming variety of local plastic mechanisms in thin-walled steel members, it has been shown [21] that even the most complicated mechanisms can be decomposed into a number of simple yet basic ones. The local plastic mechanisms can be categorised into two major classes [21, 22]: (a) "true" mechanism that can be developed by folding individual plates along the plastic hinge lines with a free deflection pattern and (b) "quasi" mechanism in which some regions of the individual plates must yield in their planes to establish the inelastic deformation pattern involved in the plastic mechanism. A descriptive summary of these different mechanisms, including eight different true mechanisms, can be found in [21]. A schematic illustration of some of the common mechanisms in webs (CW) and flanges (CF) is shown in Figure 2-3. One of the most commonly observed true mechanisms in thin-walled

columns made of channel sections is the "flip-disc" mechanism with a typical parabolic shape, which involves twist and free bending of end panels, as shown in Figure 2-3(a). It is typically observed in the web of the channel section and is generally complemented by one compression yield zone and one tension yield zone in each flange.
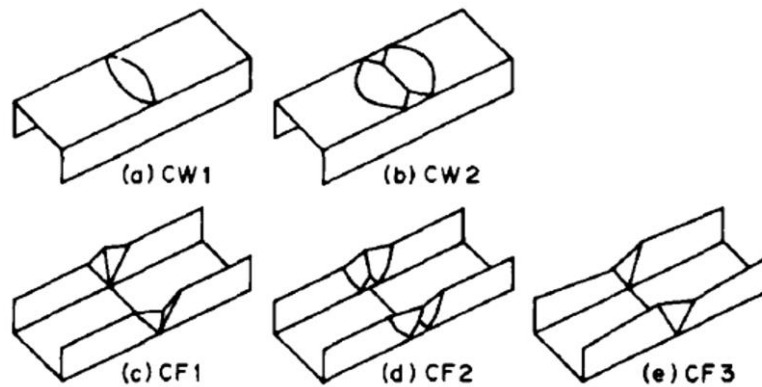
Figure 2-3: True plastic mechanisms observed in the experiments of channel columns [21]

2.3   SECTIONAL AND MEMBER BUCKLING

Buckling is influenced by many factors such as the member slenderness ratio, end boundary conditions, imperfections, loading type and eccentricity. Inelastic buckling mainly occurs in stocky to intermediate members, whereas elastic buckling is observed in moderate to slender members and comprises local, distortional and global modes [4]. The global (G) buckling mode is also known as member buckling, where the member cross-section undergoes flexural and/or torsional displacement but remains undistorted. In contrast, local (L) and distortional (D) modes only distort the cross-section and are thus categorised as sectional buckling.

Typically "signature curves", which demonstrate buckling stress versus associated half-wavelength for a CFS column and a CFS beam, are obtained from a finite strip analysis [23, 24] to assess the encountered buckling modes and evaluate the minimum buckling stress and associated half-wavelength. This concept is illustrated in Figure 2-4(a) and (b) for a lipped channel section in compression and bending, respectively. Figures display minimum local, and distortional buckling stresses and their corresponding buckling modes at associated critical

half-wavelengths; typical global buckling modes (for bending and compression) are also presented. It is noteworthy that short half-wavelength local modes may develop near holes in perforated cold-formed sections [25, 26]. This additional local mode is called L^2 mode hereafter, and it has also been observed in recent experimental tests [27] on built-up sections due to the existence of discrete fasteners.

(a)   (b)
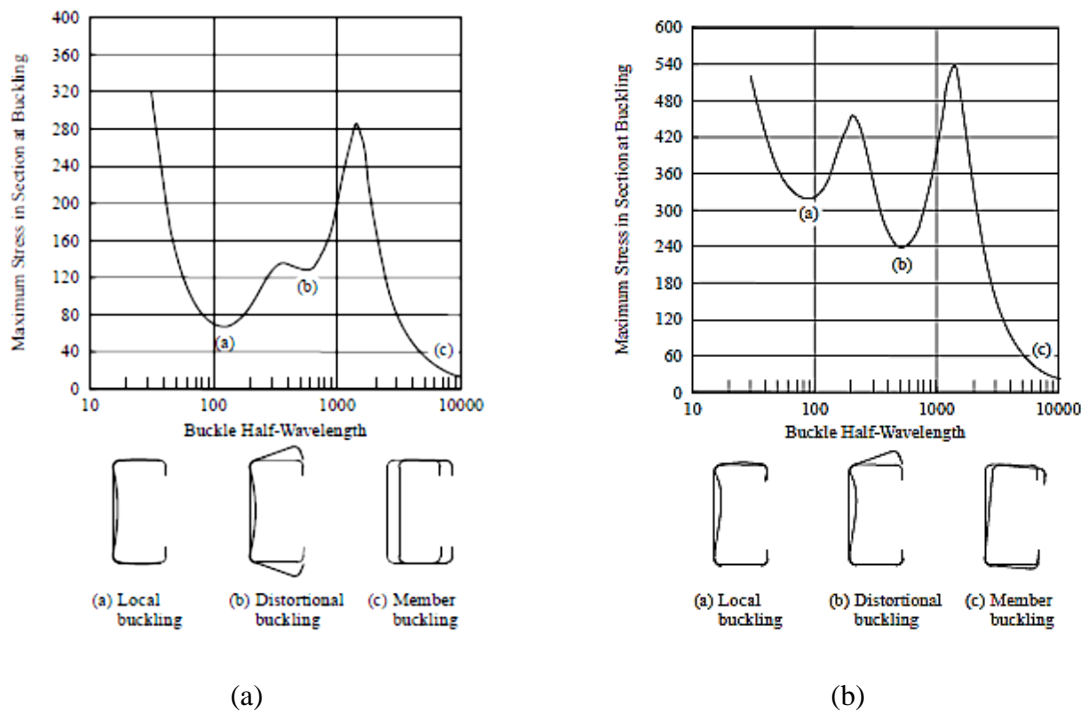
Figure 2-4: Signature curves for a lipped channel section subject to (a) compression and (b) bending.

2.3.1   Global buckling

The elastic flexural buckling of a column is expressed by the classical Euler buckling equation. The closed-form buckling capacity (N_c) is a function of elastic modulus (E_0), cross-section area (A) and member slenderness ($\lambda=L_e/r_g$) as the ratio of effective length/height (L_e) over the radius of gyration around the bending axis (r_g), viz. $N_c=\pi^2 E_0 A/\lambda^2$. If a material experiences gradual yielding, the material stiffness and capacity can reduce consequently. Engesser was the first to propose a simple modification to the Euler buckling capacity to account for inelastic overall buckling by replacing the elastic modulus (E_0) with the tangent modulus (E_t) [28]. Since the lateral bending under buckling can cause elastic unloading on the concave side of the column,

later, the so-called tangent modulus theory was revised by proposing a reduced modulus ($E_t \leq E_r \leq E_0$) as the weighted average of elastic modulus and tangent modulus over tension and compression segments of the section, respectively. However, Shanley [29] argued that a column cannot remain straight at loads above the tangent modulus buckling load. It was demonstrated that the axial force must change during overall buckling resulting in an intermediate inelastic capacity between lower and upper bounds by the tangent modulus and reduced modulus theories, respectively.

Since the inelastic post-buckling reserve for the overall buckling of columns is generally small, the inelastic column capacity can be conservatively approximated by the tangent modulus buckling load with a reasonable level of accuracy. The overall buckling, however, may differ from a pure flexural mode depending on the number of symmetry axes (two, one or none) of the section and the torsional rigidity of the member, which can provoke a pure torsional mode as twisting about the shear centre or a combined flexural-torsional mode. The latter is arguably the most frequent global buckling mode in thin-walled members, the theory of which is also very well developed in the literature [30, 31]. Most early research on this buckling mode was focused on singly symmetric open sections [32], for which design guidelines have been proposed [33]. The work by Chajes et al. [34] and Pekoz and Winter [33] were successfully incorporated into many international design standards, e.g. [15, 16].

2.3.2   *Local buckling*

Local buckling often manifests itself as the local crippling effect in the constituent plate elements of the cross-section (mainly web), which involves large plate bending deformations without significant translation of common nodes. The theory of plate buckling under in-plane loading was first developed by St. Venant [35], and the analytical solutions characterised by the plate buckling coefficient emerged later for different support conditions [36]. Lundquist et al. [37] adopted the moment distribution method for local buckling of plate assemblies under uniform compression. Later, the differential equations of each plate component were solved independently [38-40] while satisfying the static and kinematic continuity conditions at the

common junctions. The approach was later extended and resulted in the quantitative presentation of the plate buckling coefficient in design chart format for different cross-sections [41]. Von Karman [42] accounted for large deflections and established general differential equations for the post-buckling behaviour of plates under arbitrary loading and support conditions, which was later modified by Marguerre to include initial imperfections [43]. Approximate solutions were then obtained using energy methods [31, 44, 45], finite difference method [46] and perturbation theory [47].

On the subject of the inelastic plate buckling problem, one may refer to the theory proposed by Stowel [48] for instability of plates with inelastic material under in-plane compressive stress, which was based on the plastic deformation theory and founded upon an earlier theory by Ilyushin [49]. Bleich [38] proposed a semi-rational alternative theory to facilitate analytical solutions, which resulted in a simple adjustment of the plate buckling coefficient in terms of a so-called plasticity ratio as the square root of tangent modulus ratio ($\eta=\sqrt{E_t/E_0}$). The proposed theory was in good agreement with experimental data, from which it can be postulated that the inelastic buckling of plates is not affected by gradual yielding to the same extent as in columns. The plasticity ratio was later modified by Gerard [50] by replacing the tangent modulus with the secant modulus (E_s), which improved the accuracy of predictions for unstiffened plates. However, it is noted that these inelastic plate buckling loads may not be accurate estimates for the ultimate strength due to significant post-buckling strength reserve in local buckling.

The post-buckling behaviour of steel plates with material yielding and the associated ultimate strength capacity is a substantially more complex phenomenon. Upon its first experimental observations in thin steel plates, a semi-analytical formula for the ultimate capacity was developed by von Karman et al. [42], which formed the basis of the Effective Width Method (EWM) as the most extensively used design method of thin-walled members to date. The theory was established upon the observations that the longitudinal stresses redistribute towards the edges of the plate elements throughout the post-buckling regime. Following extensive tests on cold-formed steel sections and accounting for the imperfections within steel members, Winter

[51] proposed a revised equation for the effective width calculation of compressed plate elements, which has been used since then in various design standards [15, 16, 52].

2.3.3   *Distortional buckling*

Contrary to local buckling, another kind of bifurcation phenomenon was observed in the cross-section in experimental studies, which incurred fold-line motions and involved considerable membrane deformations in the flange and edge stiffeners (lips) in addition to moderate plate bending in the web [53, 54]. Thereby, the so-called distortional buckling is generally distinguished as a distortion of compression flange along the member length, and it has been characterised according to different theories in the literature, a summary of which is provided here. In one of the first theories, distortional buckling was considered another form of local buckling associated with insufficient edge stiffeners (lips) stiffness to fully support adjoining flange elements [55, 56]. Desmond [57] experimentally studied the requirement for an adequate edge stiffener and proposed an empirical solution for the plate buckling coefficient in case that cannot be satisfied. This was rolled into AISI specification for cold-formed steel structures in 1996. Another empirical design formula was later proposed by Bambach [58-60] for partially stiffened plates, which was backed by testing and parametric studies on edge stiffened plates and allowed its gradual strength prediction in between strengths for unstiffened and fully stiffened cases.

In another approach, distortional buckling is deemed a separate sectional buckling mode, first verified by Wittrick [61, 62] based on an exact stiffness method. Compared to local buckling, a lower post-buckling capacity was verified experimentally and analytically for distortional buckling, which was associated with early yielding due to the swift evolution of the membrane stress in edge stiffeners upon elastic buckling. Lau and Hancock [63] proposed one of the first and most widely used analytical models for this sectional instability by considering flexural-torsional buckling of the flange acting as an isolated column with elastic restraints provided by the web. This model originated the basic idea for the current Direct Strength Method (DSM) in Australian [16] and North American [15] specifications. It was later revised by Schafer and

Pekoz [64] and Li and Chen [65] with an allowance for modifying rotational stiffness based on the applied stresses. Another theory for distortional buckling was developed by Buhangiaer et al. [66] based on the overall buckling of the edge stiffener and an effective segment of the adjoining flange on elastic foundations, where the rigidity was defined in terms of the boundary conditions and the bending stiffness of adjacent parts. This theory was implemented in Eurocode 3 [52], in which the thickness of the effective compressed strut is reduced to account for distortional buckling. Despite rationally accounting for the interactions between constituent elements, it does not explicitly consider any post-buckling reserve for the distortional buckling mode.

2.3.4   *Buckling interactions*

The concurrence of different buckling modes is called interactive buckling, which can negatively affect the member capacity. Most typically, sectional buckling can deteriorate the sectional stiffness, resulting in a decreased overall buckling load. Although local or distortional buckling may be followed by a significant post-buckling reserve, the deformations and redistribution of stresses associated with the post-buckling reserve strength can change the global buckling response and strength of a member [67]. A comprehensive approach for the interactive local-global buckling mode was provided by van der Neut [68]. The Erosion of the Critical Bifurcation Load (ECBL) approach was later established by Dubina [69] upon the principle of van der Neut, which provides a numerical evaluation of the difference between the theoretical bifurcation point (N_{cr}) and the equilibrium limit point for the ultimate capacity (N_u) due to imperfections. The interaction between local and overall buckling has also been studied experimentally, contributing to some empirical modifications of member capacities and successful incorporation into design codes [15, 16]. For example, the effective width method explicitly accounts for this interaction by establishing the overall ultimate capacity of the member upon a reduced cross-section from local buckling effects. The direct strength method accounts for local buckling and geometric imperfections in evaluating global buckling

capacity, whereas the overall buckling in return impacts the direct strength equation for local buckling via modifying the sectional capacity limit.

In addition to interactions between sectional buckling modes (mainly local) and global buckling, the possibility for interactive local-distortional buckling has been observed in the experimental studies [70, 71]. The probable interactions between sectional buckling modes have been attributed to different sources in the literature, which can be classified into two main categories. First, in sections with closely spaced local and distortional critical buckling stresses and relatively higher yield stress, an interaction arising from a genuine mode coupling was identified by Silvestre et al. [72, 73]. By capping the distortional buckling capacity at an inelastic local capacity rather than yield capacity, they proposed a revised direct strength equation to supersede the current distortional buckling strength equation in design standards. Second, sections with predominant elastic local buckling mode and an invariably higher critical distortional buckling stress may develop a secondary bifurcation phenomenon in distortional mode and experience another type of local-distortional buckling interaction if the yield stress is still remarkably higher than the critical distortional buckling stress. A revision for the current DSM was proposed by Schafer [74, 75] to account for this interactive failure, which further limits the local buckling capacity beyond the local-global interactive capacity.

2.4   METHODS OF ANALYSIS

This section covers some existing research on methods of analysis of the behaviour of CSF members with a particular focus on built-up columns. The studies in this area can be categorised into two main branches (*i*) experimental and (*ii*) numerical investigations. Relevant studies of each group are reviewed in the following two sub-sections. Analytical methods have also been used extensively for buckling analysis of CFS members, but their range of application is almost limited to single sections, and they are thus not included in this review.

2.4.1 Experimental research

The early studies on the behaviour of built-up CFS members appear to date back to 1974, when buckling and post-buckling capacities of box and I-columns made of two channels were investigated experimentally [76]. The double-channel CFS beam was analysed by Ghersi et al. [77] to determine the buckling modes and ultimate behaviour of such beams. Stone and LaBoube [78] tested the behaviour of pin-ended built-up CFS I-sections made of screw-connected back-to-back lipped channels. The results of the modified slenderness ratio in AISI S100 [15] was shown to be optimistic for the sections with a thickness of less than 0.89 mm. Young and Chen [79] later carried out an experimental investigation on screw-connected built-up closed sections with longitudinal web stiffeners. The fixed-ended columns were tested at various lengths to provide valuable data for comparison with design strength curves.

An extensive experimental study was conducted by Whittle and Ramseyer [80] to evaluate the impacts of member characteristics on the ultimate strength of built-up closed sections formed from welded channels. Although a pin-ended boundary condition was considered in their study, a series of tests were performed later in [81] on the same section, but for different end boundary conditions, including rigid and flexible supports. The results showed that the ultimate loads were slightly affected by the type of end boundary conditions, and the modified slenderness ratio might still be used conservatively to design this type of built-up section. Moreover, Georgieva et al. [82, 83] performed a series of full-scale tests on the behaviour of bolted built-up sections made from two identical lipped Z-sections [82] and combinations of three or four Z, C and sigma sections [83]. They considered long columns with pin-ended boundary conditions and similarly showed that using the current design equations leads to a conservative prediction of the ultimate strength of these built-up sections. Later, Zhang and Young [84] investigated the behaviour of screw-connected built-up I-sections with edge and web stiffeners. The columns length varied from 300 to 3200 mm in length and had fixed-end boundary conditions with evenly spaced screws. The obtained strength curves were used to evaluate the appropriateness of the current design equations.

Li et al. [85] tested screw-connected built-up box sections and investigated the effects of various fastener arrangements on the capacity of built-up columns failing in local-global buckling mode. They showed that the spacing and arrangement of fasteners significantly affect the failure load and suggested some minimum requirements for fastener spacing. Later, Fratamico et al. [86] studied the effect of screw spacing on the sectional buckling behaviour of built-up I-sections. The test results suggested that increasing the number of equidistant fasteners along the length of the column does not substantially improve the ultimate capacity of I-sections. However, a compatible web buckling was observed for columns with screw spacing less than $L/4$. A series of compression tests were performed on various screw-connected built-up cross-sections [87], i.e. back-to-back (I), box (R) and two side-by-side connected box sections (2R), under fixed and pinned end support conditions. The ultimate capacity of the complex built-up 2R-section was 9.4 and 5.6 times the capacity of its component section for pinned- and fixed-ended columns, respectively. Moreover, the predictions of the ultimate strength of built-up sections based on the effective width method in [15, 52] were found in good agreement with the test results for columns with pinned end conditions and conservative for fixed-ended columns. In a subsequent study by Liao et al. [88] on the sectional buckling of similar built-up configurations, the ultimate capacity of a 2R-section was found to be less than or equal to double the capacity of a box section.

Liu and Zhou [89] investigated the behaviour of a T-section composed of three C-sections under compression. The primary failure mode for intermediate and long columns was flexural-torsional. The results of the effective width and direct strength methods were found conservative for this cross-section. Subsequently, Lu et al. [90] studied the buckling behaviour of I-sections with interactive failures, especially local-distortional (LD) and local-distortional-global buckling (LDG) modes. A substantial reduction in the ultimate capacity of built-up I-sections was observed due to the interactive failures. A new direct strength equation was proposed to predict the capacity of these sections failing in LD and LDG buckling modes. Fratamico et al. [91, 92] investigated the composite action in screw-connected back-to-back, sheathed and unsheathed, built-up I-sections. The results showed that end boundary conditions,

along with friction and contact, have a significant impact on the composite action of built-up members. Zhang and Young [93] studied the behaviour and possible failure modes of built-up box sections with two types of web stiffener. The component profiles of the built-up sections were connected with sufficiently small spacing along the member length using self-tapping screws, and the specimens failed in either local buckling or local-flexural interactive buckling modes. Ting et al. [94] performed extensive experimental studies on short, intermediate and slender built-up CFS columns made of two back-to-back lipped channels with various screw spacing. It was concluded that columns with screw spacing beyond the AISI specification almost displayed non-composite behaviour.

The effect of fastener spacing on the ultimate capacity of complex built-up sections composed of four component sections was studied by Meza et al. [95, 96] via a comprehensive experimental program. The component sections were flat plates, U-, and C-sections connected with either bolts or self-drilling screws. Long columns were tested between pinned supports, while the end supports of short columns were fixed. The maximum enhancement of the ultimate capacity was 11% for short columns, and the effect of fastener spacing, greater than the local half-wavelength of the section, on the ultimate strength of built-up sections was reported negligible in general. Furthermore, in several studies on the buckling of built-up CFS box sections [97-102] with various lengths and end supports, the impact of fastener spacing on the ultimate capacity was found insignificant. Lastly, Phan et al. [103] studied the local-global buckling behaviour of built-up CFS sections with multiple component sections under compression. It was found that the presence of end fastener groups (EFGs) or more screw rows along the column length does not enhance the ultimate capacity of the columns considerably. For instance, the ultimate capacity of long specimens was slightly increased (less than 5.2%) by decreasing the fastener spacing from 500 mm to 100 mm. As a concluding remark, the key parameters of the experimental studies reviewed in this section, including built-up section geometry, fastener type, end support conditions and observed failure modes, are summarised in Table 2-1.

Table 2-1: Summary of the existing experimental studies on built-up CFS columns

Researcher(s)	Year	Built-up section geometry	Fastener type(s)	Support type(s)	Failure mode(s)
Stone and LaBoube [78]	2005	Lipped I-section	Screws	Pinned	L+F
Young and Chen [79]	2008	Box of two U-shaped sections with intermediate stiffener	Screws	Fixed	L / F L+D L+D+F
Whittle and Ramseyer [80]	2009	Box of two C-sections	Welds	Pinned	F / FT
Reyes and Guzman [81]	2011	Box of two C-sections	Welds	Pinned Fixed	L / F
Georgieva et al. [82, 83]	2012	Double Z-sections Four complex sections assembled from Sigma, Z- and C-sections	Bolts	Pinned	L+D+FT
Zhang and Young [84]	2012	Lipped I-section with web stiffeners	Screws	Fixed	D / F L+D L+D+F
Li et al. [85]	2014	Lipped I-section Box of two C-sections	Screws	Pinned	L / F L+F
Fratamico et el. [86]	2016	Lipped I-section	Screws	Fixed	L L+D
Craveiro et al. [87]	2016	Lipped I-section Box of a U- and a C-section Double-box	Screws	Pinned Fixed	D+F L+D+F
Liao et al. [88]	2017	Box of a U- and a C-section A C-section connected to a box Double-box	Screws	Fixed	L / D
Liu and Zhou [89]	2017	T-section (made of three C-sections)	Screws	Pinned	FT
Lu et al. [90]	2017	Lipped I-section	Screws	Pinned	L / F L+D L+D+F
Fratamico et al. [91, 92]	2018	Lipped I-section	Screws	Fixed	F / FT
Zhang and Young [93]	2018	Box of two U-shaped sections with intermediate stiffeners	Screws	Fixed	L L+F
Ting et al. [94]	2018	Lipped I-section	Screws	Pinned	L F / FT
Roy et al. [97]	2019	Box of two C-sections	Screws	Pinned	L / F
Nie et al. [98, 99]	2020	Box of a U- and a C-section Double-box	Screws	Fixed Pinned	L L+F
Meza et al. [95, 96]	2020	Four complex sections assembled from flat plates, U- and C-sections	Bolts Screws	Fixed Pinned	L / F L +F(T)
Zhou et al. [100]	2021	Box of a U- and a C-section	Screws	Pinned	L L+F
Vy et al. [102, 104]	2021	Lipped I-section Box of two C-sections	Screws	Fixed	L / D L+D
Vy and Mahendran [101]	2021	Box of two C-sections	Screws	Fixed	F L+F
Phan et al. [103]	2021	T-section (made of three C-sections) Doubly-symmetric section (made of four C-sections)	Screws	Pinned Fixed	L / FT

2.4.2 Numerical studies

Although experimental studies such as those mentioned above provide crucial benchmark data for the stability analysis of built-up sections, their relatively high cost necessitates utilising reliable, less expensive computational approaches for extensive parametric studies. The finite element method (FEM), finite strip method (FSM) and the generalised beam theory (GBT) are the most widely used and dominant numerical methods in the analysis of CFS members. Thus, the studies based on these numerical techniques are briefly reviewed in the following subsections.

2.4.2.1 Finite element method

The finite element method (FEM) is a general numerical method to solve any partial differential equation. FEM has been successfully applied to various applications in continuum mechanics, and it is now incorporated as the core method in commercial analysis software. Two types of finite element analyses have been commonly conducted for CFS members. These are: (*i*) the linear elastic buckling analysis to estimate the critical loads and corresponding buckling modes, and (*ii*) the inelastic analysis, including geometric and material nonlinearity to capture the post-buckling response of the CFS member. A precise nonlinear finite element model should utilise suitable element type and mesh size, representative material model, realistic loading type and boundary conditions. In addition, appropriate consideration of imperfections and careful treatment of contacts and discrete constraints are necessary for accurate and successful FE modelling and simulations [12]. FEM has been successfully employed for the analysis of built-up CFS sections, and some of the most recent FE-based studies on the behaviour of built-up members are selected and briefly reviewed in the following paragraphs.

As far as modelling imperfections are concerned, the geometric imperfection is introduced as initial displacement conditions to the finite element model, where the corresponding nodal values can be generally evaluated from (*i*) an Eigen-buckling analysis, (*ii*) a limit-load analysis on a perfect configuration, or (*iii*) the actual imperfections measured experimentally [105].

Moreover, residual stresses are incorporated as initial stress conditions in numerical analysis, where one of the suggested models can be found in [106]. Finally, the influence of initial imperfections and residual stresses in CFS sections was evaluated using a probabilistic approach in [12].

Xu et al. [107] performed parametric studies in ANSYS to identify the influencing parameters on the flexural strength of built-up CFS boxes with self-tapping screws. The effect of screws was accounted for by coupling corresponding degrees of freedom (DOF) of constituent profiles at fastener locations in global coordinates. It was concluded that decreasing fastener spacing resulted in almost a six percent increase in flexural capacity. to evaluate their expected behaviour, a subsequent parametric study [108] was carried out on built-up CFS double-Z members, including columns and beams. The geometric imperfection was incorporated based on an Eigen-buckling analysis. The slip and bearing of the bolts were represented by sets of springs that connected nodes of the z-profiles at bolt locations, which revealed the importance of modelling fasteners as discrete constraints. Later, Li et al. [85] investigated the impact of installation errors and fastener spacing on the ultimate strength of built-up box- and I-columns via extensive parametric studies in ANSYS. The geometric imperfections were similarly considered via an Eigen-buckling analysis, and the effect of fasteners was considered by coupling associated DOFs at fastener locations on individual profiles. The results suggested that the spacing of fasteners and their arrangement can noticeably affect the failure load.

Laim et al. [109] conducted parametric studies in ABAQUS to determine the influence of cross-sectional dimensions on the flexural behaviour of built-up CFS open- and closed-section beams. They modelled the self-drilling screws with 3D solid elements and incorporated the geometric imperfection via an initial Eigen-buckling analysis. The numerical results suggested a strength-to-weight ratio reduction as the considered span increases. In addition, Wang and Young [110] studied the effect of cross-sectional dimensions and fastener spacing on the ultimate strength of the built-up box and I-beam sections with intermediate fasteners. They ignored the impact of imperfection in their parametric studies in ABAQUS and provided some

concluding notes for applying design equations to sections with stiffeners. Later, the effect of edge and web stiffeners on the behaviour of built-up I- and box columns was investigated in [111, 112] via extensive parametric studies in ABAQUS, where self-tapping screws were modelled by 3D solid elements and the effect of imperfection was accounted for via an initial Eigen-buckling analysis.

Liao et al. [88] numerically studied the effect of fastener spacing and width to thickness ratio in multi-component built-up closed cross-sections. Self-drilling screws were modelled using solid elements, Solid45 in ANSYS, whereas shell elements, Shell181 in ANSYS, were chosen to simulate the sections and end tracks. The results of the parametric study on short closed cross-sections, failing in local or distortional buckling, showed that the effect of screw spacing reduction on the enhancement of the ultimate load is insignificant. In a subsequent study [89] on the buckling behaviour of multi-component built-up open cross-sections, S4R shell elements in ABAQUS were used to model thin-walled sections, and the connections were simply modelled by tying the nodes at screw locations along the column length. Both studies reported that the web width to thickness ratio of multi-component built-up closed and open cross-sections is a major factor influencing the ultimate capacity and stiffness of these sections under compression. Kechidi et al. [113] proposed a nonlinear finite element modelling approach for built-up CFS I-sections and validated their model against the test data reported in [91]. The nine-node isoparametric shell element, S9R5, was adopted to model thin-walled sections, and a user-defined element was defined to model screw-fastened connections suitable for monotonic and cyclic analyses. The measured geometric imperfections were incorporated into the model using the modal imperfection decomposition method [17]. They also considered friction between the cross-section and end tracks by assuming a value of 0.19 for the coefficient of friction in the contact defined between them. The results showed that the shear demand of web screws was less than 0.4% of the axial capacity of the built-up columns. In addition, they concluded that the proposed finite element protocol can be used to find the optimal fastener arrangement for built-up columns.

Recently, in several studies [101, 102, 104] on the buckling behaviour of built-up CFS I- and box sections, the impact of fastener spacing on the ultimate load was investigated via parametric studies in ABAQUS. The component cross-sections were modelled with four-node shell elements with reduced integration, S4R, while point-based fastener elements were selected for the modelling of screws. The properties of the fastener elements were determined using the backbone curves proposed by Phan and Rasmussen [114]. The geometric imperfections were included in the model using an initial Eigen-buckling analysis, and the effect of residual stresses was ignored. These studies showed that the effect of screw size and spacing on the ultimate load of built-up I- and box sections, mainly with prevalent local buckling mode, is marginal.

2.4.2.2 Finite strip method

The Finite Strip Method (FSM) has been widely used for the elastic buckling analysis of CFS members due to its numerically efficient features, including narrow bandwidth of stiffness matrices, low computational cost, and easy implementation for prismatic members. However, its range of application is mainly limited to simple geometries and simple end boundary conditions. These limitations have been the motivation for introducing variants or enrichment of the FSM, e.g. [115-117]. Cheung [118] proposed the conventional FSM for the analysis of plates, which holds significant merits over other numerical methods due to its semi-analytical nature [119]. Nevertheless, it has two major drawbacks [119]: (*i*) deficiency in analysing problems involving material nonlinearity or collapse and (*ii*) limitation in the considered boundary conditions. The latter was the main motivation for introducing the spline finite strip method [115], which has significantly improved its versatility and applicability range.

FSM has been widely used by many researchers for elastic buckling analysis of CFS members and successfully implemented in CUFSM [24] and Thin-Wall [23] analysis programs. The semi-analytical finite strip method with some simplifying assumptions about the inclusion of fasteners and built-up section geometry [79, 120, 121] has been used for the buckling analysis of intermittently connected CFS sections. For example, CUFSM can tie a selection of

translational DOFs along the length of the member by applying nodal multi-point constraints, which can be used as an option for approximately modelling built-up sections in the context of conventional FSM. This feature was utilised by Fratamico et al. [86, 91, 92] to analyse back-to-back channel sections with or without sheeting. Despite an inherent difference with the actual effect of discrete fasteners, it can still provide a partial composite level that is typically an upper bound and lies between the curves with full and no composite actions (see Figure 2). Another notable attempt to extend the application range of conventional FSM to built-up sections, Zhang et al. [111] modelled fasteners as continuous longitudinal solid stiffeners. However, this assumption may also not represent the actual contribution of discrete fasteners and may fail to capture the composite action level accurately.
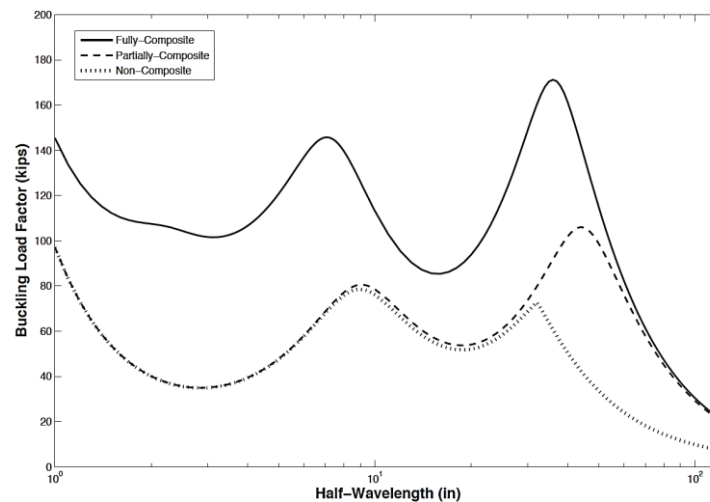
Figure 2-5: Signature curves for a built-up I-column at different levels of composite action [86]

The conventional finite strip analysis and the associated signature curve solutions may fail to provide the distinct minima in determining the proper critical local and distortional buckling modes [122]. The Generalised Beam Theory (GBT), as an analytical method, was proposed in first-order [123] and second-order [124] forms to extend conventional beam theories and capture definitively separated buckling modes and geometrical nonlinearity in thin-walled sections, respectively. Adany and Schafer [125] developed the constrained Finite Strip Method (cFSM) for the full modal decomposition of thin-walled open cross-sections by incorporating the same GBT mechanical assumptions of the buckling modes through a set of constraint

matrices. Adany [126, 127] later borrowed the same mechanical assumptions in the cFSM to enrich finite element analysis and implemented a new constrained FEM.

In contrast to the cFSM, Becque [128] proposed an alternative approach for the modal decomposition of buckled shapes based on the corresponding strain energies of different buckling modes. Another constrained approach for modal decomposition within the framework of FSM was proposed by Becque and Li [129], which was founded upon the concept of equivalent forces. At the same time, Jin et al. [130, 131] utilised a combined force-based approach to formulating an alternative cFEM using the general shell finite element formulation. One of the main shortcomings of the classic cFSM [127] was its limitations to flat plate elements forming open-branch sections. Khezri and Rasmussen [132, 133] developed a new energy-based cFSM, which can effectively decompose higher modes and restore this drawback by being equally applicable to open and closed sections.

Puckett and Gutkowski [134-136] developed the Compound Strip Method (CSM) as an extension of the semi-analytical FSM to analyse plate structures with elastic support and transverse elements. They included the stiffness of flexible supporting elements such as columns and longitudinal and transverse beams in a direct formulation [136] and hence significantly enhanced the versatility and capability of the FSM. In this method, the strain energy of the supporting elements is added to the strain energy of the component plate strips. Then the stiffness matrix is obtained by minimising the total energy with respect to displacements. The CSM was employed for the linear flexural [137] and buckling [138] analyses of straight continuous flat plates over flexible supports. For the analysis of folded plates, Puckett and Wiseman [139, 140] extended the CSM and developed a technique to include bracing elements to facilitate the analysis of folded structures. The spline compound strip method [141, 142] was also introduced as a more versatile extension of the conventional CSM and was utilised to analyse stiffened plates and braced thin-walled structures. Maleki [143] further extended the application of the CSM to the analysis of folded plates and box girders with intermediate non-rigid supports. Finally, Borković et al. [144] studied the linear

transient vibration of stiffened plates using the CSM, where the strain and the kinetic energy of stiffeners were added to those of finite strips. They also utilised the CSM for geometric nonlinear static analysis of prismatic shells with internal supports and stiffeners [145].

2.4.2.3 Generalised beam theory

The second-order Generalised Beam Theory (GBT) was developed by Schardt [146] to tackle coupled stability problems. The capability of decomposing the behaviour of a prismatic member into a series of orthogonal displacement fields and allowing the option of considering these modes in isolation or any desired combination was considered its main novelty. The GBT formulation was further developed and extensively used by Davies and colleagues [123, 124] for the elastic buckling analysis of cold-formed open cross-sections. Despite its early developments around thin-walled members with unbranched open cross-sections, its application to closed cross-sections was established later by Silvestre et al. [147] and Dinis et al. [148]. It was further extended by Goncalves et al. [149] to any arbitrary geometry and by Silvestre [150] to curved wall members. The potential applications of GBT and its favourable features have been extensively explored in the literature [151, 152], and it has been successfully implemented in GBTUL software [153] by professor Camotim and co-workers at the University of Lisbon.

2.5   METHODS OF DESIGN

Various methods exist in the literature for the design of CFS members, from which the effective width method and the direct strength method as the most common approaches are reviewed here.

2.5.1   Effective width method

The Effective Width Method (EWM) is a semi-empirical method for modelling the stress distribution in the post-buckling regime of thin plates which, as explained earlier, was first introduced by von Karman et al. [42] and later improved by Winter [51]. EWM is among the

first methods for designing thin-walled members and has been employed in many design codes [15, 16, 52]. The idea of EWM for CFS sections lies in finding the effective width for each plate element of the section and then reassembling the effective constituents to evaluate the effective overall section capacity. This method generally neglects the probable interactions between plate elements at buckling or throughout the post-buckling regime [64], which may not be necessarily true for built-up sections. Limited studies have been conducted on the applicability and accuracy of the conventional EWM for built-up columns, e.g. [85, 154].

2.5.2   *Direct strength method*

The Direct Strength Method (DSM), as a significant advancement in CFS design, is being more and more utilised as an effective tool to predict the strength of members with any general cross-section. The basic concept of the DSM lies in effectively combining the elastic local, distortional, and global buckling stresses of the considered section with the section yield stress to obtain slenderness values for each mode, which are then employed in a set of proposed direct strength equations to predict the ultimate strength of the member [155]. Hancock et al. [156] proposed the original DSM design equation for the ultimate strength of columns under distortional buckling; while the idea was later extended by Schafer and Pekoz [157] and Li et al. [158] beyond that point based on test results for a wider range of CFS cross-sections failing in local, distortional or overall (flexural or flexural-torsional) buckling modes.

Recently, DSM has become a favourable design method for CFS structures due to its simplicity, implicit nature and direct applicability to more complex geometries, and it has been successfully incorporated in North American Specification [15] and Australian/New Zealand Standard [16] as an alternative for the traditional EWM. However, since the current provisions of the DSM are mostly limited to single sections, several attempts have been made to extend the application range of DSM to built-up columns [79, 84, 111, 121, 159] and beams [110, 160]. A brief review of the recent progress in relevant research and developments is outlined here as a precursor for outlining the existing research gap and how it has been addressed in this study. In summary, an elastic buckling analysis that effectively includes the influence of

discrete fasteners and accurately determines all the elastic instabilities for the section is the first step in developing reliable direct strength equations.

In a study on built-up CFS closed sections with intermediate stiffeners by Young and Chen [79], the obtained test strengths were compared with design capacities determined using the DSM. Three sections were analysed, namely the single section, single section restrained at the flanges and double section with the flange thickness two times the web thickness. It was concluded that assuming no interaction between component profiles results in acceptable but conservative capacity predictions in built-up closed sections with stiffeners. Later, Zhang and Young [84, 111] investigated the appropriateness of the DSM for built-up CFS I-shaped and box members, where the test data were compared with the DSM capacity of composite sections with assumed web thicknesses ranging from 1.0 to 2.0 times the thickness of a single section. It was reported that assuming full composite action can overestimate the expected ultimate strength of stiffened built-up open sections and suggested an adjustment method based on introducing a scaling factor for the web thickness. For instance, the results obtained for sections with a web thickness of 1.2 times the original thickness were in good agreement with experimental data. This finding indicates that a degree of composite action between component sections is achieved in built-up members due to the presence of fasteners, which shall be carefully considered in determining the elastic buckling stresses to extend the DSM to the design of built-up sections [110].

Zhang and Young [111] proposed a method to model screws as a continuous solid stiffener along the longitudinal direction of the column. They presented a modified DSM and showed that predicted design strengths are reliable and conservative for built-up open section columns. Georgieva et al. [159] investigated the applicability of the DSM for the design of built-up CFS through experimental studies and suggested that a similar modified design methodology based on DSM can be adopted in structural standards. A modified DSM for the cold-formed built-up I-section columns was presented by Lu et al. [90], who showed that the current DSM can lead to excessively unsafe estimates for built-up I-section columns. Moreover, Phan et al. [103]

proposed a new design approach for built-up columns with complex geometries using the current direct strength equations and the effective rigidities derived theoretically in [161, 162].

2.6 RELIABILITY ASSESSMENT

A limit state function for the ultimate design of a member or structure is defined as the difference between the probability distribution functions for the provided resistance/capacity and imposed actions/demands, which is typically defined in direct or logarithmic scales. In conventional design standards, the limit state function is expressed as a design-value problem representing the gap between the characteristic values of the imposed actions and member resistance. It is vital to ensure a safe margin that can reliably keep the probability of failure below an acceptable limit for the application of interest. This objective is typically achieved by applying appropriate partial resistance or load safety factors. This differentiates the traditional allowable stress/strength design (ASD) from the load and resistance factor design (LRFD) that appreciates the uncertainties and variabilities involved in different actions and resistance.

International organisation for standardisation (ISO) and the Joint Committee on Structural Safety (JCSS) have outlined a systematic procedure based on the first-order reliability method (FORM) for the probabilistic calibration and optimisation of design standards [163, 164], which resulted in the development of probabilistic model codes and has formed the basis for the reliability-based assessment of some design standards such as Eurocodes [165] and fib model code [166]. In addition to the detailed assessment procedure, a simplified method is provided for the calibration of design factors in the design-value problem, which has been used and referenced by the national building codes of different countries such as Australia [167] and the United States [168].

The required level of safety margin is typically expressed in terms of a target reliability index, which measures the relative distance between the expected mean value of the limit state function and its critical value corresponding to the onset of failure in terms of the associated standard deviation. The target reliability index can be easily related to the probability of failure

or survival over a reference period (e.g. one year) or the design life (e.g. 50 years as typical) of the structure. The acceptable level of failure probability is usually recommended in the standards [163-165, 169] depending on the importance level or risk category associated with the structure, relative life-saving costs, the structure class for consequences of failure, mode of failure, and relative cost of safety measures. Since different plausible design scenarios in terms of the relative proportion of imposed actions versus the sustained gravity loading exist for a given structural material and member, the target reliability index (β_T) usually reflects a weighted average over the applicable range of design scenarios. This is typically established using the least-squares method considering the representative frequency associated with each case. Alternatively, the reliability index is prescribed in some design standards for a single design case that is either associated with the most probable scenario to represent the target reliability [170] or the most variable/uncertain yet still practical case to form a minimum baseline for the expected reliability [15, 16].

In ASCE7 [169], as the basis for American design standards, the lifetime (50-year) target reliability index (β_n) for structures with risk category I (structures with low-risk to human life) and II (typical structures other than I, III and IV) under typical ultimate design load cases (excluding extraordinary events such as an earthquake) is recommended as 2.5 and 3.0, respectively. These suggested values are valid as long as the failure is not sudden and does not lead to widespread damage progression; otherwise, they shall increase to 3.0 and 3.5, respectively. The international organisation for standardisation (ISO) has produced an international standard [171] regarding general principles on reliability for structures, where some recommendations for the lifetime target reliability index were provided in the 2012 version (and earlier) depending on the consequences of failure and the relative cost of safe design. These values are reproduced in Table 2-2 for reference, where β_n=3.1 is suggested as the minimum limit for ultimate limit state design. The joint committee on structural safety (JCSS) has developed a probabilistic model code [164] and suggested some tentative target reliabilities for the ultimate limit state related to a one-year reference period based on monetary optimisation, which, similar to ISO recommendations, depends on the relative cost of safety

measures and the consequence class of structure for structural failure both expressed in terms of the initial construction cost. For Class 2 structures (e.g. low-rise buildings and small industrial facilities), the recommended annual reliability index (β_1) is 3.7 ($\approx$2.55 lifetime) and 4.2 ($\approx$3.3 lifetime) for moderate and small relative costs of safety measures, respectively. The latter coincides with the prescribed value for Class 3 (e.g. mid-rise) buildings with moderate relative safety measure costs.

Table 2-2: Recommendation for lifetime target reliability index in ISO 2394-2012 [171]

Relative cost of safety measure	Consequences of failure			
	small	some	moderate	great
High	0	1.5	2.3	3.1
Moderate	1.3	2.3	3.1	3.8
Low	2.3	3.1	3.8	4.3

As far as the reliability requirements and the probabilistic-based design of cold-formed steel structures are concerned, one may refer to the commentary on AISI S100 [15] and AS/NZS4600 [16], which is established upon the seminal work of Ellingwood et al. [168] on the development of a reliability-based load criterion for American national standards including steel, concrete, timber and masonry construction. They provided the frequency associated with each gravity loading scenario and suggested a lifetime target reliability index of 3.0 for steel members (4.5 for connections) under gravity loading, which is in line with ASCE and ISO recommendations and has been adopted in AISC360 [172] and AS/NZS4100 [173] for hot-rolled steel members. Some reduced limits were also suggested for extreme events, e.g. 2.5 for wind and 1.75 for earthquakes. A relatively lower reliability index under ultimate gravity loading, 2.5 for members and 3.5 for connections, has been advised in AISI S100 and AS/NZS4600 for cold-formed steel members, which serves as the minimum requirement for reliability index over practical ranges of design cases.

2.7   GENESIS OF THE RESEARCH PROBLEM

As outlined above, a detailed investigation of local and distortional buckling and their potential interactions in built-up sections is essential for the safe design and application of this new generation of cold-formed steel sections in low- to mid-rise construction. The direct strength method also serves as the most suitable option for the design of these members due to its implicit simplicity and direct applicability to complex geometries. However, its applicability to built-up members and the need for a simple analytical tool to calculate critical elastic buckling stresses is a vital subject for further investigation. Therefore, this study is concerned with a comprehensive numerical and experimental investigation of sectional buckling in built-up CFS compression members. The reliability of the current DSM design equations for these members is assessed, and appropriate adjustments are proposed to satisfy the expected reliability requirements. In this research, a novel application of the compound strip method, as an extension of the semi-analytical finite strip method, to the elastic stability analysis of built-up members with discrete fasteners is also established to determine the critical buckling stresses of built-up sections as a DSM prerequisite. This study forms a major component of a project sponsored by the Australian Research Council on the broader topic of built-up cold-formed steel structures.

Chapter 3   ELASTIC BUCKLING ANALYSIS OF BUILT-UP SECTIONS WITH DISCRETE FASTENERS

3.1   INTRODUCTION

Cold-formed steel built-up sections are generally connected using fasteners such as screws, bolts and clinches. The presence of discrete fasteners influences the overall behaviour of the members and changes the encountered buckling modes and corresponding loads. A reliable application of these members requires an efficient analysis tool that can accurately incorporate the effects of discrete fasteners. Hence, in this study, the Compound Strip Method (CSM) is employed for the buckling analysis of built-up members, and discrete fasteners are modelled as connecting elements with adjustable stiffness properties. A simple yet accurate framework is presented for the reliable analysis of built-up sections with any desired cross-sectional composition and fastener configuration. The framework provides a useful numerical tool that expedites extensive parametric studies and can be used for the structural design of built-up sections. In Section 3.2, the semi-analytical finite strip method is briefly reviewed, and then the formulation of the connection element with the essential procedure for its inclusion in the finite strip formulation is illustrated in detail. A series of numerical examples are presented in Section 3.3 to show the accuracy and versatility of the CSM for the elastic buckling analysis of various built-up CFS sections, and the outcomes are summarised in Section 3.4.

3.2   NUMERICAL METHOD AND FORMULATION

The basic concept and methodology of the utilised technique for modelling discrete fasteners are briefly outlined in this section. The numerical method employed in this study is based on the compound strip method for plates [136], which is an extension of the semi-analytical FSM (S-a FSM) and was developed to model structures with support and connecting elements [139,

174]. In the following, the basics of S-a FSM are briefly reviewed, and subsequently, the assembly process that incorporates the fastener elements in the finite strip formulation is explained in detail.

3.2.1   Finite strip method

In the finite strip analysis of folded plates, component plates of the section are discretised using longitudinal strips, as shown in Figure 3-1. Polynomial shape functions are adopted in the transverse direction, while trigonometric functions are utilised in the longitudinal direction.
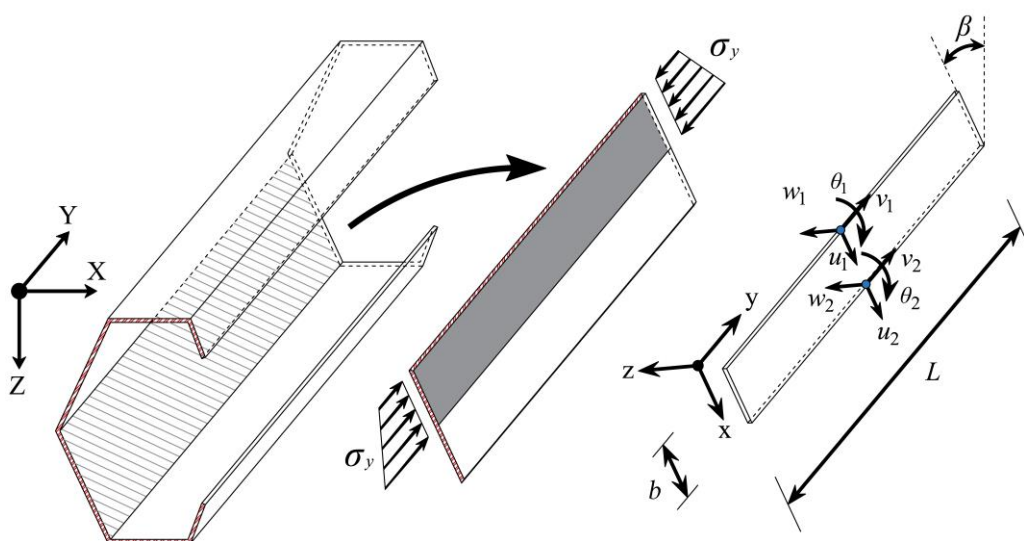
Figure 3-1: Adopted local and global coordinate systems and nodal degrees of freedom of a strip

For a typical flat finite strip, as shown in Figure 3-1, the displacement function at an arbitrary point (x, y) located on the mid-surface of the strip can be expressed as follows

$$\mathbf{u}(x, y) = \begin{Bmatrix} u(x, y) \\ v(x, y) \\ w(x, y) \end{Bmatrix} = \sum_{m=1}^{M} \mathbf{N}(x) Y_m(y) \mathbf{d}^m, \tag{3.1}$$

where $\mathbf{d}^m = \{u_1^m, v_1^m, w_1^m, \theta_1^m, u_2^m, v_2^m, w_2^m, \theta_2^m\}^{\mathrm{T}}$ is the nodal displacement vector corresponding to the m-th harmonic, M is the maximum number of harmonic terms employed in the analysis, Y_m is the shape function in the longitudinal direction that satisfies the end boundary conditions, which for common plate problems can be expressed as [175],

$$Y_m(y) = \begin{cases} \sin\left(\dfrac{\lambda_m y}{b}\right) & \text{Both ends simply supported (S-S)} \\ \sin\left(\dfrac{\lambda_m y}{b}\right)\sin\left(\dfrac{y}{b}\right) & \text{Both ends clamped (C-C)} \end{cases}, \quad \text{where} \quad \lambda_m = m\pi \quad (3.2)$$

where b is the strip width, as defined in Figure 3-1. Moreover, $\mathbf{N}(x)$ is a matrix of transverse shape functions given as

$$\mathbf{N}(x) = \begin{bmatrix} N_1 & 0 & 0 & 0 & N_2 & 0 & 0 & 0 \\ 0 & N_1 & 0 & 0 & 0 & N_2 & 0 & 0 \\ 0 & 0 & N_3 & N_4 & 0 & 0 & N_5 & N_6 \end{bmatrix}, \quad (3.3)$$

in which

$$\begin{aligned} N_1 &= 1-\bar{x}, & N_2 &= \bar{x}, \\ N_3 &= 1-3\bar{x}^2+2\bar{x}^3, & N_4 &= x\left(1-2\bar{x}+\bar{x}^2\right), & \text{where} \quad \bar{x} &= \frac{x}{b}. \\ N_5 &= 3\bar{x}^2-2\bar{x}^3, & N_6 &= x\left(\bar{x}^2-\bar{x}\right), \end{aligned} \quad (3.4)$$

By utilising the adopted displacement functions, the stiffness and stability matrices can be derived per the conventional finite strip method [118]. Following these, the elastic buckling problem can be solved as an eigenvalue problem of the following form:

$$\left(\mathbf{K} - \lambda_i\,\mathbf{K_G}\right)\boldsymbol{\varphi}_i = \mathbf{0}, \quad (3.5)$$

where $\mathbf{K}$ and $\mathbf{K_G}$ are respectively the stiffness matrix and the stability matrix of the structure, the eigenvalue λ_i is the buckling load for mode i, and the eigenvector $\boldsymbol{\varphi}_i$ is the associated buckling mode of the structure.

3.2.2   Connection element properties

This section presents a general connection element with adjustable stiffness for modelling discrete fasteners in the finite strip formulation. A three-dimensional (3D) connection element is developed by adopting linear beam theory independently in two perpendicular planes. The presented formulation is such that it can incorporate Euler-Bernoulli or Timoshenko's beam elements in the modelling by selecting corresponding stiffness constants.

<center>(a)   (b)</center>
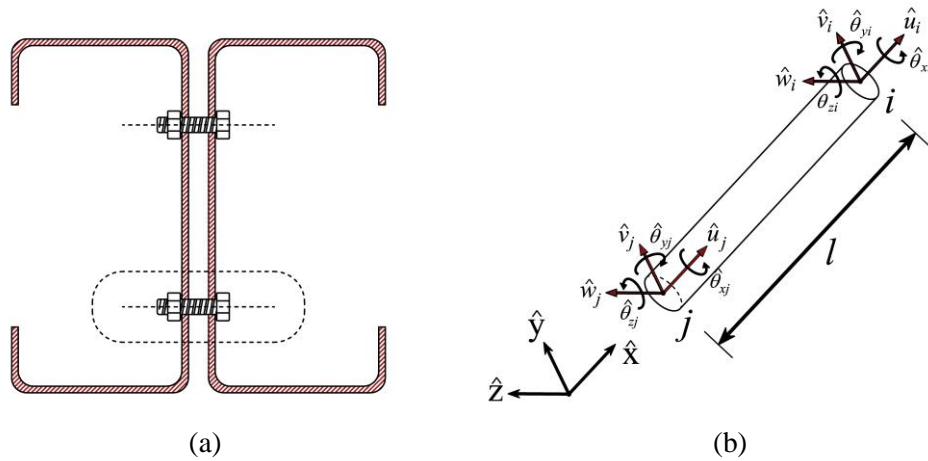
Figure 3-2: (a) Schematic view of a fastener in a built-up section, (b) local coordinates and degrees of freedom of an arbitrarily oriented connection element

The considered 3D connection element, as shown in Figure 3-2, has three translational $(\hat{u}, \hat{v}, \hat{w})$ and three rotational $(\hat{\theta}_x, \hat{\theta}_y, \hat{\theta}_z)$ DOFs at each node, where $\hat{x}$ is the direction of the longitudinal axis of the connection element. In this study, the flexural behaviour of the element is assumed to be uncoupled in perpendicular planes, where the individual flexural behaviour is described by representative shear (k_s) and rotational (k_b) stiffness. In addition, the longitudinal behaviour of the element is represented by axial (k_a) and torsional (k_t) stiffness, see Figure 3-3.

<center>(a)   (b)   (c)</center>
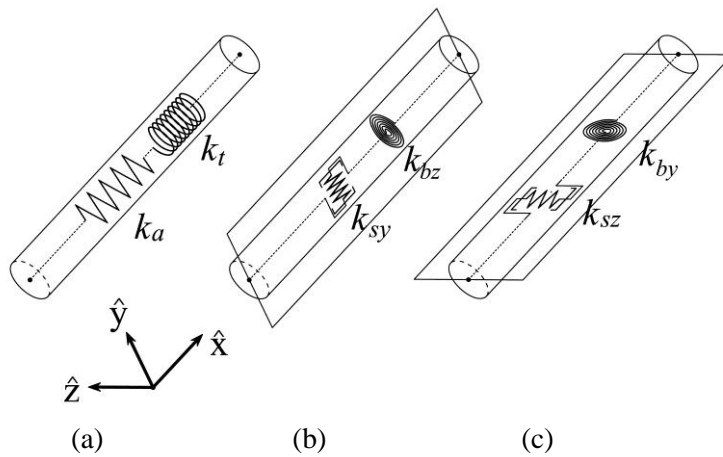
Figure 3-3: Three-dimensional connection element (a) axial and torsional springs, (b) shear and rotational springs in $\hat{x}$-$\hat{y}$ plane, and (c) shear and rotational springs in $\hat{x}$-$\hat{z}$ plane

In the local coordinate system of the element, the relation between the nodal force and nodal displacement vectors is given by

$$\left\{ \begin{array}{c} \hat{\mathbf{F}}_i \\ \hat{\mathbf{F}}_j \end{array} \right\} = \left[\begin{array}{cc} \bar{\mathbf{K}}_{ii} & \bar{\mathbf{K}}_{ij} \\ \bar{\mathbf{K}}_{ji} & \bar{\mathbf{K}}_{jj} \end{array} \right] \left\{ \begin{array}{c} \hat{\boldsymbol{\delta}}_i \\ \hat{\boldsymbol{\delta}}_j \end{array} \right\} = \bar{\mathbf{K}}_{\mathrm{c}} \, \hat{\boldsymbol{\delta}}, \tag{3.6}$$

where $\hat{\mathbf{F}}_{\mu} = \left\{ \hat{F}_{x\mu}, \hat{F}_{y\mu}, \hat{F}_{z\mu}, \hat{M}_{x\mu}, \hat{M}_{y\mu}, \hat{M}_{z\mu} \right\}^{\mathrm{T}}$, $\hat{\boldsymbol{\delta}}_{\mu} = \left\{ \hat{u}_{\mu}, \hat{v}_{\mu}, \hat{w}_{\mu}, \hat{\theta}_{x\mu}, \hat{\theta}_{y\mu}, \hat{\theta}_{z\mu} \right\}^{\mathrm{T}}$ ($\mu = i, j$), and $\bar{\mathbf{K}}_{\mathrm{c}}$ is the stiffness matrix of the connection element in its local coordinate system. By utilising a general set of slope-deflection equations [176] with the rigid-end assumption, sub-matrices of the stiffness matrix can be expressed in terms of the stiffness constants (see Figure 3-3) as follows

$$\bar{\mathbf{K}}_{ii} = \begin{bmatrix} k_a & 0 & 0 & 0 & 0 & 0 \\ 0 & k_{sy} & 0 & 0 & 0 & k_{sy}\left(\dfrac{L}{2}\right) \\ 0 & 0 & k_{sz} & 0 & -k_{sz}\left(\dfrac{L}{2}\right) & 0 \\ 0 & 0 & 0 & k_t & 0 & 0 \\ 0 & 0 & -k_{sz}\left(\dfrac{L}{2}\right) & 0 & k_{bz} + k_{sy}\left(\dfrac{L}{2}\right)^2 & 0 \\ 0 & k_{sy}\left(\dfrac{L}{2}\right) & 0 & 0 & 0 & k_{by} + k_{sz}\left(\dfrac{L}{2}\right)^2 \end{bmatrix}, \tag{3.7}$$

$$\bar{\mathbf{K}}_{jj} = \begin{bmatrix} k_a & 0 & 0 & 0 & 0 & 0 \\ 0 & k_{sy} & 0 & 0 & 0 & -k_{sy}\left(\dfrac{L}{2}\right) \\ 0 & 0 & k_{sz} & 0 & k_{sz}\left(\dfrac{L}{2}\right) & 0 \\ 0 & 0 & 0 & k_t & 0 & 0 \\ 0 & 0 & k_{sz}\left(\dfrac{L}{2}\right) & 0 & k_{bz} + k_{sy}\left(\dfrac{L}{2}\right)^2 & 0 \\ 0 & -k_{sy}\left(\dfrac{L}{2}\right) & 0 & 0 & 0 & k_{by} + k_{sz}\left(\dfrac{L}{2}\right)^2 \end{bmatrix}, \tag{3.8}$$

$$\bar{\mathbf{K}}_{ij} = \begin{bmatrix} -k_a & 0 & 0 & 0 & 0 & 0 \\ 0 & -k_{sy} & 0 & 0 & 0 & k_{sy}\left(\dfrac{L}{2}\right) \\ 0 & 0 & -k_{sz} & 0 & -k_{sz}\left(\dfrac{L}{2}\right) & 0 \\ 0 & 0 & 0 & -k_t & 0 & 0 \\ 0 & 0 & k_{sz}\left(\dfrac{L}{2}\right) & 0 & -k_{bz}+k_{sy}\left(\dfrac{L}{2}\right)^2 & 0 \\ 0 & -k_{sy}\left(\dfrac{L}{2}\right) & 0 & 0 & 0 & -k_{by}+k_{sz}\left(\dfrac{L}{2}\right)^2 \end{bmatrix}, \qquad (3.9)$$

while $\bar{\mathbf{K}}_{ji} = \bar{\mathbf{K}}_{ij}$ due to symmetry. The stiffness constants in Eqs. (3.7) to (3.9) can be calibrated from the results of experiments for determining the axial, torsional and flexural stiffness of the fasteners. These constants can be assumed alternatively according to the conventional beam theories, *viz*

$$k_a = \frac{EA}{L}, \; k_t = \frac{GJ}{L}, \; k_{by} = \frac{EI_y}{L}, \; k_{bz} = \frac{EI_z}{L}, \; k_{sy} = \frac{12EI_z}{(1+\Gamma)L^3}, \; k_{sz} = \frac{12EI_y}{(1+\Gamma)L^3}, \qquad (3.10)$$

in which Γ is the dimensionless shear parameter that is obtained from

$$\Gamma = \begin{cases} 0 & \text{Euler-Bernoulli Beam Theory} \\ \dfrac{12\left(EI/L^2\right)}{\kappa_s GA} & \text{Timoshenko Beam Theory} \end{cases} \qquad (3.11)$$

where κ_s is the shear correction factor, commonly approximated by 5/6 for rectangular sections and can be calculated for other sections with arbitrary shapes from [177].

3.2.3   *Incorporation of discrete fasteners*

In this section, the proposed connection element is incorporated in the finite strip formulation based on the concept of the compound strip method [174]. Consider two strips with parallel longitudinal axes connected with an arbitrarily oriented connection element, as shown in Figure 3-4. The total strain energy of the presented system can be expressed as the summation of the strain energy of the flat component strips and connection element(s) as follows

$$\Pi = \Pi_{S_i} + \Pi_{S_j} + \sum_{k=1}^{NC} \Pi_{C_k}, \tag{3.12}$$

in which Π_{S_μ} $(\mu = i, j)$ is the strain energy of the component strip, NC is the total number of connection elements and Π_{C_k} is the strain energy of the k-th connection element. The strain energy of a connection element in its local coordinate system $(\hat{x}, \hat{y}, \hat{z})$ is given by

$$\Pi_C = \frac{1}{2} \hat{\boldsymbol{\delta}}^{\mathrm{T}} \bar{\mathbf{K}}_{\mathbf{c}} \hat{\boldsymbol{\delta}}. \tag{3.13}$$
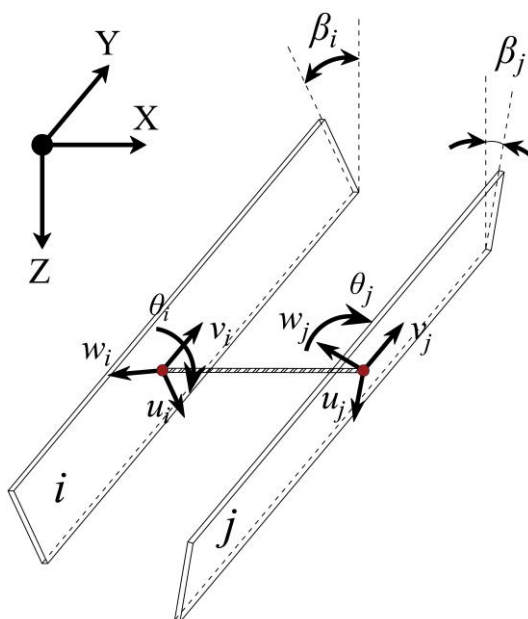
Figure 3-4: Three-dimensional model for the incorporation of connection element into associated constituent strips

In order to evaluate the strain energy, the displacements of the connection elements must be expressed in terms of the global nodal displacements of the strips [139, 142]. The first step is to transform the connection element displacements from the local coordinate to the global coordinate system, *i.e.*

$$\hat{\boldsymbol{\delta}} = \mathbf{R}\,\boldsymbol{\delta}_{\mathbf{G}}, \tag{3.14}$$

in which $\mathbf{R}$ is the transformation matrix and $\boldsymbol{\delta}_{\mathbf{G}}$ is the global displacement vector of the connection element. This transformation for a general connection element, as shown in Figure 3-2(b), is defined by the diagonal matrix, $\mathbf{R}$, as

$$\mathbf{R} = \begin{bmatrix} \hat{\mathbf{R}} & \hat{\mathbf{R}} & \hat{\mathbf{R}} & \underline{\hat{\mathbf{R}}} \end{bmatrix}, \tag{3.15}$$

where $\hat{\mathbf{R}}$ is a general rotation matrix in three dimensions that maps the local coordinate system of the connection element $(\hat{x}, \hat{y}, \hat{z})$ to the global coordinate system (X, Y, Z). This rotation matrix is constructed by the superposition of three single-axis rotations ($\mathbf{R_x}$, $\mathbf{R_y}$, and $\mathbf{R_z}$) around orthogonal axes of the local coordinate system.

It is noted that the local coordinate system of the connection element is right-handed, with the $\hat{x}$-axis being the longitudinal direction, while the adopted global system is left-handed. Thus, a reflection with respect to the X-Y plane of the element is initially performed, and then the required rotations are executed. Defining the diagonal reflection matrix $\mathbf{T_{rl}}$ and single-axis rotation tensors around the $\hat{x}$, $\hat{y}$ and $\hat{z}$ axes, as

$$\mathbf{T_{rl}} = \begin{bmatrix} 1 & 0 & 0 \\ 0 & 1 & 0 \\ 0 & 0 & -1 \end{bmatrix}, \tag{3.16}$$

$$\mathbf{R_x} = \begin{bmatrix} 1 & 0 & 0 \\ 0 & \cos\alpha & -\sin\alpha \\ 0 & \sin\alpha & \cos\alpha \end{bmatrix}, \tag{3.17}$$

$$\mathbf{R_y} = \begin{bmatrix} \cos\gamma & 0 & \sin\gamma \\ 0 & 1 & 0 \\ -\sin\gamma & 0 & \cos\gamma \end{bmatrix}, \tag{3.18}$$

$$\mathbf{R_z} = \begin{bmatrix} \cos\theta & -\sin\theta & 0 \\ \sin\theta & \cos\theta & 0 \\ 0 & 0 & 1 \end{bmatrix}, \tag{3.19}$$

The resultant transformation matrix can be obtained as follows,

$$\hat{\mathbf{R}} = \mathbf{T_{rl}}\mathbf{R_z}\mathbf{R_y}\mathbf{R_x} = \begin{bmatrix} \cos\gamma\cos\theta & -\cos\alpha\sin\theta + \sin\alpha\sin\gamma\cos\theta & \sin\alpha\sin\theta + \cos\alpha\sin\gamma\cos\theta \\ \cos\gamma\sin\theta & \cos\alpha\cos\theta + \sin\alpha\sin\gamma\sin\theta & -\sin\alpha\cos\theta + \cos\alpha\sin\gamma\sin\theta \\ \sin\gamma & -\sin\alpha\cos\gamma & -\cos\alpha\cos\gamma \end{bmatrix}, \tag{3.20}$$

where the angles α, γ, and θ are the required rotations around the local axes $\hat{x}$, $\hat{y}$ and $\hat{z}$, respectively, to construct the rotational mapping. The resultant displacements in the global

coordinate system are then transformed into local strip coordinates. Assuming that the connected strips are orientated at an angle of β_μ ($\mu = i, j$) from the z-axis, the transformation of nodal displacements to the local coordinate of the corresponding strip is defined as

$$\boldsymbol{\delta}_{\mathrm{G}} = \begin{bmatrix} \mathbf{TR}_i & \\ & \mathbf{TR}_j \end{bmatrix} \begin{Bmatrix} \boldsymbol{\delta}_i \\ \boldsymbol{\delta}_j \end{Bmatrix} = \mathbf{R}_{\mathrm{GL}}\, \boldsymbol{\delta}, \tag{3.21}$$

where $\boldsymbol{\delta}_\mu$ ($\mu = i, j$) is the displacement vector of the node μ in the local coordinate system of the corresponding strip and $\mathbf{TR}_\mu$ ($\mu = i, j$) is given as

$$\mathbf{TR}_\mu = \begin{bmatrix} \cos\beta_\mu & 0 & \sin\beta_\mu & & & \\ 0 & 1 & 0 & & & \\ -\sin\beta_\mu & 0 & \cos\beta_\mu & & & \\ & & & \cos\beta_\mu & 0 & \sin\beta_\mu \\ & & & 0 & 1 & 0 \\ & & & -\sin\beta_\mu & 0 & \cos\beta_\mu \end{bmatrix}. \tag{3.22}$$

The final step is to interpolate the connection element displacements in terms of the displacement field of the strips (see Figure 3-4) and then transform the obtained components into the global coordinate system. To this end, the interpolation matrix is expressed as

$$\boldsymbol{\delta} = \begin{Bmatrix} \boldsymbol{\delta}_i \\ \boldsymbol{\delta}_j \end{Bmatrix} = \begin{bmatrix} \boldsymbol{\psi}_i^m & \\ & \boldsymbol{\psi}_j^m \end{bmatrix} \begin{Bmatrix} \mathbf{d}_i^m \\ \mathbf{d}_j^m \end{Bmatrix} = \boldsymbol{\Psi}^m\, \mathbf{d}^m, \tag{3.23}$$

in which

$$\boldsymbol{\psi}_\mu^m = \begin{bmatrix} N_1^\mu Y_m^\mu & & & & & & & & \left(N_1^\mu\right)' Y_m^\mu \\ & N_1^\mu \left(L/\lambda_m\right)\left(Y_m^\mu\right)' & & & & & & \\ & & N_3^\mu Y_m^\mu & N_3^\mu \left(Y_m^\mu\right)' & \left(N_3^\mu\right)' Y_m^\mu & & & \\ & & N_4^\mu Y_m^\mu & N_4^\mu \left(Y_m^\mu\right)' & \left(N_4^\mu\right)' Y_m^\mu & & & \\ N_2^\mu Y_m^\mu & & & & & & & \left(N_2^\mu\right)' Y_m^\mu \\ & N_2^\mu \left(L/\lambda_m\right)\left(Y_m^\mu\right)' & & & & & & \\ & & N_5^\mu Y_m^\mu & N_5^\mu \left(Y_m^\mu\right)' & \left(N_5^\mu\right)' Y_m^\mu & & & \\ & & N_6^\mu Y_m^\mu & N_6^\mu \left(Y_m^\mu\right)' & \left(N_6^\mu\right)' Y_m^\mu & & & \end{bmatrix}^{\mathrm{T}}, \tag{3.24}$$

where $N_r^\mu = N_r(x_\mu)$, $Y_m^\mu = Y_m(y_\mu)$, and the prime sign denotes differentiation with respect to the corresponding variable x or y. Moreover, λ_m is a parameter to be determined according to the end boundary conditions, which is $m\pi$ for simply-supported and fixed end boundary conditions as defined in Eq. (3.2), and (x_μ, y_μ) indicates the location of the connection element in the local coordinates of the strip μ ($\mu = i, j$). Since the plate elements are assumed to be infinitely stiff against torsion in the normal direction, the drilling rotation ($\theta_{z\mu}$) is not incorporated as an active DOF. Thus, in the interpolation matrix in Eq. (3.23), the components of the matrix associated with this DOF are set to zero. The consequence of this assumption is that the torsional stiffness of the element is not considered for a connection element perpendicular to the strip. In other cases, where the connection element is not perpendicular to the strip, the torsional stiffness of the connection element contributes to the strip stiffness matrix. Lastly, the interpolated displacements are transformed into the global coordinate system as follows

$$\mathbf{d}^m = \mathbf{R}_{\mathbf{LG}}\, \boldsymbol{\Delta}^m = \left(\mathbf{R}_{\mathbf{GL}}\right)^{\mathrm{T}} \boldsymbol{\Delta}^m, \tag{3.25}$$

where $\boldsymbol{\Delta}^m = \left\{U_1^m, V_1^m, W_1^m, \Theta_1^m, U_2^m, V_2^m, W_2^m, \Theta_2^m\right\}^{\mathrm{T}}$ is the global displacement vector of the strip. The strain energy of a connection element can be expressed by the following equation in terms of the global displacements

$$\Pi_C = \frac{1}{2}\sum_{n=1}^{M}\sum_{m=1}^{M} \left(\boldsymbol{\Delta}^n\right)^{\mathrm{T}} \mathbf{K}_{\mathrm{c}}^{nm} \boldsymbol{\Delta}^m, \tag{3.26}$$

where $\mathbf{K}_{\mathrm{c}}^{nm}$ is the stiffness matrix of the connection element in global coordinates, which is derived by utilising Eqs. (3.14) to (3.25) and simple mathematical manipulations as

$$\mathbf{K}_{\mathrm{c}}^{nm} = \mathbf{R}_{\mathbf{GL}} \left(\boldsymbol{\Psi}^n\right)^{\mathrm{T}} \left(\mathbf{R}_{\mathbf{GL}}\right)^{\mathrm{T}} \mathbf{R}^{\mathrm{T}} \bar{\mathbf{K}}_{\mathbf{c}} \, \mathbf{R} \, \mathbf{R}_{\mathbf{GL}} \, \boldsymbol{\Psi}^m \left(\mathbf{R}_{\mathbf{GL}}\right)^{\mathrm{T}}. \tag{3.27}$$

This stiffness matrix is then added to the total stiffness matrix of the system ($\mathbf{K}$) in global coordinates for the elastic buckling analysis per Eq. (3.5). It is noteworthy that the geometric effects of the fasteners are expected to be relatively small since their out-of-plane stiffness is

much larger than the stiffness of the strips. Therefore, the contribution of the fasteners to the global stability matrix of the system ($\mathbf{K_G}$) is neglected in this study.

3.3   NUMERICAL EXAMPLES

A series of numerical examples are presented in this section to show the robustness and applicability of the introduced compound strip method to the elastic buckling analysis of various built-up cold-formed steel sections with discrete fasteners. In the following, details of the compound strip models are explained, and subsequently, the results of the proposed method for various built-up assemblies are verified against finite element (FE) simulations obtained using ABAQUS software.

3.3.1   Details of the compound strip model

For the analysis of built-up sections in the literature, four distinctive levels of composite actions are generally assumed, see Figure 3-5.
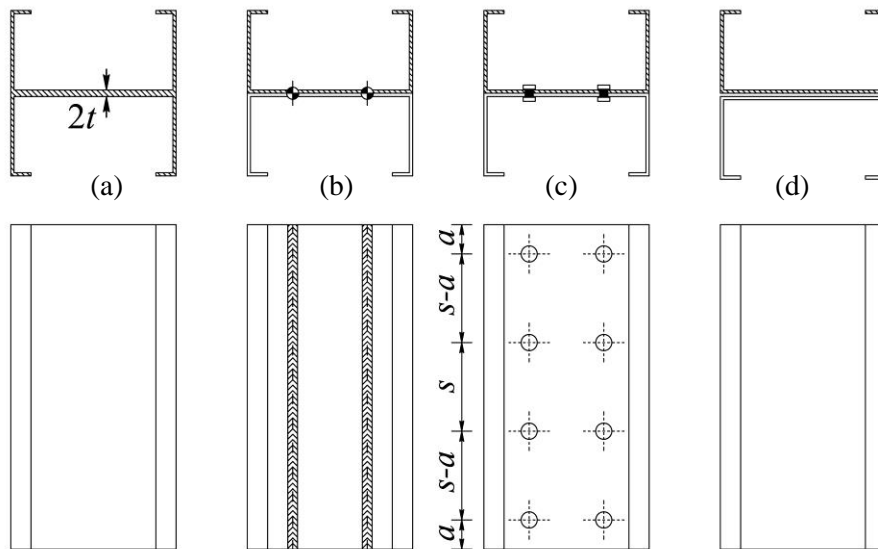
Figure 3-5: Different levels of considered composite actions: (a) fully-composite, (b) partially-composite with continuous connections, (c) partially-composite with discrete connections, (d) non-composite

The fully-composite condition (Figure 3-5(a)) implies full connection by merging the adjacent plate components of sub-sections into one flat element with the thickness equal to the

summation of the thicknesses of the elements in contact. A partially-composite state (Figure 3-5(b)) is considered by applying nodal multi-point constraints that continuously tie DOFs of the adjacent plate components over a longitudinal line at the fastener location. This study also considers an intermediate composite level (Figure 3-5(c)) by modelling discrete fasteners at arbitrary locations, representing a realistic composite state between the fully-composite and non-composite (Figure 3-5(d)) states.

3.3.2 *Details of the finite element model*

The finite element (FE) simulations are performed using Abaqus 6.14 software. As an indicative example, Figure 3-6 presents the developed FE model for a back-to-back I-section with fixed end boundary conditions. A special boundary condition enforcement is devised to replicate the boundary conditions in the FSM, details of which are given in the following.
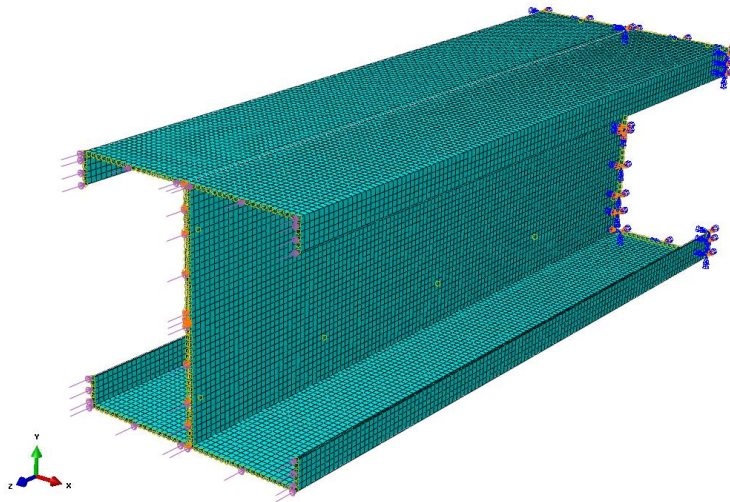
Figure 3-6: Finite element model of an I-section with fixed end boundary conditions

3.3.2.1 Enforcement of boundary conditions

The most commonly used procedures for the implementation of fixed and simply-supported end conditions (hereafter referred to as "conventional" approach) are shown in Figure 3-7(a) and Figure 3-8(a), respectively. In some previous studies, where the conventional approach was employed, a difference between the finite element and finite strip solutions was reported

[178, 179]. The difference was also observed in the preliminary investigation phase of this research, and it was explained by the fact that the conventional enforcement of end conditions in the FEA can cause stress concentrations by imposing restraints against lateral expansion due to the Poisson's effect. The imposed constraints modify the stress distribution at the ends, especially in short members, and affect mostly the local buckling stress values; however, the boundary effect becomes negligible as the span increases.

(a)

(b)
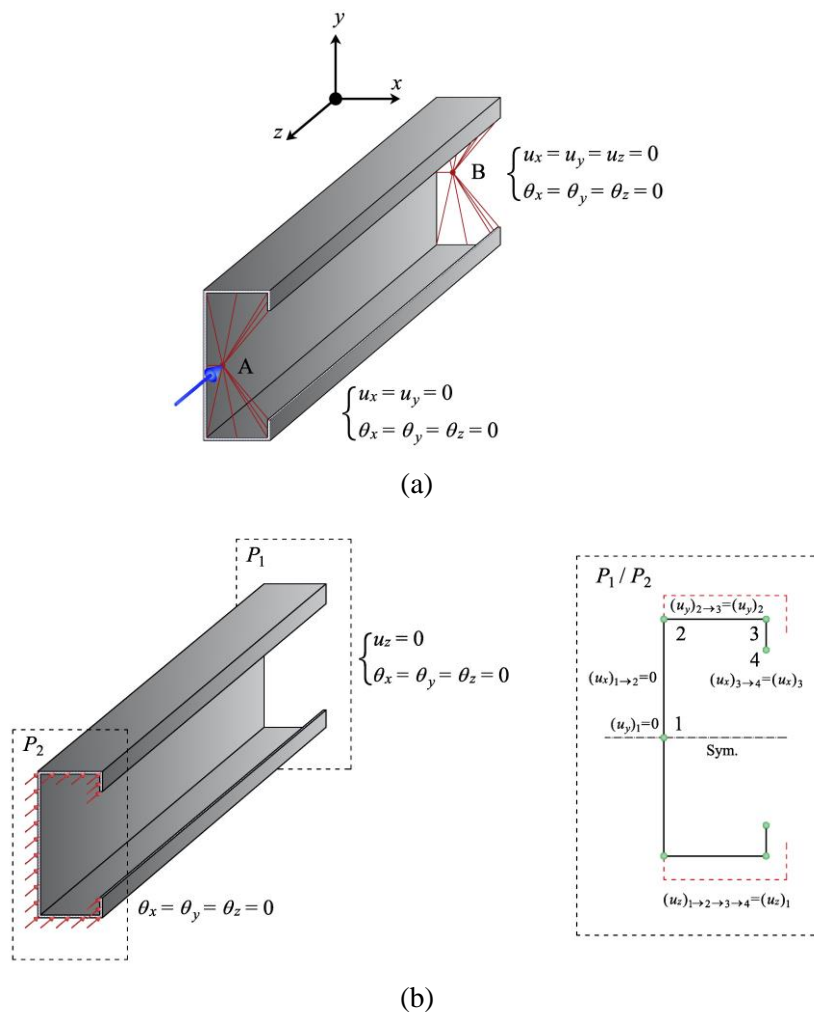
Figure 3-7: Enforcement of fixed end condition in FE simulation: (a) conventional approach, (b) modified approach for compatibility with FSM

This problem was resolved in the FE modelling by allowing free in-plane expansion of each constituent plate at the supports using Equation constraints [180], as illustrated in Figure 3-7(b) and Figure 3-8(b), which yields uniform longitudinal stress distribution throughout the length of the member, as being assumed in the FS formulation.

(a)

(b)
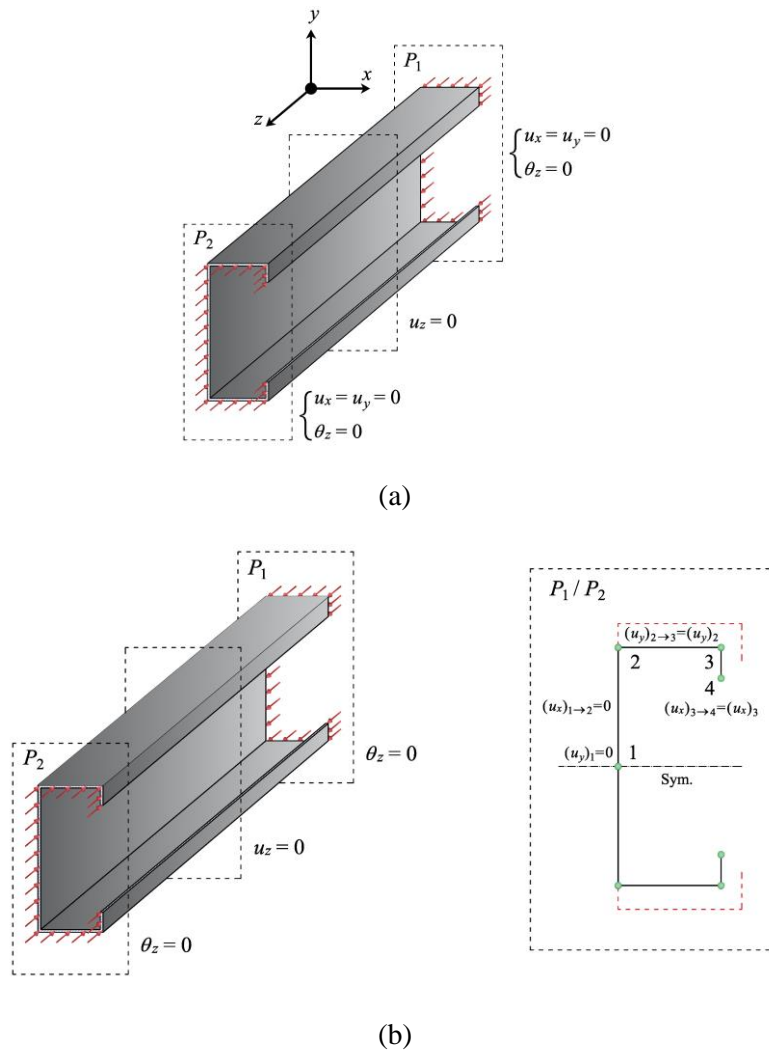
Figure 3-8: Enforcement of simply-supported end condition in FE simulation: (a) conventional approach, (b) modified approach for compatibility with FSM

3.3.2.2 Element type and mesh density

The linear shell element with reduced integration (S4R), which has three translational and three rotational degrees of freedom at each node, is assigned to plate components. A series of convergence studies were performed for the considered built-up sections with various fastener spacings to ensure that the obtained solutions are accurate and reliable. The results showed that mesh densities of 2.5 mm$\times$2.5 mm for member lengths (L) less than 1000 mm and 5 mm$\times$5 mm for longer members were adequate.

3.3.2.3 Connection element

A variety of methods are available for modelling the connectivity of built-up sections in finite element simulations. One common and practical way of modelling the connection between constituent sections of a built-up assembly in the FE simulations is coupling DOFs at the location of fasteners without introducing an element to represent the fastener. Hence, the partially-composite state with discrete connections in Figure 3-5c can be achieved in Abaqus software by utilising either discrete connection elements [180], i.e. beam or fastener element, or discrete coupling connections with tie constraints. The performance of these connection models is compared by performing several FE simulations in which the connection between the constituent sections is provided either by coupling DOFs in the location of discrete fasteners or by utilising a three-dimensional linear beam element (B31) [180] as the connection element. The obtained results and drawn conclusions are discussed later in Section 3.3.4 as the first example of a built-up section.

3.3.3   Constituent single section

In this example, the effect of mesh size and the number of longitudinal terms in the FS analysis on the elastic buckling load of a single section under compression is investigated and validated against FE solutions. Hence, a lipped channel section with the geometry shown in Figure 3-9 is analysed under uniform compression with different end boundary conditions. The assumed geometrical dimensions and material properties are reported in Table 3-1 and Table 3-2, respectively.
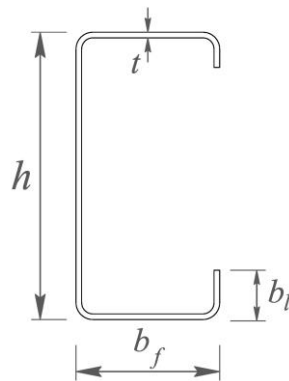
Figure 3-9: Geometry of a lipped channel section

Table 3-1: Geometric dimensions of the channel sections

Section	Dimensions (mm)			
	h	t	b_f	b_l
C1.0-100	102	1.0	51	12.5

Table 3-2: Assumed material parameters for cold-formed steel

Material	v	MPa	
		E	f_y
CFS	0.3	2.1×10^5	500

A series of convergence studies are performed according to Figure 3-10 by starting from a coarse mesh and subsequently doubling the number of strips to ensure that the adopted discretisations yield accurate and convergent solutions. For the sake of simplicity, the section is modelled using perpendicular components, implying that rounded corners are ignored. The results obtained for the convergence of the section with simply supported boundary conditions are presented in Figure 3-11 based on incorporating one longitudinal term (i.e. M=1).

Mesh 1   Mesh 2   Mesh 3   Mesh 4
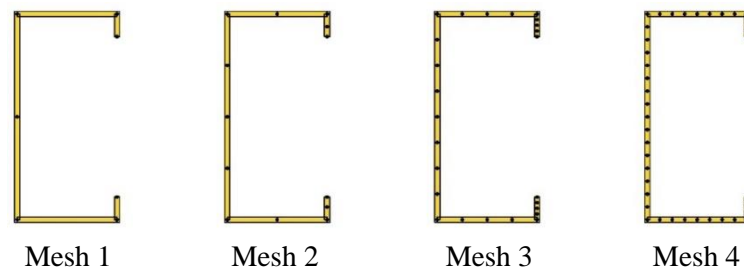
Figure 3-10: Adopted mesh discretisation for convergence study
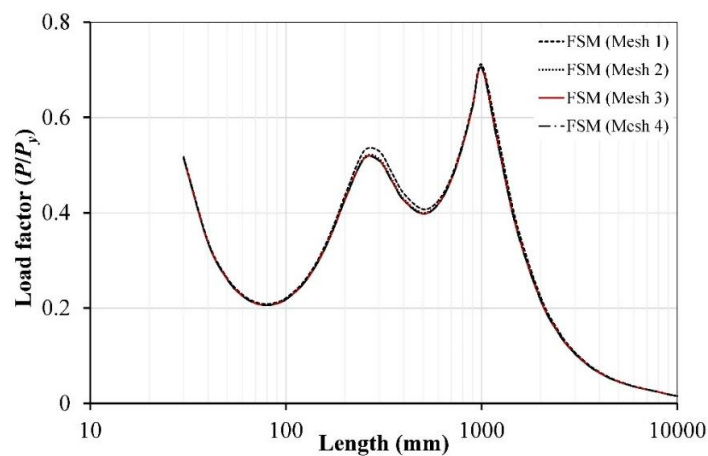
Figure 3-11: Finite strip discretisation and signature curves of a single channel section for different mesh densities under simply supported boundary conditions

As can be seen, with the refinement of discretisation in the plate components (webs, flanges, and lips), the solution converges, and further refinement of the section discretisation beyond Mesh 3 does not have a pronounced impact on the results of the buckling analysis. Moreover, a series of analyses are performed to determine the effect of the number of longitudinal terms (*M*) on the buckling load utilising the Mesh 3 discretisation (eight strips in the web and four strips per lips and flanges). The results obtained for fixed (C-C) and simply supported (S-S) end conditions are presented and compared with ABAQUS FE simulations in Figure 3-12.
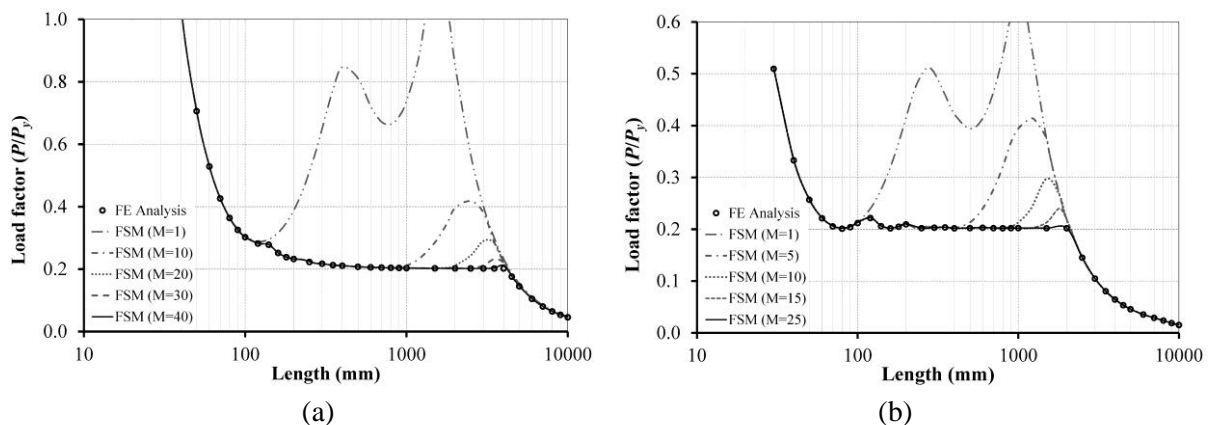
Figure 3-12: Buckling curves of the channel section for different numbers of longitudinal terms under (a) fixed and (b) simply supported boundary conditions

The results obtained for FS analysis with only one term indicate that the considered section is not prone to distortional buckling since the elastic local buckling load is substantially less than the lowest distortional buckling load. Furthermore, the figures show that the finite strip solutions converge to the FE results as the number of terms increases. For example, including 40 longitudinal terms gives satisfactory results in the C-C case, whereas a smaller number of terms (*M* = 25) is required for the S-S case. It is notable that the increase in the number of terms is more effective in the global-distortional buckling region (500 mm < *L* < 2000 mm for the S-S case and 1000 mm < *L* < 4000 mm for the C-C case) and modifies the fictitious rise in the buckling load factor in this range when adopting a small number of terms.

The last comparison is made on the mode shapes corresponding to different failure modes. Typical first mode shapes for local and global buckling of the considered single section under C-C end conditions are shown in Figure 3-13 and Figure 3-14, respectively. The obtained

modes from the compound strip analyses (with M=40) are shown to match the results of the FE simulation shown in the same figures. As expected, flexural-torsional buckling constitutes the global buckling mode of the lipped channel section.

(a)   (b)
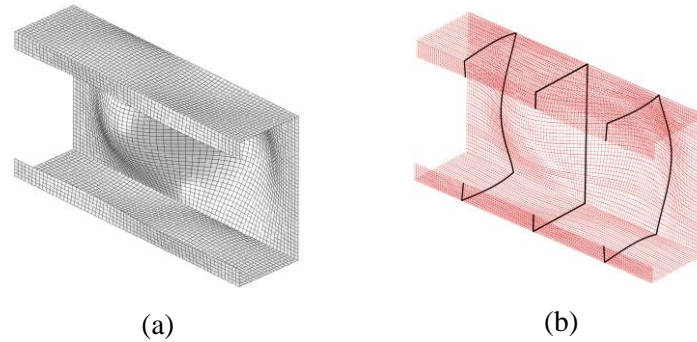
Figure 3-13: Comparison of local buckling mode shapes of the lipped channel section under C-C end boundary conditions at L = 200 mm: (a) FEM, (b) CSM

(a)   (b)
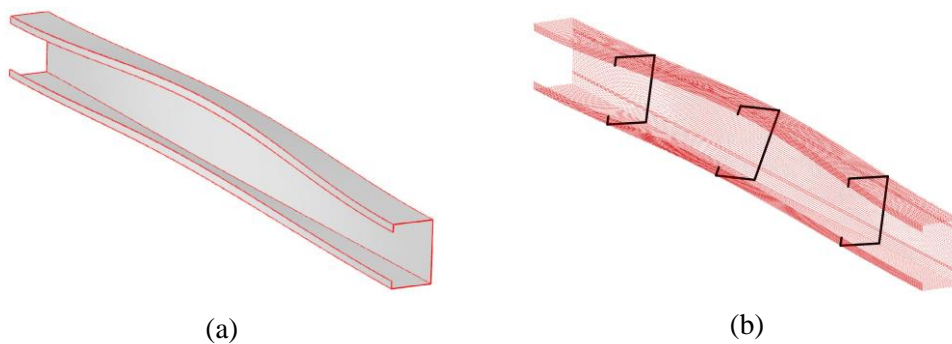
Figure 3-14: Comparison of global buckling mode shapes of the lipped channel section under C-C end boundary conditions at L = 8000 mm: (a) FEM, (b) CSM

3.3.4   Built-up I-section

In the first two examples, single-span built-up columns made of two channels are analysed for different fastener spacing ratios and end boundary conditions. First, a built-up I-section made from the back-to-back connection of two C1.0-100 channels with M4.8 fasteners is considered in this example. The geometry details of the built-up section are shown in Figure 3-15(a), and the adopted finite strip discretisation is presented in Figure 3-15(b).

(a)   (b)
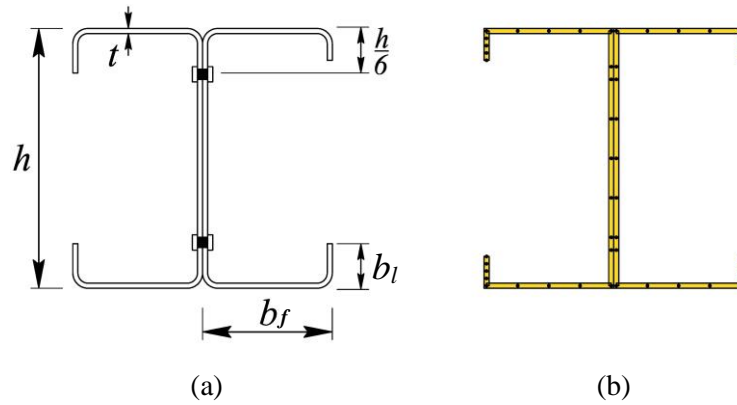
Figure 3-15: A typical built-up I-section: (a) geometry, (b) simplified finite strip discretization

Before proceeding to the FS results and discussions, the results of FE simulations of the same assembly with two different connection models as explained in Section 3.3.2.3, i.e. coupling DOFs and utilising 3D beam element, are presented in Figure 3-16 and Figure 3-17.

(a)   (b)
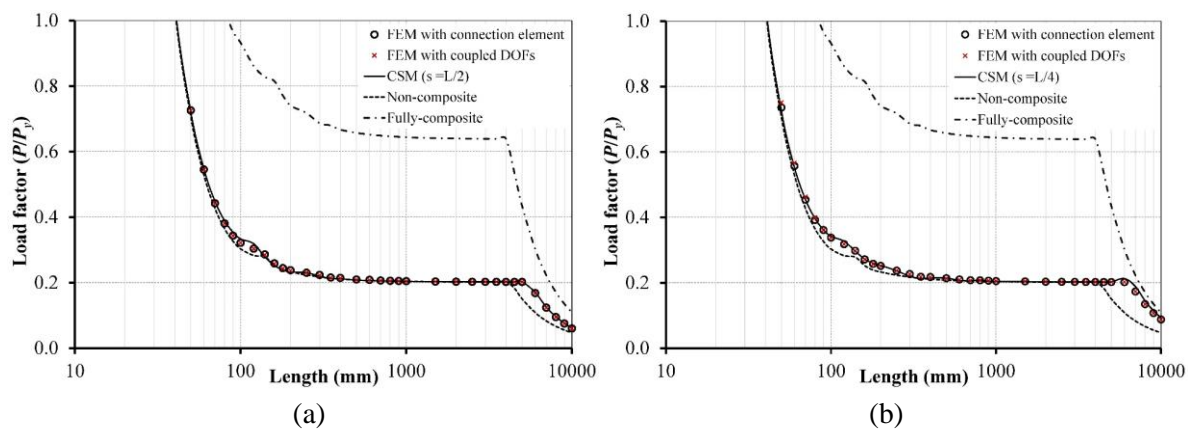
Figure 3-16: Comparison of buckling curves of the built-up I-section obtained from the finite strip and finite element simulations for fixed end conditions: (a) s = 0.5L, (b) s = 0.25L

As seen in the considered cases, the results obtained using the common type of connectivity (coupled DOFs) are almost identical to the FE solutions achieved using beam elements. Thus, only the solutions obtained using the beam element are reported in the following numerical examples, in line with the adopted approach for modelling fasteners in the CSM. The properties of a fastener with a diameter of 4.8 mm were assigned to connection elements in ABAQUS simulations and CSM analyses. Fastener spacings of s=0.5L and 0.25L were used in the analyses, corresponding to three and five equidistant fasteners along the length, respectively, including fasteners at the end cross-sections.

(a)   (b)
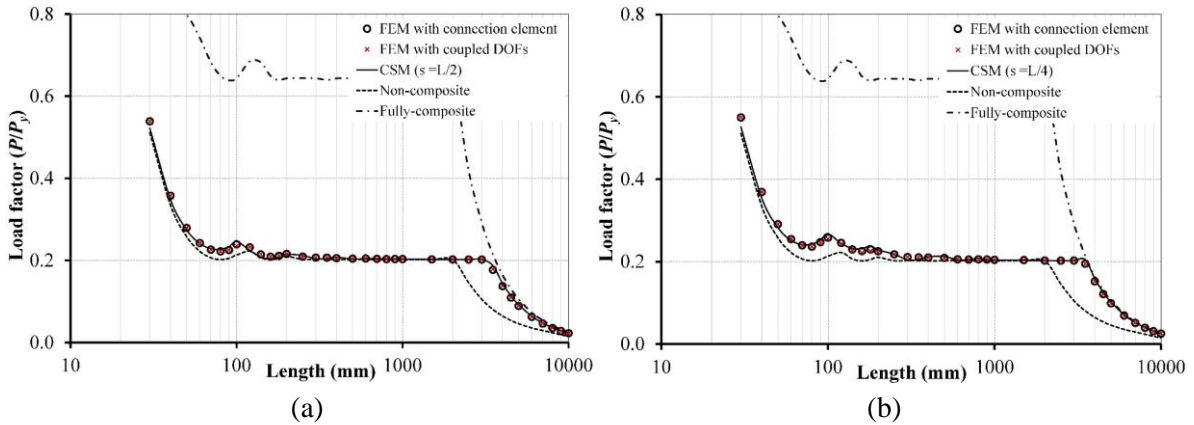
Figure 3-17: Comparison of buckling curves of the built-up I-section obtained from the finite strip and finite element simulations for simply supported end conditions and (a) $s = 0.5L$, (b) $s = 0.25L$

Utilising the proposed compound strip method, the sensitivity of the obtained buckling curves to the number of included terms is illustrated in Figure 3-18 for a fastener spacing ratio (s/L) of 0.5. Displaying a similar trend to that observed in the buckling analysis of a single section, the compound strip solutions converge to the FE results as the number of terms is increased. As expected, reasonably accurate modelling of a built-up section with discrete fasteners requires a larger number of terms in comparison with single-section analysis. According to the graphs, a good agreement between the FE and FS results is achieved by incorporating at least 60 longitudinal terms in the C-C case and 40 terms in the S-S case. The adequacy of the selected number of terms was also confirmed for various fastener spacings, i.e. $s/L = 0.25$ and 0.167, by performing a similar sensitivity analysis. Therefore, the number of included terms is set to these values in all the built-up examples presented hereafter.

(a)   (b)
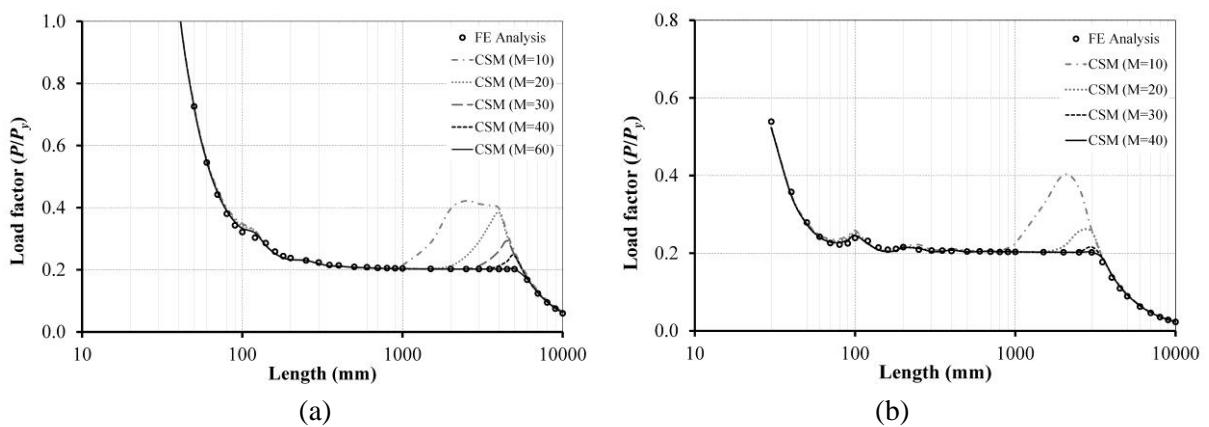
Figure 3-18: Buckling curves of built-up I-section for different numbers of longitudinal terms under (a) fixed and (b) simply supported end boundary conditions

To validate the capability of the proposed method in modelling different fastener configurations, the obtained buckling curves are compared against the FE solutions for spacing values of $L/2$ and $L/4$ inclusive of fasteners at the two ends. The results for S-S and C-C end conditions are presented in Figure 3-19 and Figure 3-20, respectively, and compared with the fully-composite and non-composite curves as the theoretical upper and lower bounds in the same figures. The results of the proposed method show reasonable agreement with the FE solutions for both cases of fastener spacing and boundary conditions. The presence of discrete fasteners in the finite strip and finite element analyses results in an intermediate-composite curve, which departs from the non-composite curve in the local and global buckling regions.

(a)   (b)
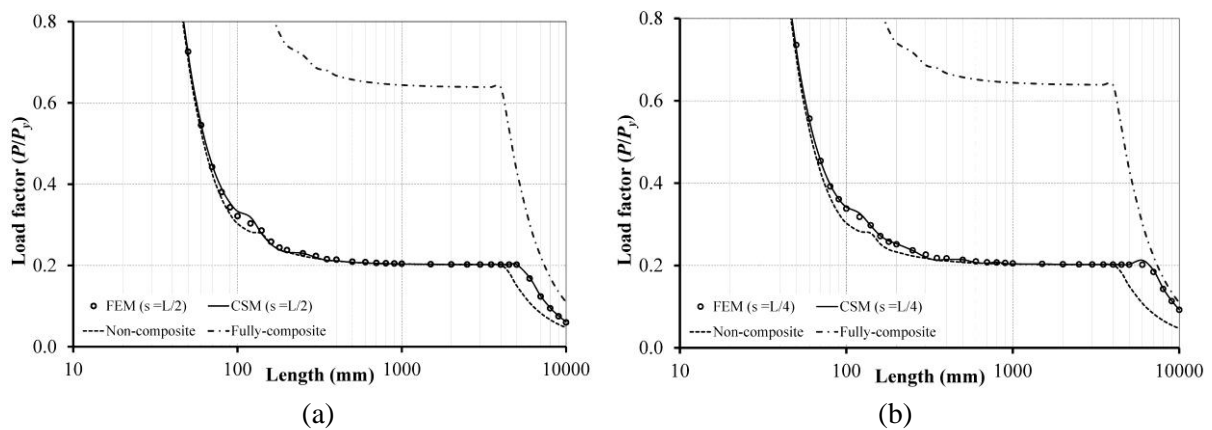
Figure 3-19: Comparison of buckling curves of the built-up I-section obtained from finite strip and finite element simulations for fixed end conditions: (a) $s = 0.5L$, (b) $s = 0.25L$

(a)   (b)
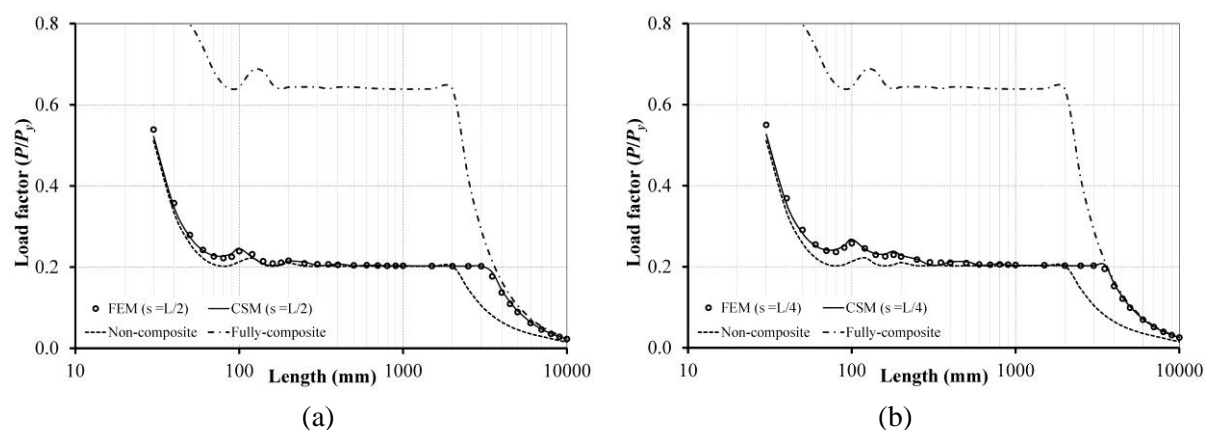
Figure 3-20: Comparison of buckling curves of the built-up I-section obtained from the finite strip and finite element simulations for simply supported end conditions and (a) $s = 0.5L$, (b) $s = 0.25L$

By decreasing the fastener spacing, a higher degree of composite behaviour is obtained, and the buckling curve shifts toward the fully-composite curve. Nevertheless, an intermediate region (500 mm $< L <$ 2000 mm for the S-S case and 500 mm $< L <$ 4000 mm for the C-C case) is observed in both spacing ratios and end boundary conditions, where the buckling curve almost follows the non-composite state suggesting that the considered fasteners are not close enough to enhance the buckling load. To further investigate the influence of fastener spacing, three cases with different spacing ratios (s/L = 0.5, 0.25 and 0.167) and an additional case with constant spacing (s = 50 mm) are adopted, and the results are compared in Figure 3-21(a) and Figure 3-22(a).

(a)   (b)
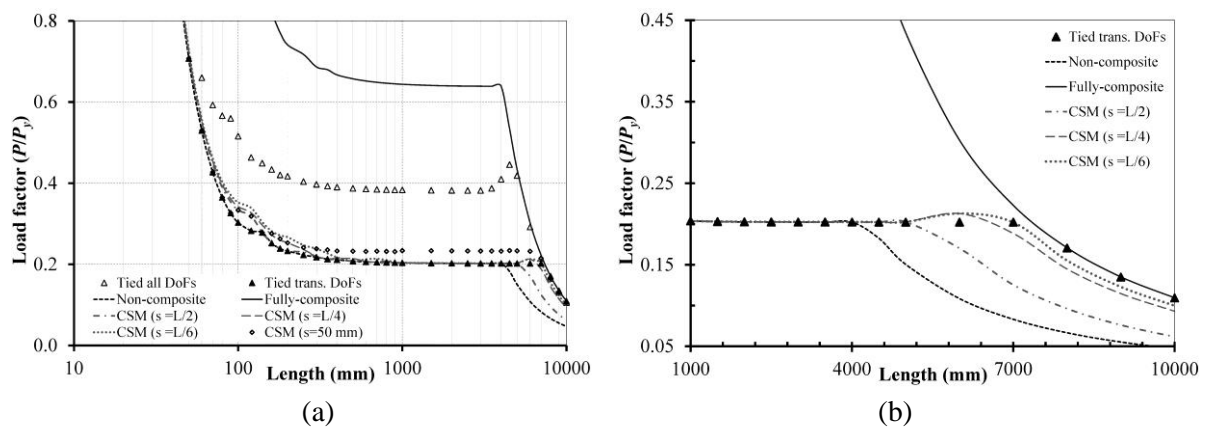
Figure 3-21: Buckling curves of the built-up I-section with fixed end conditions for different fastener spacing ratios over (a) the full range of lengths and (b) magnified global region

(a)   (b)
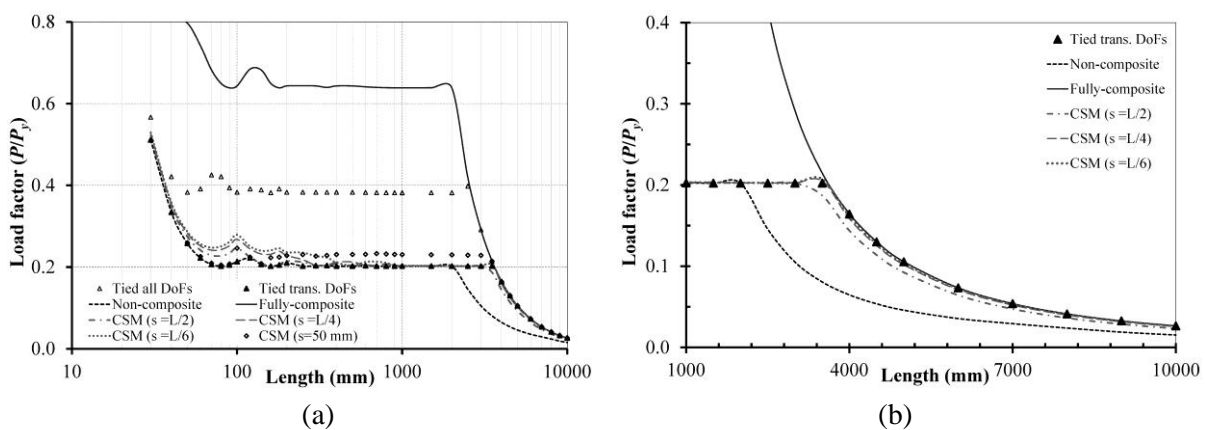
Figure 3-22: Buckling curves of the built-up I-section with simply supported end conditions for different fastener spacing ratios over (a) the full range of lengths and (b) magnified global region

In addition to the fully-composite and non-composite curves, two specific cases of the partially-composite condition are also included in the graphs. In the first case (I), only translational DOFs are tied along the nodal lines at fastener locations, whereas in the second case (II), both translational and rotational DOFs are constrained. The effect of each case on restraining the deformation of the connecting strips is illustrated schematically in Figure 3-23.
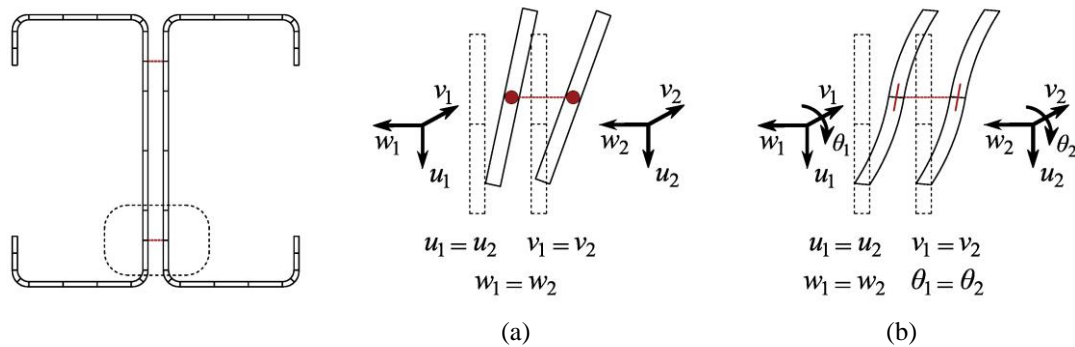
Figure 3-23: Schematic difference between two cases of partially-composite condition: (a) Case I - tied translational DOFs, (b) Case II - tied translational and rotational DOFs

Figure 3-21(a) and Figure 3-22(a) show that the results of the constraint case with only translational DOFs are not very different from a non-composite section in the local buckling region. In contrast, the inclusion of constraints on rotational DOFs results in a buckling curve between the non-composite and fully-composite curves. This curve represents the upper bound for the buckling capacity of a built-up section with discrete fasteners when the spacing tends to zero. In the global buckling region, the results of both cases are identical to those of the fully-composite section. Furthermore, the buckling curves have a transition zone from this upper bound to the non-composite curve (lower bound) that is widened the fastener spacing is reduced.

To highlight the observed trend in the global buckling region, the magnification of the results over the long span region is presented in Figure 3-21(b) and Figure 3-22(b). As can be seen, the impact of fastener spacing (s/L) is more pronounced in fixed end conditions, whereas for simply-supported boundary conditions, even introducing a fastener spacing of $s = L/2$ is sufficient to enhance the global buckling load capacity of the built-up section to almost the

fully-composite level. As a concluding remark, typical first mode shapes obtained from the compound strip analyses under C-C boundary conditions are shown in Figure 3-24 and Figure 3-25 for local and global buckling of the considered built-up section assuming fastener spacing of L/4. As can be seen, the mode shapes of FE analyses are almost identical to those of the CSM, which further validates the proposed method. Furthermore, compared with the single section, the global buckling mode shape changes from flexural-torsional buckling (Figure 3-14) to flexural buckling in the composite section (Figure 3-25).

| (a) | (b) |
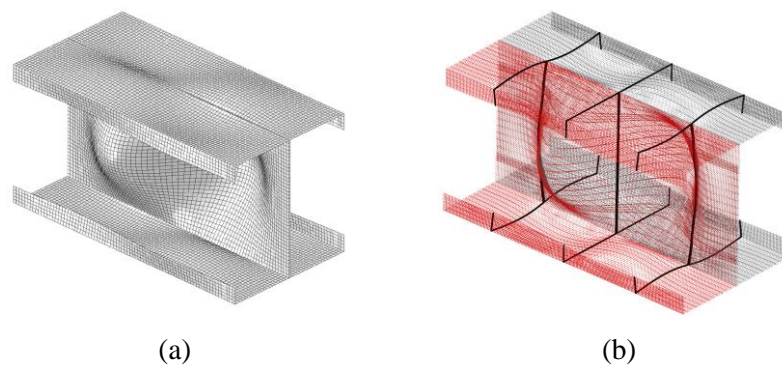
Figure 3-24: Comparison of local buckling mode shapes of the built-up I-section under C-C end boundary conditions at L = 200 mm: (a) FEM, (b) CSM

| (a) | (b) |
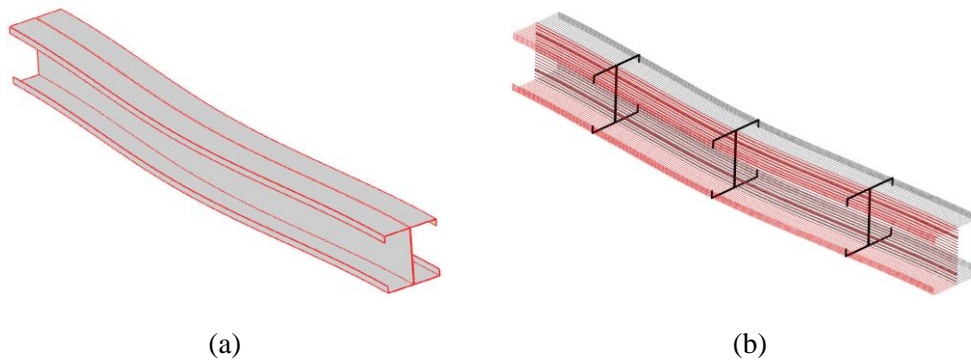
Figure 3-25: Comparison of global buckling mode shapes of the built-up I-section under C-C end boundary conditions at L = 8000 mm: (a) FEM, (b) CSM

3.3.5   Built-up box section

Next, two channel sections are connected face-to-face to make a commonly used box section, as shown in Figure 3-26(a). The same CFS material (see Table 3-1) and component sections (C1.0-100) are used, except that one of the flanges is assumed to be 2 mm longer than the other

($b_1 − b_2 = 2$ mm) to facilitate nesting of the sections. Each component plate element of the cross-section is discretised by finite strips according to Figure 3-26(b) and analysed under uniform compression with C-C and S-S end conditions. First, the buckling curves obtained for the spacing value of $L/2$ are presented in Figure 3-27, where comparisons are made with FE results. As can be seen, good agreement is obtained for both end conditions and over the entire variations of lengths.

(a)   (b)
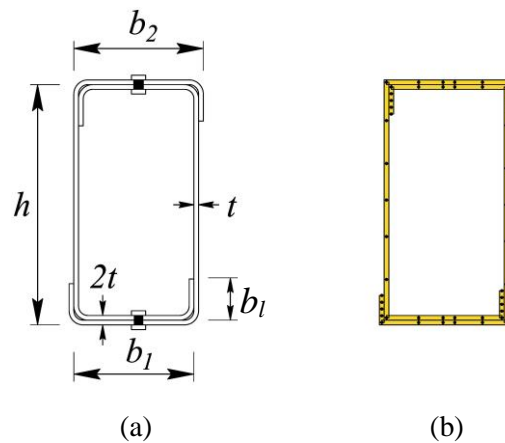
Figure 3-26: Assembly of a built-up box section: (a) geometry, (b) adopted finite strip discretisation

(a)   (b)
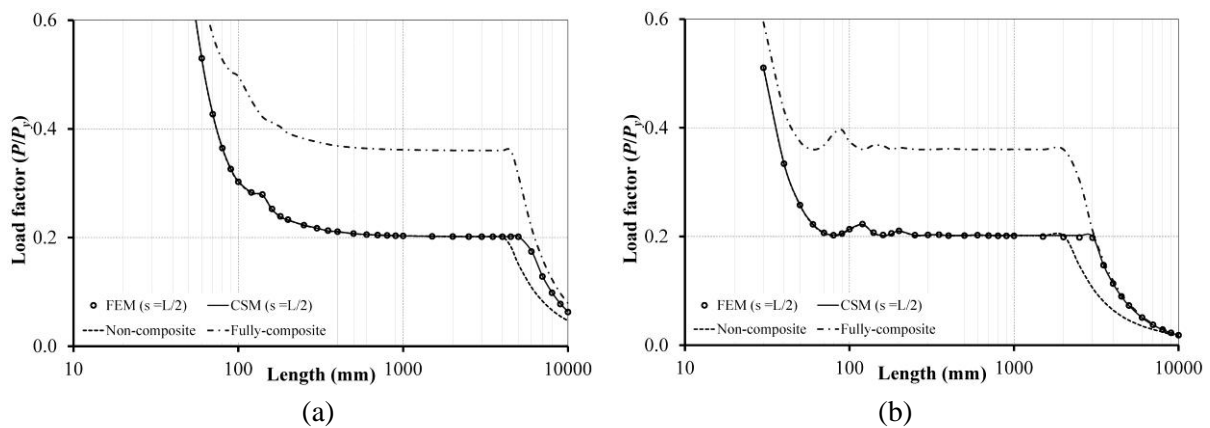
Figure 3-27: Comparison of buckling curves of the built-up box section obtained from finite strips and finite element simulations under (a) fixed and (b) simply supported boundary conditions

The obtained buckling curves for various fastener spacing ratios are presented next in Figure 3-28 and Figure 3-29 and compared with the partially-composite curves assuming continuous constraints ("Tied all DoFs", case II in Figure 3-23) as well as graphs corresponding to fully-composite and non-composite states. The results show that providing fasteners in flanges can significantly enhance the global buckling capacity of the built-up box section,

whereas the observed difference in the local buckling region is negligible. In summary, the buckling curves follow the non-composite curve in the local buckling region and tend towards the fully-composite curve in the global buckling region as the fastener spacing (s/L) is reduced. The almost non-composite behaviour of the built-up box in the local buckling region can be explained by the fact that the flange fasteners are ineffective in restraining the local buckling of the web.
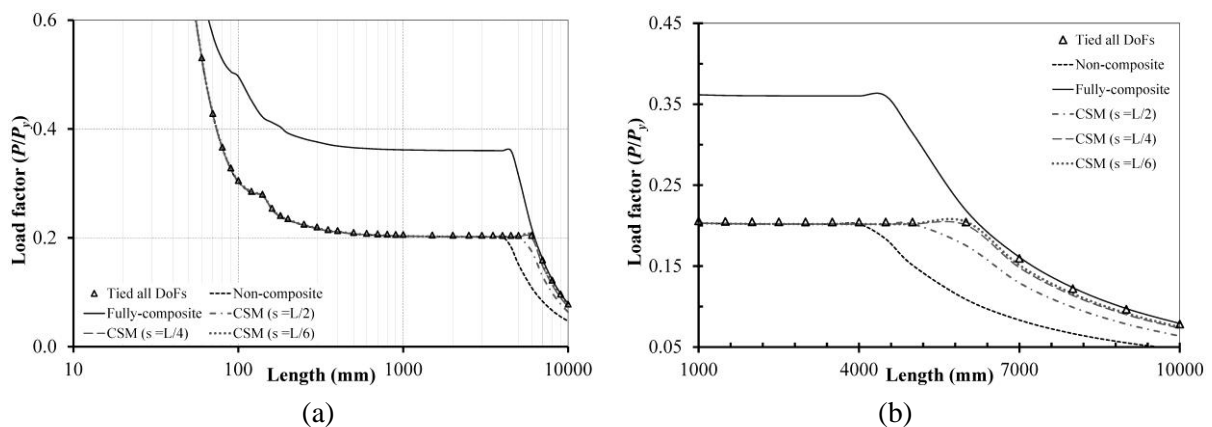
Figure 3-28: Buckling curves of the built-up box section with fixed end conditions for different fastener spacing ratios over (a) the full range of lengths and (b) magnified global region
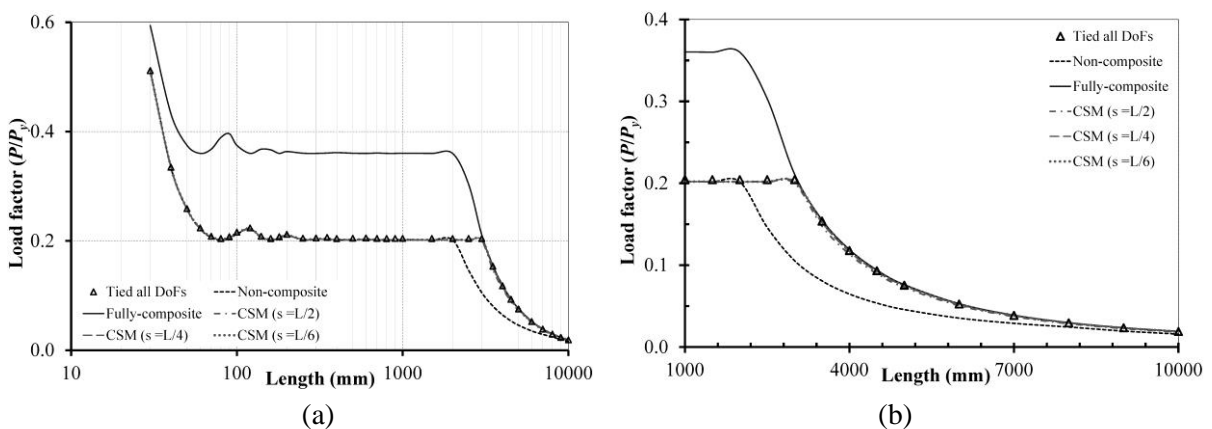
Figure 3-29: Buckling curves of the built-up box section with simply supported end conditions for different fastener spacing ratios over (a) the full range of lengths and (b) magnified global region

This example is similarly concluded by presenting typical first mode shapes obtained from the compound strip analyses under C-C boundary conditions with fastener spacing of $L/4$. The results are shown in Figure 3-30 and Figure 3-31 for local and global buckling of the box section, respectively, and are verified against the mode shapes obtained from FE simulations.

The global buckling mode shape of the built-up box section is flexural due to the formation of a doubly-symmetric cross-section by introducing discrete fasteners along the length of the member.

<table>
<tr><td>(a)</td><td>(b)</td></tr>
</table>
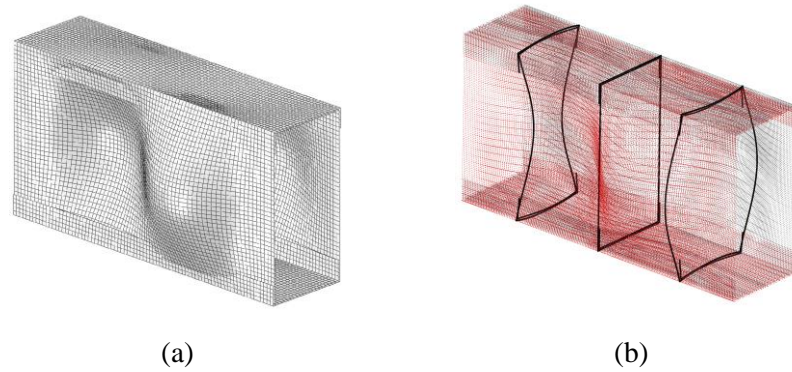
Figure 3-30: Comparison of local buckling mode shapes of the built-up box section under C-C end boundary conditions at $L = 200$ mm: (a) FEM, (b) CSM

<table>
<tr><td>(a)</td><td>(b)</td></tr>
</table>
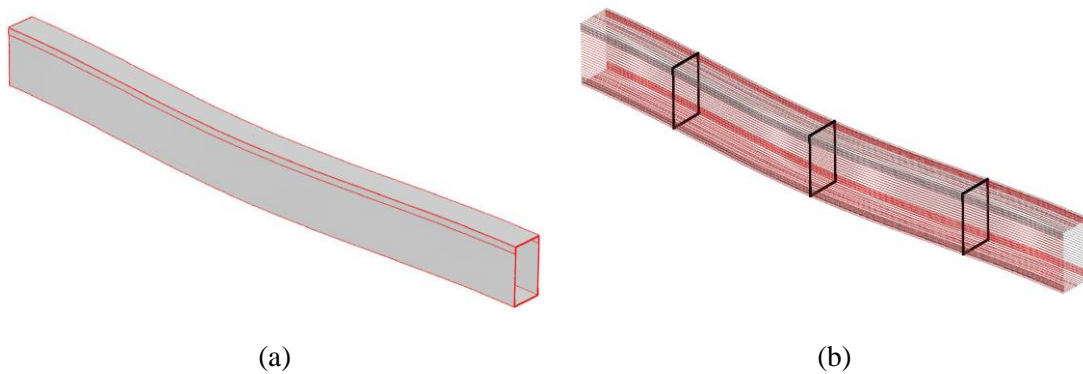
Figure 3-31: Comparison of global buckling mode shapes of the built-up box section under C-C end boundary conditions at $L = 8000$ mm: (a) FEM, (b) CSM

3.3.6   Singly-symmetric built-up corner section

In the last example, a more complicated built-up corner section is considered, as depicted in Figure 3-32(a). The so-called corner section is made by connecting three equal channel sections (C1.0-100) using a series of discrete web-to-flange and web-to-web fasteners. The finite strip discretisation of the cross-section is shown in Figure 3-32(b).

(a)   (b)
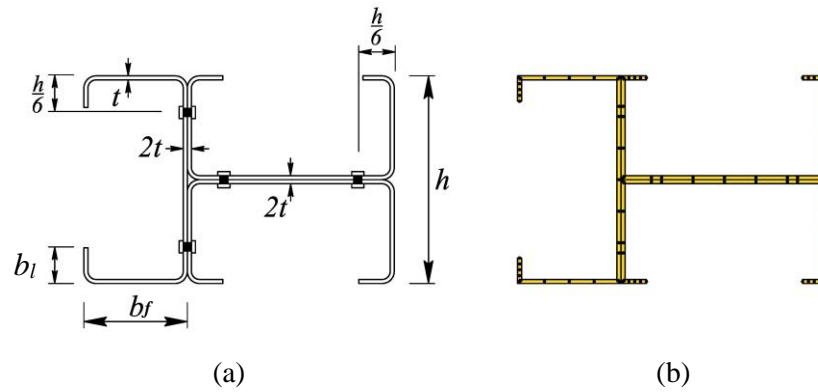
Figure 3-32: Assembly of a built-up corner section: (a) geometry, (b) finite strip discretisation

The built-up corner column is analysed under uniform compression and fixed boundary conditions at both ends (C-C), and the corresponding buckling curves are obtained. The results of the finite strip and FE simulations are compared in Figure 3-33 for $s = L/2$ and $s = L/4$, where a good level of agreement is observed, confirming the applicability of the CSM to the buckling analysis of complex built-up sections.

(a)   (b)
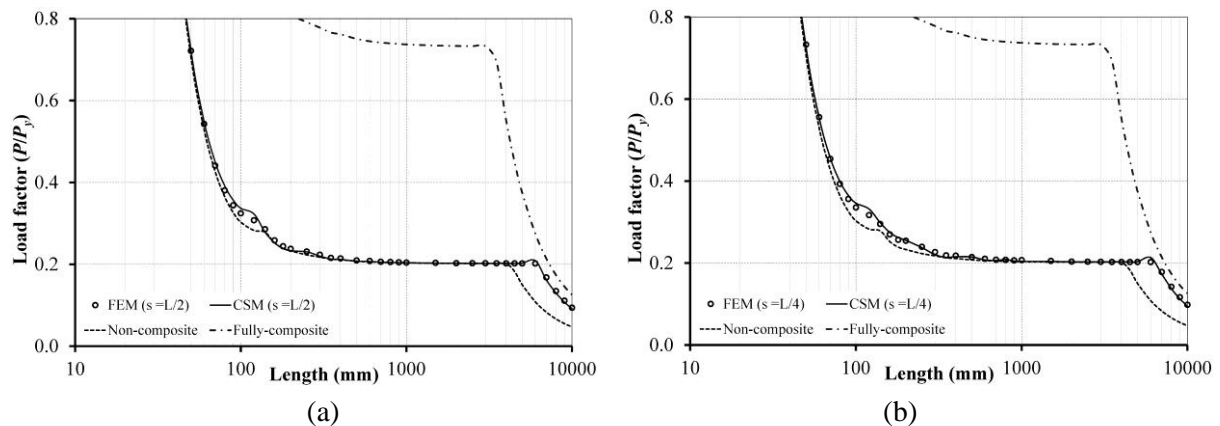
Figure 3-33: Comparison of buckling curves of the built-up corner section obtained from the finite strip and finite element simulations for fixed end conditions: (a) $s = 0.5L$, (b) $s = 0.25L$

Next, the sensitivity of the buckling curves to fastener spacing is evaluated. The results of the buckling load factor are presented in Figure 3-34 over the entire range of considered lengths as well as a specific range (1 m$<L<$10 m) for magnifying the observed effects of discrete fastener spacing in the global buckling region. The figures indicate that including fasteners with the specified spacing enhances the section buckling capacity in the local ($L<$400 mm) and global buckling regions. For lengths less than 400 mm, the smaller the spacing, the higher the enhancement in buckling capacity, whereas for global buckling, the gain in capacity by

reducing the fastener spacing is not considerable. The latter outcome means that a high degree of composite action can be obtained in global buckling, even for a small number of fasteners.

(a)   (b)
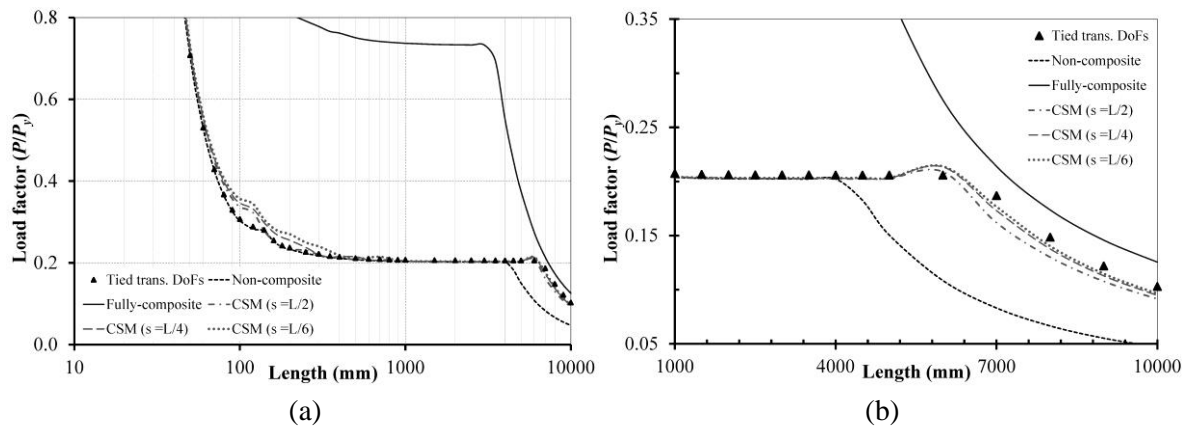
Figure 3-34: Buckling curves of the built-up corner section with fixed end conditions for different fastener spacing ratios over (a) the full range of lengths and (b) magnified global region

Lastly, the first buckling mode shapes of the built-up corner section with fastener spacing of $L/4$ are shown in Figure 3-35 and Figure 3-36, where the results of FEM and CSM indicate similar local and global buckling mode shapes. In addition, the results indicate that the global buckling mode of the singly-symmetric built-up section is flexural-torsional, the same as the single section (see Figure 3-14).

(a)   (b)
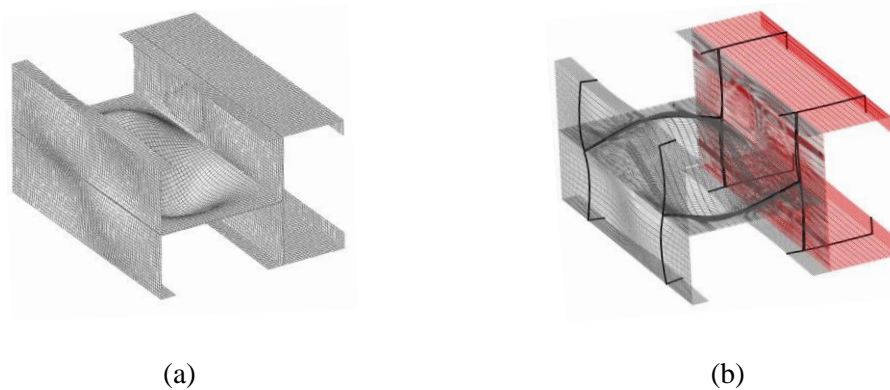
Figure 3-35: Comparison of local buckling mode shapes of the built-up corner section under C-C end boundary conditions at $L = 200$ mm: (a) FEM, (b) CSM

<center>(a)   (b)</center>
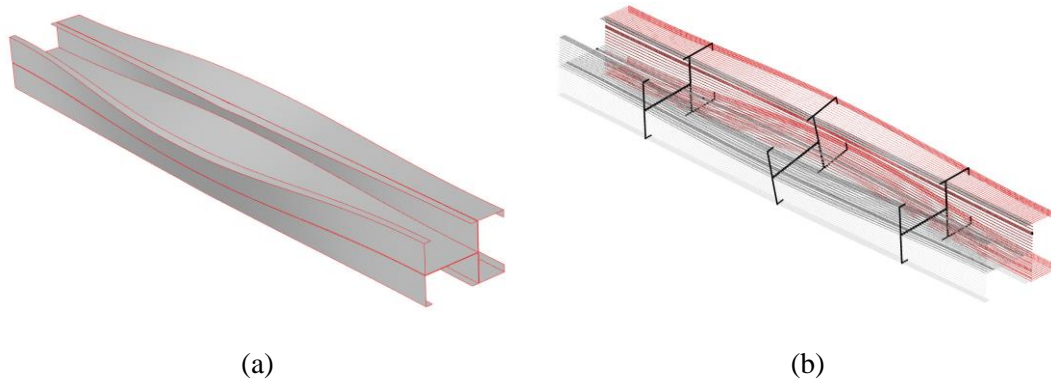
Figure 3-36: Comparison of global buckling mode shapes of the built-up corner section under C-C end boundary conditions at L = 8000 mm: (a) FEM, (b) CSM

By considering the buckling analysis results of built-up sections in the above examples, it can be concluded that the proposed CSM method can predict both the buckling capacity and corresponding mode shapes of built-up CFS sections with discrete web and flange fasteners.

3.4   SUMMARY

In this chapter, a new and practical application of the compound strip method (CSM), an extension to the finite strip method (FSM), is presented and verified. The CSM is applied for the first time to the stability analysis of cold-formed steel (CFS) built-up sections with arbitrarily-located discrete fasteners. To this end, the semi-analytical FSM was briefly introduced, and then the connection element with adjustable stiffness properties was formulated and incorporated into the conventional finite strip formulation. A simple yet accurate framework is presented for the reliable buckling analysis of built-up sections with any desired cross-sectional composition and fastener configuration.

A series of numerical examples were presented to show the performance and versatility of the CSM in the elastic buckling analysis of CFS built-up sections with increasingly complicated geometry. Several typical built-up I- and box sections and a complex corner section were analysed for various fastener configurations and boundary conditions. The proposed numerical technique is verified against finite element solutions and shown to be accurate and convergent. The extent of composite behaviour in built-up sections is determined for different fastener

spacing ratios by investigating the enhancement of buckling capacity and changes in the corresponding buckling modes for the three cross-sections studied.

The results demonstrate that reducing the fastener spacing ratio enhances the buckling capacity of built-up sections, especially in the global and local buckling regions of built-up open sections and the global buckling region of built-up closed sections. The observed difference in global buckling capacity due to the change in fastener spacing is more pronounced under fixed end conditions, whereas in the local buckling region, the impact of fastener spacing is case-dependent. It is also found that typical fastener spacing ratios have negligible influence in the intermediate buckling length region, where the buckling curve almost follows the non-composite curve assuming no interaction between sub-sections. However, the buckling capacity and the composite action in this region can still be elevated by adding fasteners with a constant spacing less than a maximum value. Lastly, the simplicity and accuracy of the CSM expedite extensive parametric studies and can facilitate the search for the optimal structural design of built-up sections and their fastener configuration in future studies and practice.

Chapter 4 EXPERIMENTAL INVESTIGATION OF SECTIONAL BUCKLING IN BUILT-UP COLUMNS

4.1 INTRODUCTION

As one of the major components of this study, an experimental program was designed to investigate the local and distortional buckling of cold-formed steel built-up sections subjected to pure compression. This experimental study elaborates on the influence of key parameters such as buckling mode, cross-section geometry and fasteners spacing. This chapter is thus dedicated to the performed experiments and is written in terms of the key steps in chronological order, commencing with the systematic procedure undertaken to design the geometry of test sections in Section 4.2. The initial preparation of test specimens is explained in Section 4.3, followed by testing for material properties in Section 4.4 using standard coupons from flat and corner parts of the sections. The procedures for measuring material and geometric imperfections are discussed in Sections 4.5 and 4.6, respectively. Section 4.7 describes the set-up and execution of the compression tests and presents the test data in graphical and tabulated forms. An in-depth discussion on the obtained results and observed behaviour is given in Section 4.8. The chapter concludes with a summary of outcomes in Section 4.9.

4.2 DESIGN OF SECTIONS GEOMETRY

The objective of the investigation was to assess the sectional buckling of the built-up cold-formed steel columns. Therefore, the individual lipped channel sections were designed to fail through local or distortional buckling modes. A series of elastic buckling analyses were performed using the finite strip method to investigate the effect of cross-section dimensions on the prevalent sectional buckling mode. The parametric study included 162 sections with

$E = 210$ GPa and nominal web heights (h) of 100, 150 and 200 mm, lip lengths (b_l) of 10, 15 and 20 mm, nominal thickness (t) of 1.2, 1.5 and 1.9 mm with flange widths (b_f) specified with respect to web depths (b_f/h varies from 0.25 to 2). These ranges were chosen based on the dimensions of conventional C-sections manufactured by LYSAGHT in Australia. A typical cross-section with key sectional parameters is shown in Figure 4-1(a), which is discretised utilising eight strips in the web and flanges and four strips per lip (see Section 3.3.3 for mesh convergence study of a lipped channel section) as illustrated in Figure 4-1(b).

(a)   (b)
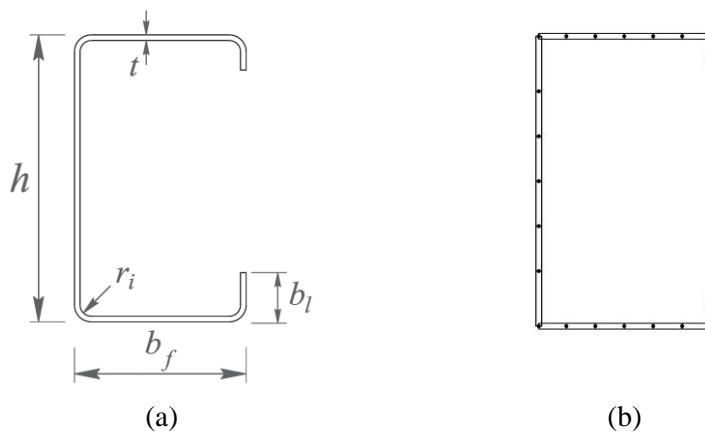
Figure 4-1: A typical lipped channel section: (a) geometry, (b) simplified finite strip discretisation

The results obtained from FS analysis with the inclusion of one harmonic term ($M=1$) are presented in Figure 4-2 for pinned-ended members under uniform compression. According to the graphs, the distortional to local critical buckling stress ratio (f_{crd}/f_{crl}) decreases as the section thickness increases or the lip length decreases. It is also evident that distortional buckling is the dominant elastic buckling mode for a wide range of b_f/h ratios. A section with a nominal web height of 150 mm and a thickness of 1.5 mm was targeted for selecting the test sections. The remaining sectional parameters were chosen as $b_f/h=0.8$ and $b_l=10$ mm, which results in $f_{crd}/f_{crl}=0.65$, i.e. well below 1.0, to ensure a dominant distortional buckling mode, as shown in Figure 4-2(b). This custom-designed section (referred to as C120) was manufactured by brake pressing high-strength G450 structural steel sheets in a specialised fabrication shop. The LYSAGHT channel section C15015 [181] was selected as the next base section for this study, with $b_f/h = 0.42$ and similar nominal height and thickness as the custom-designed sections but a dominant local buckling mode ($f_{crd}/f_{crl} = 1.70$) as depicted in Figure 4-2(b). The LYSAGHT

sections (herein referred to as C64) were roll-formed from GALVASPAN steel G450, complying with the Australian standard AS1397-2001 [182]. The nominal outer dimensions of these two cross-sections are summarised in Table 4-1 and shown in Figure 4-3, in which r_i is the inner radius of the corners. It is noted that the selected sections are identified by their flange width as the main cross-sectional variable.

(a)

(b)

(c)
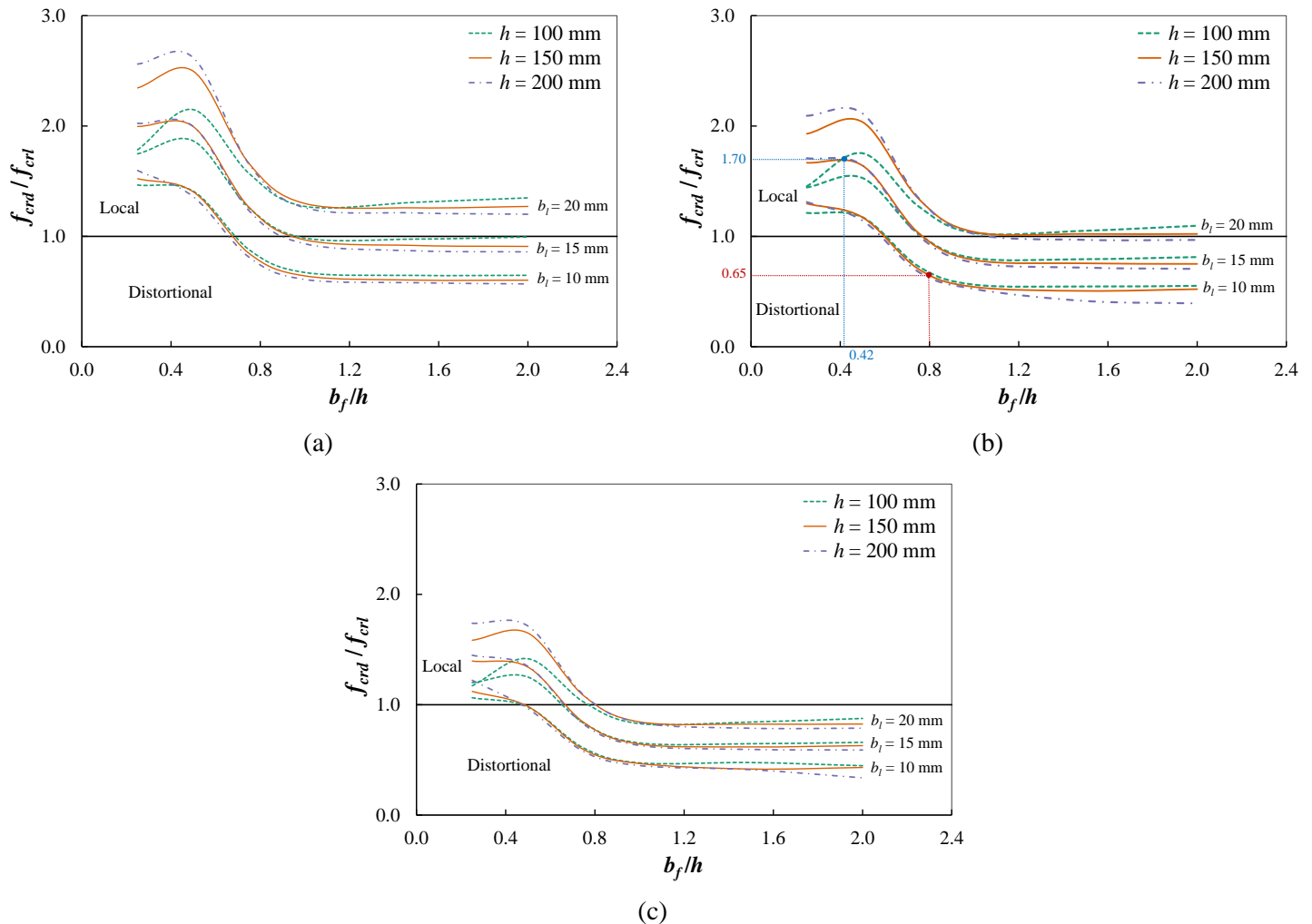
Figure 4-2: The effect of key sectional parameters on the prevalent sectional buckling mode of lipped channel sections with: (a) $t = 1.2$ mm, (b) $t = 1.5$ mm, (c) $t = 1.9$ mm

Table 4-1: Nominal cross-sectional dimensions of the designed channel sections

Section	h (mm)	b_f (mm)	b_l (mm)	t (mm)	r_i (mm)
C120	150	120	10	1.5	1.5
C64	152	64	16	1.5	5.0
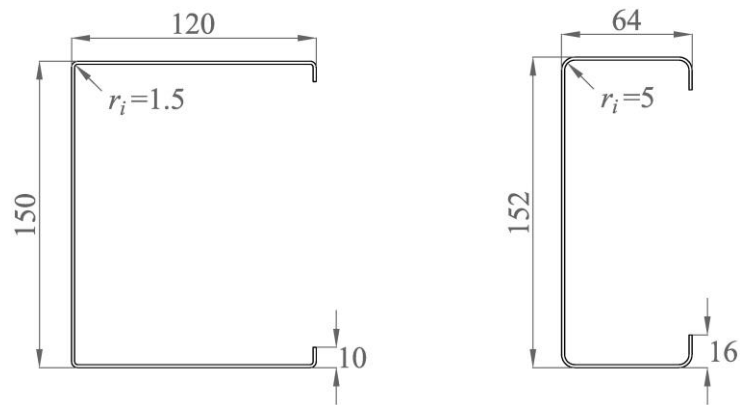
Figure 4-3: Dimensions of the lipped channel sections designed for testing (in mm)

The signature curves for the selected cross-sections obtained from the finite strip analyses with pinned end boundary conditions are presented in Figure 4-4, showing the predominant sectional mode of each section. Accordingly, the nominal length of 1 m was chosen for columns such that one distortional half-wavelength forms along the length of a fixed-ended column.
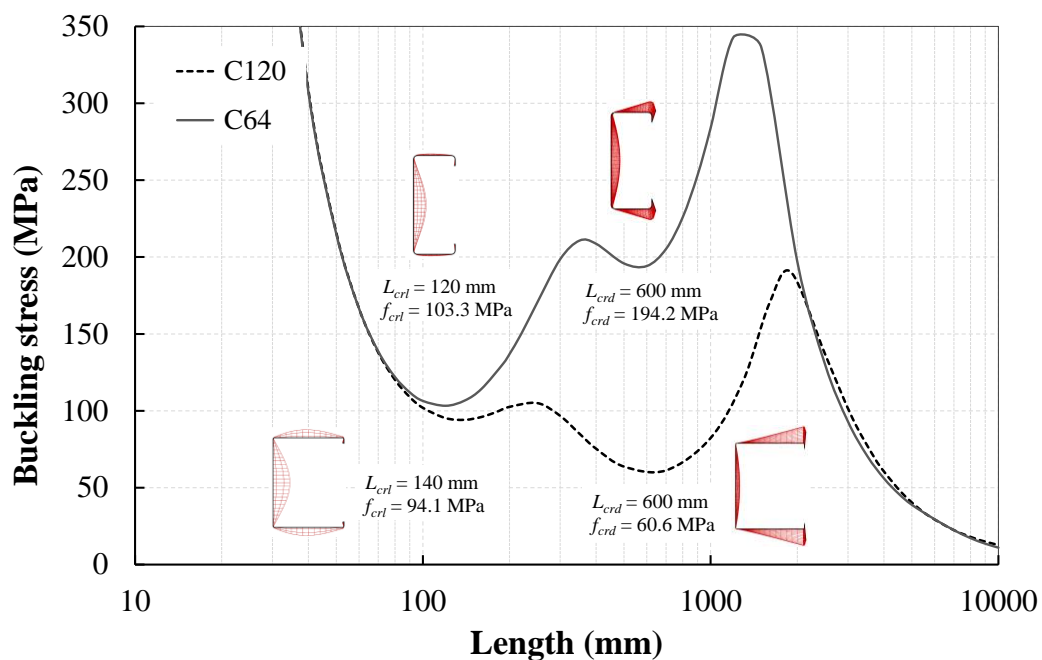
Figure 4-4: Signature curves of the selected channel sections

Different singly-symmetric and doubly-symmetric built-up assemblies were then considered comprising two, three and four channel sections, as demonstrated in Figure 4-5(a). The configuration of fasteners along the member length is also schematically drawn in

Figure 4-5(b), where the first row of fasteners was positioned nominally at 50 mm from each end in all configurations.

(a)   (b)
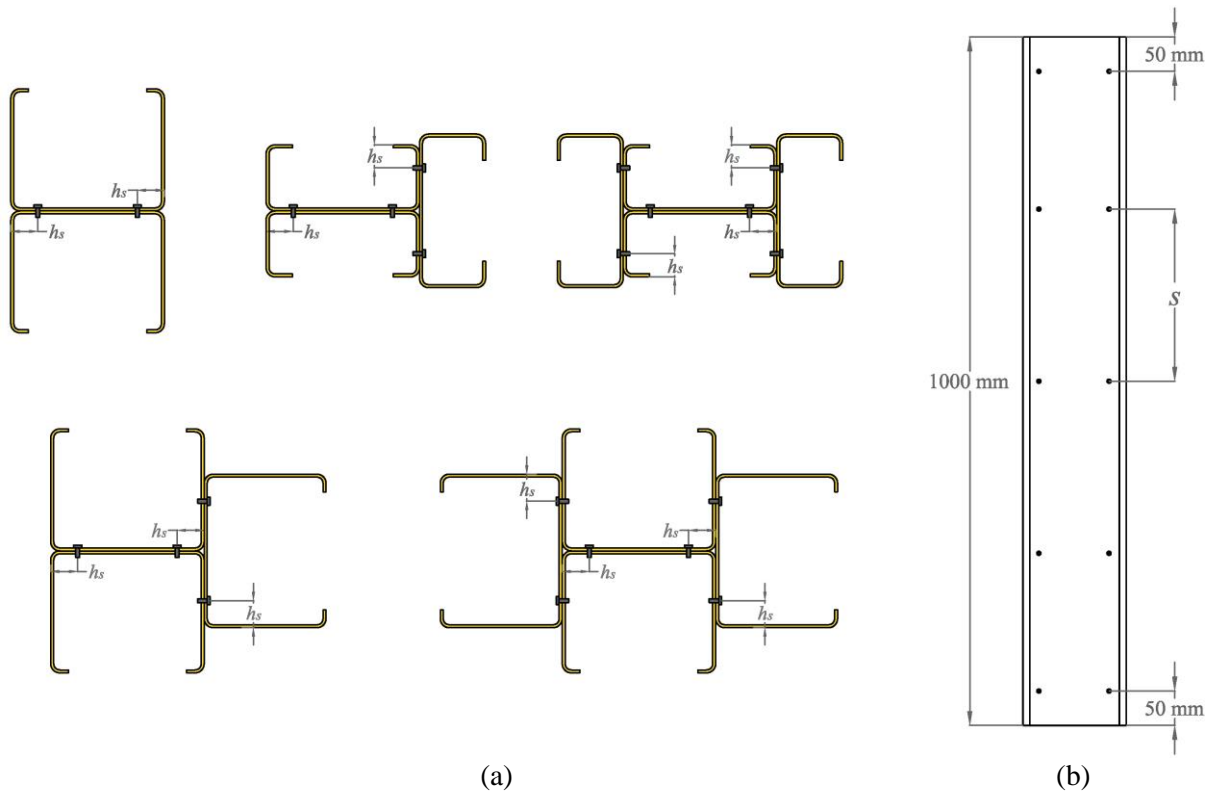
Figure 4-5: Configuration of built-up test specimens: (a) considered section assemblies, (b) longitudinal fastener arrangement

A sensitivity study was carried out on the fastener location within the member length and the cross-section by varying the fastener spacing (s) and edge distance (h_s) per Figure 4-5. The buckling analyses were performed using the Compound Strip Method (CSM) [183]. The elastic buckling results for two different built-up sections made of two (back-to-back connected) and three channel sections under fixed end boundary conditions are used for comparison. The results for different edge distance values (i.e. $h_s=h/8$, $h/6$, $h/4$) are shown in Figure 4-6 and Figure 4-7, in which the vertical axis reads the ratio of the elastic buckling stress for the built-up section (f_{cr}) with respect to that for the constituent channel section (f_{cr1}) and the horizontal axis covers different fastener spacing ratios (s/L). The results indicate that the effect of edge distance of fasteners is more pronounced in the sections with predominant distortional buckling mode (i.e. series C120). The closer the fasteners are to the web-flange intersection in the built-

up I-section of series C120, the higher the enhancement of the elastic buckling strength. This outcome can be attributed to the fact that the web supports the flange outstands that are strengthened by moving the fasteners towards the web-flange junction. In contrast, the trend is reversed for I- sections of series C64, where despite the difference between the curves being marginal, the buckling stress reduces by decreasing the edge distance of fasteners. For built-up sections made of three channel sections, the buckling stress enhancement increases with the increase of edge distance of fasteners due to the restraint provision for the flanges connected to the web. Based on these results, a nominal edge distance of 25 mm (i.e. $h/6$ for the selected sections) was chosen for the experimental investigation to allow sufficient clearance to install the screws based on the lip extent.

(a)   (b)
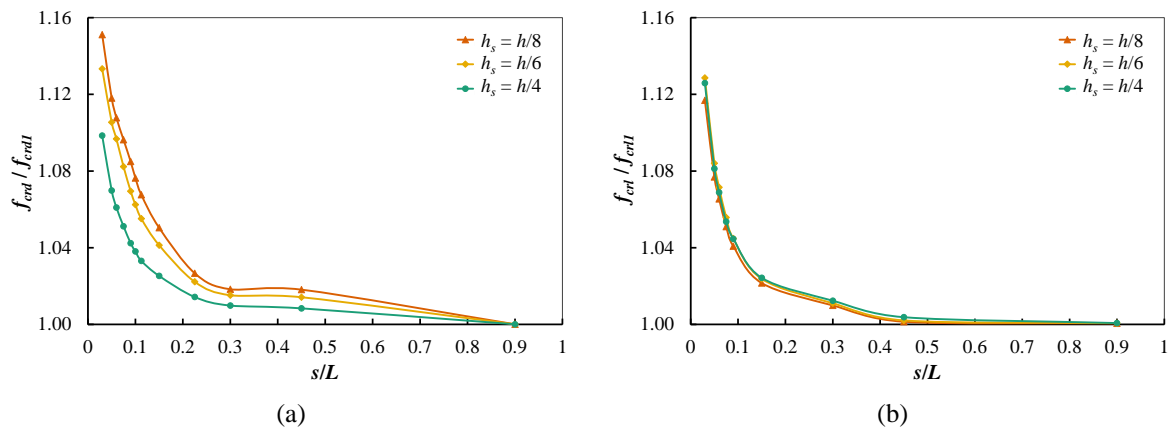
Figure 4-6: Effect of fastener spacing on the elastic buckling stress of a built-up I-section from a back-to-back connection of two channel sections: (a) C120 and (b) C64

(a)   (b)
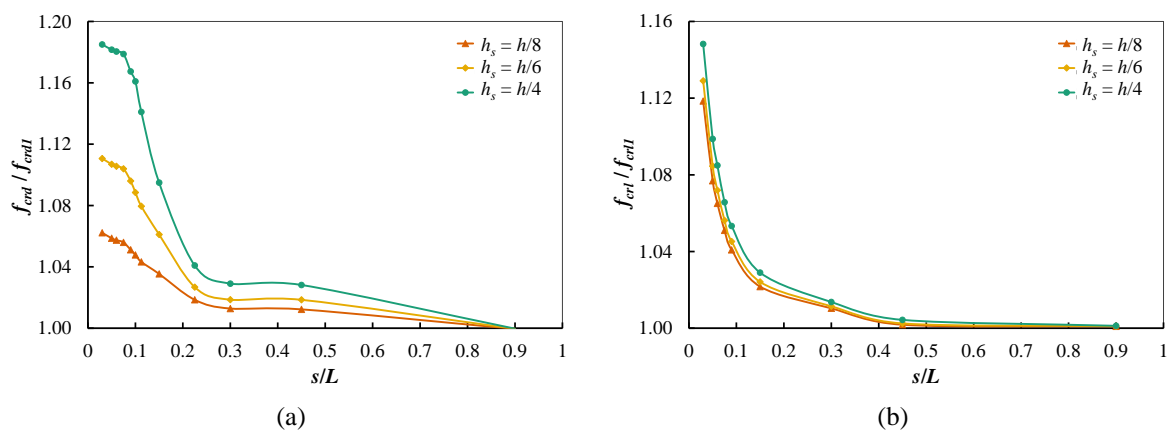
Figure 4-7: Effect of fastener spacing on the elastic buckling stress of a built-up section comprising three channel sections: (a) C120 and (b) C64

It can also be observed that the effect of fastener spacing is more evident in the built-up sections of series C120 with a maximum enhancement in the elastic buckling stress by 15% and 18% for 2C120 and 3C120 sections, respectively. According to the observed pattern, three different spacings were considered in the tests, i.e. s = 100, 300 and 900 mm. The variation was considered to study the effect of fastener spacing on the enhancement of the elastic buckling load and the subsequent increase in the ultimate strength capacity of the compression members, especially in distortional buckling mode. In addition, the possibility of secondary local modes with short half-wavelength triggered by discrete fasteners can be investigated. It is also noted that for the experimental study, the back-to-back connected assembly was not considered for section C64 with dominant local buckling mode as the effect of different parameters has already been assessed for this configuration in the literature [90, 91, 184].

4.3   PREPARATION OF TEST SPECIMENS

The sections were cut to length, and the location of screws and the centre of the webs were marked along the length of the individual specimens of built-up assemblies, as presented in Figure 4-8(a). The individual sections were then aligned to the centre of their webs and connected using POWERS #10 hex head self-drilling screws, see Figure 4-8(b). The screws comply with the requirements specified in the Australian standard AS 3566.1-2002 [185] and are capable of drilling for a maximum thickness of 3.5 mm. The test specimens were labelled to indicate the primary experimental parameters, *i.e*. the member cross-section, flange width of the channel section and fastener spacing. The specimens were first identified by the number of channel sections included in the member cross-section, "C" referring to channel section, then the nominal flange width of the channel section in millimetres, followed by the fastener spacing for built-up sections and finally, the specimen number within a common group. For instance, 3C120-100-1 is the first specimen of a built-up section comprising three channel sections with a nominal flange width of 120 mm and the fastener spacing of 100 mm.

(a)   (b)

Figure 4-8: Preparation of the built-up sections: (a) marking of the screw locations and (b) making the built-up sections using self-drilling screws

For achieving a uniform stress distribution over the member cross-section, both ends of the specimens were flattened using a linisher (see Figure 4-9) except for the specimens of Series 4C120, which exceeded the size of the linisher and were flattened by an electronic milling machine to a flatness tolerance of ±0.025 mm.

Figure 4-9: Flattening the end of specimens using a linisher

The out-to-out cross-section dimensions and web-flange and flange-lip angles were measured at both ends and middle of the specimens. The nomenclature for the cross-section dimension of each specimen is defined in Figure 4-10. As indicative examples, the measured cross-section dimensions and the actual specimen length for test series 3C120 and 3C64 are presented in

Table 4-2 and Table 4-3, respectively. The average cross-sectional dimensions and their standard deviation are also listed at the bottom of each table. The average values of the measured width of web, flanges and lips, as well as web-flange angles, are very close to the corresponding nominal values for both brake-pressed and roll-formed sections with a low standard deviation. However, there was a noticeable variation in the measured values of flange-lip angles for the roll-formed section, as reflected by a higher standard deviation, and their average value is 85.75° compared to the nominal value of 90°. The complete set of tables summarising the measured geometric dimensions for the remaining test series is given in Appendix A.
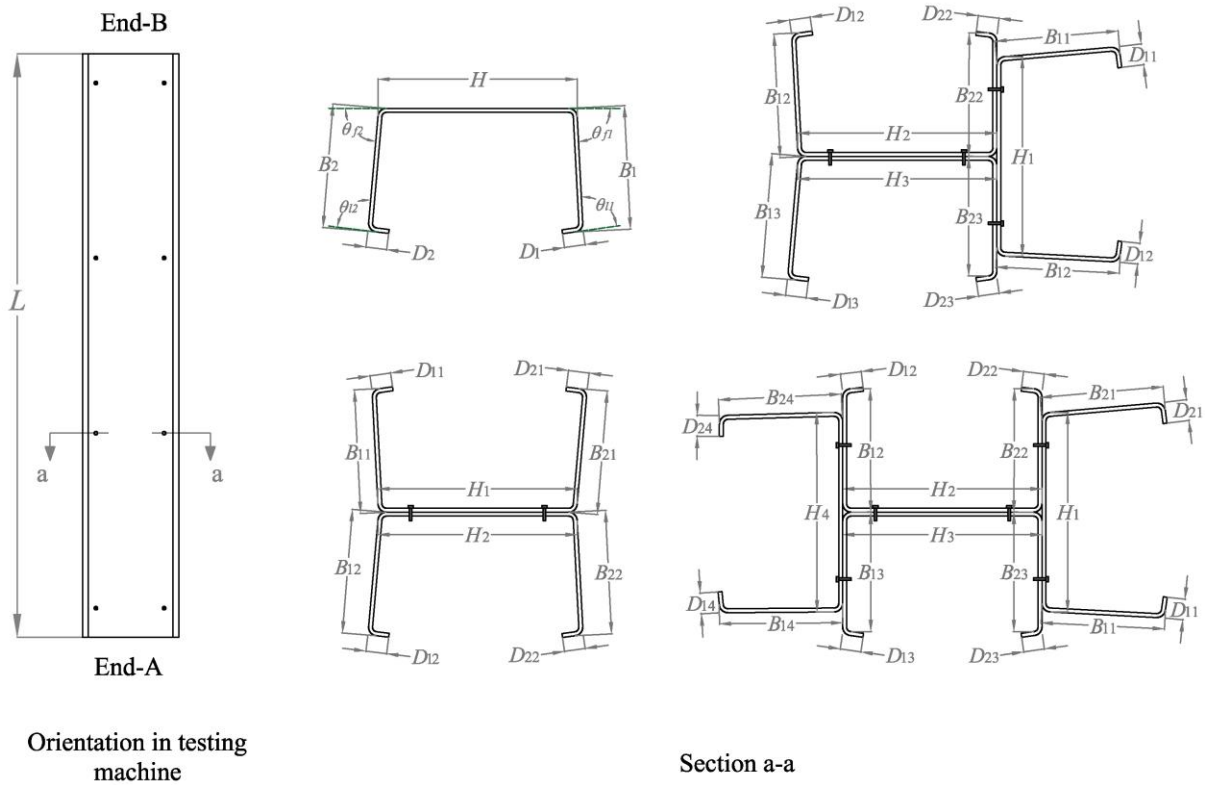
Figure 4-10: Cross-sections dimensions and measurement nomenclature

Table 4-2: Cross-section dimensions of Series 3C120

Specimen	L (mm)	i^*	h_i (mm)	b_{f1i} (mm)	b_{f2i} (mm)	b_{l1i} (mm)	b_{l2i} (mm)	θ_{f1i} (deg.)	θ_{f2i} (deg.)	θ_{l1i} (deg.)	θ_{l2i} (deg.)
Nominal			150.00	120.00	120.00	10.00	10.00	90.00	90.00	90.00	90.00
3C120-900-1	1003	1	148.08	120.45	120.48	9.84	9.80	89.85	89.91	90.21	90.10
		2	148.41	120.55	120.37	10.18	9.42	89.33	90.10	90.42	90.61
		3	148.12	120.40	120.50	9.73	9.45	90.40	89.48	89.67	89.09
3C120-900-2	1002	1	148.14	120.67	120.51	9.36	10.02	90.13	90.23	89.76	90.02
		2	148.33	120.75	120.46	9.10	10.00	90.67	90.59	91.92	89.89
		3	148.10	120.78	120.77	9.74	9.55	90.19	90.64	90.18	90.71
3C120-300-1	1003	1	148.79	120.70	120.55	9.64	9.67	90.08	90.61	90.26	90.39
		2	148.46	120.71	120.57	9.66	9.40	90.98	90.49	91.22	90.29
		3	148.19	120.77	120.69	9.70	9.37	90.31	90.80	89.89	89.68
3C120-300-2	1002	1	147.81	120.69	120.66	9.68	9.94	90.33	90.60	90.59	90.55
		2	147.77	120.68	120.60	9.62	9.56	89.89	90.33	90.44	89.49
		3	148.07	120.69	120.82	9.65	9.73	90.44	90.41	90.53	91.66
3C120-100-1	1002	1	148.58	120.72	120.74	9.57	9.85	90.55	90.02	90.76	90.59
		2	148.70	120.75	120.55	9.69	9.97	90.02	90.02	89.92	89.42
		3	148.73	120.56	120.72	9.49	9.88	90.10	90.04	89.92	88.94
3C120-100-2	1002	1	148.10	120.88	120.75	9.84	9.40	90.97	91.39	91.75	90.78
		2	147.49	120.86	120.75	9.79	9.66	90.25	90.77	90.87	91.18
		3	147.80	120.53	120.50	9.61	10.10	90.22	89.84	90.66	90.35
Average			148.20	120.67	120.61	9.66	9.71	90.26	90.34	90.50	90.21
St. Dev.			0.36	0.13	0.13	0.22	0.24	0.39	0.44	0.64	0.71

* i = 1, 2, 3 correspond to the measurements of channel section i in the built-up assembly as per Figure 4-10.

Table 4-3: Cross-section dimensions of Series 3C64

Specimen	L (mm)	$i*$	h_i (mm)	b_{f1i} (mm)	b_{f2i} (mm)	b_{l1i} (mm)	b_{l2i} (mm)	θ_{f1i} (deg.)	θ_{f2i} (deg.)	θ_{l1i} (deg.)	θ_{l2i} (deg.)
Nominal			152.00	64.00	64.00	16.00	16.00	90.00	90.00	90.00	90.00
3C64-900-1	998	1	153.96	64.26	64.50	15.70	15.99	88.32	89.82	77.62	87.33
		2	153.68	64.88	65.01	16.00	15.89	89.68	87.77	89.81	81.16
		3	154.30	64.49	64.52	16.06	15.75	88.75	91.31	83.05	90.57
3C64-900-2	998	1	154.22	64.46	64.43	15.96	16.29	88.57	91.11	83.50	87.95
		2	154.45	64.65	64.89	16.01	17.31	90.90	88.49	89.05	85.08
		3	154.07	64.45	64.76	16.13	15.56	89.90	88.29	85.87	80.37
3C64-300-1	998	1	154.45	64.34	64.91	16.45	15.24	87.57	90.73	85.67	89.98
		2	154.27	64.64	64.44	15.35	16.29	90.54	88.35	91.22	83.78
		3	153.87	65.03	64.91	16.07	15.50	89.43	88.16	91.65	80.84
3C64-300-2	998	1	154.23	64.82	64.67	16.03	15.84	87.81	90.51	83.66	92.25
		2	154.02	64.45	64.80	15.72	15.99	89.77	88.32	85.24	79.50
		3	153.79	65.39	64.56	15.61	15.67	87.92	90.21	79.85	88.98
3C64-100-1	997	1	153.52	63.71	63.84	16.35	15.19	88.27	91.28	82.96	91.18
		2	153.58	63.96	63.64	15.70	16.04	90.37	88.17	91.70	83.36
		3	153.17	64.37	63.84	15.76	15.92	89.67	88.25	89.80	80.65
3C64-100-2	997	1	153.64	63.40	63.67	16.11	15.39	88.81	90.77	83.27	90.15
		2	153.22	63.88	64.34	15.85	15.66	88.09	90.02	81.36	89.71
		3	153.07	64.13	63.97	15.86	15.81	89.48	88.00	88.28	80.69
Average			153.86	64.40	64.43	15.93	15.85	89.10	89.42	85.75	85.75
St. Dev.			0.43	0.48	0.45	0.27	0.48	1.00	1.32	4.21	4.48

* i = 1, 2, 3 correspond to the measurements of channel section i in the built-up assembly as per Figure 4-10.

4.4   MATERIAL PROPERTIES

A total of 24 tensile coupon tests were conducted to quantify the material properties at different parts of the test sections. Tensile coupons were extracted from the web, flange and corner of the two batches of roll-formed sections and web and corner of the brake-pressed sections in the longitudinal direction, as illustrated in Figure 4-11. The specimens were labelled as "Section type (C64B1, C64B2 or C120)_Coupon location (F, W or C)_Specimen number"; for instance,

"C64B1_F_2" refers to the second flange coupon test of the first batch of roll-formed section C64.

<div align="center">(a)   (b)</div>
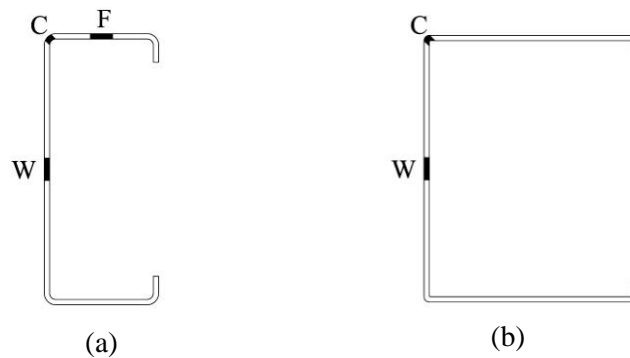
Figure 4-11: Location of coupons taken from the (a) roll-formed section, (b) brake-pressed section

4.4.1   Tensile coupon tests of flat material

Three series of tensile coupon tests were completed to determine the material properties of the flat parts of each channel section used. The flat coupon dimensions conformed to the Australian Standard AS 1391-2007 [186] and had a nominal width of 12.5 mm and a gauge length of 50 mm, as shown in Figure 4-12. The thickness (t) and the width (b) of each coupon were measured at the centre of the reduced section using a digital vernier prior to testing. The measured dimensions are given in Table 4-4.
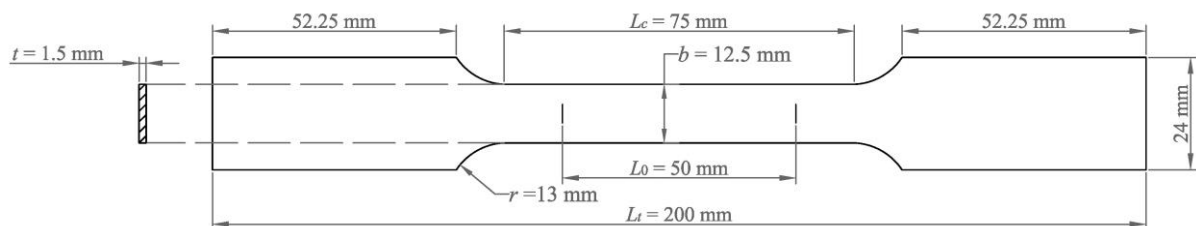
Figure 4-12: Flat coupon dimensions

The zinc coating of the first specimen was removed with Hydrochloric acid to measure the base metal thickness, and strain gauges were attached at the centre of both sides of the coupon (as shown in Figure 4-13) to capture the longitudinal strain accurately up to 1.5%. A 25 mm gauge length extensometer was also mounted on all the specimens to measure the longitudinal strain up to complete failure. The flat coupons were tested in an MTS Criterion testing machine with a capacity of 50 kN according to the Australian Standard AS 1391-2007 [186]. The tests were

operated in a displacement control mode, and the applied displacement rate was 0.2 mm/min, corresponding to a strain rate of 5×10^{-5}/s. The tests were paused for 2 minutes near the 0.2% proof stress, the ultimate strength and regular intervals between them to obtain the material properties at the static equilibrium state.

| (a) | (b) |
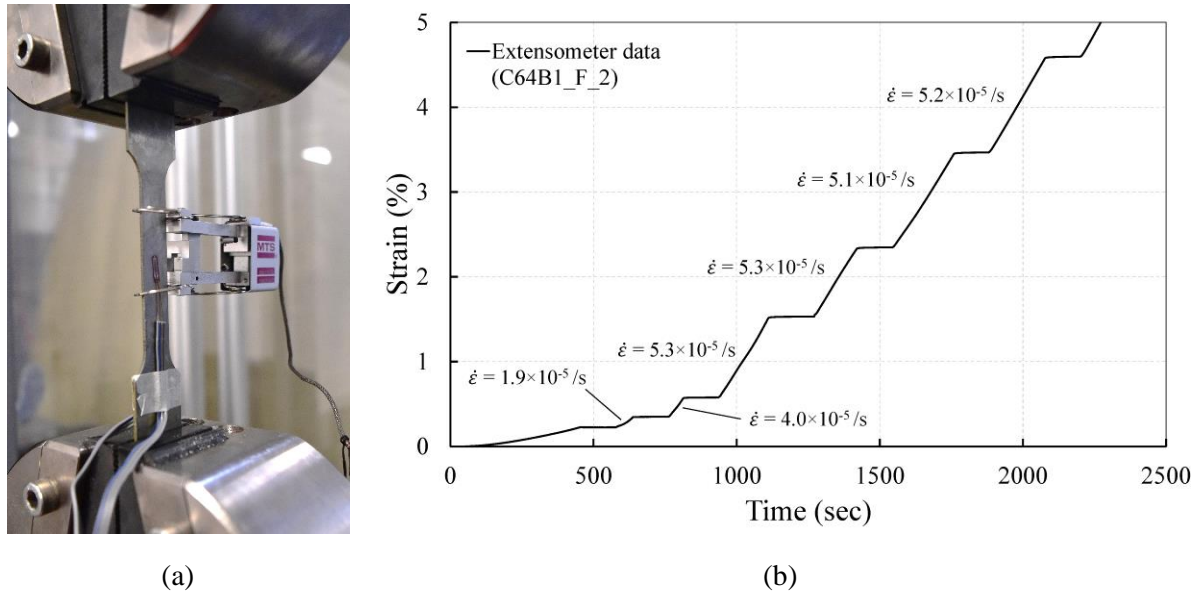
Figure 4-13: Tensile coupon test: (a) set-up, (b) a typical loading history

Typical stress-strain curves obtained from sample web and flange coupons are presented for comparison in Figure 4-14(a) and Figure 4-14(b), respectively. As can be seen, the curves follow a similar nonlinear pattern and are also quantitatively comparable in terms of displacement ductility and strength capacities. The complete set of stress-strain curves, including the static and dynamic curves, for all tensile coupon tests from flat material, can be found in Appendix B.

The obtained static material properties are summarised in Table 4-4, where E is Young's modulus, $\sigma_{0.01}$ and $\sigma_{0.2}$ are respectively the 0.01% and 0.2% proof stresses, and n is the strain hardening exponent based on Ramberg-Osgood stress-strain relation, which reads

$$\varepsilon = \frac{\sigma}{\varepsilon} + 0.002\left(\frac{\sigma}{\sigma_{0.2}}\right)^{n}, \qquad (4.1)$$

$$n = \frac{\ln(20)}{\ln(\sigma_{0.2} / \sigma_{0.01})}.$$

(4.2)

Furthermore, σ_u is the ultimate tensile strength, ε_u is the ultimate strain corresponding to the ultimate stress and ε_t is the total elongation of a gauge length of 50 mm. The results indicate that Series C120, on average, has about 10% higher 0.2% proof stress ($\sigma_{0.2}$) and ultimate stress (σ_u) capacities than Series C64.
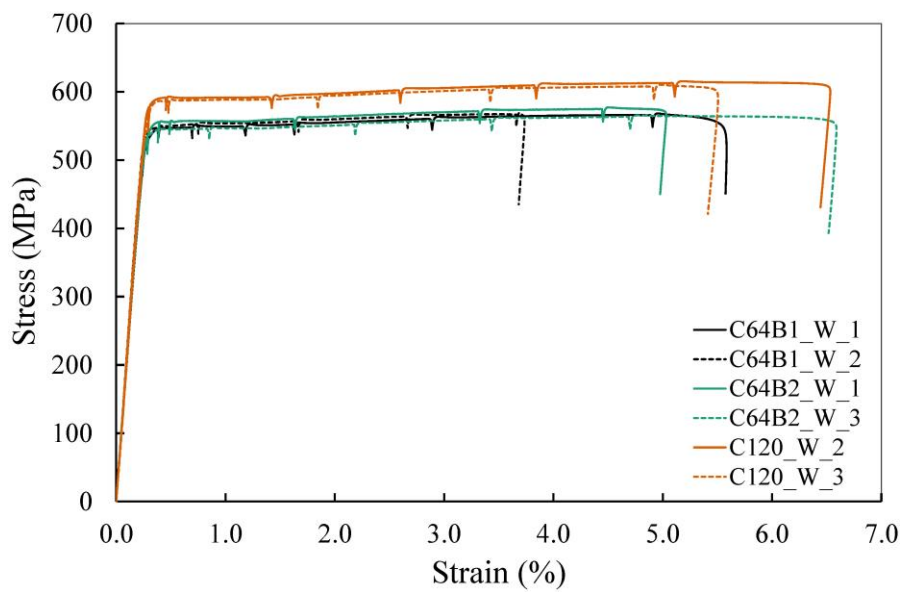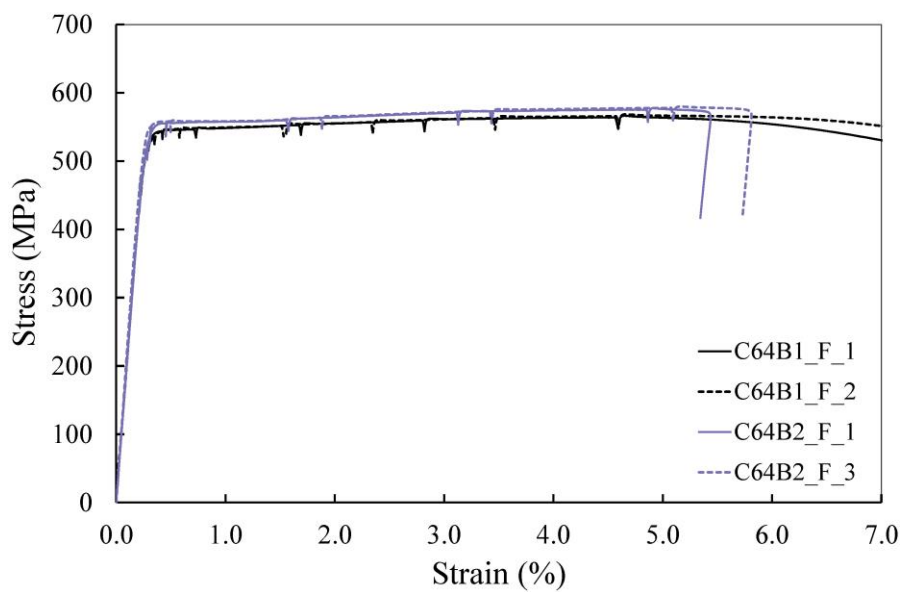
Figure 4-14: Stress-strain curves of the tested coupons from (a) web, (b) flange

Table 4-4: Flat material properties

Specimen	t (mm)	b (mm)	E (GPa)	$\sigma_{0.01}$ (MPa)	$\sigma_{0.2}$ (MPa)	n	σ_u (MPa)	ε_u (%)	ε_t (%)
C64B1_F_1		12.29	209.942	450.71	532.52	18.0	547.10	4.6	8.2
C64B1_F_2	1.48	12.20	210.402	453.12	529.31	19.3	549.12	5.0	8.8
C64B1_F_3		12.30	211.303	465.33	532.9	22.1	547.82	4.4	7.7
C64B1_W_1		12.29	211.833	476.88	533.83	26.6	548.55	4.7	10.1
C64B1_W_2	1.48	12.30	226.571	500.62	535.93	44.0	549.46	3.7	7.4
C64B1_W_3		12.30	209.026	473.06	530.44	26.2	548.85	3.8	9.3
C64B2_F_1		12.27	207.984	439.52	535.99	15.1	557.67	5.1	9.3
C64B2_F_2	1.47	12.33	214.904	438.84	540.04	14.4	560.41	5.4	9.1
C64B2_F_3		12.34	225.679	440.76	538.10	15.0	559.97	5.3	10.1
C64B2_W_1		12.39	213.338	457.70	536.02	19.0	556.89	4.8	9.6
C64B2_W_2	1.47	12.34	206.850	486.32	540.91	28.2	560.39	4.8	10.2
C64B2_W_3		12.35	223.397	454.97	527.30	20.3	546.14	5.0	10.6
C120_W_1		12.33	212.894	464.83	569.65	14.7	591.68	5.1	10.4
C120_W_2	1.48	12.41	222.628	478.58	573.20	16.6	593.64	5.8	10.1
C120_W_3		12.34	214.875	483.36	568.18	18.5	588.84	5.2	9.8

4.4.2   Tensile coupon tests of corner material

The forming process of cold-formed sections (either brake pressing or roll forming) modifies the material properties at various parts of the cross-section; however, this effect is more pronounced at the corners due to a higher degree of cold working. Therefore, three series of corner coupon tests were conducted to investigate the effect of cold working on the mechanical properties of the cold-formed sections. The width of the corner coupons is recommended to be less than the inner corner radius (r_i) for determining the properties of the cold-worked material [186]. However, it was impractical to adhere to this recommendation for the brake-pressed section due to its small inner corner radius ($r_i = 1.5$ mm). Hence, the corner coupon specimens were extracted within the outer corner radius for the brake-pressed section (3 mm wide with the gauge length of 12 mm) and the inner corner radius for the roll-formed section (6 mm wide with the gauge length of 24 mm), conforming to the Australian Standard AS 1391-2007 [186]. The nominal dimensions of the corner coupons are shown in Figure 4-15(a-b).

(a)   (b)   (c)
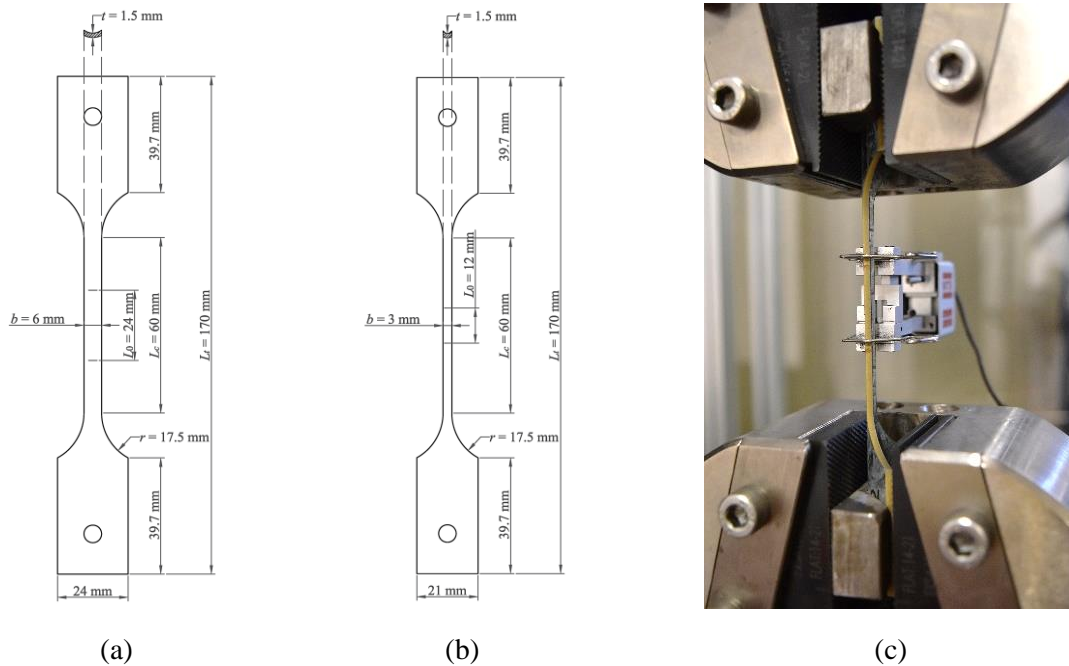
Figure 4-15: (a) Corner coupon dimensions of the roll-formed section, (b) corner coupon dimensions of the brake-pressed section, (c) tensile corner coupon test set-up

Based on the recommendations of AS 1391-2007 [186] and ASTM E8/E8M-13a [187], the gripped ends of the curved coupons may be flattened without heating to fit into flat grips. However, this method inevitably introduces loading eccentricity, which causes additional bending and considerably affects the results for Young's modulus and yield stress. In order to avoid introducing loading eccentricity, a special clamping jig was designed in [188], in which the load was transferred to the coupon specimen using end pins. The same clamping jig was utilised to perform the corner coupon tests in this thesis, as shown in Figure 4-15(c). The tests were performed in an MTS Criterion testing machine with 50 kN capacity at a displacement rate of 0.5 mm/min for Series C64B1 and 0.4 mm/min for Series C64B2 and C120. Similar to the previous section, a graphical comparison is also made in Figure 4-16 between the stress-strain curves of representative sample corner coupons. The complete set of static and dynamic curves for all tested coupons are given in Appendix B.
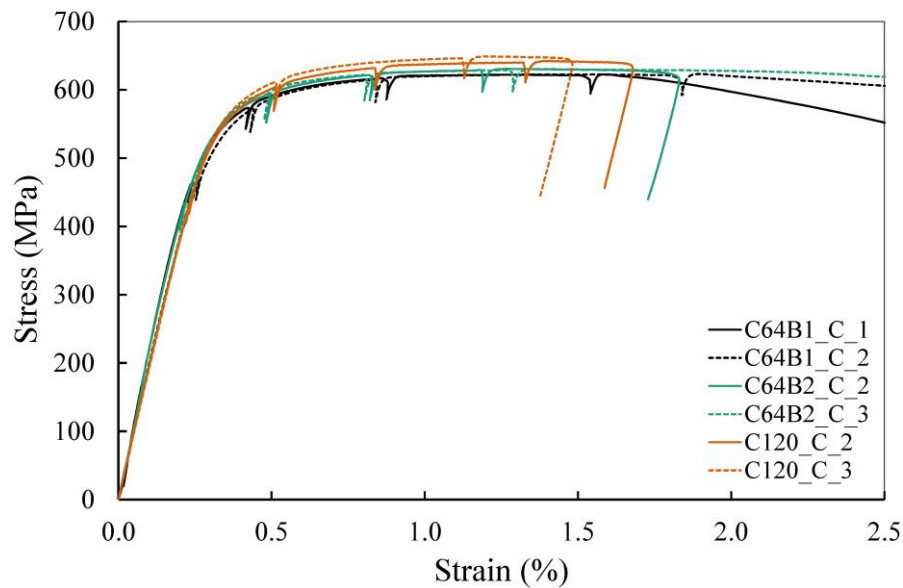
Figure 4-16: Stress-strain curves of corner coupons

The weight and density method, as stated in AS 1391-2007 [186], was utilised to determine the cross-sectional area of the curved coupons. A gauge length of 24 mm was marked on the coupons prior to testing and cut along the marks after testing. The cut piece was weighed to an accuracy of 0.01 g, and the weight obtained was divided by the density of cold-formed steel and the initial gauge length to determine the cross-sectional area, which in addition to the static material properties, are summarised in Table 4-5. The test results indicate that Series C120 has slightly higher 0.2% proof stress ($\sigma_{0.2}$) and ultimate tensile stress (σ_u) capacities.

Table 4-5: Corner material properties

Specimen	A (mm^2)	E (GPa)	$\sigma_{0.01}$ (MPa)	$\sigma_{0.2}$ (MPa)	n	σ_u (MPa)	ε_u (%)	ε_t (%)
C64B1_C_1	9.30	218.169	383.87	556.28	8.1	594.60	1.5	5.3
C64B1_C_2	9.23	198.577	377.30	549.49	8.0	594.49	2.0	5.7
C64B1_C_3	9.36	194.731	430.04	561.47	11.2	597.07	1.3	4.0
C64B2_C_1	9.35	221.715	409.35	557.35	9.7	597.98	1.2	2.6
C64B2_C_2	9.47	216.185	386.66	548.91	8.5	598.71	1.4	4.3
C64B2_C_3	9.24	195.984	402.89	557.23	9.2	598.77	1.4	6.2
C120_C_1	5.50	187.232	398.67	566.40	8.5	602.83	0.99	4.2
C120_C_2	5.36	194.591	406.45	565.94	9.0	613.48	1.42	3.4
C120_C_3	5.31	191.741	405.74	576.50	8.5	619.86	1.23	2.7

A comparison of the results of Table 4-4 and Table 4-5 shows that the cold forming process enhances the yield stress and ultimate strength at the corners by 6% and 9%, respectively, while it decreases the ductility. It also highlights a more pronounced modification of the strain hardening exponent (n) from the range of 14 to 44 for flat parts to a range of 8 to 11 for the corner coupons, which implies a more rounded stress-strain curve (see Figure 4-16).

4.5   MEASUREMENT OF RESIDUAL STRESSES

Residual stresses are induced in cold-formed sections as a result of manufacturing and fabricating processes. The coiling-uncoiling process mainly creates residual stresses and strains in the longitudinal direction, depending on the radius of the coils. In contrast, the cold forming process mainly introduces additional residual stresses and strains in the transverse direction and corners [11]. The through-thickness residual stress variation of a thin plate is commonly assumed to be linear and is decomposed into the membrane and bending stress components [12], as shown in Figure 4-17. However, a third "layering" component of residual stress is also present, varying through the thickness [189].
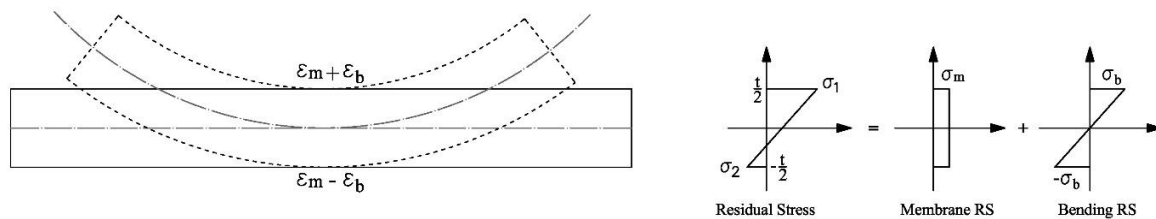
Figure 4-17: Membrane and bending stress components of residual stresses

The effect of the bending and layering stress components is implicitly considered in the material behaviour obtained from a tensile coupon test as the coupons are straightened by the grips of the testing machine, which approximately reintroduces the bending residual stresses into the specimen. Moreover, experimental studies have shown that the membrane residual stresses induced by brake pressing are rather small [12, 13] and can be generally ignored in numerical modelling. Hence, the membrane residual stresses were measured only for the roll-formed section in this study.

Strain gauges were attached to both sides of a C64 specimen at the centre of the web, and, as schematically presented in Figure 4-18(a), a sequence of longitudinal and transverse cuts was made to measure the residual stresses at the centre of the web using the sectioning method [190]. The temperature should be controlled in this method so as not to affect the residual stresses; hence a metal shear with a cutting capacity of 2.5 mm was used, as shown in Figure 4-18(b). Metal shear devices are known to produce less heat compared to a band saw. The room temperature was 21°C, and the maximum measured temperature at the cutting line was 22.4°C, which was deemed to be within an acceptable range from the ambient room temperature.

(a)   (b)
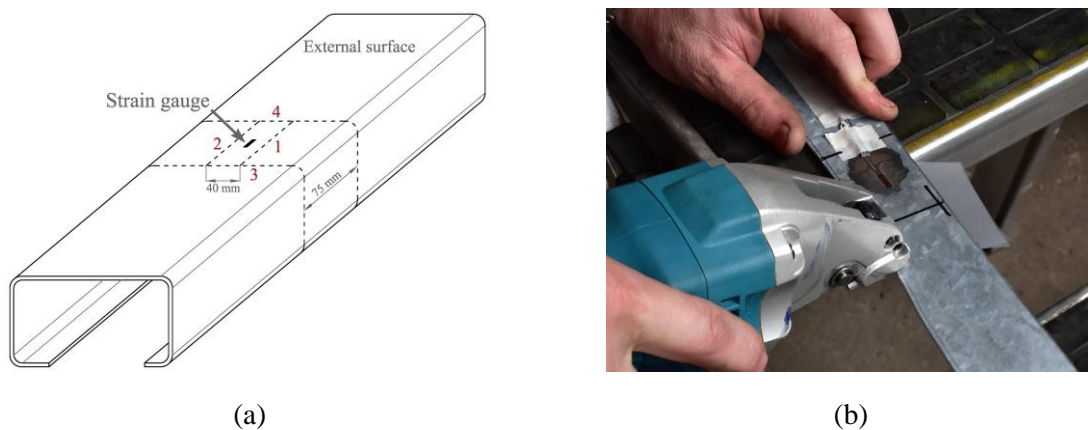
Figure 4-18: The sectioning technique: (a) cut lines location and sequence, (b) cutting tool
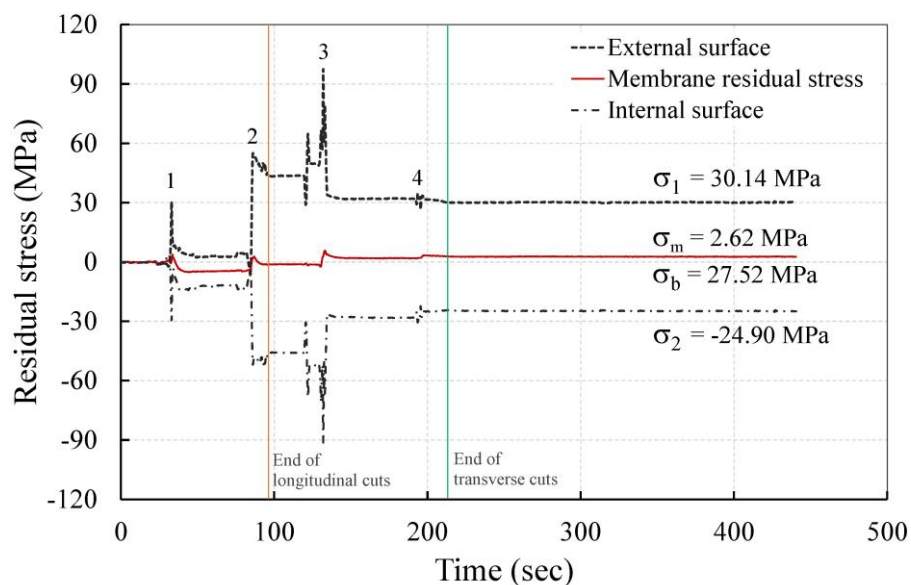
Figure 4-19: Released residual stresses measured on both sides of the section during cutting

The longitudinal strains released during the cutting process were measured using the attached strain gauges on the internal and external surfaces of the web. The measured surface strains were converted to residual stresses using Young's modulus obtained from the tensile coupon tests of the roll-formed section, as reported in Table 4-4. The residual stresses were then decomposed into the membrane (constant) and bending (linearly varying) stress components. As seen in Figure 4-19, most of the residual stresses were released after the longitudinal cuts and reached constant values of 30.13 MPa and -24.89 MPa at the external and internal surfaces of the web after the last cut respectively. The obtained membrane residual stress is 2.62 MPa. Therefore, it was concluded that the membrane residual stresses induced in the section due to roll forming are negligible and can be ignored in the numerical modelling of the structural behaviour of this section.

4.6 MEASUREMENT OF GEOMETRIC IMPERFECTIONS

The manufacturing process may introduce different geometric imperfections (e.g. camber, twist or waviness) in a cold-formed steel member. In addition, shipping, storage and construction processes may cause localised imperfections in the form of, e.g. dents, holes or squeezed flanges. The geometric imperfections significantly influence the expected behaviour and failure modes of thin-walled members. Consequently, geometric imperfections were measured before testing.

4.6.1 Measurement rig

In order to evaluate the shape and magnitude of the imperfections, measurements need to be taken in transverse and longitudinal directions at discrete points. In this study, laser recording devices were used to measure imperfections. The details of the locations of the lasers in the transverse direction and their positive measuring direction for each section assembly are presented in Figure 4-20. Imperfections were measured at the centre of the web and flanges and 5 mm inwards from the rounded corners and the lips. However, because of the impeded access to the web of the built-up sections, the location of the lasers for the top and bottom of

the web was adjusted to 30 mm from the centre of the web, which also facilitated investigating the influence of screws on the imperfections.
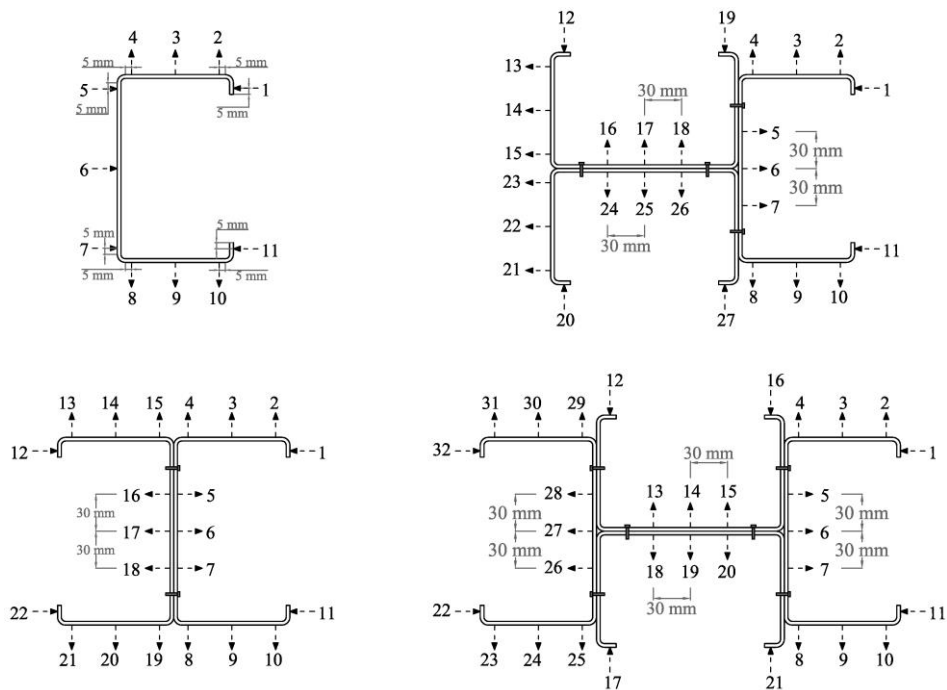
Figure 4-20: Location of laser lines for a single section and built-up assemblies
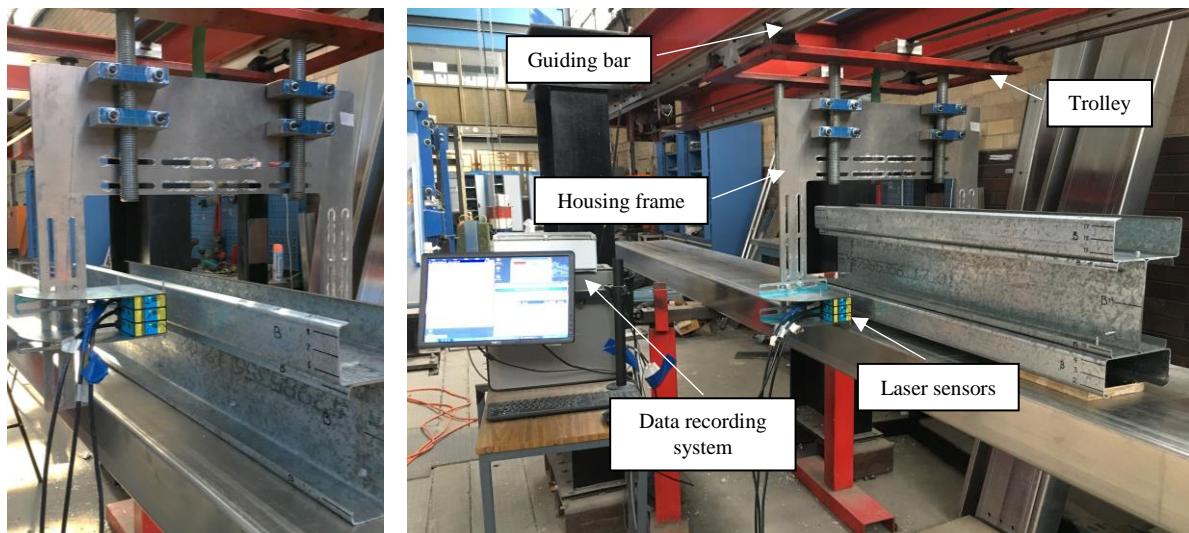
Figure 4-21: Imperfection measurement rig

Figure 4-21 shows the utilised imperfection measurement set-up. The measurement rig consists of a housing frame mounted on a trolley, which is pulled along high-precision guiding bars by a motor. The calibrated laser displacement sensors were connected to the housing frame using 3 mm steel brackets in order to measure the absolute distance to the specimen. Since the data

sampling rate was 10 Hz, the speed of the trolley was set to 10 mm/s to allow reading every millimetre along the member length. The specimens were cleaned and levelled on the table to ensure the results would not be affected by other factors such as dust. The imperfections were then measured twice, and the readings were averaged.

4.6.2   *Measurement results*

The main imperfection readings for the built-up specimen 2C120-300-1 are given in Figure 4-22 as an indicative example, which desirably shows a negligible noise level from external excitations such as vibrations of the test set-up. The locations of fasteners are also indicated in the diagram of web measurements, the effect of which can be observed as a localised disturbance in the overall pattern of imperfections (see Figure 4-22(a)).
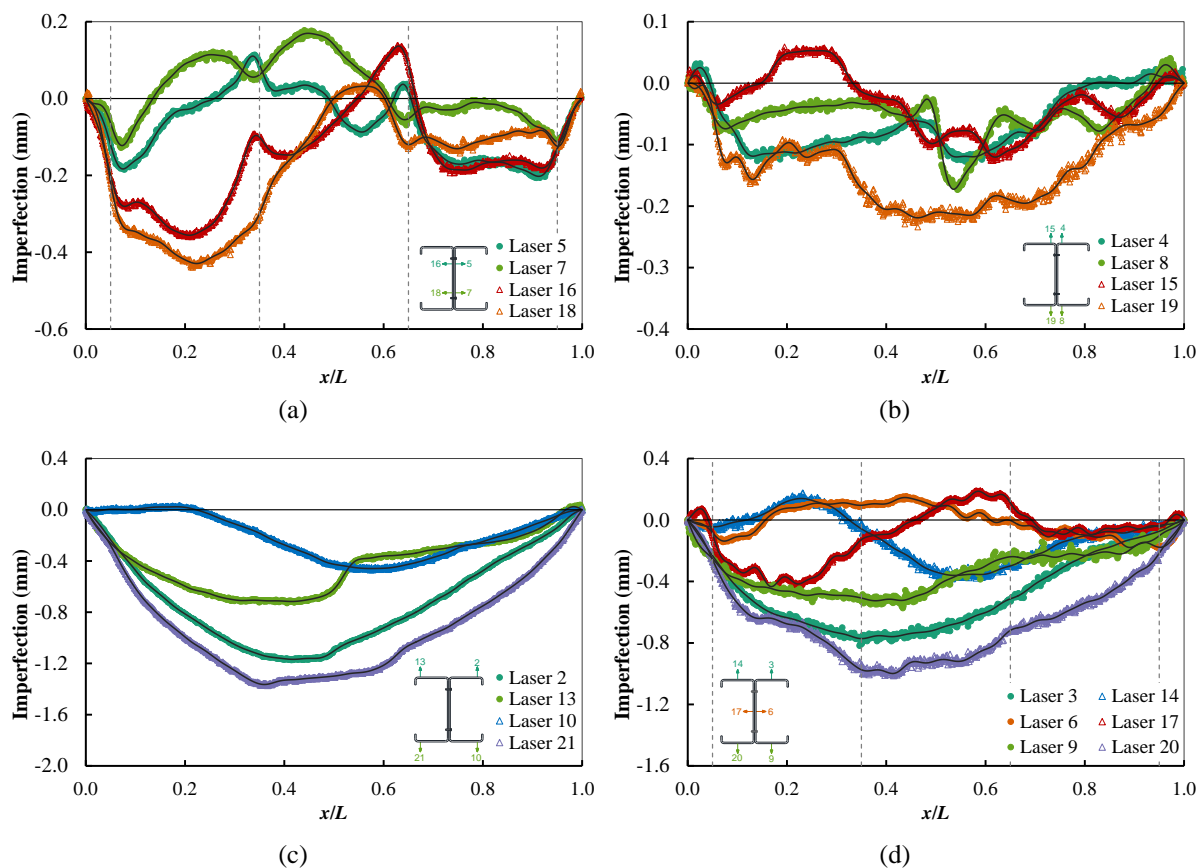
Figure 4-22: A typical imperfection measurement data with Fourier approximations (black lines)

The raw data of each line were approximated analytically by sinusoidal Fourier series as per the following discretised form for convenience in presentation and future use:

$$f(x) = \sum_{n=1}^{N_t} a_n \sin \frac{n\pi x}{L} \quad \forall \ 0 \le x \le L, \tag{4.3}$$

where N_t is the number of terms retained for the approximation, and the coefficient a_n is the amplitude associated with each wavelength ($\lambda_n = 2L/n$) that can be obtained using N_p discrete data points (where $N_p \ge N_t$) from the following equation:

$$a_n = \frac{2}{N} \sum_{n=1}^{N_p} f(x_n) \sin \frac{n\pi x_n}{L}. \tag{4.4}$$

In this analysis, a total number of 30 sinusoidal terms (i.e. $N_t = 30$) was retained to eliminate the contribution of high-frequency vibrations while including enough terms well beyond short half-wavelengths associated with local buckling and the minimum fastener spacing in this study (i.e. $s_{min}=L/10$). The approximations of imperfection measurements using finite Fourier series are shown with black lines in Figure 4-22, which show a good agreement with the measured data. The coefficients of the Fourier approximation of each imperfection reading for the test specimens are tabulated in Appendix C.

Measured imperfections can be decomposed into the critical eigenmodes of the sections as a common way of incorporating imperfections in numerical modelling [17-19]. In this method, a combination of scaled critical buckling mode shapes of the section is employed to form the imperfection field as follows

$$f = \sum_i \alpha_i \varphi_i, \tag{4.5}$$

where f is the imperfection field, and α_i is the scale factor corresponding to the normalised critical buckling mode shape φ_i obtained from an elastic buckling analysis as described in Chapter 3. The imperfection magnitude of each mode, α_i, can be determined based on the statistics of actual imperfection measurements. For instance, the typical critical buckling mode shapes of a back-to-back I-section are shown in Figure 4-23. The magnitude of global vertical translation and twist of the section can be obtained from the readings of lasers 5, 7, 16 and 18,

and the global horizontal translation can be captured by the readings of lasers 4, 8, 15 and 19. Similarly, the readings along lasers 2, 10, 13 and 21 determine the distortion of the section, whereas lasers 3, 6, 9, 14, 17 and 20 capture the local imperfections of the section.
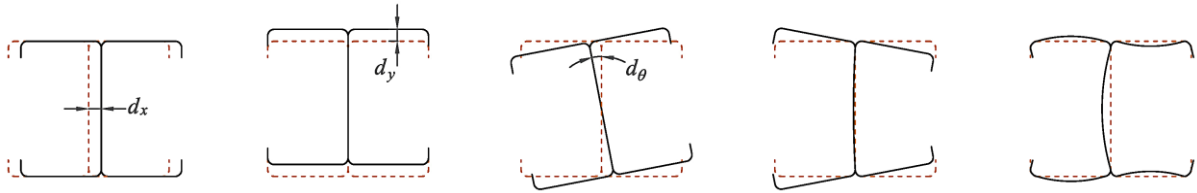
Figure 4-23: Critical buckling mode shapes of a built-up I-section

Figure 4-24 depicts the representative parameters of local and distortional imperfections for a lipped channel section and the built-up assemblies indicating the positive direction considered for each parameter. A summary of the imperfection parameters derived at the mid-length of each specimen is presented in Table 4-6 and Table 4-7 for tests Series C120 and C64, respectively. Considerable variation in all imperfection parameters was observed, as reflected by a high standard deviation compared to the average values. The global imperfection components about the minor and major axes were fairly small for both test series as the specimens were short and connected back-to-back in built-up assemblies.
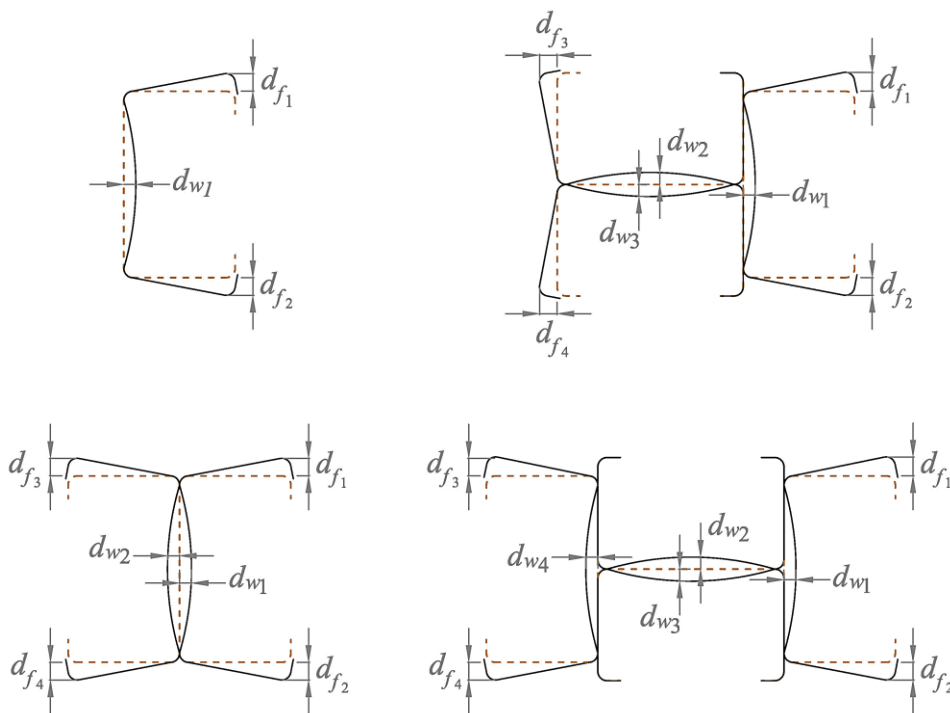
Figure 4-24: Representative imperfection parameters of the test sections

Table 4-6: Imperfection parameters measured at mid-length for test series C120

Specimen	Global		Distortional				Local			
	d_x (mm)	d_y (mm)	d_{f1}/t	d_{f2}/t	d_{f3}/t	d_{f4}/t	d_{w1}/t	d_{w2}/t	d_{w3}/t	d_{w4}/t
1C120-1	-0.216	-0.048	-0.238	-0.181	-	-	0.120	-	-	-
1C120-2	-0.064	0.033	-0.346	-0.308	-	-	0.141	-	-	-
2C120-900-1	-0.026	0.004	0.775	-0.529	-0.080	0.079	-0.055	0.054	-	-
2C120-900-2	0.034	-0.015	-0.248	-0.425	-0.647	0.262	-0.173	-0.048	-	-
2C120-300-1	0.031	0.023	-0.731	-0.406	-0.271	-0.862	-0.082	-0.071	-	-
2C120-300-2	0.012	0.062	-0.197	-0.305	0.213	-0.834	-0.091	0.050	-	-
2C120-150-1	0.036	0.042	0.244	-0.885	0.327	-0.511	-0.041	0.178	-	-
2C120-150-2	-0.039	0.002	-0.219	-0.554	-0.194	-0.340	0.057	0.161	-	-
2C120-100-1	0.010	-0.075	-0.245	-0.145	-0.410	0.180	0.003	-0.220	-	-
2C120-100-2	-0.005	0.025	-0.916	0.009	-0.139	-0.857	0.081	-0.012	-	-
3C120-900-1	-0.238	0.034	0.033	-0.214	-0.155	-0.219	0.143	0.047	0.019	-
3C120-900-2	-0.234	-0.017	-0.621	-0.345	-0.194	-0.193	0.176	0.139	-0.015	-
3C120-300-1	-0.536	-0.052	0.268	-0.701	-0.521	-0.546	0.406	0.109	0.063	-
3C120-300-2	-0.180	0.040	0.239	0.120	-0.246	0.152	0.148	0.008	-0.032	-
3C120-100-1	-0.163	0.010	-0.109	0.600	-0.754	-0.352	0.002	-0.162	-0.189	-
3C120-100-2	-0.105	0.082	-0.165	-0.138	-0.155	-0.343	-0.066	-0.066	0.200	-
4C120-900-1	0.023	-0.006	-0.649	-0.316	-0.319	-0.440	0.112	-0.232	-0.185	0.194
4C120-900-2	-0.019	0.005	-0.476	-0.495	-0.834	-0.442	0.252	0.056	0.059	0.040
4C120-300-1	-0.007	-0.102	0.368	-0.629	-0.505	-0.516	0.023	-0.205	-0.004	-0.077
4C120-300-2	-0.012	-0.038	-0.355	0.209	0.014	-0.306	0.275	-0.249	-0.251	0.258
4C120-100-1	0.047	-0.037	-0.537	-1.387	-0.134	-0.629	0.216	-0.060	-0.011	0.205
4C120-100-2	0.061	0.028	-0.856	-0.813	-0.666	-0.130	0.329	0.065	0.049	0.519
|Average|*	L/11005	L/28611	0.406				0.126			
St. Dev.*	L/7749	L/35930	0.268				0.107			

* Statistics are based on the absolute values of imperfection parameters for built-up sections.

Table 4-7: Imperfection parameters measured at mid-length for test series C64

Specimen	Global		Distortional				Local			
	d_x (mm)	d_y (mm)	d_{f1}/t	d_{f2}/t	d_{f3}/t	d_{f4}/t	d_{w1}/t	d_{w2}/t	d_{w3}/t	d_{w4}/t
1C64-1	-0.421	-0.192	-0.761	0.152	-	-	-0.038	-	-	-
1C64-2	-0.103	-0.088	-0.182	-0.448	-	-	-0.079	-	-	-
3C64-900-1	0.336	-0.104	0.524	0.012	0.328	0.093	-0.140	0.251	-0.288	-
3C64-900-2	0.059	0.051	-0.311	0.136	0.255	-0.151	-0.151	-0.197	-0.147	-
3C64-300-1	0.100	0.196	-1.905	0.186	0.234	-0.371	-0.442	-0.196	-0.200	-
3C64-300-2	0.149	0.072	-0.544	0.371	-0.058	-0.085	-0.177	-0.509	0.097	-
3C64-100-1	0.072	0.058	-0.415	0.572	0.179	-0.123	-0.026	-0.293	-0.026	-
3C64-100-2	0.154	0.098	-0.507	0.113	-0.240	-0.364	-0.300	-0.100	-0.183	-
4C64-900-1	0.103	0.039	0.106	-0.066	0.196	-0.216	0.439	-0.146	-0.073	-0.123
4C64-900-2	-0.099	0.024	0.116	-0.172	-0.047	-0.348	0.000	-0.033	-0.096	0.170
4C64-300-1	-0.026	0.076	0.168	-0.263	-0.092	-0.111	0.074	-0.083	-0.107	-0.045
4C64-300-2	-0.074	0.107	0.201	-0.485	0.018	0.066	0.293	0.050	-0.208	-0.138
4C64-100-1	-0.080	0.028	0.210	-0.407	-0.063	-0.313	0.290	-0.131	-0.036	0.006
4C64-100-2	0.046	-0.049	0.147	-0.150	0.106	-0.114	0.120	-0.125	0.085	-0.038
|Average|[*]	L/9250	L/13317	0.261				0.145			
St. Dev.[*]	L/12374	L/21125	0.288				0.107			

[*] Statistics are based on the absolute values of imperfection parameters for built-up sections.

Another important imperfection data reported in the literature for cold-formed steel sections is the maximum imperfection, which is typically utilised for the nonlinear computational modelling of these sections. In the Australian standard AS/NZS 4600 [16], the imperfection amplitudes for local (ω_l) and distortional (ω_d) buckling are prescribed as follows

$$\omega_l = 0.3t\sqrt{f_y / f_{crl}}, \tag{4.6}$$

$$\omega_d = 0.3t\sqrt{f_y / f_{crd}}, \tag{4.7}$$

in which t is the section thickness. A summary of the measured maximum imperfection components for the built-up specimens of both test series is reported in Table 4-8 compared to the AS/NZS 4600 [16] recommendations. The sectional imperfections are normalised relative to the section thickness, and the critical local and distortional buckling stresses are obtained using the CSM, which will be explained in detail later in Chapter 6. The measured distortional

imperfection amplitudes are comparable to the Australian standard recommended values, while the local imperfection values are reasonably smaller. These imperfection amplitudes can be utilised in numerical simulations to incorporate geometrical imperfections as the combination of scaled sectional buckling mode shapes per Eq. (4.5).

Table 4-8: The measured maximum sectional imperfections for built-up specimens in comparison with the Australian standard AS/NZS4600 [16] recommendations

Specimen	Local (d_w/t)		Distortional (d_f/t)	
	Measured	AS4600	Measured	AS4600
2C120-900-1	0.26	0.74	0.82	0.77
2C120-900-2	0.21	0.74	0.75	0.74
2C120-300-1	0.31	0.74	0.90	0.75
2C120-300-2	0.24	0.74	0.91	0.75
2C120-150-1	0.21	0.74	0.91	0.76
2C120-150-2	0.44	0.74	0.60	0.76
2C120-100-1	0.32	0.73	0.54	0.76
2C120-100-2	0.21	0.73	0.97	0.76
3C120-900-1	0.31	0.72	0.34	0.76
3C120-900-2	0.33	0.72	0.66	0.77
3C120-300-1	0.55	0.72	0.79	0.75
3C120-300-2	0.28	0.72	0.32	0.74
3C120-100-1	0.22	0.71	0.78	0.72
3C120-100-2	0.31	0.71	0.47	0.71
4C120-900-1	0.43	0.71	0.78	0.76
4C120-900-2	0.34	0.71	0.85	0.76
4C120-300-1	0.23	0.71	0.75	0.74
4C120-300-2	0.39	0.71	0.53	0.75
4C120-100-1	0.30	0.70	1.53	0.71
4C120-100-2	0.53	0.69	1.00	0.71
3C64-900-1	0.42	0.68	0.62	0.44
3C64-900-2	0.39	0.68	0.58	0.44
3C64-300-1	0.44	0.68	1.90	0.43
3C64-300-2	0.69	0.68	0.85	0.43
3C64-100-1	0.32	0.67	0.62	0.43
3C64-100-2	0.46	0.67	0.71	0.43
4C64-900-1	0.35	0.68	0.52	0.44
4C64-900-2	0.41	0.68	0.80	0.44
4C64-300-1	0.44	0.68	0.68	0.44
4C64-300-2	0.35	0.68	0.89	0.43
4C64-100-1	0.60	0.67	0.78	0.43
4C64-100-2	0.66	0.67	0.69	0.43
Average	0.37	0.70	0.78	0.63

4.7 COMPRESSION TESTS

A total of 36 compression tests were carried out on the designated single and built-up cross-sections with a nominal height of 1 m under fixed-ended conditions.

4.7.1 Test arrangements

To guarantee a fixed-ended boundary condition, a special end plate was designed for each cross-section and was filled with Patternstone. The end plates were composed of two 16 mm thick steel plates connected using four M12 bolts, as shown in Figure 4-25. The bottom plate was intact, while the cross-section of each test series with a thickness of 15 mm was extracted from the top plate so that the centroid of the section and the plate coincide, see Figure 4-10 for cross-section dimensions. Each specimen was carefully placed at the centre of the end plates, and the major and minor axes of the cross-section were aligned with the centre lines of the plate. A mixture of Patternstone (ultra-hard gypsum) with a compressive strength of 28 MPa at 1 hour (and 70 MPa at 24 hours) was then poured into the gap between the section and the end plate and was allowed to set for at least 30 minutes or until it was completely hardened. The specimen was flipped afterwards, and the same procedure was conducted for the other end. The explained process of preparing the specimen for the test may be seen in Figure 4-26. Using this type of end plate also facilitates uniform compression loading and prevents localised damage to the section edges at the ends [191].
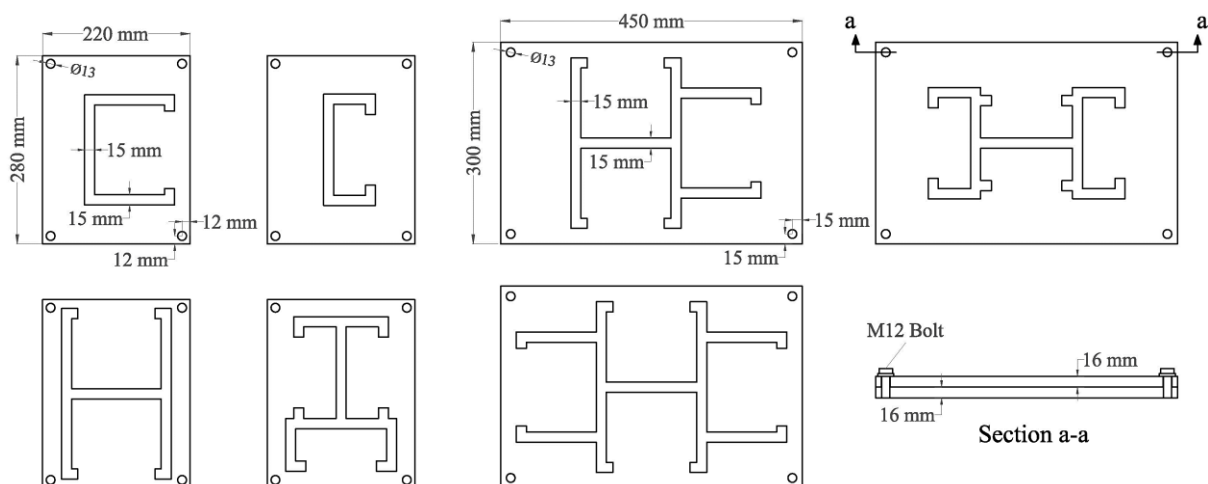
Figure 4-25: End plates details
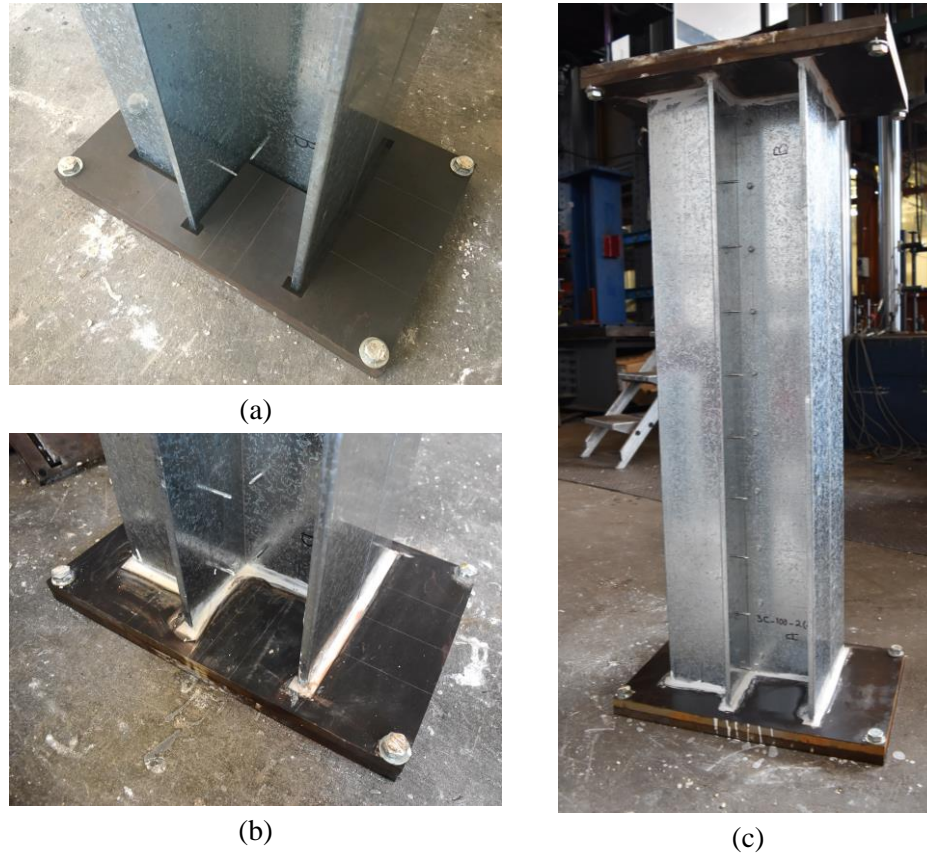
Figure 4-26: Process of preparing a specimen for testing: (a) alignment of the specimen, (b) pouring Patternstone for the first end, (c) final specimen

4.7.2 Test set-up

All specimens were tested between fixed ends under monotonically increasing concentric compression. The test set-up is shown schematically in Figure 4-27. To ensure concentric loading, a 600×300×16 mm steel plate was fixed to the centre of the bottom platen of the testing machine, and the bottom end-plate of each specimen was then perfectly aligned with the centre lines of the fixed plate. Once the specimen was set in place, a layer of a thick mixture of Patternstone was poured on top of the end plate to maintain a uniform compression loading, and the loading plate was then driven down gradually to squeeze out the Patternstone layer around the loading plate. The Patternstone was allowed to harden fully before applying load. To assess whether the uniform distribution of the load on the built-up section was achieved, eight strain gauges were fitted at the mid-height of two test specimens, i.e. 2C120-300-2 and

2C120-100-2, with two gauges near the junctions of the flanges and lips and two gauges near the junctions of the flanges and web of each individual section, as illustrated in Figure 4-28.

(a)   (b)
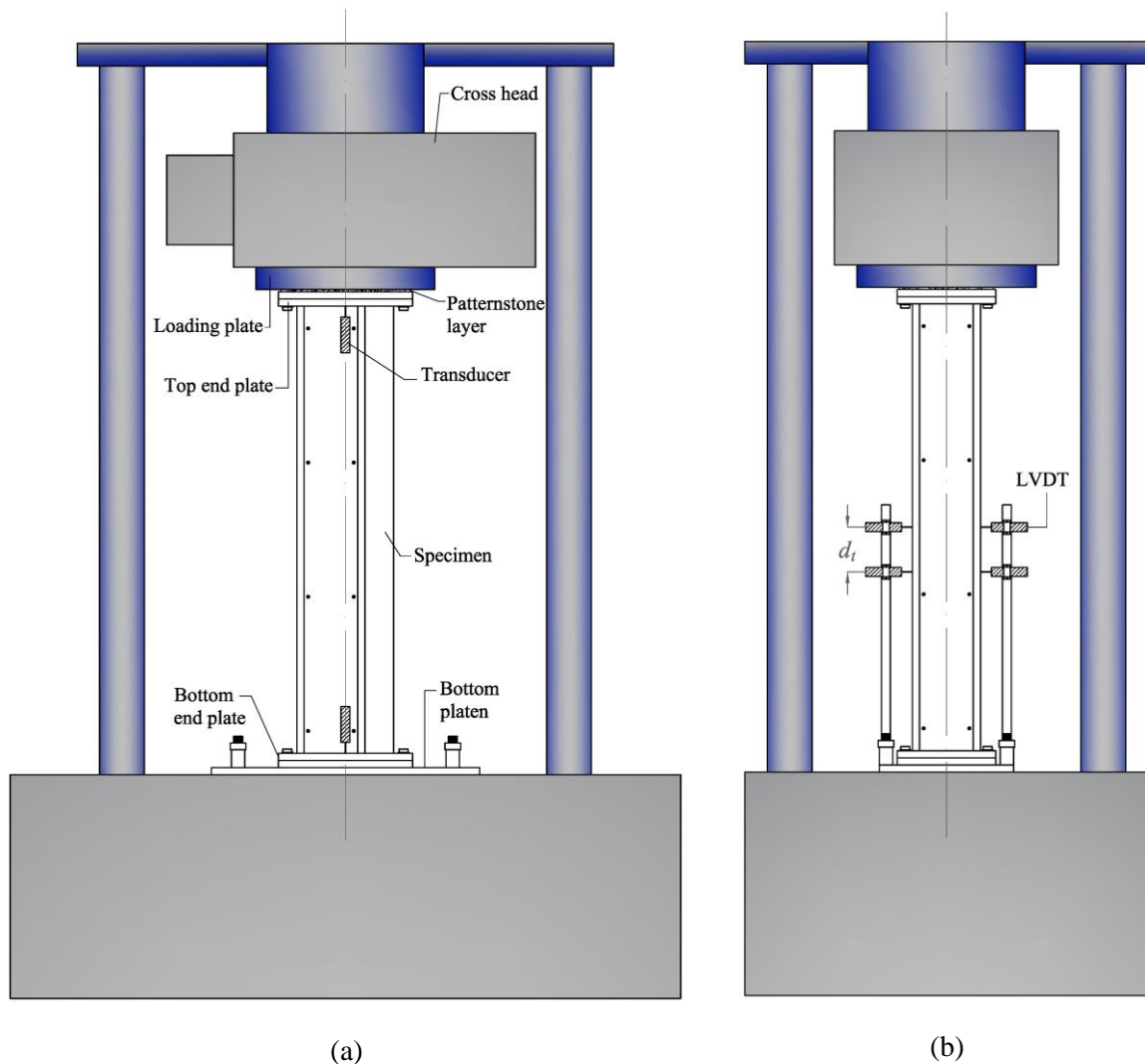
Figure 4-27: Compression test set-up: (a) front view, (b) side view

To monitor local and distortional deformations, LVDTs (Linear Variable Displacement Transducers) were mounted on each specimen in the middle of the web and at the junctions of the flanges and lips at two different locations along the member length. The arrangements of transducers around each cross-section and along the member length are presented in Figure 4-28 and Figure 4-27(b), respectively. The longitudinal locations were at the mid-height of the specimens and the distance d_t down from the mid-height. This distance (d_t) was chosen as 100 mm for the specimens of Series C64 such that it was less than the local buckling half-

wavelength of the section and provided adequate room for installation. For the specimens of Series C120, this distance was 250 mm, which corresponded to the half-wavelength of the second distortional mode to capture the out-of-plane behaviour of the section in the longitudinal direction. Three and five LVDTs were respectively placed around the channel sections and the built-up sections at each longitudinal location, as shown in Figure 4-28. The clearance of transducers from the edge of the section was 10 mm; however, for the two specimens with fitted strain gauges, the transducers were mounted at a distance of 15 mm to allow the strain gauges to be attached at the flange-lip junctions. In addition, four transducers were installed on the end plates according to Figure 4-27(a), i.e. two on the bottom end plate and two on the top end plate, close to the centroid of the cross-section to measure the actual axial shortening of the specimens.
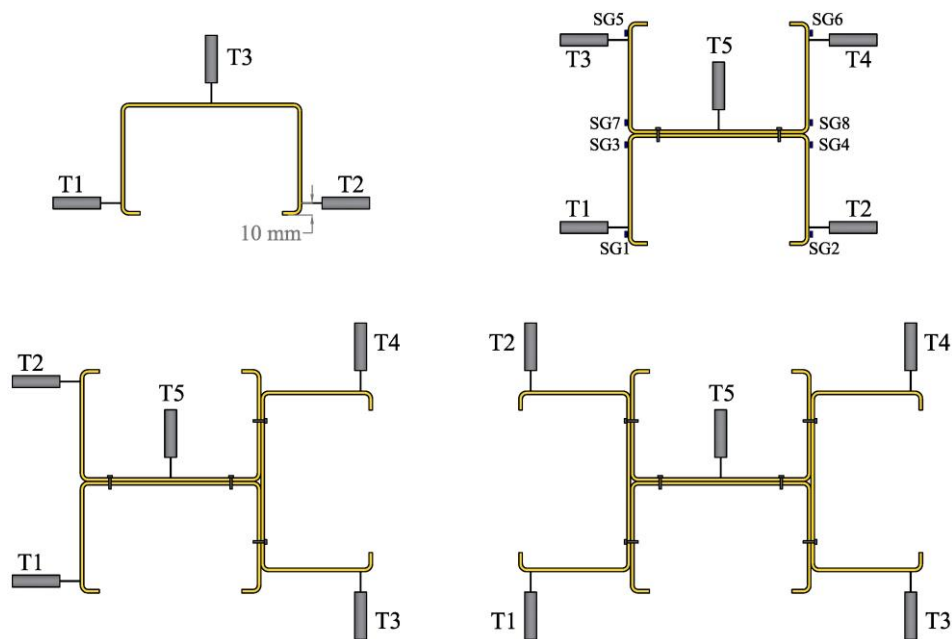
Figure 4-28: Location of LVDTs and strain gauges around the cross-sections

Once the transducers were set, the displacement-controlled loading was applied to all specimens using a DARTEC testing machine with a 2000 kN capacity. The loading rate was 0.2 mm/min except for specimen 4C120-900-1, which had a rate of 0.5 mm/min. Similar to the tensile coupon tests, the loading was paused regularly for two minutes to obtain the static load. The applied load and transducer readings were recorded continuously by a data acquisition system. The details of the actual test set-up are shown in Figure 4-29.
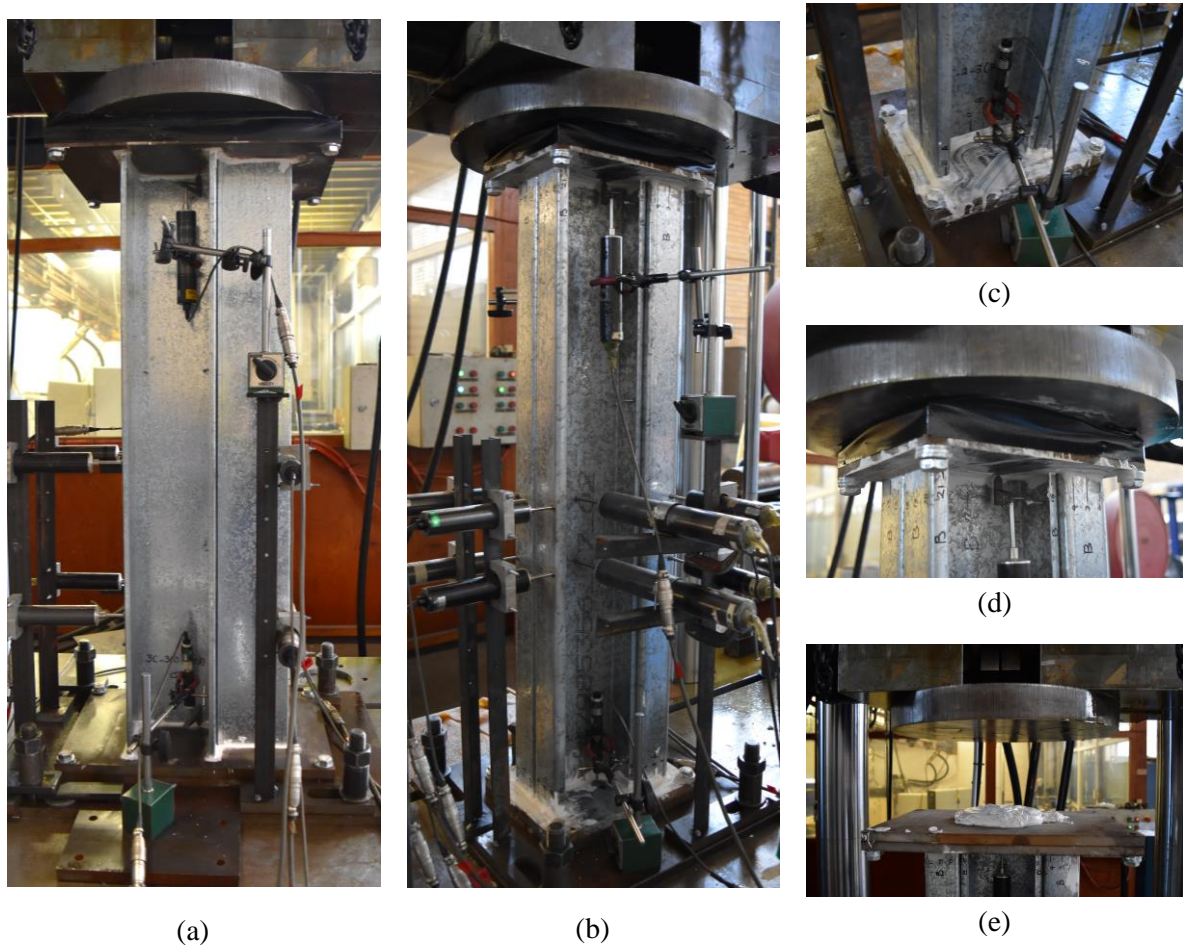
Figure 4-29: Details of the test set-up: (a) Series C120, (b) Series C64, (c) mounted transducers on the bottom end plate, (d) mounted transducers on the top end plate and (e) Patternstone layer between the loading plate and the top end plate before lowering cross-head

4.7.3   Test results

The results of the experimental tests on different built-up section assemblies are provided in the following subsections in terms of the constituent section and the prevalent buckling mode. First, the results are shown for test series C120, for which the distortional buckling mode is the critical mode, and the results for test series C64 with predominant local buckling mode are presented next.

4.7.3.1 Test series C120

As observed from the tests, all the specimens of Series C120 underwent distortional buckling before the peak load and localised failure in the post-peak phase. Figure 4-30 shows the

transducer measurements at the mid-height of specimens, denoted by 'M', and at the distance of 250 mm below the mid-height, denoted by 'D', for one of the specimens of each cross-section tested, as representative examples. The sign convention for displacements and the arrangement of transducers around each cross-section are included in the graphs with a detailed description in Section 4.7.2. The complete set of load vs. transducer displacement graphs for test Series C120 is presented in Appendix D.

According to the graphs, significant distortional buckling occurred during testing of all cross-sections with a typical maximum displacement of 20 mm. Following the onset of distortional buckling, large deformations developed in the flanges at the M-location for the single section and at the D-location, mainly for the built-up sections. These large distortional deformations provoked a reversal in the direction of flange movement at the M-location for built-up sections. This result also highlights the change of distortional buckling shape from a single half-wave curve in a channel section, corresponding to the first mode, to an antisymmetric double half-wave curve in built-up sections, corresponding to the second distortional buckling mode, particularly in back-to-back I-sections, as indicated in Figure 4-31. Another observation is that the flanges of each lipped channel section were distorted in the same direction, i.e. inwards or outwards, with almost the same pattern for all different built-up assemblies except for specimen 4C120-100-1, which will be discussed later in this Section.
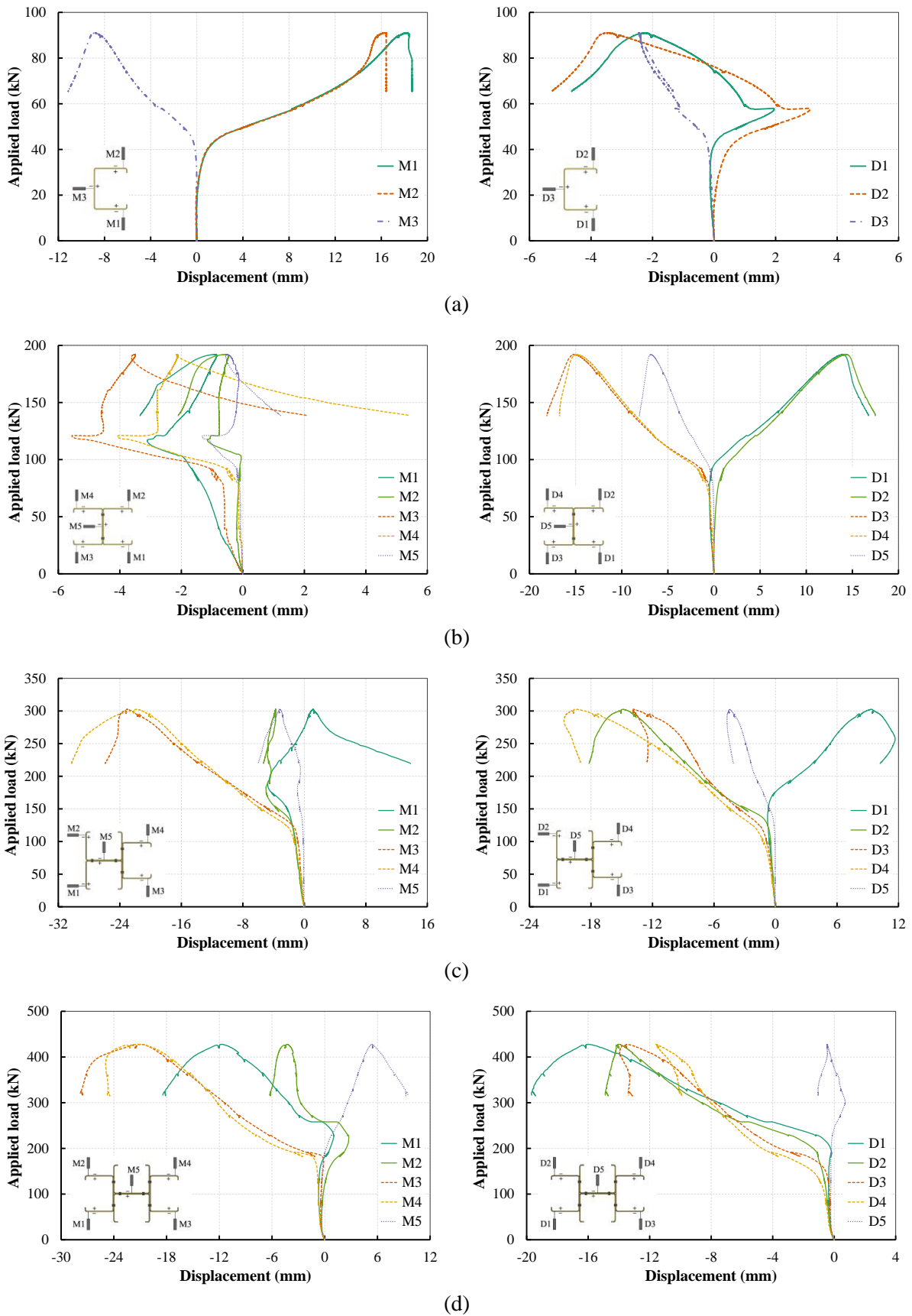
Figure 4-30: Transducers data at mid-height (M) and 250 mm down from the mid-height (D) for specimen (a) 1C120-2, (b) 2C120-300-2, (c) 3C120-300-2 and (d) 4C120-300-1

(a)   (b)   (c)
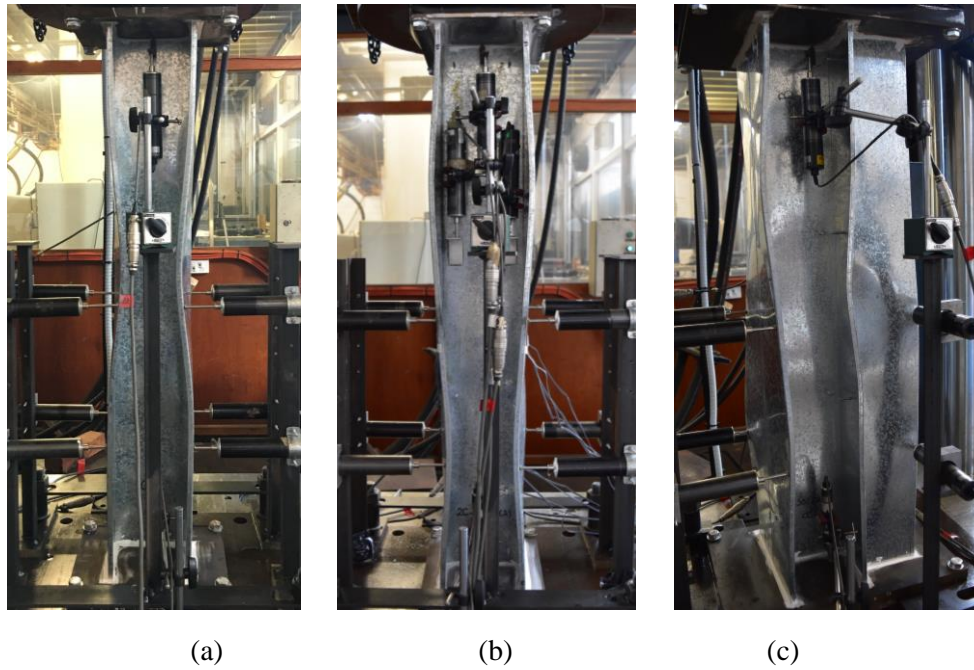
Figure 4-31: Distortional buckling shape (following the occurrence of large deformations) of specimen (a) 1C120-2, (b) 2C120-300-2 and (c) 3C120-300-2

The measured data of the four transducers mounted on the top and bottom end plates are presented in Figure 4-32(a) for specimen 2C120-100-1. As can be seen, the recorded data of the two bottom transducers, i.e. B1 and B2, and the two top transducers, i.e. T1 and T2, are virtually identical, which indicates that the transducers on both sides of the cross-section were close enough to the centroid to capture the actual top and bottom displacements. Since the top and bottom transducers measured displacements in the opposite direction, the actual axial shortening of the specimen along the centroidal line was obtained from

$$\text{Axial shortening} = -(\delta_{T1} + \delta_{T2})/2 - (\delta_{B1} + \delta_{B2})/2 \qquad (4.8)$$

Figure 4-32(b) presents the load versus axial shortening curves for 2C120-100-1 utilising the transducers data, Eq.(4.8), and the recorded data from the stroke of the testing machine. The stroke data gives an initially nonlinear response curve, whereas the initial relationship obtained from Eq.(4.8) is almost linear. As a common practice, the initial portion of the curve before the onset of elastic buckling is adjusted to a line with a slope of the axial stiffness of the column, *EA/L*, as illustrated in Figure 4-32(b). The adjusted curve is shown to be very similar to the

curve obtained from the transducers data, and the latter approach has thus been used hereafter for presenting the load vs. axial shortening curves.

(a)   (b)
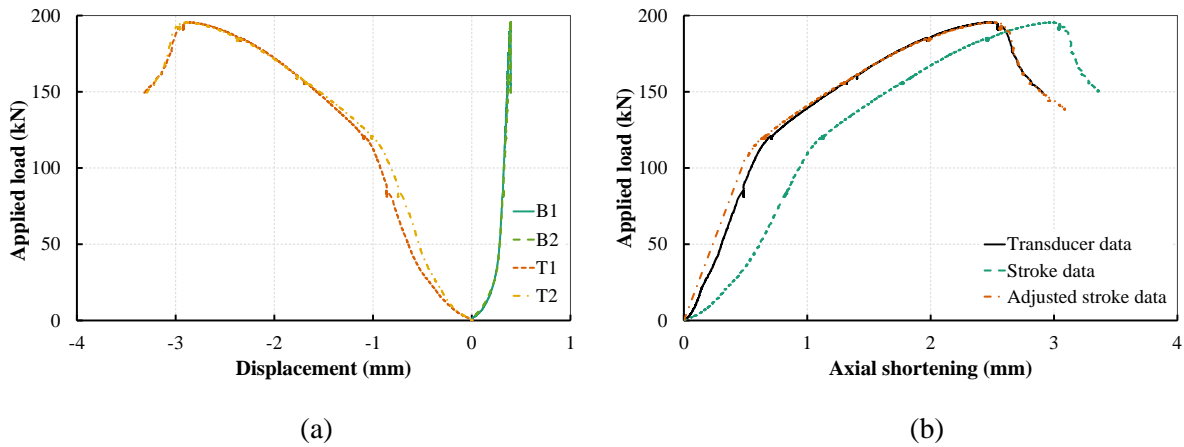
Figure 4-32: Specimen 2C120-100-1: (a) Load vs. displacement measured by transducers mounted on the top and bottom end plates, (b) Load vs. axial shortening curves

The nonlinear capacity curves for all specimens in this test series are presented in Figure 4-33. The recorded load of the single channel sections (1C120) is multiplied by the number of channel sections (n) included in each section assembly, and the adjusted load-displacement curve is included in the figures for comparison with the results of built-up sections. A summary of test results for this series is also provided in Table 4-9, which lists the elastic stiffness, the conformal web buckling observation, the static ultimate capacity of the section (P_u) and the capacity enhancement ratio.

According to the results, the ultimate load capacity of the built-up sections increases as the screw spacing decreases. The increase in the ultimate capacity may be decomposed into two components; one due to the end connectivity and one due to the intermediate fasteners. The former can be identified as the enhancement of the ultimate capacity of the built-up section with only end fasteners ($P_u|_{s=0.9L}$) with respect to multiple single sections without interactions (nP_{u1}), which includes the effect of contact initiated between the constituent plates and a potential shift of the buckling mode towards the higher modes in one or multiple individual cross-sections. The latter is responsible for the additional enhancement of the ultimate capacity ($\Delta P_{us} = P_u - P_u|_{s=0.9L}$) with the introduction of intermediate fasteners and the reduction in fastener spacing.
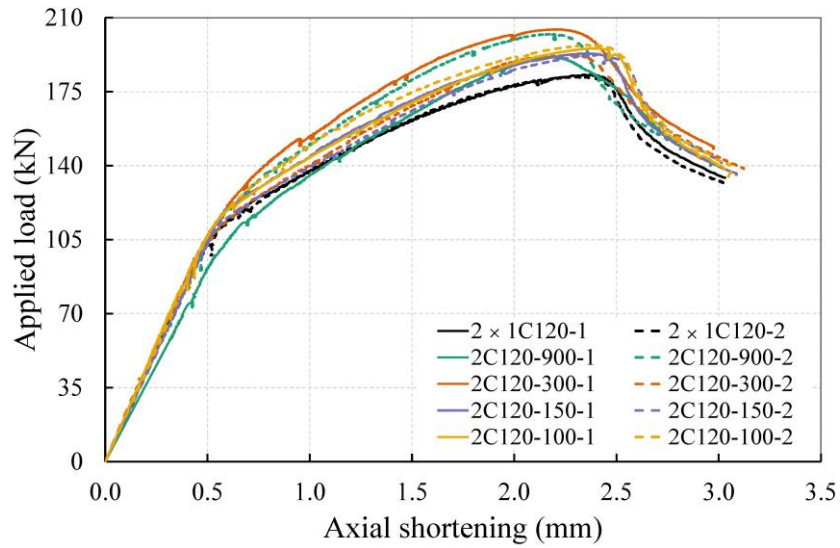
(a)
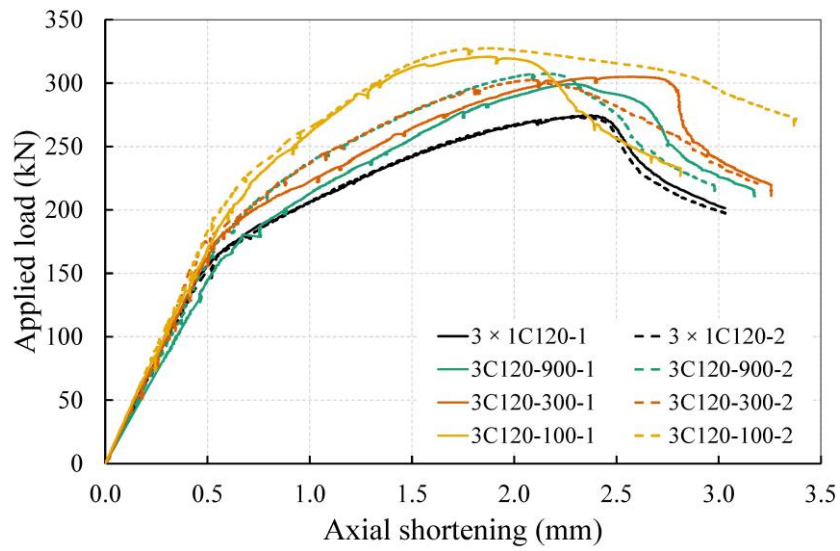
(b)
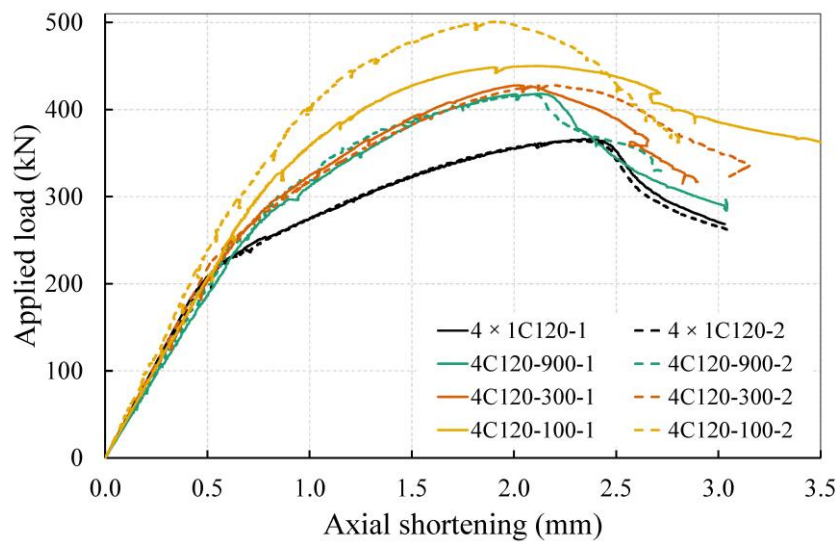
(c)

Figure 4-33: Load vs. Axial shortening curves of test series (a) 2C120, (b) 3C120 and (c) 4C120

Table 4-9: Summary of compression test results of Series C120

Specimen	Stiffness (kN/mm)	Conformal web buckling*	P_u (kN)	$\Delta P_{u1}/nP_{u1}$ (%)	$\Delta P_{us}/P_u\vert_{s=0.9L}$** (%)
1C120-1	114.2	-	90.3	-	-
1C120-2	120.9	-	89.9	-	-
2C120-900-1	180.4	No	188.9	4.8	-
2C120-900-2	206.2	No	199.6	10.8	-
2C120-300-1	217.6	Yes	202.2	12.2	7.0
2C120-300-2	220.1	Yes	190.4	5.7	0.8
2C120-150-1	207.1	Yes	190.8	5.9	1.0
2C120-150-2	205.5	Yes	191.2	6.1	1.2
2C120-100-1	223.3	Yes	193.0	7.1	2.2
2C120-100-2	213.9	Yes	195.2	8.3	3.3
3C120-900-1	285.6	No	295.9	9.5	-
3C120-900-2	312.2	No	303.7	12.4	-
3C120-300-1	321.6	Yes	300.7	11.2	1.6
3C120-300-2	352.8	Yes	299.6	10.8	1.3
3C120-100-1	336.7	Yes	317.2	17.4	7.2
3C120-100-2	360.5	Yes	322.8	19.4	9.1
4C120-900-1	380.8	No	411.2	14.1	-
4C120-900-2	393.8	No	410.7	14.0	-
4C120-300-1	407.8	Yes	420.3	16.6	2.3
4C120-300-2	436.1	Yes	422.1	17.1	2.8
4C120-100-1	411.7	Yes	442.9	22.9	7.8
4C120-100-2	470.9	Yes	492.1	36.5	19.8

* Conformal web buckling of the two back-to-back connected sections in each built-up assembly

** This capacity enhancement ratio is calculated with respect to the minimum capacity of the two nominally identical specimens with a fastener spacing of 0.9L.

By increasing the number of sections included in a built-up section (2C, 3C, 4C), the contribution of end connectivity to the enhancement of the built-up section capacity increases (by 4.8%, 9.5%, 14%), and the intermediate fastener contribution varies to a lesser extent for the same fastener spacing between built-up assemblies comprising of three and four channel sections (excluding the specimen 4C120-100-2).

The results also accentuate the effect of screw spacing on the initial stiffness and the conformity of the buckling of connected webs in each built-up assembly. From general observation, the initial stiffness of the built-up section increases slightly as the screw spacing decreases and tends towards the initial stiffness of the single section multiplied by the number of channel sections included in each section assembly. The conformal buckling of the connected webs was sought during the test and is reported in Table 4-9. For all the specimens with a fastener spacing of 0.3L or less, the conformal web buckling was achieved, suggesting that a minimum fastener spacing is required to form a built-up section by connecting single sections with predominant distortional buckling mode.

The two nominally identical specimens gave very close results in most cases with a difference of less than 2.5%, except for trials 2C120-900, 2C120-300 and 4C120-100, where the difference is 5.7%, 6.2% and 11.1%, respectively. The higher capacity of 2C120-900-2 and 2C120-300-1 is partially inherited from their cross-sectional dimensions, resulting in a higher elastic buckling load than other tested back-to-back cross-sections, as reported later in Section 4.8.1. The lower capacity of specimen 2C120-900-1 can be explained by the fact that its constituent sections buckled and failed in independent modes, with one in the first mode (f_{cr} = 85.9 MPa) and the other in the second mode (f_{cr} = 89.2 MPa), as shown in Figure 4-34(a). In contrast, both lipped channel sections in the nominally identical specimen 2C120-900-2 buckled in the second mode, as illustrated in Figure 4-34(b). Furthermore, the considerable discrepancy between the capacities of the nominally identical 4C120-100 specimens is related to the formation of local buckling in the back-to-back connected sections of 4C120-100-2, as clearly indicated in Figure 4-35(b). As can be seen, distortional buckling occurred in the back-to-back connected sections of 4C120-100-1 with an outward movement of flanges at the mid-height of the column, whereas local half-wavelengths formed between the fastener pairs on the web and restrained flanges of 4C120-100-2. The restraint provisions in the web and flanges of the back-to-back connected cross-sections matched the local half-wavelength of the section (as reported in Section 4.2), which, together with the pattern of local imperfections along the length of the member, might have triggered the higher mode in 4C120-100-2. The recorded transducer

data at the mid-height of the sections are also included in Figure 4-35, from which the results of transducer M5 further confirm the formation of local buckling in the web of 4C120-100-2 with a higher elastic buckling load compared to 4C120-100-1.

(a)   (b)
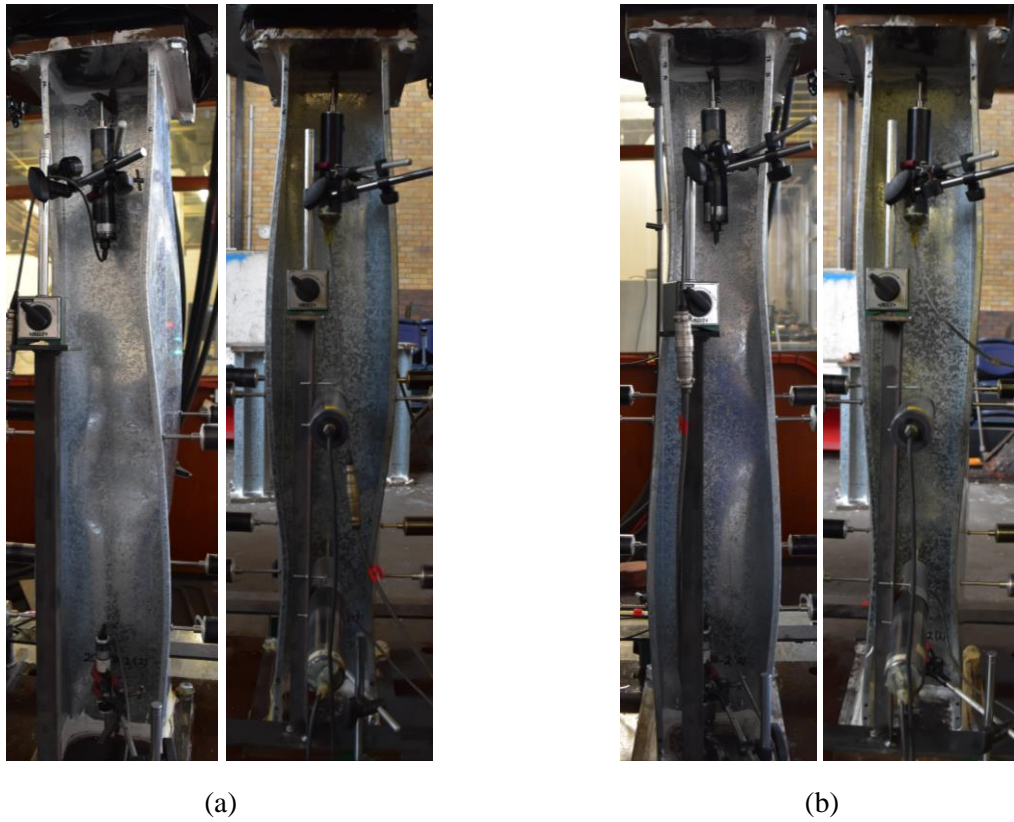
Figure 4-34: Front and back views of the buckling mode shape of specimen (a) 2C120-900-1 and (b) 2C120-900-2 during testing
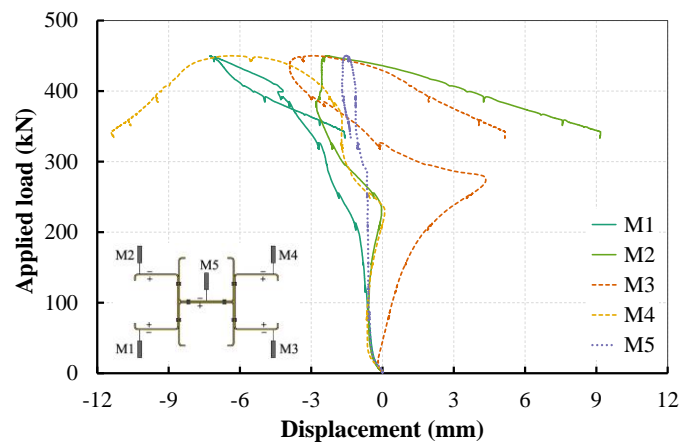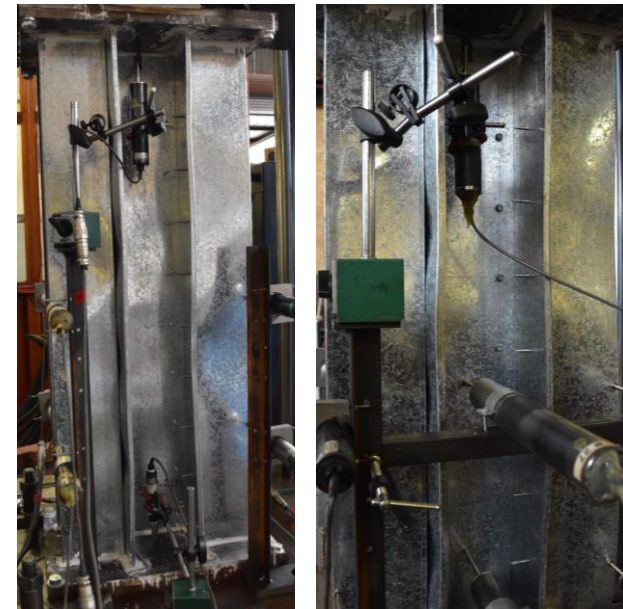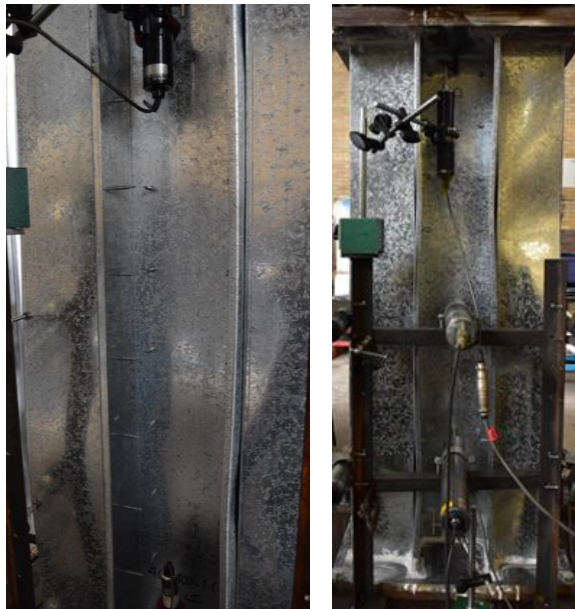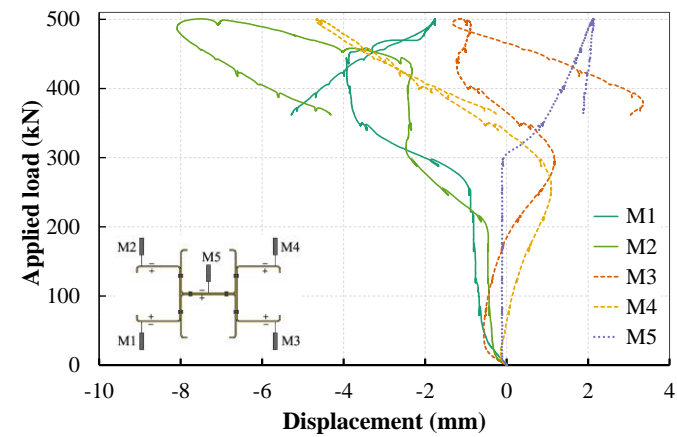
Figure 4-35: Buckling behaviour of specimens, (a) 4C120-100-1 and (b) 4C120-100-2 during testing

Another parameter assessed was the evolution of the longitudinal strain in the constituent sections over the course of loading using the strain gauges installed on back-to-back I-sections per Figure 4-28. The load-strain curves obtained from the reading of eight strain gauges fitted on the back-to-back built-up sections are presented in Figure 4-36. The results show that all the individual cross-sections were subjected to compression strain from the start of loading, and the strains were developed uniformly in the entire built-up cross-section, which verifies the effectiveness of the adopted support conditions.

(a)

(b)
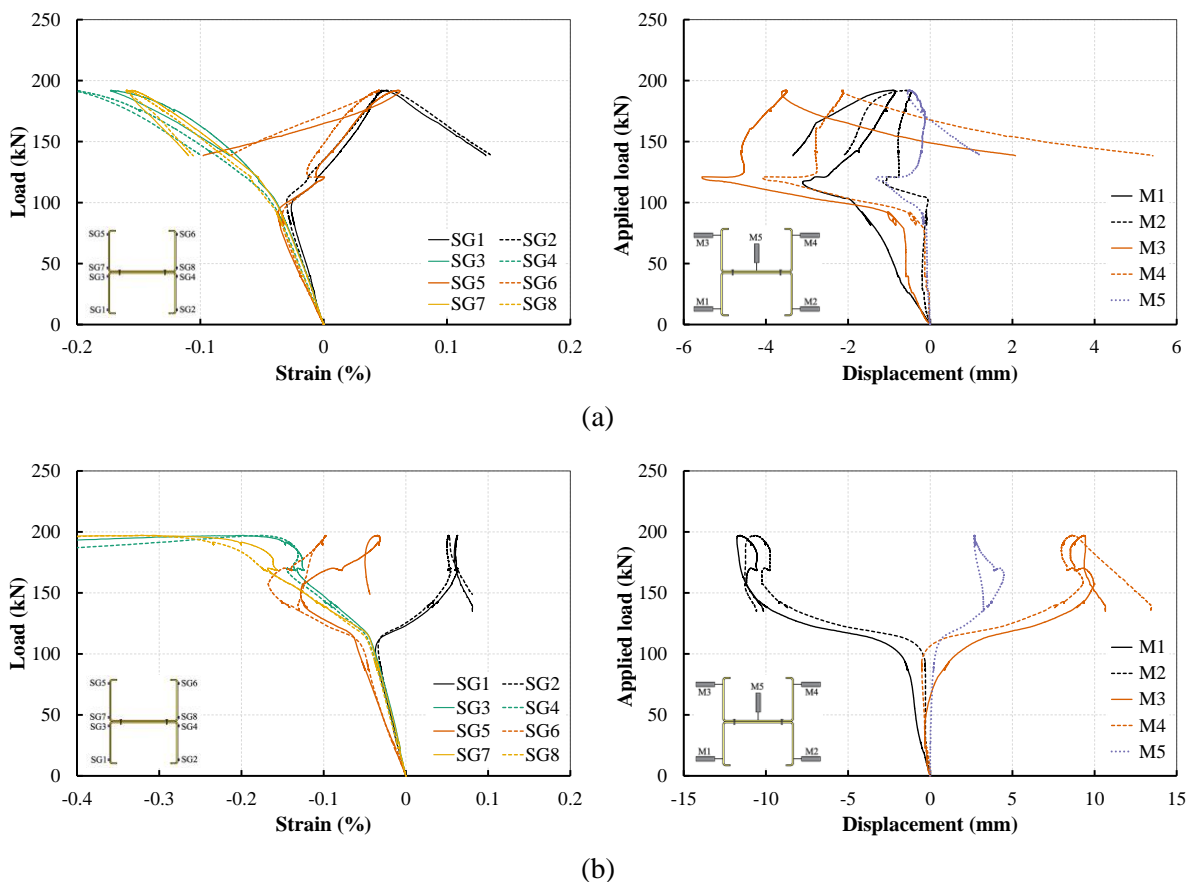
Figure 4-36: Load vs. strain curves and load vs. transducers displacement at the mid-height of test specimen (a) 2C120-300-2 and (b) 2C120-100-2

Furthermore, the sudden change in the slope of the load-strain curves obtained at the junction of the flange and lips (i.e. SG1, SG2, SG5 and SG6) indicates the onset of distortional buckling, which can be utilised for determining the elastic buckling load of the section as will be further explained in Section 4.8.1. After the occurrence of elastic buckling and during the loading stage, some parts of the cross-sections were subjected to compressive stresses, while the

remaining parts close to the flange-lip junctions were under tensile stresses. By comparing the results obtained from strain gauges to the movement of the flanges from transducers data, it can be concluded that flanges with outward movement (depicted by negative displacements in the recorded transducers data in Figure 4-36) started to develop tensile stresses after the onset of elastic buckling, while those with inward movement remained in a compression stress state, as depicted in Figure 4-36(b).

4.7.3.2   Test series C64

In contrast to Series C120 with distortional failure mode, the local-distortional interactive buckling was prevalent for the specimens of Series C64 from general test observations. Figure 4-37 presents the transducer measurements at the mid-height and at 100 mm below it for one of the specimens of each cross-section assembly tested as an indicative example. The sign convention for the measured displacements of web and flanges is similar to that of test series C120, as shown in each graph. The complete set of load vs. transducers displacement curves for test series C64 is provided in Appendix D. The buckling behaviour of two representative built-up specimens during testing is also presented in Figure 4-38 and Figure 4-39.

An evident local elastic buckling mode was observed in all cross-sections tested, as indicated by a sharp change in the slope of the load-displacement curves of transducers M3 and D3 for a single section and transducers M5 and D5 for built-up sections mounted on the web. At this stage, the deformations developed in the flanges of all cross-sections were negligible, see Figure 4-38(a) and Figure 4-39(a). However, as the axial load increased, a change occurred in the slope of the load-displacement curves of the transducers mounted on the flanges, which signals the onset of distortional buckling in the section. Following that, noticeable distortional deformations developed in the flanges of all cross-sections before reaching the peak load, as shown in Figure 4-38(b) and Figure 4-39(b), suggesting the occurrence of failure through the interaction of local and distortional buckling modes. Eventually, the deformations localised somewhere along the length of the column in the post-peak regime, and a flip-disc plastic

mechanism formed in the specimens, as clearly indicated in Figure 4-38(c) and Figure 4-39(c). The local plastic mechanism observed in testing will be discussed in detail later in Section 4.8.2.

(a)

(b)

(c)
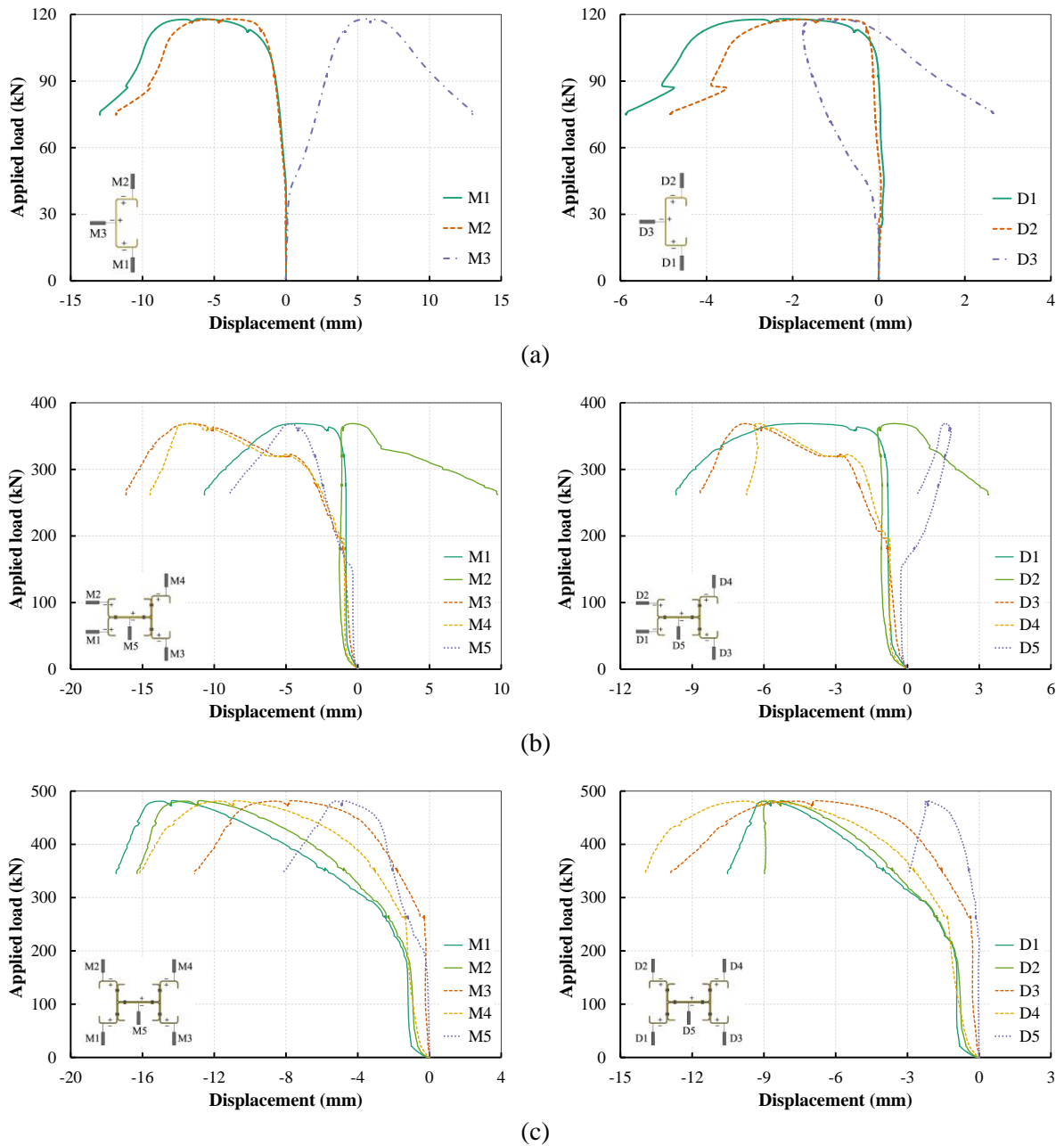
Figure 4-37: Transducers data at mid-height (M) and 100 mm down the mid-height (D) for specimen (a) 1C64-2, (b) 3C64-300-1 and (c) 4C64-300-1

<center>(a)   (b)   (c)</center>
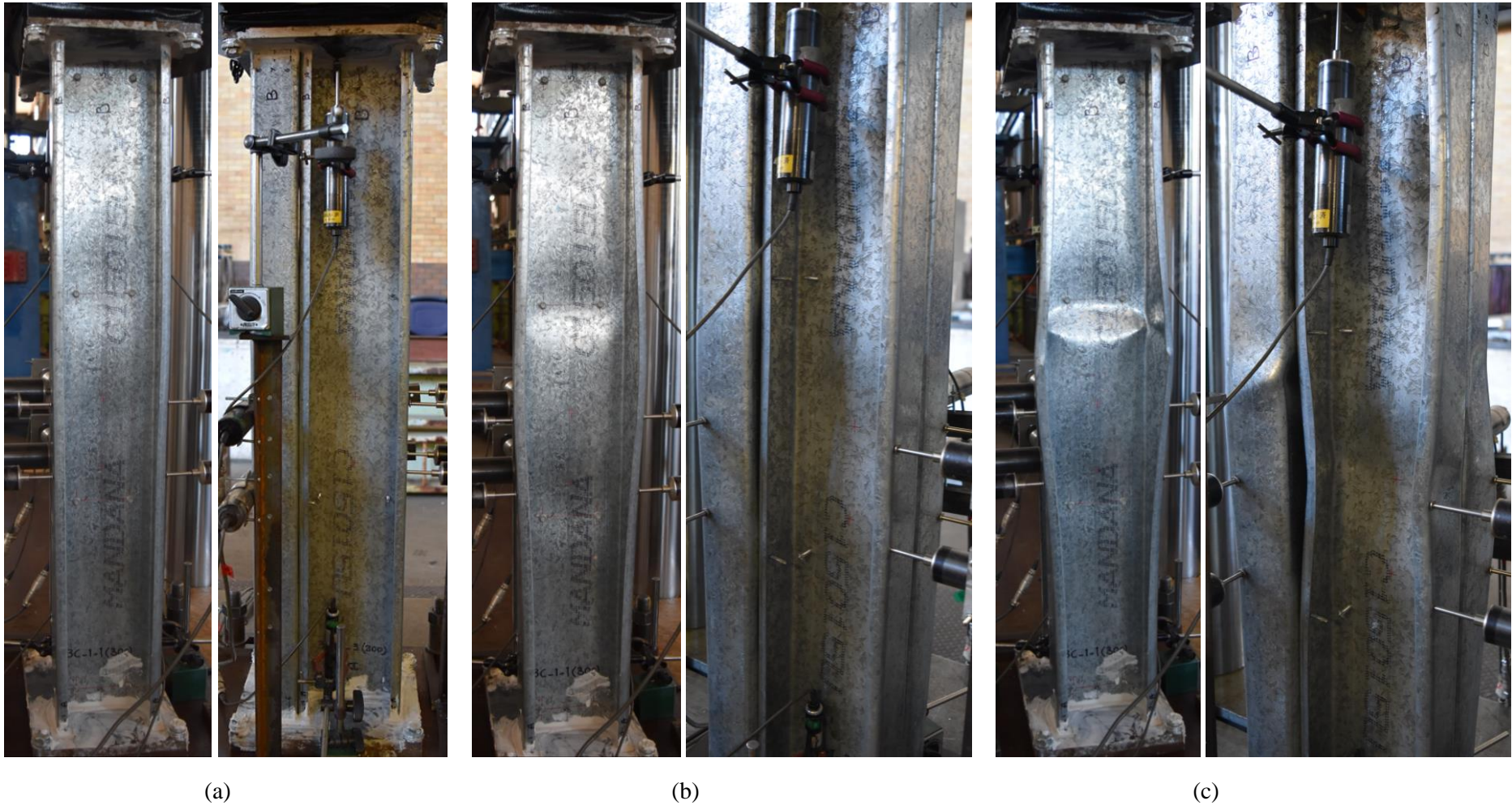
Figure 4-38: Buckling deformations of specimen 3C64-300-1 at (a) the onset of local buckling, (b) peak load and (c) post peak

(a)   (b)   (c)
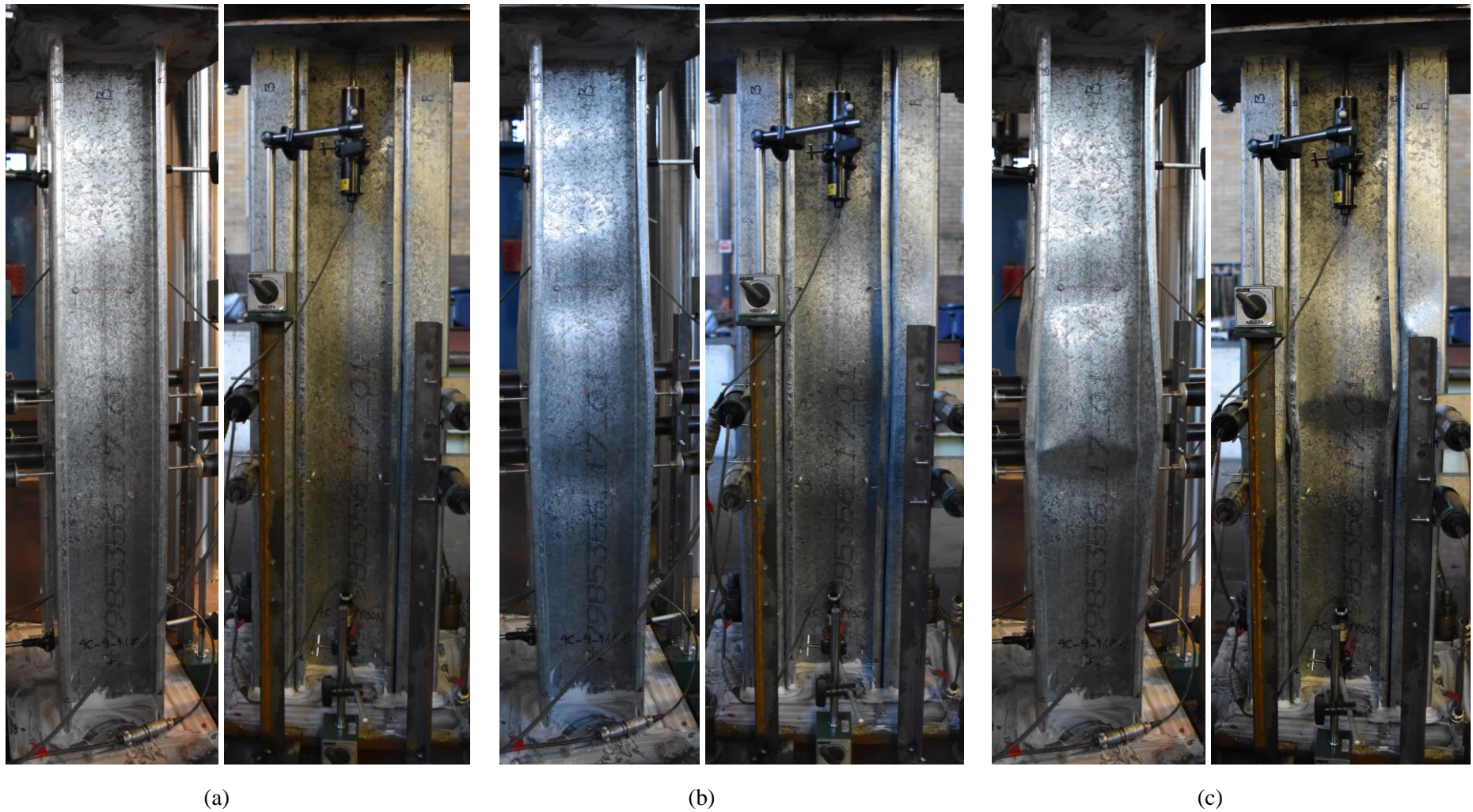
Figure 4-39: Buckling deformations of specimen 4C64-300-1 at (a) the onset of local buckling, (b) peak load and (c) post peak

Figure 4-40(a) presents the measurements of top and bottom transducers for specimen 3C64-100-2, and a comparison between the load vs. axial shortening curves is provided in Figure 4-40(b) using the different techniques explained in Section 4.7.3.1. Similar to Series C120, the axial shortening calculated by Eq.(4.8) is utilised to plot representative capacity curves for different section assemblies, as shown in Figure 4-41. A summary of test results is also provided in Table 4-10, including the initial stiffness, the conformal web buckling observation, the static ultimate capacity of the section (P_u), and the capacity enhancement ratio.

| (a) | (b) |
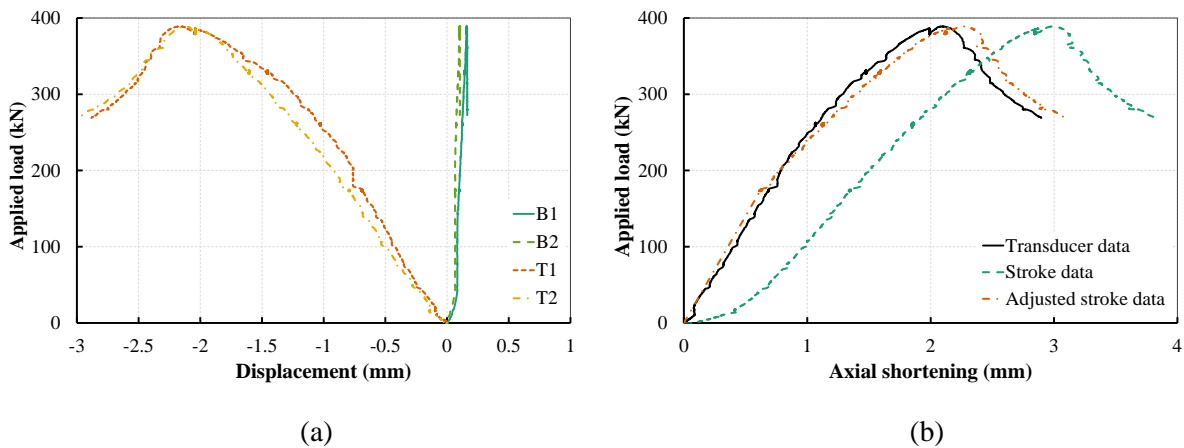
Figure 4-40: Specimen 3C64-100-2: (a) Load vs. displacement measured by transducers mounted on the top and bottom end plates, (b) Load vs. axial shortening curves

For assessing the enhancement of ultimate capacity due to intermediate fasteners, a reference capacity curve is provided in the figures that are established by multiplying the recorded load of the single channel sections (1C64) by the number of channel sections included in each section assembly. Comparing the curves of single sections to that of trials 3C64-900 and 4C64-900, which include no intermediate connections, a marginal increase in capacity and a slight decrease in initial stiffness is evident. As also highlighted in Table 4-10, this result contrasts Series C120, which showed a considerable increase in the capacity of specimens with no intermediate fastener ($P_u|_{s=0.9L}$). Since all the sections followed the first local buckling mode shape, it is reasonably justifiable that the capacity was not influenced by the end connectivity and the resultant contact between the sections.

The addition of evenly-spaced intermediate screws did not yield a significant improvement in the ultimate capacity of the built-up sections ($\Delta P_{u1} / nP_{u1}$), which is in line with the observed enhancement in the capacities of Series C120 due to intermediate fasteners ($\Delta P_{u1} / P_u|_{s=0.9L}$). Lastly, the results for the nominally identical repetitions of each built-up assembly are generally consistent, with a less than 2% difference.
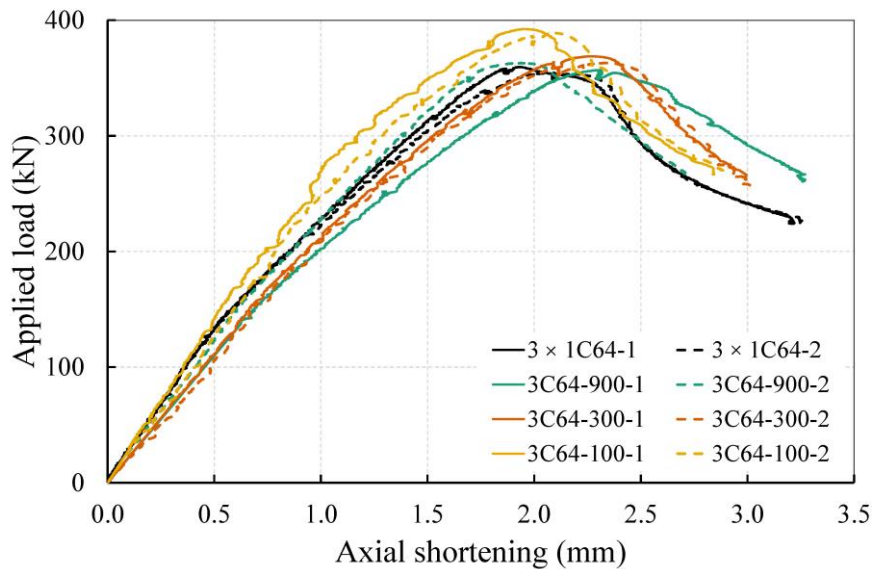
(a)
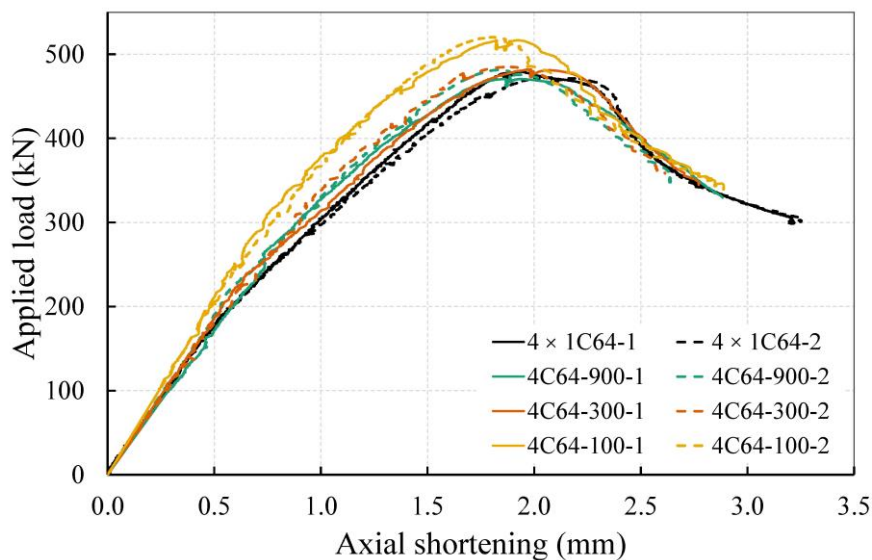
(b)

Figure 4-41: Load vs. Axial shortening curves of test series (a) 3C64, (b) 4C64

Table 4-10: Summary of compression test results of Series C64

Specimen	Stiffness (kN/mm)	P_u (kN)	$\Delta P_{u1} / nP_{u1}$ (%)
1C64-1	89.1	117.9	-
1C64-2	90.4	116.4	-
3C64-900-1	219.8	352.0	0.2
3C64-900-2	246.9	358.5	2.0
3C64-300-1	224.2	362.4	3.1
3C64-300-2	213.4	356.3	1.4
3C64-100-1	283.1	386.8	10.1
3C64-100-2	271.1	381.0	8.4
4C64-900-1	333.7	468.8	0.0
4C64-900-2	375.0	474.6	1.3
4C64-300-1	371.3	477.9	2.0
4C64-300-2	369.5	477.5	1.9
4C64-100-1	417.1	505.6	7.9
4C64-100-2	423.2	513.1	9.5

The progression of longitudinal strain was evaluated at the centre of the web of individual sections at the mid-height location of built-up specimen 4C64-100-2, and the results are shown in Figure 4-42.
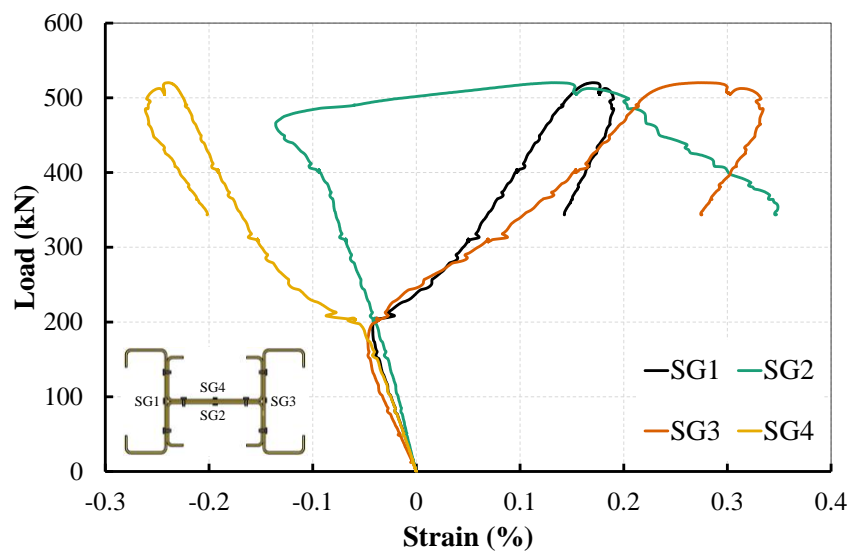
Figure 4-42: Load vs. strain curves at the mid-height of test specimen 4C64-100-2

Uniform compression was developed in all individual cross-sections over the elastic regime, which as for similar observations for Series C120, confirms the ability of the end conditions and loading procedure employed in the testing to provide uniformly applied strain. As the load increased, local buckling occurred in the web of each constituent section which caused a sharp change in the slope of the load-strain curves except for SG2. This strain gauge did not capture the onset of local buckling due to its slight offset from the centre of the web for accommodating the installation of transducer M5.

4.8   DISCUSSION

4.8.1   *Elastic buckling load*

The first discussion on the experimental results is dedicated to the elastic buckling load level and its comparison with the prediction of the Compound Strip Method. The critical buckling load of the constituent plates or the overall section can be evaluated from the interpretation of load and displacement or strain measurements by various direct methods, a summary of which can be found in [192]. Most of these methods rely on the axial strain data either in differential or average forms, which require strain gauge installation and measurements. A simple yet effective approach is plotting the load versus the average axial strain, where the elastic buckling point can be approximated by the onset of nonlinearity as a sharp change in the slope of the curve. The vertical tangent method is a more precise and algorithmic variant of the mean strain measure. In this method, the graph is plotted with a spline curve approximating the measurements, and the critical buckling load is obtained from the intercept of the plotted curve and the vertical line tangent to the curve. Where no axial strain readings are available, the axial shortening may be used to track the onset of elastic buckling from the nonlinearity in the load-displacement curve. Despite being less reliable than the mean strain method, this approach can still yield satisfactory approximations. Following these, the data from strain gauge measurements in the 2C120-300-2 and 2C120-100-2 test specimens are post-processed to evaluate the onset of elastic buckling from the direct method, whereas the load vs. axial

shortening curve is used for the rest of the test specimens of Series C120. This method is denoted by the M-1 technique in this study. Since there was no discernible change in the slope of load-displacement curves of test series C64 after the onset of local buckling (see Figure 4-41), the elastic buckling load cannot be calculated from this method.

Some of the direct interpretation methods rely on lateral displacement measurements at peak locations. One commonly used method is the load versus deflection squared ($P\text{-}\delta^2$) approach [193], which is expected to yield satisfactory results that are typically lower bounds to the critical buckling load [58, 194]. This method requires recording the transverse buckling displacements of one (i.e., the critical) or a number of plate elements of the section at typically the location expected to have the maximum displacement. Then, the load versus buckling displacement squared is plotted, in which the intercept of the tangent line to the post-buckling regime with the load axis is taken as the critical load. When the buckling displacements are measured for both flanges and web, either the buckling load for the critical element is reported, or the values for each element are averaged over the section. The former method is usually more popular, giving the bucking load of that particular element, whereas, in the latter, an average buckling load is obtained for the cross-section.

Based on the measurements from the LVDTs installed on the test specimens, the critical buckling loads for flange and web elements are evaluated using this technique, referred to as the M-2 method. The buckling loads of the web and flanges are averaged to determine the elastic buckling load of the section in the distortional mode. In contrast, only the web is used to determine the local buckling mode as the transducer arrangement in the flanges was not suitable for recording local buckling deformations. However, the average buckling load of the flanges is also included to indicate when the local-distortional interaction occurred. The direct evaluations of the critical buckling stress (f_{cr}) using these methods are listed in Table 4-11 for test series C120 and C64 and compared with the predictions of the Compound Strip Method as the semi-analytical solution to the elastic buckling problem.

Table 4-11: Experimental and numerical elastic buckling stresses for built-up test sections

Specimen	Experimental				CSM	FEM	
	Web (min)	Flange (average)	Section (M-2)	Section (M-1)		Fastener (FE-1)	Solid (FE-2)
2C120-900-1	81.3	77.8	79.6	88.3	86.4	86.4	86.4
2C120-900-2	100.0	79.5	89.8	99.2	92.9	92.6	92.6
2C120-300-1	96.8	74.9	85.8	97.7	92.2	91.0	92.5
2C120-300-2	81.7	82.4	82.1	90.1	90.5	89.2	90.9
2C120-150-1	94.0	88.6	91.3	92.0	87.9	86.6	89.7
2C120-150-2	92.0	88.6	90.3	92.4	88.5	87.7	91.1
2C120-100-1	93.7	86.7	90.2	94.1	89.2	86.8	91.9
2C120-100-2	97.2	91.8	94.5	95.4	88.9	86.5	91.8
3C120-900-1	95.0	90.8	92.9	92.8	88.6	88.6	88.6
3C120-900-2	94.0	89.8	91.9	92.6	86.7	86.7	86.8
3C120-300-1	92.5	88.5	90.5	94.5	90.6	90.7	92.6
3C120-300-2	94.5	84.7	89.6	94.5	92.8	92.8	94.4
3C120-100-1	99.5	91.3	95.4	103.9	99.1	98.8	102.3
3C120-100-2	102.7	89.0	95.8	104.3	101.1	100.8	103.8
4C120-900-1	88.9	73.8	81.3	90.6	88.8	88.9	90.2
4C120-900-2	103.8	83.8	93.8	94.7	88.3	88.5	92.8
4C120-300-1	94.3	84.3	89.3	96.6	92.6	92.7	95.2
4C120-300-2	95.4	83.7	89.6	96.9	92.0	92.1	94.0
4C120-100-1	113.0	90.8	101.9	105.1	101.7	101.6	105.6
4C120-100-2	131.5	95.1	113.3	117.9	102.2	102.2	109.3
3C64-900-1	104.9	121.5	104.9	-	104.4	103.9	104.1
3C64-900-2	105.1	109.6	105.1	-	104.1	103.6	103.8
3C64-300-1	106.2	118.6	106.2	-	104.8	104.2	105.0
3C64-300-2	104.8	128.6	104.8	-	105.0	104.4	105.2
3C64-100-1	118.6	141.9	118.6	-	107.0	106.4	112.3
3C64-100-2	114.6	135.8	114.6	-	107.3	106.7	112.5
4C64-900-1	107.1	121.7	107.1	-	104.3	103.9	104.1
4C64-900-2	105.6	116.7	105.6	-	104.4	103.9	104.1
4C64-300-1	106.9	123.4	106.9	-	104.8	104.3	105.1
4C64-300-2	107.6	120.5	107.6	-	104.7	104.2	105.0
4C64-100-1	110.4	184.3	110.4	-	106.4	105.7	111.8
4C64-100-2	112.0	185.3	112.0	-	106.7	107.8	113.9

It is noted that the results correspond to the buckling mode shape that formed in the test specimens and do not necessarily reflect the results of the first buckling mode. For a comprehensive comparison, the finite element solutions are also provided that correspond to the elastic eigenvalue solution for two different fastener modelling approaches. In the FE-1 model, each discrete screw is modelled using the fastener element in Abaqus, which is expected to yield almost identical results to the CSM, as discussed in Chapter 3. In a more sophisticated modelling approach (FE-2), solid elements are utilised to represent the self-drilling screws, which will be explained in Chapter 5 in detail. As can be seen, the results of the M-2 method as an indication of the buckling strength of critical elements within the section are always lower than those from the M-1 technique as an overall measure obtained from the load-displacement curve. The CSM and FE-1 model predictions match and are in line with the M-2 evaluations that form a lower bound estimate of the elastic buckling load of the built-up sections. In contrast, the FE-2 results compare well with the M-1 estimations of the elastic buckling capacity for the whole section.

4.8.2   *Local plastic mechanisms*

The local failure mechanisms observed in the tests are more closely investigated in this Section. Despite the overwhelming variety of local plastic mechanisms in thin-walled steel members, it has been shown [21] that even the most complicated mechanisms can be decomposed into a number of simple yet basic ones. The local plastic mechanisms can be categorised into two major classes [21, 22]: (a) "true" mechanism that can be developed by folding individual plates along the plastic hinge lines with a free deflection pattern and (b) "quasi" mechanism in which some regions of the individual plates must yield in their planes to establish the inelastic deformation pattern involved in the plastic mechanism. The former can be observed in different forms, some of which may rely on some degree of twisting and out-of-plane bending of end panels that can still be counted as a true mechanism due to the much greater flexibility of the plates in these actions. In contrast, the latter is typically observed in stiffened plates and requires certain regions of the mechanism to undergo large in-plane plastic deformations. This

mechanism can manifest in three types of yielding in direct tension, compression or pure shear or combinations thereof.

A descriptive summary of these different mechanisms, including eight different true mechanisms, can be found in [21]. A schematic illustration of some of the mechanisms in webs (CW) and flanges (CF) is shown in Figure 2-3. One of the most commonly observed true mechanisms in thin-walled columns made of channel sections is the "flip-disc" mechanism with a typical parabolic shape, which involves twist and free bending of end panels, as shown in Figure 2-3(a). It is typically observed in the web of the channel section and is generally complemented by one compression yield zone and one tension yield zone in each flange. This mechanism was observed in the majority of the test specimens, as indicated in Figure 4-43 for Series C120 and in Figure 4-38(c) and Figure 4-39(c) for Series C64, and is the main local plastic mechanism in the web of the tested specimens in this study.

The flip-disc mechanism in the web of the columns was also accompanied by another basic true mechanism formed in the flanges of the channel sections. Interestingly, the flange failure mechanism is different between the sections that failed in distortional buckling (Series C120) and the sections with the interactive local-distortional buckling failure (Series C64). As can be seen in Figure 4-43, the flange failure mechanism of type CF3, according to Figure 2-3(e), formed in built-up test specimens of Series C120. On the contrary, the failure mechanism of type CF1 per Figure 2-3(c) developed in the flanges of test specimens of Series C64, which can be observed in Figure 4-38(c) and Figure 4-39(c). It is also noted that two nominally identical specimens may not have precisely the same mechanisms as observed in the tests (see Figure 4-43), which can be explained by the fact that the initial imperfections impact the initial location for plasticity development, and the mechanism is mostly locked-in to that location once yielding commences.
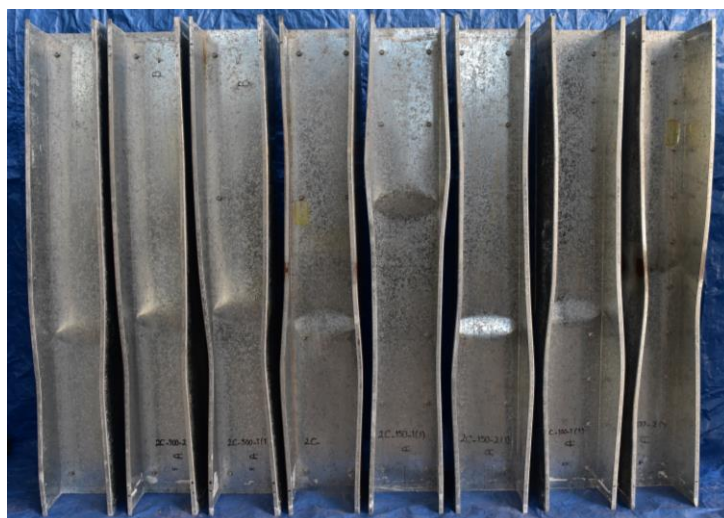
(a)
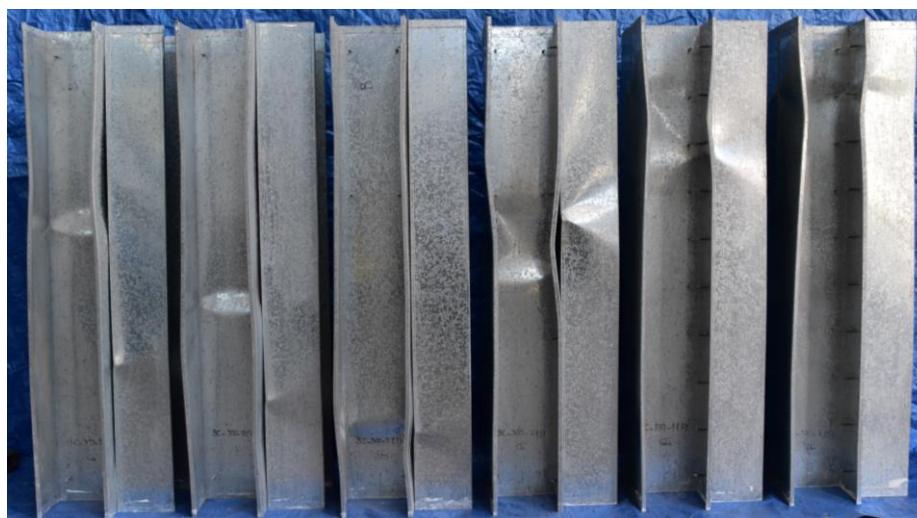
(b)

(c)

Figure 4-43: Localised failure deformations formed in the tested specimens of series (a) 2C120, (b) 3C120 and (c) 4C120

4.9   SUMMARY

In order to investigate the sectional buckling behaviour of cold-formed steel built-up columns, two cross-sections were designed, one with the prevalent distortional buckling (C120) and one with the predominant local buckling (C64). Three different singly- and doubly-symmetric built-up assemblies were considered for the testing program with three different screw spacings ($s = 100$, 300 and 900 mm). The custom-designed C120 section was manufactured by brake pressing, and the C64 section was selected from the available roll-formed industrial sections. A set of tensile coupon tests was conducted to determine the material properties of the flat and corner parts of the sections. The results indicated a nonlinear material behaviour with a considerably higher 0.2% proof and ultimate tensile stresses for test series C120. The residual membrane stress was also measured at the web of the roll-formed section and was found to be negligible.

Prior to testing, the geometrical imperfections were measured along the length of the member at different transverse locations on the web, flanges, and lips of the cross-sections. Then, the measured imperfections were decomposed to the critical eigenmodes of the sections (i.e., global, local, and distortional) for further utilisation in numerical modelling. The amplitude of the global imperfections was relatively small due to the short length of the members and the symmetry of the built-up cross-sections. The maximum sectional imperfections measured were also compared with the AS4600 recommendations. The measured distortional imperfection amplitudes were comparable to the Australian standard recommended values, while the local imperfection values were reasonably smaller.

A total of 36 specimens with a length of 1 m were tested under axial compression between fixed ends. An idealised fixed-ended condition was achieved by designing a special end plate for each cross-section filled with Patterstone to facilitate the confinement of the specimens at the ends. All the specimens of Series C120 buckled and failed in distortional buckling, while a local buckling was observed for the specimens of Series C64 in the elastic region, followed by an interactive local-distortional buckling failure. According to the results, the ultimate load

capacity of built-up columns increases as the screw spacing decreases. This increase is more significant for the specimens of Series C120, with a maximum enhancement of 36.5% compared to a single section capacity. This result is mainly attributed to the change of the buckling mode from a single half-wave curve in a single section to an antisymmetric double half-wave curve in the built-up specimens. In contrast, all the C64 sections failed in a local-distortional interactive mode following initial buckling in the local mode shape, and their capacity was not influenced by the end connectivity or contact between the sections. Therefore, the ultimate capacity of the built-up sections was compared to the capacity of specimens with no intermediate connection ($P_u|_{s=0.9L}$) to investigate the effect of the addition of evenly-spaced intermediate screws. The results showed that the improvement of the ultimate capacity of all built-up assemblies due to intermediate fasteners was of limited significance for both test series, with a general increase of less than 10%. It is also noteworthy that for both test series, the noticeable enhancement occurred where the fasteners spaced below the half-wavelength associated with the critical buckling mode of the section, i.e. $s/L=0.3<L_{crd}/L=0.6$ for Series C120 and $s/L=0.1<L_{crl}/L=0.12$ for Series C64. This observation suggests the influence of s/L_{crs} as a design parameter, which will be closely investigated in Chapter 6.

The local plastic mechanism observed in the experiments was assessed in both test series. The primary plastic mechanism forming in the web of all sections was the flip-disc plastic mechanism; however, the failure mechanism developed in the flanges was different between the sections that failed in distortional and local-distortional interactive modes. Lastly, the elastic buckling load of the built-up sections was estimated from the experimental results and was compared with the predictions of the compound strip method and finite element models. A reasonable level of agreement was observed across different methods, and the results obtained from the CSM will later be utilised in Chapter 6 for the design of cold-formed steel built-up columns.

Chapter 5   NUMERICAL MODELLING OF BUILT-UP SECTIONS

5.1   INTRODUCTION

This chapter elaborates on the details of finite element simulations performed in this study for the collapse modelling of cold-formed steel built-up columns. First, the theoretical background and features of the finite element models are explained in Section 5.2, and the numerical models are validated against the results of the experimental tests presented in Section 5.3. Subsequently, the calibrated FE models are utilised as the basis for extensive parametric studies into the effect of cross-section dimensions, built-up section geometry and fastener spacing on the ultimate strength of built-up columns, outlined in Section 5.4 with a comprehensive discussion. Finally, this chapter concludes with a summary of the key outcomes and closing remarks in Section 5.5.

5.2   DETAILS OF FINITE ELEMENT MODELLING

Comprehensive finite element analyses are performed to understand better the effect of different parameters, e.g. geometric imperfections, fastener spacing and built-up section geometry, on the sectional buckling behaviour of cold-formed steel built-up sections under compression. The FE model is first validated against experimental data (see Chapter 4 for test details), for which details of the model developed in Abaqus 6.14 software are explained in the following sections, including material properties, boundary condition enforcement, implementation of geometric imperfections, contact modelling, utilised element types and solution techniques.

5.2.1   Nonlinear material model

The results from the tensile coupon tests, outlined in Chapter 4, are utilised to define the material behaviour of cold-formed steel in numerical analysis for the flat and corner parts of the test sections. These experimental data are obtained by employing the initial dimensions of the test coupons, referred to as engineering stress (σ) and engineering strain (ε). However, for inelastic constitutive modelling based on finite strain assumption, these components must be converted to true stress (σ') and true strain (ε') based on the instantaneous geometric properties. As a result, the true strain is expressed by the following integral form

$$\varepsilon' = \int dl/l = \ln\left(l/l_0\right),$$
(5.1)

which yields the following relationship between engineering and true strain, given that the engineering stress is defined as the ratio of the measured elongation to the initial length of the coupon, i.e. $\varepsilon = \Delta l/l_0$

$$\varepsilon' = \ln\left(1+\varepsilon\right).$$
(5.2)

In addition, true stress is defined as $\sigma = P/A$, which, based on the assumption of an incompressible material, i.e. $A = A_0(l_0/l)$, and some simple mathematical manipulations, results in the following correlation between true and engineering stress and strain

$$\sigma' = \sigma\left(1+\varepsilon\right).$$
(5.3)

Then the true plastic strain (ε'_p) can be calculated as

$$\varepsilon'_p = \varepsilon' - \frac{\sigma'}{E}.$$
(5.4)

The engineering and true stress-strain curves considered for the numerical simulations of test series C120 and C64 are presented in Figure 5-1, both starting with an initially linear elastic portion followed by a gradual yielding portion. The difference between the curves is marginal at low strains and becomes noticeable as the strain evolves into the high range. The Abaqus input data for metal plasticity calculations is based on the true stress vs true plastic strain, which

is tabulated in Table 5-1 for the material behaviour employed for the flat and corner parts of the test sections in numerical analyses. It is noted that the static stress-strain curves, as explained in Section 4.4, are directly used for the modelling of material behaviour in FE model calibration, while the representative Ramberg-Osgood expressions derived from the coupon test results of the industrial section (C64) are utilised for further numerical simulations and parametric studies. The complete set of engineering stress-strain curves are presented in Appendix B. Poisson's ratio is also considered 0.3 in all computational models.
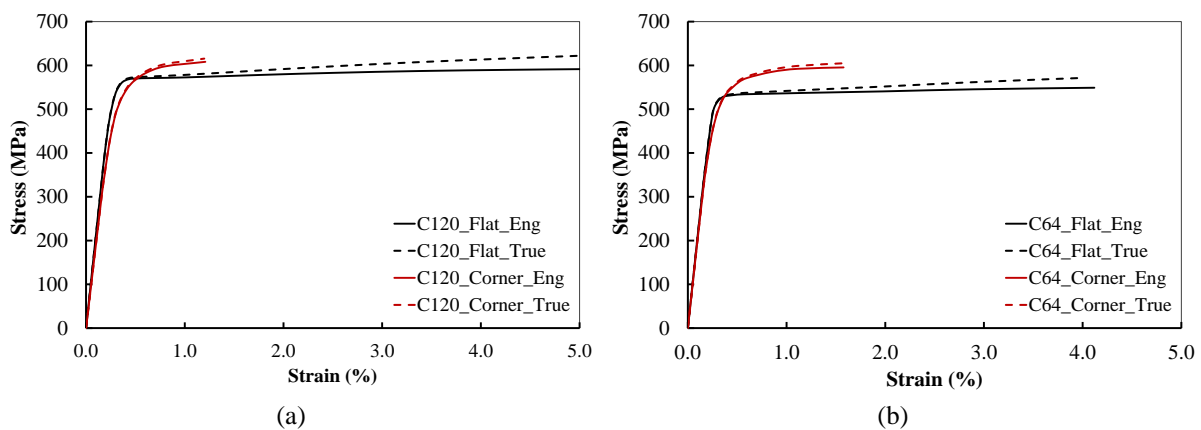
Figure 5-1: Engineering and true stress-strain curves considered for (a) Series C120, (b) Series C64

Table 5-1: Abaqus input data for determination of elastic and plastic behaviour of flat and corner parts of test series C120 and C64

C120_Flat (E = 212.894 GPa)		C120_Corner (E = 190.911 GPa)		C64_Flat (E = 211.833 GPa)		C64_Corner (E = 203.826 GPa)	
σ' (MPa)	ε'_p (%)	σ' (MPa)	ε'_p (%)	σ' (MPa)	ε'_p (%)	σ' (MPa)	ε'_p (%)
372.02	0.000	310.11	0.000	314.44	0.000	315.57	0.000
437.99	0.005	351.31	0.004	383.13	0.004	401.86	0.012
473.61	0.011	393.02	0.008	431.24	0.008	454.64	0.030
502.81	0.023	442.59	0.020	474.44	0.014	495.65	0.058
523.69	0.034	491.20	0.043	499.61	0.024	524.10	0.096
545.00	0.055	523.79	0.079	512.68	0.041	541.23	0.137
564.72	0.107	545.50	0.119	525.05	0.077	564.38	0.236
572.32	0.197	568.76	0.196	531.70	0.127	575.13	0.322
578.44	0.736	586.39	0.298	537.15	0.317	590.11	0.557
597.64	2.201	602.54	0.480	551.25	1.692	598.84	0.815
621.99	4.704	615.51	0.879	571.59	3.77	604.77	1.268

The classical metal plasticity with associated flow rule and isotropic hardening can be adopted for the collapse modelling of cold-formed steel members under static loading conditions, where loading is relatively monotonic and creep effects are insignificant. As discussed in Section 4.5, bending residual stresses are implicitly considered in the stress-strain curves of the tensile coupons, and the measured membrane residual stresses induced by cold-forming were quite small and hence are not incorporated in the numerical modelling. Thereby, the isotropic von Mises yield criterion with isotropic hardening and associated flow rule, known as the isotropic elasto-plasticity material model in Abaqus [195], is utilised in this study. This material model has been conventionally employed in cold-formed steel modelling, where residual stresses are neglected [19]. The Mises yield function is commonly defined as

$$F = \sigma_{eq} - \sigma_y, \tag{5.5}$$

where σ_{eq} is the equivalent Mises stress that is defined as

$$\sigma_{eq} = \sqrt{3J_2} = \sqrt{\frac{3}{2} s_{ij} s_{ij}}, \tag{5.6}$$

in which J_2 is the second invariant of the deviatoric stress tensor ($\mathbf{s}$). The components of the deviatoric stress tensor are equal to $s_{ij} = \sigma_{ij} - p\delta_{ij}$, where $p = \sigma_{ii}/3$ (sum on double-index i) is the hydrostatic pressure and δ_{ij} is the Kronecker delta. The yield stress (σ_y), as an indicator for the development of plasticity, can be expressed in the following general form

$$\sigma_y = \sigma_y^0 (\varepsilon_{eq}^p) R(\dot{\varepsilon}_{eq}^p), \tag{5.7}$$

in which σ_y^0 is the initial static yield stress limit as a function of equivalent plastic strain (ε_{eq}^p) with the consideration of isotropic hardening for the evolution of plasticity, while function R accounts for the strain-rate dependence of the yield limit. In lieu of high strain rates in loading, such as the test conditions of this study, rate-independent yielding can be reasonably assumed, which means $R=1$. The equivalent plastic strain is defined as

$$\varepsilon_{eq}^p = \sqrt{\frac{2}{3} \varepsilon_{ij}^p \varepsilon_{ij}^p}, \tag{5.8}$$

where ε_{ij}^p is the plastic component of the total strain tensor that is obtained by subtracting ε_{ij}^e as the elastic component, i.e. $\varepsilon_{ij}^p = \varepsilon_{ij} - \varepsilon_{ij}^e$. The evolution rate for the plastic strain components can be evaluated based on the associated flow rule as follows

$$\dot{\varepsilon}_{ij}^p = \left(\partial F / \partial \sigma_{ij} \right) \dot{\varepsilon}_{eq}^p = \frac{3}{2} \frac{s_{ij}}{\sigma_{eq}} \dot{\varepsilon}_{eq}^p, \tag{5.9}$$

in which $\dot{\varepsilon}_{eq}^p$ is the equivalent plastic strain rate, which is the rate of change in the equivalent plastic strain at each increment. In essence, the constitutive relationship in terms of equivalent stress (σ_{eq}) versus the equivalent plastic strain (ε_{eq}^p) in combination with the Mises yield function controls the initiation and evolution of this conventional metal plasticity model, which can be considered as the extension of uniaxial stress-strain relationship to three-dimensional problems.

5.2.2 Geometric imperfections

The buckling behaviour and ultimate strength of thin-walled structures are generally imperfection sensitive; therefore, implementing geometric imperfections in the numerical modelling of these structures is crucial. The measured imperfection data was directly incorporated into the FE models using a series of Python scripts for model validation. An overview of the scripts is presented in Figure 5-2. First, the FE model with perfect geometry was created through a Python script using the measured dimensions, as per Appendix A, and material properties obtained from the tensile coupon tests, as explained in Section 5.2.1. Then, the mesh coordinates of the perfect geometry were extracted, and the geometric imperfections of each node were calculated based on its longitudinal and transversal locations, viz. web, flanges, lips or corners, using the measured imperfections data (see Section 4.6 for details). Following that, the perfect mesh coordinates were updated by adding the geometric imperfections, and the FE model with imperfect geometry was generated for the nonlinear static analysis.
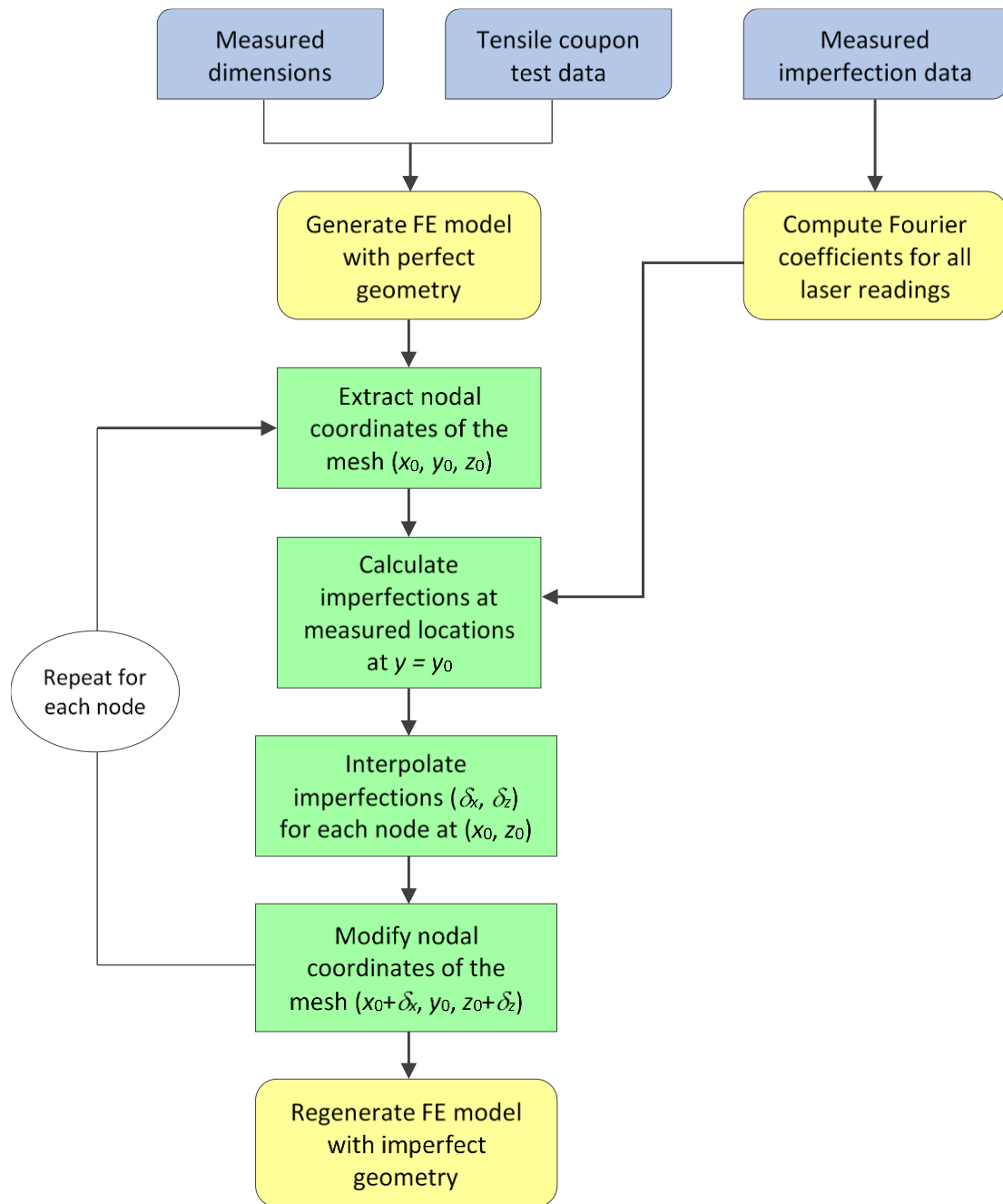
Figure 5-2: Flowchart of the Python scripts for the implementation of geometric imperfections into the FE model

For each node with the coordinates of (x,y,z), the y-coordinate indicates the longitudinal location of the node, and the (x, z) coordinates represent the transversal location of the node on the cross-section. For computing the magnitude of geometric imperfections at each node, the imperfections were first calculated at the measured locations using the y-coordinate of the node and the Fourier coefficients obtained from the measured data for each laser reading.

Subsequently, the magnitude of imperfections was determined based on the transversal location of the node using a quadratic interpolation for the web and flanges and a linear interpolation for the lips, as illustrated in Figure 5-3 for the tested cross-sections. As can be seen in the figure, for the flanges connected to the web in built-up assemblies consisting of three and four channel sections, a compatible imperfection to that of the connected web was imposed. This assumption was made in lieu of the geometric imperfection measurements for these flanges due to the impeded access.
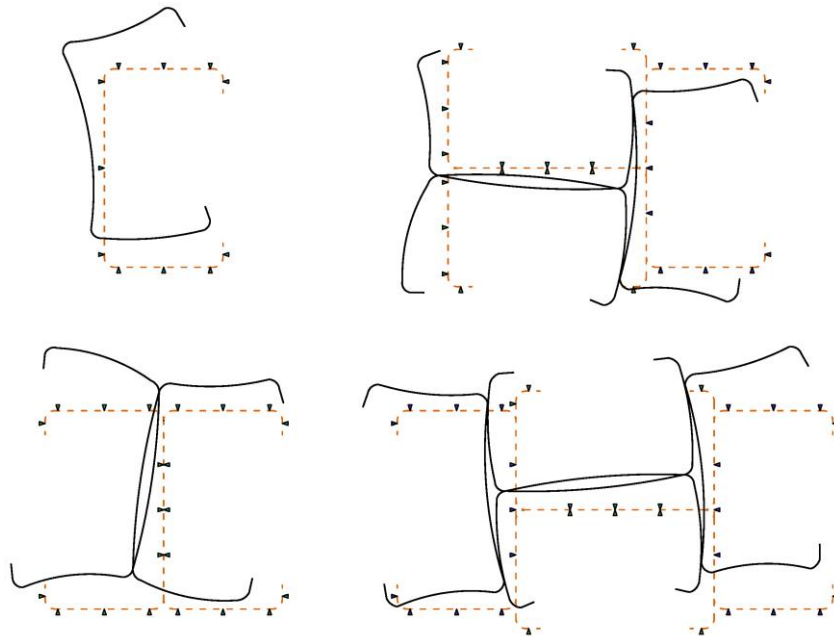
Figure 5-3: Schematic illustration of the implementation of geometric imperfections in the tested cross-sections at $y=y_0$ using the laser reading at the locations shown on the perfect cross-section

Figure 5-4 shows 3D representations of the imperfections (with a magnification factor of 100) incorporated in the FE models of the built-up sections comprising two and three channel sections. The imposed compatible imperfections of the flanges connected to the web are evident in Figure 5-4(a). More details on the interpolation and implementation of imperfections can also be found in [196]. It is noted that the traditional modal approach is employed in parametric studies to define geometric imperfections, which will be explained in Section 5.4.2.1 in detail.

(a)   (b)
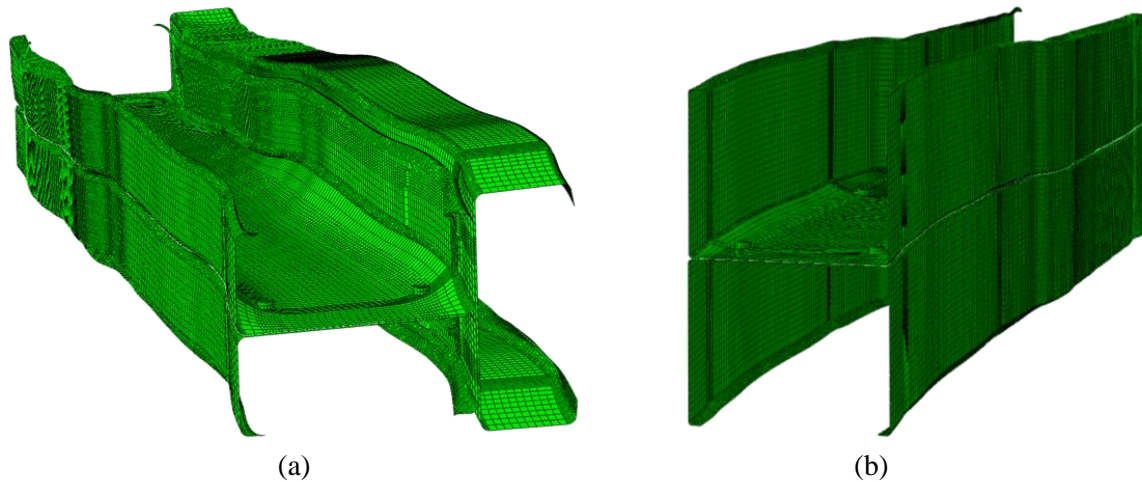
Figure 5-4: Magnified imperfections (scale factor = 100) incorporated into the FE model for the test specimen (a) 3C64-900-1 and (b) 2C120-300-2

5.2.3   Boundary conditions

In order to make meaningful comparisons between numerical and experimental results, adequate modelling of end support conditions is essential. The specimens were tested between fixed ends, the details of which are described in Section 4.7.1. Various methods exist for implementing the desired end conditions in FE models with shell elements. In this study, the fixed-ended condition was modelled by two different approaches:

1) a complex model comprising two solid homogeneous loading plates in contact with the specimen at both ends, as illustrated in Figure 5-5(a) for an I-section,

2) a simplified model utilising the multi-point constraint (MPC) feature, as shown in Figure 5-5(b) for the same section.

In the first approach, contact between the end sections and the loading plates was modelled using a node-to-surface contact pair. The surface of end plates in contact with the column ends was defined as the master surface, and the edge of end sections was specified as the node-based slave surfaces. Hard contact was considered for the normal contact behaviour, which allows no penetration between the two surfaces. The tangential behaviour was defined as rough, meaning that infinite friction restrained any slip between the end sections and loading plates. All degrees of freedom were restrained at the bottom and top end plates to impose a fixed boundary

condition, except for the translational DoF in the axial direction of the top plate to allow for an axial displacement-controlled loading regime matching the experiments.

In the second approach, the multi-point constraint (MPC) option has been utilised to form a spider web link between the nodes on the essential/Dirichlet boundaries (i.e. the support end of the specimen), which is constrained over the desired degrees of freedom by a set of linear equations. The objective boundary conditions are then enforced by restraining the corresponding displacements and rotations of the central point. As the clamped ends were the desired support conditions for this study, the translational and rotational degrees of freedom of the pivot have been fixed.
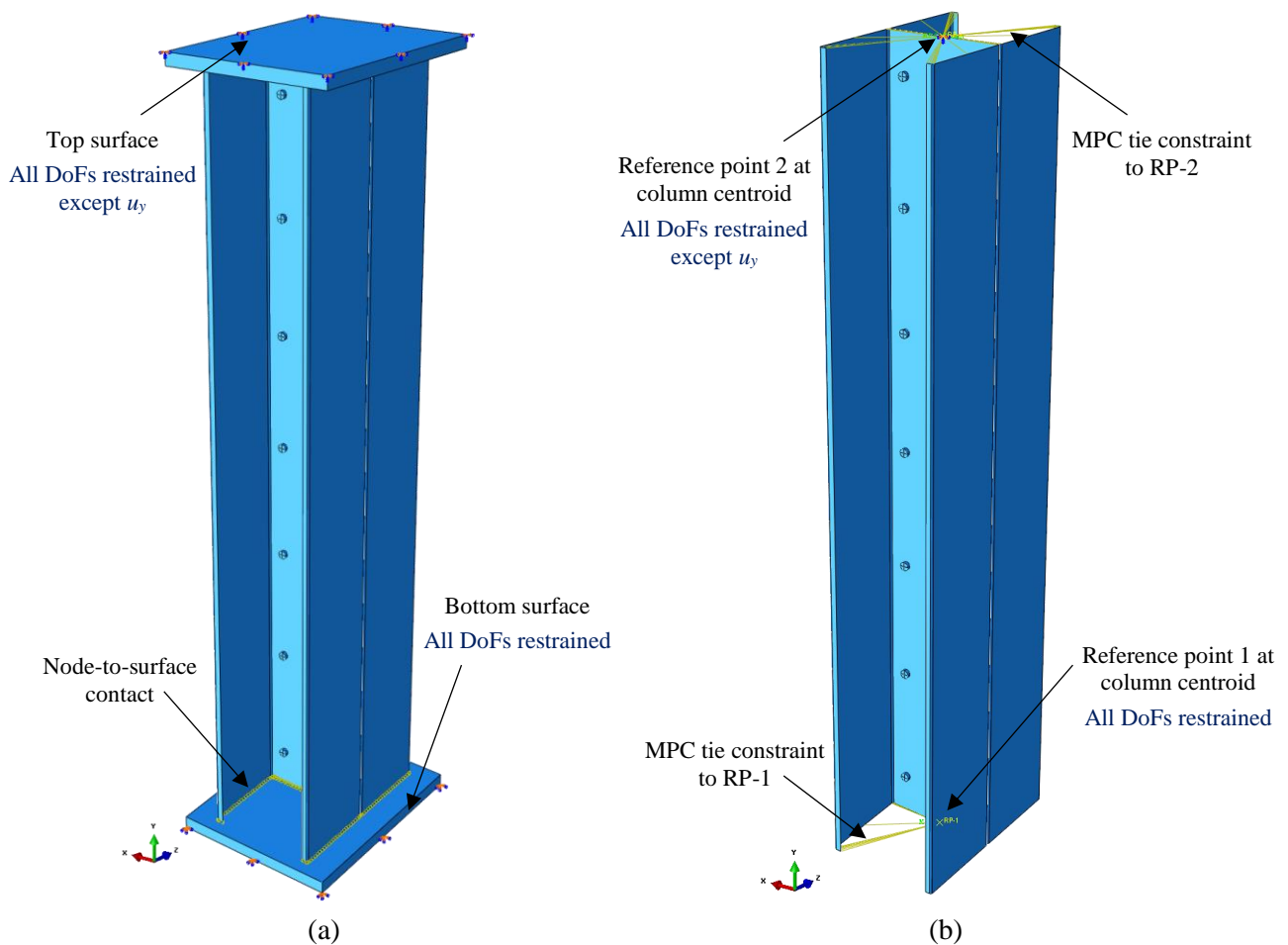
Figure 5-5: Fixed end boundary condition modelling: (a) complex approach, (b) simplified approach

The load vs. axial shortening FE results obtained for one of the single sections, 1C120-2, and one of the built-up sections trials, 2C120-150-1, are presented in Figure 5-6 and Figure 5-7, respectively.
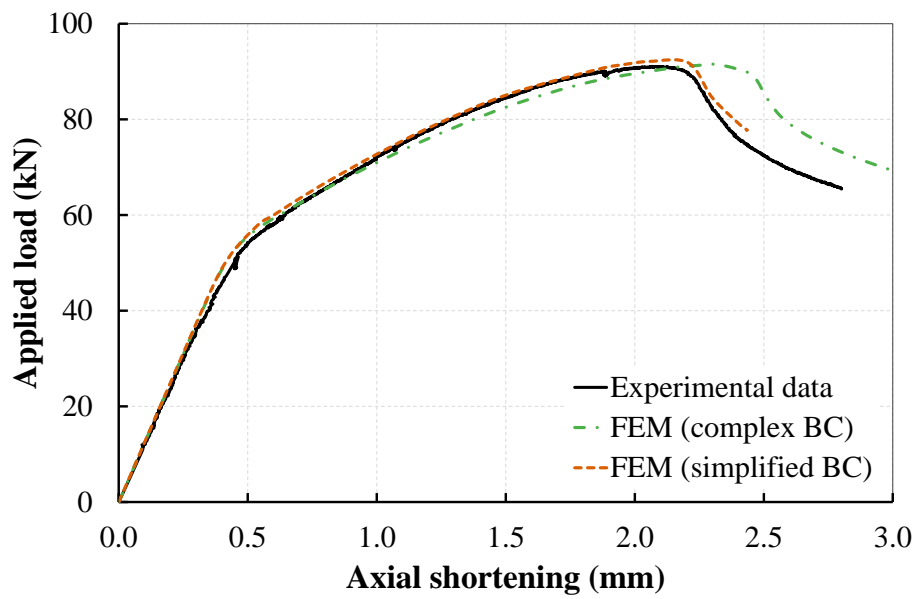
(a)
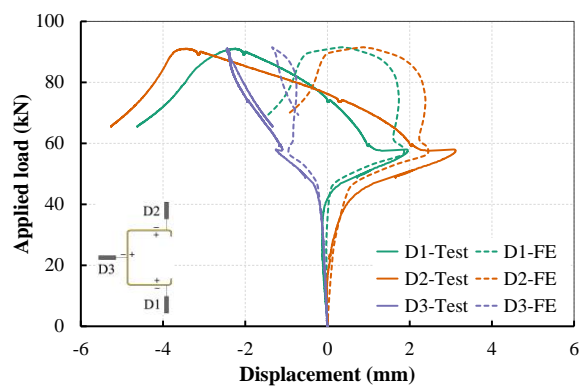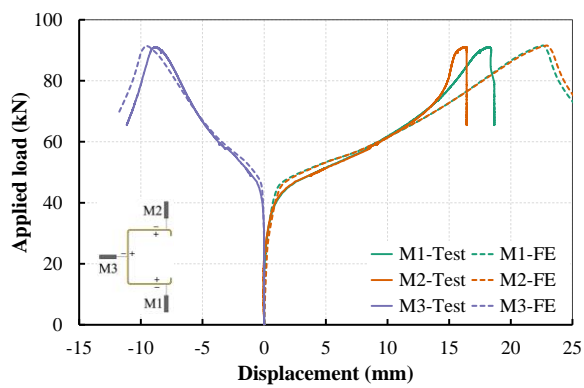
(b)
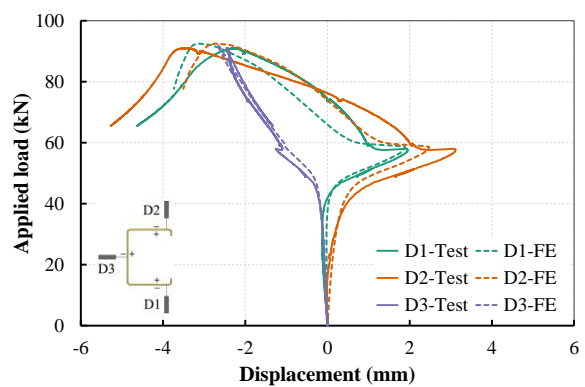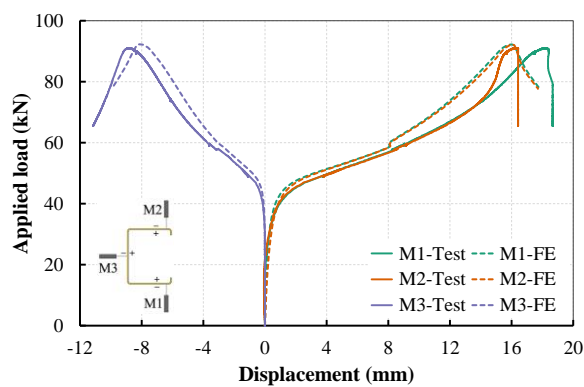
(c)

Figure 5-6: Comparison of the results of FE models with different boundary condition enforcement methods for test specimen 1C120-2: (a) load vs. axial shortening, (b) transducers data for the complex approach, and (c) transducers data for the simplified approach
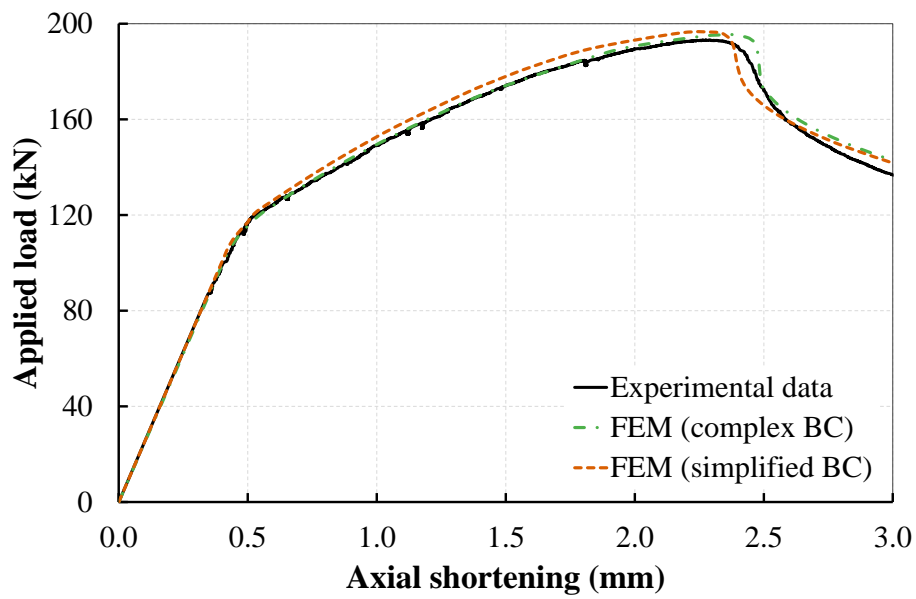
(a)
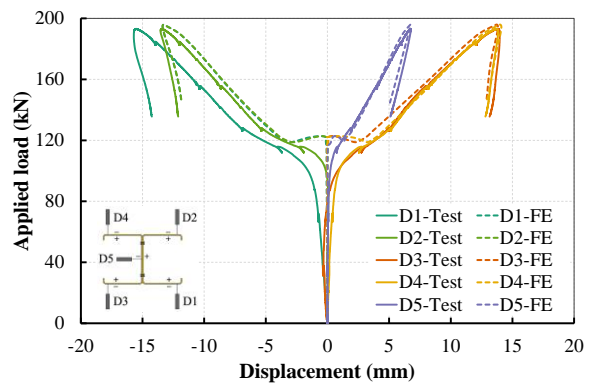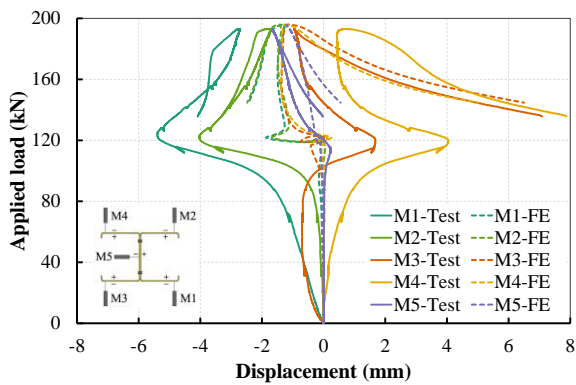
(b)
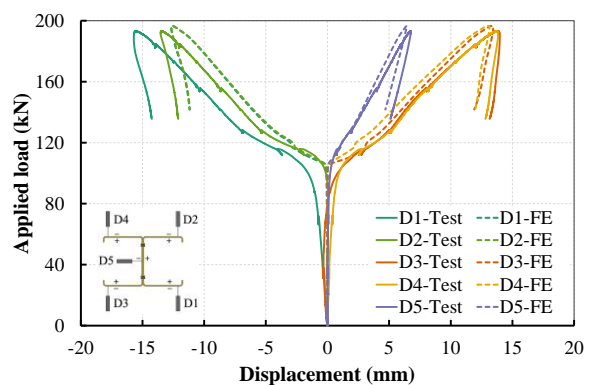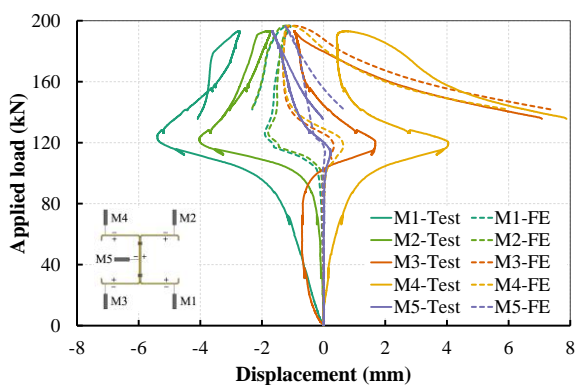
(c)

Figure 5-7: Comparison of the results of FE models with different boundary condition enforcement methods for test specimen 2C120-150-1: (a) load vs. axial shortening, (b) transducers data for the complex approach, and (c) transducers data for the simplified approach

The results indicate that the ultimate strength is predicted well utilising both boundary condition modelling approaches. However, the first approach gives a closer result to the test data in terms of tangent stiffness after the occurrence of elastic buckling compared to the second approach, which is slightly stiffer. The comparison of the FE results with the recorded transducers data, see Figure 5-6(b-c) and Figure 5-7(b-c), also show that the buckling mode shape and the post-buckling behaviour are not affected by simplifying the boundary condition modelling and are well predicted. Thereby, for the sake of computational efficiency and stability, the second approach has been utilised to enforce the fixed-end boundary condition in this study.

5.2.4   Contact modelling

The problem of the sectional buckling of thin-walled steel built-up members can potentially involve localised stress transfer between the constituent plate elements via surface contact conditions. This can be observed at various potential locations in the member, such as the vicinity of discrete fasteners and at loading and support regions, some of which must be explicitly modelled to capture the nonlinear behaviour of such structures reliably. Abaqus FE package offers a wide range of contact conditions ranging from hard contact to a variety of softened contact relationships with arbitrary (e.g. linear, exponential, or custom-made tabular piecewise-linear) functions for pressure-overclosure behaviour as the relationship between the imposed contact pressure versus the interface displacement or the clearance between the contact surfaces in the normal direction.

In this study, a hard surface-to-surface contact condition is considered, which minimises the penetration of the slave surface into the master surface and does not permit the interfacial transfer of tensile stress. The tangential behaviour is considered frictionless, allowing pressure-independent sliding between the surfaces. The pressure-overclosure relationship in this most common contact condition is illustrated in Figure 5-8(a), where the idealised zero-penetration condition may or may not be strictly enforced depending on the enforcement method used. The methods supported by Abaqus are the direct enforcement method [197], the conventional

penalty method as the stiff approximation of hard contact, and the Augmented Lagrange method. The direct method may cause over-constraint issues because of the strict interpretation of contact constraints and thereby be more susceptible to numerical instability and convergence issues. The penalty method, in contrast, approximates the hard contact condition with optional linear or nonlinear behaviour as desired and can yield some degree of penetration. These two options can mitigate the over-constraint issue and improve solver efficiency and performance. Lastly, the Augmented Lagrange method is the enrichment of the linear penalty method by using augmentation iterations that drive down the penetration distance and improve the stiff approximation accuracy.

(a)   (b)
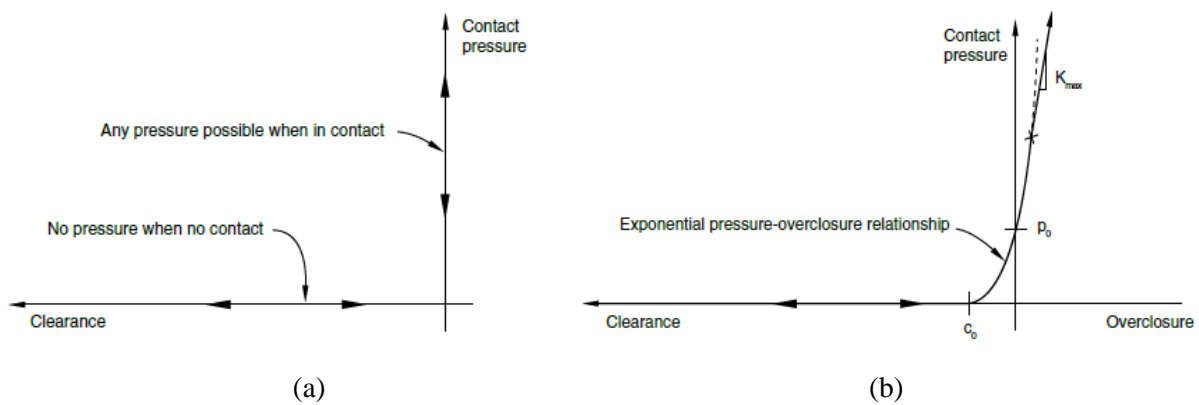
Figure 5-8: Contact conditions [197]: (a) idealised hard contact, (b) softened contact with exponential pressure-overclosure relationship

Following these, the Augmented Lagrange method is utilised in this study to enforce hard surface-to-surface contact conditions, where the surface smoothing option is also activated to improve convergence and accuracy of contact stresses (for nearly axisymmetric surfaces) by geometry correction and smoothing faceted regions. Furthermore, the slave surface adjustment option is also activated to ensure the probable alteration of the contact surfaces if already penetrated prior to contact application due to the consideration of geometric imperfections. As an alternative to hard contact, one may use softened contact to model the interaction between the thin layers for numerical reasons as it may resolve the contact condition faster and mitigate convergence issues compared with hard contact. An exponential pressure-overclosure relationship, as shown in Figure 5-8(b), would be a suitable option in this scenario; in which

the contact pressure will be transmitted once the clearance between the surfaces reaches a critical limit (c_0) and below that, the imposed stress will subsequently increase exponentially to resemble a hard contact condition. Specifying an optional limit (k_{max}) on the contact stiffness in Abaqus/Explicit that the model can attain during overclosure (infinity or large penalty stiffness by default) may assist in mitigating the side effect of large stiffness on reducing the stable time increment. The tangential behaviour between the section parts in contact with each other in a built-up member is modelled as frictionless, which allows sliding motions between surfaces without inducing forces in the corresponding direction.

As far as the contact tracking approach for the relative motion of the interfacing surfaces is concerned, the general finite-sliding option [197] has been mainly considered in the FE simulations of this geometrically nonlinear problem as it allows for arbitrary relative separation, sliding and rotation of the surfaces in contact. In this method, the connectivity of the active contact constraints and the load transfer paths are updated upon the relative tangential motion. This approach is more computationally expensive than the small-sliding approach that relies on the assumption of small sliding of one surface over the other with the planar approximations of the master surface per averaging region of the slave surface. Nevertheless, the small-sliding approach still allows for arbitrary large rotations and can be used for geometrically nonlinear analyses as long as a slave node interacts with the same local area of the master surface throughout the analysis, as shown in Figure 5-9 for a built-up section failing in a local-distortional interactive mode.

(a)   (b)   (c)
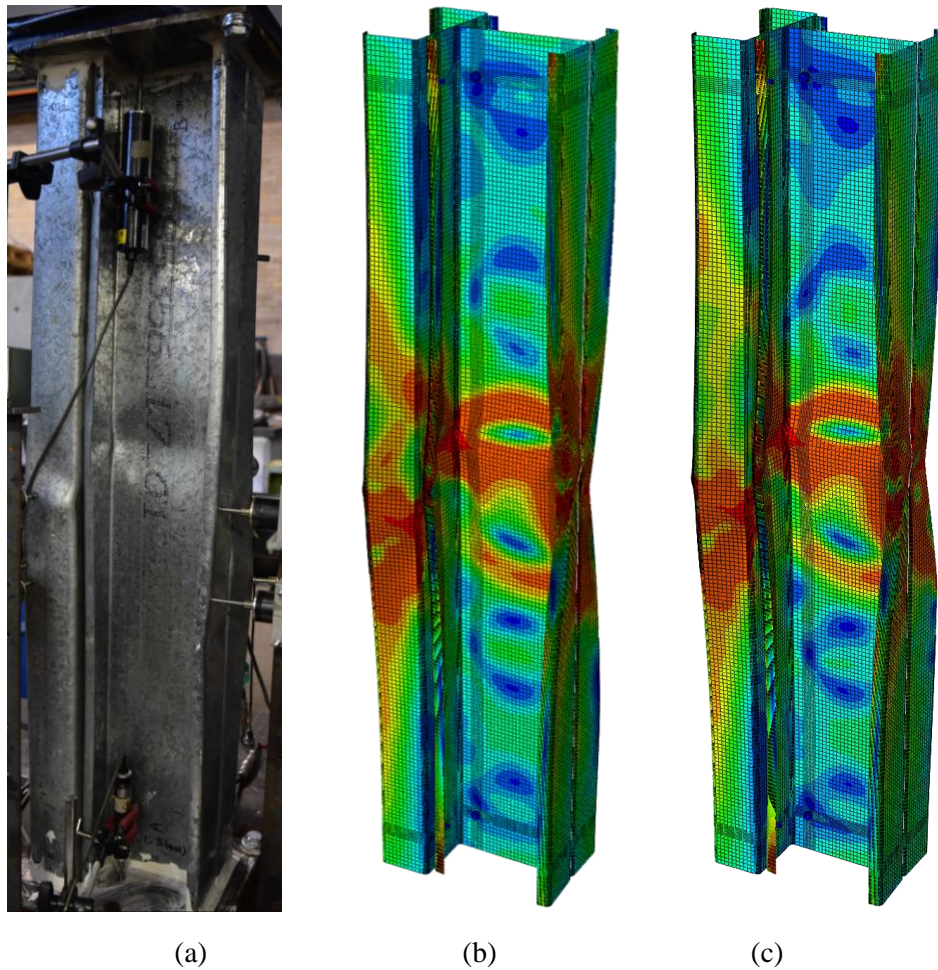
Figure 5-9: Comparison of the post-peak deformations of FE models with different contact tracking approaches for the test specimen 3C64-900-1: (a) test result, (b) finite sliding approach, and (c) small sliding approach

Both tracking approaches yield the same post-peak deformations as the test results, with a slight difference in the von Mises stress distribution around the localised failure area. However, for built-up assemblies failing in distortional buckling modes, large rotations form in the web and flanges of the lipped channel sections in contact, which necessitate the use of the finite sliding tracking approach, as presented in Figure 5-10 for a back-to-back I-section. The results indicate that the failure was localised in a different area on the web compared to the test results using the small sliding tracking approach, which resulted in a higher ultimate capacity. These results also highlight the importance of the sliding assumptions on the buckling behaviour of built-up sections in numerical simulations.

<div align="center">(a)   (b)   (c)</div>
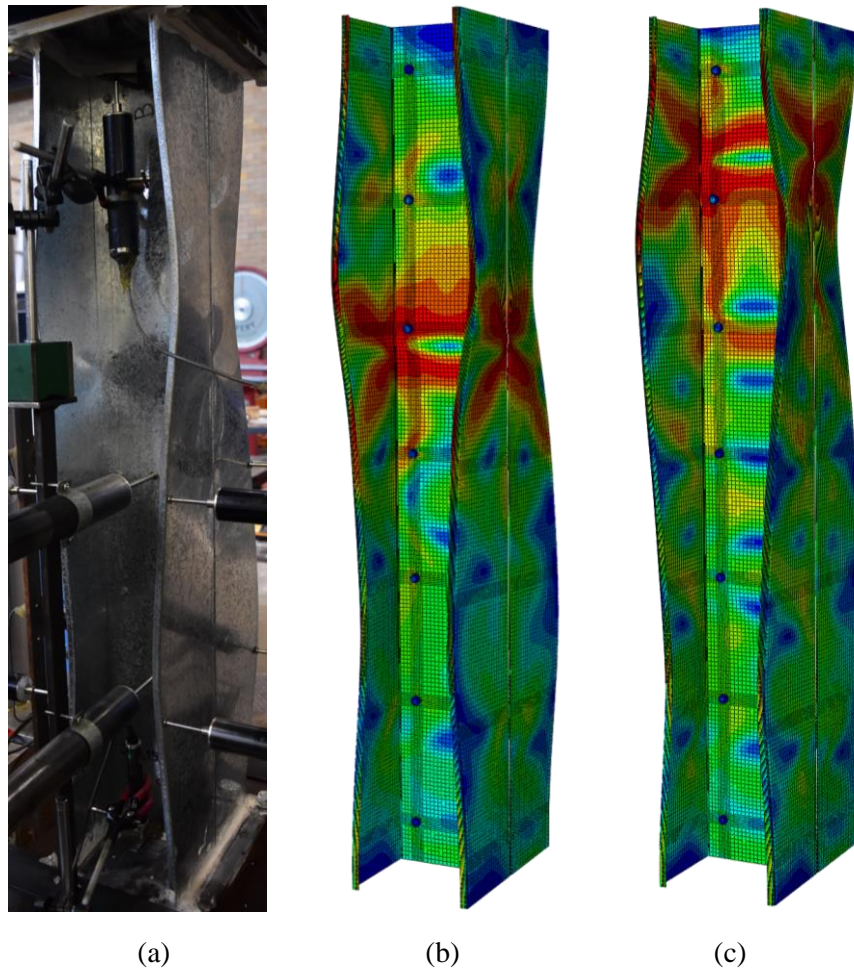
Figure 5-10: Comparison of the post-peak deformations of FE models with different contact tracking approaches for the test specimen 2C120-150-1: (a) test result, (b) finite sliding approach, and (c) small sliding approach

5.2.5 Connection element

Four different modelling options were investigated in Abaqus that are briefly discussed and compared here to select an appropriate connection element for capturing the nonlinear response of the built-up sections with discrete fasteners. These different screw modelling options are schematically illustrated in Figure 5-11. In the first and the simplest modelling option (i), the nodes on the constituent plates located on the screw centre lines were tied together in terms of both translational and rotational degrees of freedom, as shown in Figure 5-11(a). This option may be considered equivalent to introducing rigid links, given that the free space between the plates is negligible. In modelling option (ii), the connectivity between the plates was extended to a surface/region (see Figure 5-11(b)) instead of individual nodes as in option (i), where the

same degrees of freedom were tied over a surface representing the screw intrusion using the surface-to-surface tie constraint [197].

$$u_{x1} = u_{x2} \quad \theta_{x1} = \theta_{x2}$$
$$u_{y1} = u_{y2} \quad \theta_{y1} = \theta_{y2}$$
$$u_{z1} = u_{z2} \quad \theta_{z1} = \theta_{z2}$$

$$u_x|_{S1} = u_x|_{S2} \quad \theta_x|_{S1} = \theta_x|_{S2}$$
$$u_y|_{S1} = u_y|_{S2} \quad \theta_y|_{S1} = \theta_y|_{S2}$$
$$u_z|_{S1} = u_z|_{S2} \quad \theta_z|_{S1} = \theta_z|_{S2}$$

$$f_x = k_{sx}(u_{x2} - u_{x1})$$
$$f_y = k_{sy}(u_{y2} - u_{y1})$$
$$f_z = k_a(u_{z2} - u_{z1})$$

- Surface-to-surface contact between S_1 & S_2
- Shell-to-solid coupling on Γ_1 & Γ_2

(a)   (b)   (c)   (d)
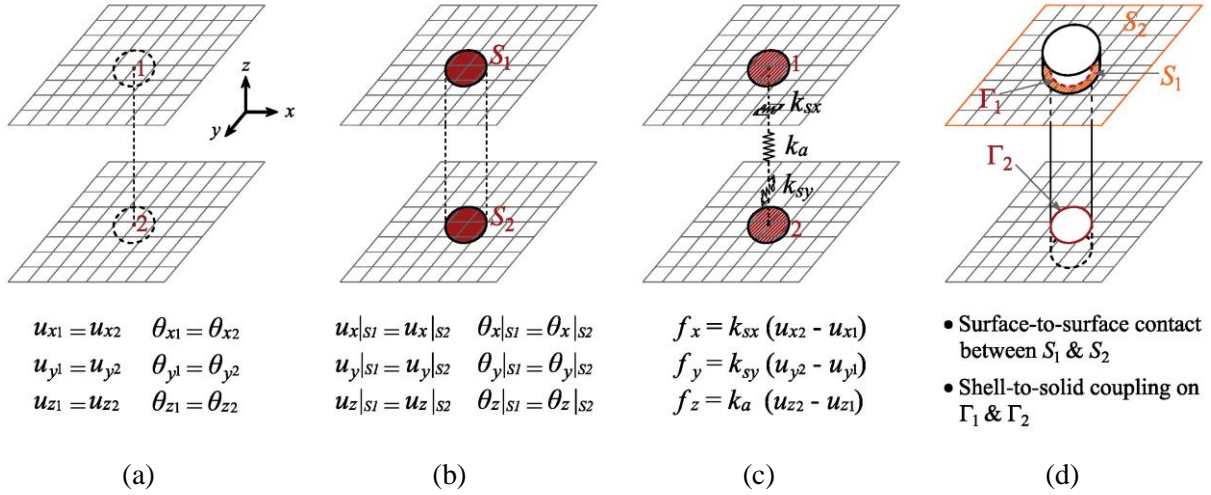
Figure 5-11: Different options considered for the FE modelling of a screw-fastened connection: (a) tied DoFs at the centre of the fastener location, (b) tied DoFs over the fastener area, (c) mesh-independent fastener element, (d) solid element

In the third scenario (iii), the mesh-independent fastener element feature in Abaqus [197] was considered, where the areas of the plates connected by the screws are linked by representative springs, as illustrated in Figure 5-11(c). The stiffness of these springs can be adjusted by the calibration against available test data through an inverse analysis. In this study, the shear stiffness and strength of the screw-fastened connections were determined from the backbone curves proposed by Phan and Rasmussen [114]. The multi-linear backbone curve considered for a single shear screw-fastened connection is presented in Figure 5-12, for which the representative stiffness and displacement parameters are defined as follows

$$K_* = \alpha_* \left(\frac{d}{t}\right)^{\beta_*} E t \tag{5.10}$$

$$\Delta_* = \alpha_* \left(\frac{d}{t}\right)^{\beta_*} t \tag{5.11}$$

where α_* and β_* are dimensionless coefficients corresponding to the stiffness K_* ($= K_e$, K_s, K_p, K_r) or displacement Δ_* ($= \Delta_y$, Δ_m, Δ_r), d is the screw diameter, t is the ply thickness, and E is

Young's modulus of the connected plates. The trend coefficients (α_* and β_*) proposed by Phan and Rasmussen [114] are reported in Table 5-2.
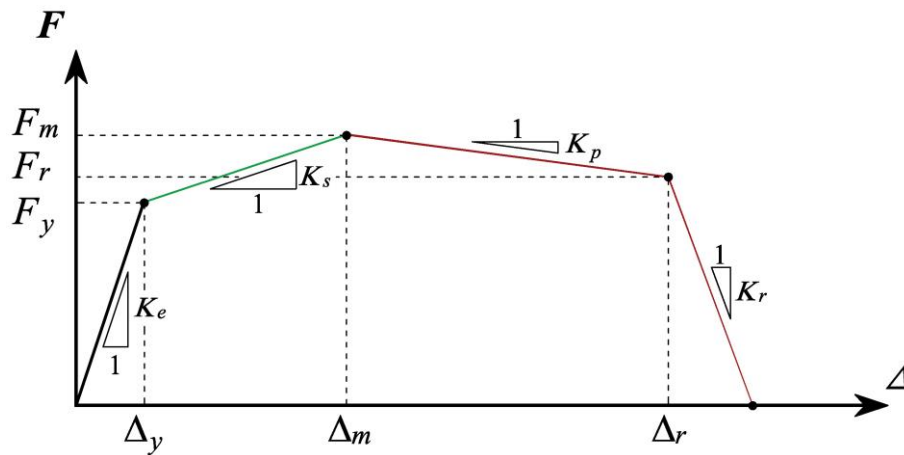
Figure 5-12: Backbone curve considered for the behaviour of a single shear connection

Table 5-2: Coefficients of the backbone curve for stiffness and displacement parameters [114]

Parameters	K_e	K_s	K_p	K_r	Δ_y	Δ_m	Δ_r
α_*	0.0136	0.0232	-0.0349	-0.0220	0.0680	0.0415	0.0445
β_*	0.5	-1.1	-2.5	0.2	1.3	2.9	3.4

The last option (iv) was the explicit modelling of the screws as solid elements with representative material properties. This technique is the most realistic option but implies a higher computational cost and requires additional considerations, such as contact conditions and connectivity to the surrounding shell/plate elements, as shown in Figure 5-11(d). The interaction between the screw surface and the bearing surface of steel plates has been provided by the shell-to-solid coupling of translational degrees of freedom, while normal hard contact and frictionless tangential behaviour have been prescribed for the interface between the screws head and steel shell surface. The solid screws were modelled with a nominal shank diameter of 4.8 mm, length of 10 mm, nominal head diameter of 10.8 mm, and thickness of 4.3 mm as per the dimensions of the sections used in the tests. Material properties of the self-drilling screws were defined according to the recommendations of the Australian Standard AS4291.1-2015 [198], i.e. the yield stress was assumed as 720 MPa and the ultimate strength as 900 MPa with Young's modulus the same as the web of the connected sections as per Table 5-1. These

assumptions align with the material properties that Roy et al. [199] obtained from the tensile coupon tests of self-drilling screws. Although only these four options were considered in this study, one may consider other alternatives for modelling the connectivity between constituent plate elements. One example is introducing a conventional or generalised beam element with representative stiffness properties, which share similarities with the third option in concept and is expected to yield comparable results.

The inelastic capacity curves obtained from the four modelling options are compared in Figure 5-13 for the back-to-back CFS built-up column C120-150-1. As can be seen, all the capacity curves obtained and the ultimate load predicted by different fastener modellings are in good agreement with the experimental results. However, considering the solid connection elements is the most accurate option among the methods considered. This method not only predicts the nonlinear capacity curve with reasonable accuracy but also can capture the expected failure mode, unlike the other techniques, as illustrated in Figure 5-14. This conclusion was also found valid for the more complex built-up section geometries. Therefore, option (iv) is considered for the numerical simulations and parametric studies included in this study.
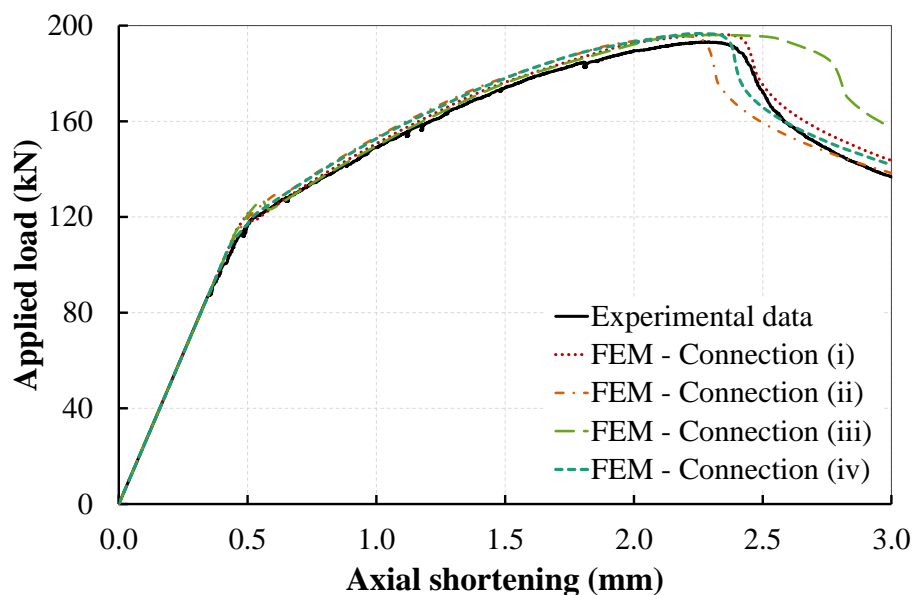
Figure 5-13: Comparison of load vs. axial shortening curves obtained from different FE modellings of screw-fastened connections for the test specimen 2C120-150-1

(a)   (b)   (c)   (d)   (e)
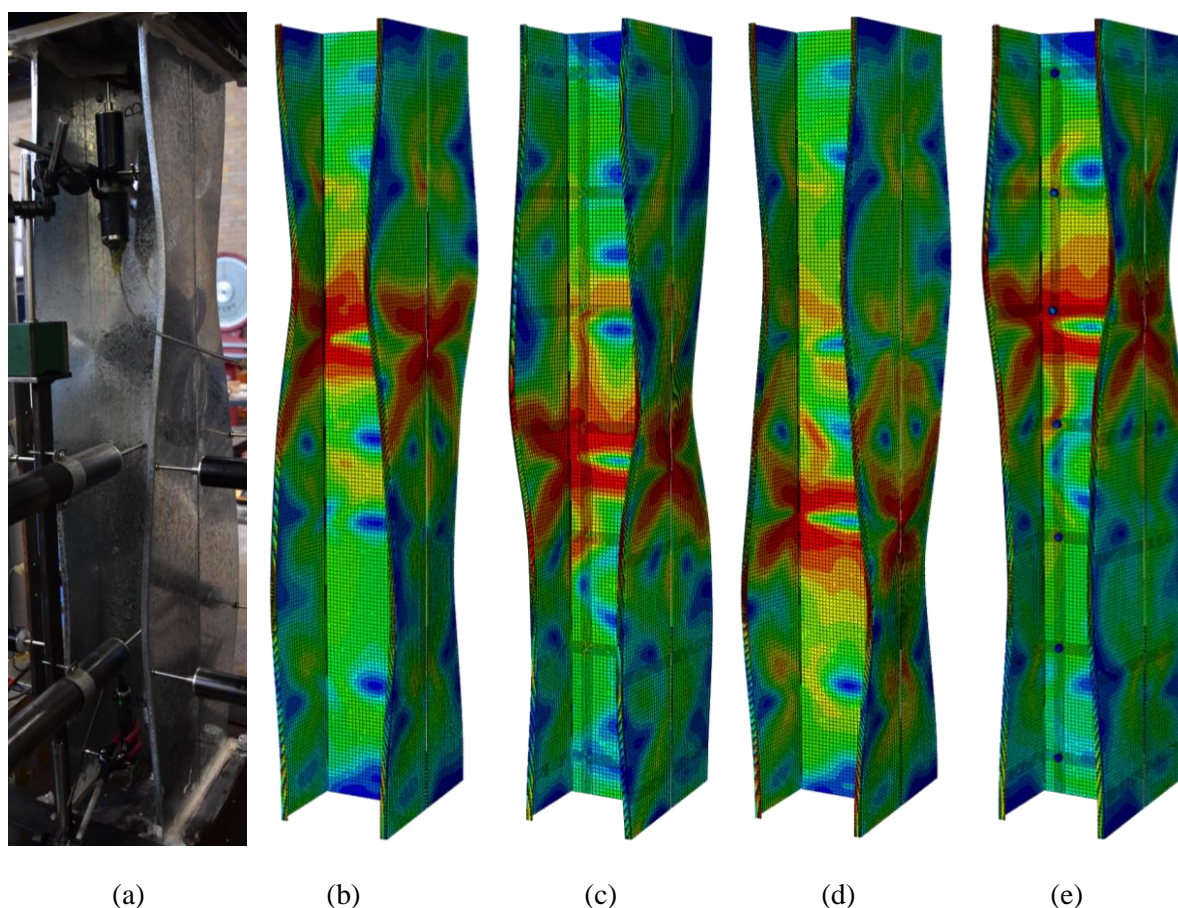
Figure 5-14: Comparison of post-peak deformations predicted by different FE modellings of screw-fastened connections for the test specimen 2C120-150-1: (a) test result, (b) tied DoFs at the centre of the fastener location, (c) tied DoFs over the fastener area, (d) mesh-independent fastener element, (e) solid element

5.2.6 *Element selection and mesh density*

As discussed in the previous Section, solid elements were utilised for the modelling of discrete fastener elements, whereas shell elements are used for modelling the constituent plates of the cold-formed steel single/built-up members. The fasteners were meshed by 3D linear hexahedron solid elements with a reduced integration scheme (C3D8R) available in Abaqus [180]. Abaqus supports a variety of shell elements ranging from conventional shell elements to continuum shell elements. The former group constitutes 2D triangular or quadrilateral elements representing the mid-plane/surface with translational and rotational degrees of freedom. In contrast, the latter class holds full 3D geometric representation based on only translational degrees of freedom for the top/positive (SPOS) and bottom/negative (SNEG)

surfaces that geometrically resemble solid elements and facilitate their direct connectivity. These elements employ first-order layered composite theory, and their constitutive modelling shares some similarities with the conventional shell elements, but unlike them, the continuum 3D shell elements can be stacked to provide a more refined through-thickness response. The stress in the thickness direction may not be zero in contrast to the plane stress assumption in the conventional shell elements, which may cause additional effective thickness strain beyond that considered in the conventional shells due to the Poisson's effect.

Since the CFS plates are very thin, conventional shell elements have been considered for this study. Specifically, the S4R elements [180] as the general-purpose quadrilateral (Quad) shell elements were used. It relies on a first-order approximation of the displacement field with a reduced (lower-order) integration scheme for forming the stiffness matrix (not for the mass matrix nor the distributed loading). Due to its linear nature and the use of reduced integration, this element also incorporates hourglass stabilisations for the control of spurious hourglass membrane and flexural modes, including the probable butterfly and crop-circle modes in transverse shear. These elements account for finite membrane strains and large rotations. They also allow transverse shear deformation using thick shell theory and yield Kirchhoff thin shell elements when the transverse shear deformation becomes very small as the shell thickness decreases. One may also save further on the computational cost by using four-node thin shell elements with five (instead of six) degrees of freedom per node (S4R5) [180], which is established upon the Kirchhoff plate theory for bending and small strain assumption for membrane behaviour. The quadratic version of this thin shell element, i.e. S9R5 [180], may show better performance due to its higher convergence rate requiring a lower number of elements and can also facilitate modelling the corners and lips due to its curved nature [19].

Last to note is the number of integration points through the shell thickness, which impacts the accuracy of the model and the sensitivity to the initiation and propagation of the yielding. A recommended default value for models with material nonlinearity is the use of the modified Simpson's rule with five integration points; however, more integration points may be required

at the cost of computational time. Typically, nine through-thickness integration points have been considered for the post-buckling and collapse simulations in this study.

A series of mesh sensitivity studies were performed for different cross-sections tested to ensure that the results were accurate. Six different mesh configurations were considered, with the aspect ratio of 1:1 for the flat parts of the section and a maximum aspect ratio of 4:1 for the rounded corners and connection regions. The flat parts element size varied from 20 mm to 4 mm, and a more refined mesh grade in the corner and lip segments was considered as required. The results of the mesh sensitivity study are presented in Figure 5-15 for a lipped channel section, 1C120-1, and one of the tested I-columns, 2C120-150-1. The ultimate load obtained from the FE analysis is normalised to the test values, and the total number of shell elements (NE_t) is divided by the number of sections included in a section (n).
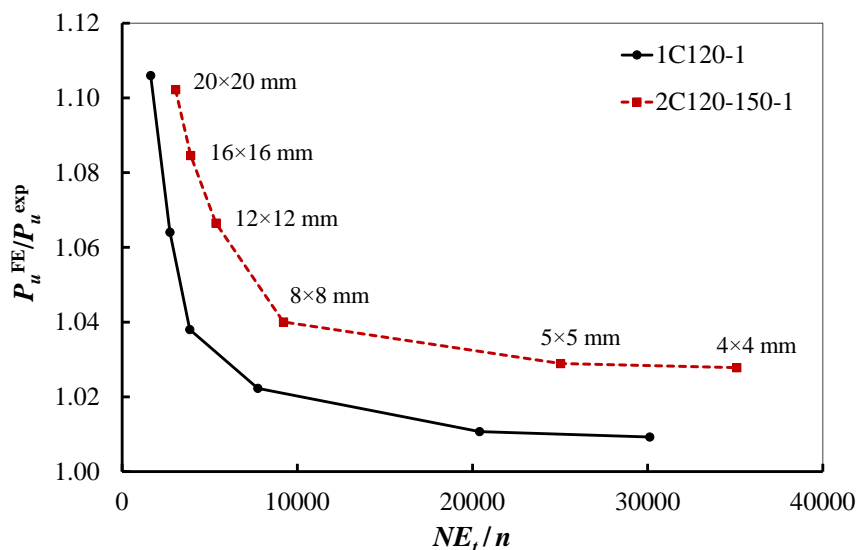
Figure 5-15: Convergence of the ultimate load with mesh refinement

Based on the results, a regular FE discretisation of the spatial domain with a typical maximum mesh density of 5-8 mm can yield a reasonably accurate nonlinear response for both sections. The FE simulations were performed on the University of Sydney's high-performance computing cluster (Artemis); therefore, the extra computational cost was not a major concern, and a finer mesh with a maximum element size of 5 mm was chosen for this numerical study.

Typical FE meshes adopted for modelling the connection regions in a built-up section and solid screws are shown in Figure 5-16.

<center>(a)   (b)</center>
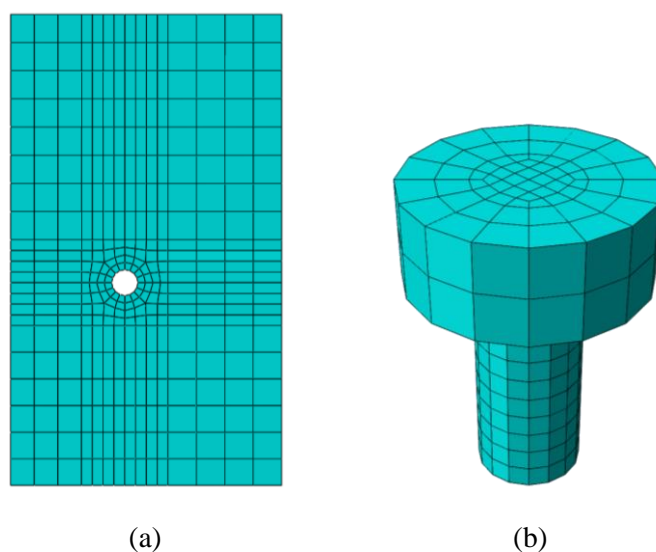
Figure 5-16: Adopted FE mesh for (a) connection regions in channel sections and (b) screws

5.2.7   *Loading and solution schemes*

A similar strategy, as that illustrated for the enforcement of boundary conditions in Section 5.2.3, has been utilised to impose the concentric compression objective loading condition on the built-up columns. The nodes and degrees of freedom on the loading surface have been constrained by assigning multi-point constraints (MPC) to the nodes. The concentric (uniform) compression loading has been applied by imposing displacement to the central point of the spider web, while the support reaction is monitored as a measure of the external force applied. Thereby, displacement-controlled analyses have been performed to investigate the inelastic behaviour of the sections up to failure, where the full Newton-Raphson (NR) method has been considered as the nonlinear solution strategy. For more efficiency in the computational cost, the automatic incrementation in Abaqus [200] for the consideration of pseudo time steps has been used rather than fixed increments. Furthermore, the line search algorithm (instead of event-to-event stepping) has been utilised to enrich the refinement of time increments and prevent divergence of equilibrium iterations, which is most effective when the quasi-Newton (also known as modified NR) solution is tested.

Due to the incremental marching of the imposed loading with irregular steps and depending on the degree of nonlinearity involved, the solution may become unstable or suffer from convergence problems in critical increments due to high strain/stress gradient or geometrical instability, i.e. buckling. This issue is exacerbated by the localised stress transfer in contact regions and localised failure in the critical areas. The problem is thus pronounced in the vicinity of critical response regions, which in the case of nonlinear behaviour of slender thin-walled metal members are the elastic buckling and ultimate capacity points. In the nonlinear solution of quasi-static problems with the NR method, Abaqus can introduce artificial mass-proportional damping [200] to stabilise the imposed gradient and alleviate the convergence issue. Introducing artificial damping and pseudo viscous force to the problem can aid in satisfying the equilibrium between the internal and external forces and finding convergent solutions. Of course, reverting to nonlinear dynamic (implicit/explicit) analysis with direct time integration and material damping would be an alternative solution to the problem at the expense of higher computational costs.

Automatic viscous stabilisation in any nonlinear quasi-static procedure can be simply illustrated as the following modification to the equilibrium equation between internal and external forces

$$P - F_i - F_v = 0;$$
(5.12)

where F_i is the vector of internal forces induced in the member due to external loading P, commonly approximated in numerical methods by $F_i = \mathbf{K}_p u$ as the multiplication of the inelastic stiffness matrix ($\mathbf{K}_p$) and the vector of nodal displacements (u). Moreover, F_v is the vector of viscous forces due to the introduction of artificial mass-proportional damping that takes the following form

$$F_v = c\mathbf{M}^* v,$$
(5.13)

in which c is the constant damping factor introduced, $\mathbf{M}^*$ is an artificial mass matrix calculated with unity density, and $v = \Delta u / \Delta t$ is the vector of nodal velocities from pseudo-time increments.

Abaqus supports the automatic stabilisation using either a constant damping factor or the adaptive automatic stabilisation damping factor. In the adaptive method, the damping factor can vary from initial values in spatial and temporal domains to effectively control the convergence and distortion issues from which the solution based on the constant damping factor may suffer. The automatic stabilisation assigns a damping factor that satisfies a specified limit for the ratio of dissipated energy for a given increment with characteristics similar to the first increment to the extrapolated strain energy. The default limit for the dissipated energy fraction is 0.02%, but it can be overwritten as desired. In contrast, the adaptive method adjusts the damping factor when and where required to ensure convergent results, but the energy dissipated by viscous damping would always grow [200]. Abaqus will limit the ratio of the energy dissipated by the viscous damping (ALLSD) to the total strain energy (ALLSE) to an adjustable accuracy tolerance (5% by default) to keep the deviation from the exact solution within an acceptable range.

Despite the efficiency of the adaptive automatic stabilisation in resolving the convergence issues, one may like to manually control the introduction of the damping factor by nominating variable user-defined values when required, e.g. critical steps only. However, no matter which option is chosen, the user's responsibility is to ensure the results are accurate. This can be confirmed by checking the following items:

- The value of damping factor (c) assigned to be reasonable, which depends on the problem and requires an experienced user,
- The viscous forces (F_v) to be relatively small in comparison with the overall internal forces (F_i) in the model;
- The viscous damping energy (ALLSD) to be relatively small compared to the total strain energy (ALLSE).

All the three options illustrated for viscous stabilisation, i.e. constant, adaptive automatic and user-defined, have been tested in this study. A comparison of the inelastic axial load-displacement curve obtained for the test specimen 3C120-900-1 is made in Figure 5-17. A

maximum damping factor value of 1×10^{-4} was obtained by trial and error for the solution convergence and applied as the constant damping factor for the first two options. The maximum stabilisation energy to strain energy ratio was set to 0.05 in the adaptive automatic stabilisation scheme. The load was applied in three stages with a constant damping factor in the user-defined option, for which the optimal value was determined by trial and error to minimise the ratio of energy dissipated by viscous damping to the total strain energy. The damping factor was set to zero for the initial stage from the start of the solution up to the onset of elastic buckling. From this point onwards, a value of 1×10^{-5} was applied up to the occurrence of the inelastic buckling, beyond which the maximum value of 1×10^{-4} was utilised through the post-buckling regime.
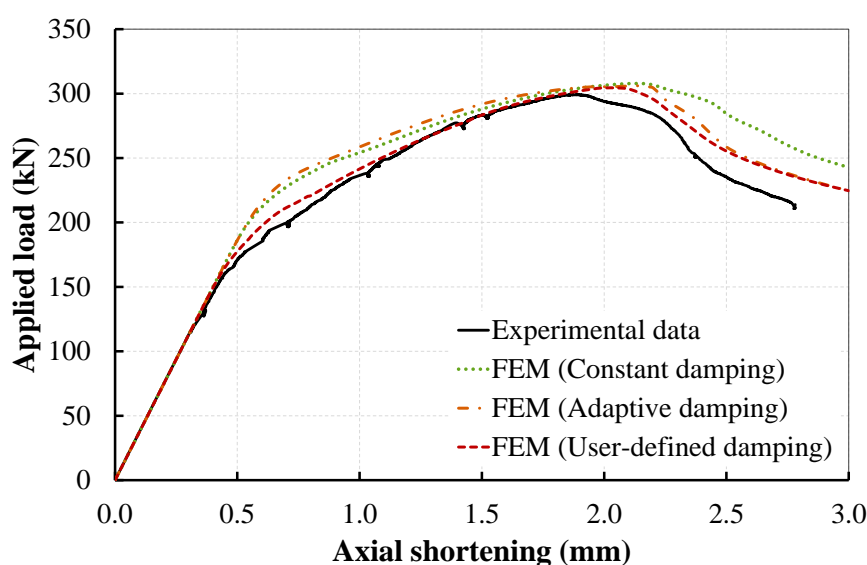
Figure 5-17: Comparison of load vs. axial shortening curves of different options of the viscous stabilisation scheme in Abaqus for test specimen 3C120-900-1

As can be seen, the user-defined damping option gives the closest prediction of the inelastic capacity curve. On the other hand, the adaptive automatic stabilisation method (referred to as adaptive damping in Figure 5-1) had the highest computational efficiency, but its continuously increasing pattern of dissipated viscous damping energy resulted in the observed overestimations of the capacity curve from the onset of elastic buckling up to the ultimate load despite the imposed criteria to keep the maximum ratio of stabilisation to strain energy reasonably small. Nonetheless, the predicted ultimate capacity is still within an acceptable tolerance for all the options. As a result, the variable user-defined damping factor was utilised

in this study, where a maximum damping factor value of 2×10^{-6} (with ALLSD/ALLSE ratio limited to 0.1%) was required for convergent solutions in I-sections, whereas a higher value at about 3×10^{-4} (with ALLSD/ALLSE ratio limited to 1.0%) was necessary for more complex built-up sections comprising of three and four lipped channel sections.

5.3   MODEL VALIDATION

The proposed model for the nonlinear finite element analysis of cold-formed steel built-up sections is summarised in this Section, where the performance and accuracy of the model predictions are validated against the results of experimental tests performed in this study, as presented in Chapter 4. The process starts with validating the model predictions for single-section columns of both test series C120 and C64. Then, the results of FE simulations are compared with the test data in Figure 5-18 and Figure 5-19, which contain the nonlinear overall load-displacement curves and the lateral displacement curves obtained from the LVDT measurements.

The figures show that good agreement has been achieved between the numerical predictions and the test data in terms of the inelastic force and displacement capacities and the expected displacement pattern. In addition to the quantitative comparison of capacities, the predicted failure mode is compared in Figure 5-20 with that obtained from testing and shows a reasonably matching prediction. The predominant buckling mode is distortional buckling for specimen 1C120-2, while a combined local-distortional buckling constitutes the ultimate failure mode of test specimen 1C64-1. As seen in Figure 5-20(b), the predicted deformations of the test specimen 1C64-1 are localised in a slightly higher position compared to the test, which in turn resulted in a difference between the recorded transducers data in testing and the FE model, as shown in Figure 5-19(b). All in all, these examples corroborate the suitability of the numerical model in simulating the loading and support conditions as well as modelling the geometric imperfections with reasonable accuracy.

(a)   (b)
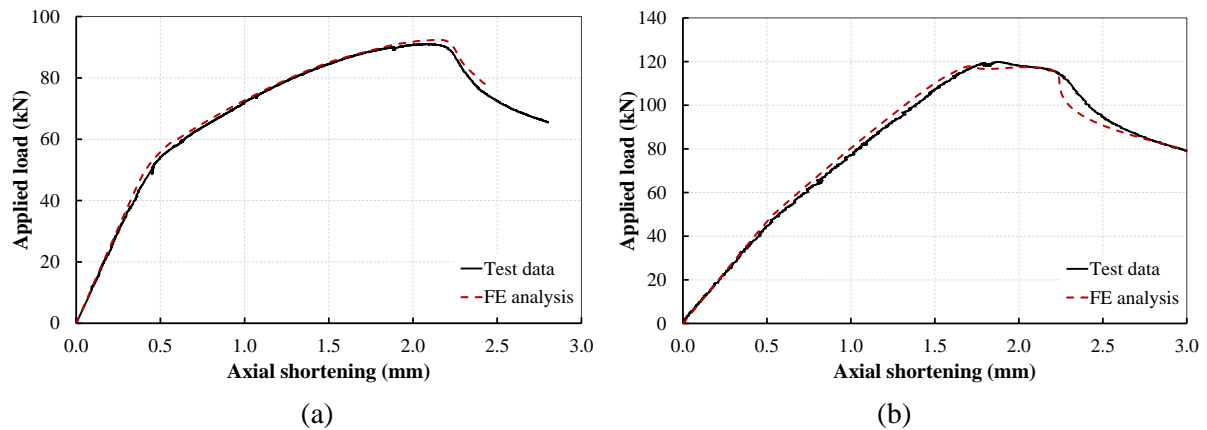
Figure 5-18: Comparison between numerical predictions and experimental results of load vs. axial shortening curve of lipped channel sections: (a) 1C120-2 and (b) 1C64-1

(a)

(b)
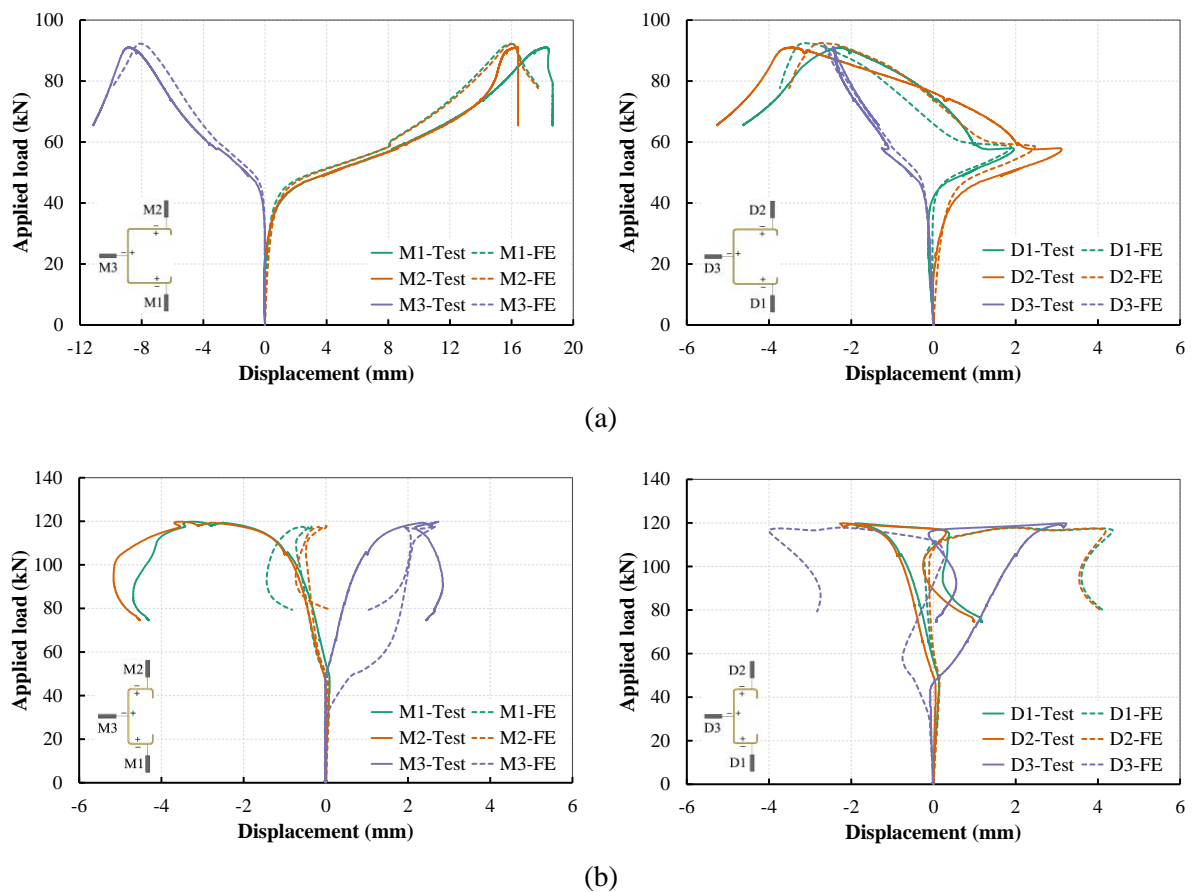
Figure 5-19: Comparison between numerical predictions and experimental results of transducers data of lipped-channel sections: (a) 1C120-2 and (b) 1C64-1

<div align="center">(a)   (b)</div>
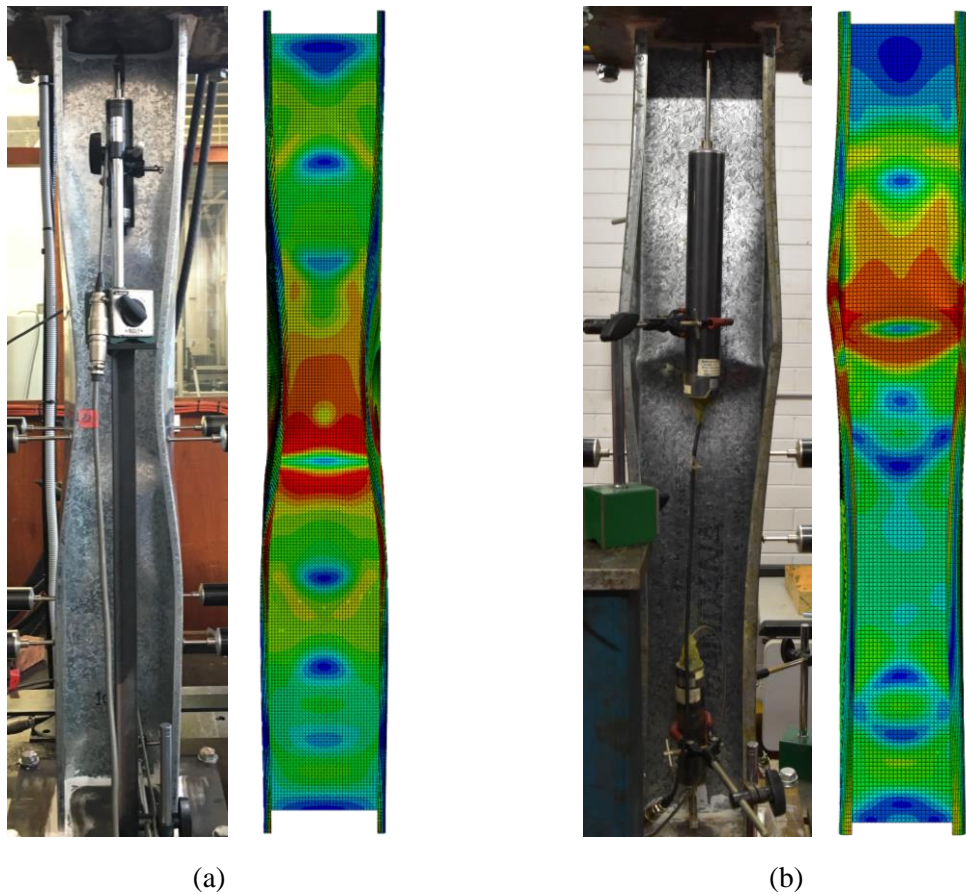
Figure 5-20: Comparison between numerical and experimental results of post-peak deformations of lipped-channel sections: (a) 1C120-2 and (b) 1C64-1

In the next step, the FE modelling of the first group of built-up sections is tested, which are made of simple back-to-back connections of lipped-channel sections. This teat aims to validate the contact modelling and incorporation of discrete fasteners. The inelastic capacity curves obtained from the FE simulations for different fastener spacings are presented in Figure 5-21 and compared with the experimental data of compression load vs. axial shortening. Figure 5-22 shows the predictions of lateral displacements at quarter- and half-height stations compared to the measurements from LVDTs. Lastly, the predicted failure modes at the post-peak state are presented in Figure 5-23 for the fastener configurations considered and compared side-by-side with those observed in testing.

As can be seen, the FE model can qualitatively and quantitatively capture the inelastic behaviour of the built-up columns with web-to-web screw connections at various spacings up to the ultimate capacity and even beyond that into the post-peak regime. The ultimate load is

predicted with excellent accuracy for different screw spacings. However, the FE models typically show a marginally higher stiffness than the test specimens after the onset of elastic buckling, which is related to the simplified modelling of the boundary conditions as discussed in Section 5.2.3. The FE results also demonstrate excellent agreement with the recorded transducer data and the observed post-peak deformations in all different screw spacing cases. Moreover, conformal web buckling of back-to-back connected sections is achieved numerically for screw spacing less than $L/3$, as shown in Figure 5-23, which matches with the experimental observations. Considering the results obtained, it can be concluded that the proposed method for modelling screw-fastened connections and contact between the constituent plates has been quite effective and accurate in capturing the inelastic behaviour, ultimate capacity and failure mode.

(a)

(b)

(c)

(d)
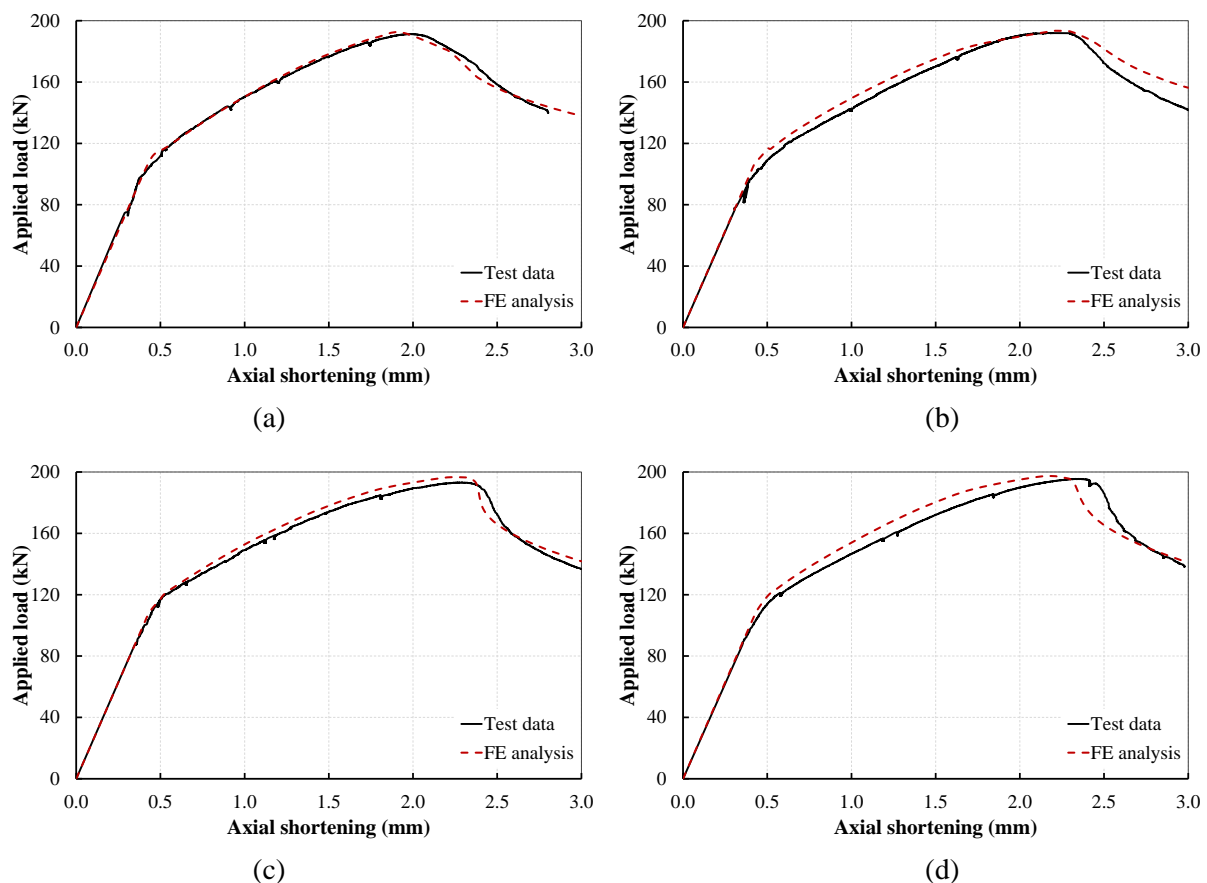
Figure 5-21: Comparison between numerical predictions and experimental results of load vs. axial shortening curve of built-up I-sections with different screw spacings: (a) 2C120-900-1, (b) 2C120-300-2, (c) 2C120-150-1 and (d) 2C120-100-1
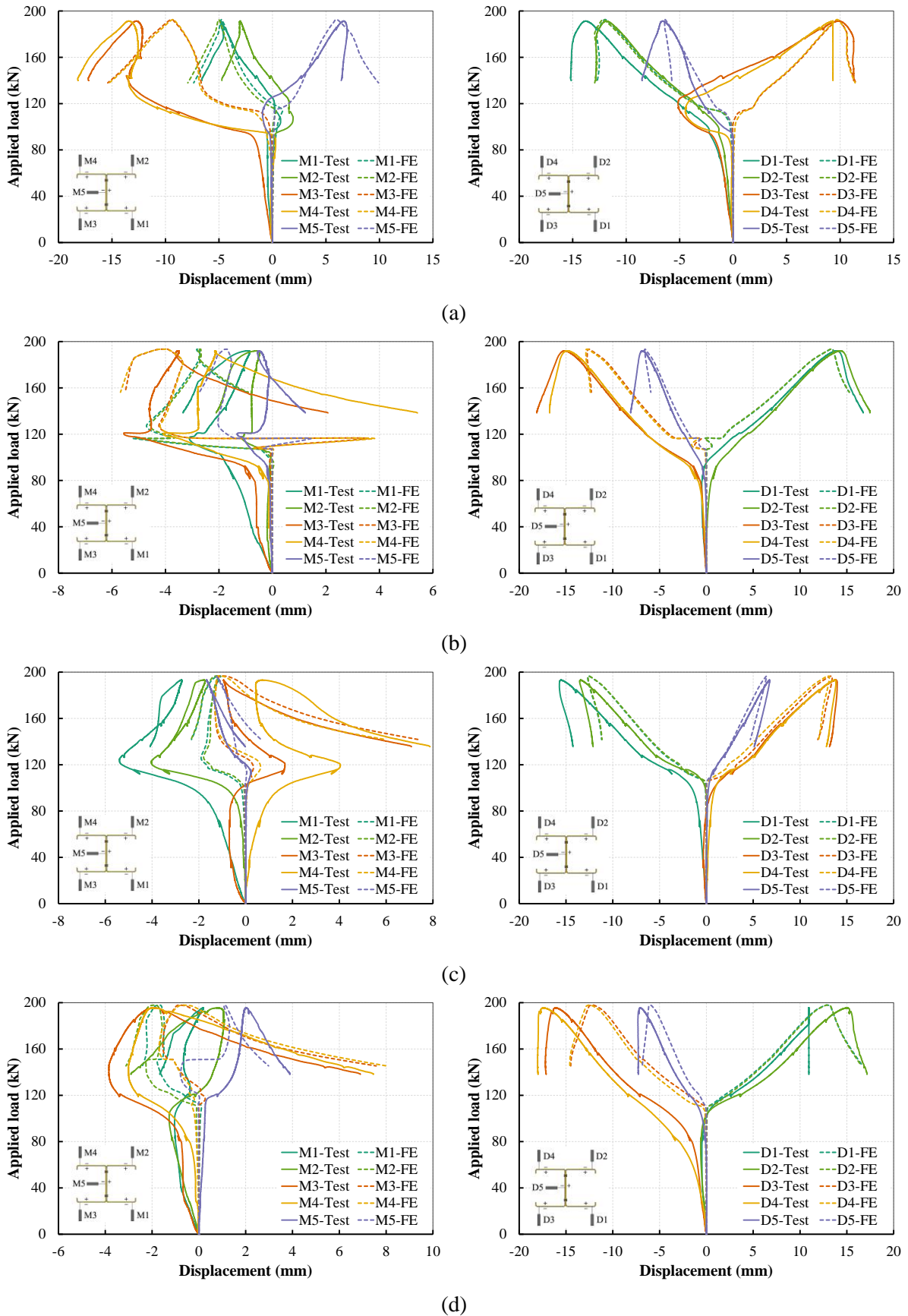
Figure 5-22: Comparison between numerical predictions and experimental results of transducers data of built-up I-sections: (a) 2C120-900-1, (b) 2C120-300-2, (c) 2C120-150-1 and (d) 2C120-100-1

(a)

(b)

(c)

(d)
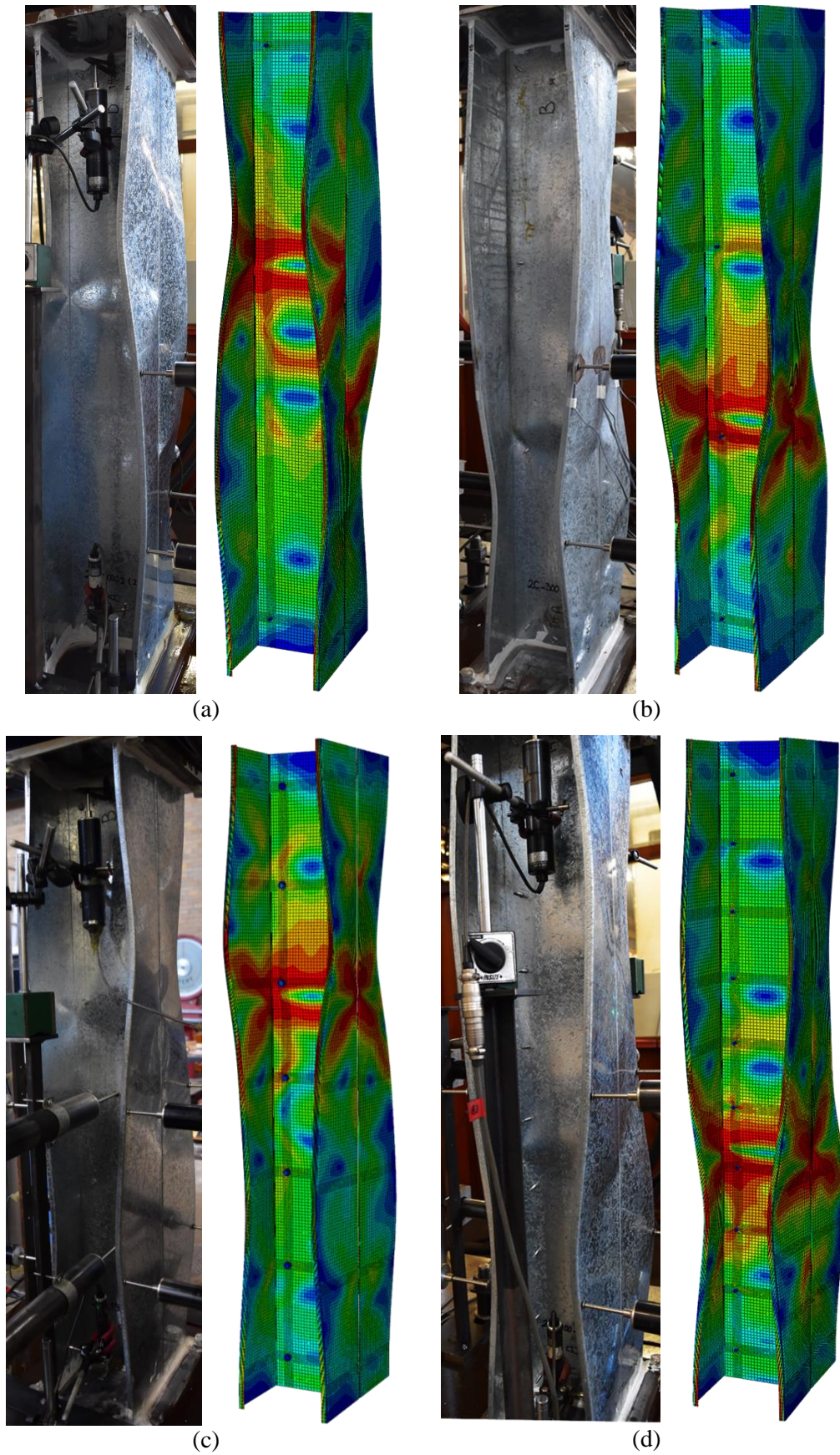
Figure 5-23: Comparison between numerical and experimental results of post-peak deformations of built-up I-sections: (a) 2C120-900-1, (b) 2C120-300-2, (c) 2C120-150-1 and (d) 2C120-100-1

Following these preliminary validations, the effectiveness of the proposed FE modelling approach in capturing the inelastic behaviour of more sophisticated built-up section assemblies is tested. The numerical predictions are verified against the experimental data for the remainder of the test specimens, i.e. 3C and 4C series, which are made of multiple sections with mixed-type connectivity (web-to-web and web-to-flange).

The nonlinear capacity curves and lateral displacement graphs for the built-up sections made of three lipped-channel sections with a screw spacing of 300 mm are presented in Figure 5-24 and Figure 5-25 as indicative examples. An excellent agreement with the test data is achieved in terms of the ultimate load and the recorded lateral deformations for both sections that inherently differ in their failure modes. Subsequently, the predicted deformations by the numerical simulations are compared with the test observations at the peak-load state for test specimen 3C120-300-2 in Figure 5-26 and at the post-peak regime for test specimen 3C64-300-1 in Figure 5-27. The results show identical failure mechanisms to the experimental observations, indicating the FE analysis has accurately reproduced the failure modes formed in the built-up sections, viz. distortional buckling for test series C120 and local-distortional buckling interaction for test series C64.

The same comparisons are made between the FE results of built-up columns comprising four lipped-channel sections with the experimental data in Figure 5-28 to Figure 5-30. As can be seen, with a very good level of accuracy, the FE results match the experimental data and the observed post-buckling deformations for both test series. The complete load vs. axial shortening curves and load vs. transducer displacement graphs obtained from the FE analyses are given in Appendix D for both test series and compared with the experimental data.

As a concluding remark for this Section, the ultimate capacity of the built-up test specimens is quantitatively compared with the FE predictions, and the results are summarised in Table 5-3. The average ratio of the ultimate capacity predicted by the FE models to the experimental strength of the specimens is 1.02, with a standard deviation of 0.02. In summary, excellent agreement is achieved for all different built-up assemblies with various screw spacings, which

confirms the capability of the incorporated model to predict the structural behaviour of different built-up configurations.

(a)   (b)
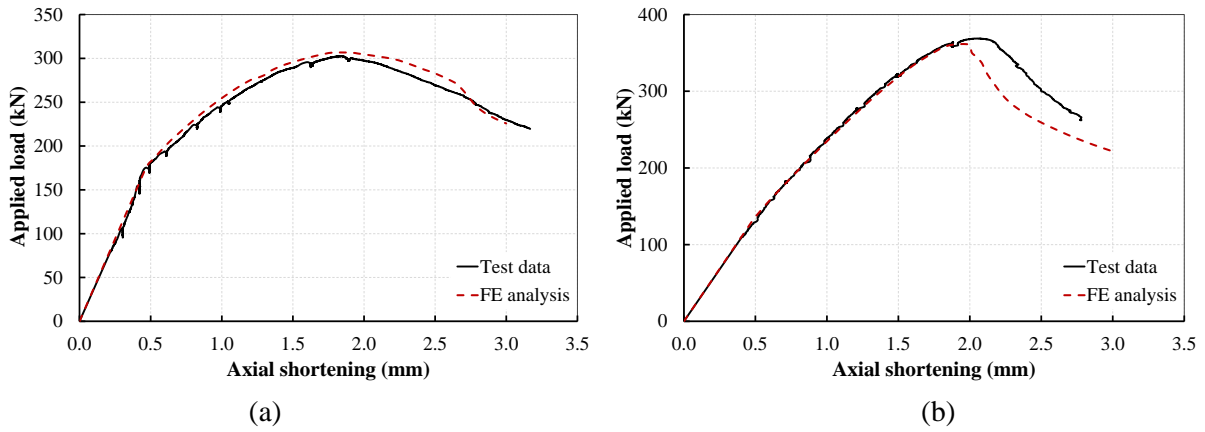
Figure 5-24: Comparison between numerical predictions and experimental results of load vs. axial shortening curve of built-up 3C series: (a) 3C120-300-2 and (b) 3C64-300-1

(a)

(b)
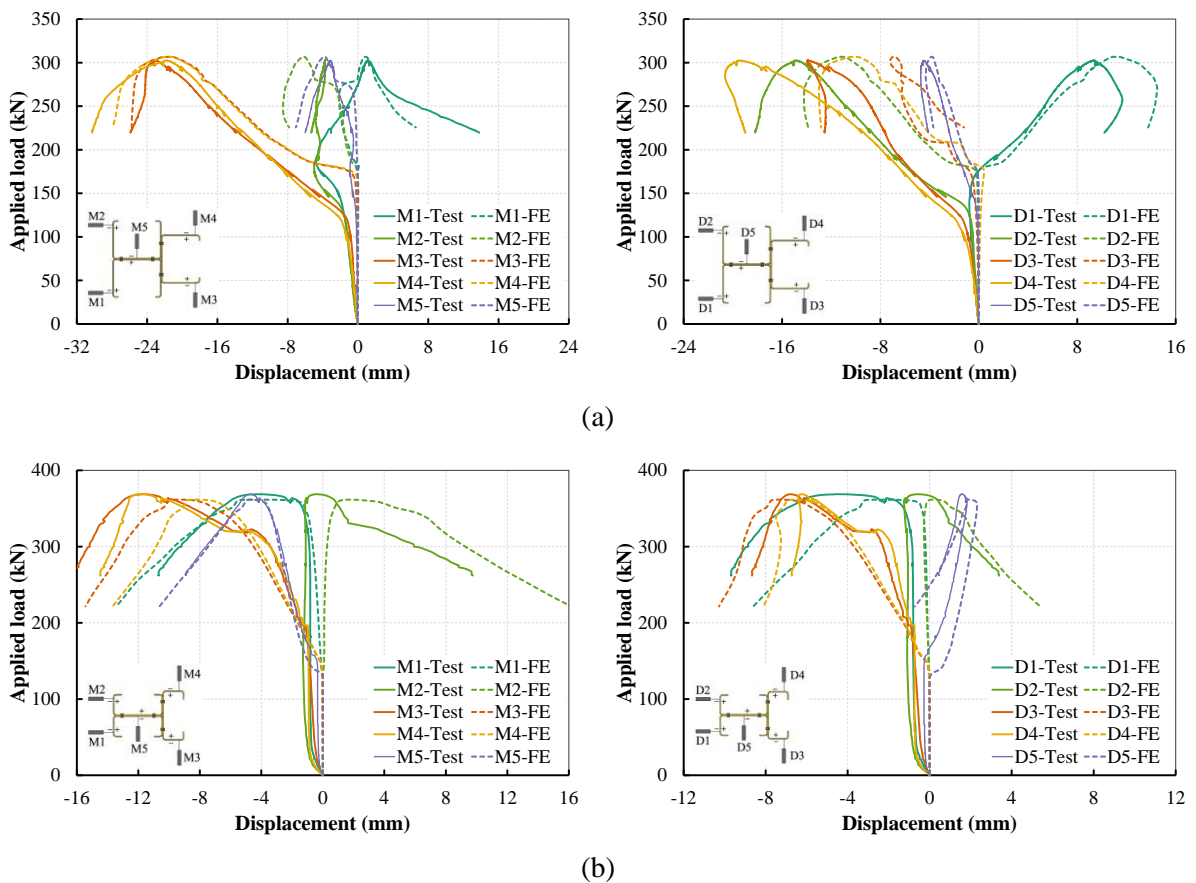
Figure 5-25: Comparison between numerical predictions and experimental results of transducers data of built-up 3C series: (a) 3C120-300-2 and (b) 3C64-300-1

(a)

(b)

(c)
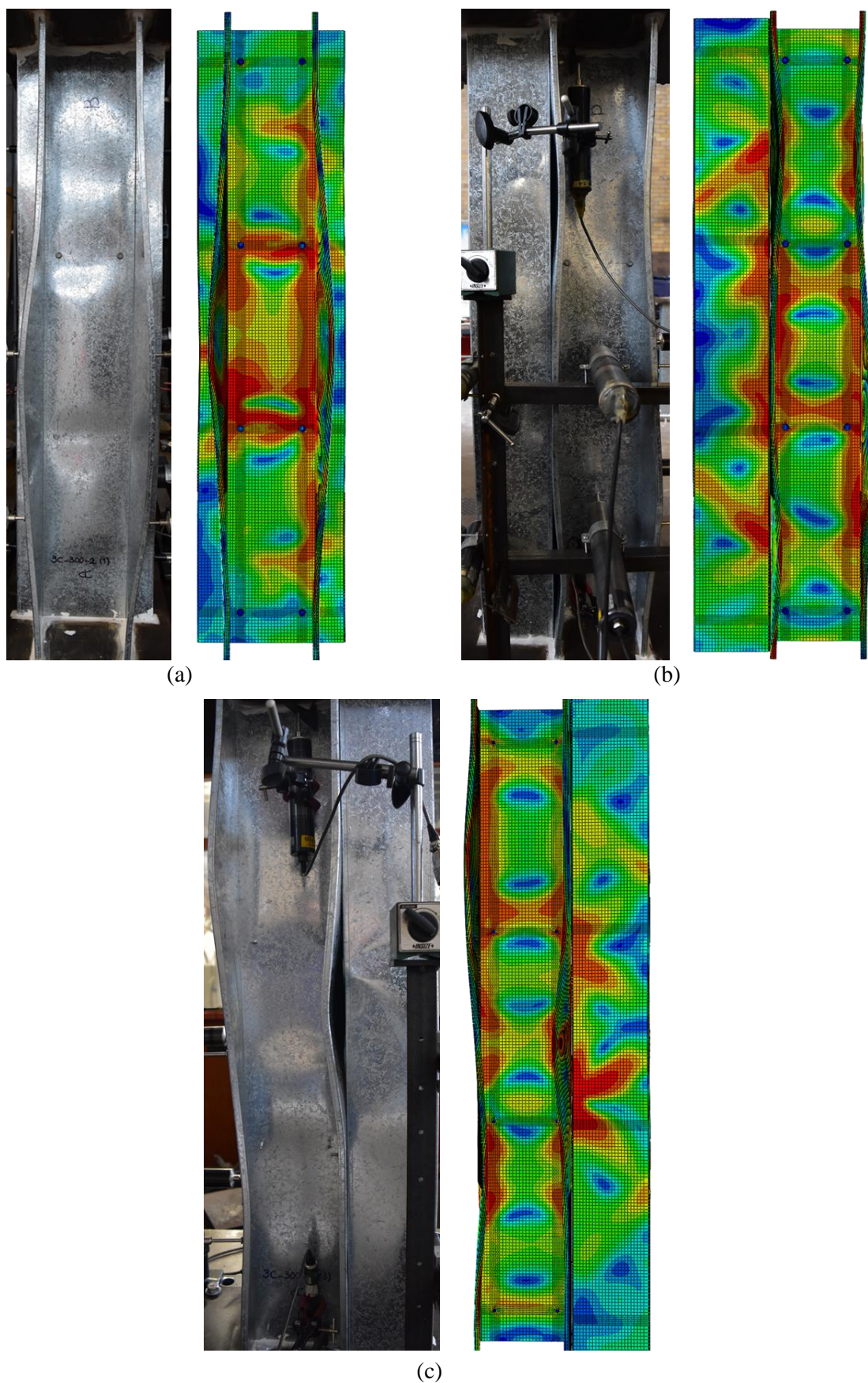
Figure 5-26: Comparison between numerical predictions and experimental results of deformation pattern at peak-load state for specimen 3C120-300-2: (a) side view, (b) back view and (c) front view

(a)

(b)

(c)
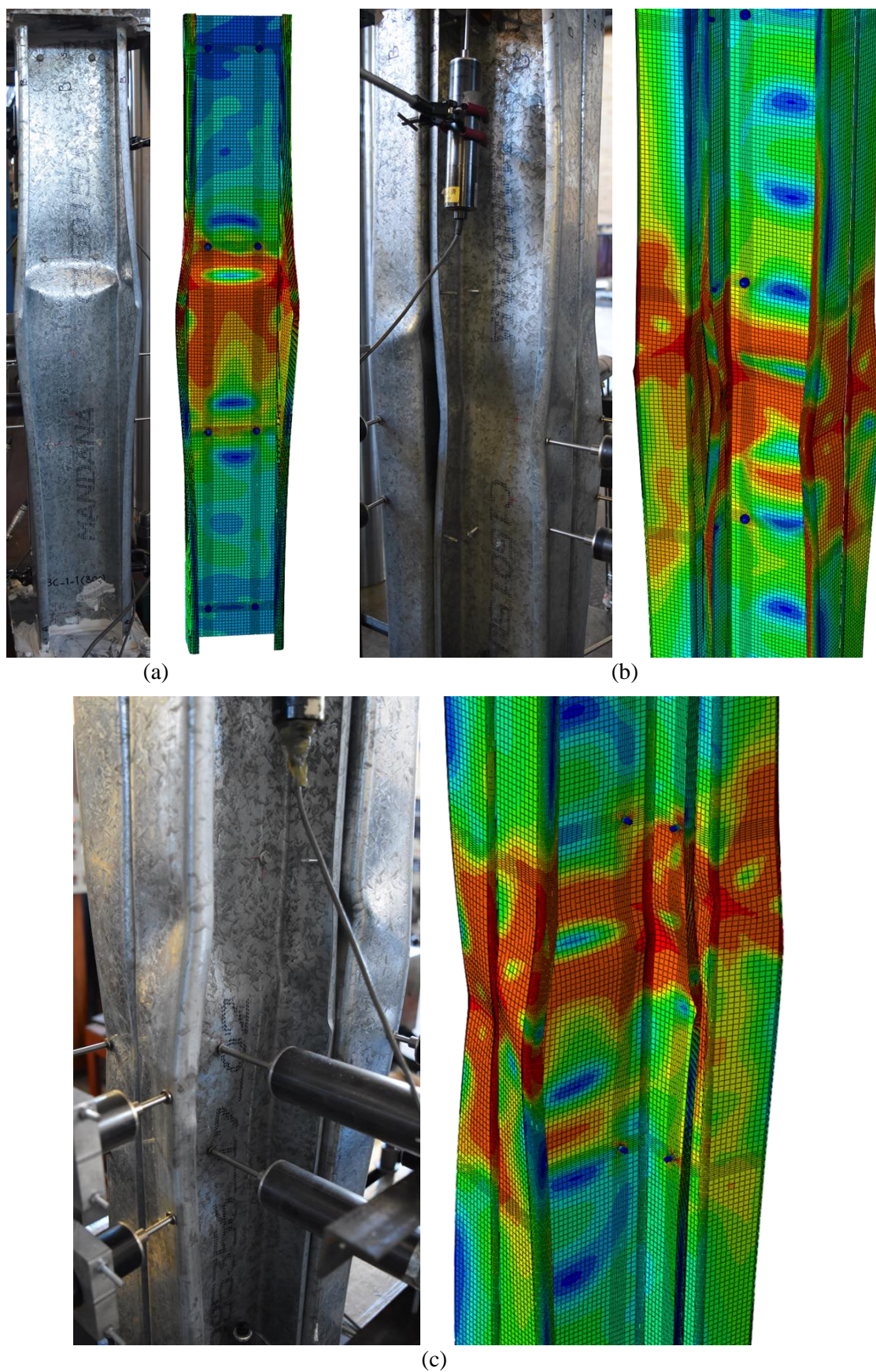
Figure 5-27: Comparison between numerical predictions and experimental observations of post-peak deformation pattern for specimen 3C64-300-1: (a) side view, (b) back view and (c) front view

(a)

(b)
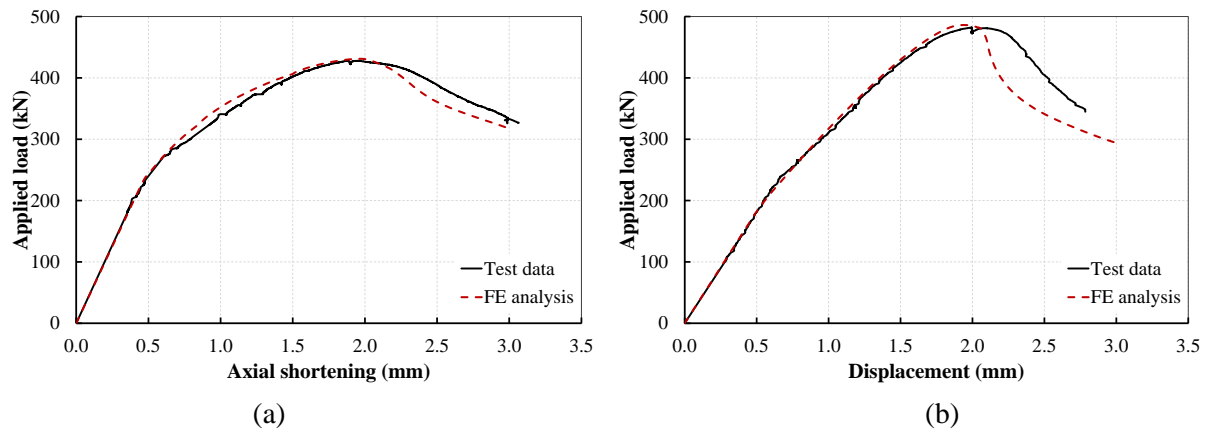
Figure 5-28: Comparison between numerical predictions and experimental results of load vs. axial
shortening curve of built-up 4C series: (a) 4C120-300-2 and (b) 4C64-300-1

(a)

(b)
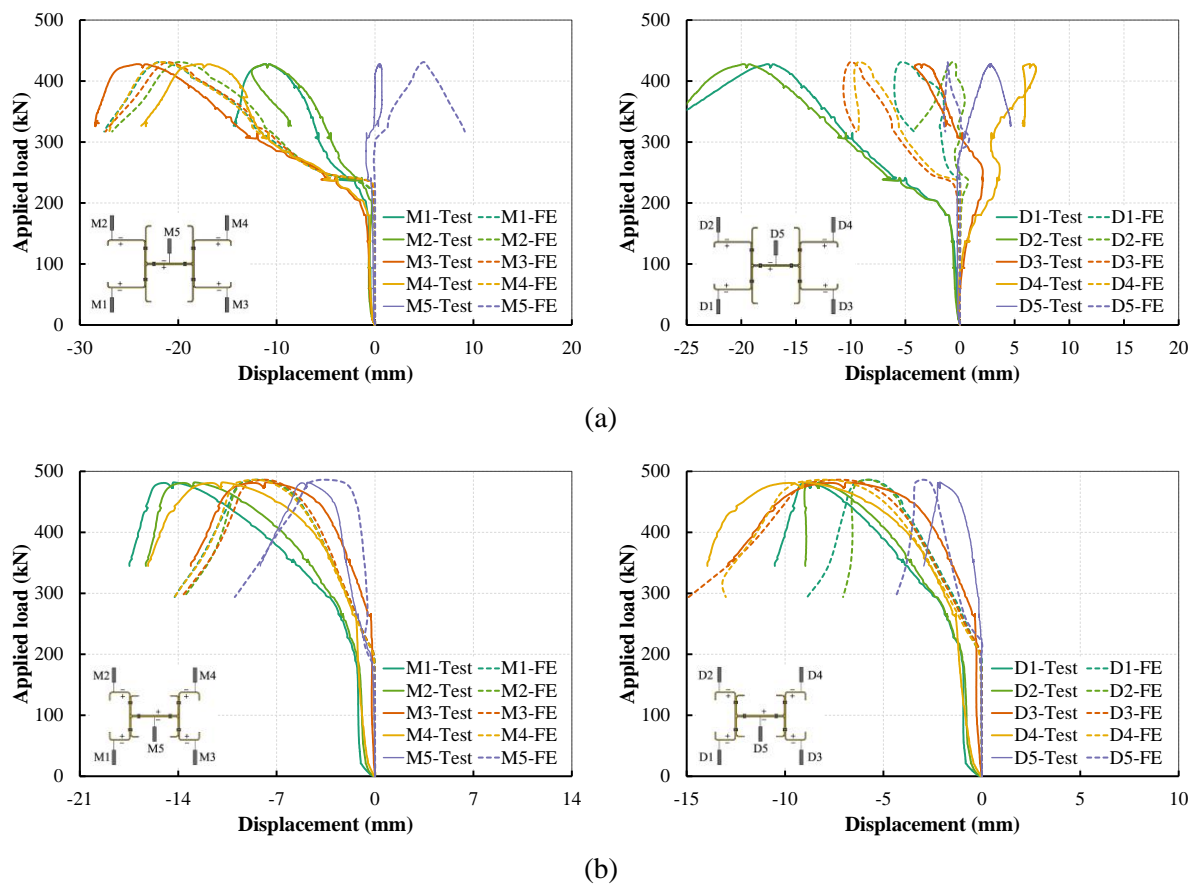
Figure 5-29: Comparison between numerical predictions and experimental results of transducers data
of built-up 4C series: (a) 4C120-300-2 and (b) 4C64-300-1

(a)

(b)
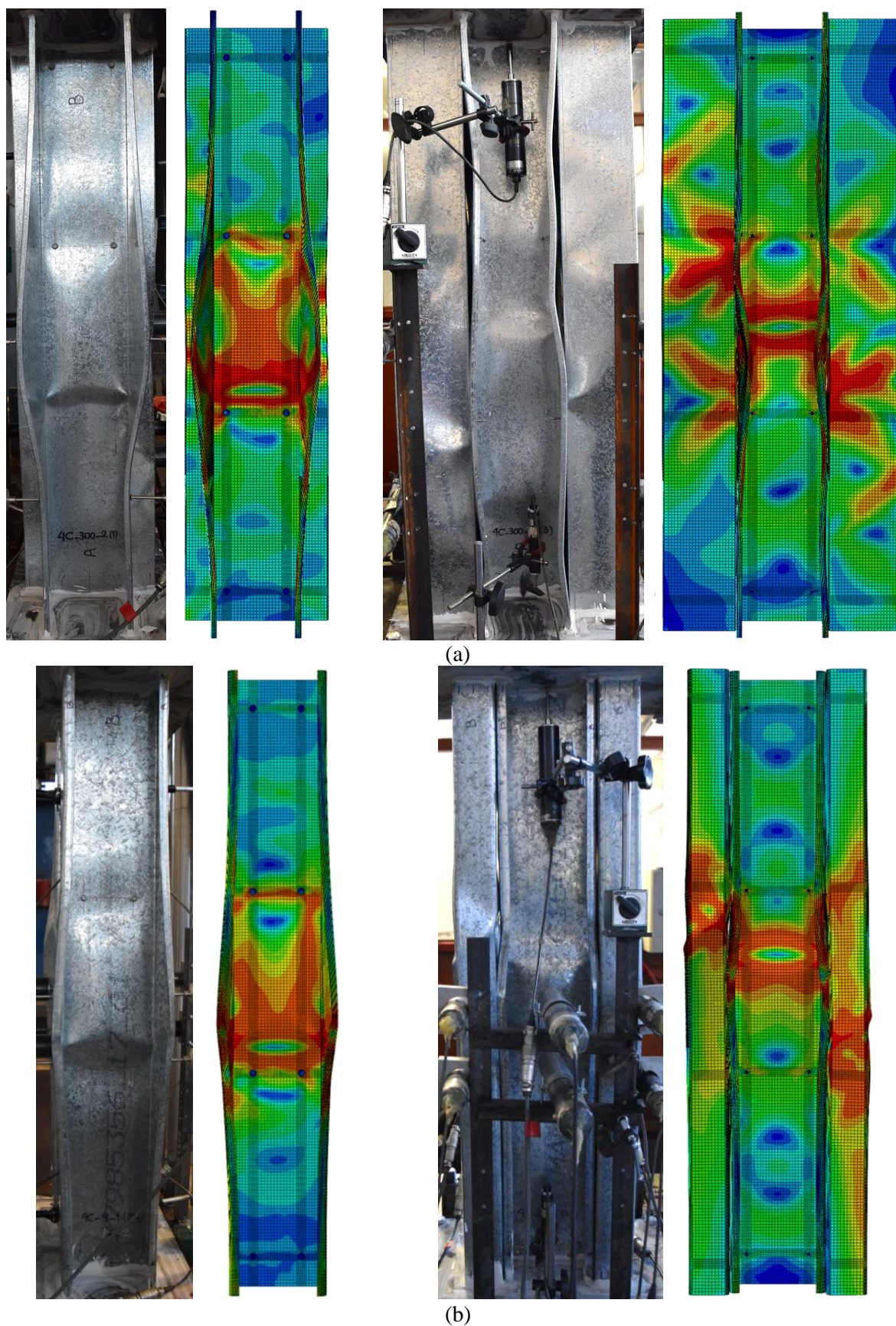
Figure 5-30: Comparison between numerical predictions and experimental results of the post-peak deformations for specimen (a) 4C64-300-2, (b) 4C64-300-1 from the side (left) and front (right) views

Table 5-3: Comparison of the ultimate load obtained from the FE analyses with the test results for various built-up columns

Specimen	P_u^{exp} (kN)	P_u^{FE} (kN)	P_u^{FE} / P_u^{exp}
2C120-900-1	188.9	192.5	1.02
2C120-900-2	199.6	193.3	0.97
2C120-300-1	202.2	198.3	0.98
2C120-300-2	190.4	193.4	1.02
2C120-150-1	190.8	196.5	1.03
2C120-150-2	191.2	195.3	1.02
2C120-100-1	193.0	197.7	1.02
2C120-100-2	195.2	198.4	1.02
3C120-900-1	295.9	308.6	1.04
3C120-900-2	303.7	307.9	1.01
3C120-300-1	300.7	304.4	1.01
3C120-300-2	299.6	306.5	1.02
3C120-100-1	317.2	330.2	1.04
3C120-100-2	322.8	331.1	1.03
4C120-900-1	411.2	422.3	1.03
4C120-900-2	410.7	421.5	1.03
4C120-300-1	420.3	424.8	1.01
4C120-300-2	422.1	431.1	1.02
4C120-100-1	442.9	476.4	1.08
4C120-100-2	492.1	480.7	0.98
3C64-900-1	352.0	367.1	1.04
3C64-900-2	358.5	368.4	1.03
3C64-300-1	362.4	361.6	1.00
3C64-300-2	356.3	363.6	1.02
3C64-100-1	386.8	392.5	1.01
3C64-100-2	381.0	392.4	1.03
4C64-900-1	468.8	485.9	1.04
4C64-900-2	474.6	486.7	1.03
4C64-300-1	477.9	486.2	1.02
4C64-300-2	477.5	484.4	1.01
4C64-100-1	505.6	532.9	1.05
4C64-100-2	513.1	527.6	1.03
		Average	1.02
		St. Dev.	0.02

5.4   PARAMETRIC STUDY

Upon successful validation of the numerical framework for the inelastic analysis of built-up sections, extensive parametric studies are performed in this Section to investigate the influence of different design parameters in preparation for the validation of design equations according to the Direct Strength Method. Variations in design parameters are considered in addition to those already reflected in the experimental investigation phase. These include changes in the section depth, width, thickness, built-up section geometry and screw spacing.

5.4.1   Cross-sections geometry

To design cross-sections for the parametric study, signature curves were first obtained for single lipped channel sections with different web height (h), flange width to web height ratio (b_f/h), thickness (t) and lip length (d) to find critical elastic buckling stresses for design purposes. The results obtained for the ratio of the critical local buckling load (f_{crl}) to the critical distortional buckling load (f_{crd}) were presented previously in Figure 4-2 as a function of the relative flange width ratio and the lip length. The chosen geometric dimensions were based on the signature curves and the acknowledgment of practicality in construction to cover sections with distinct local and distortional elastic buckling modes.

Following these results, the final geometric parameters for the parametric studies were carefully selected with the aim of further assessing the sectional buckling of built-up sections with varying sectional slenderness. The sectional slenderness (λ_s) is defined as

$$\lambda_s = \sqrt{f_y / f_{crs}} \tag{5.14}$$

in which f_y is the yield stress obtained from the tensile coupon tests, and f_{crs} is the critical sectional buckling stress for either local or distortional modes. According to the practical sections used in industry, three values of section depth, i.e. h=100, 200, and 300 mm, with two different nominal thicknesses were chosen. Furthermore, two sets of b_f/h-ratios were selected for each section depth such that the prevalent buckling mode of the section was local buckling

mode in the first set (set-L) and a distinctive distortional mode in the second set (set-D). The inner radius of the corners (r_i) was chosen as 4.0 and 3.0 mm for the sections of set-L and set-D, respectively.

The height of the columns in set-L was considered such that multiple (at least three) local buckling half-wavelength is expected in the specimen. This consideration would result in the isolation of the fixed end conditions effect as it is expected to diminish by increasing the member length. Therefore, the end conditions are not expected to influence the local buckling capacity and associated half-wavelength. This was observed previously in the results of elastic buckling analyses in Chapter 3; see Figures 3-18 and 3-27 as indicative examples. Thereby, the critical buckling stress (f_{crl}) can be obtained either from reference signature curves for the simply-supported condition or directly from an elastic buckling analysis under clamped end conditions using the Finite Strip Method. The critical buckling length (L_{crl}), as the half-wavelength associated with the local buckling, can also be evaluated directly from the signature curves or indirectly from fixed-end analysis by accounting for the number of local buckling half-wavelengths (n_l) observed over the length, i.e. $L_{crl} \approx L/n_l$. It is noted that the length of each specimen was also selected such that one distortional buckling half-wavelength can be potentially induced under clamped end conditions, which would allow studying any probable sectional buckling interactions if available. This concept is illustrated for one of the sections in this set (C200-80-1.5) in Figure 5-31(a), in which the signature curve under S-S boundary conditions and the buckling stress for different member lengths under C-C end conditions (for M=30) are included. The results of the elastic buckling analysis are presented versus the reference length, which is the buckle half-wavelength for the simply-supported condition and the actual column length for the fixed-ended columns. The key parameters, including critical sectional buckling stresses and associated half-wavelengths, are indicated. As can be seen, the critical buckling stress under fixed ends, which is almost stabilised upon induction of multiple local half-wavelengths in the member, is in line with the minimum local buckling stress from the signature curve with m=1, which is not modified by increasing the number of terms.
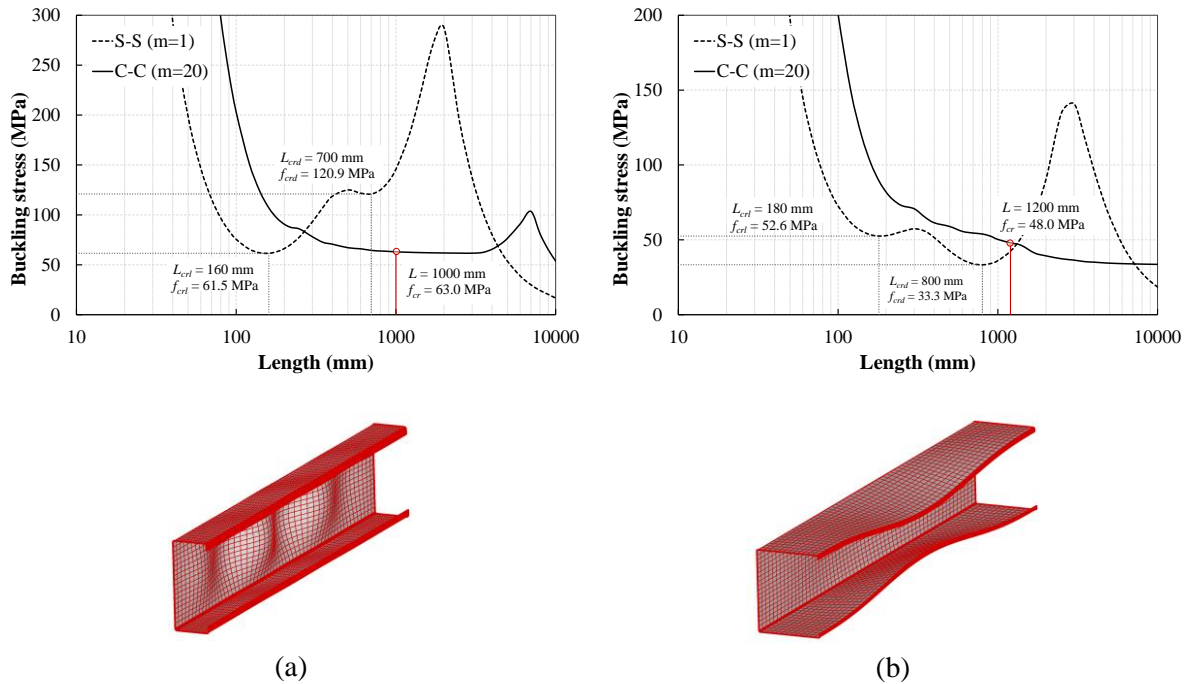
Figure 5-31: Buckling stress versus reference length curves and buckling mode shapes of (a) section C200-80-1.5 from set-L and (b) section C200-160-1.5 from set-D

The same effect is expected to be observed in distortional buckling as the first few buckling half-wavelengths are expected to be influenced by the support conditions, where clamped end conditions can enhance distortional buckling stress. However, the effect is similarly expected to vanish, and the results would tend towards those for simply-supported cases by increasing the member length such that multiple (at least three) distortional buckling half-wavelength are generated in the specimen. Therefore, the critical buckling half-wavelength (L_{crd}) can be assessed from the signature curves for simply-supported cases, and the minimum distortional buckling stress (f_{crd}) can be conservatively evaluated from the same signature curve. However, the impact of boundary conditions should be accounted for in calculating the distortional buckling stress (f_{crd}) if enough distortional buckles are not induced along the length of the column. As an illustrative example, the results of the elastic buckling analysis for section C200-160-1.9 from set-D are presented in Figure 5-31(b). As can be seen, the height of the columns in the distortional set was chosen such that one distortional buckling half-wavelength is induced under fixed end conditions while the length is still short enough to minimise the influence of

global buckling. In this case, the distortional buckling stress should be determined from the C-C curves.
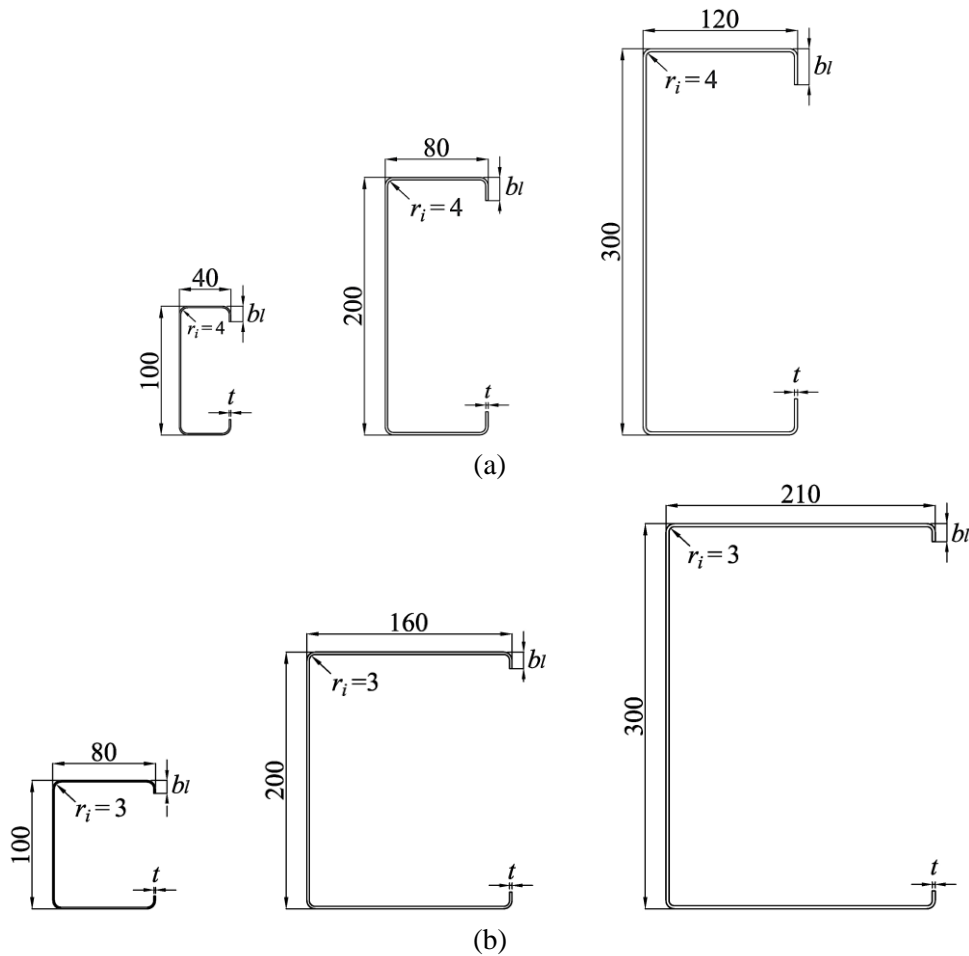
Figure 5-32: Geometry of the lipped channel sections considered in the parametric studies: (a) Set-L with prevalent local buckling mode and (b) Set-D with predominant distortional buckling mode

Figure 5-32 shows the geometry of the selected lipped channel sections for each set of the parametric studies, where their sectional dimensions and design parameters, including their critical sectional buckling stress and slenderness ratios, are listed in Table 5-4. The characteristic half-wavelength as critical lengths for each sectional buckling mode is also included in the table. These variations resulted in a broad coverage of sectional slenderness values for each sectional buckling mode, i.e. ranging from 1.13 to 3.49 for set-L and from 0.96 to 3.71 for set-D. These sections were labelled with an initial C (representing one lipped channel section) followed by three numbers indicating the web height, flange width and thickness of the section. For example, C100-40-1.2 refers to a section from the set-L with

h=100 mm, b_f =40 mm, and t=1.2 mm. Note that λ_{crs} and L_{crs} are the critical sectional slenderness and half-wavelength corresponding to the dominant buckling mode of the cross-section, i.e. minimum of the local (f_{crl}) and distortional (f_{crd}) buckling stresses.

Table 5-4: Summary of section dimensions and design parameters of the lipped channel sections considered in the parametric studies

Set	Section	L (mm)	h (mm)	b_f (mm)	b_l (mm)	t (mm)	f_{crl} (MPa)	f_{crd} (MPa)	L_{crs} (mm)	λ_{crs}	P_u^{FE} (kN)
L	C100-40-1.2	500	100	40	12	1.2	163.8	302.7	80	1.80	73.2
	C100-40-1.9	500	100	40	16	1.9	413.6	602.8	80	1.13	149.0
	C200-80-1.5	1000	200	80	16	1.5	61.5	125.0	160	2.94	118.4
	C200-80-1.9	1000	200	80	18	1.9	99.0	181.5	160	2.32	187.4
	C300-120-1.9	1500	300	120	24	1.9	43.6	103.3	220	3.49	195.5
	C300-120-2.4	1500	300	120	28	2.4	69.8	155.5	220	2.76	321.3
D	C100-80-1.2	800	100	80	10	1.2	139.9	141.4	500	1.94	61.3
	C100-80-1.9	700	100	80	12	1.9	352.4	342.5	500	1.25	157.6
	C100-80-2.4	700	100	80	16	2.4	569.8	577.1	500	0.96	261.6
	C200-160-1.5	1200	200	160	10	1.5	52.6	48.0	800	3.33	91.1
	C200-160-1.9	1200	200	160	13	1.9	85.4	84.1	800	2.51	152.7
	C300-210-1.9	1500	300	210	12	1.9	39.3	38.6	1000	3.71	148.4
	C300-210-2.4	1500	300	210	14	2.4	62.8	59.8	1000	2.98	232.6

Three different built-up assemblies were considered similar to the test configurations, i.e. a typical back-to-back I-section with web-to-web connections and complex combinations of three and four C-sections with web-to-web and web-to-flange connectivity. The geometric configurations of these built-up sections are presented in Figure 5-33, which includes the location of fasteners within the cross-section. The impact of intermediate discrete fasteners on the degree of coupling and interaction between individual sections was studied by considering six variations for the screw spacing to length ratios, i.e. s/L=1, 1/2, 1/4, 1/5, 1/8 and 1/16. It is noted that the first row of fasteners was located at a relative distance of 0.02L from each end (see Figure 5-33). The same labelling conventions as channel sections were followed by

replacing the initial letter with the number of channel sections included in the built-up assemblies and adding an end suffix indicating the L/s ratio for the fastener configuration. For instance, 2C200-160-1.5-2 represents a built-up I-section from set-D with h=200 mm, b_f=160 mm, t=1.5 mm, and s=$L/2$.
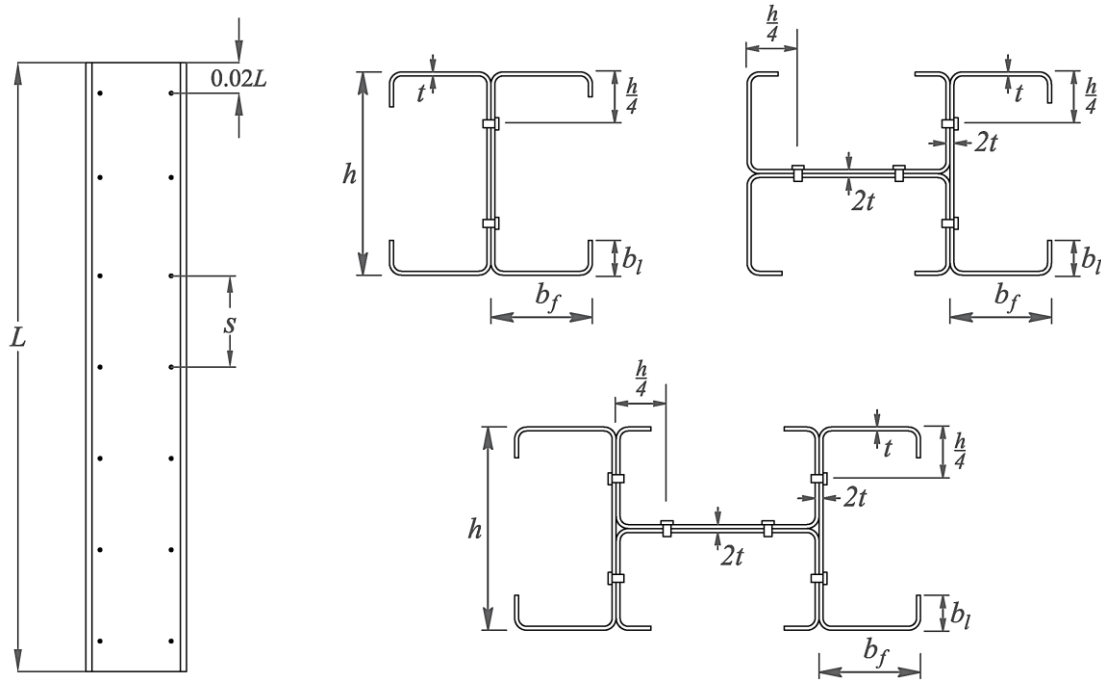
Figure 5-33: Configuration of the built-up sections considered in the parametric studies

5.4.2   Finite element analyses

As per the objectives of this study, concentric compression and fixed-ended boundaries were imposed as the loading and support conditions for the finite element simulations, for which the same modelling strategy as being introduced and utilised earlier in Section 5.2.3 was followed. For the material properties of flat (web/flange) and corner parts of the sections, the same stress-strain curves as for the C64 test series, as explained in Section 5.2.1 and in line with the tensile coupon test measurements, were adopted to allow a direct comparison between different parametric configurations. Therefore, only the adopted approach for incorporating nominal geometric imperfections in the models and the results of FE simulations with an appropriate level of discussions are provided in the following subsections.

5.4.2.1 Implementation of geometric imperfections

For the advanced analyses involved in these parametric studies that form the basis for the reliability-based assessment of the current design methods for built-up sections, the traditional modal approach for incorporating geometric imperfections in numerical models is utilised. This approach is advised in the Australian [16] and North American [15] specifications for the geometric and material analysis with imperfections (GMNAI) and advanced analysis of CFS framing systems, in which the imperfection field is approximated as a weighted combination of a selected normalised buckling mode shapes. The imperfection field (δ_0) is thus approximated by the following expression

$$\delta_0(x, y, z) = \sum_i c_i \omega_i \Phi_i(x, y, z), \tag{5.15}$$

where w_i is the magnitude of each imperfection mode to be included, and $\Phi_i(x,y,z)$ is the corresponding buckling mode shape accounting for the spatial distribution of the imperfection field, which is obtained from a rational elastic stability analysis based on the finite element or finite strip methods. Lastly, c_i is a coefficient that controls the sign and relative contribution of the imperfection mode. Due to the orthogonality of buckling modes, a linear modal combination (c_i=1), also referred to as the "square-max" approach, is typically used for combining individual imperfections. This approach ensures the intended magnitude of a given mode and ignores interactions of imperfection mode shapes.

Generally, geometric imperfections are divided into member (Global) and sectional (Local and Distortional) components. For overall member imperfections, typically, one half-sinewave with a maximum magnitude of $L/1000$ shall be taken [16], where the member length is the distance between the supporting elements. Since this study is concerned with short, stocky members subject to sectional buckling, and as confirmed by the experimental measurements in Chapter 4, the global imperfections are expected to be relatively negligible, and therefore only sectional imperfections are considered here.

Since the Compound Strip Method is used for the elastic buckling analysis of built-up sections, the mode shape function is decomposed here to a sectional mode shape $\varphi_i(x,z)$ and a longitudinal shape function $Y_i(y)$, where the former reads the normalised mode shapes for local and distortional buckling in the critical cross-section and the latter is assumed as the trigonometric shape functions of the FSM in the longitudinal direction with half-wavelength consistent with the mode considered. The two sets of sectional imperfections are schematically shown in Figure 5-34, where the scaled Local (Type 1) mode approximates the maximum local imperfections in the stiffened element while the adjusted distortional (Type 2) mode measures the maximum out-of-straightness deviation of the flanges.

(a)   (b)
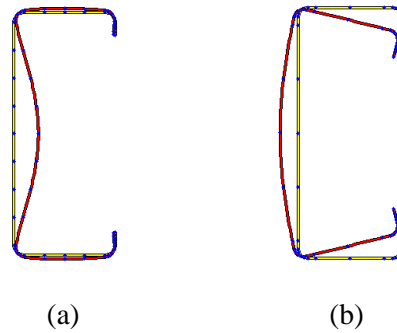
Figure 5-34: Different sectional geometric imperfections: (a) Local, (b) Distortional modes.

Following these assumptions, the imperfection field in Eq. (5.15) can be simplified to

$$\delta_0(x,y,z) = \sum_i \omega_i Y_i(y) \varphi_i(x,z), \tag{5.16}$$
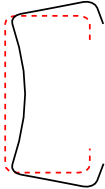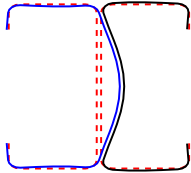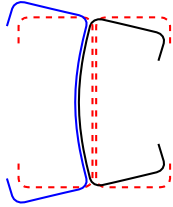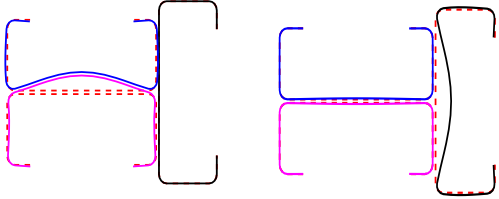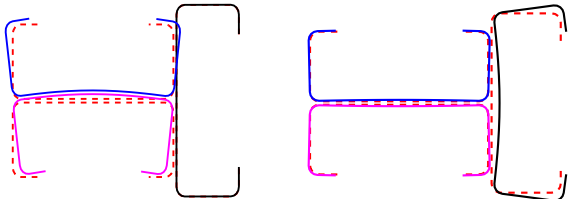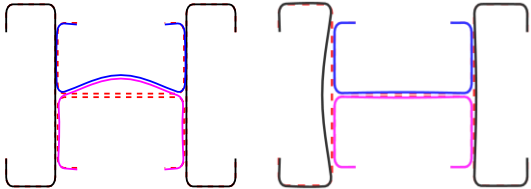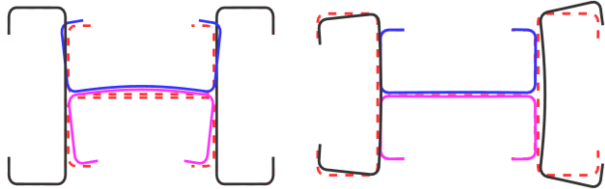
where Y_i for clamped end conditions is defined as

$$Y_i(y) = \sin\left(\frac{m\pi y}{L}\right)\sin\left(\frac{\pi y}{L}\right), \tag{5.17}$$

in which m refers to the number of buckling half-wavelengths over the member length considered for each sectional mode. In the Australian standard AS 4600 [16], the imperfection amplitudes for local and distortional buckling are prescribed based on the study by Walker [201], as per Eqs. (4.6) and (4.7). The Australian standard recommendations are generally preferred over the equations proposed by Schafer and Pekoz [12], where ω_i is defined as a pure function of thickness, e.g. $\omega_l \approx 6t\exp(-2t)$ and $\omega_d \approx t$. This preference is mainly because such

functions do not differentiate slender from stocky members, which are expected to be less susceptible to developing significant initial imperfections, whereas the Walker equation depends on the slenderness of the section. It is also noted that the c_i is set for each section such that the incorporated distortional imperfection has the outward flange-lip movement, which results in a lower column strength [73]. Lastly, a summary of sectional buckling modes considered for each built-up section is provided schematically in Table 5-5.

Table 5-5: Sectional mode shapes used in the implementation of imperfections for parametric study

Section geometry	Sectional mode shapes	
	Local	Distortional
1C		
2C		
3C		
4C		

5.4.2.2 Results and Discussions

The inelastic capacity curves are compared in Figure 5-35 for different sets (L/D), in which only the results for sections with a common thickness (i.e. $t = 1.9$ mm) between all sets are included. A detailed comparison is made next between the inelastic buckling mechanism in different section sets, where the progression of sectional deformations throughout the loading regime is captured at various timeframes in Figure 5-36, including initial, elastic, peak-load and post-peak states. For this comparison, specimens C200-160-1.9 from set-D and C200-80-1.9 from set-L were selected as representative examples, where the former expectedly failed in pure distortional mode, whereas the latter followed an interactive local-distortional failure mechanism. The ultimate capacities of the studied lipped channel sections are included in Table 5-4. It is noted that the specimens C100-80-1.2 and C100-80-1.9 from set-D failed in distortional-local interactive mode rather than pure distortional mode.
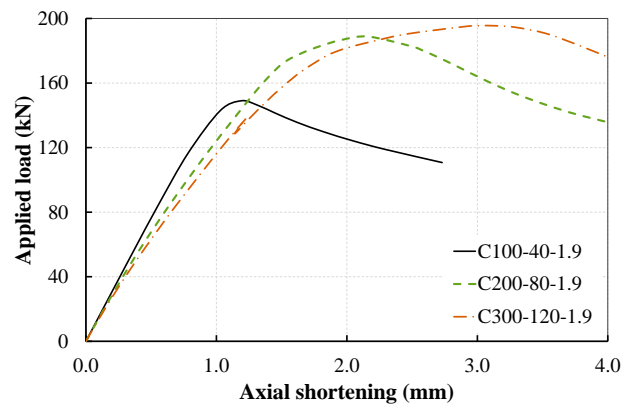
(a)
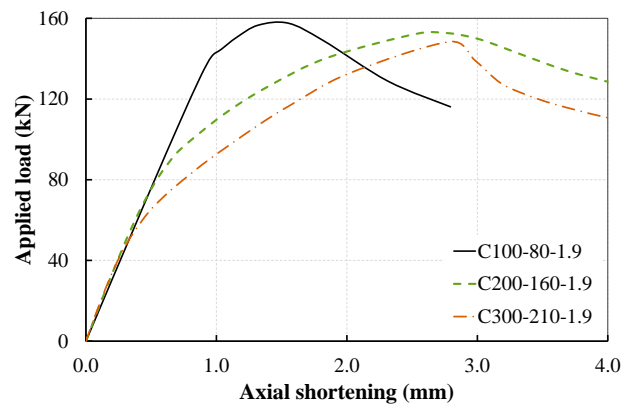
(b)

Figure 5-35: Inelastic capacity curves of the lipped channel sections with $t = 1.9$ mm for: (a) Set-L with prevalent local buckling mode and (b) Set-D with predominant distortional buckling mode
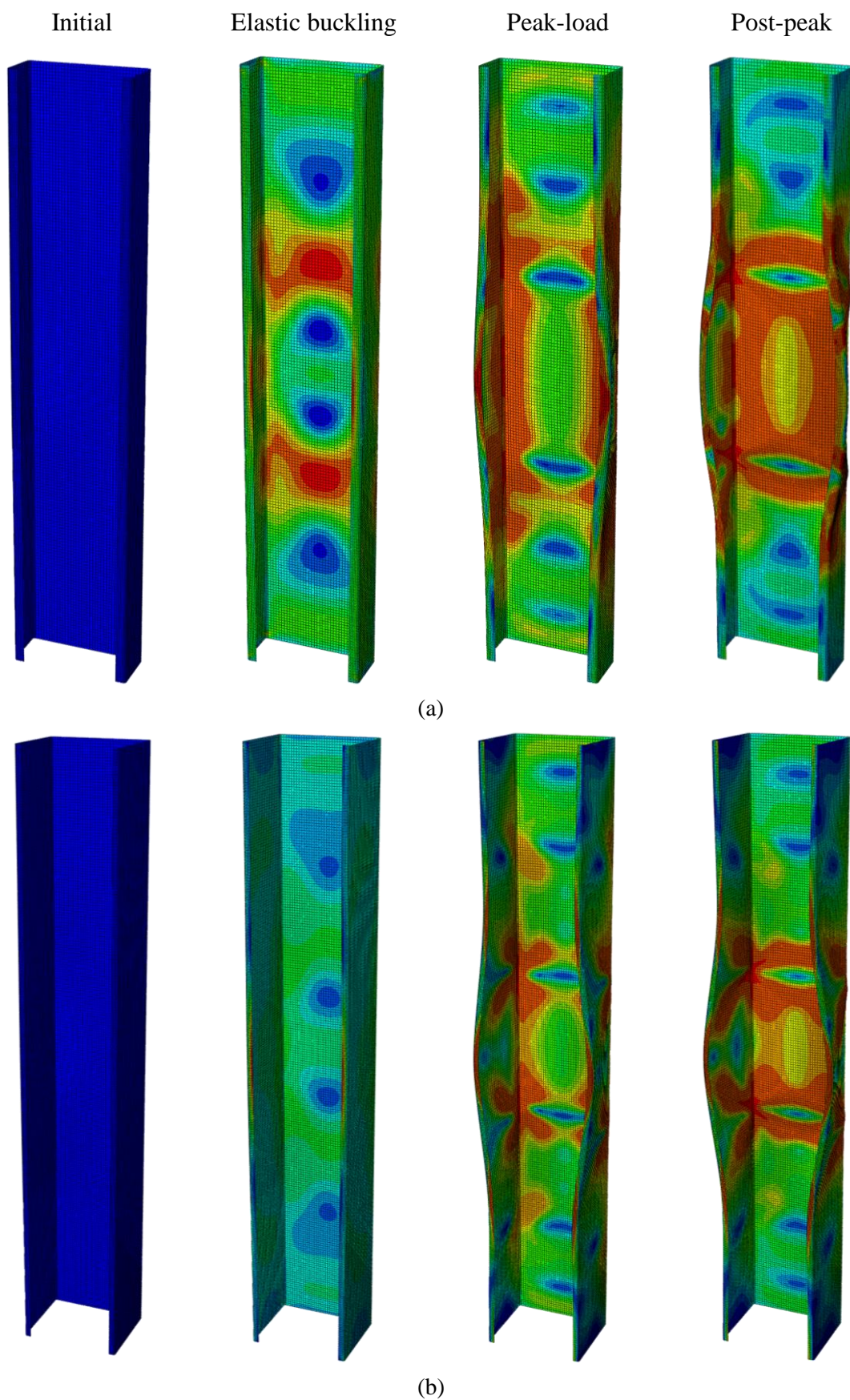
Figure 5-36: Deformed shapes of the lipped channel sections at various loading states for: (a) C200-80-1.9 specimen from set-L and (b) C200-160-1.9 specimen from set-D

The inelastic capacity curves are presented in Figure 5-37 for the built-up section 2C200-80-1.9 with different fastener spacing from set-L with predominant local buckling mode. In addition, the capacity curve for the single section with the load scaled by the number of constituent sections is included in the figure to highlight the effect of composite action provided by contact conditions and discrete fasteners between the sections. According to the results, the ultimate load capacity of the section increases slightly as the screw spacing decreases, which matches the outcomes of the experimental study. To illustrate the development of sectional buckling, the deformations of the built-up I-section 2C200-80-1.9-6 at various stages of loading are given in Figure 5-38 as an example. As can be seen, the failure buckling mode is similar to that for the single section C200-80-1.9 (see Figure 5-36(a)).
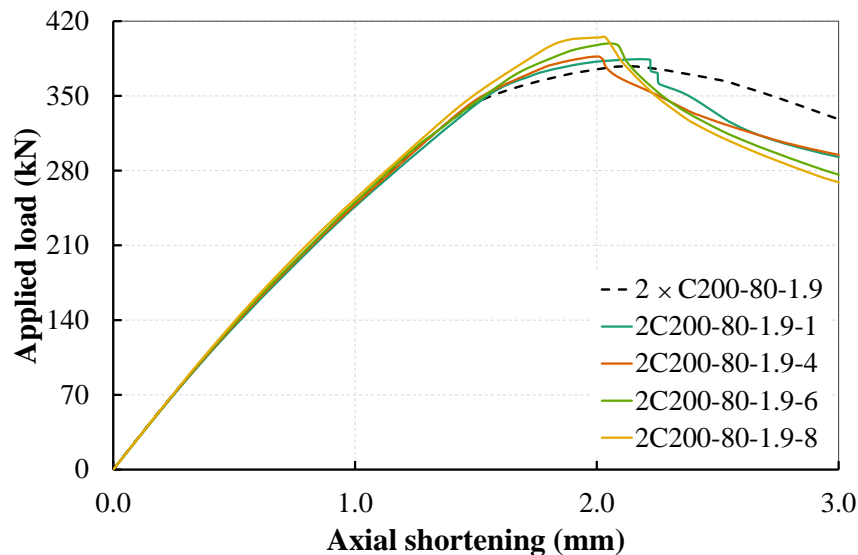
Figure 5-37: Inelastic capacity curves of the built-up I-section 2C200-80-1.9 with different fastener spacings

The primary results of the parametric studies for different built-up sections from set-L and set-D are summarised in Table 5-6 and Table 5-7, respectively. These tables cover the relative ultimate capacity ratios of each built-up section with respect to individual sections without any connectivity and with end connectivity, i.e. $P_u/(nP_{u1})$ and $P_u/P_u|_{s=L}$, which demonstrate the effects of end connectivity and intermediate discrete fasteners, respectively. The enhancement of the ultimate capacity of the built-up sections by reducing the fastener spacing is also illustrated in Figure 5-39 and Figure 5-40 for set-L and set-D, respectively.
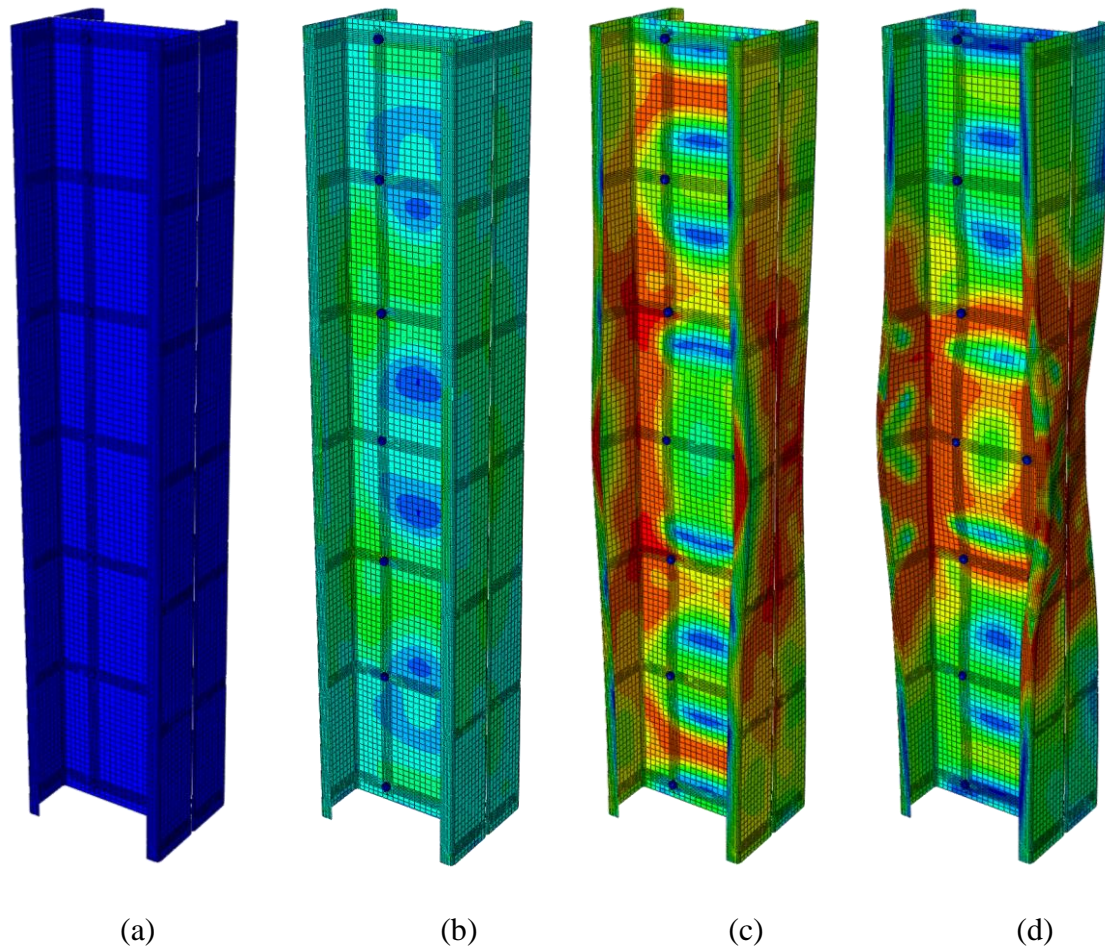
Figure 5-38: Deformed shapes of the built-up I-section 2C200-80-1.9-6 at various loading states: (a) initial, (b) elastic buckling, (c) peak-load and (d) post-peak

As can be seen, the maximum increase of the ultimate capacity compared to two individual single sections, i.e. $\Delta P_{u1}/(2P_{u1})$, is 15.7% and 11.0% for the I-sections of set-L and set-D, respectively. Figure 5-39(a) suggests that the influence of equidistant discrete fasteners on local buckling reduces as the web depth increases. According to the results, the variations of sectional dimensions and sectional slenderness ratio do not have noticeable impacts on the ultimate capacity of an I-section. It is concluded from the tests and the FE analyses that providing screws in the web of a built-up back-to-back I-configuration cannot effectively restrain the sectional buckling in the individual channel sections and alter the sectional buckling mode shape. As a result, a built-up I-section may be conservatively considered as two individual sections for design purposes. However, this statement may not necessarily be valid

and deemed uneconomical for more complex built-up assemblies with mixed connectivity as it yields considerably conservative estimates.

These enhancements can be considerably improved, especially in distortional buckling, by increasing the number of sections and introducing mixed web-flange connectivity. The magnitude and pattern for the relative enhancement of the ultimate capacity of these built-up sections by reducing fastener spacing in different geometry configurations with respect to multiple single sections without interactions are also illustrated in Figure 5-39(b-c) and Figure 5-40(b-c) for each sectional buckling set. The maximum enhancement ratio for the minimum spacing $s=L/16$ ($\approx L_{crd}/10$) with respect to non-composite level was 30.2 and 43.9 percent for distortional buckling, and 24.0 and 32.0 for local buckling of 3C and 4C sections, respectively. These figures indicate 19 and 32 percent enhancement compared to the basic I-section with the same fastener spacing but simple web-to-web connections for set-L, and 7 and 13 percent enhancement for set-L. For the practical range of fastener spacing that is likely to be between 1 and 3 times the section height, which roughly corresponds to $s/L=0.2\sim0.5$ in this parametric study, the average capacity enhancement ratio is about 3% for 2C, 12% for 3C and 15% for 4C sections of set-D and 3%, 9% and 12% for 2C, 3C and 4C sections of set-L, respectively.

Table 5-6: Summary of the results of the parametric study for the built-up sections of set-L

Section	P_u^{FE}/nP_{u1}			$P_u^{FE} / P_u|_{s=L}$		
	2C	3C	4C	2C	3C	4C
C100-40-1.2-1	1.041	1.027	1.026	1.000	1.000	1.000
C100-40-1.2-2	1.044	1.067	1.069	1.003	1.039	1.042
C100-40-1.2-4	1.047	1.088	1.097	1.006	1.059	1.069
C100-40-1.2-5	1.050	1.122	1.126	1.009	1.093	1.098
C100-40-1.2-8	1.103	1.156	1.178	1.059	1.126	1.148
C100-40-1.2-16	1.137	1.240	1.302	1.092	1.207	1.269
C100-40-1.9-1	1.028	1.015	1.019	1.000	1.000	1.000
C100-40-1.9-2	1.046	1.071	1.077	1.018	1.055	1.057
C100-40-1.9-4	1.047	1.082	1.094	1.019	1.067	1.073
C100-40-1.9-5	1.048	1.089	1.095	1.020	1.073	1.074
C100-40-1.9-8	1.099	1.141	1.176	1.070	1.124	1.154
C100-40-1.9-16	1.157	1.210	1.242	1.126	1.192	1.218
C200-80-1.5-1	1.014	1.032	1.048	1.000	1.000	1.000
C200-80-1.5-2	1.017	1.085	1.129	1.003	1.052	1.078
C200-80-1.5-4	1.022	1.095	1.139	1.008	1.061	1.088
C200-80-1.5-5	1.023	1.100	1.142	1.009	1.066	1.090
C200-80-1.5-8	1.056	1.154	1.200	1.042	1.118	1.146
C200-80-1.5-16	1.059	1.205	1.263	1.044	1.168	1.206
C200-80-1.9-1	1.026	1.034	1.045	1.000	1.000	1.000
C200-80-1.9-2	1.031	1.088	1.117	1.005	1.052	1.069
C200-80-1.9-4	1.033	1.100	1.133	1.007	1.064	1.084
C200-80-1.9-5	1.044	1.107	1.176	1.018	1.070	1.125
C200-80-1.9-8	1.080	1.145	1.188	1.053	1.107	1.136
C200-80-1.9-16	1.094	1.211	1.269	1.066	1.171	1.214
C300-120-1.9-1	1.011	1.037	1.074	1.000	1.000	1.000
C300-120-1.9-2	1.013	1.077	1.146	1.001	1.039	1.066
C300-120-1.9-4	1.014	1.092	1.160	1.003	1.052	1.080
C300-120-1.9-5	1.015	1.111	1.161	1.004	1.071	1.081
C300-120-1.9-8	1.029	1.138	1.185	1.018	1.097	1.103
C300-120-1.9-16	1.044	1.177	1.260	1.033	1.135	1.173
C300-120-2.4-1	1.011	1.051	1.063	1.000	1.000	1.000
C300-120-2.4-2	1.015	1.083	1.120	1.004	1.030	1.054
C300-120-2.4-4	1.016	1.087	1.127	1.005	1.034	1.061
C300-120-2.4-5	1.016	1.105	1.148	1.005	1.051	1.081
C300-120-2.4-8	1.044	1.136	1.179	1.032	1.081	1.109
C300-120-2.4-16	1.049	1.178	1.225	1.037	1.120	1.153

Table 5-7: Summary of the results of the parametric study for the built-up sections of set-D

Section	P_u^{FE}/nP_{u1}			$P_u^{FE}/P_u|_{s=L}$		
	2C	3C	4C	2C	3C	4C
C100-80-1.2-1	1.040	1.073	1.133	1.000	1.000	1.000
C100-80-1.2-2	1.049	1.121	1.174	1.008	1.045	1.036
C100-80-1.2-4	1.049	1.139	1.210	1.009	1.062	1.068
C100-80-1.2-5	1.051	1.169	1.241	1.010	1.089	1.095
C100-80-1.2-8	1.062	1.225	1.304	1.020	1.142	1.151
C100-80-1.2-16	1.092	1.302	1.439	1.049	1.214	1.270
C100-80-1.9-1	1.006	1.056	1.080	1.000	1.000	1.000
C100-80-1.9-2	1.023	1.120	1.135	1.018	1.060	1.051
C100-80-1.9-4	1.026	1.133	1.174	1.020	1.073	1.087
C100-80-1.9-5	1.031	1.159	1.186	1.025	1.098	1.099
C100-80-1.9-8	1.054	1.180	1.229	1.048	1.117	1.138
C100-80-1.9-16	1.110	1.228	1.315	1.104	1.163	1.217
C100-80-2.4-1	1.003	1.041	1.056	1.000	1.637	1.000
C100-80-2.4-2	1.013	1.072	1.086	1.011	1.685	1.028
C100-80-2.4-4	1.015	1.102	1.107	1.012	1.000	1.049
C100-80-2.4-5	1.038	1.121	1.131	1.035	1.000	1.072
C100-80-2.4-8	1.043	1.124	1.151	1.040	1.000	1.091
C100-80-2.4-16	1.056	1.174	1.193	1.053	1.000	1.130
C200-160-1.5-1	1.047	1.098	1.161	1.000	1.000	1.000
C200-160-1.5-2	1.052	1.118	1.187	1.004	1.018	1.022
C200-160-1.5-4	1.056	1.128	1.212	1.009	1.028	1.044
C200-160-1.5-5	1.057	1.134	1.230	1.009	1.033	1.059
C200-160-1.5-8	1.060	1.210	1.302	1.012	1.102	1.121
C200-160-1.5-16	1.093	1.293	1.433	1.043	1.178	1.234
C200-160-1.9-1	1.013	1.065	1.116	1.000	1.000	1.000
C200-160-1.9-2	1.018	1.085	1.164	1.005	1.019	1.043
C200-160-1.9-4	1.019	1.097	1.199	1.006	1.030	1.074
C200-160-1.9-5	1.021	1.129	1.213	1.008	1.060	1.087
C200-160-1.9-8	1.043	1.162	1.296	1.029	1.091	1.161
C200-160-1.9-16	1.067	1.285	1.413	1.053	1.207	1.266
C300-210-1.9-1	1.023	1.081	1.156	1.000	1.000	1.000
C300-210-1.9-2	1.024	1.108	1.181	1.002	1.024	1.021
C300-210-1.9-4	1.024	1.143	1.228	1.002	1.058	1.062
C300-210-1.9-5	1.025	1.162	1.239	1.003	1.075	1.072
C300-210-1.9-8	1.033	1.197	1.322	1.010	1.107	1.143
C300-210-1.9-16	1.050	1.257	1.424	1.027	1.162	1.232
C300-210-2.4-1	1.031	1.094	1.160	1.000	1.000	1.000
C300-210-2.4-2	1.034	1.126	1.186	1.003	1.029	1.022
C300-210-2.4-4	1.036	1.143	1.227	1.004	1.044	1.058
C300-210-2.4-5	1.036	1.143	1.230	1.005	1.045	1.060
C300-210-2.4-8	1.046	1.229	1.286	1.014	1.123	1.109
C300-210-2.4-16	1.069	1.295	1.449	1.037	1.183	1.249
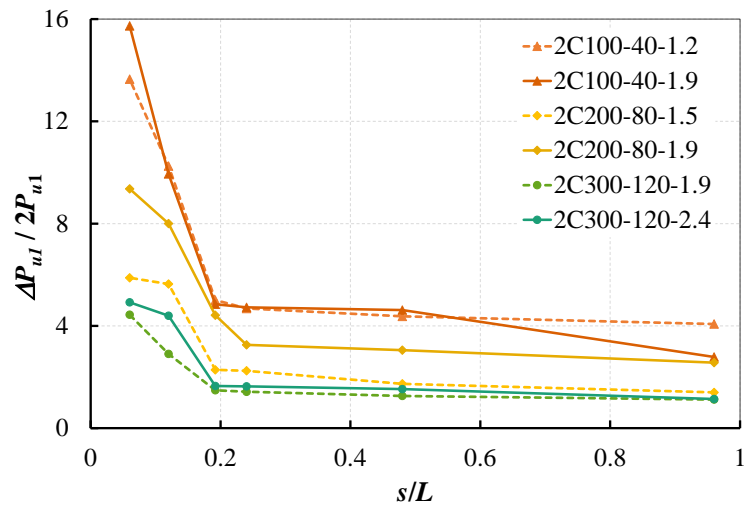
(a)
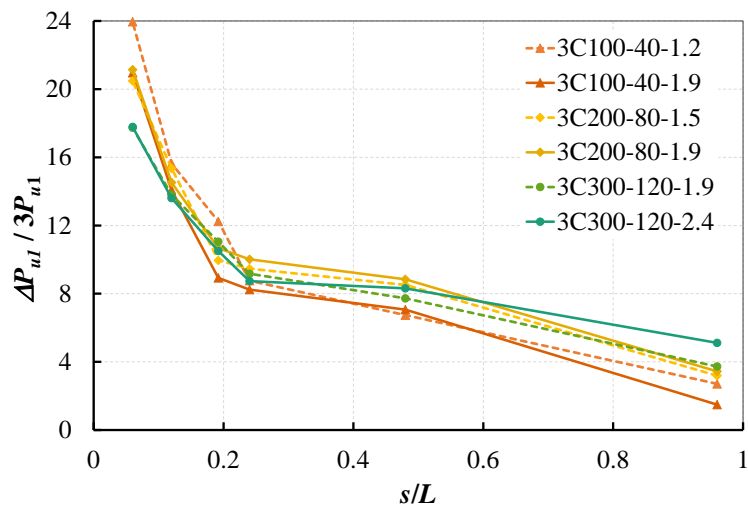
(b)
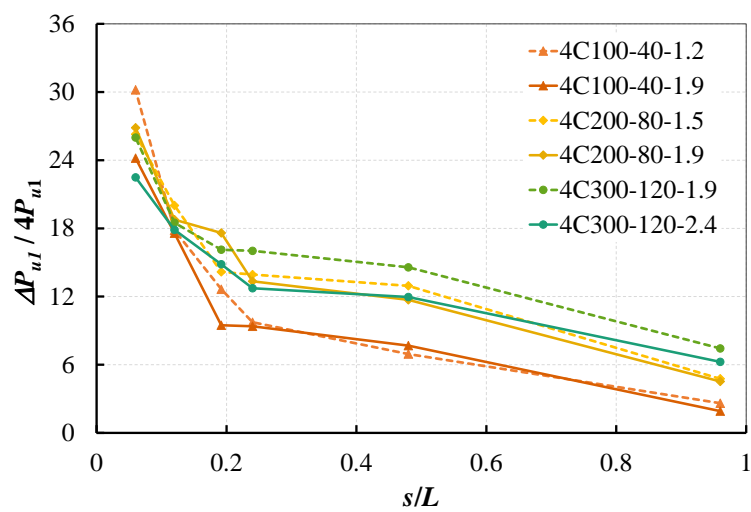
(c)

Figure 5-39: Effect of fastener spacing on the ultimate load of the built-up sections in Set-L: (a) 2C,

(b) 3C and (c) 4C sections.
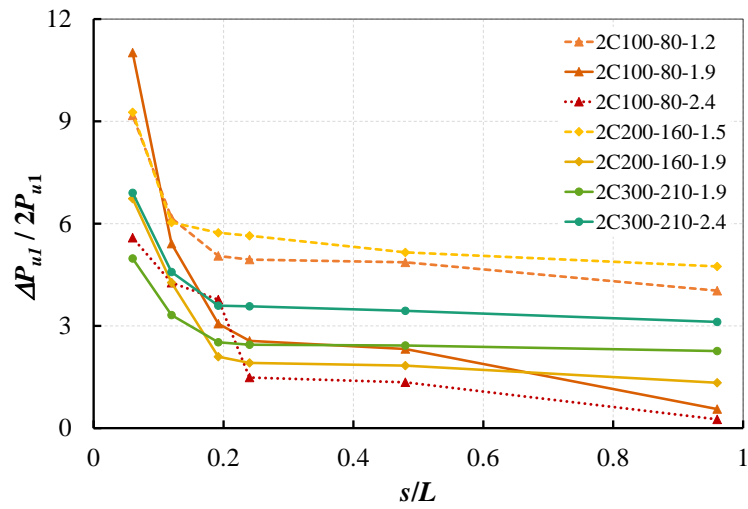
(a)
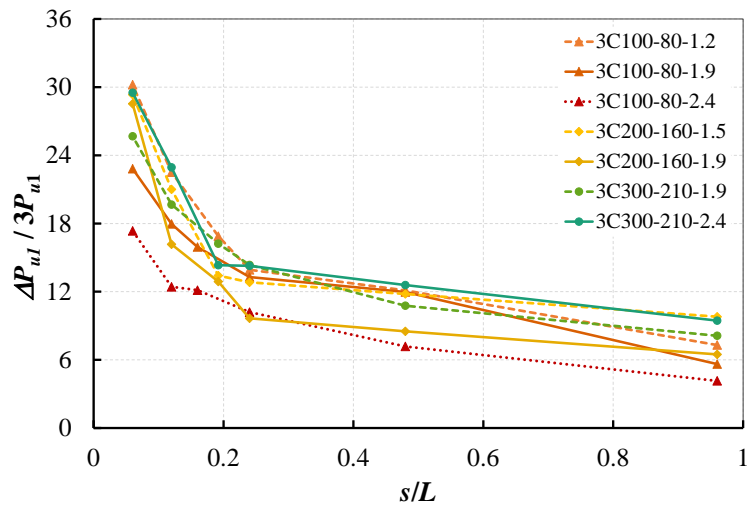
(b)
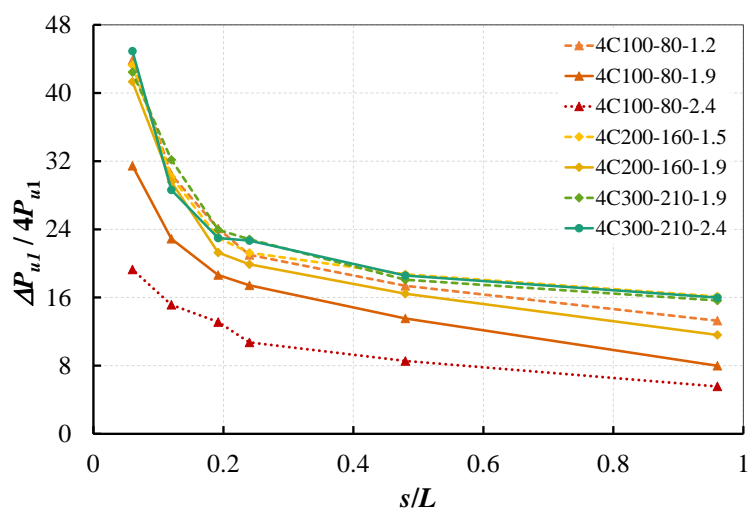
(c)

Figure 5-40: Effect of fastener spacing on the ultimate load of the built-up sections in Set-D: (a) 2C, (b) 3C and (b) 4C sections.

5.5 SUMMARY

In this chapter, a detailed finite-element model was developed for the reliable nonlinear analysis and design of built-up cold-formed steel sections with discrete screw connections. The model was established using conventional shell finite elements with an isotropic J2 plasticity constitutive model. It used appropriate connection elements and contact conditions to realistically model the interactions between the constitutive plates. The geometric imperfections were incorporated into the FE model using the Fourier series approximations of the measured imperfections as in-built perturbations for nonlinear buckling analysis. The Newton-Raphson method with dynamic time stepping and adaptive viscous regularisation was adapted as the nonlinear solution scheme for the quasi-static problem. These main components of the computational model were discussed in different subsections, including discussions on the available options for each component, their main features (merits and drawbacks) and rational justifications for the options chosen for this study. This includes a detailed theoretical background with conclusive comparisons of the available options for the nonlinear constitutive model, the systematic implementation of geometric imperfections, the enforcement of end support conditions, the application of contact conditions between the constituent plates, the selection of connection elements for representing intermediate screw fasteners, type of elements to be used with mesh sensitivity, and finally the incremental load stepping and nonlinear solution schemes.

The predictions of the proposed methodology were compared against the experimental results to calibrate the influencing parameters and validate the accuracy of the numerical simulations, which were shown to be in excellent agreement with the test data in terms of the inelastic behaviour (up to ultimate capacity and beyond) and the failure mode. The results confirmed the conclusions in Chapter 4 on the influence of discrete fasteners and contact between the constituent elements on the elastic buckling capacity and the ultimate capacity of the built-up sections with different assemblies and configurations. Although the computational model is established within the framework of Abaqus software, it can be applied to other commercial

software with similar features and characteristics, including the available finite element library, contact models, nonlinear analysis and solution options. The calibrated FE model was utilised to perform extensive parametric studies into the effects of various design parameters on the ultimate strength of built-up columns, including cross-section dimensions, sectional slenderness, built-up section geometry and fastener spacing. These results form the basis for the following investigative phase in Chapter 6, which is concerned with the assessment of currently available design equations for CFS built-up columns, especially the Direct Strength Method (DSM), and adjustments to this required to accurately predict the strength of built-up members with multiple component sections.

Chapter 6 EVALUATION OF DESIGN METHODS FOR BUILT-UP SECTIONS

6.1 INTRODUCTION

In Section 6.2 of this final technical chapter, the most common methods in international standards for the design of cold-formed steel members are briefly reviewed. Their applicability to the built-up sections is examined and discussed in Section 6.3 by comparison against the experimental test data of this study. The basic principles of first-order reliability analysis and its application to CFS members are explained in Section 6.4, and the reliability of current standardised design procedures is then assessed based on the numerical parametric studies. Some adjustments are proposed in Section 6.5 to improve the accuracy of the ultimate capacity predictions to meet the target reliability index in the Australian and North American specifications. This chapter concludes with a summary of accomplishments in Section 6.6.

6.2 CURRENT DESIGN METHODS

The current design methods in Australian, North American and European standards include the conventional Effective Width Method (EWM), which modifies the width of the constituent plate elements for sectional capacity calculations based on their buckling state. An alternative design procedure is the Direct Strength Method (DSM), which correlates the ultimate capacity of the member with the critical buckling loads of the section. It has been successfully incorporated into the Australian standard and North American specification for the design of cold-formed steel structural members. The design procedures for compression members based on these methods are explained in the following subsections.

6.2.1 *Effective width method*

6.2.1.1 Eurocode Approach

Different steel sections are classified in Clause 5.5.2 of EN1993-1-1 [52], where cold-formed steel sections are categorised as Class 4 with the high possibility of local buckling in one or more parts of the cross-section before attaining the yield stress. The sectional resistance of a CFS section is evaluated from Clause 6.2.4 of EN1993-1-1 or Clause 6.1.3 of EN1993-1-3 [202] as

$$N_{c,Rd} = f_y A_{eff} / \gamma_{M0},$$ (6.1)

in which γ_{M0} is the resistance factor for the sectional resistance and A_{eff} is the effective area of the cross-section accounting for the local buckling according to the concept of the effective width method. Subsequently, the buckling resistance of the member is defined in Clause 6.3.1 as follows

$$N_{b,Rd} = \chi f_y A_{eff} / \gamma_{M1},$$ (6.2)

where γ_{M1} is the resistance factor for buckling resistance and χ is a reduction factor for the relevant global buckling mode of the member, i.e. flexural or flexural-torsional buckling as applicable. The resistance factors, which can be interpreted as the inverse of strength reduction factors (ϕ), are defined by default in [52, 202] as unity with more specific definitions in the national annex of each country. The effective width of the constituent parts of the cross-section for calculating A_{eff} is obtained from Clause 4.4 of EN1993-1-5 [203]. For any part of the cross-section, the associated effective width (b_{ej}) can be obtained from the following equation

$$b_{ej} = \rho_j b_j,$$ (6.3)

where the reduction factor ρ_j relevant to part *j* can be cast in the following generalised form

$$\rho_j = \begin{cases} 1 & \forall \lambda_{pj} \leq \lambda_{pj.\lim}, \\ \left(1 - \dfrac{\beta_{pj}}{\lambda_{pj}}\right) \dfrac{1}{\lambda_{pj}} & \forall \lambda_{pj} > \lambda_{pj.\lim}. \end{cases}$$ (6.4)

The limiting slenderness ratio ($\lambda_{pj.\text{lim}}$) can be simply obtained by satisfying the conditional provision of the effective width factor. This means solving the following quadratic equation

$$\lambda_{pj.\text{lim}}^2 - \lambda_{pj.\text{lim}} + \beta_{pj} = 0, \tag{6.5}$$

which yields the following expression for the limiting slenderness ratio

$$\lambda_{pj.\text{lim}} = 0.5\left(1 + \sqrt{1 - 4\beta_{pj}}\right). \tag{6.6}$$

For internal/stiffened parts with restraints at both edges (e.g. webs) and in the uniform compression stress state, i.e. stress gradient factor $\psi = 1$, the prefactor β_{pi} is specified as 0.22, which yields $\lambda_{pi.\text{lim}} = 0.673$. The effective width factor for flange outstands under uniform compression is obtained using a slightly different effective width factor based on $\beta_{po} = 0.18$ and $\lambda_{po.\text{lim}} = 0.748$.

In Eq. (6.3), the slenderness ratio for each constituent plate is also defined in terms of the ratio of yield stress over the critical stress for initiating local buckling as follows

$$\lambda_{pj} = \sqrt{f_y / f_{crj}}. \tag{6.7}$$

The critical local buckling stress for the part of interest (f_{crj}) can be found from

$$f_{crj} = \frac{k_{\sigma j} \pi^2 E_s}{12\left(1 - \upsilon^2\right)}\left(\frac{t_j}{b_j}\right)^2, \tag{6.8}$$

which based on the explicit assumption of Elastic modulus in EC3, i.e. $E_s = 210$ GPa, can result in further simplification of λ_{pj} into

$$\lambda_{pj} \approx \frac{\left(b_j / t_j\right)}{28.4\varepsilon\sqrt{k_{\sigma j}}}, \tag{6.9}$$

where $\varepsilon = \sqrt{f_y / 235}$. The buckling stress factor $k_{\sigma j}$ is prescribed in Tables 4.1 and 4.2 of EN1993-1-5 [203], depending on the stress ratio and boundary conditions. For internal and outstand compression elements, $k_{\sigma i} = 4.0$ and $k_{\sigma o} = 0.43$ can be considered, respectively.

Lastly, the reduction factor χ for the buckling resistance is expressed by

$$\chi = \frac{1}{\Phi + \sqrt{\Phi^2 - \bar{\lambda}^2}}, \qquad (6.10)$$

where the imperfection function Φ for steel members has been commonly approximated by

$$\Phi = 0.5\left[1 + \alpha\left(\bar{\lambda} - \lambda_1\right)^\beta - \alpha\lambda_0 + \bar{\lambda}^2\right]. \qquad (6.11)$$

This general expression has been simplified in EC3 by assuming $\beta=1$, $\lambda_0=0$ and $\lambda_1=0.2$, viz.

$$\Phi = 0.5\left[1 + \alpha\left(\bar{\lambda} - 0.2\right) + \bar{\lambda}^2\right], \qquad (6.12)$$

where the imperfection factor α is prescribed in Table 6.1 of [52] based on the type of buckling curve as indicated in Table 6.2 for different section geometries and classes. The buckling curve for Class 4 channel sections is nominated as type (c), and the associated imperfection factor is set as $\alpha=0.49$. The slenderness ratio for global buckling ($\bar{\lambda}$) is also defined in EC3 as

$$\bar{\lambda} = \sqrt{A_{eff}\, f_y / N_{cr}}, \qquad (6.13)$$

where N_{cr} is the elastic buckling load associated with the prevalent global buckling mode, i.e. flexural ($N_{cr.F}$) or flexural-torsional ($N_{cr.TF}$) modes, based on gross cross-sectional properties. As an example, the elastic buckling load for flexural buckling can be expressed by the Euler buckling equation, which can then be utilised to derive the following expression upon some simple mathematical manipulations

$$\bar{\lambda} = \sqrt{\frac{A_{eff}}{A_g}}\left(\frac{l_e}{r_g}\right)\frac{1}{\bar{\lambda}_1}, \qquad (6.14)$$

in which A_g is the gross cross-section area, l_e is the effective length of the member, r_g is the radius of gyration, and $\bar{\lambda}_1$ is defined as

$$\bar{\lambda}_1 = \pi\sqrt{E_s / f_y} \approx 93.9\varepsilon. \qquad (6.15)$$

As the above equations show, the approach merely accounts for local and global buckling and potential interactions. For sections subject to distortional buckling, such as elements with edge and/or intermediate stiffeners, further adjustments shall be made per clause 5.5.3 of EN1993-1-3 [202] by reducing the thickness of cross-section parts undergoing distortional buckling based on the associated minimum buckling stress. For example, the effective width of a single edge stiffener (b_{es}) in lipped channel sections is calculated using the reduction factor for outstand elements, where the associated buckling stress factor ($k_{\sigma s}$) for calculating the critical local buckling stress (f_{crs}) and establishing the slenderness ratio (λ_{ps}) is obtained from the following expression:

$$k_{\sigma s} = \begin{cases} 0.5 & d_l/b \leq 0.35, \\ 0.5 + 0.83\sqrt[3]{(d_l/b - 0.35)^2} & 0.35 < d_l/b \leq 0.6, \end{cases} \tag{6.16}$$

where d_l is the lip length and b is the flange width. As can be seen, the buckling stress factor for $d_l/b < 0.35$ slightly differs from the default value ($k_{\sigma o}=0.43$) for outstand elements. The effective cross-sectional area of the stiffener (or generally parts undergoing distortional buckling) shall be taken as the effective width of the edge stiffener plus the effective portion of the adjoining flat element (e.g. flange), where the effective width of the flange might be obtained in the first trial by assuming it is doubly supported as an internal element.

The reduction factor for distortional buckling resistance (χ_d), which is simply the overall flexural buckling of the stiffener, should be obtained from the following expression

$$\chi_d = \begin{cases} 1.0 & \lambda_d \leq 0.65, \\ 1.47 - 0.723\lambda_d & 0.65 < \lambda_d < 1.38, \\ 0.66/\lambda_d & \lambda_d \geq 1.38. \end{cases} \tag{6.17}$$

In the above equation, the relative slenderness for distortional buckling is defined as

$$\lambda_d = \sqrt{f_y/\sigma_{cr,s}}, \tag{6.18}$$

where the associated critical buckling stress ($\sigma_{cr,s}$) can be either evaluated from the analytical methods provided in Clauses 5.5.3.2-4 or obtained from a rational elastic first-order buckling

analysis. For $\chi_d<1$, the strength of the stiffener area shall be reduced accordingly, and the process of effective width calculation may be refined iteratively until reaching a convergent solution. The final effective section properties shall be based on a reduced thickness (t_r) for the effective stiffener area corresponding to the final value of χ_d.

It is noted that the EWM in Eurocode is only applicable to a range of prequalified sections in terms of their geometrical dimension, for which adequate experience and testing already exist. For instance, the approach only applies to unstiffened channel sections with $b/t \leq 50$ that can be increased to 60 for lipped channel sections as long as $d_l/t \leq 50$. Other cross-sections with larger width-to-thickness ratios may also be used, provided their ultimate capacity is verified by an appropriate number of tests and/or detailed calculations. In addition, the depth of the edge stiffener in lipped sections should be within 20 to 60 percent of the flange width, i.e. $0.2 \leq d_l/b \leq 0.6$, so that it provides sufficient stiffness for the flange and the primary buckling of the stiffener itself is avoided. Otherwise, the lip and its favourable contribution shall be conservatively ignored according to Eurocode.

It is noteworthy that Eurocode does not include any specific provisions for built-up sections. However, the effect of fasteners may be taken into account in the strength calculation by using the results of critical distortional buckling stress ($\sigma_{cr,s}$) from the compound strip analysis (considering partially-composite action) in Eq. (6.18). This approach will be tested later in Section 6.3 and Section 6.4 for the strength prediction of built-up sections.

6.2.1.2 Australian and North American Specifications

Although the effective width approach in the Australian standard AS4600 [16] and North American specification AISI S100 [15] shares the same principles as in the European standard, it has some differences with some caveats and additional rules for built-up members that will be discussed in this section. The unfactored section and member capacities for a CFS column under compression is defined as follows

$$N_s = A_{eff} f_y \text{ and } N_c = A_{eff} f_n, \tag{6.19}$$

where A_{eff} is the effective cross-section area as defined later in the section, and f_n is the critical stress level representing the nominal strength of the member with consideration of buckling. The critical stress ratio (f_n/f_y), which resembles the reduction factor χ in EC3, has been expressed with a different function as

$$\frac{f_n}{f_y} = \begin{cases} 0.658^{\lambda_c^2} & \lambda_c \leq 1.5, \\ \dfrac{0.877}{\lambda_c^2} & \lambda_c \geq 1.5, \end{cases} \tag{6.20}$$

where λ_c is a dimensionless slenderness ratio, which differs slightly from $\bar{\lambda}$ in EC3 in terms of definition considering both yielding and buckling capacities based on gross cross-section area, viz.

$$\lambda_c = \sqrt{f_y / f_{oc}}. \tag{6.21}$$

The global buckling stress ($f_{oc}=N_{cr}/A_g$) is the least of flexural, torsional and flexural-torsional buckling capacities, as applicable, that can be obtained from a rational elastic buckling analysis or the analytical expressions provided in Appendix D1.1 of AS/NZS 4600 [16] or sections C4.1.1-2 of AISI S100 [15]. A comparison is made in Figure 6-1 between the above global/overall ultimate capacity adjustment for imperfections and that in Eurocode, assuming the section is fully effective ($A_{eff}=A_g$) for different slenderness ratios. The ultimate theoretical capacity bounded by the yield and elastic member buckling capacities is also provided that corresponds to an ideal scenario without any imperfections and serves as the upper bound for the capacity.

In AS/NZS 4600 [16], the member capacity for monosymmetric sections subject to distortional buckling is also bounded by the following limit depending on the distortional buckling stress level (f_{od})

$$N_{c.\max} = \begin{cases} A_g \left(1-0.25\, f_y/f_{od}\right) f_y & f_{od} > f_y/2, \\ A_g \left[0.055\left(\sqrt{f_y/f_{od}} - 3.6\right)^2 + 0.237 \right] f_y & f_y/13 \leq f_{od} \leq f_y/2, \end{cases} \tag{6.22}$$

where f_{od} can be obtained from a rational elastic stability analysis or relevant equations in Appendix D1.2 of AS/NZS 4600 [16].
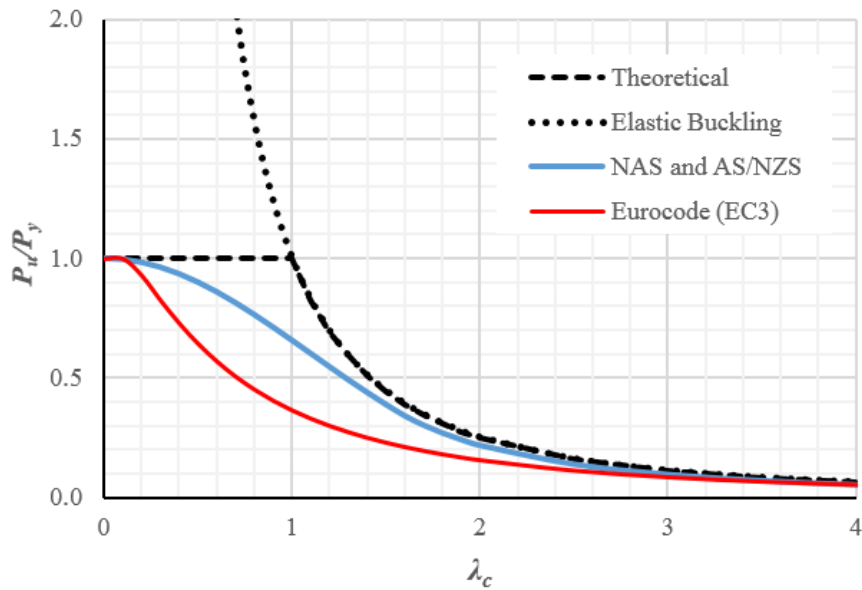
Figure 6-1: Adjustment of the ultimate capacity due to global buckling for imperfections

The effective area (A_{eff}) of the section is established based on the effective width of the constituent elements, which follows the same principle as that introduced for EC3 in Section 6.2.1.1 with the following two exceptions:

A. The same equation is used for compressed stiffened (internal) and unstiffened (outstand) elements, i.e. $\beta_{pi}=\beta_{po}=0.22$ and $\lambda_{pi.\text{lim}}=\lambda_{po.\text{lim}}=0.673$. The only difference between these two elements is their relevant buckling stress factor, which is similarly considered as $k_{\sigma i}=4.0$ and $k_{\sigma o}=0.43$.

B. The slenderness parameter (λ_{pj}) for each element is defined more generally as

$$\lambda_{pj} = \sqrt{f^*/f_{crj}}, \tag{6.23}$$

in which f^* is the design stress in the compression element based on its effective area, as illustrated in Figure 6-2. For calculating section capacity (N_s), A_{eff} is the effective area at the yield stress state and f^* shall be taken as f_y, whereas for calculating the member capacity (N_c), the effective area corresponds to the critical stress state and f^* must therefore be considered equal to f_n.

(a) stiffened/internal elements   (b) unstiffened/outstand elements
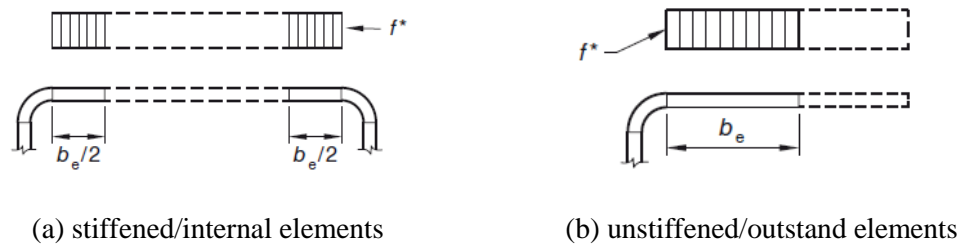
Figure 6-2: Effective width and design stress state in plate elements under uniform compression [16]

For the effective width calculation of uniformly compressed elements with an edge stiffener, such as lipped channel sections, an adjustment is necessary to account for the effect of distortional buckling of the edge stiffener and its relative stiffness as it may not be stiff enough to restrain the flange fully. The required corrections for the effective width calculation of edge stiffeners (lips) and flanges (including the appropriate buckling coefficient k_σ) are introduced in Clauses 1.3 of the AISI specification and 2.4.2 of AS/NZS 4600. For example, for a simple lip stiffener, the adjustments applicable to $b/t > 0.3285$ are as per the following equations with a schematic illustration of the concept as per Figure 6-3

$$d_s = d_{se}\left(I_s/I_a\right),$$
(6.24)

$$b_1 = 0.5b_e\left(I_s/I_a\right),$$
(6.25)

$$k_\sigma = \begin{cases} 3.57\left(I_s/I_a\right)^n + 0.43 & \left(d_l/b\right) \leq 0.25, \\ \left(4.82 - 5d_l/b\right)\left(I_s/I_a\right)^n + 0.43 & 0.25 < \left(d_l/b\right) \leq 0.8, \end{cases}$$
(6.26)

where d_{se} is the effective width of the lip edge stiffener for local buckling and b_e is the effective width of the flange for local buckling calculated using k_σ in Eq. (6.26). Moreover, I_s is the second moment of area of the stiffener (not to be taken greater than I_a), and I_a is the minimum second moment of area deemed adequate so that the flange element behaves as a stiffened element. These values (I_s, I_a) and the exponent n are defined as follows

$$I_s = \frac{d^3 t \sin^2\theta}{12},$$
(6.27)

$$I_a = 399t^4 \left[\frac{(b/t)}{S} - 0.328 \right]^3 \leq 5t^4 \left[23\frac{(b/t)}{S} + 1 \right],$$
(6.28)

$$n = 0.582 - \frac{(b/t)}{4S} \geq \frac{1}{3},$$
(6.29)

in which $S = 1.28\sqrt{E/f^*}$ is the slenderness factor. For $b/t \leq 0.3285$, no further adjustment is required for the lips ($d_{se}=d_s$), and flanges are expected to be fully effective ($b_1=b_2=b/2$) irrespective of I_s, which can be interpreted as stating that no edge stiffener is required.

(a) actual and effective stiffener   (b) effective elements and their stress state
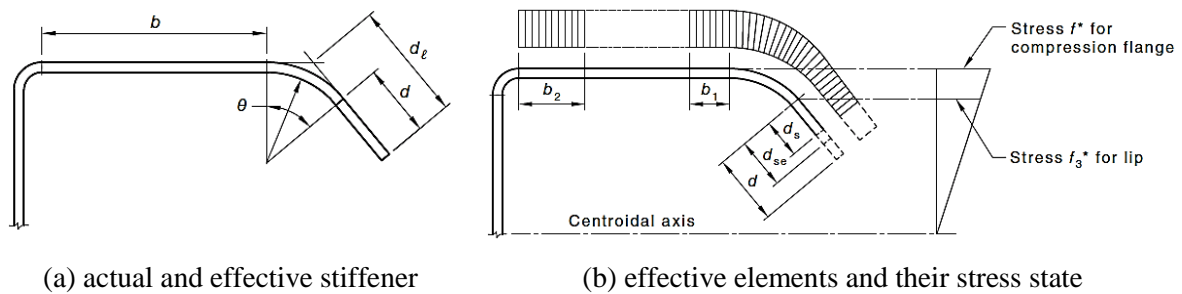
Figure 6-3: Adjustments for the effective width of elements with simple-lip edge stiffener [16]

Lastly, for built-up compression members made of two sections in contact, such as back-to-back connection of two channel sections forming an I-section, the global slenderness ratio (l_e/r_g) can be modified due to the potential enhancement of the buckling capacity as long as the buckling mode involves relative deformations of the sections imposing shear demand in the fastener elements. The proposed modification and some essential requirements for the intermediate fastener(s) or spot welds to ensure such enhancement are elaborated in the next section on the Direct Strength Method.

6.2.2   Direct Strength Method

It is well understood that the effective width method is a powerful well-established method with a sound rational basis that can account for yielding, global buckling and local sectional buckling and their probable interactions. However, it has several drawbacks, such as requiring the effective section to be calculated for any given value of global buckling stress f^*, implicitly

accounting for the effect of distortional buckling and being currently applicable to a range of prequalified sections with certain width-to-thickness ratio limitations for the constituent plate elements. In addition, its application to built-up members and more complex geometries is either cumbersome or not a straightforward task. In contrast, the Direct Strength Method (DSM) effectively addresses these shortcomings by establishing direct correlations between the ultimate member capacity and characteristic elastic buckling capacities in different global and sectional modes that can be obtained from a rational stability analysis.

The basic idea and concept of the DSM were initially proposed by Hancock [156], in which a correlation was suggested between the ultimate strength and the elastic buckling stress of CFS columns under distortional buckling. Later, this alternative design approach was extended [74, 204] for a broader range of cross-sections failing in local, distortional, overall flexural, or flexural-torsional buckling modes. As a result, the DSM has been successfully incorporated into international standards, including the Australian standard [16] and North American specifications [15] for the design of CFS members. Despite being extensively validated for single CFS sections, its accuracy and calibration for the design of built-up sections have been the subject of research and discussion in the literature for the past few years.

In contrast to the effective width method, the DSM provides a set of column curve equations based on gross sectional properties to determine the reduced strength of a steel member, such as columns in a given mode due to buckling or yielding. Thereby, the nominal axial capacity (P_n) of a CFS compression member in DSM is defined as the minimum of the nominal axial strengths for the flexural buckling (P_{ne}), local buckling (P_{nl}) and distortional buckling (P_{nd}) limit states. Based on extensive compression tests performed on CFS columns failing in distortional buckling, e.g. [156, 205], the following curve fit to the test data was proposed and implemented in the standards [15, 16] to estimate the nominal capacity in distortional buckling

$$P_{nd} = \begin{cases} P & \forall \lambda_d \leq 0.561, \\ \left[1-0.25\left(\dfrac{P_{crd}}{P}\right)^{0.6}\right]\left(\dfrac{P_{crd}}{P}\right)^{0.6} P & \forall \lambda_d > 0.561, \end{cases} \tag{6.30}$$

where P_{crd} is the critical elastic distortional buckling load ($=f_{crd}A_g$) that is obtained from a rational elastic buckling analysis, and P is the cap for the capacity that typically corresponds to the squash load capacity based on yielding ($P_y=f_yA_g$) when the interaction with other modes is neglected, otherwise it reflects the limiting stress state of a mode that may interact with distortional buckling. Lastly, λ_d is the slenderness ratio for the distortional buckling failure that is defined as $\lambda_d = \sqrt{P_y / P_{crd}}$.

The column curve for the global Euler buckling capacity (P_{ne}) has been typically expressed by the following direct strength equation,

$$P_{ne} = \begin{cases} \left(0.658^{\lambda_c^2}\right)P_y & \forall \lambda_c \leq 1.5, \\ \left(\dfrac{0.877}{\lambda_c^2}\right)P_y & \forall \lambda_c > 1.5, \end{cases}$$

$$(6.31)$$

which is equivalent to Eq. (6.20) for the nominal buckling resistance of the member in the EWM. The slenderness ratio for global buckling is similarly defined as $\lambda_c = \sqrt{P_y / P_{cre}}$ based on the ratio of squash/yield capacity (P_y) and the critical load for global buckling ($P_{cre}=f_{cre}A_g$) obtained as the minimum of the critical loads for the flexural, torsional and flexural-torsional buckling modes with appropriate effective length consideration. The associated buckling stress (f_{cre}) can be determined from a rational elastic stability analysis or in accordance with Appendix D of AS/NZS 4600 [16] or Sections C4.1.1-2 of the North American Specification [15]. For instance, the flexural buckling stress for doubly symmetric sections, closed cross-sections, and any other sections that can be shown not to fail in torsional or flexural-torsional buckling modes can be evaluated from the Euler equation as follows

$$f_{cre} = \pi^2 E_s / \lambda_m^2,$$

$$(6.32)$$

where λ_m is the modified slenderness defined as the ratio of effective length (half-wavelength) of the member (L_e) for the flexural buckling over the modified radius of gyration of the section (r_m), i.e. $\lambda_m=L_e/r_m$. The modified slenderness ratio for a built-up section must account for the introduced level of composite action resulting from discrete fasteners that lies between the states of fully composite and non-composite action. For compression members composed of

two sections in contact, when the buckling mode creates shear forces in the connectors due to relative deformations between the constituent sections, the following equation for the modified slenderness ratio is recommended in the AISI and AS/NZS specifications

$$\lambda_m = \sqrt{\lambda_0^2 + \left(L_z/r_{y1}\right)^2},$$

(6.33)

where $\lambda_0 = L_e/r_0$ is the overall slenderness ratio of the entire section about the built-up member axis, L_z is the buckling length about the minor axis of an individual built-up section component between fasteners along the column height, i.e. $L_z = s$. Lastly, r_{y1} is the minimum radius of gyration of the full unreduced cross-sectional area of an individual built-up section component. In addition, for the enhancement of buckling capacity, the fastener capacity and spacing shall satisfy the following requirements [16]:

(a) The maximum allowable spacing for intermediate fasteners or spot welds is limited such that (s/r_{min}) does not exceed one-half of the governing slenderness ratio of the built-up member to ensure that the buckling of individual studs between fasteners does not occur before the global buckling of the entire built-up section,

(b) The ends of a built-up compression member are connected by fasteners spaced longitudinally not more than four diameters apart for a distance equal to 1.5 times the maximum width of the member or by a weld having a length not less than the maximum width of the member, and

(c) The intermediate fastener(s) or weld(s) at any longitudinal tie location can transmit at least 2.5 percent of the available axial compression capacity of the built-up member.

In summary, direct strength design equations, such as Eq. (6.30) for distortional buckling, can be treated as the generalisation of the column curves for global buckling in Eq. (6.31) to other modes. Thereby, direct strength design equations for different buckling modes can be written in the following generalised form

$$\frac{P_{ni}}{P_{mi}} = \begin{cases} 1 & \forall \lambda_i \leq \lambda_{i.\text{lim}}, \\ \left(a_i - \dfrac{b_i}{\lambda_i^{c_i}}\right)\dfrac{1}{\lambda_i^{c_i}} & \forall \lambda_i > \lambda_{i.\text{lim}}, \end{cases}$$

(6.34)

where $P_{mi}=f_{mi}A_g$ is the maximum nominal capacity associated with the mode of interest (i) acting as the cap for the ultimate capacity, and λ_i is the slenderness ratio for the buckling mode i that is proportional to the ratio of peak strength (f_{mi}) to the critical buckling stress (f_{cri}) in that mode, i.e. $\lambda_i = \sqrt{f_{mi}/f_{cri}}$. Furthermore, a_i, b_i, and c_i are the coefficients corresponding to the mode of interest (i) that are typically obtained from regression to test data with an aim to meet an acceptable level of target reliability index in design. Lastly, $\lambda_{i.\lim}$ is the limiting slenderness ratio associated with each buckling mode that must adhere to the following correlation for compatibility between the conditions

$$\lambda_{i.\lim} = \left[\frac{a_i - \sqrt{a_i^2 - 4b_i}}{2b_i} \right]^{\frac{-1}{c_i}}. \tag{6.35}$$

Following this generalised expression and based on existing work for beams [204], the following equation was suggested for the nominal local buckling capacity of columns in NAS and AS/NZS standard, accounting for possible local-global buckling interaction

$$P_{nl} = \begin{cases} P_{ne} & \forall \lambda_l \leq 0.776, \\ \left[1 - 0.15\left(\frac{P_{crl}}{P_{ne}}\right)^{0.4}\right]\left(\frac{P_{crl}}{P_{ne}}\right)^{0.4} P_{ne} & \forall \lambda_l > 0.776, \end{cases} \tag{6.36}$$

in which $\lambda_l = \sqrt{P_{ne}/P_{crl}}$ with $P_{crl}=f_{crl}A_g$ being the critical elastic local buckling load. It is noteworthy that Yap and Hancock [191] proposed the following equation for the local buckling capacity of CFS sections with web stiffeners

$$P_{nl} = \begin{cases} P_{ne} & \forall \lambda_l \leq 0.673, \\ \left[1 - 0.22\left(\frac{P_{crl}}{P_{ne}}\right)^{0.5}\right]\left(\frac{P_{crl}}{P_{ne}}\right)^{0.5} P_{ne} & \forall \lambda_l > 0.673, \end{cases} \tag{6.37}$$

which was shown to provide relatively more accurate predictions than Eq. (6.36) for these sections due to the consideration of local instability in multiple compression elements. The key parameters of the current direct strength equations for local and distortional buckling are summarised in Table 6-1.

Table 6-1: Parameters of current direct strength design equations for sectional buckling

Buckling Mode	a_i	b_i	c_i	$\lambda_{i.\text{lim}}$	P_{mi}
Local	1.0 (1.0*)	0.15 (0.22*)	0.8 (1.0*)	0.776 (0.673*)	P_{ne}
Distortional	1.0	0.25	1.2	0.561	P_y

* where the values in parenthesis correspond to sections with web stiffeners

6.3 COMPARISON WITH TEST DATA

Prior to performing any detailed reliability assessment, a comparison is made between the predictions of the current commonly-used design methods, as explained in Section 6.2, and the experimental data of this study, as provided in Chapter 4. For the use of DSM in the design of built-up sections, the most challenging task is the determination of critical elastic buckling stresses. Due to the deficiency of the current conventional Finite Strip Method (FSM) in explicitly accounting for discrete fasteners, researchers and practitioners have trialled various techniques, as discussed previously in Chapter 3 and summarised below, to obtain signature curves for the elastic buckling of different built-up assemblies as the prerequisite for the evaluation of the critical length and load for different buckling modes:

- Uncoupled constituent sections without composite action (NC) as the lower-bound and conservative estimate, which is expected to be a reasonable assumption for most design scenarios when the spacing of fasteners is not adequate to enhance the elastic buckling and ultimate capacities,

- Fully-composite (FC) section with constituent sections being merged where applicable to test the theoretical yet practically unachievable upper-bound for the capacities, and

- Partially-composite (PC) scenario accounting for discrete fasteners, which has been achieved via either locally stiffening parts of the section in the vicinity of fastener locations or via tying the degrees of freedom at those locations along the member length. The latter is expected to serve as a practical upper-bound estimate when fasteners are spaced sufficiently close to enhance the capacity.

The Compound Strip Method (CSM), as developed in Chapter 3 for built-up members with discrete fasteners, serves as a superior alternative for the above techniques and a unified solution for the elastic buckling analysis of built-up members at various levels of composite actions. For example, the signature curve for the test specimen 2C120-900-1 with primary distortional buckling mode is obtained using different FSM techniques (i.e. NC, FC) under simply-supported end conditions. The results are compared in Figure 6-4 with those from the CSM with different fastener spacing (i.e. s = 900 mm, 150 mm, 50 mm, 25 mm corresponding to s/L_{crd}=1.5, 0.25, 0.08, 0.04).
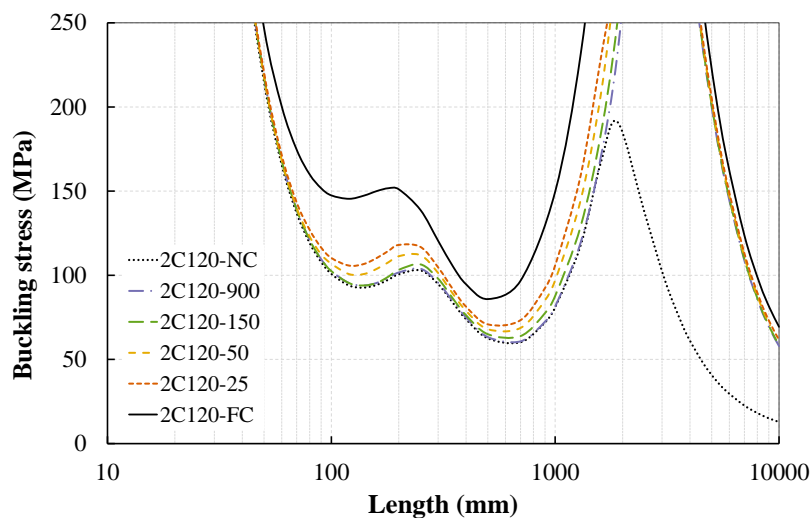
Figure 6-4: Impact of intermediate fasteners spacing on the signature curve of a built-up I-section

As can be seen, the introduction of discrete fasteners with spacings below the half-wavelength associated with minimum distortional buckling load (i.e. s/L_{crd}≤1.0) resulted in the elevation of the critical distortional buckling capacity (f_{crd}). Since for the above section L_{crd}/L_{crl}≈4.0, further reduction of fastener spacing below the half-wavelength corresponding to the characteristic minimum local buckling load of the section (i.e. s/L_{crd}≤0.25) also resulted in the enhancement of critical local buckling capacity and the tendency of the signature curve towards its upper-bound. Since the critical buckling lengths (L_{crd}, L_{crl}) for the built-up sections under various design scenarios are almost identical to those for a single section (L_{crd1}, L_{crl1}), it can be concluded that for sections with fastener spacing exceeding L_{crd1}, both critical distortional (f_{crd}) and local (f_{crl}) buckling stress can be conservatively estimated from signature curves for a

single constituent section with no coupling consideration (NC), and the ultimate capacity (P_u) is the direct sum of the uncoupled capacities of the constituent sections. For sections with $s>L_{crl1}$, the critical local buckling stress is still not expected to change from its non-composite value, whereas for all other scenarios, the enhancement in the critical local or distortional buckling stresses can be captured if necessary with the aid of the CSM or a rational finite element model. These stresses can then be used to assess the subsequent improvement in estimating the ultimate capacity of built-up members per the Direct Strength Method.

The critical length (L_{cri}) for different buckling modes and associated stress (f_{cri}), as required for direct strength design equations, were evaluated according to the procedure provided in Section 5.4.1. Firstly, the signature curves for the elastic buckling of various built-up sections under pinned end conditions were used to evaluate critical parameters (especially local buckling), which were obtained using the CSM. The critical half-wavelengths associated with local and distortional buckling are presented in Table 6-2 for the test sections.

Table 6-2: Critical half-wavelength of sectional buckling modes for tested cross-sections

Test series	FSM/CSM (S-S, $m=1$)					
	L_{crl} (mm)			L_{crd} (mm)		
	NC	PC	FC	NC	PC	FC
C120	140	140	120	600	600	500
C64	120	120	120	600	600	500

The critical buckling length and stress were also estimated from the elastic buckling analyses under fixed end conditions, where multiple half-sinewaves ($M=40$) were used to obtain the critical buckling load and associated half-wavelength. As expected, the results were almost identical for local buckling. For distortional buckling, higher buckling stress is achieved due to the influence of end conditions, which is expected to diminish by increasing the member length to form multiple distortional half-wavelengths while not long enough to be influenced by global buckling. However, this may not be directly assessable in sections with predominant local buckling mode. Modal decomposition techniques or the development of a constrained compound strip method would desirably serve as a solution for this objective. The results of

the elastic buckling analyses for test specimens with different levels of composite action under pinned and fixed end boundary conditions are reported in Table 6-3 and compared with the elastic buckling stress obtained from the test results (see Section 4.8.1 for more details).

As per distinctions made on the data sets depending on their prevalent buckling mode, i.e. Series C120 with distortional and Series C64 with local buckling modes, the results for each test series are provided in Table 6-4 and Table 6-5, respectively. The predictions by the EWM per EC3 [52, 202] and AS/NZS 4600 [16], as well as the current DSM in Australian and North American provisions, are compared with the test data. As can be seen, the EWM per EC3 appears to be the most conservative approach among these methods for both series. However, this conservatism is partially rectified in design by adopting no further strength reduction factor on the capacity predictions, i.e. $\gamma_m=1/\phi=1$. On the contrary, the current DSM based on FC evaluation of elastic buckling is significantly unconservative for both C64 and C120 test sets due to the inherent optimism in expecting the achievement of full composite behaviour. The remaining methods have a reasonable level of accuracy for different test series with some potential room for improvement subject to detailed reliability analysis. The results suggest that the current EWM in AS/NZS 4600 seems to be the most accurate method for Local (C64) test series and both sets combined, while the current DSM based on PC evaluation is found to be the most precise method for Distortional (C120) test series due to a lower coefficient of variation. This finding will also be investigated quantitatively through reliability analysis in Section 6.4.1.3 using more extensive data sets based on the results of numerical parametric studies from Chapter 5.

Table 6-3: Critical elastic buckling stress predictions for built-up test specimens

Specimen	Tests f_{cr} (MPa)	FSM/CSM (S-S, M=1) f_{crl} (MPa)			FSM/CSM (S-S, M=1) f_{crd} (MPa)			FSM/CSM (C-C, M=40) f_{cr} (MPa)		
		NC	PC	FC	NC	PC	FC	NC	PC	FC
2C120-900-1	79.6	92.7	93.9	145.4	58.9	60.7	85.8	84.8	86.4	124.7
2C120-900-2	89.8	93.3	94.6	146.4	60.6	62.2	89.0	87.5	92.9	129.3
2C120-300-1	85.8	93.7	94.7	146.0	59.6	63.3	87.9	86.0	92.2	127.8
2C120-300-2	82.1	93.1	94.6	145.7	59.4	62.6	86.2	86.0	90.5	125.4
2C120-150-1	91.3	93.5	94.5	145.1	58.4	64.2	84.9	83.4	87.9	122.7
2C120-150-2	90.3	93.4	94.6	145.4	58.6	64.1	85.2	84.2	88.5	123.6
2C120-100-1	90.2	93.3	96.3	144.9	58.3	64.7	84.3	83.6	89.2	122.2
2C120-100-2	94.5	93.1	96.2	145.2	58.2	64.6	84.4	83.5	88.9	122.3
3C120-900-1	92.9	93.6	99.6	149.8	59.3	65.5	98.4	85.4	88.6	142.4
3C120-900-2	91.9	93.5	99.2	146.9	58.7	64.9	91.9	84.2	86.7	132.1
3C120-300-1	90.5	93.1	99.2	148.2	58.7	67.3	95.3	84.5	90.6	137.8
3C120-300-2	89.6	93.8	99.7	148.2	59.2	68.0	94.9	85.4	92.8	137.2
3C120-100-1	95.4	93.2	100.7	148.0	59.7	68.4	94.3	85.9	99.1	136.3
3C120-100-2	95.8	93.6	101.8	148.4	59.2	67.9	95.6	85.3	101.1	138.2
4C120-900-1	81.3	94.1	101.1	154.6	60.1	65.0	110.1	86.7	88.8	157.5
4C120-900-2	93.8	94.4	101.4	154.0	60.9	65.5	109.1	87.8	88.3	156.1
4C120-300-1	89.3	93.9	100.8	153.9	58.8	67.9	107.7	84.8	92.6	154.1
4C120-300-2	89.6	94.1	100.9	153.6	60.0	67.7	108.1	86.5	92.0	154.2
4C120-100-1	101.9	93.6	105.8	153.0	58.9	68.3	105.2	84.4	101.7	150.6
4C120-100-2	113.3	94.3	106.4	152.2	61.0	68.6	107.5	88.0	102.2	153.7
3C64-900-1	104.9	102.5	104.2	370.7	193.0	248.4	455.5	104.4	104.4	370.2
3C64-900-2	105.1	102.2	103.8	369.7	192.3	254.5	458.0	104.1	104.1	369.2
3C64-300-1	106.2	101.9	104.0	370.3	191.6	257.7	449.1	103.8	104.8	369.7
3C64-300-2	104.8	102.2	104.3	371.0	190.8	259.3	449.1	104.1	105.0	370.4
3C64-100-1	118.6	103.3	105.4	374.1	194.4	265.9	459.3	105.2	107.0	373.5
3C64-100-2	114.6	103.2	105.7	375.0	194.4	265.0	462.7	105.1	107.3	374.4
4C64-900-1	107.1	102.2	104.3	421.3	191.7	245.1	479.6	102.2	104.3	420.7
4C64-900-2	105.6	102.3	104.3	421.3	191.6	244.9	480.1	102.3	104.4	420.8
4C64-300-1	106.9	102.1	104.3	421.2	191.8	255.4	480.9	102.1	104.8	420.6
4C64-300-2	107.6	102.2	104.2	420.8	191.7	256.8	481.4	102.2	104.7	420.1
4C64-100-1	110.4	102.1	105.0	421.3	190.2	258.8	477.2	102.1	106.4	420.7
4C64-100-2	112.0	102.8	105.3	423.1	192.7	261.8	483.7	102.8	106.7	422.4

It is also noted that for the sections of test series C120, the ratio of lip length to flange width (d_l/b) is below the threshold of EC3 for considering the contribution of the lips in the capacity calculations. As a result, two sets of values are reported in Table 6-4, one complying with the strict code requirements on conservatively ignoring the contribution of the lips and one considering the lips in the capacity calculations. As can be seen, the former approach results in a significant conservatism in the predictions, whereas the latter, though still conservative, may be deemed unsafe for design if used without a strength reduction factor. In these scenarios, the approach proposed in AS/NZS 4600 yields better estimates due to its accurate consideration of the edge stiffener and adjacent elements with potential interactions.

Table 6-4: Summary of the ultimate load predictions for test series C120 using the current design methods

Specimen	P_u^{exp} (kN)	P_u^{exp}/P_u^{design}				
			DSM		EWM	EWM
		NC	PC	FC	(AS4600)	(Eurocode)
2C120-900-1	188.9	0.95	0.94	0.77	0.94	1.37 (1.00)*
2C120-900-2	199.6	0.99	0.96	0.80	0.99	1.44 (1.05)
2C120-300-1	202.2	1.01	0.98	0.82	1.00	1.46 (1.06)
2C120-300-2	190.4	0.96	0.93	0.78	0.94	1.38 (1.00)
2C120-150-1	190.8	0.98	0.95	0.79	0.94	1.38 (1.01)
2C120-150-2	191.2	0.97	0.95	0.79	0.95	1.38 (1.01)
2C120-100-1	193.0	0.98	0.95	0.80	0.96	1.40 (1.02)
2C120-100-2	195.2	1.00	0.96	0.81	0.97	1.41 (1.03)
3C120-900-1	295.9	1.00	0.98	0.76	0.97	1.43 (1.04)
3C120-900-2	303.7	1.03	1.01	0.81	0.99	1.46 (1.07)
3C120-300-1	300.7	1.02	0.98	0.78	0.99	1.45 (1.06)
3C120-300-2	299.6	1.01	0.96	0.78	0.98	1.44 (1.05)
3C120-100-1	317.2	1.06	0.98	0.83	1.04	1.53 (1.11)
3C120-100-2	322.8	1.09	0.99	0.84	1.05	1.56 (1.13)
4C120-900-1	411.2	1.03	1.02	0.75	1.01	1.49 (1.08)
4C120-900-2	410.7	1.02	1.02	0.75	1.00	1.48 (1.08)
4C120-300-1	420.3	1.07	1.02	0.77	1.03	1.52 (1.10)
4C120-300-2	422.1	1.06	1.02	0.78	1.03	1.53 (1.11)
4C120-100-1	442.9	1.13	1.02	0.82	1.09	1.60 (1.15)
4C120-100-2	492.1	1.22	1.13	0.91	1.20	1.78 (1.28)
	Average	1.03	0.99	0.80	1.00	1.47 (1.07)
	St. Dev.	0.06	0.04	0.04	0.06	0.09 (0.06)

* () The ratio of ultimate load estimation (P_u^{exp}/P_u^{design}) according to Eurocode by including the contribution of the lips in the effective area of the test specimens with $d_l/b<0.2$

Table 6-5: Summary of the ultimate load predictions for test series C64 using the current design methods

Specimen	P_u^{exp} (kN)	P_u^{exp}/P_u^{design}				
		DSM			EWM (AS4600)	EWM (Eurocode)
		NC	PC	FC		
3C64-900-1	188.9	1.05	1.03	0.70	0.93	1.16
3C64-900-2	199.6	1.07	1.05	0.71	0.95	1.18
3C64-300-1	202.2	1.09	1.06	0.73	0.96	1.21
3C64-300-2	190.4	1.07	1.04	0.72	0.95	1.19
3C64-100-1	190.8	1.16	1.13	0.78	1.03	1.29
3C64-100-2	191.2	1.15	1.11	0.76	1.01	1.26
4C64-900-1	193.0	1.06	1.03	0.69	0.93	1.16
4C64-900-2	195.2	1.07	1.04	0.70	0.95	1.17
4C64-300-1	295.9	1.08	1.05	0.70	0.95	1.20
4C64-300-2	303.7	1.08	1.05	0.70	0.95	1.19
4C64-100-1	300.7	1.14	1.10	0.74	1.01	1.26
4C64-100-2	492.1	1.16	1.12	0.75	1.02	1.27
Average		1.10	1.07	0.72	0.97	1.21
St. Dev.		0.04	0.04	0.03	0.04	0.05

For a more specific discussion on the current Direct Strength Method with a more refined assessment of the effect of different fastener spacings and induced levels of composite action, the predictions by the DSM are shown in Figure 6-5 and Figure 6-6 for distortional and local buckling strengths, respectively. The relevant test data for each buckling mode with slenderness ratio calculated using different techniques are also included in the same figure for comparison. It is noted that each built-up section is differentiated with a distinctive marker and colour, and different fastener spacings for each section are distinguished by colour shading that ranges from a light shade to a dark one indicating the reduction in fastener spacing within the selection considered in the tests. As can be seen, the effect of fastener spacing is more pronounced on the distortional buckling slenderness, as reducing the fastener spacing below the critical half-wavelength for distortional buckling ($s/L_{crd}<<1.0$), but still within practical limits of construction, can give a noticeable rise to the buckling load. However, a less practical scenario with fastener spacing below the critical half-wavelength for local buckling ($s/L_{crl}<1.0$) is required to effectively restrain the local buckling of the section and enhance its capacity as

a built-up member. Therefore, a revised configuration of the section, e.g., stiffened webs or adjusted fastener configuration, may seem a more practical and effective means of increasing the local buckling load.
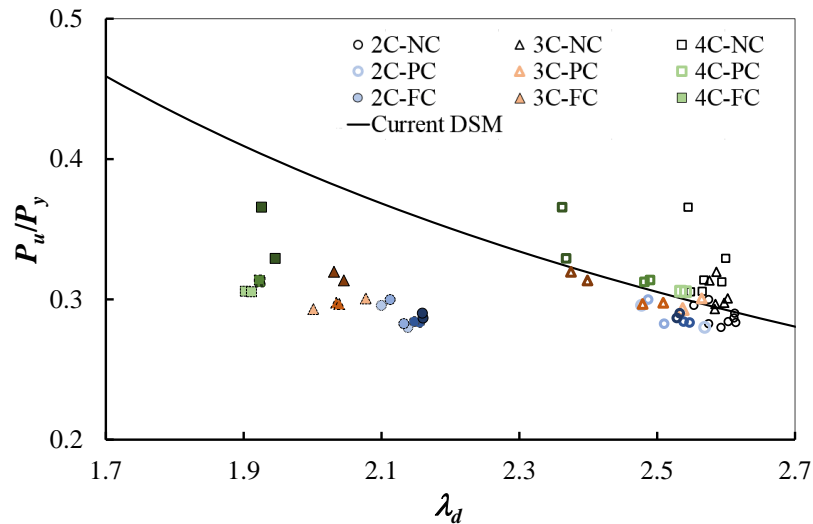
Figure 6-5: Variation of P_u/P_y with distortional slenderness ratio λ_d obtained with different levels of composite action for the specimens of test series C120
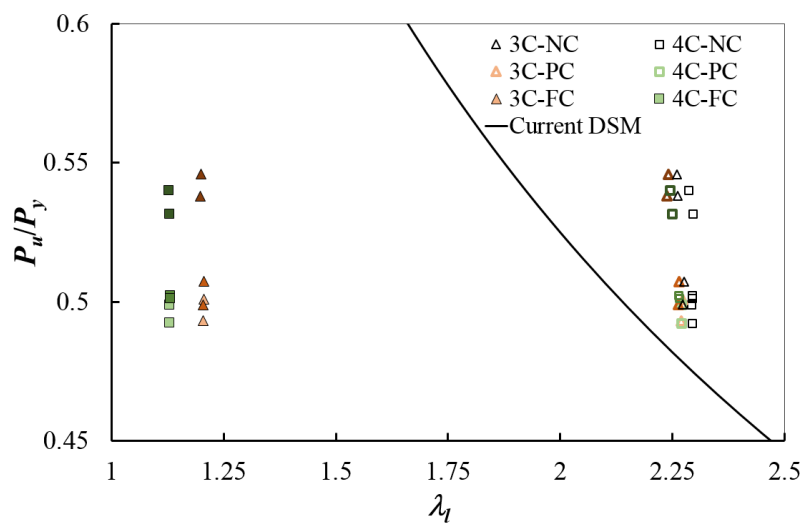
Figure 6-6: Variation of P_u/P_y with local slenderness ratio λ_l obtained with different levels of composite action for the specimens of test series C64

The non-composite (NC) approach provides a conservative estimate, especially for close spacing fasteners. The main shortcoming is that it does not differentiate the slenderness difference between the specimens with different fastener spacings and configurations. On the other side, the fully composite assumption yields highly unsafe predictions, which cannot be

reached under typical fastener configurations and spacings. The CSM can partially address this concern and distinguish the slenderness difference between various specimens with different fastener spacings, especially for distortional buckling. Nevertheless, it still provides conservative estimates for more complicated built-up sections with mixed connectivity, including flange-to-web connections in addition to typical web-to-web connections. This can be attributed to the probable contact between different plate elements involved in those complex assemblies that can cause a restraining effect and increase the critical buckling load and enhancement in the built-up member post-elastic reserve capacity.

6.4   RELIABILITY ANALYSIS

6.4.1.1 Basic principles

A limit state function $g(\mathbf{x})$ with $\mathbf{x}$ being the vector of basic design variables relevant to the problem is generally defined as the difference between the probability distribution functions (PDF) for resistance/capacity $R(\mathbf{x})$ and actions/loads $S(\mathbf{x})$, where the limiting condition $g(\mathbf{x})=0$ indicates a critical state below which failure is expected. Two indicative PDFs for load and resistance are schematically shown in Figure 6-7, which under practical design scenarios unavoidably overlap over a region as shaded in the graph. The probability of failure when design actions may exceed the available member capacity shall be evaluated and limited to an acceptable value in the design process.
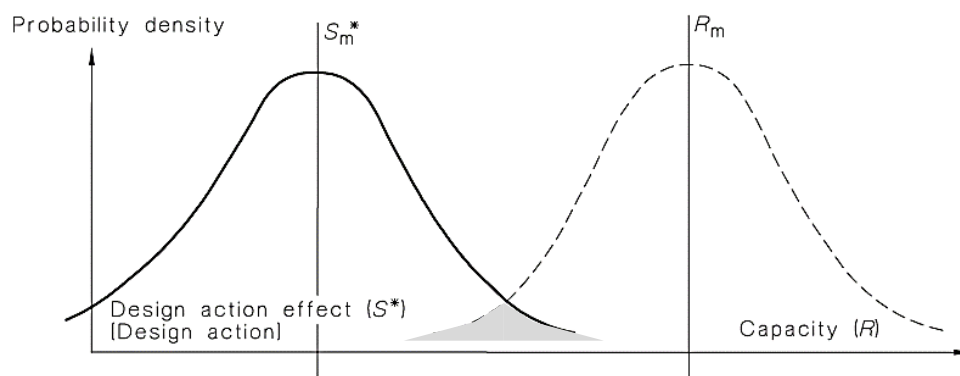
Figure 6-7: Probability distributions for member capacity and design action effects [206]

In the load and resistance factor design (LRFD) method, as commonly adopted in various international design standards, an acceptable strength design for an ultimate limit state (ULS) is defined such that the available design resistance (R_d) exceeds the design level of imposed actions (S_d), viz.

$$g_d = R_d - S_d \geq 0, \tag{6.38}$$

where in the definition of design values for load and resistance, a safety margin is introduced between the characteristic values of design actions (S_n) and resistance (R_n) by employing partial strength (reduction ↓) and load (amplification ↑) factors. The design resistance level is typically defined by

$$R_d = \eta R_n / \gamma_m, \tag{6.39}$$

where R_n is the nominal design resistance of the member obtained based on nominal section properties and characteristic strength of the material, which is typically defined as a five percentile value. Furthermore, γ_m is the partial safety factor of the material in the element of interest (section, member or connection) and under the design action of interest (if treated differently due to the nature of associated failure) that can be considered as the reciprocal of strength reduction factor ($\phi=1/\gamma_m$). Lastly, if applicable, η is a modification factor accounting for other influencing parameters, such as load duration (creep), moisture content, temperature and size effect. As far as a representative PDF is concerned, typically, a log-normal distribution with a minimum coefficient of variation (V_R) of 10 percent is considered. However, for materials with brittle nature, e.g. concrete, a different family of PDFs such as Weibull distribution is deemed more appropriate, which interpolates between the exponential and Rayleigh distributions.

The design level of actions imposed on the member can be expressed by the following generalised function accounting for the possible combinations of different load cases

$$S_d = \gamma_G G_n + \sum_i \psi_{Qi} Q_{ni}, \tag{6.40}$$

in which γ_G and G_n are, respectively, the partial load factor and nominal value for permanent gravity loading, including the self-weight (SW) and superimposed dead loads (SDL). Similarly, γ_{Qi} and Q_{ni} are defined as the partial load factors and nominal values for different imposed actions, i.e. live load (Q) alone or in combination with other loads such as wind (W), earthquake (E) and snow (S), while the combination probability factors ψ_{Qi} account for the reduced probability of the simultaneous occurrence of two or more extreme events at once in that load combination. Different load combinations and associated load factors and combination probability factors for the Australian building practice can be found in AS 1170.0 [207]. A summary of probability distribution parameters for dead and live loads is provided in Table 6-6 with reference to the background research and some supporting standards. As can be seen, a normal or log-normal distribution with almost mean value as the nominal level ($G_m \approx G_n$) and a relatively small coefficient of variation (V_G=0.1) are commonly assumed for dead loads due to their deterministic nature. In contrast, an extreme value (EV) Type 1 (Gumbel) distribution with typically 98 percentile as the characteristic value and relatively higher coefficient of variation has been assumed for the imposed live load.

Table 6-6: Summary of probability distribution parameters for gravity loading

Action	PDF	Standards	Reference	X_m/X_n	V_X	γ_X
Dead Load	Log-normal	ASCE 7 [169] AS1170.1 [208]	Ellingwood [168] Pham et al. [209]	1.05	0.1	1.4[a] (1.2)[b]
	Normal	Eurocode [165], NCC 2019 [167]	ISO 2394 [163] JCSS [164]	1.0	0.1	per code
Live Load	Gumbel (EV Type 1)	ASCE 7 AS1170.1	Ellingwood [168] Pham et al. [209]	1.0[c]	0.25	1.6[d]
		Eurocode, NCC 2019[c]	ISO 2394 [163] JCSS [164]	0.5[e]	0.4[e]	per code

[a] value for dead load acting alone, it has been prescribed as 1.35 in AS1170.1 and EC0
[b] value for dead load acting in combination with live load or wind
[c] value for live load in areas (e.g. small) not entitled to live load reduction
[d] load factor for live load is prescribed as 1.5 in AS1170.1 and EC0
[e] values may slightly differ depending, and those in ISO 2394 are only provided for the sake of comparison

In the first-order reliability method (FORM), the limit state function $g(\mathbf{x})$, defined as the difference between the design resistance and actions, is commonly considered as either the

direct difference between the PDFs or the difference between the natural logarithms of the functions, where the latter has been widely adopted in the design of steel structures including cold-formed steel members. This yields the following expression for the limit state function

$$g(\mathbf{x}) = \ln R(\mathbf{x}) - \ln S(\mathbf{x}) = \ln(R/S), \qquad (6.41)$$

where the associated mean (μ_g) and standard deviation (σ_g) can be obtained based on the assumption of log-normal distributions and the consideration of R and S being statistically independent variables, i.e. cov(R,S)≈0. Therefore, one may obtain

$$\mu_g = \ln\left(\frac{R_m}{\sqrt{c_R}}\right) - \ln\left(\frac{S_m}{\sqrt{c_S}}\right) = \ln\left(\frac{R_m}{S_m}\sqrt{\frac{c_S}{c_R}}\right), \qquad (6.42)$$

$$\sigma_g = \sqrt{\sigma_R^2 + \sigma_S^2} = \sqrt{\ln(c_R c_S)}, \qquad (6.43)$$

in which $c_i = 1 + V_i^2$ with V_i being the coefficient of variation of variable i. The reliability index (β), as a commonly considered measure for the structural safety margin, can then be evaluated from the following expression

$$\beta = \frac{\mu_g}{\sigma_g} = \frac{\ln\left[(R_m/S_m)\sqrt{c_S/c_R}\right]}{\ln\sqrt{c_R c_S}}. \qquad (6.44)$$

Assuming the coefficient of variation of load and resistance are small such that $V_i^2 \to 0$, some approximations can be made as follows

$$\ln c_R \simeq V_R^2, \ln c_S \simeq V_S^2 \text{ and } c_S/c_R \simeq 1, \qquad (6.45)$$

which yields the following simplified expression for the reliability index based on the approximations of the mean and standard deviation of the limit state function

$$\beta \simeq \frac{\ln(R_m/S_m)}{\sqrt{V_R^2 + V_S^2}}. \qquad (6.46)$$

This approximation is only valid for $V_i \leq 0.25\text{-}0.30$ and assumed in the seminal work of Ellingwood et al. [168] on the development of probability-based load criterion for American

national standards that served as the basis for the reliability assessment in many design standards, including AISC 360 [172], ACI 318 [210], AISI S100 [15], AS 4100 [173] and AS 4600 [16]. As derived, the reliability calculation per Eq. (6.46) depends only on the mean and coefficient of variation of the resistance and loads and is referred to as the First Order Second Moment (FOSM) Method. Importantly, it is premised on the assumption that the load effect (*S*) is also log-normal.

From a statistical point of view, the reliability index indicates the distance between the mean value for the limit state function and its critical value g(**x**)=0 as the onset of failure, which is expressed relatively in terms of the associated standard deviation. This is illustrated schematically in Figure 6-8.
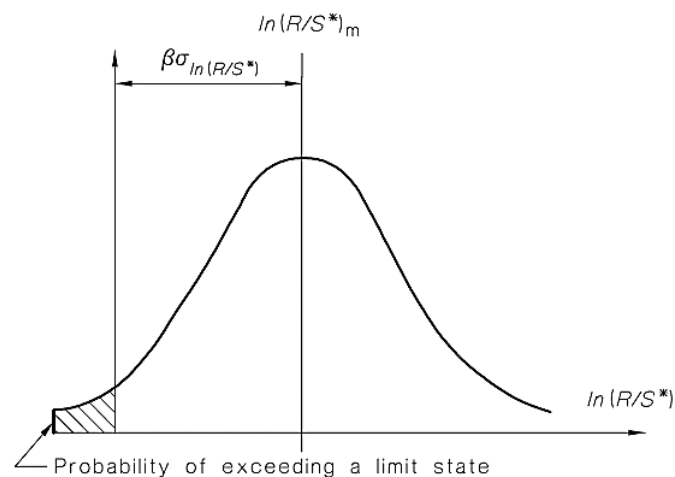
Figure 6-8: Limit state function with the associated reliability index and probability of failure [206]

The probability of failure (*P_f*) for a given member can be expressed by

$$P_f = \Pr\left[g(\mathbf{x}) < 0\right] = 1 - P_s,$$ (6.47)

where P_s is the probability of survival. Assuming the limit state function is normally distributed, the associated probability distribution function can be written as

$$f(x) = \frac{1}{\sigma_g \sqrt{2\pi}} \exp\left[-\frac{1}{2}\left(\frac{x - \mu_g}{\sigma_g}\right)^2\right].$$ (6.48)

The cumulative distribution function (CDF) can then be established as

$$F(x) = \int_{-\infty}^{x} f(t)dt = \frac{1}{2}\left[1 + \text{erf}\left(\frac{x - \mu_g}{\sigma_g}\right)\right]. \tag{6.49}$$

The relationship between the probability of failure and the associated reliability index, as tabulated in Table 6-7, can be mathematically established as follows

$$P_f = \Phi(-\beta) \text{ or } \beta = -\Phi^{-1}(P_f), \tag{6.50}$$

where $\Phi(-\beta)$ is essentially equal to $F(0)$ as the CDF at the onset of failure, viz.

$$\Phi(-\beta) = 0.5\left[1 + \text{erf}(-\beta/\sqrt{2})\right] = 0.5\text{erfc}(\beta/\sqrt{2}). \tag{6.51}$$

Table 6-7: Relationship between the probability of failure and the reliability index

P_f	10^{-1}	10^{-2}	10^{-3}	10^{-4}	10^{-5}	10^{-6}	10^{-7}
β	1.3	2.3	3.1	3.7	4.2	4.7	5.2

Different plausible design scenarios exist for a given structural material and member in terms of the relative proportion of dead and live loads, i.e. $\alpha_{ni} = G_{ni}/Q_{ni}$. Therefore, the target reliability index (β_T) is usually determined to reflect a representative value over the applicable range of design scenarios considering the frequency associated with each case. Assuming m different numbers of appropriate design scenarios, β_T is sought to be as close as possible to individual indices β_i corresponding to each design scenario $i \leq m$. The measure of closeness is typically defined as follows and aimed to be minimised

$$\sum_{i=1}^{m} \omega_i \left(\beta_i - \beta_T\right)^2 \to 0, \tag{6.52}$$

where the normalised weight factor ω_i represents the relative frequency of the appearance or the importance of each design case such that $\sum\omega_i = 1$. A range of design scenarios α_i and some proposed frequencies ω_i for different building materials in the American practice is provided in Ellingwood et al. [168]. For instance, their suggested weight factors for conventional steel and light gauge steel/aluminium are reproduced in Table 6-8 for reference.

Table 6-8: Suggested frequency/weight factors for different design gravity load scenarios

Material	G_n/Q_n					
	2.0	1.0	2/3	1/2	1/3	1/5
Steel	0.10	0.20	0.25	0.35	0.07	0.03
Light Gauge/Aluminium	0.00	0.06	0.17	0.22	0.33	0.22

The target reliability index (β_T) itself is also suggested in terms of either the annual index (for a one-year reference period) or the lifetime index over the service life of the structure, i.e. typically a 50-year reference period. The relationship between the annual reliability index and its lifetime value over n years can be simply established based on the survival probability over those years as follows

$$\Phi(\beta_n) = \left[\Phi(\beta_1)\right]^n \quad \text{where: } \Phi(\beta_n) = 1 - \Phi(-\beta_n) = P_{sn}. \tag{6.53}$$

As discussed in Section 2.6, the acceptable level of failure probability is usually defined in the standards [163, 169, 211] in terms of the importance level or risk category associated with the structure, relative life-saving costs, the structure class for consequences of failure, mode of failure and relative cost of safety measures. ASCE 7 [169], as the basis for minimum design actions in American design standards, prescribes the minimum lifetime (50-year) target reliability index (β_n) for different structural classes in terms of their risk category (i.e. equivalent to importance level). This value for typical ultimate design load cases (excluding extraordinary events such as an earthquake) is recommended as 2.5 and 3.0 for structures with risk category I (structures with low risk to human life) and II (typical structures other than I, III and IV), respectively. These limits are valid if the failure is not sudden and does not lead to widespread damage progression; otherwise, they shall increase to 3.0 and 3.5, respectively. Ellingwood et al. [168] suggested a lifetime target reliability index of 3.0 for steel members (4.5 for connections) under gravity loading, which is in line with ASCE recommendations and has been adopted in AISC 360 [172] and AS 4100 [173] for hot-rolled steel members. Some reduced limits were also suggested for extreme events, e.g. 2.5 for wind and 1.75 for earthquakes.

A relatively lower reliability index, 2.5 for members and 3.5 for connections, has been advised in AISI S100 [15] and AS/NZS 4600 [16] for cold-formed steel members, which serves as the minimum limit for the reliability index over practical ranges of design cases ($\alpha_n=G_n/Q_n$). This prescribed minimum baseline is typically associated with $\alpha_n=1/5$, whereas the target reliability index would generally exceed this limit, accounting for other design scenarios with higher gravity load contribution. For instance, the Canadian Standard Association (CSA) prescribes the reliability index as 3.0 for CFS members [170] but associated with $\alpha_n=1/3$, roughly representing the target reliability index. The conceptual difference between the target reliability index and the minimum baseline is schematically illustrated in Figure 6-9, where some sample reliability indices (β_i) for different design cases (α_{ni}) are plotted over the range of applicable design scenarios ($\alpha_{n,min}\leq\alpha_{ni}\leq\alpha_{n,max}$) per Table 6-8, and the target reliability index (β_T) as the weighted average and the baseline reliability index (β_{min}) as the minimum value are indicatively provided for comparison.
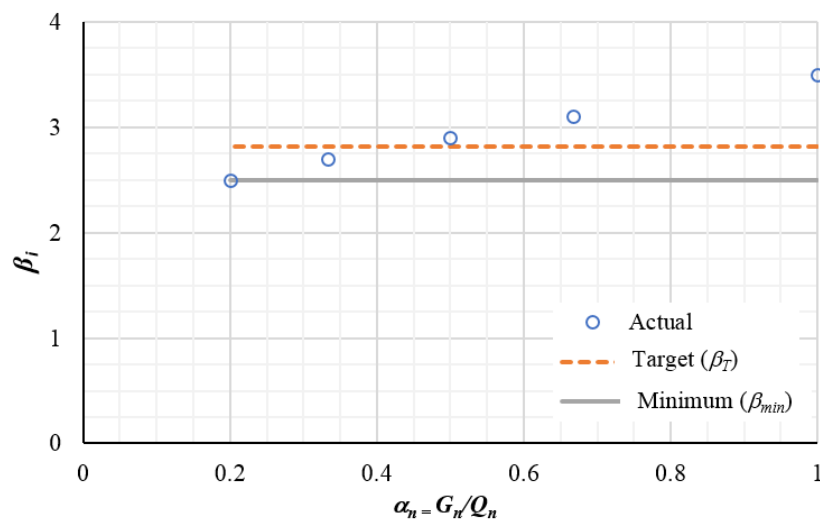
Figure 6-9: Schematic presentation of variation in reliability index over practical design range

6.4.1.2 Application to cold-formed steel

Following the First Order Second Moment (FOSM) method proposed by Ravindra and Galambos [212], the following correlation can be established between the mean (R_m) and nominal (R_n) resistance of a member and its associated coefficient of variation (V_R)

$$R_m = \left(P_m M_m F_m\right) R_n, \quad V_R = \sqrt{V_P^2 + V_M^2 + V_F^2}. \tag{6.54}$$

In the above equation, the professional factor P accounts for the model uncertainty as to the ratio of the experimental value of the ultimate capacity (P_u^{exp}) over its model prediction using the standard design equations (P_u^{design}). The model prediction is obtained from the effective width or direct strength methods in the case of CFS members with the actual measured dimensions and material properties as explained previously in the relevant subsections. The material factor M accounts for the material variability, which for steel members is mainly quantified based on the ratio of the actual yield stress (F_{ya}) to its nominal value (F_{yn}) specified by the manufacturer. Lastly, the fabrication factor F considers the variability in the section properties effective in calculating the member resistance to the action of interest, which for the case of axial compression would be the ratio of actual cross-section area (A_{ga}) over its nominal value (A_{gn}). These correlation factors can thus be summarised as follows

$$P = P_u^{exp} / P_u^{design}, \quad M = f_{ya} / f_{yn}, \quad F = A_{ga} / A_{gn}. \tag{6.55}$$

Based on the values for these parameters from examining available test data on beams, Hsiao et al. [213, 214] developed statistical parameters for the above factors as listed in Table 6-9, which lead to $R_m/R_n \approx 1.22$ and $V_R \approx 0.14$. However, these parameters can be refined based on the relevant experimental data for CFS compression members.

Table 6-9: Statistical parameters for resistance factors [213, 214]

Factor	Mean	CV
Professional (P)	1.11	0.09
Material (M)	1.10	0.10
Fabrication (F)	1.00	0.05

Due to the predominant nature of live load in light steel frames, the characteristic value of design actions under ultimate gravity case can be cast according to Eq. (6.40) as follows

$$S_n = \gamma_G G_n + \gamma_Q Q_n = Q_n \left(\alpha_n \gamma_G + \gamma_Q\right), \tag{6.56}$$

whereas the mean value for ultimate gravity action can be expressed as

$$S_m = G_m + Q_m = Q_n \left[\alpha_n \left(G_m / G_n \right) + \left(Q_m / Q_n \right) \right]. \tag{6.57}$$

As dead and live loads are independent variables, the standard deviation for ultimate design gravity action (σ_S) can be obtained from the square root of the sum of squares (SRSS) of the standard deviations for dead (σ_G) and live (σ_Q) loads, i.e. $\sigma_S^2 = \sigma_G^2 + \sigma_Q^2$. This yields the following expression for the coefficient of variation of design gravity actions (V_S)

$$V_S = \frac{\sigma_S}{S_m} = \frac{\sqrt{\left[\alpha_n \left(G_m / G_n \right) V_G \right]^2 + \left[\left(Q_m / Q_n \right) V_Q \right]^2}}{\alpha_n \left(G_m / G_n \right) + \left(Q_m / Q_n \right)}. \tag{6.58}$$

By utilising Eqs. (6.54) and (6.57), and considering the critical value for the limit state function, i.e. $S_n = \phi R_n$, the ratio of the mean values for capacity and design load can be expressed in the following format

$$R_m / S_m = P_m M_m F_m \left(c_\phi / \phi \right), \tag{6.59}$$

where the coefficient c_ϕ is defined as follows

$$c_\phi = \frac{\alpha_n \gamma_G + \gamma_Q}{\alpha_n \left(G_m / G_n \right) + \left(Q_m / Q_n \right)}. \tag{6.60}$$

The reliability index for a given strength reduction factor (ϕ) can then be evaluated according to Eq. (6.46) by utilising Eqs. (6.54) and (6.58) as

$$\beta = \frac{\ln(P_m M_m F_m c_\phi / \phi)}{\sqrt{V_R^2 + V_S^2}}. \tag{6.61}$$

Alternatively, the above equation can be rearranged such that the strength reduction factor corresponding to a target level of reliability index is obtained, viz.

$$\phi = c_\phi P_m M_m F_m \exp\left(-\beta \sqrt{V_R^2 + V_S^2} \right). \tag{6.62}$$

Following the recommendations for the minimum reliability index in the Australian standard [16] and North American specification [15] for the design of CFS members, i.e. $\beta = 2.5$ corresponding to $\alpha_n = 1/5$, and the suggested statistical parameters in Table 6-6 for dead and live

loads by Ellingwood et al. [168] as the basis for ASCE 7 [169] and AS 1170.1 [208] loading codes, the statistical parameters participating in the evaluation of the strength reduction factor can be further simplified to

$$c_\phi = 0.826\left(0.2\gamma_G + \gamma_Q\right), \quad V_S = 0.21. \tag{6.63}$$

6.4.1.3 Assessment of the current design methods

It is understood that the number of experimental tests in this study was still limited compared to what would be desirable for a reliability-based verification of the current design equations or their modifications if necessary. Moreover, their range of slenderness ratios for different sectional buckling modes was limited, which further limits their applicability for such study. In fact, the experimental program of this study was merely designed to provide insights into the sectional buckling of cold-formed steel compression members with a reasonable variation of some design parameters to study different sectional buckling modes, their interactions and the effect of discrete fasteners for various geometries of built-up open sections. The results were aimed to validate the refined finite element models proposed in this study, which were then utilised to carry out extensive parametric studies to various design scenarios, including the variation of the constituent single sections to improve the understanding of the influencing parameters with enhanced coverage of slenderness ratios.

The results of FE simulations are thus included to perform the reliability assessment and propose recommendations for modifying the current direct strength method for the design of CFS built-up compression members. However, using only numerical data would be characteristically different from a conventional reliability-based assessment using experimental data for the following reasons:

- Reliability is always assessed with respect to real behaviour and natural variations of the influencing parameters, which can be captured by experimental studies or in-situ testing of actual members. A finite element or any numerical simulation will only approximately predict the actual behaviour depending on the variability of material, its

failure modes, and the accuracy of the numerical model. This variation, even slight, may impact the accuracy of the reliability assessment, which may require some adjustments in the reliability-based validation of design equations.

- An experimental study with a reasonable number of tests and variations is expected to inherently incorporate the natural scatter in material properties and geometric imperfections, whereas the same statement is not necessarily true for a FE model as it usually employs only the statistical mean of local and global imperfections with typically a continuous Fourier series approximation (or similar) for the longitudinal variation and no allowance for variance around the mean value.

In lieu of a more advanced reliability assessment, revising the professional factor P and its associated coefficient of variation VP may seem rational when using numerical data in the validation process. Denoting $P_1 = P_u^{exp}/P_u^{FE}$ and $P_2 = P_u^{FE}/P_u^{design}$, one may simply incorporate the following adjustments for this purpose

$$P_m = P_{m1} \times P_{m2}, \quad V_P \cong \sqrt{V_{P1}^2 + V_{P2}^2}, \tag{6.64}$$

which is based on assuming that the joint variability of P_1 and P_2 is insignificant, i.e. $cov(P_1, P_2) \approx 0$. It is noted that P_1 and its associated coefficient of variation V_{P1} is a measure of closeness between FE model predictions and experimental variations, which has been already established in Chapter 5 for different experimental sets. In contrast, P_2 and its associated coefficient of variation V_{P2} for a given standard design method show the correlation between the model predictions and FE results from the parametric studies. In the best-case scenario where the FE model predicts the test data with a high degree of accuracy ($P_{m1} \approx 1$) and a small coefficient of variation, whether in absolute term ($V_{P1} \approx 0$) or in relation to other contributing factors (e.g. $V_{P1} << V_{P2}$), it may seem permissible to not modify the professional factor and its statistical parameters, i.e. $P_m \approx P_{m2}$ and $V_P \approx V_{P2}$. In this study, the statistical parameters for FE predictions were included in the assessment according to Eq. (6.64) with $P_{m1} = 0.98$ and $V_{P1} = 0.02$.

The predictions of the current design strength equations are first compared with the numerical FE data points obtained from parametric studies in Chapter 5 with slenderness ratios calculated using the compound strip method. The results of the elastic buckling analyses and predictions for the ultimate load of the sections based on different design methods are presented in Appendix E. Similar to the preliminary evaluations based on experimental data in Section 6.3, the comparisons with strengths obtained from FE-based parametric studies are similarly made separately for distortional and local buckling, and the results are provided in Figure 6-10 and Figure 6-11, respectively. It is noted that the numerical strengths are given in these figures with respect to two sets of slenderness ratios: 1) using the slenderness ratio corresponding to a single section (λ_1) without any coupling consideration between sections, and 2) using the slenderness of the built-up section obtained using the compound strip method. The results suggest that the latter approach is more representative due to its capability to make distinctions between the various fastener spacings considered and levels of composite action attained, which produce a distributed scatter of data points in closer agreement with the direct strength curve (Figure 6-10(b)), rather than vertically distributed data points at discrete slenderness ratios, as shown Figure 6-10(a).

Despite the general agreement between the ultimate capacities and the direct strength curve, some localised deviations were identified in the scattering of data points around the current DSM curve for distortional buckling in Figure 6-10. The deviations are associated with the observed interaction between the sectional buckling modes in the specimens made of sections C100-40-1.2 and C100-40-1.9, which is not considered in the current DSM. Upon a closer investigation of the inelastic response and the encountered failure modes, an interactive local-distortional mode was identified for those sections, which inherently had very close critical sectional buckling stresses ($f_{crd} \approx 0.98 f_{crl}$) with reasonably spaced critical sectional buckling lengths ($L_{crd}/L_{crl} \approx 5.5$).
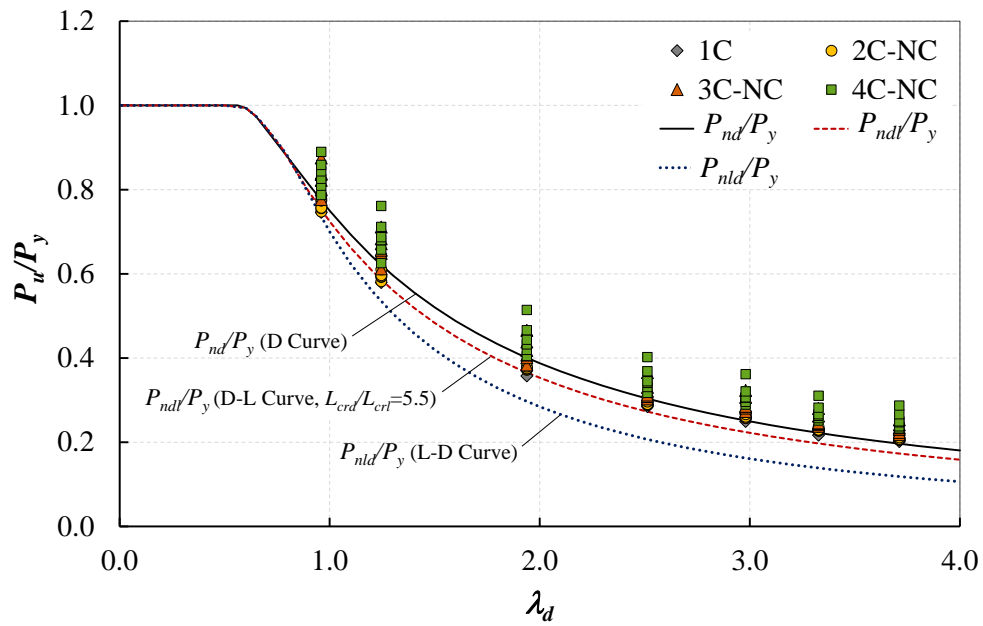
(a)
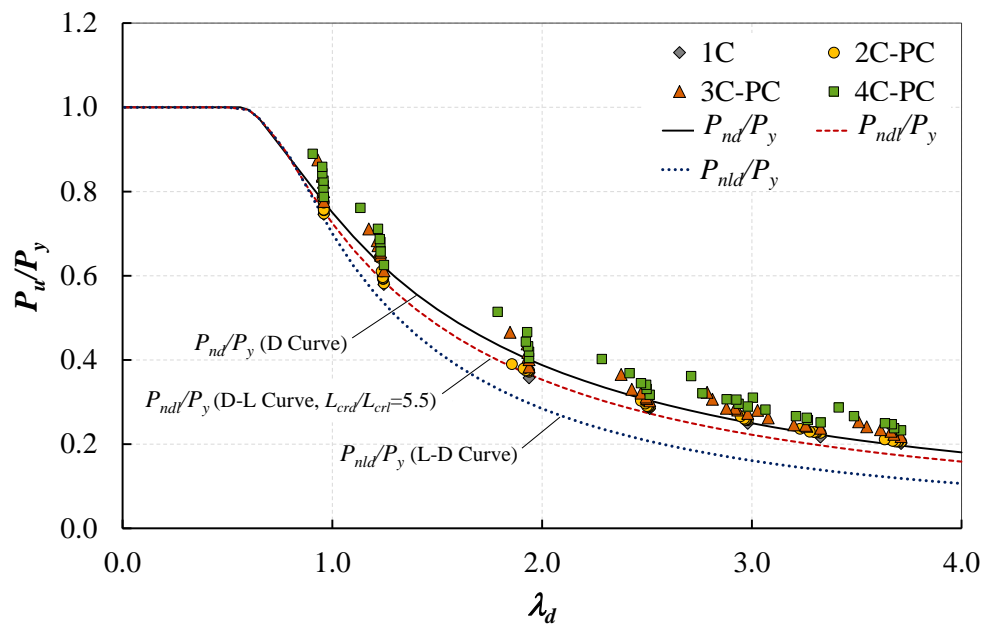
(b)

Figure 6-10: Variation of P_u/P_y with distortional slenderness ratio λ_d obtained with different levels of composite action: (a) non-composite, (b) partially-composite for the columns considered in the parametric study
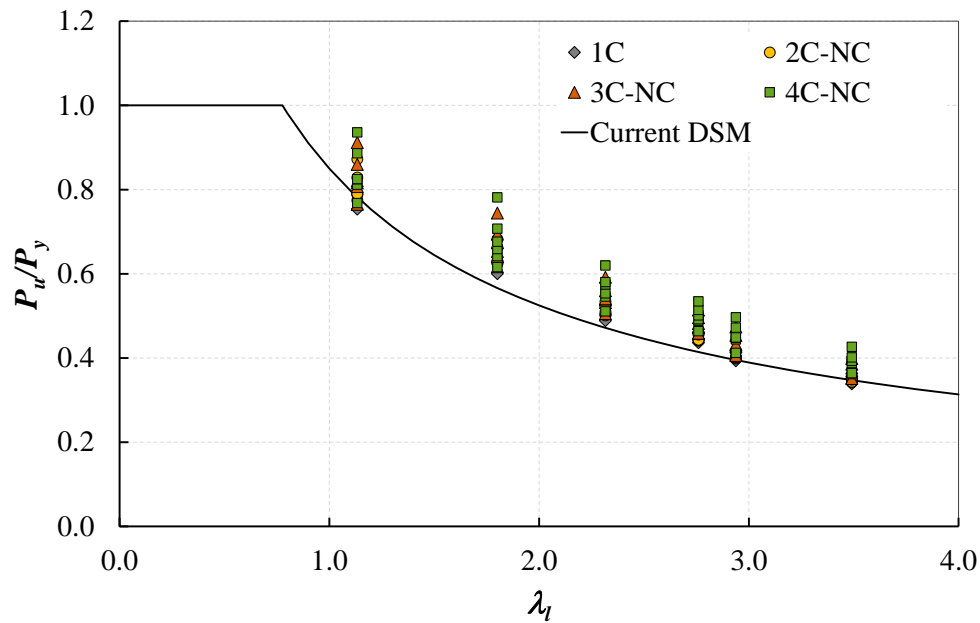
(a)
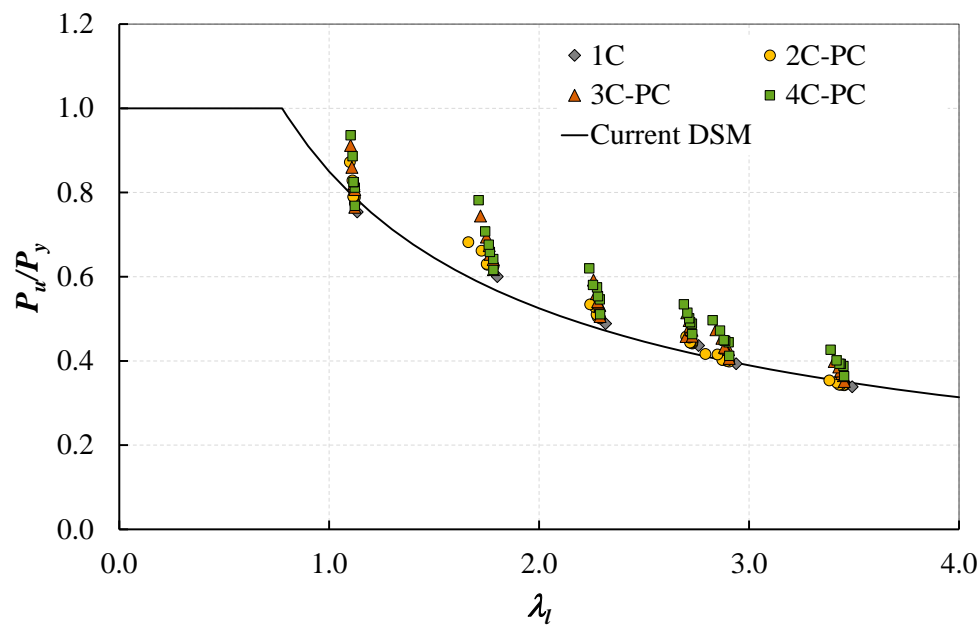
(b)

Figure 6-11: Variation of P_u/P_y with local slenderness ratio λ_l obtained with different levels of composite action: (a) non-composite, (b) partially-composite for the columns considered in the parametric study

Different sources of local-distortional buckling interactions have been debated in the literature [70-74], which have been considered by some proposed modifications of the current DSM. These sectional buckling interactions may be categorised into the following two groups:

- An interaction arising from a genuine mode coupling, which is characterised by very close local and distortional critical buckling stresses ($f_{crd} \approx f_{crl}$). This phenomenon was thoroughly investigated by Silvestre et al. [72, 73], wherein the so-called NDL approach, the following expression for the improved nominal strength against distortional-local interactive failures was proposed

$$\frac{f_{ndl}}{f_{nl}} = \begin{cases} 1 & \forall \lambda_{dl} \le 0.561, \\ \left[1 - 0.25\left(\frac{f_{crd}}{f_{nl}}\right)^{0.6}\right]\left(\frac{f_{crd}}{f_{nl}}\right)^{0.6} & \forall \lambda_{dl} > 0.561, \end{cases} \tag{6.65}$$

where $\lambda_{dl} = \sqrt{f_{nl} / f_{crd}}$ is the NDL interactive slenderness, and f_{nl} is the nominal local strength, which is obtained from Eq. (6.36) with the exception that f_{ne} is replaced with f_y to isolate the influence of global buckling. As a result, Eq. (6.65) was generalised in their research to supersede the original distortional buckling strength Eq. (6.30), by using a pseudo local strength (f^*_{nl}) that was proposed as a linear interpolation between f_{nl} and f_y depending on the critical buckling length ratio L_{crd}/L_{crl} in the range of 4.0 to 8.0 as follows:

$$f_{nl} \le f^*_{nl} = f_y + (1 - 0.25 L_{crd} / L_{crl})(f_y - f_{nl}) \le f_y. \tag{6.66}$$

- An interaction in sections dominated by local elastic buckling and with a higher secondary distortional buckling stress. In fact, the post-elastic reserve capacity in local buckling is understood to be higher than the distortional buckling stress, as also reflected in the direct strength design equations. This local-distortional interactive failure (NLD) can further limit the local buckling capacity below its nominal local-global interactive capacity, which can be potentially accounted by the following expression for the corresponding ultimate capacity as proposed by Schafer [74, 75]

$$\frac{f_{nld}}{f_{nd}} = \begin{cases} 1 & \forall \lambda_{ld} \le 0.776, \\ \left[1 - 0.15\left(\frac{f_{crl}}{f_{nd}}\right)^{0.4}\right]\left(\frac{f_{crl}}{f_{nd}}\right)^{0.4} & \forall \lambda_{ld} > 0.776, \end{cases} \tag{6.67}$$

in which $\lambda_{dl} = \sqrt{f_{nd} / f_{crl}}$ is the NLD interactive slenderness, and f_{nd} is the nominal distortional strength obtained from Eq. (6.30).

Following the same argument, the NDL approach may be considered to be also applicable to sections with prevalent elastic distortional buckling mode and substantially higher yield stress than the critical local buckling stress. The proposed NDL and NLD revisions of the DSM predictions are included in Figure 6-10 for comparison using a red dashed line and a blue dotted line, respectively. As can be seen, Eq. (6.65) for NDL interaction with f^{*}_{nl} per Eq. (6.66) provides a close lower bound fit to the ultimate FE strengths.

As discussed in Section 5.4.2.2, the parametric study results showed that the ultimate capacity of built-up sections can be increased by reducing the fastener spacing below the critical buckling half-wavelength associated with each mode. Although the compound strip method reasonably captures the enhancement of the elastic buckling load, which results in a modification of the slenderness ratio and hence an adjustment of capacity prediction, the direct strength predictions lack accuracy at low slenderness ratios. This observation suggests the relative fastener spacing s/L_{crd} should be considered a design parameter for calibrating the direct strength curves for built-up sections. The figures also show further enhancement of ultimate capacity in the more complex built-up sections (3C, 4C) with mixed-type connections providing restraints for flanges compared to a conventional built-up I-section with only web-to-web connections. This enhancement seems to be correlated with the relative number of restrained flanges in the cross-section, where the induced additional contacts and the change in the critical sectional buckling mode to a higher mode are found to provide the observed improvement in the post-elastic response and the ultimate capacity of the member. Therefore, this variable is considered as an additional influencing factor and included in the proposed modifications of the current DSM design equations in the next section.

The DSM generally appears conservative for the local buckling of built-up sections, especially in the intermediate slenderness ratios (e.g. $1.0 \leq \lambda_l \leq 2.0$). For distortional buckling, DSM reasonably captures the ultimate capacity of single sections and is reasonably accurate for built-

up I-sections at moderate to high slenderness ratios. Nevertheless, it becomes conservative for more complex sections (3C, 4C) with mixed connectivity and members with lower fastener spacing ratios (e.g. $s/L_{crd} \leq 0.5$). Using the current form of the standard design methods in Section 6.2, a reliability analysis is performed according to Eq. (6.61) to evaluate the reliability index assuming $\alpha_n = G_n/Q_n = 1/5$ for each design method using ultimate gravity load combinations and strength reduction factors consistent with each design standard, i.e. $\gamma_m = 1.0$ in EC, and $\phi = 0.85$ in AS/NZS and AISI. The results are summarised in Table 6-10, including the mean (μ_i) and standard deviation (σ_i) for the predictions in terms of P_u^{FE}/P_u^{design}, which includes values corresponding to each individual L/D data set as well as averaged values for one combined set. Despite the similarity of the DSM and EWM design equations in the AISI and AS/NZS provisions, two different reliability indices are obtained as the load factors for the ultimate gravity case in these standards differ slightly. As can be seen, the current EWM in EC3 shows a closer match to target reliability for ultimate capacity prediction of sections with predominant local buckling mode, but it provides substantially conservative predictions for distortional buckling set. On the contrary, the EWM in AS/NZS4600 yields consistent but slightly unsafe predictions for both sets. The current DSM also offers almost consistent predictions for both sets, but they are on the conservative side, which will be investigated and adjusted in the next section.

Table 6-10: Reliability index for built-up members using the current design equations

Mode	Variable	Direct Strength Method		Effective Width Method	
		AS4600	AISI S100	AS4600	EC3
Local	μ_L	1.10	1.10	1.02	1.23
	σ_L	0.08	0.08	0.08	0.09
	β_L	2.91	3.14	2.42	2.58
Distortional	μ_D	1.07	1.07	1.02	1.49
	σ_D	0.08	0.08	0.10	0.17
	β_D	2.77	3.00	2.43	3.25
Sectional (Combined)	μ_o	1.08	1.08	1.02	1.37
	σ_o	0.08	0.08	0.09	0.19
	β_o	2.84	3.06	2.43	2.80

Conversely, the required level of strength reduction factor ($\phi=1/\gamma_m$) for each method is obtained according to Eq. (6.62) such that a reliability index of 2.5 associated with $\alpha_c=G_c/Q_c=1/5$ is satisfied. This target was chosen to ensure conformity with the requirements in the AS and AISI provisions, as illustrated previously in Section 6.4.1.1. The results are given in Table 6-11, which includes separate strength reduction factors (ϕ_L, ϕ_D) for different sectional modes for comparison and one averaged value (ϕ_{LD}) for overall predictions with both L and D sets combined as having different strength reduction factors for each buckling mode is not common in design standards. Furthermore, separate reliability analyses were performed for each built-up configuration (2C, 3C, 4C), and the obtained strength reduction factors are reported in the Table to closely observe the variations in the reliability of DSM predictions for each configuration. Like in the previous study, two slightly different strength reduction factors are obtained for AISI and AS/NZS due to their inherent difference in the live load factor for ultimate gravity load combination.

Table 6-11: Strength reduction factors (ϕ) for built-up members using the current design equations

Mode	Section geometry	Direct Strength Method		Effective Width Method	
		AS4600	AISI S100	AS4600	EC3
Local	2C	0.85	0.90	0.79	0.99
	3C	0.90	0.96	0.84	1.03
	4C	0.93	0.98	0.87	1.04
	All	0.89	0.94	0.83	1.02
Distortional	2C	0.81	0.86	0.77	1.14
	3C	0.88	0.93	0.85	1.22
	4C	0.93	0.98	0.89	1.34
	All	0.87	0.93	0.83	1.22
Sectional (Combined)	2C	0.83	0.88	0.79	1.08
	3C	0.90	0.95	0.84	1.10
	4C	0.93	0.99	0.88	1.13
	All	0.88	0.93	0.83	1.09

In terms of the observed gap between the strength reduction factors obtained for each method versus its target value, the current EWM in EC3 shows the closest match for local buckling but the highest difference for distortional buckling due to its inherent conservative limitations. It is

noteworthy that by using the results of critical distortional buckling obtained from the CSM for the strength prediction based on EC3, as explained in Section 6.2.1.1, the strength reduction factor of the EWM for local buckling is improved from 1.05 toward the target value of 1.0. As far as direct strength design equations are concerned, the strength reduction factors obtained for sectional buckling of single channel sections are in agreement with the background reliability assessment in the commentary on AISI specification [15], which was based on an extensive experimental data set on local and distortional buckling combined. The current DSM almost satisfies the target limit for built-up I-sections (2C) with variations in different sectional buckling modes. However, the strength reduction factor obtained for other built-up sections tested in this study is expectedly found to be noticeably over the target limit, which is the main subject of proposed revisions in the next Section.

6.5   MODIFICATION OF THE DIRECT STRENGTH DESIGN EQUATIONS

As explained earlier, the obtained strength reduction factors in Table 6-11 for the current DSM noticeably differ for some cases, especially for 3C and 4C sections, from the prescribed standard value of ϕ=0.85 for concentrically loaded compression members in the North American and Australian standards. Therefore, some revisions are proposed for the current DSM equations to bring the strength reduction factors for all sections tested as close as possible to their target value while satisfying the expected reliability index in these standards.

6.5.1   *Distortional buckling*

The DSM predictions for distortional buckling in single sections and built-up I-sections based on the North American practice were generally in agreement with the prescribed strength reduction factor for achieving the required reliability level using the FOSM reliability method. Thereby, a lower strength reduction factor (ϕ≈0.8), as reported in Table 6-11, was achieved based on the Australian practice due to the live load combination factor difference. It is noteworthy that the discrepancy between the strength reduction factors for US and AU/NZ practices is perceived when the FOSM reliability method is used. However, the current strength

reduction factors in the Australian standards were obtained using the first-order reliability method (FORM) and assuming Gumbel distribution for live load rather than a simple log-normal distribution as in the FOSM reliability approach. Therefore, using the same strength reduction factor (ϕ=0.85) for US and AU/NZS practices is still valid for designing built-up sections using the current direct strength equation for distortional buckling.

Following an initial verification for commonly used single and built-up back-to-back channel sections, it is now attempted to address the observed conservatism in the current DSM predictions for distortional buckling in more complex sections. To this end, the built-up I-section and AISI specification are selected as the reference baseline for recovering the conservatism in target reliability. A meaningful dependency of ultimate capacities on s/L_{crd} was observed, which was pronounced at low distortional buckling slenderness ratios corresponding to a transition from squash sectional capacity to inelastic distortional buckling capacity. Moreover, an overall dependency on the assembly configuration of the built-up sections was observed with a more significant impact at intermediate to high distortional slenderness ratios, which is simply characterised in this study based on the relative number of restrained elements/flanges (n_{fr}) with respect to the total number of elements/flanges (n_{ft}) undergoing distortional buckling, i.e. $n_{rd}=n_{fr}/n_{ft}$. Thereby, these two factors are chosen as the main parameters in the proposed modifications to the direct strength design equation. The definition of restrained elements is illustrated in Figure 6-12 for all the built-up cross-sections considered in set-D, and the corresponding values of n_{fr}, n_{ft} and n_{rd} are presented in Table 6-12.
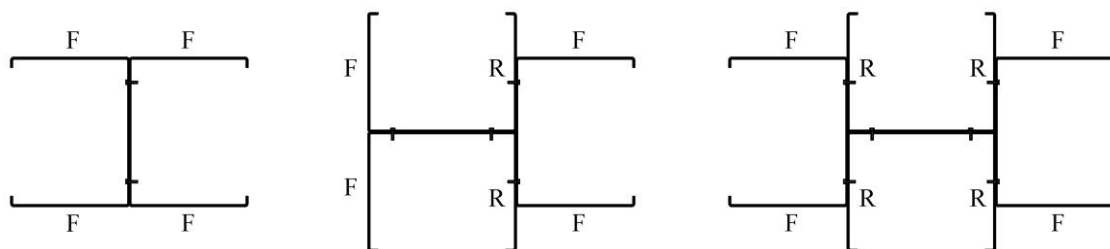
Figure 6-12: Illustration of restrained and free flanges of the built-up cross-sections of set-D

Table 6-12: Values of the relative number of restraint elements subject to distortional buckling for the studied built-up cross-sections

Section geometry	n_{ft}	n_{fr}	n_{rd}
2C	4	0	0.00
3C	6	2	0.33
4C	8	4	0.50

By following these observations, the following paragraphs on the proposed adjustments of the current DSM are written in a more general form to be directly interpreted for local buckling as the proposed procedure is almost unified between the sectional buckling modes. According to the nature of a general direct strength curve per equation (6.34) and the dependency of its slope and pattern at different slenderness ratios on the participating parameters (a_i, b_i, c_i), the reduction in the following two parameters was sought in this study for each sectional buckling mode:

- Calibration of b_i for adjusting the conservatism at low slenderness ratios, and

- Adjustment of c_i to account for the observed shift over the tail of the curve and the change in the rate of degradation.

While keeping a_i constant, these adjustments essentially shift the normalised direct strength equation for distortional buckling towards that for local buckling, which is also intended as a rational justification for the proposed modifications. A generalised reduction function f_r in the form of a generalised nonlinear interpolation function with adjustable power is utilised in this study for the quantification of reductions in the DSM parameters with respect to the influencing design variables:

$$f_r(\xi_i) = \chi_{r\xi} + (1 - \chi_{r\xi})\xi_i^{m_\xi}, \tag{6.68}$$

in which ξ_i (i.e. n_{fi}=1−n_{ri} or s/L_{cri}) is the influencing design variable, $\chi_{r\xi}$ is the maximum reduction ratio for the parameter of interest when ξ_i=0 as the ideal constraint condition (i.e. n_{ri}→1 or s/L_{cri}→0), and m_ξ is the associated exponent that controls the rate of reduction over intermediate design values (0<ξ_i<1). It is noted that the term n_{ri} is generalised from the

previously explained parameter n_{rd}, and it now refers to the relative number of restrained elements undergoing the sectional mode of interest i. For the case of m_ξ=1, the function (f_r) is the simple linear interpolation between $\chi_{r\xi}$ and 1. This form for the proposed reduction function is selected so that the proposed expressions for different sectional buckling modes (i=L/D) can be unified. It also somewhat resembles the participating modification function in the general form of the direct strength equations $a_i−b_i/\lambda_i^{ci}$, where the slenderness (λ_i) can be considered as λ_i=$1/\xi_i$ and the other parameters are defined as a_i=$\chi_{r\xi}$, b_i=$a_i−1$=$\chi_{r\xi}−1$, c_i=m_ξ. This highlights another rational feature of the proposed reduction function over an arbitrary regression, which is its gradual reduction with an adjustable rate from an initial value of unity (i.e. non-composite case) towards an asymptote ($\chi_{r\xi}$) as the reduction factor at high slenderness ratios ($\lambda_i→\infty$).

By adopting the generalised reduction function, the following unified adjustment expression is proposed for the revision of the current DSM parameters in either of the sectional buckling modes

$$b_{ir} = b_{i0} f_r (s / L_{cri})^{1/f_r (1-n_{ri})},$$ (6.69)

$$c_{ir} = c_{i0} f_r (1-n_{ri})^{1/f_r (s/L_{cri})},$$ (6.70)

where b_{i0} and c_{i0} refer to the current values of these parameters in the relevant DSM design equation prior to any adjustments. This function contains a primary reduction function for each DSM parameter depending on the primary influencing design variable (e.g. $1−n_{ri}$ for c_{ir}), which is further modified using the secondary design variable (e.g. s/L_{cri} for c_{ir}) by adjusting the exponent in charge of regulating the rate of enhancement. It is noted that the regression parameters for the adjusted DSM variables were back-calculated through nonlinear regression analysis to test data at different slenderness ratios to meet the target strength reduction factor for DSM predictions.

For the case of distortional buckling, i.e. suffix i in the equations to be replaced with d, the obtained regression parameters are summarised in Table 6-13, which can then be used to evaluate the reduced DSM parameters associated with ultimate distortional buckling capacity

(b_{dr}, c_{dr}) depending on the relative number of restrained flanges in the built-up section assembly ($1-n_{rd}$) and the normalised fastener spacing ratio (s/L_{crd}).

Table 6-13: Regression parameters for the adjustment of DSM variables in distortional buckling

Design variable (ξ)	maximum reduction ($\chi_{r\xi}$)	exponent (m_ξ)
$n_{fd}=1-n_{rd}$	0.75	0.8
s/L_{crd}	0.70	0.8

Following the proposed modifications, the DSM equation for distortional buckling of built-up columns is revised as follows

$$\frac{P_{nd}}{P_y} = \begin{cases} 1 & \forall \lambda_d \leq \lambda_{d.\lim}, \\ \left(1-\dfrac{b_{dr}}{\lambda_d^{c_{dr}}}\right)\dfrac{1}{\lambda_d^{c_{dr}}} & \forall \lambda_d > \lambda_{d.\lim}, \end{cases} \tag{6.71}$$

where

$$\lambda_{d.\lim} = \left[\frac{1-\sqrt{1-4b_{dr}}}{2b_{dr}}\right]^{\frac{-1}{c_{dr}}}, \tag{6.72}$$

$$b_{dr} = 0.25\left(0.7+0.3\left(s/L_{crd}\right)^{0.8}\right)^{\frac{1}{0.75+0.25\left(1-n_{fd}\right)^{0.8}}}, \tag{6.73}$$

$$c_{dr} = 1.2\left(0.75+0.25\left(1-n_{fd}\right)^{0.8}\right)^{\frac{1}{0.7+0.3\left(s/L_{crd}\right)^{0.8}}}, \tag{6.74}$$

in which s/L_{crd} shall not be taken as more than 1.0. Upon the systematic adjustment of direct strength design equations with parametric variables, the strength reduction factor and reliability index for more complex built-up sections were successfully restored to levels consistent with baseline built-up I-sections as commonly used and verified in building research and practice. A comparison of the accuracy and scatter of the DSM predictions prior to and after proposed adjustments are made in Figure 6-13 for various sections. The results of the proposed DSM show a substantial improvement in the accuracy of ultimate load predictions for different built-up section configurations.
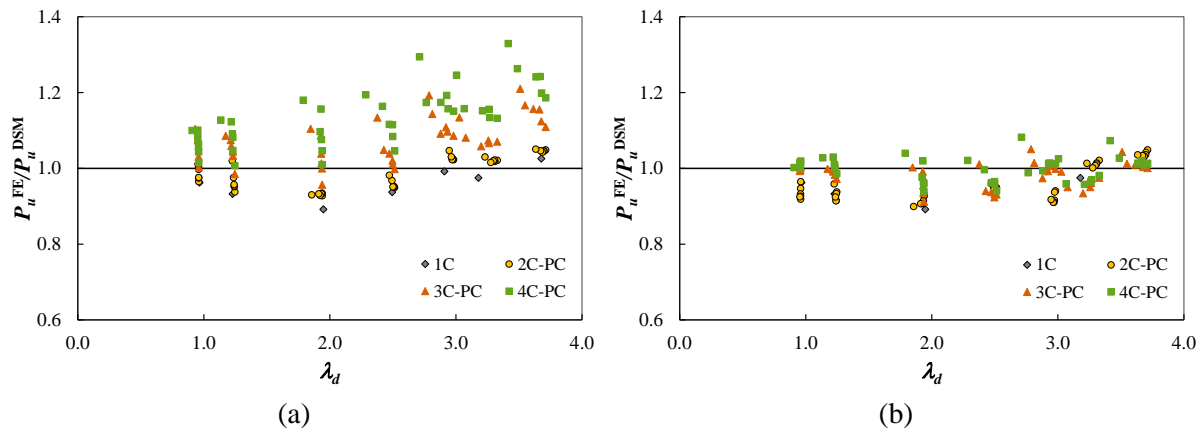
Figure 6-13: Scatter of data points for ultimate distortional buckling capacity around model predictions based on the: (a) current DSM, (b) proposed DSM

Next, the updated predictions of the DSM are compared separately for each built-up configuration with the numerical data points, and the results are provided in Figure 6-14. Theoretical lower (LB) and upper bounds (UB) for the design ultimate capacity of each cross-section under distortional buckling is also included in the figure by assuming ineffective connectivity ($s/L_{crd} \geq 1$) and full continuous connection at fastener location along the length of the member, ($s/L_{crd} \rightarrow 0$), respectively. As can be seen, the pattern for enhancing ultimate capacity due to the spacing of discrete fasteners is captured with reasonable accuracy across different configurations using the proposed parametric adjustments. Thus, the proposed modification holds significant promise for incorporation in the US and AS/NZS standards for the design of built-up members subject to distortional buckling. However, a potential ground for improvement was identified in Section 6.4.1.3 for cases with closely spaced sectional buckling strengths involving probable sectional mode coupling, e.g. $0.9 \leq f_{crd}/f_{crl} \leq 1.1$ as advised in [73], where the use of NDL approach with f^*_{nl} per Eq. (6.66) seems promising as an effective replacement for distortional buckling strength equation. This statement can be further validated in future research using a more specific parametric study on this phenomenon in built-up members.
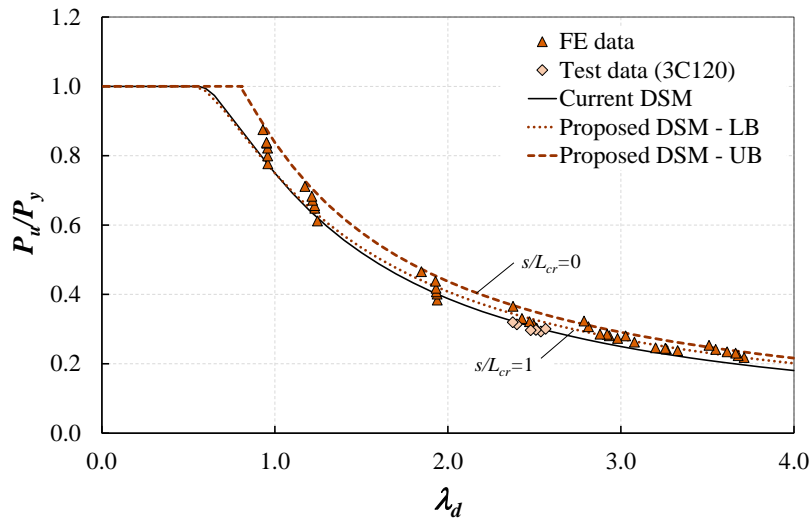
(a)
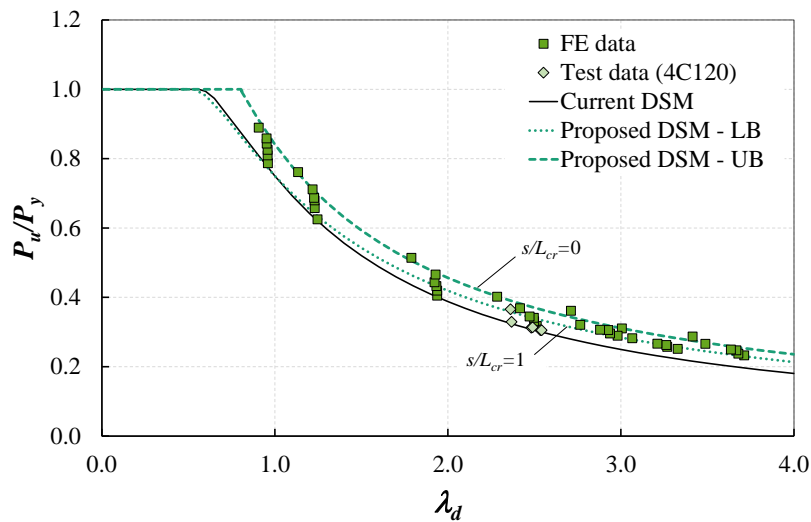
(b)

Figure 6-14: Comparison of the adjusted direct strength design method predictions of the ultimate distortional buckling capacity for (a) 3C and (b) 4C sections.

In conclusion, the expected enhancement of ultimate distortional buckling capacity (P_{nd}) of CFS built-up members is decomposed into three components as follows:

A. Enhancement as a result of the elevation in elastic distortional buckling stress (f_{crd}) and subsequent reduction in the associated slenderness ratio (λ_d), which is captured via evaluation of the critical distortional buckling capacity from the CSM and then using basic unmodified DSM predictions with $f_r(s/L_{crd})=1$ and $n_{rd}=0$;

B. Enhancement of the ultimate capacity based on the level of restraint provided for flanges in the built-up section configuration, e.g. 3C or 4C sections, which is characterised by the proposed modification of the direct strength parameters (b_d, c_d) based on the relative number of restrained flanges ($0 \leq n_{rd} \leq 1$); and

C. Further enhancement of the ultimate capacity due to intermediate fasteners with spacing less than the critical distortional buckling half-wavelength ($s/L_{crd} < 1$), if applicable, is captured via further adjustments of the same DSM parameters (b_d, c_d) using the proposed reduction function $f_r(s/L_{crd})$.

For a hypothetical case of a built-up section with continuous connections at fastener locations along the length of the member ($s/L_{crd} \rightarrow 0$) and a configuration such that all flanges are partially restrained using the fasteners ($n_{rd} \rightarrow 1$), these components will effectively shift the direct strength curve for distortional buckling towards that for local buckling, i.e. $b_d \approx b_l = 0.15$ and $c_d \approx c_l = 0.8$. This hypothetical scenario means that the section is expected to undergo local buckling as effectively restrained for distortional buckling, which serves as the theoretical upper bound for ultimate distortional buckling capacity of practical built-up geometries with discrete fasteners. All other possible design scenarios are considered to lie between this theoretical upper limit and the current DSM curve as the lower bound, associated with built-up sections with no composite action.

6.5.2 Local buckling

The DSM predictions for local buckling in single sections and built-up I-sections were slightly more conservative than those for distortional buckling. The strength reduction factor obtained for AS/NZS 4600 was in agreement with the prescribed limit, whereas a higher factor ($\phi \approx 0.9$), as reported in Table 6-11, was achieved for AISI S100. A reasonable level of agreement was attained over the full slenderness range, but a higher scatter of data points was observed at lower values of local buckling slenderness ratios. In addition, a higher post-elastic reserve capacity was obtained using more complex cross-sections, which is attributed to the mixed connectivity and partial restraint of some of the webs and flanges. This resulted in additional

conservatism in DSM predictions and yielded higher strength reduction factors for those sections.

Similar to the procedure adopted for adjusting distortional buckling capacity predictions, the built-up I-section and AISI specification are selected as the reference baseline for recovering the conservatism in target reliability for sections with mixed connectivity. Furthermore, the parameter a_l in the direct strength design equation was kept constant, and the adjustments for built-up sections were incorporated through modification of the other two parameters (b_l, c_l) to slide and push the direct strength predictions for local buckling in built-up sections away from the baseline predictions for single sections to match the data points for different built-up configurations with the target reliability level using the current strength reduction factors of 0.90 and 0.85 applicable to the AISI and AS specifications. The same form of the generalised reduction function (f_r) was utilised for quantifying the effect of cross-section configuration and fastener spacing; however, the participating coefficients ($\chi_{r\xi}$) and exponents (m_ξ) were adjusted so that the target goal as outlined above can be achieved. These values were evaluated from a nonlinear regression analysis of local buckling data points, and the obtained values are listed in Table 6-14.

Table 6-14: Regression parameters for the adjustment of DSM variables in local buckling

Design variable (ξ)	maximum reduction ($\chi_{r\xi}$)	exponent (m_ξ)
$n_{fl}=1-n_{rl}$	0.75	0.8
s/L_{crl}	0.70	4.0

The proposed reduction in DSM parameters for local buckling was therefore quantified using the generalised adjustments per Eqs. (6.69) and (6.70) by replacing design variables relevant to local buckling, i.e. L_{crl} and n_{rl}. It is noted that the relative ratio of restrained elements in the context of local buckling (n_{rl}) refers in this study to the relative number of major constituent elements undergoing local buckling (e.g. webs as considered here) that are partially constrained in the built-up configuration (n_{wr}) with respect to the total number of elements undergoing local buckling (n_{wt}). This ratio is equivalent to one minus the relative number of free/unrestrained elements (n_{fl}), i.e. $n_{fl}=1-n_{rl}$, which characterises the proposed adjustments. Definition of

restrained elements for local buckling is shown in Figure 6-15, and the determination of n_{rl} for each cross-section is illustrated in Table 6-15. It is noted that connecting the webs of channel sections in a built-up I-section using typical fasteners is not expected to prevent local buckling, and therefore, the webs in this scenario are not counted as restrained elements for the determination of n_{rl}, as reported in Table 6-15.
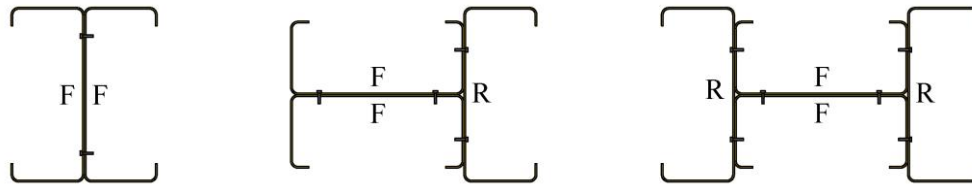
Figure 6-15: Illustration of restrained and free flanges of the built-up cross-sections in set-L

Table 6-15: Values of the relative number of restraint elements subject to local buckling for the studied built-up cross-sections

Section geometry	n_{wt}	n_{wr}	n_{rl}
2C	2	0	0.00
3C	3	1	0.33
4C	4	2	0.50

The modified DSM equation for local buckling of built-up columns is expressed as follows

$$\frac{P_{nl}}{P_y} = \begin{cases} 1 & \forall \lambda_l \leq \lambda_{l.\lim}, \\ \left(1 - \frac{b_{lr}}{\lambda_l^{c_{lr}}}\right)\frac{1}{\lambda_l^{c_{lr}}} & \forall \lambda_l > \lambda_{l.\lim}, \end{cases} \tag{6.75}$$

where

$$\lambda_{l.\lim} = \left[\frac{1 - \sqrt{1 - 4b_{lr}}}{2b_{lr}}\right]^{\frac{-1}{c_{lr}}}, \tag{6.76}$$

$$b_{lr} = 0.15\left(0.7 + 0.3\left(s/L_{crl}\right)^4\right)^{\frac{1}{0.75 + 0.25\left(1 - n_{fl}\right)^{0.8}}}, \tag{6.77}$$

$$c_{lr} = 0.8\left(0.75 + 0.25\left(1 - n_{fl}\right)^{0.8}\right)^{\frac{1}{0.7 + 0.3\left(s/L_{crl}\right)^4}}, \tag{6.78}$$

in which s/L_{crl} shall not be taken as more than 1.0.

Upon the adjustment of direct strength design equations with parametric variables and successful restoration of the strength reduction factor for more complex built-up sections to levels consistent with baseline built-up I-sections, the updated DSM predictions for each built-up configuration are compared in Figure 6-16(b) with the corresponding numerical test data. The accuracy and scatter of the current DSM model predictions are also included in Figure 6-16(a) for comparison, which shows the robustness of the proposed modification to the current DSM and its improvement in terms of accuracy and observed variations over different built-up configurations. The detailed calculations based on the current design equations and the proposed design equations for local and distortional buckling capacities of built-up columns are provided in Appendix F for three tested built-up cross-sections as indicative examples. The results are compared with the experimental results, which demonstrate the increase in design strength made possible by the proposed design equations.
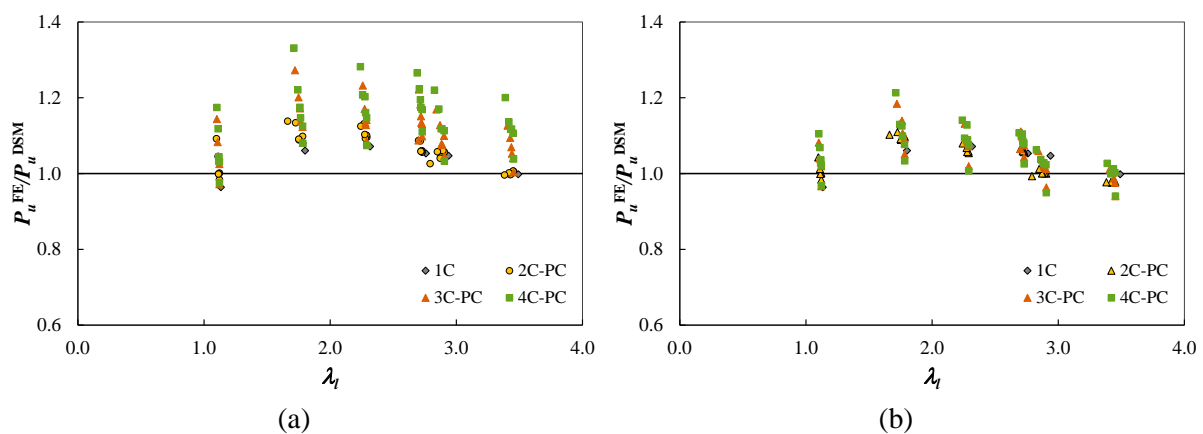
Figure 6-16: Scatter of data points for ultimate local buckling capacity around model predictions based on: (a) current DSM, (b) proposed DSM

Despite the considerable contribution of $f_r(s/L_{crl})$ factor for the effect of fastener spacing on the additional enhancement of local buckling reserved capacity, it may be safely neglected in the majority of practical design cases as the provision of such closely spaced fasteners ($s<L_{crl}$) may be deemed impractical. This is due to the short critical half-wavelength of local instabilities, which is typically in the order of section depth ($L_{crl}\approx h_w$) and slightly reduced by decreasing fastener spacing. Therefore, in most design cases, typical fastener spacings are not expected to substantially modify the critical elastic local buckling stress and associated half-wavelength

from their basic values for single sections that can be obtained from a conventional finite strip analysis available in software such as CUFSM [24] or Thin-Wall [23]. A nominal enhancement in the ultimate local buckling capacity (P_{nl}) with respect to multiple single sections without composite action can thus be obtained using the proposed modification for b_l and c_l with or without consideration of $f_r(s/L_{crl})$ adjustment as desired.

6.6   SUMMARY

This chapter was devoted to the assessment of current standardised procedures, namely the traditional Effective Width Method (EWM) and the Direct Strength Method (DSM), in the European, North American and Australian/New Zealand standards for the design of cold-formed steel (CFS) members. The theoretical frameworks of these two methods and their application to CFS built-up members were explained, and their predictions of sectional buckling capacity were compared against the experimental data. Subsequently, some basic concepts of the first-order reliability method for assessing current design methods and the calibration of code partial safety factors were reviewed, and its applicability to CFS members was discussed. The results from extensive parametric studies carried out in Chapter 5 were then utilised to perform a reliability-based assessment, where the suitability and performance of the two design standard methods were evaluated for the design of CFS built-up compression members under sectional buckling.

The strengths and weaknesses areas of each design method were highlighted based on the outcomes of the reliability assessment. It was found that the effective width method provides the best estimates for the local buckling capacity; however, its application is not straightforward that is further limited by several slenderness limitations in place. On the contrary, the direct strength method as a simple alternative approach shows superior performance for distortional buckling while still showing safe and reasonable predictions for local buckling. The DSM, in combination with the compound strip method for elastic buckling analysis, was found to be applicable to built-up members and a wider range of sections compared to the EWM, which promotes its use even as the default design method due to its

simplicity and extended range of applicability. A more specific and detailed level of discussion was provided for using the DSM predictions as the design method of interest in this study. Some particular issues were identified, such as interactive local-distortional buckling failure and the enhancement of post-elastic sectional capacity in complex built-up members, and some remedial solutions were discussed.

A rational modification for the DSM design parameters for local and distortional buckling capacities of built-up columns was proposed based on the relative number of restrained components (n_{ri}) undergoing the sectional buckling mode of interest and the normalised fastener spacing ratio in terms of the associated critical buckling half-wavelength (s/L_{cri}). The proposed modifications were shown to be reasonably accurate and robust for different cross-section assemblies and fastener configurations and allowed the strength enhancement produced by intermittent fasteners to be accurately accounted for. Lastly, an upper limit for enhancing the direct strength curves was proposed based on considering theoretical upper limits for the proposed influencing factors, i.e. $n_{ri} \rightarrow 1$ for the relative number of restrained components in the built-up cross-section assembly and $s/L_{cri} \rightarrow 0$ for the relative spacing of discrete fasteners.

Chapter 7 CONCLUSIONS

7.1 SUMMARY AND OUTCOMES

This study was mainly concerned with the sectional buckling of open built-up sections under uniform compression, which included experimental and numerical investigations with extensive parametric studies to assess the reliability of the current design equations. The primary outcomes and accomplishments of this study are concisely summarised in the following sections.

7.1.1 Elastic buckling analysis

A new and practical application of the Compound Strip Method (CSM) was presented and verified in this research, which extends the use of the semi-analytical Finite Strip Method (FSM) for modelling members with support and connecting elements. For the first time, the CSM was applied to the stability analysis of built-up Cold-Formed Steel (CFS) sections with arbitrarily located discrete fasteners. First, the basics of the semi-analytical FSM were briefly introduced in Chapter 3, and the formulation of discrete connection elements with adjustable stiffness properties and their incorporation in the conventional finite strip formulation was explained in detail. This enrichment of the conventional FSM and the proposed framework serves as a useful tool for the buckling analysis and the structural design of built-up sections with any desired cross-sectional composition and fastener configuration. The simplicity and accuracy of the CSM can expedite extensive parametric studies and the search for the optimal structural design of built-up sections in future studies and practice.

A series of numerical examples were presented in that chapter to show the performance and versatility of the CSM in the elastic buckling analysis of built-up CFS sections with complicated geometry. Several typical built-up I- and box sections and a complex corner

section were analysed for various fastener configurations and boundary conditions. The proposed numerical technique was verified against the Finite Element (FE) solutions obtained using ABAQUS software, and it was shown to be both accurate and convergent. The extent of composite behaviour in built-up sections was investigated for different fastener spacing ratios in terms of the enhancement of buckling capacity and changes in the corresponding buckling modes for the three cross-sections studied. The results demonstrated that reducing the fastener spacing ratio can effectively enhance the global buckling capacity of both open and closed built-up sections. However, the sectional buckling capacity of open built-up sections can also be increased, though to a lesser extent and through much more effort, by reducing the fastener spacing below the critical half-wavelength for each buckling mode. The observed change in global buckling capacity is more pronounced under fixed end conditions, whereas the impact of fastener spacing is case-dependent in the local buckling region.

7.1.2   *Experimental investigation*

Chapter 4 describes the experimental program of this study, which was designed and carried out to investigate the local and distortional buckling of built-up cold-formed steel sections subjected to pure compression with a particular focus on the influence of cross-section geometry and fasteners spacing. To this end, two cross-sections were designed, which included one custom-made press-braked section (C120) with the prevalent elastic distortional buckling mode and one roll-formed industrial section (C64) with the predominant local elastic buckling mode. For each set, three different singly-symmetric and doubly symmetric built-up sections were considered, and each configuration was tested with three different screw spacings ($s = 100$, 300 and 900 mm).

The material properties of the flat and corner parts of the sections were obtained using standard coupon tests, and the results indicated a nonlinear material behaviour with a considerably higher 0.2% proof and ultimate tensile stresses for test series C120. In addition, the membrane residual stress in the web of the roll-formed section was tested and found to be negligible. Prior to testing, the geometrical imperfections were measured along the length of the member at

different transverse locations on the web, flanges, and lips of the cross-sections. The measured imperfections were decomposed into the critical eigenmodes of the sections (i.e., global, local, and distortional) using the Fourier series technique and were compared with the Australian standard recommendations. The amplitude of the global imperfections was relatively small due to the short length of the members and the symmetry of the built-up cross-sections. The measured distortional imperfection amplitudes were comparable to the Australian standard recommended values, while the local imperfection values were reasonably smaller. A total of 36 specimens with a nominal length of 1 m, as the critical distortional half-wavelength of the sections, were tested under uniform axial compression between idealised fixed ends. The fixed end condition was achieved using a special end plate for each cross-section filled with Patternstone to facilitate the confinement of the specimens at the ends.

All the specimens of Series C120 buckled and failed in the distortional mode. On the contrary, a local buckling mode was observed for the specimens of Series C64 in the elastic region, followed by an interactive local-distortional buckling failure at the ultimate state. The results indicated an increase in the ultimate load capacity of built-up columns with the reduction of screw spacing. This was more pronounced in Series C120 with a maximum enhancement of 36.5% compared to a single section capacity once connecting four sections with the minimum fastener spacing considered. This maximum capacity enhancement can be attributed to the observed change of buckling mode from distortional to local in the back-to-back connected cross-sections in the built-up configuration with four component sections, in which the restraints provided to the web and flanges matched the local half-wavelength of the section and together with the pattern of local imperfections along the length of the member triggered buckling in the higher local mode. In contrast, the ultimate capacity of C64 sections was not noticeably influenced by the discrete connections or contact between the sections. Upon a detailed comparison of the ultimate capacity of specimens with that of specimens with no intermediate fasteners, it was noticed that the improvement in the ultimate capacity of all built-up sections due to evenly-spaced intermediate fasteners was of limited significance for both test series with an average observed increase of less than 10%.

As far as the local plastic mechanisms were concerned, the commonly known flip-disc mechanism was identified as the primary mode in the web of almost all sections, while the local failure mechanisms that developed in the flanges were different between the sections failing in distortional and local-distortional interactive modes. The elastic buckling load of the built-up sections was estimated from the experimental load-displacement curve and compared with the predictions of the compound strip method and finite element models, where a reasonable level of agreement was observed across both methods.

7.1.3   *Numerical studies*

A detailed finite-element model was developed for the reliable nonlinear collapse analysis of built-up cold-formed steel sections with discrete screw connections, elaborated in Chapter 5. The model was established upon conventional shell finite elements using the isotropic von-Mises (J2) plasticity constitutive model. Some of the most appropriate connection elements and contact conditions in ABAQUS were employed to capture the interactions between the constitutive plates to the best of their capabilities. The geometric imperfections were incorporated into the FE model using the Fourier series approximations of the measured imperfections as in-built perturbations for nonlinear buckling analysis. The nonlinear solution scheme for the quasi-static problem was based on the full Newton-Raphson method with dynamic time stepping and adaptive viscous regularisation. The main components of the computational model were discussed, including their available options and comparison between these, followed by a rational justification for the options chosen in this study. Specifically, a detailed theoretical background was provided with conclusive comparisons of the available options for the nonlinear constitutive model, the systematic implementation of geometric imperfections, the enforcement of end support conditions, the application of contact conditions between the constituent plates, the selection of connection elements for representing intermediate screw fasteners, type of elements to be used with mesh sensitivity, and finally the incremental load stepping and nonlinear solution schemes.

The accuracy and performance of the proposed FE modelling strategy were verified against the experimental data, contributing to the calibration of the influencing parameters. The predictions of the proposed methodology were shown to be in excellent agreement with the test data in terms of the failure mode and the inelastic capacity curve up to ultimate capacity and beyond. Upon its successful calibration, the FE model was utilised to perform extensive parametric studies into the effects of various design parameters on the ultimate strength of built-up columns. This included practical variations of cross-section dimensions, sectional slenderness, built-up section geometry, and fastener spacing beyond those considered in the experimental investigation. The outcomes further confirmed the earlier experimental observations on the influence of discrete fasteners and contact between the constituent elements on the elastic buckling capacity and the ultimate capacity of the built-up sections with different assemblies and configurations. This numerical data set was then utilised for the reliability-based assessment of the currently available standard design equations for built-up CFS columns, especially the direct strength method, and any adjustments required. It is noted that though the computational model was established within the framework of ABAQUS software, it can be applied to any other commercial analysis software with similar features and capabilities, including the available FE library, contact models, nonlinear analysis and solution options.

7.1.4   *Evaluation of the current design methods*

In the final chapter, the common design methods of cold-formed steel members in international standards, namely the Effective Width Method (EWM) and the Direct Strength Method (DSM), were briefly reviewed. The applicability of these design methods to the built-up sections was examined and discussed through comparison with the experimental test data as well as the results of numerical parametric studies in this study. Detailed reliability analysis was performed to assess the suitability of these design methods and highlight their strengths and weaknesses when applied to the sectional buckling of built-up CFS compression members. It was found that the EWM provides the best estimates for the local buckling capacity, and it also yields reasonably accurate predictions for distortional buckling when using the additional provisions

in AS/NZS 4600 and the AISI specification. Nevertheless, its application was not as straightforward as the DSM and is further limited by several slenderness limitations for the constituent elements. The direct strength method, in combination with the compound strip method for the elastic buckling analysis, showed superior performance in predicting the distortional buckling strength while still providing safe and efficient predictions of the local buckling strength.

The DSM was shown to be applicable to built-up members, where specific issues such as local-distortional buckling interactions and the enhancement of post-elastic sectional capacity were identified and addressed. Some adjustments were proposed to improve the accuracy of the current direct strength design equations for the ultimate capacity predictions of built-up compression members to comply with the expected reliability index in the Australian and North American provisions while conserving the prescribed strength reduction factor. The proposed adjustments were established upon a rational modification of the participating factors in the direct strength equations for local and distortional buckling capacities based on the relative number of restrained components undergoing the sectional buckling mode of interest and the fastener spacing relative to the associated critical buckling half-wavelength. The proposed modifications were shown to be reasonably accurate and robust for different cross-section and fastener configurations. In addition, upper limits for the enhancements of inelastic sectional capacities were proposed based on theoretical upper limits for the proposed influencing factors.

7.2 POTENTIAL FUTURE WORKS

This study was mainly concerned with the sectional buckling of open built-up sections under uniform compression. The compound strip method was employed and verified for these members. Based on the scope and outcomes of this study, the following potential subjects are recommended for future works in this area:

- The experimental and numerical investigations of closed built-up sections and the effect of flange restraints on their sectional buckling load and ultimate capacity, which can

also be used to validate the proposed hypothetical upper-bound limits for the enhancement of ultimate sectional capacity in built-up compression members,

- Application of the compound strip method to built-up sections under pure bending or in combination with axial load to study the influence of discrete fasteners on the elastic buckling capacity and modes of built-up members with and without sheathing,

- A thorough study of the effect of imperfections on the behaviour of built-up sections using the modal decomposition techniques to propose new recommendations for the magnitude of imperfection associated with each critical buckling mode shape.

REFERENCES

[1] J. Rhodes, N.E. Shanmugam, *Cold-Formed Steel Structures*, in: W.F. Chen, J.Y.R. Liew (Eds.), The Civil Engineering Handbook (2nd ed.), CRC Press, 2002.

[2] J.M. Davies, Recent research advances in cold-formed steel structures, *Journal of Constructional Steel Research* 55(1) (2000) 267-288.

[3] L.W. Williams, *1 - Introduction to recent trends in cold-formed steel construction*, in: C. Yu (Ed.), Recent Trends in Cold-Formed Steel Construction, Woodhead Publishing, 2016, pp. 1-35.

[4] W.W. Yu, R.A. LaBoube, *Cold-formed steel design*, John Wiley & Sons, 2010.

[5] W. Ramberg, W.R. Osgood, *Description of Stress-Strain Curves by Three Parameters*, National Aeronautics and Space Administration Washington DC, 1943.

[6] R. Hill, *A theory of the yielding and plastic flow of anisotropic metals*, Proceedings of the Royal Society of London A: Mathematical, Physical and Engineering Sciences, The Royal Society, 1948, pp. 281-297.

[7] W.F. Hosford, *On yield loci of anisotropic cubic metals*, Proceedings of the seventh North American metalworking research conference, 1979, pp. 191-196.

[8] R. Hill, *Theoretical plasticity of textured aggregates*, Mathematical Proceedings of the Cambridge Philosophical Society, Cambridge Univ Press, 1979, pp. 179-191.

[9] N. Abdel-Rahman, K. Sivakumaran, Material properties models for analysis of cold-formed steel members, *Journal of Structural Engineering* 123(9) (1997) 1135-1143.

[10] V. Zeinoddini-Meimand, *Geometric imperfections in cold-formed steel members*, PhD Thesis, The Johns Hopkins University, 2011.

[11] W.M. Quach, J.G. Teng, K.F. Chung, Residual stresses in steel sheets due to coiling and uncoiling: a closed-form analytical solution, *Engineering Structures* 26(9) (2004) 1249-1259.

[12] B.W. Schafer, T. Peköz, Computational modeling of cold-formed steel: characterizing geometric imperfections and residual stresses, *Journal of Constructional Steel Research* 47(3) (1998) 193-210.

[13] E. de M. Batista, F.C. Rodrigues, Residual stress measurements on cold-formed profiles, *Experimental Techniques* 16(5) (1992) 25-29.

[14] C.D. Moen, T. Igusa, B.W. Schafer, Prediction of residual stresses and strains in cold-formed steel members, *Thin-walled structures* 46(11) (2008) 1274-1289.

[15] AISI Standard, *North American Cold-Formed Steel Specification for the Design of Cold-Formed Steel Structural Members*, AISI S100-16, American Iron and Steel Institute (AISI), Washington, DC, 2016.

[16] Australian Standard, *Cold-formed steel structures*, AS 4600-2018, Standards Australia, NSW, 2018.

[17] V.M. Zeinoddini, B.W. Schafer, Simulation of geometric imperfections in cold-formed steel members using spectral representation approach, *Thin-Walled Structures* 60 (2012) 105-117.

[18] K.J.R. Rasmussen, G.J. Hancock, Geometric imperfections in plated structures subject to interaction between buckling modes, *Thin-Walled Structures* 6(6) (1988) 433-452.

[19] B.W. Schafer, Z. Li, C.D. Moen, Computational modeling of cold-formed steel, *Thin-Walled Structures* 48(10) (2010) 752-762.

[20] M. Shinozuka, G. Deodatis, Simulation of Multi-Dimensional Gaussian Stochastic Fields by Spectral Representation, *Applied Mechanics Reviews* 49(1) (1996) 29-53.

[21] N.W. Murray, P.S. Khoo, Some basic plastic mechanisms in the local buckling of thin-walled steel structures, *International Journal of Mechanical Sciences* 23(12) (1981) 703-713.

[22] N.W. Murray, *Introduction to the theory of thin-walled structures*, Clarendon Press, Oxford, 1984.

[23] J.P. Papangelis, G.J. Hancock, Computer analysis of thin-walled structural members, *Computers & Structures* 56(1) (1995) 157-176.

[24] Z. Li, B.W. Schafer, Buckling analysis of cold-formed steel members with general boundary conditions using CUFSM conventional and constrained finite strip methods, (2010).

[25] Z. Yao, K.J. Rasmussen, Inelastic local buckling behaviour of perforated plates and sections under compression, *Thin-Walled Structures* 61 (2012) 49-70.

[26] C.D. Moen, B. Schafer, Elastic buckling of cold-formed steel columns and beams with holes, *Engineering Structures* 31(12) (2009) 2812-2824.

[27] I. Georgieva, L. Schueremans, L. Pyl, L. Vandewalle, Experimental investigation of built-up double-Z members in bending and compression, *Thin-Walled Structures* 53 (2012) 48-57.

[28] M.M. Attard, G.W. Hunt, Column buckling with shear deformations—A hyperelastic formulation, *International Journal of Solids and Structures* 45(14) (2008) 4322-4339.

[29] F.R. Shanley, Inelastic Column Theory, *Journal of the Aeronautical Sciences* 14(5) (1947) 261-268.

[30] T.V. Galambos, *Structural members and frames*, Courier Dover Publications, 2016.

[31] S.P. Timoshenko, J.M. Gere, *Theory of elastic stability*, Courier Corporation, 2009.

[32] A. Chilver, *Thin-Walled Structures*, John Wiley and Sons, New York, 1967.

[33] T.B. Pekoz, G. Winter, Torsional-Flexural Buckling of Thin-Walled Sections Under Eccentric Load, *Journal of the Structural Division* 95(5) (1969) 941-963.

[34] A. Chajes, P.J. Fang, G. Winter, *Torsional flexural buckling, elastic and inelastic, of cold formed thin-walled columns*, School of Civil Engineering, Cornell University, 1966.

[35] R. Von Mises, On Saint Venant's Principle, *Bulletin of the American Mathematical Society* 51(8) (1945) 555-562.

[36] G.H. Bryan, On the Stability of a Plane Plate under Thrusts in its own Plane, with Applications to the Buckling of the Sides of a Ship, *Proceedings of the London Mathematical Society* 1(1) (1890) 54-67.

[37] E.E. Lundquist, E.Z. Stowell, E.H. Schuette, *Principles of Moment Distribution Applied to Stability of Structures Composed of Bars or Plates*, National Aeronautics and Space Administration Washington DC, 1945.

[38] F. Bleich, *Buckling strength of metal structures*, New York, 1952.

[39] A. Chilver, A generalised approach to the local instability of certain thin-walled struts, *Aeronautical Quarterly* 4(3) (1953) 245-260.

[40] P. Bulson, Local stability and strength of structural sections, *Thin-Walled Structures* (1967) 153-207.

[41] P.S. Bulson, *The stability of flat plates*, Chatto and Windus, London, 1970.

[42] T. Von Kármán, E.F. Sechler, L.H. Donnell, The strength of thin plates in compression, *Transactions of the American Society of Mechanical Engineers* 54(5) (1932) 53-70.

[43] E. Ventsel, T. Krauthammer, *Thin Plates and Shells: Theory, Analysis, and Applications*, Marcel Dekker, New York 2001.

[44] N. Yamaki, Postbuckling behavior of rectangular plates with small initial curvature loaded in edge compression, *Journal of Applied Mechanics* 26 (1959) 407-414.

[45] J. Rhodes, J. Harvey, Plates in uniaxial compression with various support conditions at the unloaded boundaries, *International Journal of Mechanical Sciences* 13(9) (1971) 787-802.

[46] A.K. Basu, J.C. Chapman, Large Deflection Behaviour of Transversely Loaded Rectangular Orthotropic Plates, *Proceedings of the Institution of Civil Engineers* 35(1) (1966) 79-110.

[47] A. Walker, The post-buckling behaviour of simply-supported square plates, *Aeronautical Quarterly* 20(3) (1969) 203-222.

[48] E. Stowell, *A Unified theory of plastic buckling of columns and plates*, National Advisory Committee for Aeronautics, Wshington DC, 1948.

[49] A. Ilyushin, Stability of plates and shells beyond the proportional limit, *National Advisory Committee for Aeronautics – Technical Memorandums* (Memo 1116) (1947) 1-44.

[50] G. Gerard, Secant modulus method for determining plate instability above the proportional limit, *Journal of the Aeronautical Sciences* 13(1) (1946) 38-44.

[51] G. Winter, Strength of thin steel compression flanges, *Transactions of the American Society of Civil Engineers* 112(1) (1947) 527-554.

[52] European Standard, *Eurocode 3: Design of steel structures, Part 1.1: General rules and rules for buildings*, EN 1993-1-1, European Committee for Standardization, Brussels, 2005.

[53] G.J. Hancock, Local, distortional, and lateral buckling of I-beams, *Journal of the Structural Division* 104(11) (1978) 1787-1798.

[54] G.J. Hancock, Distortional buckling of steel storage rack columns, *Journal of Structural Engineering* 111(12) (1985) 2770-2783.

[55] A. Chilver, The stability and strength of thin-walled steel struts, *The engineer* 196(5089) (1953) 180-183.

[56] A. Chilver, The behaviour of thin-walled structural members in compression, *Engineering* 172(4466) (1951) 281-282.

[57] T. Desmond, *The behavior and strength of thin-walled compression elements with longitudinal stiffness*, Ph.D. Thesis, Cornell University, Ithaca, New York, 1977.

[58] M.R. Bambach, Photogrammetry measurements of buckling modes and interactions in channels with edge-stiffened flanges, *Thin-Walled Structures* 47(5) (2009) 485-504.

[59] M.R. Bambach, Design of uniformly compressed edge-stiffened flanges and sections that contain them, *Thin-walled structures* 47(3) (2009) 277-294.

[60] M. Bambach, Unified element and section approach to design of cold-formed steel structures, *Journal of structural engineering* 136(4) (2010) 343-353.

[61] W. Wittrick, General sinusoidal stiffness matrices for buckling and vibration analyses of thin flat-walled structures, *International Journal of Mechanical Sciences* 10(12) (1968) 949-966.

[62] W. Wittrick, A unified approach to the initial buckling of stiffened panels in compression, *Aeronautical Quarterly* 19(3) (1968) 265-283.

[63] S.C. Lau, G.J. Hancock, Distortional buckling formulas for channel columns, *Journal of Structural Engineering* 113(5) (1987) 1063-1078.

[64] B. Schafer, T. Peköz, Laterally braced cold-formed steel flexural members with edge stiffened flanges, *Journal of Structural Engineering* 125(2) (1999) 118-127.

[65] L. Li, J. Chen, An analytical model for analysing distortional buckling of cold-formed steel sections, *Thin-walled structures* 46(12) (2008) 1430-1436.

[66] D. Buhagiar, J. Chapman, P. Dowling, Design of C-sections against deformational lip buckling, *11th International Specialty Conference on Cold-Formed Steel Structures*, St Louis, MO, 1992.

[67] T.V. Galambos, *Guide to stability design criteria for metal structures*, John Wiley & Sons, 1998.

[68] A. Van der Neut, *The interaction of local buckling and column failure of thin-walled compression members*, in: M. Hetényi, W.G. Vincenti (Eds.), Applied Mechanics. International Union of Theoretical and Applied Mechanics, Springer Berlin, Heidelberg, 1969, pp. 389-399.

[69] D. Dubina, The ECBL approach for interactive buckling of thin-walled steel members, *Steel and Composite Structures* 1(1) (2001) 75-96.

[70] Y.B. Kwon, B.S. Kim, G.J. Hancock, Compression tests of high strength cold-formed steel channels with buckling interaction, *Journal of Constructional Steel Research* 65(2) (2009) 278-289.

[71] B. Young, N. Silvestre, D. Camotim, Cold-Formed Steel Lipped Channel Columns Influenced by Local-Distortional Interaction: Strength and DSM Design, *Journal of Structural Engineering* 139(6) (2013) 1059-1074.

[72] N. Silvestre, D. Camotim, P. Dinis, Direct strength prediction of lipped channel columns experiencing local-plate/distortional interaction, *Advanced Steel Construction* 5(1) (2009) 45-67.

[73] N. Silvestre, D. Camotim, P.B. Dinis, Post-buckling behaviour and direct strength design of lipped channel columns experiencing local/distortional interaction, *Journal of Constructional Steel Research* 73 (2012) 12-30.

[74] B. Schafer, Local, distortional, and Euler buckling of thin-walled columns, *Journal of structural engineering* 128(3) (2002) 289-299.

[75] B.W. Schafer, *Distortional buckling of cold-formed steel columns*, AISI Research Report RP00-1, AISI, Washington DC, 2000.

[76] J.T. Dewolf, T. Pekoz, G. Winter, Local and overall buckling of cold-formed members, *Journal of the Structural Division* 100(10) (1974) 2017-2036.

[77] A. Ghersi, R. Landolfo, F.M. Mazzolani, Buckling modes of double-channel cold-formed beams, *Thin-Walled Structures* 19(2) (1994) 353-366.

[78] T.A. Stone, R.A. LaBoube, Behavior of cold-formed steel built-up I-sections, *Thin-Walled Structures* 43(12) (2005) 1805-1817.

[79] B. Young, J. Chen, Design of Cold-Formed Steel Built-up Closed Sections with Intermediate Stiffeners, *Journal of Structural Engineering* 134(5) (2008) 727-737.

[80] J. Whittle, C. Ramseyer, Buckling capacities of axially loaded, cold-formed, built-up C-channels, *Thin-Walled Structures* 47(2) (2009) 190-201.

[81] W. Reyes, A. Guzmán, Evaluation of the slenderness ratio in built-up cold-formed box sections, *Journal of Constructional Steel Research* 67(6) (2011) 929-935.

[82] I. Georgieva, L. Schueremans, L. Pyl, Composed columns from cold-formed steel Z-profiles: Experiments and code-based predictions of the overall compression capacity, *Engineering Structures* 37 (2012) 125-134.

[83] I. Georgieva, L. Schueremans, L. Pyl, L. Vandewalle, Innovative cross-section shapes for built-up CFS columns. Experimental investigation, (2012).

[84] J.H. Zhang, B. Young, Compression tests of cold-formed steel I-shaped open sections with edge and web stiffeners, *Thin-Walled Structures* 52 (2012) 1-11.

[85] Y. Li, Y. Li, S. Wang, Z. Shen, Ultimate load-carrying capacity of cold-formed thin-walled columns with built-up box and I section under axial compression, *Thin-Walled Structures* 79 (2014) 202-217.

[86] D.C. Fratamico, B.W. Schafer, *Numerical studies on the composite action and buckling behavior of built-up cold-formed steel columns*, 22nd international specialty conference on cold-formed steel design and construction, 2014, pp. 213-228.

[87] H.D. Craveiro, J.P.C. Rodrigues, L. Laím, Buckling resistance of axially loaded cold-formed steel columns, *Thin-Walled Structures* 106 (2016) 358-375.

[88] F. Liao, H. Wu, R. Wang, T. Zhou, Compression test and analysis of multi-limbs built-up cold-formed steel stub columns, *Journal of Constructional Steel Research* 128 (2017) 405-415.

[89] X. Liu, T. Zhou, Research on axial compression behavior of cold-formed triple-lambs built-up open T-section columns, *Journal of Constructional Steel Research* 134 (2017) 102-113.

[90] Y. Lu, T. Zhou, W. Li, H. Wu, Experimental investigation and a novel direct strength method for cold-formed built-up I-section columns, *Thin-Walled Structures* 112 (2017) 125-139.

[91] D.C. Fratamico, S. Torabian, X. Zhao, K.J.R. Rasmussen, B.W. Schafer, Experimental study on the composite action in sheathed and bare built-up cold-formed steel columns, *Thin-Walled Structures* 127 (2018) 290-305.

[92] D.C. Fratamico, S. Torabian, X. Zhao, K.J.R. Rasmussen, B.W. Schafer, Experiments on the global buckling and collapse of built-up cold-formed steel columns, *Journal of Constructional Steel Research* 144 (2018) 65-80.

[93] J.H. Zhang, B. Young, Experimental investigation of cold-formed steel built-up closed section columns with web stiffeners, *Journal of Constructional Steel Research* 147 (2018) 380-392.

[94] T.C.H. Ting, K. Roy, H.H. Lau, J.B. Lim, Effect of screw spacing on behavior of axially loaded back-to-back cold-formed steel built-up channel sections, *Advances in Structural Engineering* 21(3) (2018) 474-487.

[95] F.J. Meza, J. Becque, I. Hajirasouliha, Experimental study of the cross-sectional capacity of cold-formed steel built-up columns, *Thin-Walled Structures* 155 (2020) 106958.

[96] F.J. Meza, J. Becque, I. Hajirasouliha, Experimental study of cold-formed steel built-up columns, *Thin-Walled Structures* 149 (2020) 106291.

[97] K. Roy, T.C.H. Ting, H.H. Lau, J.B.P. Lim, Experimental and numerical investigations on the axial capacity of cold-formed steel built-up box sections, *Journal of Constructional Steel Research* 160 (2019) 411-427.

[98] S.F. Nie, T.H. Zhou, Y. Zhang, B. Liu, Compressive behavior of built-up closed box section columns consisting of two cold-formed steel channels, *Thin-Walled Structures* 151 (2020) 106762.

[99] S. Nie, T. Zhou, M.R. Eatherton, J. Li, Y. Zhang, Compressive behavior of built-up double-box columns consisting of four cold-formed steel channels, *Engineering Structures* 222 (2020) 111133.

[100] X. Zhou, Y. Xiang, Y. Shi, L. Xu, Y. Zou, Simplified design method of cold-formed steel columns with built-up box sections, *Engineering Structures* 228 (2021) 111532.

[101] S.T. Vy, M. Mahendran, Behaviour and design of slender built-up nested cold-formed steel compression members, *Engineering Structures* 241 (2021) 112446.

[102] S.T. Vy, M. Mahendran, T. Sivaprakasam, Built-up nested cold-formed steel compression members subject to local or distortional buckling, *Journal of Constructional Steel Research* 182 (2021) 106667.

[103] D.K. Phan, K.J.R. Rasmussen, B.W. Schafer, Tests and design of built-up section columns, *Journal of Constructional Steel Research* 181 (2021) 106619.

[104] S.T. Vy, M. Mahendran, T. Sivaprakasam, Built-up back-to-back cold-formed steel compression members failing by local and distortional buckling, *Thin-Walled Structures* 159 (2021) 107224.

[105] J. Becque, M. Lecce, K.J. Rasmussen, The direct strength method for stainless steel compression members, *Journal of Constructional Steel Research* 64(11) (2008) 1231-1238.

[106] S. Niu, K. Rasmussen, F. Fan, Local–Global Interaction Buckling of Stainless Steel I-Beams. II: Numerical Study and Design, *Journal of Structural Engineering* 141(8) (2014) 04014195.

[107] L. Xu, P. Sultana, X. Zhou, Flexural strength of cold-formed steel built-up box sections, *Thin-Walled Structures* 47(6–7) (2009) 807-815.

[108] I. Georgieva, L. Schueremans, L. Pyl, L. Vandewalle, Numerical study of built-up double-Z members in bending and compression, *Thin-Walled Structures* 60 (2012) 85-97.

[109] L. Laím, J.P.C. Rodrigues, L.S.d. Silva, Experimental and numerical analysis on the structural behaviour of cold-formed steel beams, *Thin-Walled Structures* 72 (2013) 1-13.

[110] L. Wang, B. Young, Behavior of Cold-Formed Steel Built-Up Sections with Intermediate Stiffeners under Bending. II: Parametric Study and Design, *Journal of Structural Engineering* (2015) 04015151.

[111] J.H. Zhang, B. Young, Numerical investigation and design of cold-formed steel built-up open section columns with longitudinal stiffeners, *Thin-Walled Structures* 89 (2015) 178-191.

[112] J.H. Zhang, B. Young, Finite element analysis and design of cold-formed steel built-up closed section columns with web stiffeners, *Thin-Walled Structures* 131 (2018) 223-237.

[113] S. Kechidi, D.C. Fratamico, B.W. Schafer, J. Miguel Castro, N. Bourahla, Simulation of screw connected built-up cold-formed steel back-to-back lipped channels under axial compression, *Engineering Structures* 206 (2020) 110109.

[114] D.K. Phan, K.J.R. Rasmussen, *Cold-formed steel bolted and screw-fastened connections in shear*, The 8th International Conference on Thin-Walled Structures, University of Lisbon, Lisbon, Portugal, 2018.

[115] S.C.W. Lau, G.J. Hancock, Buckling of thin flat-walled structures by a spline finite strip method, *Thin-walled structures* 4(4) (1986) 269-294.

[116] M. Khezri, M.A. Bradford, Z. Vrcelj, Thin plate bending analysis and treatment of material discontinuities using the generalised RKP-FSM, *Computer Modeling in Engineering and Sciences* 87(4) (2012) 271-306.

[117] M. Khezri, M. Abbasi, K.J.R. Rasmussen, A combined meshfree/finite strip method for analysis of plates with perforations and cracks, *Thin-Walled Structures* 111 (2017) 113-125.

[118] Y.K. Cheung, L. Tham, *The finite strip method*, CRC Press, 1997.

[119] Y.K. Cheung, *Finite strip method in structural analysis*, Elsevier, 2013.

[120] J.-H. Zhang, B. Young, Compression tests of cold-formed steel I-shaped open sections with edge and web stiffeners, *Thin-Walled Structures* 52 (2012) 1-11.

[121] G. Aruna, S. Sukumar, V. Karthika, Study on Cold-formed Steel Built-up Square Sections with Intermediate Flange and Web Stiffeners, *Asian Journal of Civil Engineering* 16(7) (2015) 919-931.

[122] S. Ádány, B. Schafer, Buckling mode decomposition of single-branched open cross-section members via finite strip method: derivation, *Thin-walled structures* 44(5) (2006) 563-584.

[123] J. Davies, P. Leach, First-order generalised beam theory, *Journal of Constructional Steel Research* 31(2-3) (1994) 187-220.

[124] J. Davies, P. Leach, D. Heinz, Second-order generalised beam theory, *Journal of Constructional Steel Research* 31(2) (1994) 221-241.

[125] S. Ádány, B. Schafer, A full modal decomposition of thin-walled, single-branched open cross-section members via the constrained finite strip method, *Journal of Constructional Steel Research* 64(1) (2008) 12-29.

[126] S. Ádány, Constrained shell Finite Element Method for thin-walled members, Part 1: constraints for a single band of finite elements, *Thin-Walled Structures* 128 (2018) 43-55.

[127] S. Ádány, D. Visy, R. Nagy, Constrained shell Finite Element Method, Part 2: application to linear buckling analysis of thin-walled members, *Thin-Walled Structures* 128 (2018) 56-70.

[128] J. Becque, A new approach to modal decomposition of buckled shapes, *Structures* 4 (2015) 2-12.

[129] J. Becque, X. Li, B. Davison, Modal decomposition of coupled instabilities: The method of the equivalent nodal forces, *Thin-Walled Structures* 143 (2019) 106229.

[130] S. Jin, D. Gan, H. Chen, R. Cheng, X. Zhou, A force-based method for identifying the deformation modes of thin-walled members, *Thin-Walled Structures* 129 (2018) 473-487.

[131] S. Jin, Z. Li, F. Huang, D. Gan, R. Cheng, G. Deng, Constrained shell finite element method for elastic buckling analysis of thin-walled members, *Thin-Walled Structures* 145 (2019) 106409.

[132] M. Khezri, K. Rasmussen, An energy-based approach to buckling modal decomposition of thin-walled members with arbitrary cross sections, Part 1: Derivation, *Thin-Walled Structures* 138 (2019) 496-517.

[133] M. Khezri, K. Rasmussen, An energy-based approach to buckling modal decomposition of thin-walled members with arbitrary cross-sections, Part 2: Modified global torsion modes, examples, *Thin-Walled Structures* 138 (2019) 518-531.

[134] J. Puckett, G. Lang, Compound strip method for free vibration analysis of continuous plates, *Journal of engineering mechanics* 112(12) (1986) 1375-1389.

[135] J.A. Puckett, R.M. Gutkowski, *Compound strip method for the analysis of continuous elastic plates*, Colorado State University, 1983.

[136] J.A. Puckett, R.M. Gutkowski, Compound strip method for analysis of plate systems, *Journal of Structural Engineering* 112(1) (1986) 121-138.

[137] J.A. Puckett, Application of the compound strip method for the analysis of slab-girder bridges, *Computers & Structures* 22(6) (1986) 979-986.

[138] J.A. Puckett, D.L. Wiseman, K.P. Chong, Compound strip method for the buckling analysis of continuous plates, *Thin-Walled Structures* 5(5) (1987) 383-400.

[139] J. Puckett, D. Wiseman, Compound strip method for folded plates with connecting elements, *Journal of Structural Engineering* 117(1) (1991) 255-267.

[140] D.L. Wiseman, J.A. Puckett, Applications of compound strip method for folded plates with connecting elements, *Journal of Structural Engineering* 117(1) (1991) 268-285.

[141] C.J. Chen, R.M. Gutkowski, J.A. Puckett, B-spline compound strip analysis of stiffened plates under transverse loading, *Computers & Structures* 34(2) (1990) 337-347.

[142] C.J. Chen, R.M. Gutkowski, J.A. Puckett, B-spline compound strip formulation for braced thin-walled structures, *Journal of Structural Engineering* 117(5) (1991) 1303-1316.

[143] S. Maleki, Compound strip method for box girders and folded plates, *Computers & Structures* 40(3) (1991) 527-538.

[144] A. Borković, N. Mrđa, S. Kovačević, Dynamical analysis of stiffened plates using the compound strip method, *Engineering Structures* 50(Supplement C) (2013) 56-67.

[145] A. Borković, S. Kovačević, D.D. Milašinović, G. Radenković, O. Mijatović, V. Golubović-Bugarski, Geometric nonlinear analysis of prismatic shells using the semi-analytical finite strip method, *Thin-Walled Structures* 117(Supplement C) (2017) 63-88.

[146] R. Schardt, Generalized beam theory—an adequate method for coupled stability problems, *Thin-walled structures* 19(2-4) (1994) 161-180.

[147] N. Silvestre, D. Camotim, Non-linear generalized beam theory for cold-fromed steel members, *International Journal of Structural Stability and Dynamics* 03(04) (2003) 461-490.

[148] P.B. Dinis, D. Camotim, N. Silvestre, GBT formulation to analyse the buckling behaviour of thin-walled members with arbitrarily 'branched' open cross-sections, *Thin-Walled Structures* 44(1) (2006) 20-38.

[149] R. Gonçalves, P.B. Dinis, D. Camotim, GBT formulation to analyse the first-order and buckling behaviour of thin-walled members with arbitrary cross-sections, *Thin-Walled Structures* 47(5) (2009) 583-600.

[150] N. Silvestre, Generalised beam theory to analyse the buckling behaviour of circular cylindrical shells and tubes, *Thin-Walled Structures* 45(2) (2007) 185-198.

[151] J. Rondal, Cold-formed steel members and structures: General Report, *Journal of Constructional Steel Research* 55(1) (2000) 155-158.

[152] D. Camotim, C. Basaglia, N. Silvestre, GBT buckling analysis of thin-walled steel frames: A state-of-the-art report, *Thin-Walled Structures* 48(10) (2010) 726-743.

[153] R. Bebiano, D. Camotim, R. Gonçalves, GBTul 2.0 − A second-generation code for the GBT-based buckling and vibration analysis of thin-walled members, *Thin-Walled Structures* 124 (2018) 235-257.

[154] C.H.T. Ting, H.H. Lau, *Compression Test on Cold-Formed Steel Built-up Back-to-Back Channels Stub Columns*, Advanced Materials Research, Trans Tech Publ, 2011, pp. 2900-2903.

[155] B.W. Schafer, Review: the direct strength method of cold-formed steel member design, *Journal of constructional steel research* 64(7) (2008) 766-778.

[156] G.J. Hancock, Y.B. Kwon, E.S. Bernard, Strength design curves for thin-walled sections undergoing distortional buckling, *Journal of Constructional Steel Research* 31(2) (1994) 169-186.

[157] B.W. Schafer, T. Pekoz, *Direct strength prediction of cold-formed steel members using numerical elastic buckling solutions*, 14th International Specialty Conference on Cold-Formed Steel Structures, University of Missouri, Rolla, 1998, pp. 69-76.

[158] Z. Li, B.W. Schafer, Application of the finite strip method in cold-formed steel member design, *Journal of Constructional Steel Research* 66(8–9) (2010) 971-980.

[159] I. Georgieva, L. Schueremans, L. Vandewalle, L. Pyl, Design of Built-up Cold-Formed Steel Columns According to the Direct Strength Method, *Procedia Engineering* 40 (2012) 119-124.

[160] L. Wang, B. Young, Beam tests of cold-formed steel built-up sections with web perforations, *Journal of Constructional Steel Research* 115 (2015) 18-33.

[161] D.K. Phan, K.J.R. Rasmussen, Flexural rigidity of cold-formed steel built-up members, *Thin-Walled Structures* 140 (2019) 438-449.

[162] K.J.R. Rasmussen, M. Khezri, B.W. Schafer, H. Zhang, The mechanics of built-up cold-formed steel members, *Thin-Walled Structures* 154 (2020) 106756.

[163] ISO Standard, *General principles on reliability for structures*, ISO 2394:2015, International Organization for Standardization, Geneva, 2015.

[164] Report of JCSS, *Probabilistic model code*, Joint Committee on Structural Safety, JCSS, 2001.

[165] European Standard, *Eurocode 0: Basis of structural design*, EN 1990:2002, European Committee for Standardization, Brussels, 2002.

[166] federation internationale du beton, *fib Model Code for Concrete Structures 2010*, Ernst & Sohn, 2013.

[167] Australian Buildings Codes Board, *Building Code of Australia - Volume 1*, NCC 2019, Standards Australia, NSW, 2019.

[168] B. Ellingwood, T.V. Galambos, J.G. MacGregor, *Development of a probability based load criterion for American National Standard A58: Building code requirements for minimum design loads in buildings and other structures*, Department of Commerce, National Bureau of Standards, 1980.

[169] ASCE Standard, *Minimum Design Loads and Associated Criteria for Buildings and Other Structures*, ASCE/SEI 7-16, American Society of Civil Engineers, NY, 2016.

[170] Canadian Standard, *North American Cold-Formed Steel Specification for the Design of Cold-Formed Steel Structural Members*, CAN/CSA S136-12, Canadian Standards Association, Mississauga, Ontario, 2012.

[171] ISO Standard, *General principles on reliability for structures*, ISO 2394:2012, International Organization for Standardization, Geneva, 2012.

[172] AISC Standard, *Specification for Structural Steel Buildings*, ANSI/AISC 360-16, American Institute of Steel Construction, Chicago, IL, 2016.

[173] Australian Standard, *Steel structures*, AS 4100-1998, Standards Australia, NSW, 2016.

[174] J.A. Puckett, R.M. Gutkowski, *Compound strip method for analysis of continuous elastic plates*, Engineering Mechanics in Civil Engineering, ASCE, 1983, pp. 240-243.

[175] M.A. Bradford, M. Azhari, Buckling of plates with different end conditions using the finite strip method, *Computers & Structures* 56(1) (1995) 75-83.

[176] J. Dario Aristizabal-Ochoa, Slope-deflection equations for stability and second-order analysis of Timoshenho beam–column structures with semi-rigid connections, *Engineering Structures* 30(9) (2008) 2517-2527.

[177] F. Gruttmann, W. Wagner, Shear correction factors in Timoshenko's beam theory for arbitrary shaped cross-sections, *Computational Mechanics* 27(3) (2001) 199-207.

[178] B.W. Schafer, *Cold-formed steel behavior and design: analytical and numerical modeling of elements and members with longitudinal stiffeners*, PhD Thesis, Cornell University, New York, 1997.

[179] Z. Li, *Buckling analysis of the finite strip method and theoretical extension of the constrained finite strip method for general boundary conditions, Research report*, J.H.U. Press, Johns Hopkins University, 2009.

[180] D.S. Simulia, Abaqus 6.14–Analysis Users's Guide: Volume IV: Elements, *Dassault Systemes Simulia Corporation, Providence, RI* (2014).

[181] Lysaght, Zeds & Cees User Guide for Design and Installation Professionals, 2019. https://cdn.dcs.lysaght.com/download/lysaght-zeds-cees-purlins-and-girts-user-guide. (Accessed 8 June 2020).

[182] Australian Standard, *Steel sheet and strip—Hot-dip zinc-coated or aluminium/zinc-coated*, AS 1397-2001, Standards Australia, NSW, 2001.

[183] M. Abbasi, M. Khezri, K.J.R. Rasmussen, B.W. Schafer, Elastic buckling analysis of cold-formed steel built-up sections with discrete fasteners using the compound strip method, *Thin-Walled Structures* 124 (2018) 58-71.

[184] D.C. Fratamico, S. Torabian, K.J. Rasmussen, B.W. Schafer, Experimental investigation of the effect of screw fastener spacing on the local and distortional buckling behavior of built-up cold-formed steel columns, *International Specialty Conference on Cold-Formed Steel Structures*, Baltimore, Maryland, 2016.

[185] Australian Standard, *Self-drilling screws for the building and construction industries - Part 1: General requirements and mechanical properties*, AS 3566.1–2002, Standards Australia, NSW, 2002.

[186] Australian Standard, *Metallic materials—tensile testing at ambient temperature*, AS 1391-2007, Standards Australia, NSW, 2007.

[187] ASTM Standard, E8/E8M-13a, *Standard test methods for tension testing of metallic materials. ASTM International, West Conshohocken, PA* (2013).

[188] S. Niu, *Interaction Buckling of Cold-Formed Stainless Steel Beams*, PhD Thesis, The University of Sydney, Sydney, 2014.

[189] P.W. Key, S.W. Hasan, G.J. Hancock, Column Behavior of Cold-Formed Hollow Sections, *Journal of Structural Engineering* 114(2) (1988) 390-407.

[190] N. Tebedge, G. Alpsten, L. Tall, Residual-stress measurement by the sectioning method, *Experimental Mechanics* 13(2) (1973) 88-96.

[191] D.C.Y. Yap, G.J. Hancock, Experimental Study of High-Strength Cold-Formed Stiffened-Web C-Sections in Compression, *Journal of Structural Engineering* 137(2) (2011) 162-172.

[192] J. Singer, J. Arbocz, T. Weller, *Buckling Experiments: Experimental Methods in Buckling of Thin Walled Structures: Basic Concepts, Columns, Beams and Plates – Volume 1* John Wiley & Sons, Inc, New York, 1998.

[193] K. Venkataramaiah, J. Roorda, Analysis of local plate buckling experimental data, *Proc. Sixth International Speciality Conference on Cold-Formed Steel Structures*, St. Louis, 1982.

[194] M. Paszkiewicz, T. Kubiak, Selected problems concerning determination of the buckling load of channel section beams and columns, *Thin-Walled Structures* 93 (2015) 112-121.

[195] D.S. Simulia, Abaqus 6.14–Theory Guide, *Dassault Systemes Simulia Corporation, Providence, RI* (2014).

[196] A.N. Trouncer, *Steel storage racks with locally unstable members*, PhD Thesis, The University of Sydney, Sydney, 2014.

[197] D.S. Simulia, Abaqus 6.14–Analysis Users's Guide: Volume V: Prescribed conditions, constraints & interactions, *Dassault Systemes Simulia Corporation, Providence, RI* (2014).

[198] Australian Standard, *AS 4291.1 - Mechanical properties of fasteners made of carbon steel and alloy steel - Part 1: Bolts, screws and studs*, Standards Australia, NSW, 2015.

[199] K. Roy, H.H. Lau, T.C. Huon Ting, R. Masood, A. Kumar, J.B.P. Lim, Experiments and finite element modelling of screw pattern of self-drilling screw connections for high strength cold-formed steel, *Thin-Walled Structures* 145 (2019) 106393.

[200] D.S. Simulia, Abaqus 6.14–Analysis Users's Guide: Volume II: Analysis, *Dassault Systemes Simulia Corporation, Providence, RI* (2014).

[201] A.C. Walker, *Design and analysis of cold-formed sections*, John Wiley & Sons, 1975.

[202] European Standard, *Eurocode 3: Design of Steel Structures, Part 1.3: General rules - Supplementary rules for cold-formed members and sheeting*, EN 1993-1-3, European Committee for Standardization, Brussels, 2006.

[203] European Standard, *Eurocode 3: Design of steel structures - Part 1.5: Plated structural elements*, EN 1993-1-5, European Committee for Standardization, Brussels, 2006.

[204] B.W. Schafer, T. Pekoz, Direct strength prediction of cold-formed steel members using numerical elastic buckling solutions, *14th International Specialty Conference on Cold-Formed Steel Structures*, 1998.

[205] D.C. Yap, G.J. Hancock, Experimental study of complex high-strength cold-formed cross-shaped steel section, *Journal of Structural Engineering* 134(8) (2008) 1322-1333.

[206] Australian Standard, *Cold-formed steel structures - Commentary*, AS 4600 Supplement 1:1998, Standards Australia, NSW, 1998.

[207] Australian Standard, *Structural design actions - General principles*, AS/NZS 1170.0-2002, Standards Australia, NSW, 2002.

[208] Australian Standard, *Structural design actions - Permanent, imposed and other actions*, AS/NZS 1170.1:2002, Standards Australia, NSW, 2002.

[209] L. Pham, Reliability analyses of reinforced concrete and composite column sections under concentric loads, *Institution of Engineers (Australia) Civ Eng Trans* (1) (1985).

[210] ACI Standard, *Building Code Requirements for Structural Concrete*, ACI 318-19, American Concrete Institute, Farmington Hills, MI, 2019.

[211] Australian Standard, *General principles on reliability for structures*, AS 5104:2017, Standards Australia, NSW, 2017.

[212] M.K. Ravindra, T.V. Galambos, Load and resistance factor design for steel, *Journal of the Structural Division* 104(9) (1978) 1337-1353.

[213] L.E. Hsiao, W.W. Yu, T.V. Galambos, *Load and resistance factor design of cold-formed steel: Calibration of the AISI design provisions*, University of Missouri-Rolla, Rolla, MO, 1988.

[214] L.E. Hsiao, W.W. Yu, T.V. Galambos, AISI LRFD method for cold-formed steel structural members, *Journal of Structural Engineering* 116(2) (1990) 500-517.

Appendix A   Measured Cross-Sectional Dimensions

This appendix represents the measured cross-sectional dimensions of the specimens tested in this study, as explained in Chapter 4. The measurement nomenclature is illustrated in Figure 4-10 in Section 4.3.

Table A-1: Cross-section dimensions of Series 1C120

Specimen	L (mm)	$i*$	h_i (mm)	b_{f1i} (mm)	b_{f2i} (mm)	b_{l1i} (mm)	b_{l2i} (mm)	θ_{f1i} (deg.)	θ_{f2i} (deg.)	θ_{l1i} (deg.)	θ_{l2i} (deg.)
Nominal	1000		150.00	120.00	120.00	10.00	10.00	90.00	90.00	90.00	90.00
1C120-1	1002	1	148.44	120.78	120.76	9.66	9.69	90.32	90.33	91.02	90.75
1C120-2	1002	1	147.88	120.61	120.19	9.78	9.57	89.67	90.04	90.92	88.91

* i = 1 correspond to the measurements of channel section i in the built-up assembly as per Figure 4-10.

Table A-2: Cross-section dimensions of Series 1C64

Specimen	L (mm)	$i*$	h_i (mm)	b_{f1i} (mm)	b_{f2i} (mm)	b_{l1i} (mm)	b_{l2i} (mm)	θ_{f1i} (deg.)	θ_{f2i} (deg.)	θ_{l1i} (deg.)	θ_{l2i} (deg.)
Nominal	1000		152.00	64.00	64.00	16.00	16.00	90.00	90.00	90.00	90.00
1C64-1	995	1	153.54	64.03	64.08	16.25	15.34	87.88	90.9	83.82	90.25
1C64-2	996	1	153.38	64.50	64.57	15.93	15.55	89.96	87.97	91.79	81.37

* i = 1 correspond to the measurements of channel section i in the built-up assembly as per Figure 4-10.

Table A-3: Cross-section dimensions of Series 2C120

Specimen	L (mm)	$i*$	h_i (mm)	b_{f1i} (mm)	b_{f2i} (mm)	b_{l1i} (mm)	b_{l2i} (mm)	θ_{f1i} (deg.)	θ_{f2i} (deg.)	θ_{l1i} (deg.)	θ_{l2i} (deg.)
Nominal	1000		150.00	120.00	120.00	10.00	10.00	90.00	90.00	90.00	90.00
2C120-900-1	997	1	148.69	120.70	120.55	9.70	9.60	90.12	90.60	89.92	90.84
		2	149.14	120.84	120.83	9.68	9.50	89.47	90.06	89.31	91.70
2C120-900-2	998	1	148.23	120.71	120.78	9.88	10.16	91.07	90.82	91.27	91.93
		2	148.69	120.74	120.75	9.71	9.97	91.03	90.83	90.97	91.21
2C120-300-1	999	1	147.92	120.77	120.94	9.56	9.79	91.71	90.95	91.73	91.31
		2	148.45	120.63	120.75	9.86	10.09	90.78	90.54	92.67	89.99
2C120-300-2	998	1	147.62	120.96	120.63	9.90	9.45	90.12	90.41	90.57	89.65
		2	148.79	120.53	120.71	9.53	9.75	89.79	90.19	89.92	90.71
2C120-150-1	999	1	148.19	120.64	120.38	8.88	10.16	89.89	89.74	89.60	90.55
		2	148.37	120.59	120.61	9.70	9.73	90.08	90.63	91.31	89.98
2C120-150-2	997	1	147.99	120.77	120.54	9.82	9.52	90.04	90.22	90.73	89.84
		2	148.32	120.48	120.55	9.93	9.09	89.85	89.62	88.71	91.19
2C120-100-1	997	1	148.07	120.80	120.68	9.92	9.04	89.89	89.84	90.42	91.58
		2	148.55	120.55	120.57	9.88	9.32	89.71	89.59	90.02	90.24
2C120-100-2	999	1	148.13	120.63	120.37	9.80	9.05	90.06	89.89	90.62	89.83
		2	148.70	120.47	120.66	9.12	10.02	90.59	90.57	89.54	90.22
Average			148.36	120.67	120.64	9.68	9.64	90.26	90.28	90.45	90.67
St. Dev.			0.37	0.13	0.15	0.29	0.37	0.58	0.44	0.97	0.72

* i = 1, 2 correspond to the measurements of channel section i in the built-up assembly as per Figure 4-10.

Table A-4: Cross-section dimensions of Series 3C120

Specimen	L (mm)	i	h_i (mm)	b_{f1i} (mm)	b_{f2i} (mm)	b_{l1i} (mm)	b_{l2i} (mm)	θ_{f1i} (deg.)	θ_{f2i} (deg.)	θ_{l1i} (deg.)	θ_{l2i} (deg.)
Nominal	1000		150.00	120.00	120.00	10.00	10.00	90.00	90.00	90.00	90.00
3C120-900-1	1003	1	148.08	120.45	120.48	9.84	9.80	89.85	89.91	90.21	90.10
		2	148.41	120.55	120.37	10.18	9.42	89.33	90.10	90.42	90.61
		3	148.12	120.40	120.50	9.73	9.45	90.40	89.48	89.67	89.09
3C120-900-2	1002	1	148.14	120.67	120.51	9.36	10.02	90.13	90.23	89.76	90.02
		2	148.33	120.75	120.46	9.10	10.00	90.67	90.59	91.92	89.89
		3	148.10	120.78	120.77	9.74	9.55	90.19	90.64	90.18	90.71
3C120-300-1	1003	1	148.79	120.70	120.55	9.64	9.67	90.08	90.61	90.26	90.39
		2	148.46	120.71	120.57	9.66	9.40	90.98	90.49	91.22	90.29
		3	148.19	120.77	120.69	9.70	9.37	90.31	90.80	89.89	89.68
3C120-300-2	1002	1	147.81	120.69	120.66	9.68	9.94	90.33	90.60	90.59	90.55
		2	147.77	120.68	120.60	9.62	9.56	89.89	90.33	90.44	89.49
		3	148.07	120.69	120.82	9.65	9.73	90.44	90.41	90.53	91.66
3C120-100-1	1002	1	148.58	120.72	120.74	9.57	9.85	90.55	90.02	90.76	90.59
		2	148.70	120.75	120.55	9.69	9.97	90.02	90.02	89.92	89.42
		3	148.73	120.56	120.72	9.49	9.88	90.10	90.04	89.92	88.94
3C120-100-2	1002	1	148.10	120.88	120.75	9.84	9.40	90.97	91.39	91.75	90.78
		2	147.49	120.86	120.75	9.79	9.66	90.25	90.77	90.87	91.18
		3	147.80	120.53	120.50	9.61	10.10	90.22	89.84	90.66	90.35
Average			148.20	120.67	120.61	9.66	9.71	90.26	90.34	90.50	90.21
St. Dev.			0.36	0.13	0.13	0.22	0.24	0.39	0.44	0.64	0.71

* i = 1, 2, 3 correspond to the measurements of channel section i in the built-up assembly as per Figure 4-10.

Table A-5: Cross-section dimensions of Series 3C64

Specimen	L (mm)	i^*	h_i (mm)	b_{f1i} (mm)	b_{f2i} (mm)	b_{l1i} (mm)	b_{l2i} (mm)	θ_{f1i} (deg.)	θ_{f2i} (deg.)	θ_{l1i} (deg.)	θ_{l2i} (deg.)
Nominal			152.00	64.00	64.00	16.00	16.00	90.00	90.00	90.00	90.00
		1	153.96	64.26	64.50	15.70	15.99	88.32	89.82	77.62	87.33
3C64-900-1	998	2	153.68	64.88	65.01	16.00	15.89	89.68	87.77	89.81	81.16
		3	154.30	64.49	64.52	16.06	15.75	88.75	91.31	83.05	90.57
		1	154.22	64.46	64.43	15.96	16.29	88.57	91.11	83.50	87.95
3C64-900-2	998	2	154.45	64.65	64.89	16.01	17.31	90.90	88.49	89.05	85.08
		3	154.07	64.45	64.76	16.13	15.56	89.90	88.29	85.87	80.37
		1	154.45	64.34	64.91	16.45	15.24	87.57	90.73	85.67	89.98
3C64-300-1	998	2	154.27	64.64	64.44	15.35	16.29	90.54	88.35	91.22	83.78
		3	153.87	65.03	64.91	16.07	15.50	89.43	88.16	91.65	80.84
		1	154.23	64.82	64.67	16.03	15.84	87.81	90.51	83.66	92.25
3C64-300-2	998	2	154.02	64.45	64.80	15.72	15.99	89.77	88.32	85.24	79.50
		3	153.79	65.39	64.56	15.61	15.67	87.92	90.21	79.85	88.98
		1	153.52	63.71	63.84	16.35	15.19	88.27	91.28	82.96	91.18
3C64-100-1	997	2	153.58	63.96	63.64	15.70	16.04	90.37	88.17	91.70	83.36
		3	153.17	64.37	63.84	15.76	15.92	89.67	88.25	89.80	80.65
		1	153.64	63.40	63.67	16.11	15.39	88.81	90.77	83.27	90.15
3C64-100-2	997	2	153.22	63.88	64.34	15.85	15.66	88.09	90.02	81.36	89.71
		3	153.07	64.13	63.97	15.86	15.81	89.48	88.00	88.28	80.69
Average			153.86	64.40	64.43	15.93	15.85	89.10	89.42	85.75	85.75
St. Dev.			0.43	0.48	0.45	0.27	0.48	1.00	1.32	4.21	4.48

* i = 1, 2, 3 correspond to the measurements of channel section i in the built-up assembly as per Figure 4-10.

Table A-6: Cross-section dimensions of Series 4C120

Specimen	L (mm)	i	h_i (mm)	b_{f1i} (mm)	b_{f2i} (mm)	b_{l1i} (mm)	b_{l2i} (mm)	θ_{f1i} (deg.)	θ_{f2i} (deg.)	θ_{l1i} (deg.)	θ_{l2i} (deg.)
Nominal	1000		150.00	120.00	120.00	10.00	10.00	90.00	90.00	90.00	90.00
4C120-900-1	1002	1	147.66	120.36	120.23	9.91	9.87	89.69	90.19	90.17	90.17
		2	147.76	120.68	120.51	9.92	9.65	90.02	90.46	90.85	91.03
		3	147.84	120.39	120.46	9.99	9.67	89.93	90.17	90.21	90.03
		4	147.50	120.50	120.60	9.90	9.52	90.09	90.56	90.60	89.93
4C120-900-2	1003	1	147.19	120.58	120.59	9.81	9.81	90.91	90.39	88.49	90.24
		2	147.92	120.61	120.46	9.88	9.98	90.59	90.44	90.48	89.05
		3	147.57	120.48	120.46	9.80	10.00	90.01	89.57	91.44	90.33
		4	147.35	120.41	120.31	9.91	9.87	90.07	89.91	89.39	89.53
4C120-300-1	1003	1	148.04	120.74	120.49	9.88	9.67	90.37	90.71	90.99	90.27
		2	146.65	121.43	121.13	9.64	9.69	88.66	91.41	89.35	91.97
		3	146.35	121.09	121.11	9.49	9.59	91.40	88.30	91.45	89.76
		4	147.56	120.46	120.47	10.00	9.95	90.08	90.22	89.66	91.20
4C120-300-2	1000	1	147.90	120.45	120.64	9.83	9.73	91.30	90.36	90.70	90.66
		2	147.83	120.59	120.54	9.85	9.85	91.06	91.75	90.88	91.33
		3	147.85	120.43	120.33	9.79	9.59	90.84	90.87	90.86	91.02
		4	147.63	120.74	120.48	9.86	9.54	90.68	91.21	91.14	90.62
4C120-100-1	1002	1	147.97	120.68	120.79	9.96	9.71	91.32	91.62	91.12	91.96
		2	147.48	120.65	120.76	9.74	9.66	89.61	90.21	90.24	91.06
		3	147.49	120.22	120.68	10.09	9.03	89.59	89.75	89.17	93.36
		4	148.20	120.67	120.55	9.50	9.79	90.10	90.73	89.99	90.53
4C120-100-2	1002	1	147.88	120.69	120.39	9.84	10.12	91.02	90.89	90.78	93.70
		2	147.71	120.59	120.38	9.87	10.04	90.69	90.84	90.91	90.06
		3	147.74	120.64	120.69	9.82	9.90	90.95	91.65	92.73	91.23
		4	145.45	121.30	121.19	9.81	9.93	91.01	90.08	91.96	88.57
Average			147.49	120.67	120.62	9.82	9.77	90.51	90.54	90.59	90.82
St. Dev.			0.64	0.29	0.25	0.14	0.23	0.68	0.80	0.99	1.24

* i = 1, 2, 3, 4 correspond to the measurements of channel section i in the built-up assembly as per Figure 4-10.

Table A-7: Cross-section dimensions of Series 4C64

Specimen	L (mm)	i	h_i (mm)	b_{f1i} (mm)	b_{f2i} (mm)	b_{l1i} (mm)	b_{l2i} (mm)	θ_{f1i} (deg.)	θ_{f2i} (deg.)	θ_{l1i} (deg.)	θ_{l2i} (deg.)
Nominal	1000		152.00	64.00	64.00	16.00	16.00	90.00	90.00	90.00	90.00
4C64-900-1	998	1	154.21	64.59	64.69	16.30	15.35	88.61	91.01	84.28	90.60
		2	154.26	64.59	64.80	16.33	15.64	88.24	91.25	83.37	92.02
		3	153.81	64.99	64.69	15.49	16.08	89.79	88.43	89.27	79.72
		4	154.17	64.34	64.86	15.94	15.56	88.51	91.28	82.43	90.65
4C64-900-2	997	1	153.82	64.68	64.67	15.98	15.82	87.95	89.67	78.88	89.08
		2	153.82	64.52	64.95	15.71	16.10	89.89	89.76	79.79	89.53
		3	154.29	64.55	64.29	16.20	15.49	91.18	88.21	90.25	81.19
		4	154.17	64.73	64.39	15.14	16.31	87.85	90.97	83.20	89.88
4C64-300-1	997	1	153.97	64.62	64.74	15.41	16.22	88.43	89.73	80.35	89.59
		2	154.08	64.46	64.88	15.43	16.39	88.50	89.77	79.75	89.12
		3	154.09	64.61	64.38	15.83	15.58	90.96	88.73	91.38	83.19
		4	154.30	64.48	64.69	15.82	15.82	88.50	90.86	83.08	92.54
4C64-300-2	997	1	153.86	64.79	64.71	15.66	16.02	88.02	89.49	80.22	90.09
		2	154.00	64.74	65.04	15.85	15.75	88.16	89.77	81.08	91.09
		3	154.29	64.59	64.65	15.72	16.11	90.82	88.38	90.54	82.70
		4	154.27	64.65	64.59	16.27	15.57	88.29	91.04	82.63	90.86
4C64-100-1	997	1	153.82	64.72	64.93	15.71	15.49	88.16	90.02	80.82	89.70
		2	153.90	64.87	65.00	15.56	15.60	88.40	89.52	81.74	90.34
		3	154.15	64.65	64.59	15.53	15.69	90.93	88.42	89.29	84.10
		4	154.34	64.50	64.66	16.26	15.37	87.62	91.27	84.72	88.97
4C64-100-2	998	1	153.63	64.69	64.43	16.12	15.60	88.63	90.96	83.01	91.34
		2	153.99	64.35	64.59	16.30	15.19	88.40	90.74	83.68	89.91
		3	153.51	64.39	64.94	16.02	15.60	88.56	89.68	80.01	89.12
		4	153.53	64.70	64.58	15.70	16.03	88.13	89.96	80.06	89.12
Average			154.01	64.61	64.70	15.84	15.76	88.85	89.95	83.49	88.52
St. Dev.			0.24	0.15	0.20	0.32	0.32	1.07	0.99	3.76	3.45

* i = 1, 2, 3, 4 correspond to the measurements of channel section i in the built-up assembly as per Figure 4-10.

Appendix B   Tensile Coupon Test Results

B.1. FLAT PARTS

The results of the tensile coupon tests of flat parts for both test series C120 and C64 are presented in this section. The static curve of each coupon test and the magnified gradual yielding region are also included in the figures. The test procedure and the summary of the results can be found in Section 4.4.1.
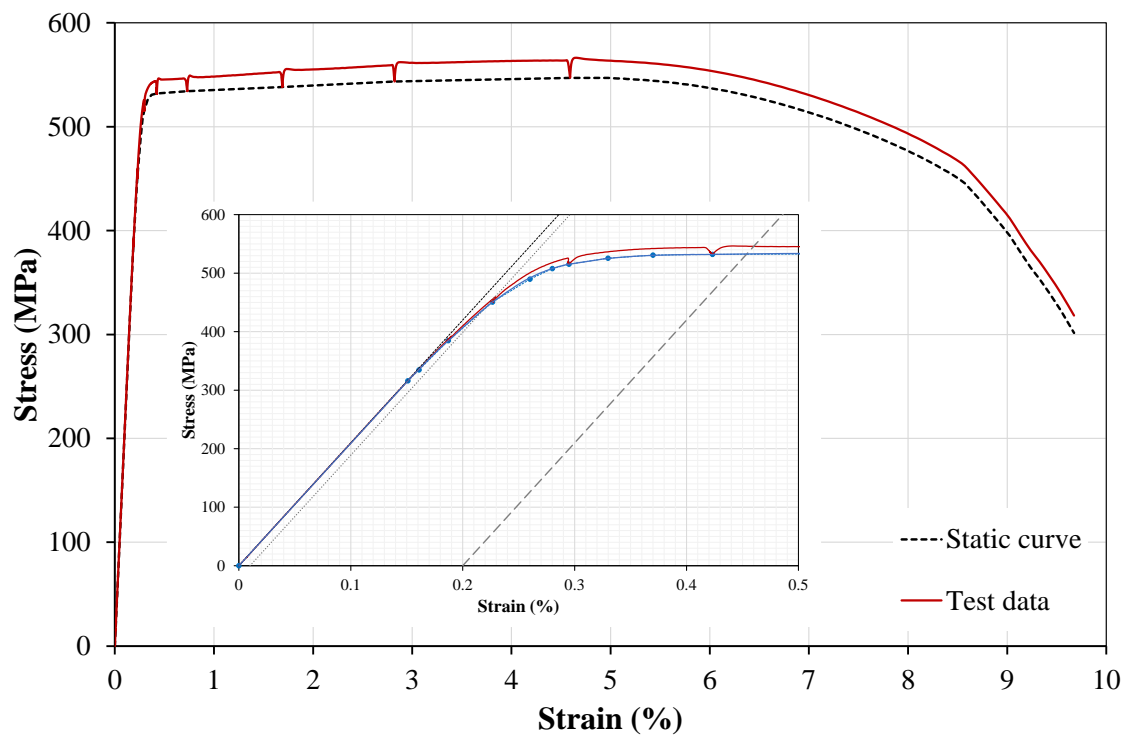
Figure B-1: Stress-strain curve of coupon specimen C64B1_F_1
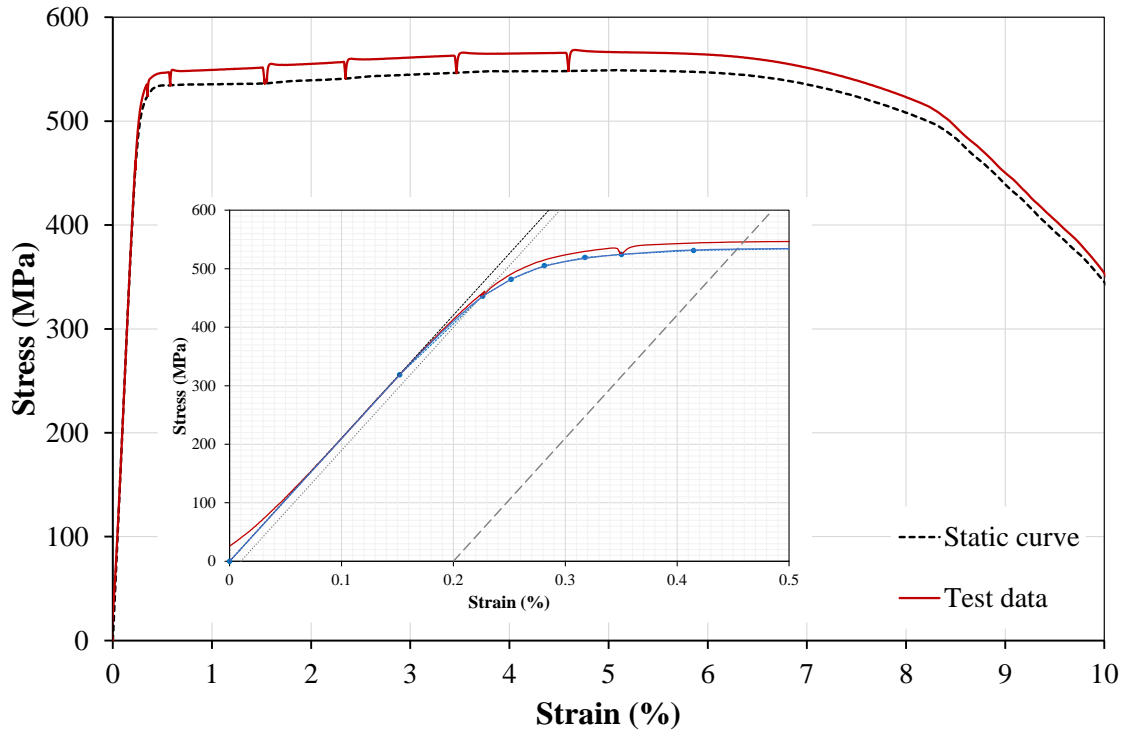
Figure B-2: Stress-strain curve of coupon specimen C64B1_F_2
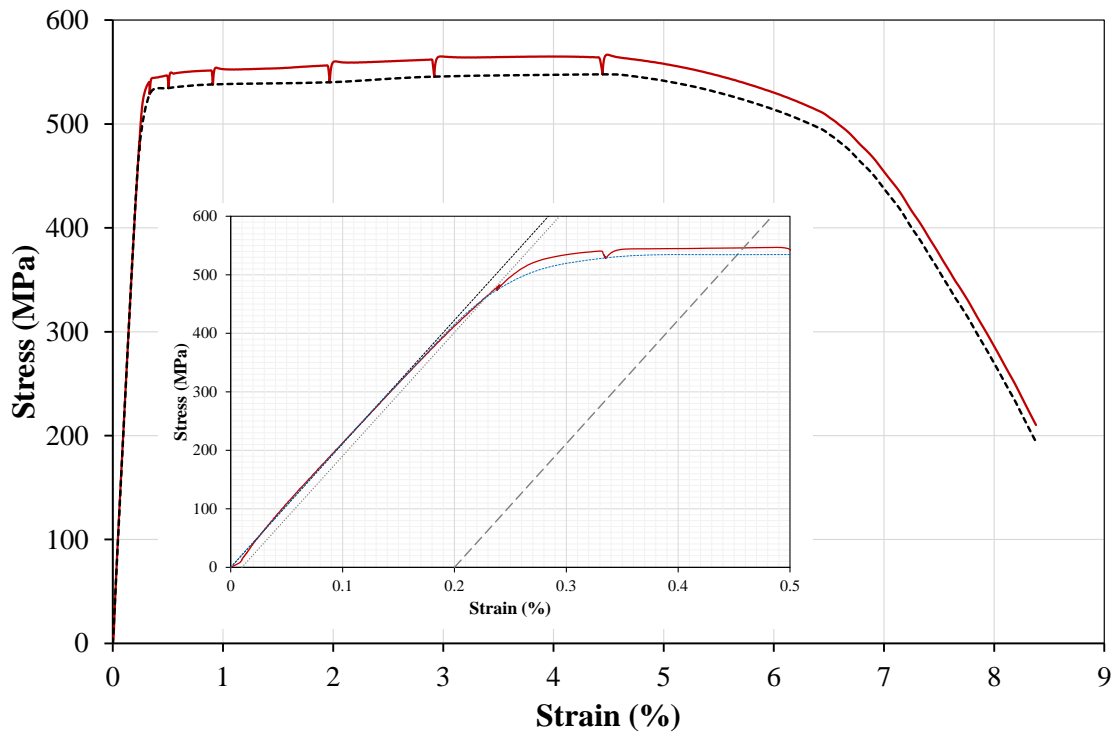
Figure B-3: Stress-strain curve of coupon specimen C64B1_F_3
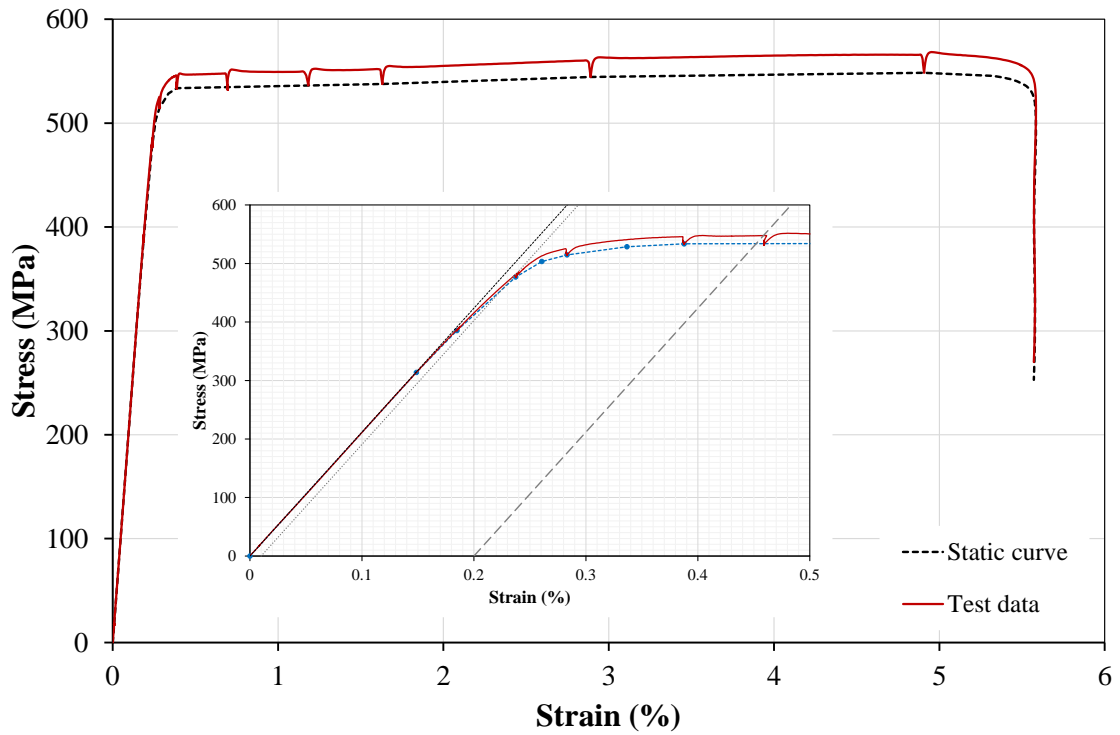
Figure B-4: Stress-strain curve of coupon specimen C64B1_W_1
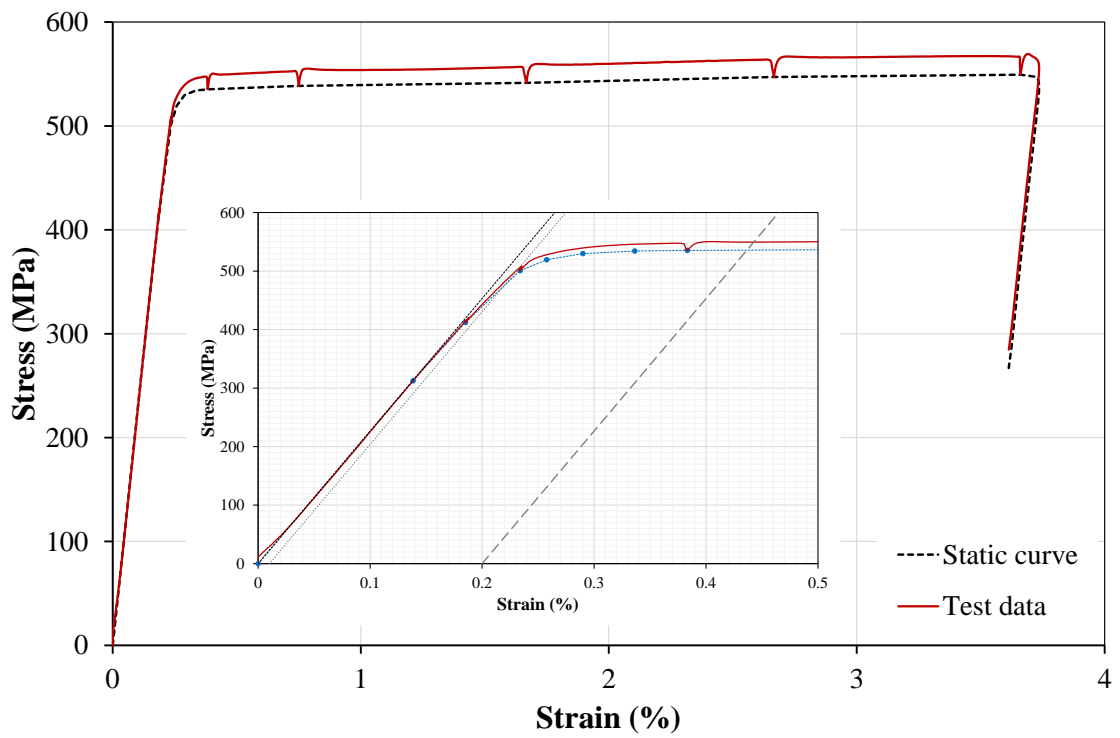
Figure B-5: Stress-strain curve of coupon specimen C64B1_W_2
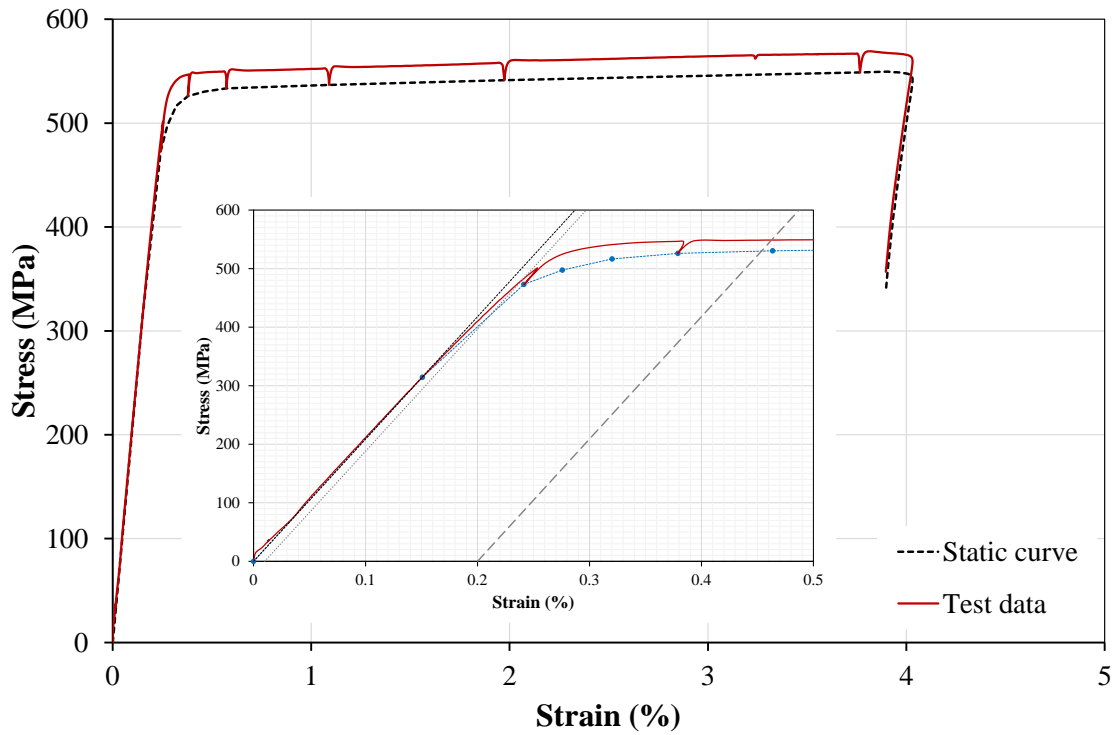
Figure B-6: Stress-strain curve of coupon specimen C64B1_W_3
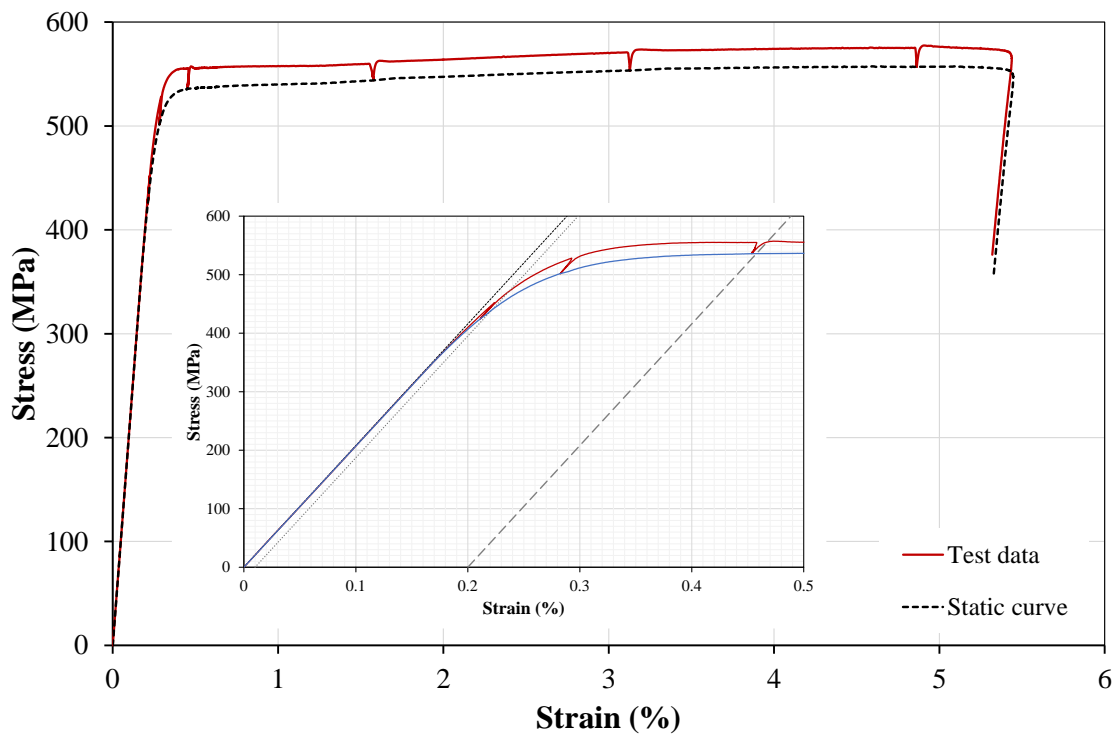
Figure B-7: Stress-strain curve of coupon specimen C64B2_F_1
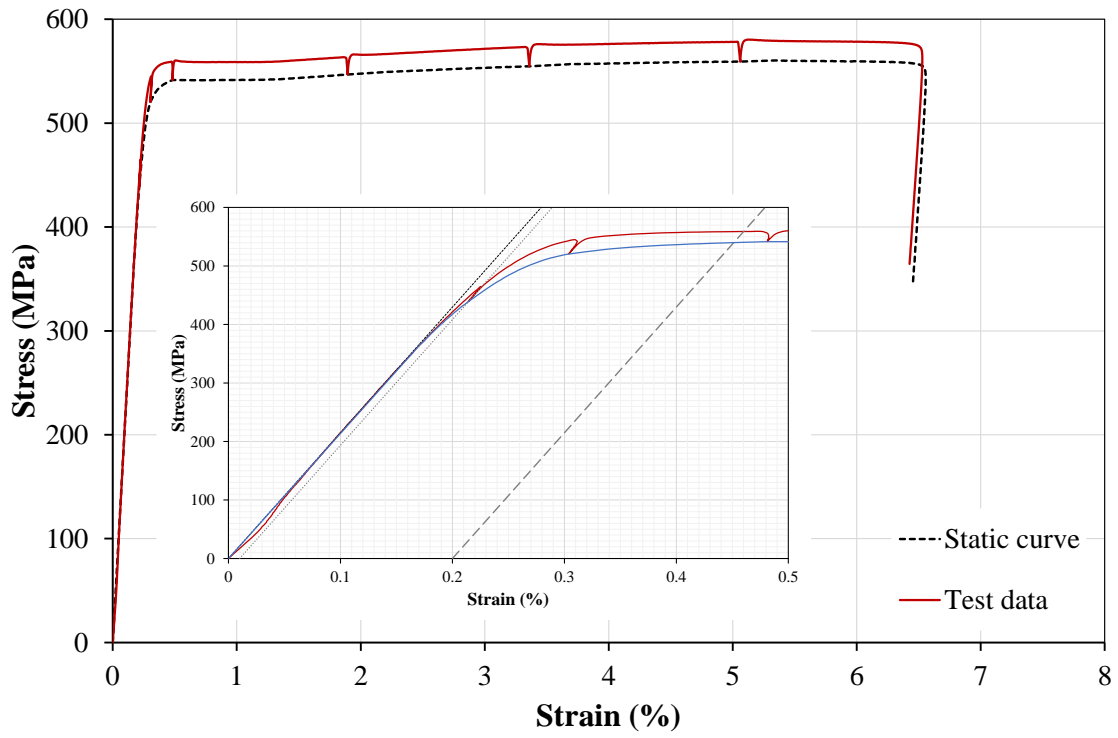
Figure B-8: Stress-strain curve of coupon specimen C64B2_F_2
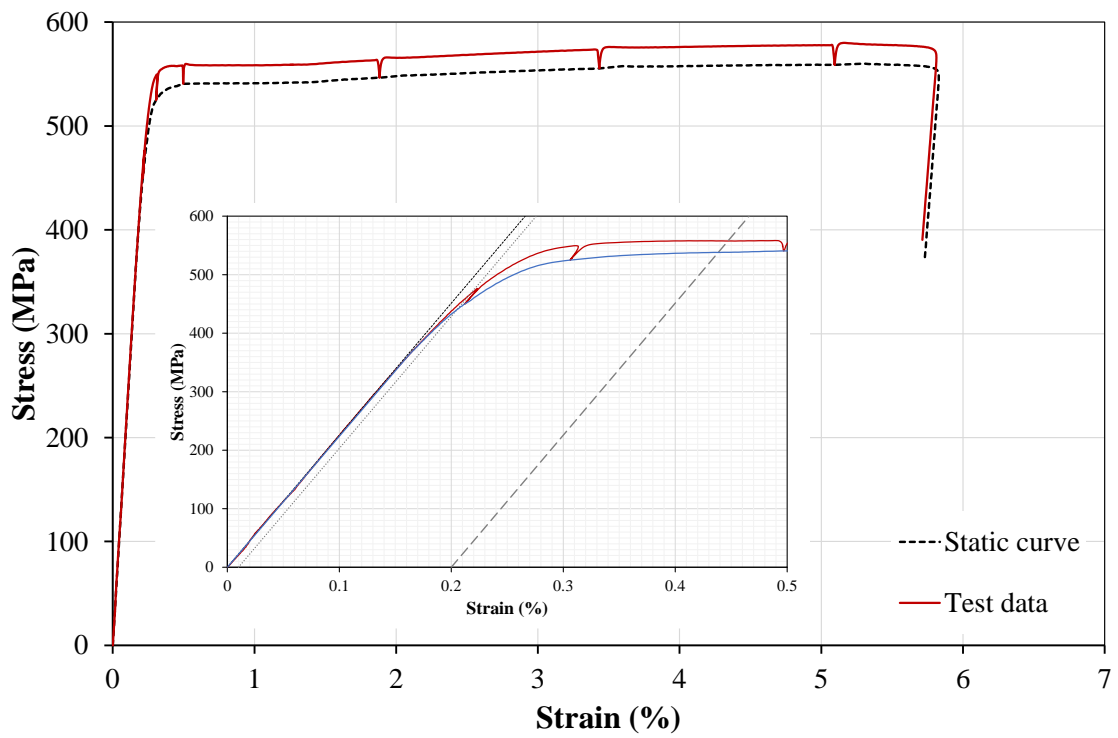
Figure B-9: Stress-strain curve of coupon specimen C64B2_F_3
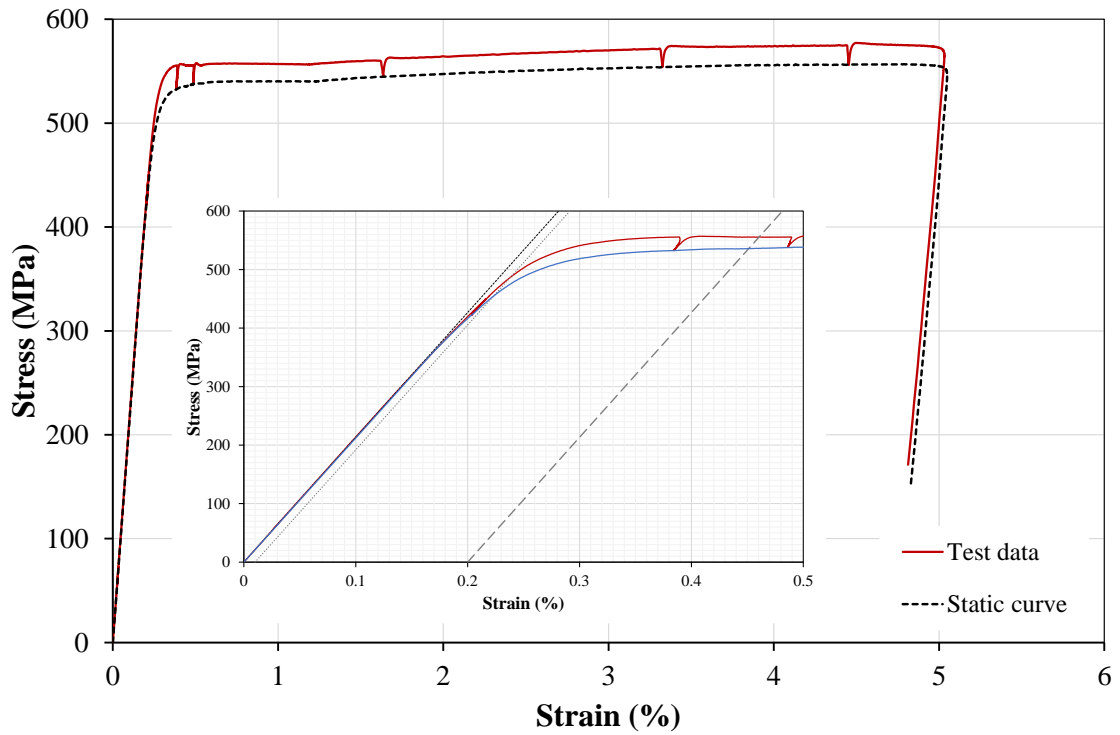
Figure B-10: Stress-strain curve of coupon specimen C64B2_W_1
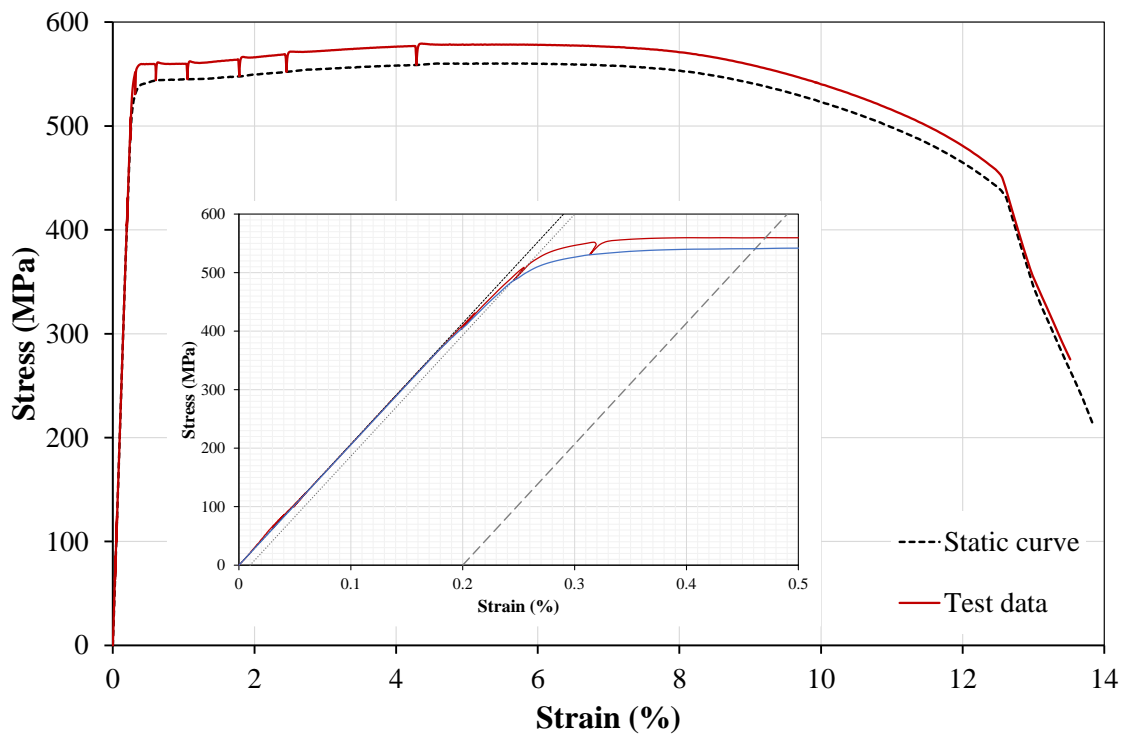
Figure B-11: Stress-strain curve of coupon specimen C64B2_W_2
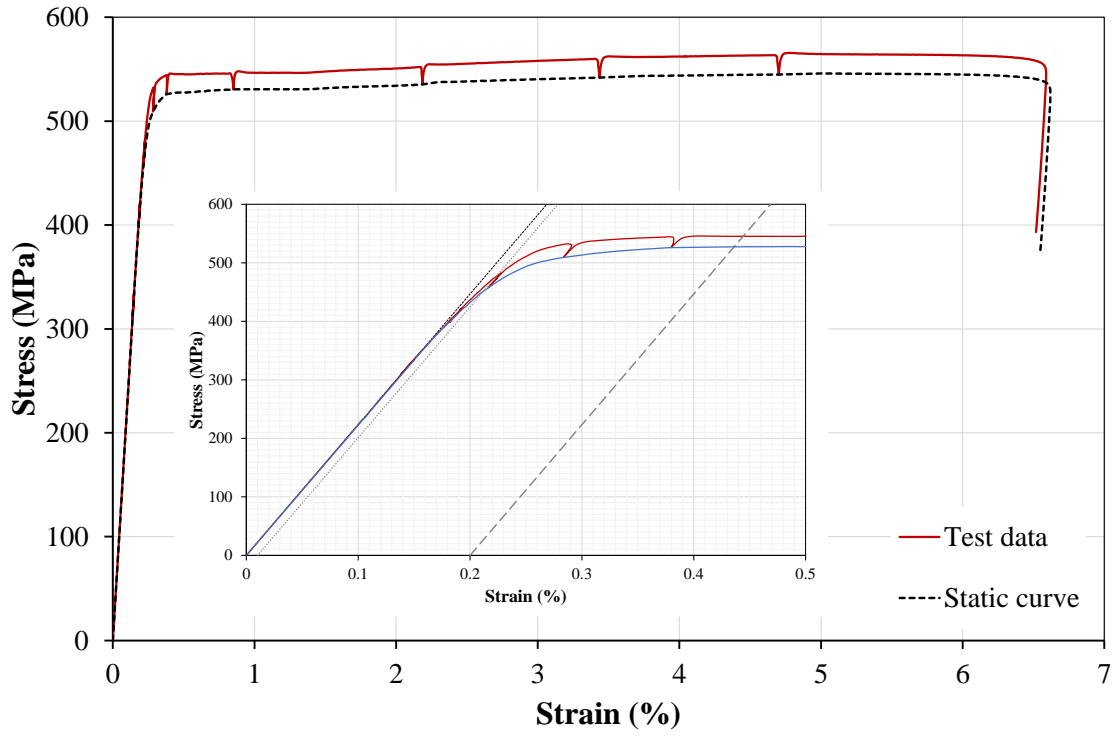
Figure B-12: Stress-strain curve of coupon specimen C64B2_W_3
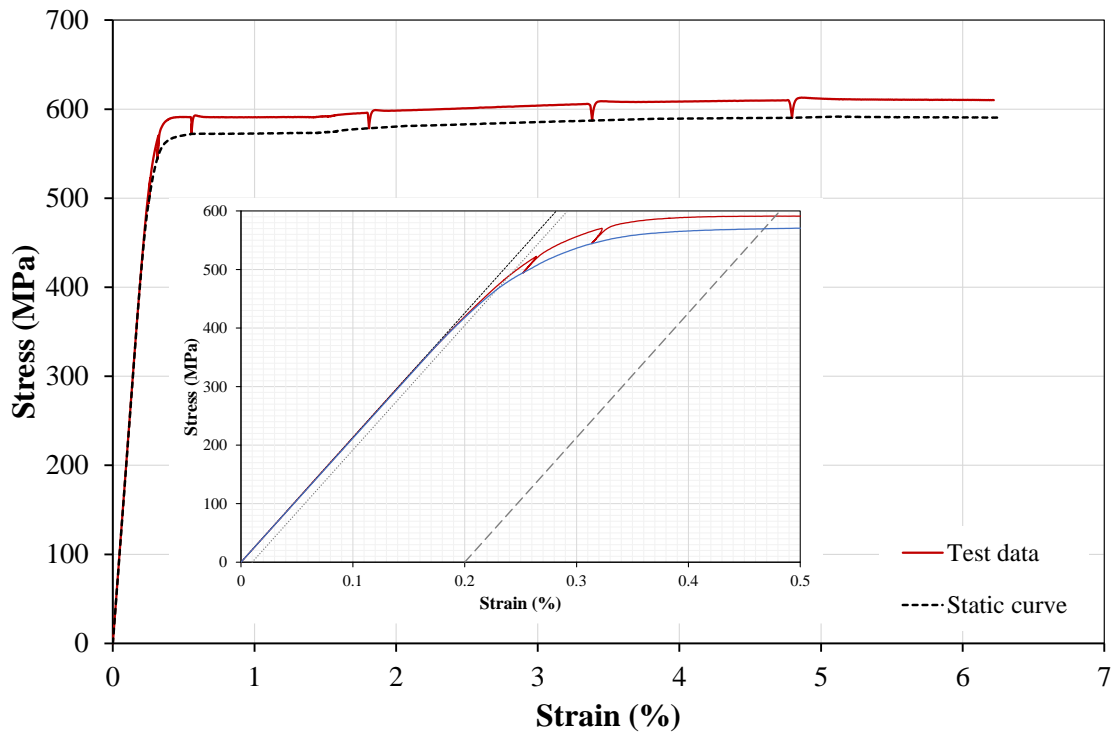
Figure B-13: Stress-strain curve of coupon specimen C120_W_1
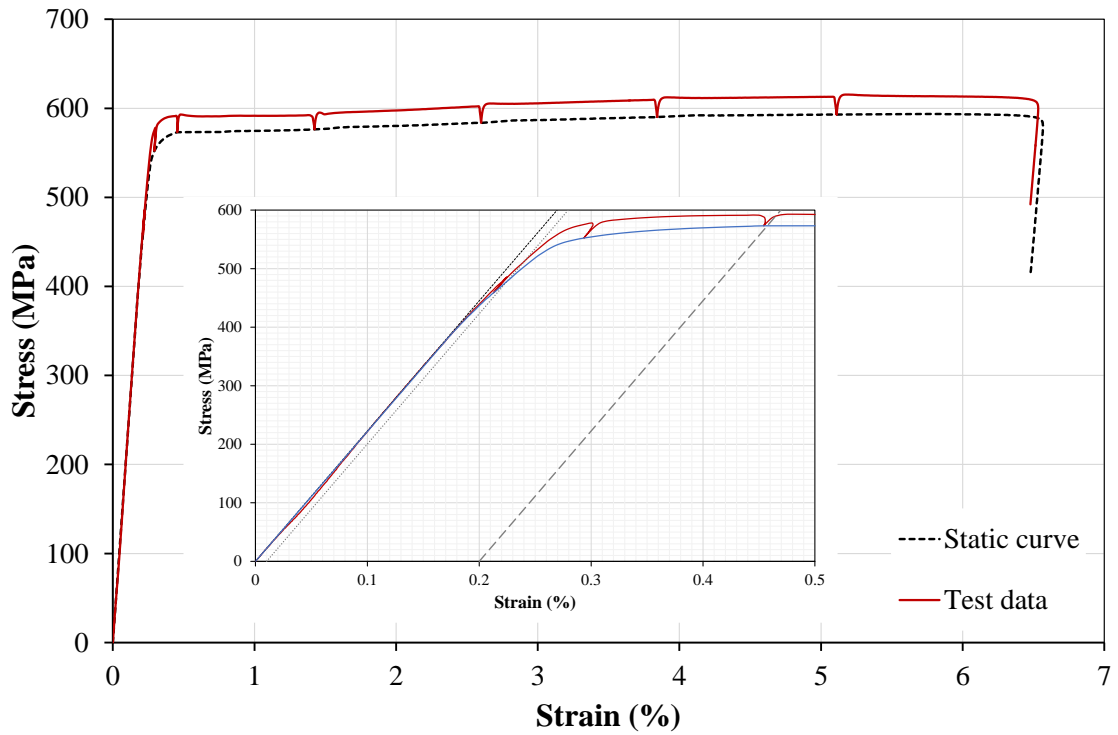
Figure B-14: Stress-strain curve of coupon specimen C120_W_2
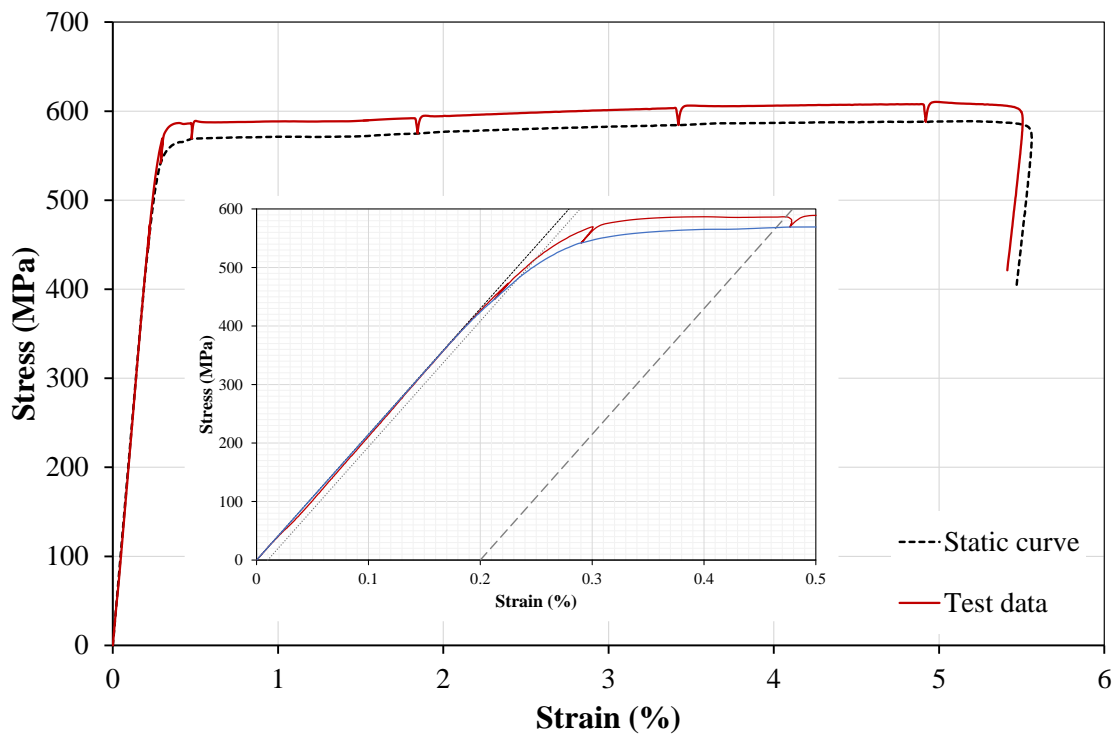
Figure B-15: Stress-strain curve of coupon specimen C120_W_3

B.2. CORNER PARTS

The results of the tensile coupon tests of corner parts for both test series C120 and C64 are presented in this section. The static curve of each coupon test and the magnified gradual yielding region are also included in the figures. The test procedure and the summary of the results can be found in Section 4.4.2.
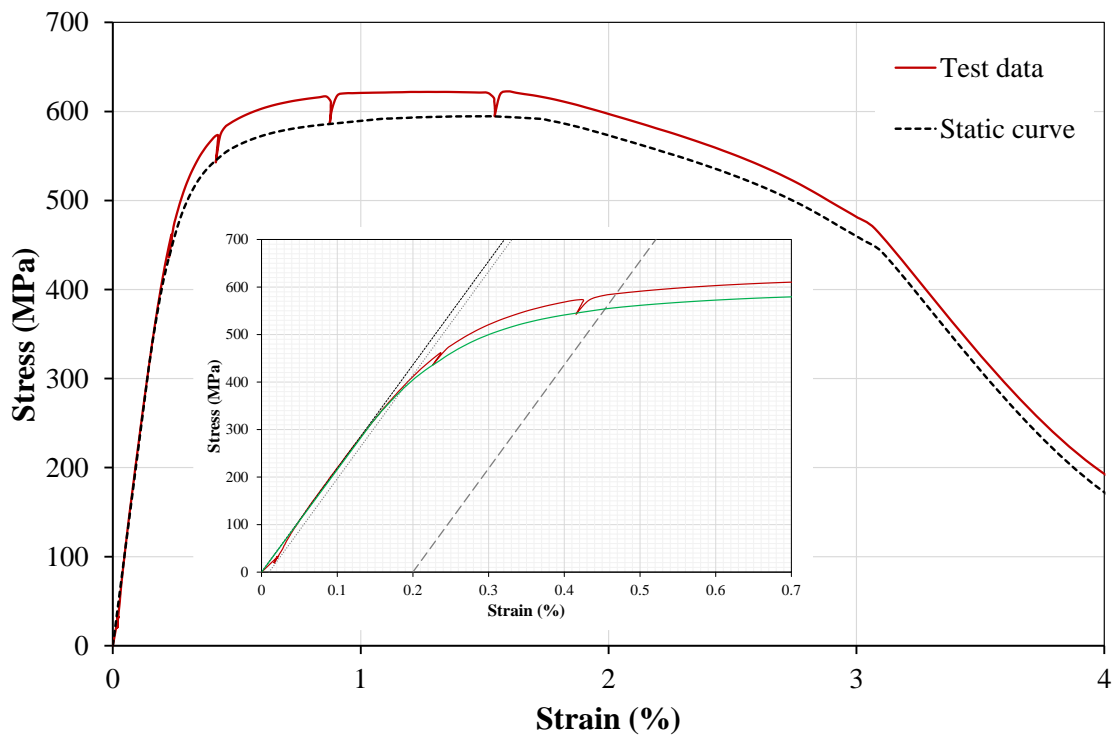
Figure B-16: Stress-strain curve of coupon specimen C64B1_C_1
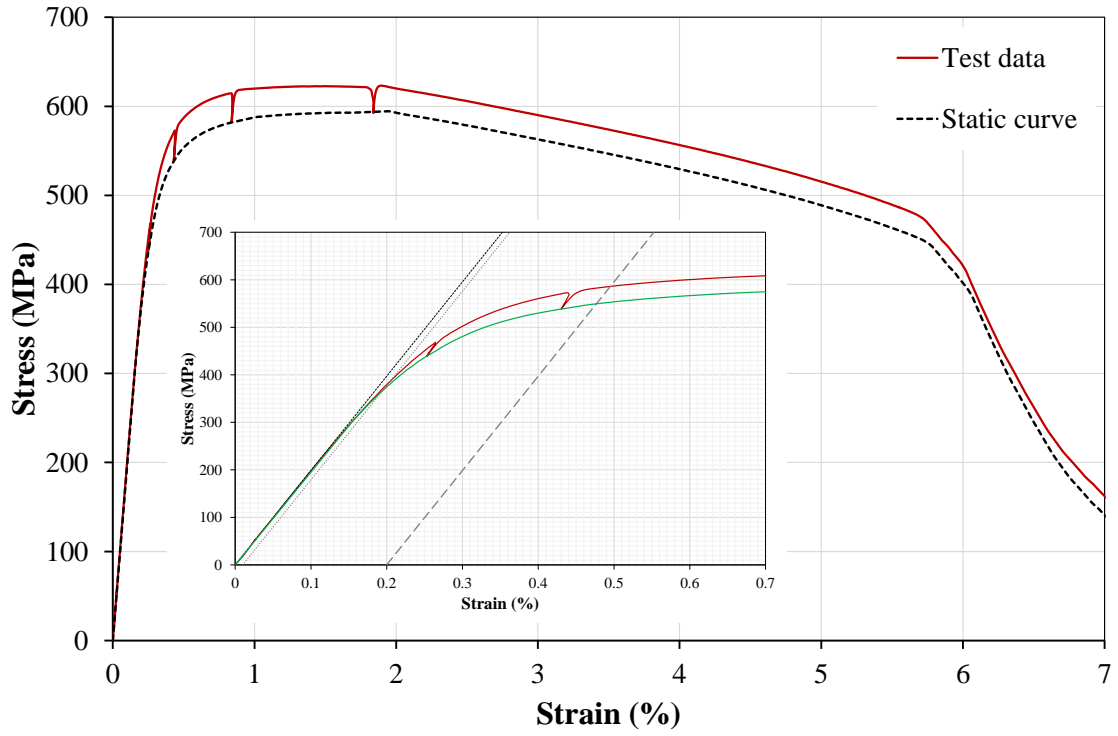
Figure B-17: Stress-strain curve of coupon specimen C64B1_C_2
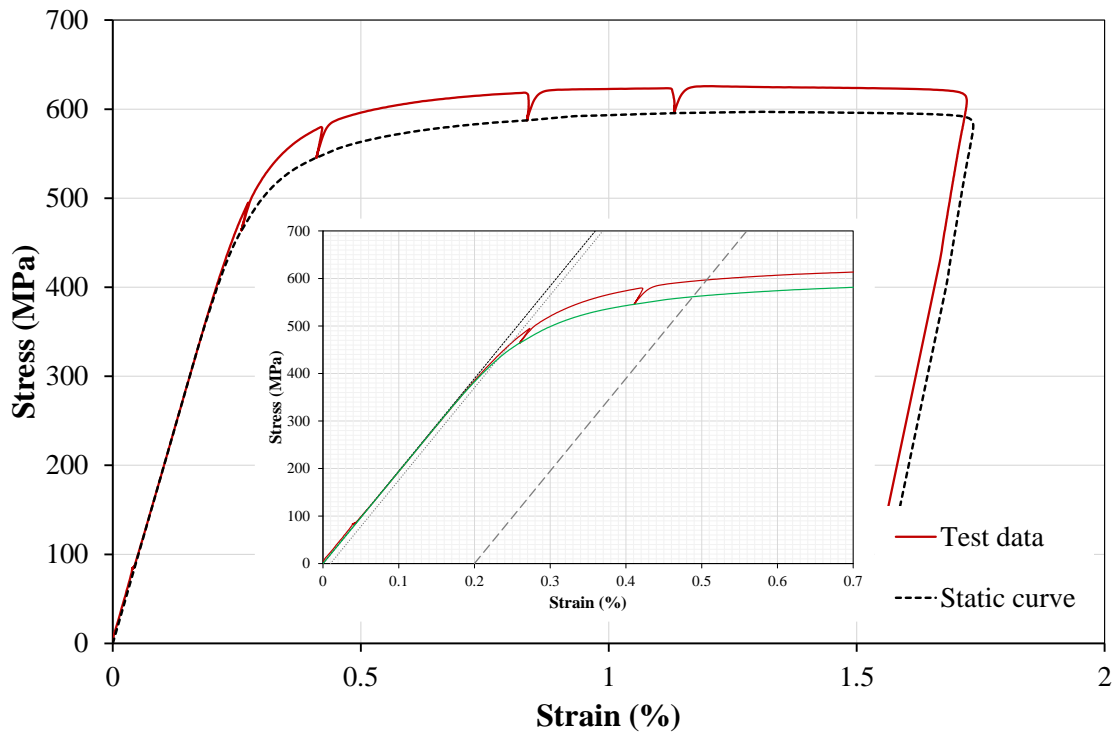
Figure B-18: Stress-strain curve of coupon specimen C64B1_C_3
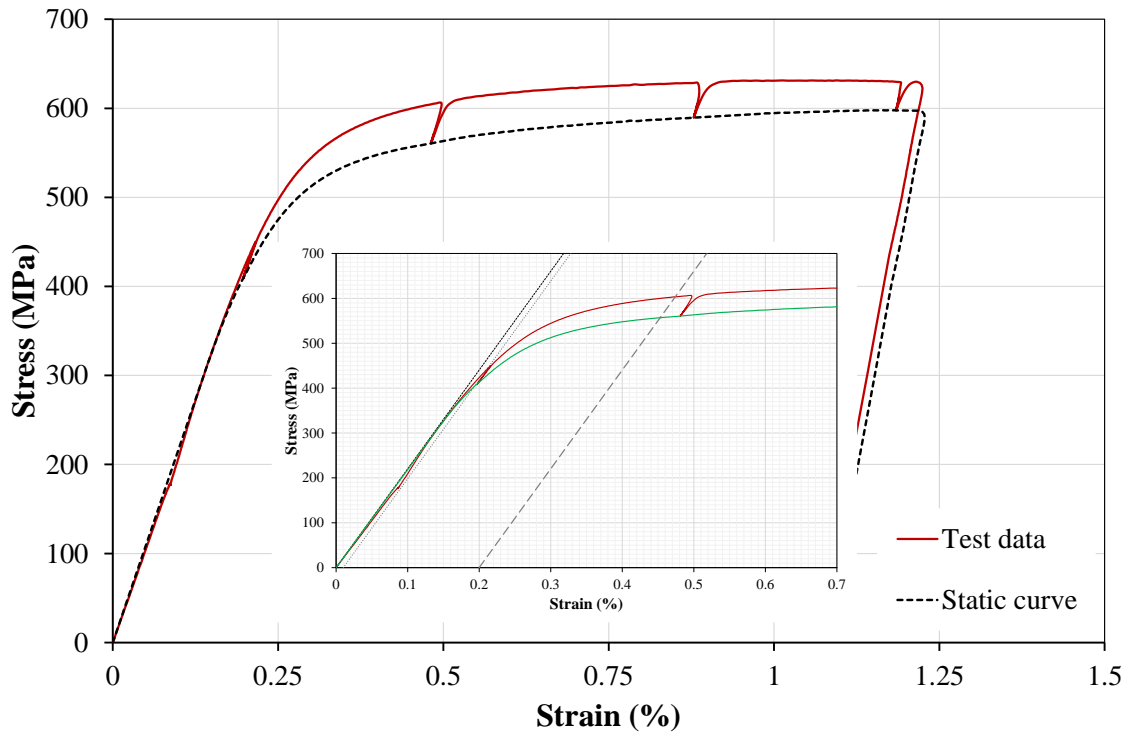
Figure B-19: Stress-strain curve of coupon specimen C64B2_C_1
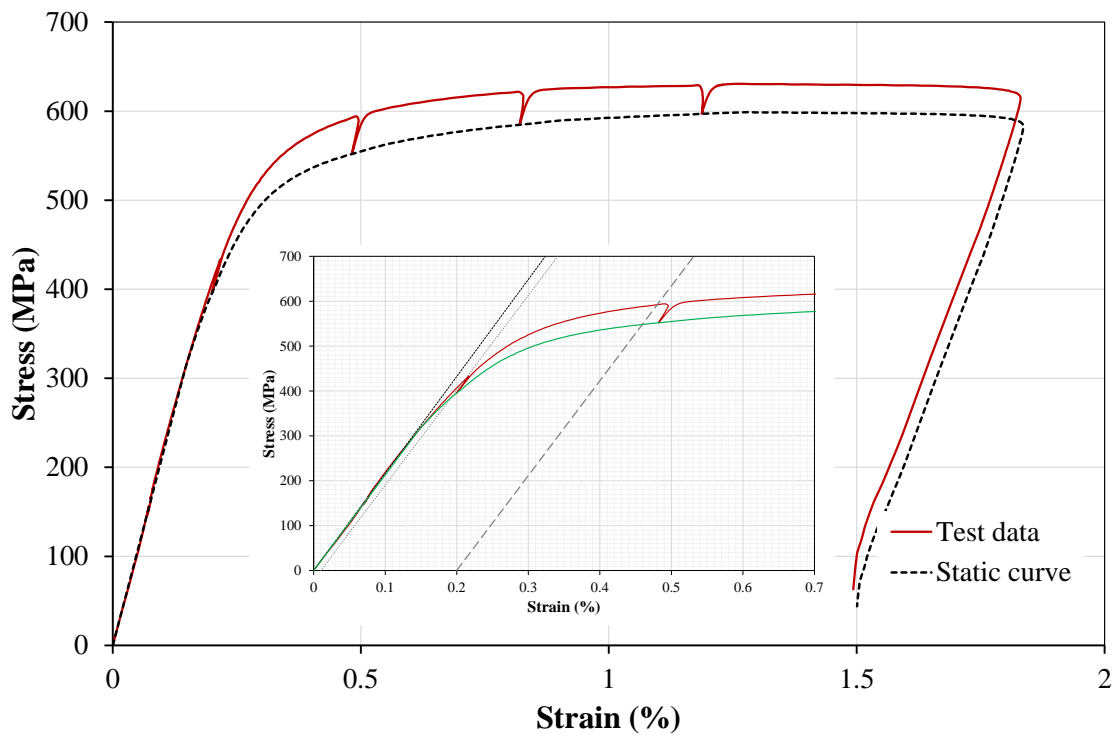
Figure B-20: Stress-strain curve of coupon specimen C64B2_C_2
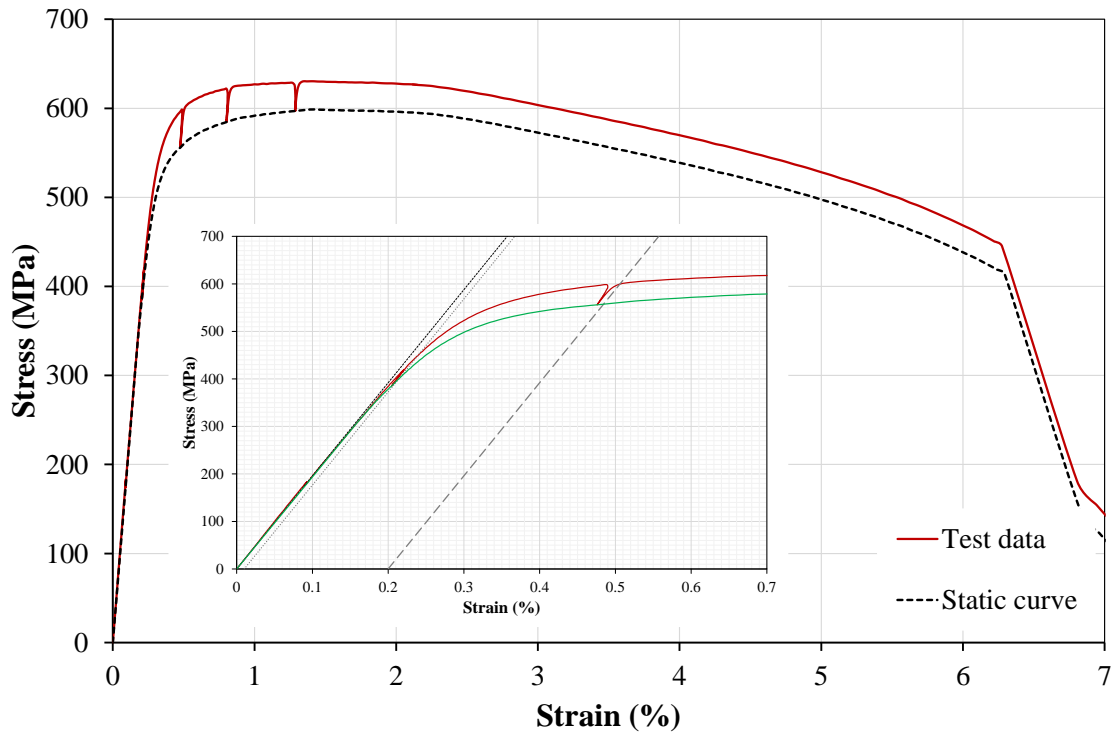
Figure B-21: Stress-strain curve of coupon specimen C64B2_C_3
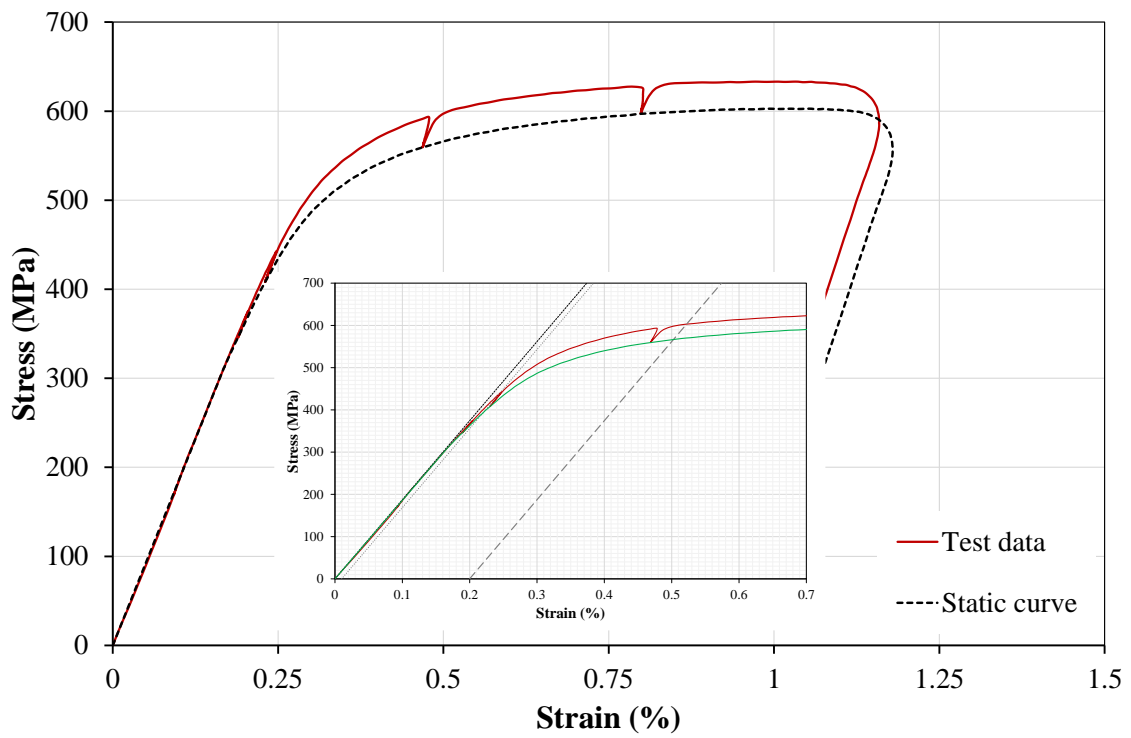
Figure B-22: Stress-strain curve of coupon specimen C120_C_1
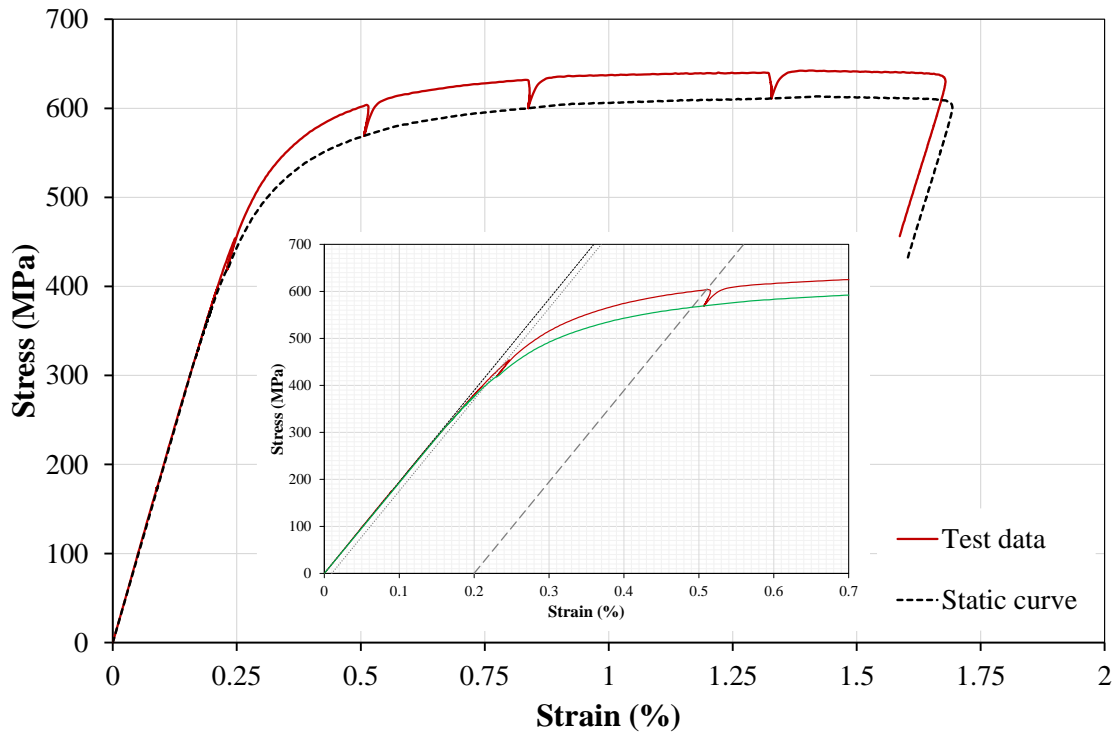
Figure B-23: Stress-strain curve of coupon specimen C120_C_2
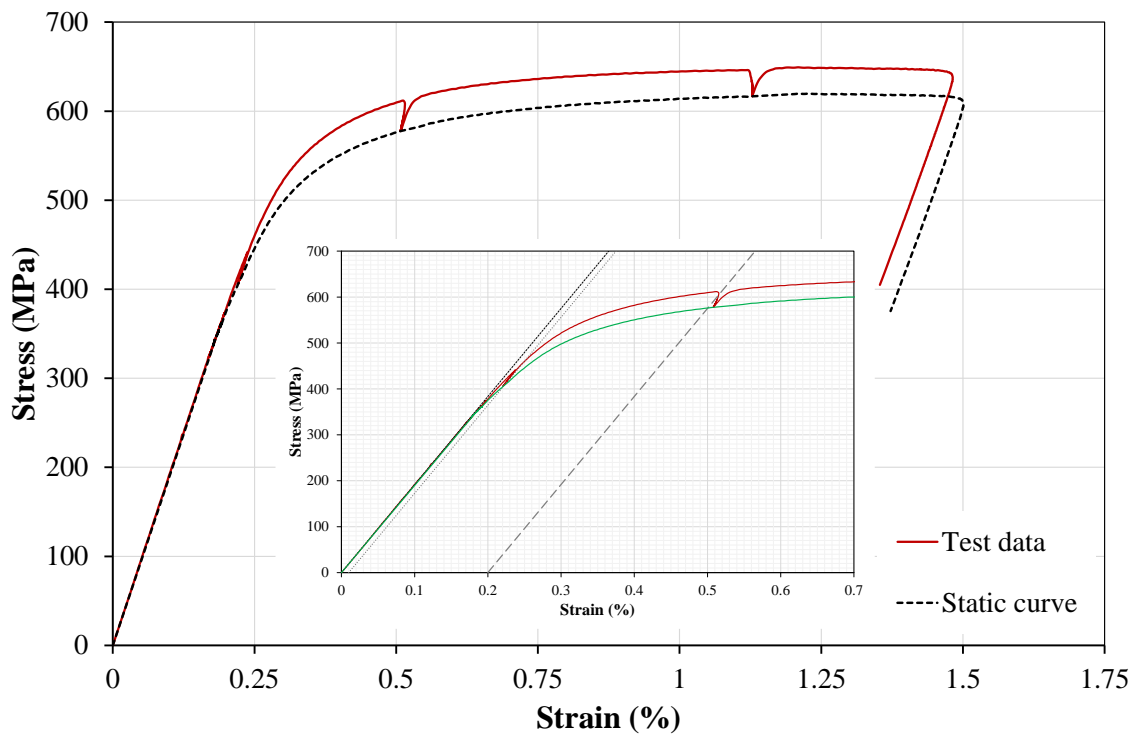
Figure B-24: Stress-strain curve of coupon specimen C120_C_3

Appendix C   Measured Geometrical Imperfections

The coefficients of the Fourier approximation (a_n) of each imperfection reading for the test specimens of Series C120 and C64 are presented in this Appendix. The details of the locations of the lasers in the transverse direction and their positive measuring direction for each section assembly can be found in Figure 4-20.

Table C-1: Fourier coefficients (10^{-5} mm) for the measured imperfections of specimen 1C120-1

Line	a_1	a_2	a_3	a_4	a_5	a_6	a_7	a_8	a_9	a_{10}	a_{11}	a_{12}	a_{13}	a_{14}	a_{15}
1	1477	-3406	480	-3939	1319	-868	-1660	-76	1226	-1514	-926	605	489	-1138	230
2	53036	-19777	7583	-643	-2294	-881	2487	-1794	-895	-229	610	-1416	-172	253	-105
3	33744	-11504	5262	-101	-136	-957	1649	-934	479	-34	425	-402	621	5	128
4	6876	2482	-1287	-1181	1642	-804	-1576	-789	654	-1176	-1041	106	392	-564	22
5	-9743	-6383	3505	1188	-1184	-589	2617	-158	-259	1203	593	-201	-362	910	351
6	-29	-15290	1909	1494	-97	-999	2423	-728	-96	2091	-456	343	158	283	152
7	-23145	-8416	2379	232	-699	-397	614	-820	343	488	-76	-446	-487	-142	-474
8	-413	-1538	-2066	-1453	487	-428	-925	984	-759	378	-422	325	-83	-120	-158
9	28092	-9629	-458	499	1601	-213	1645	1051	692	1414	360	350	436	351	212
10	27500	-11330	-6721	2182	-1740	1298	1057	1539	-175	1702	72	501	-19	788	-283
11	13769	1847	-532	1286	-920	-842	-1252	414	-215	-330	-667	86	-372	-336	-227

Table C-2: Fourier coefficients (10^{-5} mm) for the measured imperfections of specimen 1C120-2

Line	a_1	a_2	a_3	a_4	a_5	a_6	a_7	a_8	a_9	a_{10}	a_{11}	a_{12}	a_{13}	a_{14}	a_{15}
1	30005	-3529	-5004	4401	167	1462	-106	-1754	-1765	499	18	-441	277	-22	604
2	46593	2788	-81	5756	1572	-1212	-526	678	-190	-137	466	-226	416	181	735
3	48015	6305	2468	12514	4396	1732	992	860	-679	1179	988	-242	675	359	1237
4	5979	-2816	-3727	3502	123	1202	-560	-570	-2138	1256	568	-340	103	170	39
5	-17852	4062	-47	4007	3184	161	-834	1592	-630	-831	673	-271	-88	392	652
6	-8149	-13047	-12361	13658	12258	-743	41	2506	816	-1510	1343	-979	674	628	859
7	-6544	-2581	-4480	1366	4203	-844	411	1285	118	-1227	477	-620	124	93	-115
8	10766	859	-1990	1174	1426	673	351	269	987	-280	293	-318	-6	132	522
9	19303	-15289	-10159	5377	10480	-519	995	2042	2005	-805	794	1	238	228	547
10	33449	-16097	-4829	2829	5365	1154	927	1176	683	-6	1205	311	281	166	264
11	2002	-5689	-3803	2219	1906	149	-568	578	527	-228	-466	-235	-166	30	153

Table C-3: Fourier coefficients (10^{-5} mm) for the measured imperfections of specimen 1C64-1

Line	a_1	a_2	a_3	a_4	a_5	a_6	a_7	a_8	a_9	a_{10}	a_{11}	a_{12}	a_{13}	a_{14}	a_{15}
1	31847	-31316	-5619	-22848	-3685	4414	3202	-4517	2173	-27	-460	-2342	237	-1871	-509
2	154536	6973	26288	1642	2691	712	225	-436	638	-330	535	-614	-798	176	-464
3	87107	7241	18253	1352	907	-194	230	-636	1384	-389	728	-712	-230	-431	-366
4	38081	16156	12920	3136	796	1726	926	860	1247	546	914	212	405	38	137
5	-79971	-16091	-20371	-6150	-3366	-1642	-189	-2495	-467	-1023	179	-1086	-202	-1059	-64
6	-56727	-14597	-10019	-6723	-2515	-5743	-2644	-4100	-539	-720	704	-1394	438	-986	-110
7	-27056	-12641	-6862	-4469	387	-1196	-698	-2073	-1098	-302	699	-572	407	-985	-364
8	-7878	1659	1960	-3790	-3423	-3024	-531	-152	936	210	-181	-1205	-869	-425	53
9	-11576	-5213	-1997	-10986	-5857	-3465	-1020	-2123	-815	-547	-424	-1405	-1331	-993	-466
10	3048	2394	-998	-9049	-4130	1211	1787	1335	1104	2419	1375	1412	663	1411	961
11	27859	-28578	13252	-14242	-5716	3861	-165	-7834	-2346	-3235	-469	-5407	-2802	-3307	-1560

Table C-4: Fourier coefficients (10^{-5} mm) for the measured imperfections of specimen 1C64-2

Line	a_1	a_2	a_3	a_4	a_5	a_6	a_7	a_8	a_9	a_{10}	a_{11}	a_{12}	a_{13}	a_{14}	a_{15}
1	34703	16186	2855	5429	24	1631	4266	3095	2868	434	84	1705	420	1625	575
2	45989	27412	9538	-320	-3405	-2304	-1242	575	-59	-483	-980	-306	-365	31	-883
3	15651	20657	3109	2264	-1926	517	-711	763	833	508	-871	508	348	419	-783
4	-6193	15488	112	3051	-918	1820	-825	413	590	985	114	527	171	-43	-415
5	-2343	-4981	-2025	-800	-74	-179	1761	367	494	-1394	661	-588	449	33	499
6	-40938	-16970	-13709	-7899	2152	-5021	-1194	-1624	917	-1139	-1110	-801	380	-303	685
7	-24331	-4760	-9353	-4643	-4271	-512	-78	-79	1329	362	1539	-125	1048	552	328
8	-16211	7087	5962	6534	91	1107	-322	1077	-1693	714	-526	619	-269	694	22
9	36226	19418	20991	7022	-696	1181	-584	874	-1533	783	-1109	1416	161	1166	-47
10	114096	30338	41773	4401	3370	-1655	900	-1524	-572	-579	229	307	1080	368	746
11	106382	22810	27870	3060	-1963	-97	4592	3670	2931	-1074	795	652	1243	-120	291

Table C-5: Fourier coefficients (10^{-5} mm) for the measured imperfections of specimen 2C120-900-1

Line	a_1	a_2	a_3	a_4	a_5	a_6	a_7	a_8	a_9	a_{10}	a_{11}	a_{12}	a_{13}	a_{14}	a_{15}
1	23861	-2357	-689	8	2945	-233	-1330	27	1319	-729	-902	427	766	-614	-227
2	-114572	-25042	-7449	377	-4054	-249	1367	-193	-1696	1062	1187	-676	-261	936	81
3	-61485	-19734	-5810	-1936	-1026	-1182	518	-271	-76	405	322	-130	-139	121	-178
4	-8953	-2710	-4222	-467	2184	-261	-2226	234	1065	-274	-137	1036	930	-407	-162
5	8455	-8044	1797	4463	-2264	2689	703	3318	-264	2988	835	818	314	173	96
6	16921	-11189	3639	4667	-3301	1548	-190	1909	-958	3268	336	-11	515	-400	294
7	7289	-9178	3660	3567	-4349	1022	-694	1628	-1825	2222	-160	82	-454	379	-108
8	12091	575	-915	-3705	783	-641	-1850	-1208	-594	-854	922	392	427	-164	-8
9	41902	-17094	2048	-3440	1054	-2005	230	-780	-5	-117	550	24	488	294	-99
10	87887	-24193	9026	-2113	1928	-857	1342	-95	-261	155	783	-157	290	92	-93
11	12582	-2838	458	-2197	1879	-955	-443	-305	487	-589	213	-125	254	-538	111
12	-52	-9809	-5766	2163	-81	1769	-843	504	909	-939	-376	196	259	-93	-385
13	8722	-22439	-2040	2908	3907	-351	1674	436	-741	876	532	189	23	380	39
14	-10222	-21225	-11774	2880	2745	-22	1944	877	556	-655	573	147	-46	323	78
15	2832	-2786	-5135	1309	-545	1222	-1449	281	429	-666	101	142	147	-114	-314
16	-13023	-8900	-10610	12904	-3664	2024	2388	2685	-588	2880	429	963	-94	393	-159
17	-13018	-15140	-14378	11919	-3940	628	2018	1691	-735	1974	-96	38	-280	-72	-263
18	-14174	-7167	-13620	10005	-3156	1892	281	2589	-1763	1200	-986	977	-515	506	-455
19	-4245	-9191	-4303	800	-1888	-1465	-211	-1173	-364	-136	7	-322	-119	-99	5
20	-8049	-30356	-11995	6363	-4957	-3362	2266	-1633	-578	877	654	2	79	333	416
21	-21033	-33481	-14686	3083	-3718	-1584	-503	-20	-892	394	662	82	80	276	360
22	24488	-5755	-3453	3727	-428	-529	1302	-666	93	278	18	-33	-194	-52	135

Table C-6: Fourier coefficients (10^{-5} mm) for the measured imperfections of specimen 2C120-900-2

Line	a_1	a_2	a_3	a_4	a_5	a_6	a_7	a_8	a_9	a_{10}	a_{11}	a_{12}	a_{13}	a_{14}	a_{15}
1	1971	2200	-3024	-2843	-3739	-1112	620	-347	76	-895	-162	-641	-314	-431	-40
2	28330	25012	-3876	1015	-420	-263	-1071	-1717	317	-98	-362	-466	-354	-107	-1019
3	13099	21200	-7169	1850	-1845	-352	-1287	-1670	1602	461	95	-163	19	266	-531
4	5561	5671	-4569	-21	-1260	-912	497	-213	246	-871	-469	-390	-503	-248	-211
5	12221	891	-10803	-4366	-1462	1569	-562	-260	-871	1416	1581	277	-452	1456	-154
6	9423	6167	-14292	-3600	-4227	1330	-2957	-941	-560	1301	-695	303	-834	708	-598
7	13680	5581	-7924	-2843	-2678	44	-2859	-1782	581	1093	-308	-319	-46	177	-355
8	3799	-867	-3440	-2665	484	275	1289	368	260	1016	1049	9	-68	1081	-406
9	32400	8103	-6128	-8812	1792	-536	3653	-801	1649	610	1817	110	871	-12	447
10	60819	14960	-545	-4729	1184	73	1856	-425	447	387	162	-53	-12	-24	-95
11	-5688	2632	-1629	-222	-1942	472	220	299	45	1022	163	519	-184	379	-158
12	6391	4130	3088	695	-130	415	-869	50	354	226	-774	313	7	-214	-415
13	102656	-21034	7269	-974	733	-1647	1862	372	-29	792	253	59	-160	508	-259
14	58597	-15687	4004	-2491	1704	-1151	1436	-12	678	898	386	175	168	381	126
15	10533	-1114	531	-1957	2236	160	144	218	852	945	-707	83	135	268	-320
16	4150	-17756	-469	675	-2112	-1146	243	220	-1356	498	-184	68	-599	566	352
17	5983	-23659	-1131	-222	-1740	-2541	333	-693	-339	-432	130	-656	-355	-399	-27
18	7467	-20115	-1702	125	-1388	-1886	-526	-318	-849	87	-374	-273	-49	-203	331
19	2718	3153	-391	594	2928	680	-442	-78	1802	-51	-715	228	956	42	-517
20	-13997	-12109	661	-1099	-403	-1805	1461	-563	506	-430	116	-298	-66	-36	37
21	-27631	-16949	2786	1307	-2520	-1792	2667	142	-1569	-863	920	-164	-1181	283	675
22	-229	-3122	1940	-3140	930	578	-1414	-1063	1287	0	-1201	-537	919	-204	-723

Table C-7: Fourier coefficients (10^{-5} mm) for the measured imperfections of specimen 2C120-300-1

Line	a_1	a_2	a_3	a_4	a_5	a_6	a_7	a_8	a_9	a_{10}	a_{11}	a_{12}	a_{13}	a_{14}	a_{15}
1	-990	-3805	2162	-623	-2039	-1620	-406	100	-777	-1131	-460	62	-371	-677	-67
2	110028	18192	590	-453	1099	969	648	-851	67	-109	-414	-444	-182	216	-245
3	72447	19196	2613	3912	2322	572	1342	-16	24	-434	-321	-189	44	7	29
4	9874	3257	556	3322	-86	-833	234	25	-723	-814	-602	176	-723	-633	-225
5	-5826	6970	-9204	-1006	-6298	-1098	-845	-802	-2694	1244	-1160	-1518	1816	1253	58
6	3301	8080	-8249	-769	-4514	-498	-4388	-268	-1924	1505	-558	477	132	1077	134
7	6284	5784	-4782	-2368	-898	-134	-5324	-928	-1114	945	-419	416	-886	320	609
8	7849	-1149	468	2063	1933	-187	-444	2032	-176	-258	-335	1494	-817	-931	625
9	47643	14654	8583	-612	5647	2767	1466	225	956	882	649	461	-35	330	248
10	62164	20886	7553	-2754	2808	3811	310	-541	832	2590	-759	-236	290	1226	-646
11	-75	-1161	1063	4510	-1836	-3054	193	1687	-1398	-1161	376	826	-1073	-387	783
12	-5814	-1774	-1083	4336	-391	827	427	788	-861	-61	-352	331	-157	293	-128
13	33447	-13623	-7810	1128	1049	191	444	682	43	383	-386	51	-160	-40	-81
14	19303	-12419	-10313	3613	5082	1499	2072	514	291	-295	-471	155	296	368	11
15	5078	-4473	-2343	1493	1819	577	1492	15	-308	711	-1076	231	201	413	-652
16	-16242	-9324	-17592	1395	-4128	-2988	2316	2216	-4109	-46	-1290	-1554	1204	854	-809
17	-8985	-16406	-18767	-696	446	-2287	2461	2302	-798	509	553	331	1775	1390	806
18	-20800	-15471	-17717	-2022	1103	-1240	-2959	718	-1527	-603	-577	1125	-785	392	519
19	20905	-684	550	1627	1997	1912	860	-549	120	-780	-7	-281	-443	-858	-338
20	97520	9575	7126	-616	5836	1965	3339	1296	-832	-2212	-172	-376	-932	-688	-328
21	137564	13381	8467	-1086	2842	-1221	1799	714	-383	-1820	-153	-311	-348	-17	-160
22	683	-4900	-1685	-1782	-1664	1931	507	-561	-332	412	66	136	-86	-262	-54

Table C-8: Fourier coefficients (10^{-5} mm) for the measured imperfections of specimen 2C120-300-2

Line	a_1	a_2	a_3	a_4	a_5	a_6	a_7	a_8	a_9	a_{10}	a_{11}	a_{12}	a_{13}	a_{14}	a_{15}
1	19622	2317	-461	-1541	1747	2933	-78	-1538	160	1800	295	-680	-72	1132	296
2	34863	-18551	-3913	3477	-1932	-2726	-180	1466	-1168	-1045	139	844	-98	-818	-45
3	26803	-12917	-2379	2488	-77	-1111	-376	670	-1386	303	853	414	-296	-181	147
4	7720	-1647	-2617	-601	34	1916	-1016	-737	-1288	1750	1088	-250	-1023	1228	-13
5	8763	-19160	-3634	-2687	-2476	-942	2292	-1955	-1237	-374	-331	1556	2019	-1217	596
6	13175	-20001	-1957	-1358	-1976	-1356	-634	-280	397	-618	-687	1354	-341	-462	646
7	12841	-19262	521	-1365	105	-2928	-1551	-485	5	-933	-521	814	-335	137	622
8	8050	3270	-542	-146	1255	594	-1364	405	-401	82	404	-286	-63	454	-172
9	41391	-16941	2078	-504	1560	-865	-2406	664	-470	-106	638	-238	-126	199	363
10	55686	-33182	1892	-1125	-1803	-530	-2439	996	-1436	-1089	812	-385	-5	-189	-9
11	21169	1641	938	-1587	1851	1571	-399	-253	601	857	-54	-189	607	402	-140
12	20151	-1038	-1075	1319	2373	-1823	-1257	1279	1170	-954	-812	601	734	-598	-748
13	-16564	21372	-2175	-728	-2826	2404	1164	-929	-1938	537	1367	-353	-741	350	738
14	-451	18494	-1146	1289	28	1599	1685	118	-281	-559	1229	62	294	-91	482
15	-2725	2281	-1772	903	1056	-1350	-932	162	802	-1351	295	723	663	-607	-327
16	-3313	14712	-6703	-1195	-2368	3665	2314	-1579	-1087	-1027	650	918	1690	-774	65
17	-10514	11863	-6797	-3085	-3286	1626	-221	-2255	-961	-994	250	-706	-59	-505	-31
18	-4614	11037	-1729	-1448	-894	2042	-965	-1571	-1068	-467	246	24	-2035	104	1622
19	21528	-5716	1477	2143	2100	-1235	-736	668	425	238	423	-248	297	-81	148
20	87446	11388	4801	3930	3301	295	-737	941	-24	873	797	-272	-22	146	208
21	136170	16172	5635	1756	783	2360	6	344	-706	1517	229	-2	-383	647	51
22	19562	-1990	2620	1844	1250	-1076	168	398	238	-738	95	201	245	-622	93

Table C-9: Fourier coefficients (10^{-5} mm) for the measured imperfections of specimen 2C120-150-1

Line	a_1	a_2	a_3	a_4	a_5	a_6	a_7	a_8	a_9	a_{10}	a_{11}	a_{12}	a_{13}	a_{14}	a_{15}
1	-4168	364	1601	-6425	540	-21	399	-526	-496	45	611	-266	274	182	142
2	-34765	35316	-2379	-4921	1693	-595	650	-1187	-449	-762	654	-435	219	-445	322
3	-11645	29451	-5261	-8088	5130	-715	877	-717	-1151	-799	1488	-641	0	-205	481
4	5737	6609	-864	-2964	1496	-692	528	-712	-978	-994	1344	-320	-177	10	75
5	-4739	-2054	-9127	-2993	631	-414	-1048	-349	-2811	2018	228	132	748	-560	-969
6	-11823	-1440	-14377	-5078	-407	-152	-1899	-46	-2957	2001	-381	-631	-244	58	-291
7	-8134	-339	-11559	-4406	119	-748	-2316	-1032	-1393	1696	-184	-1159	872	28	-325
8	18587	7132	-1939	-497	1088	-790	580	836	-395	865	-8	578	-1109	807	486
9	91704	4980	3773	888	2531	113	3104	441	-2953	1845	-144	916	-1110	428	-569
10	144325	1252	7939	708	1688	1343	1897	617	-1547	1425	58	509	-289	-22	-563
11	4496	5909	-385	1203	-497	-1988	13	716	-318	43	-569	479	-649	321	-200
12	3781	-106	676	3498	2297	-819	-2066	504	1402	118	-1098	-513	755	473	-399
13	-30594	32122	5886	61	-3487	732	1773	1130	-1732	450	1053	646	-470	-533	403
14	-13989	24530	1491	1543	-1665	1745	683	1765	-622	664	611	766	1171	15	-297
15	5239	104	-921	131	1978	300	-983	418	775	818	-593	-94	2185	656	-371
16	-32877	7401	-7125	-192	-7965	1049	-4421	-4	-3175	604	-1611	-368	-5344	-115	461
17	-23030	11485	-3203	2173	-7895	2717	-2814	1167	-1888	1391	-155	132	-2018	98	36
18	-28554	5093	-5580	1668	-8631	1621	-3158	374	-3542	1511	-1949	175	-5663	-638	281
19	10320	3428	521	1021	1694	-233	24	-701	359	-1027	393	-427	1552	-201	-19
20	52395	23359	6226	429	2316	264	2799	-1212	1034	-1393	1396	-297	1343	-420	125
21	90604	33647	10537	233	1582	773	2038	-875	28	-1492	536	-121	194	-523	58
22	2664	-2809	2512	-1469	306	374	-1007	-383	274	222	-454	-134	-61	355	81

Table C-10: Fourier coefficients (10^-5 mm) for the measured imperfections of specimen 2C120-150-2

Line	a_1	a_2	a_3	a_4	a_5	a_6	a_7	a_8	a_9	a_{10}	a_{11}	a_{12}	a_{13}	a_{14}	a_{15}
1	18660	2656	246	-1549	2038	2928	-441	-1405	792	2142	278	-704	346	1159	41
2	38673	-23397	-194	2612	-2084	-3523	801	1329	-963	-890	487	721	-257	-1050	80
3	31557	-17343	554	1420	399	-2321	1733	855	-173	274	725	812	-223	-409	304
4	8158	-3253	-1328	-1647	776	1335	724	-543	108	1345	1125	-447	-970	470	325
5	-442	-15156	1163	2660	1244	-822	-6141	638	-3293	-690	-1152	175	631	-1084	-241
6	-6010	-16788	1761	3490	755	-1778	-6717	770	-3379	-452	-1148	-492	-1676	100	-277
7	-8182	-13758	-1215	2117	-600	-1399	-4931	114	-2951	-753	-47	-716	398	339	71
8	10451	3685	-743	-917	191	1020	-215	-497	24	5	796	119	-418	496	325
9	50197	-7420	-4086	-1368	-625	-866	-958	-767	-643	-228	457	-25	-334	132	-15
10	80655	-6763	-4269	792	-1072	-1839	-652	-323	-882	-1262	139	20	-158	-368	-92
11	16496	3516	1763	-1037	1260	1786	148	-14	332	992	105	-75	260	594	105
12	3842	367	-3949	-3619	-733	-573	24	-594	-245	99	434	-24	-12	170	81
13	23475	10269	-6610	-2651	-450	163	280	-623	-154	-872	816	60	288	-114	-15
14	12382	8206	-10285	-7387	-1207	-179	673	139	366	-416	1898	661	1397	-69	-220
15	8359	2507	-3072	-2463	457	-486	-239	-195	59	-89	1299	688	1665	-253	4
16	-27435	13677	-14485	-1637	-4644	378	-4711	-3090	-3950	-97	-2928	-1628	-4489	-103	101
17	-34616	22980	-20615	-751	-6503	2167	-4241	-2742	-4671	1165	-2500	-48	-2364	1211	68
18	-28161	10551	-20752	-4808	-6448	-56	-2414	-4683	-4224	629	-2339	-1507	-5648	387	627
19	5229	757	-4231	648	-1106	-1678	-65	-534	1140	586	1297	85	1471	51	219
20	22427	15277	-6916	2981	-2503	-1889	-951	-2825	1310	1398	1746	79	1100	541	-37
21	46864	17372	-3707	3325	-837	147	-1130	-1136	21	1548	562	-16	215	499	-103
22	18881	5738	-3262	-357	-1286	-985	976	264	647	-303	276	-121	-64	-381	163

Table C-11: Fourier coefficients (10^{-5} mm) for the measured imperfections of specimen 2C120-100-1

Line	a_1	a_2	a_3	a_4	a_5	a_6	a_7	a_8	a_9	a_{10}	a_{11}	a_{12}	a_{13}	a_{14}	a_{15}
1	-9399	-965	-6746	5499	-340	-363	-177	-65	-385	-133	691	-157	-20	-300	-180
2	22653	-26783	-8102	5349	-857	338	409	283	-12	-424	379	319	-96	164	73
3	3393	-22625	-14989	8653	-2852	-823	733	-355	248	-711	1301	-330	186	159	4
4	-592	-6580	-4703	3511	-1650	-585	441	-658	216	-1072	829	-476	-90	-135	-51
5	-15918	-7810	-9473	3152	-2214	-2121	-3645	2424	1228	-5347	4024	922	-938	1536	1894
6	-9902	-4830	-9056	5835	-301	-222	-3202	4083	2249	-4498	4115	394	-426	607	777
7	-9035	726	-7546	5877	53	978	-2164	2964	1496	-1085	3029	-502	350	471	-283
8	1729	-4821	-3513	-695	-622	1053	1383	1062	1050	-106	-331	-287	-152	-310	-320
9	3896	-40274	-6602	-1755	-2543	877	1103	2815	432	-880	-204	-192	95	-722	-191
10	16774	-55065	-2307	2152	-3003	366	1576	113	537	-124	-995	454	74	-648	448
11	18878	-6510	-2425	779	-723	1515	653	-429	920	263	-32	216	-30	345	-166
12	18125	-8504	-4895	-346	-975	696	309	185	730	-295	223	210	67	183	-24
13	59295	-26495	7085	1666	1313	-1134	549	1013	782	-1343	361	-55	267	-552	-155
14	25306	-24944	-1275	24	-3647	-919	815	961	1331	-815	975	-235	-86	-408	-18
15	13186	-4150	-2869	657	-1885	351	936	-715	1915	-848	-365	-242	-63	102	53
16	11485	-6951	-8356	6138	4322	-1554	-5874	1755	1342	-1236	3477	439	-2312	1295	1828
17	12558	-13365	-9858	2361	5419	-964	-7242	4941	1068	-1759	2415	460	-1747	-73	507
18	5410	-6852	-5551	-189	4701	1762	-5270	6571	-129	-434	1558	410	-748	457	212
19	-14797	-6976	-2958	3172	-1673	1279	878	1183	-909	371	223	-385	689	-618	-32
20	-30554	-25137	-8976	7302	-4280	2009	2879	1770	-905	837	556	-463	869	-553	-283
21	-38466	-31408	-6884	4860	-1170	1507	662	1008	-121	1279	598	203	364	323	-59
22	-4442	20	-5397	6444	356	-353	225	446	-311	546	535	-109	97	-121	-51

Table C-12: Fourier coefficients (10^-5 mm) for the measured imperfections of specimen 2C120-100-2

Line	a_1	a_2	a_3	a_4	a_5	a_6	a_7	a_8	a_9	a_{10}	a_{11}	a_{12}	a_{13}	a_{14}	a_{15}
1	29149	-1604	-3136	1173	722	1872	80	-306	376	591	-299	-60	-652	-402	-117
2	135483	21570	-4220	-796	-440	-1003	1572	1505	-665	-654	-558	9	-483	256	-686
3	95332	15132	-3090	-176	3186	759	3095	2963	-805	-1174	-386	156	-185	89	-631
4	15138	308	-3185	121	1620	1160	863	640	340	-266	-344	469	47	-295	-355
5	-14341	-8505	-7501	5487	-1763	1384	-1434	658	-1273	359	1307	-347	-341	1901	-31
6	-14635	-11632	-7425	8086	-1845	379	394	1589	-1377	1084	149	-923	-691	798	147
7	-11134	-9183	-3971	5716	-27	-1106	1639	1049	-725	1263	-632	-1743	-1757	-870	79
8	-1254	-6852	-3175	2797	1706	-335	357	367	-182	-823	508	250	360	-559	79
9	-14039	-29115	-15632	7317	5149	-1438	488	710	-527	-910	764	719	598	-649	329
10	-11564	-38364	-12763	4968	1066	128	-154	542	23	-578	798	100	612	-85	372
11	-75	-2215	-395	7437	1763	-137	121	243	-145	-388	637	226	232	66	-91
12	4112	-2057	-3799	6700	1325	-137	-183	518	-357	-635	21	133	321	-65	-144
13	5543	-10638	-17126	1007	145	74	-585	502	-272	-722	578	-95	227	-191	579
14	-5868	-12975	-17422	3255	3057	-702	-4	842	-560	-1905	941	664	1194	-248	269
15	-8254	-2990	-5382	2071	404	297	-383	721	-678	-1319	474	515	911	-241	64
16	2590	-59	-5551	-71	-284	4311	-265	-568	-3468	-780	1439	-1222	-672	1676	-432
17	-4476	-9479	-7051	804	3249	2556	-564	-911	-1138	-113	1086	-1946	-1009	-335	525
18	-22957	-12063	-8824	1908	2489	1098	-1429	-465	-823	817	-359	-1179	-2361	-442	565
19	22388	4155	-946	-1895	2620	-262	1785	-501	280	382	-318	-101	43	482	-152
20	94834	8311	5549	-2381	5663	2661	4568	-359	-1133	1298	-125	412	175	492	-175
21	135110	65	3740	-230	1543	2277	2940	761	-969	1143	284	223	287	280	-330
22	17059	-4576	-2268	1073	1152	1236	-431	-314	564	-84	-500	-235	-512	-22	74

Table C-13: Fourier coefficients (10^{-5} mm) for the measured imperfections of specimen 3C120-900-1

Line	a_1	a_2	a_3	a_4	a_5	a_6	a_7	a_8	a_9	a_{10}	a_{11}	a_{12}	a_{13}	a_{14}	a_{15}
1	-350	-833	-3543	598	932	-1057	393	-990	715	778	566	625	165	236	-100
2	-6817	21608	-5116	254	-1202	737	-171	-1277	-1022	190	107	77	-71	385	115
3	-3767	20047	-5744	2709	-1908	945	-893	-1852	283	1261	631	-92	331	227	412
4	-2493	3480	-3004	-223	-691	-665	464	53	329	734	-70	1	175	-219	238
5	-4320	17250	-2385	-3231	1137	-2481	2147	-4464	1626	426	1689	-2	-85	534	-906
6	-88	13460	-2133	-6922	1840	-1528	2198	-2562	1502	1718	1324	704	173	738	-548
7	11817	2407	-2018	-7169	1482	-103	2107	-823	1084	2231	1963	1489	691	691	137
8	1108	1218	-5594	-1852	-1118	-733	-372	-316	-565	-161	824	263	78	-90	-206
9	12237	16414	-11108	-7359	-1672	481	644	-373	507	428	2152	854	619	-52	96
10	32301	22744	-5657	-2101	-420	1220	988	1479	284	1749	1471	586	830	531	-263
11	14092	7764	-5203	1760	-1218	-1444	443	-59	750	499	-22	220	-154	-100	16
12	5972	-342	-5182	955	2	1084	988	648	-387	647	-189	205	-189	284	-155
13	-1567	-86	-1327	1781	-116	-891	45	-141	-577	1130	-383	109	-53	-190	-21
14	11795	-16821	-11687	9118	-5326	-2627	1752	250	-1100	1582	-138	677	-436	839	192
15	19262	-24035	-9560	3130	-2306	-1505	60	-122	-724	449	559	126	-106	-8	246
16	-15328	-2504	-13912	12017	-4295	-2354	1710	549	-1345	753	-7	-85	-136	304	-5
17	-22963	-7330	-21265	12673	-5957	-2632	372	375	-2101	308	-665	-337	-264	290	397
18	-30712	-3758	-21531	11268	-6843	-870	-1610	1297	-3092	246	-1695	151	-719	715	-72
19	-9872	-5552	-7325	1261	-574	2323	-728	440	1327	-1194	-281	10	409	-325	-178
20	16879	2202	2051	1338	2819	457	1060	-365	1563	556	755	109	155	651	84
21	7580	1878	-1	-917	910	-54	-526	-101	35	375	338	120	255	-36	25
22	28744	-22031	-1464	-3791	611	-3482	-457	-407	-429	-12	111	-363	84	-562	-116
23	46083	-26577	-2185	-158	-1113	-2175	724	190	-149	99	1146	165	-58	-69	832
24	1143	-11637	-3768	-2170	-3805	-3343	-1064	-1386	-754	590	944	312	155	225	75
25	1607	-9936	-5072	-1363	-5434	-3695	-2350	-846	-1267	507	937	443	-343	729	260
26	515	-8674	-3654	-657	-5975	-3740	-2635	-650	-2528	689	247	1125	-447	944	739
27	6431	-345	-1996	291	2202	1421	-794	-1758	422	1472	-135	-791	284	857	-97

Table C-14: Fourier coefficients (10^{-5} mm) for the measured imperfections of specimen 3C120-900-2

Line	a_1	a_2	a_3	a_4	a_5	a_6	a_7	a_8	a_9	a_{10}	a_{11}	a_{12}	a_{13}	a_{14}	a_{15}
1	14320	-1357	-859	2772	1494	265	-229	-112	-482	-985	131	-185	-82	386	-712
2	100592	4831	4544	3260	168	-753	359	-673	-2640	-1495	-449	-954	-81	63	-201
3	66948	-5953	2876	-1886	3149	-1028	2303	-1658	-2246	-1711	249	-735	580	-116	19
4	5475	-4597	-627	45	1743	889	610	-874	-297	-970	-317	-322	-317	51	-27
5	-6718	3631	-1712	4023	4147	-608	3212	-1124	-1405	-3070	645	-1998	369	-1479	-304
6	-9502	-6996	-4402	4341	4548	-326	1753	696	-885	-1101	169	-131	203	-20	-121
7	-9397	-12064	-5565	4935	4395	1297	1430	2573	-807	214	918	2109	674	1143	202
8	6152	-1771	-886	2814	1981	1009	279	88	203	378	-77	173	176	100	-36
9	19951	-11136	-5547	3056	4871	-3	320	-180	-130	-584	166	615	393	-41	140
10	49324	-9052	2887	1915	3576	-322	1016	-149	96	-441	560	75	940	-62	330
11	22434	-6919	572	1960	1221	834	-728	-663	161	-318	-377	-314	-273	99	-12
12	21442	3106	-3764	-290	-1474	-1287	619	98	660	70	326	52	120	-55	80
13	2627	3028	-3567	202	-345	-78	130	675	676	-417	830	265	-172	-477	19
14	34388	26061	-3541	5335	1040	2426	127	-931	1707	521	1343	623	965	1093	435
15	29057	39114	-154	4131	3	3604	-555	-346	-400	1009	601	765	21	896	-172
16	-22474	14572	-9188	-5254	-6196	-3150	-2071	-5776	28	-2069	291	-1493	-6	-235	69
17	-25779	14631	-13068	-6861	-7877	-1837	-2922	-4731	-625	-1714	885	-974	430	-325	346
18	-27875	8644	-13667	-6907	-8099	-796	-3282	-2749	-1678	-1771	609	-752	530	-608	342
19	12535	271	-2264	-3080	-1008	-1016	-619	-897	-131	-585	134	245	-33	-18	13
20	8935	1654	-2156	1746	-1727	-1797	-799	410	-1689	-1191	594	77	-1256	-412	373
21	6218	-2760	1031	1731	2101	-1239	442	979	486	-1916	324	608	121	-617	311
22	23715	12026	3862	1582	1935	2812	620	331	1084	-222	377	308	9	1178	176
23	23758	15272	5105	-3590	-94	3204	788	-2357	1594	-24	-309	-1119	835	310	-295
24	-4297	16126	-3349	-905	-2197	504	-2517	-3050	-1444	-838	77	-1630	-313	-644	159
25	-3149	20615	-4451	1705	-3269	1895	-3495	-1494	-1952	-80	273	-1092	194	-255	-150
26	-6875	18846	-4899	2390	-3764	2308	-4118	-453	-2422	-122	-442	-958	-359	-192	263
27	22477	1257	633	1420	1597	-829	-956	564	456	-587	-132	-249	463	-322	-243

Table C-15: Fourier coefficients (10^{-5} mm) for the measured imperfections of specimen 3C120-300-1

Line	a_1	a_2	a_3	a_4	a_5	a_6	a_7	a_8	a_9	a_{10}	a_{11}	a_{12}	a_{13}	a_{14}	a_{15}
1	29088	4276	1396	-2811	1248	-915	-355	-36	1165	-357	-402	300	375	-454	-334
2	-34729	-36194	-5705	3889	-1831	-4253	-92	1551	-1229	-1935	483	908	-326	-609	-80
3	-8154	-23763	-4013	-192	-44	-3433	-475	277	44	-843	923	-485	57	144	452
4	-9194	-851	-2192	-432	1718	760	-1358	-344	705	728	207	-848	542	1261	-78
5	-7538	-14466	1353	-4580	2221	1700	2124	-197	1199	-1191	269	2372	-160	-1532	-188
6	-9222	-16962	-488	-6079	2809	1649	1393	1938	1739	-34	240	2072	-632	477	-458
7	974	-19576	1803	-7089	4029	-454	1786	2727	2486	30	1027	1872	-88	2174	193
8	17996	3228	-177	1082	1229	396	-450	16	936	382	-772	51	313	-162	-190
9	61588	-11084	-2685	2074	-604	-824	-262	-392	602	380	-228	16	-22	165	71
10	103570	-6963	301	6722	76	1560	2307	2205	1389	331	306	864	62	439	436
11	30650	3135	-401	-1974	1856	2544	-658	-1277	478	1778	-124	-626	26	1211	21
12	23746	-6115	3332	2567	1459	-1777	1516	-451	571	-160	-30	299	376	-416	-31
13	21881	-3156	1885	599	1812	-810	170	-454	1201	-917	-244	241	-367	-249	-32
14	86949	11260	6455	728	3201	903	501	-1438	1089	-865	-19	427	100	-244	173
15	140649	26125	5354	1610	737	2931	983	-16	365	736	-548	193	-708	850	-28
16	-5250	18986	-3883	1495	-2822	-2945	-642	-2845	-833	-393	-56	-2094	-87	-360	-181
17	-8671	18915	-3128	-542	-3935	-4135	-670	-2023	-1429	-103	-101	-2086	-26	-324	304
18	-15647	15629	-2741	-990	-4817	-1777	-590	559	-1951	920	-532	-939	44	806	258
19	30935	-3093	-374	2016	2352	-1478	-1402	1212	1742	-896	-945	212	699	-297	-677
20	16146	4284	1593	1449	2437	-878	-1412	1289	1388	-796	-874	543	484	-186	-721
21	18766	-61	-356	1215	2931	-1492	-342	437	1861	-1514	-517	781	116	-381	-212
22	14084	22208	-712	3442	370	4540	17	2001	399	1219	-125	1973	-1205	1447	-430
23	25562	22548	4346	-1830	-557	2235	1958	-953	-687	898	445	3	-1367	732	503
24	-4315	12056	-3407	2672	-5901	-736	179	-3787	-2062	-553	218	-2030	570	-428	563
25	-10364	10532	-4256	4067	-7263	-748	-432	-2657	-2757	82	-224	-1309	554	118	256
26	-19513	8474	-6460	3577	-8013	189	-2113	-1216	-4033	711	-2214	-546	169	451	-528
27	30687	2996	1771	1878	122	-641	-618	215	170	-958	-163	313	-138	-595	46

Table C-16: Fourier coefficients (10^{-5} mm) for the measured imperfections of specimen 3C120-300-2

Line	a_1	a_2	a_3	a_4	a_5	a_6	a_7	a_8	a_9	a_{10}	a_{11}	a_{12}	a_{13}	a_{14}	a_{15}
1	8422	-3781	-448	-1265	2806	40	-1924	-851	1194	35	-1025	30	694	-146	-740
2	-26011	-23451	2951	-700	-3643	-1762	2894	144	-719	1081	2232	55	476	242	1310
3	-21954	-21928	901	-1214	-3377	-907	-253	-262	782	1597	38	116	188	468	572
4	-5875	-3701	-2077	-2601	731	287	-2323	-590	1137	738	-1734	130	635	-518	-434
5	-1078	-5836	-4025	-1020	-51	-3508	2712	-1923	-3292	103	2883	-2666	-1178	-131	-1974
6	-5530	-1859	-6445	-351	298	-3544	1968	-589	-1755	-55	1897	-1568	-747	1097	-629
7	-3188	-4627	-5381	-2931	-1453	-4956	-422	186	-1410	-1113	404	-2335	-754	2140	-590
8	-4346	-3822	-1679	-1174	155	-521	-1242	-886	-196	-1125	-199	225	-233	-962	-236
9	-8064	-19469	-800	-1553	-620	489	-205	-888	102	-563	371	44	73	-711	39
10	-13524	-20900	1292	1981	191	1766	799	705	332	128	279	332	-706	815	108
11	15294	-827	-1065	-399	1208	-897	-1247	-312	439	-703	-229	-215	-17	-130	-65
12	5535	383	446	654	2723	223	-2046	702	1471	503	-993	813	745	28	-577
13	31262	-8804	8385	545	-551	1432	3487	115	-385	197	762	-879	-386	856	443
14	17842	-4651	2405	-1419	-1501	3231	1312	-663	230	-199	-283	-439	-474	-408	34
15	18753	2138	-524	-704	2606	2593	-228	675	1355	-774	-785	773	563	-822	149
16	-2093	-31994	460	-3155	-2546	-11802	2939	214	232	874	862	-3206	1078	2813	-606
17	-2213	-37775	-450	-3711	-3211	-12267	1367	249	198	1197	-511	-1853	396	2749	-783
18	-2719	-32524	868	-3782	-4184	-9851	1542	980	-6	1559	-1539	-1273	438	2779	-1067
19	11870	-3626	-99	-1013	128	-618	-1203	-127	17	-76	-938	283	-130	68	-222
20	15938	1077	1534	1803	2154	-1103	-973	833	1617	-1027	-592	780	868	-471	-432
21	-28545	18724	3604	-1009	25	3386	2507	-564	-1476	-41	1156	39	-220	437	1263
22	773	24000	4049	1569	2549	6058	2888	693	411	-379	1601	1473	1388	595	1285
23	4016	-172	-703	119	2336	625	-591	355	447	-1655	-633	635	973	-581	-305
24	5704	6685	-3213	-2014	-2602	-5950	390	-542	-1359	-570	792	-2156	-530	1622	300
25	-9236	-11203	-4050	-4305	-7400	111	-575	2419	-2536	-626	-272	852	773	-373	364
26	11481	10967	-3794	-1404	-3127	-3898	-444	-145	-2585	-244	-1249	-1549	-814	1692	-528
27	23508	-3830	2809	683	404	-901	-286	2	91	-1104	172	198	81	-850	83

Table C-17: Fourier coefficients (10⁻⁵ mm) for the measured imperfections of specimen 3C120-100-1

Line	a_1	a_2	a_3	a_4	a_5	a_6	a_7	a_8	a_9	a_{10}	a_{11}	a_{12}	a_{13}	a_{14}	a_{15}
1	9396	-2296	446	2898	1264	1078	-459	534	37	784	235	-115	271	464	-149
2	32548	21517	13577	-2127	1387	468	3699	751	662	-1042	1170	128	672	642	305
3	3724	14528	2540	-2922	-543	899	1089	716	1732	-396	607	237	488	76	168
4	-101	-789	-2036	-615	476	489	-458	101	1056	-281	103	-63	393	252	263
5	31694	8961	2538	697	3502	-145	-840	-6443	-4964	-5178	-2460	-2135	-2253	-1748	-585
6	19983	4577	2884	-1276	3242	957	-2192	-6422	-5420	-3203	-1475	-1243	-2141	-1559	-746
7	4248	2598	2945	-3682	1834	1574	-2196	-5343	-4570	-1252	-738	-1343	-3039	-1543	-1619
8	-7832	1726	-1194	1459	1492	-242	-675	1610	2775	808	-986	277	1692	834	-461
9	-45985	20335	-1377	3793	-2447	557	2064	2010	1844	323	728	729	865	123	419
10	-86823	17654	-5785	-1586	-3964	-949	1865	-381	85	-632	717	-1015	-388	-308	500
11	22697	-1196	-475	148	3400	127	-959	-272	852	270	-458	-153	808	235	-191
12	21154	-4792	-4144	1990	-82	1893	648	580	-279	499	708	456	210	-134	25
13	96466	8698	611	3150	2735	-599	1671	2375	-469	-175	1069	321	203	470	-51
14	70499	2185	-2638	2481	4705	-293	4758	2560	-1300	-627	1236	-317	-166	-226	-123
15	18811	-4897	-1252	1480	2174	1436	937	461	-153	829	792	200	382	35	-146
16	17793	2319	-3384	-123	-2514	3891	-2672	-98	-2530	-654	-1003	-2641	-2351	544	-1623
17	14714	-3052	-10392	-1691	-2185	1303	-3098	-182	-2324	-521	-1236	-1789	-2129	485	-883
18	13591	-2944	-11882	-994	658	-656	-1199	1473	-941	267	-543	218	-1824	783	-445
19	17594	-5210	-859	4707	2913	1014	823	-75	-342	-57	1041	420	427	171	363
20	12101	-2570	-543	2006	1791	10	51	239	379	-932	-571	-335	-175	-187	194
21	22089	-28653	-8661	-1130	6126	-209	933	262	642	127	970	-338	484	-333	214
22	-17712	-33404	-20618	2009	7668	-4162	-632	-516	243	-803	-526	-1164	-511	-1064	-855
23	-692	-7040	-2632	1615	2695	-985	222	501	460	285	264	-315	267	-213	435
24	10513	-6300	-6443	9846	1859	2640	-3728	877	807	-250	-766	-2338	-2517	94	-946
25	16974	-2423	-8870	12034	22	1050	-4468	902	-1022	-189	-1725	-1405	-2185	-55	-945
26	14529	4846	-9047	12280	-1581	-116	-4149	1992	-2166	332	-3183	-930	-3455	3	-1052
27	30194	-150	-1385	3639	16	551	47	-1683	-518	734	-557	-335	180	345	551

Table C-18: Fourier coefficients (10⁻⁵ mm) for the measured imperfections of specimen 3C120-100-2

Line	a_1	a_2	a_3	a_4	a_5	a_6	a_7	a_8	a_9	a_{10}	a_{11}	a_{12}	a_{13}	a_{14}	a_{15}
1	6172	2529	921	-3476	2480	1837	-561	-988	2269	1213	-445	-709	1196	711	-422
2	30659	-33333	3912	443	-1799	-3426	1796	527	-1360	-1864	875	-559	-458	-504	1248
3	17224	-28060	1573	-2897	-756	-2811	-172	-1504	-47	-284	778	132	58	-366	970
4	1566	-2111	-1502	-2455	872	1600	-1037	-1431	236	1355	-294	-428	-161	664	391
5	21942	-6345	-2073	-2565	1691	-1059	3793	547	-3377	1086	1613	-3515	607	-603	-2980
6	23867	-6018	-3323	-5156	2238	-2763	2394	-730	-4203	468	1852	-1761	-50	-438	-1283
7	24739	-8053	-974	-6545	2965	-4635	1272	-2255	-3858	-366	2649	-327	-197	-186	491
8	-2788	1379	940	1609	-234	1903	-33	71	298	946	84	39	275	449	34
9	22513	-20237	-2132	2843	-1061	532	-488	232	315	465	332	202	297	63	149
10	26216	-31727	-9230	2850	-4442	-1679	-1135	-363	-1927	-1462	-752	559	-538	-168	-374
11	3274	3290	418	-3501	-396	1395	-49	-498	279	602	52	-216	126	353	98
12	2156	-812	-505	-3476	2739	2281	-682	-306	1674	1532	113	-256	1498	1139	-158
13	25032	-28064	3150	2411	-1255	-2684	1784	787	-854	-455	1050	-163	-1430	-290	531
14	18431	-19185	1333	-612	622	-1778	2241	1078	1769	590	790	-574	547	471	1143
15	1704	-503	-1338	-1742	1788	645	-665	-413	1543	1286	-602	-282	275	317	-499
16	12010	-21507	4167	143	-3133	-4639	324	-3203	-2185	-383	-652	-1581	720	-1947	118
17	12706	-22262	5739	-428	-4481	-3729	-1098	-2298	-2846	-1599	-281	-426	1026	-1042	118
18	14586	-21160	4261	-1292	-3902	-2735	-1945	-1044	-3411	-2903	-448	816	812	-35	-444
19	-10306	6215	87	-3410	-362	2723	-439	207	-701	1196	-343	344	-285	196	592
20	6557	-5698	-4332	1957	-2586	679	792	-1249	894	549	-16	110	-152	175	67
21	35954	-27188	-3972	-2868	-1182	-2428	-1843	797	-241	-975	-653	-591	-622	-1027	-796
22	29146	-22525	-5990	-1495	-921	-1008	524	2637	1635	-39	1049	73	460	-264	-149
23	8964	-1425	-4036	709	-1143	274	425	357	1167	1333	-498	1141	-486	124	-11
24	-12398	-16947	-4437	3773	-5109	-2135	-691	35	59	-1562	-398	-1991	1180	-1992	-848
25	-22879	-19725	-7462	9185	-8427	320	-1326	1642	-1161	-1345	-998	-686	596	-285	-559
26	-15398	-20795	-6017	8019	-7447	-718	-204	1067	-1025	-2896	-1112	-1178	331	-76	-1561
27	32469	-2495	2388	-1640	509	794	-352	-92	387	1052	-3	-232	13	665	162

Table C-19: Fourier coefficients (10^{-5} mm) for the measured imperfections of specimen 3C64-900-1

Line	a_1	a_2	a_3	a_4	a_5	a_6	a_7	a_8	a_9	a_{10}	a_{11}	a_{12}	a_{13}	a_{14}	a_{15}
1	-53158	-27696	22975	-649	11001	-10325	1749	1078	2933	-2834	2979	-1343	1107	-2248	1524
2	-32564	-47067	36312	-1270	5130	947	3442	-847	390	-13	-357	696	-928	716	-633
3	-46893	-26966	16812	-3304	1908	224	1500	-2278	149	-1225	-596	-1014	-765	-447	13
4	-24014	-15728	7141	-3680	456	2275	992	-998	176	-1157	1019	-907	259	-787	95
5	-18464	574	-13972	5737	-5704	-5452	-393	1638	-4282	1835	871	-501	264	2181	-582
6	14668	-1489	-12686	9171	-5602	-4125	1460	4116	-7546	3285	937	-955	-468	2959	-1879
7	31768	-3897	-6786	7490	-1975	-2996	1759	4301	-5110	2066	492	-993	-1086	1852	-1278
8	-19297	-7207	-2202	1222	371	-1134	-17	-2589	-231	-233	138	-171	-305	-592	124
9	-18329	-14702	1268	-724	1660	-2486	834	-2788	-200	-1165	456	-88	99	-348	363
10	-2747	-27339	8902	218	4806	-4205	3610	-3271	1396	-1372	1456	-546	265	-642	526
11	-50076	9140	-4014	-503	2	-7828	184	1204	1899	-2062	718	-2007	474	-1965	1109
12	-37952	3686	-6617	5576	2979	5971	3463	-267	1130	2540	1100	1460	1087	1652	555
13	-7241	40300	5517	-2187	3968	3881	4222	3013	1114	932	1223	869	29	582	602
14	-24112	27788	-948	-2955	674	2714	1158	3426	562	391	-81	1331	-268	1230	93
15	-20827	18323	-1189	-2163	192	2591	132	3367	103	474	239	1071	-194	981	427
16	31533	-24656	-1022	-5717	-4447	-4120	-291	-2708	-1385	-2673	-1701	-1929	-1138	-1695	-596
17	30236	-28506	-4123	-2970	-4938	-6276	167	-3128	-2087	-2895	-766	-2070	-1737	-1120	-1071
18	25931	-26409	-1487	-3095	-4805	-4066	-920	-1935	-1617	-2226	-1478	-1222	-2014	-863	-1421
19	10549	9464	16032	-3432	3942	9298	8005	-2971	980	6121	3165	-401	1927	1470	1497
20	-51466	31723	-1138	23870	-2490	82	608	1105	1549	-558	-288	986	452	452	384
21	38095	-922	20606	308	5683	-4716	2758	1122	158	607	425	631	-947	520	-1100
22	7531	-4578	11303	1579	2947	-4218	1363	206	-50	-228	486	623	-129	273	-461
23	8245	-17518	8287	-495	1461	-4599	1125	-1629	932	-768	616	-464	219	-286	284
24	-36747	29209	-787	7528	-4359	7899	-4910	3398	-2147	1515	-1281	691	-1022	504	-547
25	-27223	26935	5474	7543	-3070	9682	-4559	3332	-1300	1156	-919	1054	-849	524	-385
26	-8771	21081	1720	7712	-2515	8162	-4750	2361	-2374	767	-2032	812	-1546	607	-913
27	-20445	14144	6244	11135	1590	-3257	4467	5047	-3729	1506	-709	3569	-1781	2249	-83

Table C-20: Fourier coefficients (10^{-5} mm) for the measured imperfections of specimen 3C64-900-2

Line	a_1	a_2	a_3	a_4	a_5	a_6	a_7	a_8	a_9	a_{10}	a_{11}	a_{12}	a_{13}	a_{14}	a_{15}
1	-26455	-25157	-1100	-21555	-2603	4897	192	-3179	2563	246	189	-214	496	63	-906
2	66212	-912	27288	-517	4327	17	2072	-561	-568	-669	-1113	-1857	-852	-889	814
3	40371	-1354	19126	-433	3772	545	2102	-682	418	-420	-378	-1015	19	-401	390
4	28772	12155	11857	3637	2689	1923	870	195	1122	458	23	159	-31	188	182
5	-35184	-7966	-8483	-6914	-3485	-2410	-3342	-1363	-1393	-1397	-623	-540	-340	29	-96
6	-19873	-2023	-5252	-5965	-4890	-2689	-5058	419	-2405	-349	-1632	102	-812	335	-83
7	-15041	213	-8069	-4401	-5220	7	-5638	2004	-2373	631	-1699	598	-257	249	167
8	-2476	1770	5763	-2740	-767	-3465	-99	-723	942	130	-630	-1791	-410	-52	404
9	-12594	-7204	2357	-10272	-3274	-4984	-741	-1430	163	-251	-437	-1622	-893	-677	-93
10	-8487	-4957	1210	-8823	-3321	724	1327	996	502	1910	557	1030	602	1277	445
11	22705	-7518	12995	-10962	-696	4505	2694	-6185	-3050	-2074	-447	-4540	-1666	-2782	-900
12	11633	-25087	1107	-13636	-58	-578	4337	-6233	-2859	-1822	153	-4266	-1947	-2482	-775
13	-28238	14396	311	5113	-3942	-1916	-1394	-403	425	-1718	841	-1256	537	-1177	763
14	-21435	11852	2058	3936	-4391	1238	-2638	1373	-134	353	-371	828	-781	586	244
15	-1033	611	6549	751	-1527	1285	-1047	680	988	375	-694	931	-493	291	255
16	-6741	10611	-1199	2530	-1786	4871	-2322	2742	-2223	1377	-969	984	-803	502	-541
17	-19569	8910	-331	354	-5762	6444	-3449	2208	-2870	1486	-1365	1256	-1036	372	-359
18	-38039	12032	-5657	5272	-7923	7522	-3211	3546	-2267	2008	-796	1496	-293	833	71
19	-37625	-31448	3243	-25019	-2024	1833	2199	-2758	800	188	-526	152	1427	-185	-1332
20	-10884	-5401	-1783	4514	-1975	-2794	1041	874	-1344	-134	741	-623	509	-307	931
21	35870	-29149	7771	120	3349	-3792	2715	-2118	1339	-1694	1144	-614	185	-424	180
22	13728	-19749	4080	-2034	-695	-3883	-175	-1811	340	-1893	360	-1098	114	-906	-152
23	9182	-11573	5781	-1324	-1146	-2567	34	-1508	648	-370	312	9	561	-607	-117
24	-26274	6717	-13540	720	-1565	271	-2485	1001	-2505	624	-1684	298	-1592	798	-1250
25	-40425	9037	-18475	2266	-3989	884	-2022	375	-3201	1495	-811	1173	-1286	893	-918
26	-44596	11209	-15514	5066	-3253	1179	-3013	964	-2697	1014	-1172	776	-1154	532	-611
27	-1733	1268	13903	8262	2549	-3136	8601	2107	1454	-1841	2082	-212	1899	-343	-142

Table C-21: Fourier coefficients (10^{-5} mm) for the measured imperfections of specimen 3C64-300-1

Line	a_1	a_2	a_3	a_4	a_5	a_6	a_7	a_8	a_9	a_{10}	a_{11}	a_{12}	a_{13}	a_{14}	a_{15}
1	-18178	-15887	170	-20988	-7614	-422	1576	1598	-2847	-4091	1226	1218	-1922	-566	1330
2	189499	32781	-7937	-16143	24927	11425	-5802	-7113	5142	4390	-2032	-3436	1675	-65	-644
3	108124	20176	-2928	-7632	13332	5984	-1803	-3256	2524	1810	-856	-1512	1	202	174
4	52585	18196	1847	2875	5568	3440	1582	60	1268	1396	839	201	-56	524	159
5	-77020	-21395	-11239	-5696	-9003	-4608	-4663	-3403	-3226	-1904	-2442	-1183	-1231	-1483	156
6	-64047	-8722	-12797	-4381	-8257	-3243	-6680	28	-2767	-1405	-2257	-302	-827	350	513
7	-56083	-597	-15171	-2546	-6064	139	-5298	1910	-3247	-1013	-2229	622	-33	1391	43
8	3537	103	4917	-2452	-2116	-1841	968	-907	1346	-273	-315	-1259	-372	-150	172
9	-7725	-8613	-768	-6906	-3169	-2322	1309	-2694	-224	-758	-184	-1073	-1029	-840	181
10	-6141	-8093	-3055	-6852	-2973	1474	831	-459	766	1558	565	930	483	1327	1234
11	30572	-13082	13372	-13094	-1055	1784	-404	-5824	-3702	-2265	-2476	-4344	-2779	-3365	-1740
12	2843	20535	10000	8752	-5058	-3594	4839	6813	-3879	2933	-613	3394	-2539	3756	-1647
13	-21616	15109	-3278	6643	-3546	-2393	457	-99	731	-2226	1153	-1347	685	-1867	1239
14	-19123	12440	-1332	5465	-4517	1155	-828	1574	-511	-188	307	809	-423	54	472
15	-1066	1076	5067	1286	-3150	1544	-314	1015	555	-246	399	908	-250	177	351
16	-6540	6486	-5902	3750	-3684	5216	-3949	2728	-1697	232	-1919	748	-446	505	444
17	-12074	7146	-3151	5565	-4754	5385	-5519	3645	-2827	755	-1831	659	-419	593	-208
18	-28511	11323	-6681	7776	-2692	3902	-4976	3066	-3336	1676	-1587	592	-884	717	-465
19	-33320	16636	-689	23138	-16	-1522	6602	4303	1842	-873	537	1075	969	1114	18
20	-7012	-267	-4280	-1330	-1179	-7232	101	979	-493	-1428	-94	-503	135	-784	348
21	73430	-43116	8114	-181	4476	-3319	4191	-2525	1055	-1364	1205	-768	294	-917	774
22	32318	-27695	3446	-641	1260	-2752	2772	-2503	300	-1343	962	-517	-566	-827	180
23	8806	-16607	1012	-1729	531	-2227	1279	-1827	13	-247	216	-353	-400	-860	-166
24	-45358	6776	-9029	605	-4663	1173	-2022	2162	-208	-489	-2072	-135	133	1475	176
25	-56944	9535	-12167	142	-5291	1602	-2151	1408	-1863	667	-1233	318	-246	1355	-248
26	-51330	10319	-8375	2484	-5904	1132	-1775	6	-967	938	-774	365	-256	411	-172
27	26948	-955	17492	-580	5403	-5561	3978	-754	208	-1957	2491	-1620	2034	-2051	-409

Table C-22: Fourier coefficients (10^{-5} mm) for the measured imperfections of specimen 3C64-300-2

Line	a_1	a_2	a_3	a_4	a_5	a_6	a_7	a_8	a_9	a_{10}	a_{11}	a_{12}	a_{13}	a_{14}	a_{15}
1	8710	-10458	809	-19646	-3082	6966	4957	-743	232	1829	-350	75	431	965	-223
2	100011	3276	30585	1395	2082	837	-257	-603	195	605	451	-311	-729	0	-868
3	52657	3624	20055	1925	1658	988	214	-860	248	86	731	-841	288	-763	87
4	20999	14442	12315	5767	2892	1644	1808	1075	864	1589	1024	12	658	212	-13
5	-18921	-11946	-5400	-3151	1831	-7543	-7125	-4647	-480	-2676	-552	-2139	-1371	-1468	84
6	-20661	-17434	-8009	-7656	-36	-7744	-3896	-4403	-1359	-3978	-150	-1458	-911	-1160	-275
7	-40650	-21566	-13780	-9849	-2679	-6468	-310	-4487	-1756	-4305	-725	-1560	736	-532	-46
8	-25143	2620	1859	-3297	-5772	-3605	-603	-649	626	281	-936	-1365	-1037	-373	-43
9	-48130	-5062	-3178	-6473	-8180	-3718	-1726	-1595	-289	-180	-521	-1282	-1320	-519	-245
10	-42207	-59	-1532	-3704	-4824	720	752	1925	1098	2524	1019	1585	660	2012	852
11	-11611	-14362	8717	-9296	-2280	4246	908	-7888	-4274	-3809	-418	-5196	-3043	-3085	-1104
12	-19958	-7682	-10380	141	-2310	5970	1582	-2562	115	1845	536	-195	861	508	1072
13	36230	42082	10170	-1905	2675	4301	4979	1188	948	1644	818	612	80	655	144
14	4661	28172	3216	126	-815	4642	2576	1964	143	2429	56	803	-336	1106	242
15	-5385	15248	2171	1101	-545	2821	973	1689	869	859	447	547	-391	999	-217
16	-51108	-13631	-6874	-12118	-4044	-7729	-5800	-4724	-3209	-2771	-1577	-1994	-603	-192	-694
17	-82238	-28624	-18408	-13792	-8138	-7626	-8265	-4447	-3867	-3238	-1273	-1655	-1919	-116	-554
18	-74377	-34516	-17130	-14355	-6269	-5212	-7176	-3288	-1723	-3731	-1540	-1303	-2394	-503	-152
19	14228	25659	17585	-1745	7304	8832	6084	-4186	1910	3209	2636	1169	1528	391	1564
20	26732	16575	21242	-4520	5739	5325	4051	-498	624	1850	1250	672	1624	1239	248
21	67934	54549	39110	3103	-592	1408	1787	744	1190	-817	-469	-1641	-790	-481	61
22	6609	36590	18936	6384	-1157	3223	2105	2291	1847	2311	563	189	279	707	-12
23	-25653	20544	5753	6294	799	1704	116	1969	2641	3053	1014	1477	1469	941	-22
24	-11128	-10596	-1671	3994	-1365	-5626	1226	-1925	-3715	-2880	282	-2784	-2298	36	-506
25	13585	6710	2673	12748	5009	-1959	4285	1808	-2091	-1015	1409	-1437	-1701	366	-753
26	72645	35887	24967	21757	16778	9904	7776	8652	4599	4136	3469	3335	454	2597	1461
27	-27010	2423	-4522	1886	1362	6338	4026	1788	111	1140	755	1504	2023	1283	909

Table C-23: Fourier coefficients (10^{-5} mm) for the measured imperfections of specimen 3C64-100-1

Line	a_1	a_2	a_3	a_4	a_5	a_6	a_7	a_8	a_9	a_{10}	a_{11}	a_{12}	a_{13}	a_{14}	a_{15}
1	6009	-25287	285	-25602	-5280	3502	1682	-2188	-12	1320	-144	-276	536	-35	346
2	78473	2124	26046	830	5401	1527	1556	-2266	-1174	-997	-377	-1490	-613	-1198	177
3	37917	4409	17533	1394	4594	1207	1426	-1849	-1150	-965	409	-488	-72	-642	326
4	20470	16754	11596	6369	6408	3456	2049	1295	954	1239	774	634	467	615	363
5	-3674	6824	-11706	1944	-2497	-2646	-487	879	723	-439	-2219	-104	-1652	-1047	-1457
6	-9109	7117	-11876	-2274	-976	-4019	-369	-1027	-1036	209	-2784	-1549	-864	-1824	-982
7	-12682	6772	-16669	849	-7023	-3294	307	-1282	-1123	552	-2445	-1994	-4389	-2297	-3294
8	-26741	-633	3542	-2887	362	-4780	-1036	-1416	-743	-1598	-1013	-1452	-598	-661	352
9	-62528	-19224	-1091	-8266	-2066	-6066	-2488	-2864	-2313	-2099	-823	-2085	-1157	-1307	-245
10	-74054	-20210	133	-4709	-1116	384	543	238	-811	1331	491	1399	305	1776	1177
11	16643	-12350	16339	-11934	2165	3584	3357	-6443	-1760	-1513	304	-2728	-693	-2510	-802
12	18553	6324	6730	16831	-2301	1177	-704	7906	-3545	3762	-1790	5704	-2809	2910	-1138
13	-20808	11695	-5203	5614	123	-1416	2232	-1915	417	-1717	1105	-1808	1206	-1637	1098
14	-31309	8647	-7163	7037	-1427	1734	-609	128	-1149	915	-507	727	-264	198	292
15	-18877	-3537	422	1920	164	1591	124	-287	459	560	-718	236	-408	-111	351
16	-31432	11611	-11005	-2870	-6513	1983	-1884	1208	-3565	783	-1368	397	-735	-1046	-277
17	-37856	10843	-10593	-3285	-8681	2725	-787	1378	-2953	-306	-1049	-152	-173	-777	-290
18	-40177	12718	-11590	-1780	-7230	1667	-555	1850	-892	-473	-177	72	121	-1008	-891
19	-26989	22423	3318	25038	-1352	-2668	1504	4388	2003	-1148	-145	876	790	1212	-427
20	-7463	-255	-9490	1994	2069	3252	1310	84	1758	1784	1234	1914	1047	1076	1695
21	30529	-43045	6462	-1645	6565	-4618	4494	-1306	767	-1520	1007	-1227	280	-621	427
22	2886	-26268	193	-1215	3793	-3778	1575	-1584	-558	-761	-496	-1325	132	-398	-94
23	-9772	-11597	-1917	-526	3089	-1679	1234	-1489	-667	-182	-543	-999	-82	-603	492
24	-4278	2913	-4180	-872	-3150	-749	971	2283	-2010	1814	-784	-5	-218	-415	-65
25	-9131	5991	-6725	-138	-4295	210	1192	508	-2020	1870	215	487	1	-412	-793
26	-53	6689	-395	525	-2312	-999	915	-994	389	835	516	284	515	-1021	-1044
27	-19931	9168	7540	-5488	3148	2794	7009	193	610	1630	1831	1096	1157	477	494

Table C-24: Fourier coefficients (10^{-5} mm) for the measured imperfections of specimen 3C64-100-2

Line	a_1	a_2	a_3	a_4	a_5	a_6	a_7	a_8	a_9	a_{10}	a_{11}	a_{12}	a_{13}	a_{14}	a_{15}
1	-51471	-33273	-7265	-25111	770	2313	3486	-3863	-890	835	442	-493	717	-237	776
2	90103	-6146	27460	-6285	2164	258	-902	-930	-438	-779	-231	-1522	-1281	-873	-1122
3	57463	-3028	20089	-3347	1988	234	-76	-644	1226	-20	191	-554	-699	-788	-94
4	39186	9954	15000	2727	1020	1493	715	393	1332	651	628	103	397	-30	-53
5	-32903	7418	-17470	-5798	-3456	18	-2266	-730	-1649	-575	-762	-1296	-233	-839	-745
6	-38951	7035	-15603	-4036	-3292	1497	225	-1094	-2614	-3215	55	-1313	-1453	1	-1262
7	-46998	1015	-11168	679	-1706	392	480	127	-4338	347	-915	204	-2561	308	-1671
8	8034	-2239	5896	729	-1488	-1981	-415	196	1024	-749	267	-465	-565	-188	10
9	-4200	-15280	1028	-4182	-2792	-2650	-69	-291	-348	-673	-115	-248	-803	252	-162
10	165	-17924	2743	-4217	-2246	1053	490	2209	569	2203	1235	1709	820	1885	1087
11	-10962	-10232	-1258	-18045	-1644	1062	3114	-8944	-4577	-2993	-1016	-4310	-2694	-3407	-1463
12	306	-8270	12970	8193	5599	-2132	1640	1263	-371	-2172	1453	-246	507	-1099	120
13	67127	-37784	19923	-5384	3747	-3988	886	-1791	1115	-1524	-246	7	-668	-580	54
14	18915	-19100	7915	-2975	1841	-3644	1830	-1668	750	-2493	426	-489	-88	-949	335
15	4726	-12334	5593	-3311	1848	-2032	1636	-1633	843	-2599	1077	-1036	518	-755	579
16	-26666	18822	-6973	2373	4904	1788	-778	3202	-4080	3439	-853	2364	-426	681	-757
17	-18499	13554	-13049	1056	6478	3181	2795	3495	-6031	4953	-1366	3042	35	1302	-1182
18	-3760	2280	-9484	-3878	5919	2910	5219	1792	-6220	4327	-1806	2310	749	1680	-903
19	-48968	-5301	-17894	2997	4610	-6599	-151	-1136	200	-41	1690	741	917	-1012	1173
20	4123	-8528	-1837	1621	869	9521	211	95	1399	3275	734	2135	1405	1307	1667
21	77881	-25250	6391	-362	3049	-4376	3902	-1429	709	-916	1203	-1281	-120	-893	-1
22	28429	-17385	-1144	-2256	-817	-4899	795	-2029	-558	-1403	183	-1253	-361	-820	-221
23	8303	-9613	36	-1854	155	-2934	1095	-2191	160	-977	538	-914	248	-800	531
24	-18289	-800	2600	8088	107	2020	678	2588	-3949	1270	-1480	423	-231	-106	-699
25	-32138	642	-5471	11034	-2820	1470	4859	218	-4487	2919	-811	1295	544	798	-522
26	-39078	5678	-10500	14389	-4339	432	6116	-146	-5018	4124	-1605	1844	930	2212	-823
27	-5806	9024	12702	-5012	10090	5025	3433	-703	2502	2941	2672	879	1710	-474	1872

Table C-25: Fourier coefficients (10^{-5} mm) for the measured imperfections of specimen 4C120-900-1

Line	a_1	a_2	a_3	a_4	a_5	a_6	a_7	a_8	a_9	a_{10}	a_{11}	a_{12}	a_{13}	a_{14}	a_{15}
1	1098	-2376	-709	-1936	-1010	-181	73	-649	21	199	-47	-95	219	-123	-48
2	97247	-38527	-3621	1528	-3505	-858	22	-1019	-274	152	-179	-362	-373	-5	-342
3	62977	-30596	653	6115	-4805	765	1696	-1697	516	143	-433	-141	-377	233	-320
4	19964	-5300	-758	2955	-91	-101	1097	115	-141	608	4	-114	7	-26	2
5	-17849	-16604	-12502	8802	-3148	-6066	3170	-1984	108	-59	600	171	425	498	620
6	-27950	-19525	-16463	9883	-5530	-5471	1511	-1583	-981	49	-852	352	-514	630	-291
7	-14796	-15868	-13566	6608	-2309	-4572	1667	-421	-1481	-75	-2054	722	-1188	1122	-502
8	12184	-2979	-3963	3497	395	2036	-783	1254	390	-643	-142	416	-219	-28	-379
9	10257	-14112	-14067	3541	1325	820	1018	1536	930	346	-371	266	71	-113	552
10	44120	-15658	76	4032	3451	-172	1801	1212	141	942	-148	354	227	352	356
11	-7782	-6535	-3738	-1228	-2003	2221	-466	-607	821	-1041	-491	90	-252	-159	-520
12	20341	-7615	-3330	4020	-98	1650	456	-1068	-1320	837	23	-559	25	-399	127
13	17464	-15874	-967	10848	5319	-5743	-295	-1257	-690	-1120	-124	-914	-155	336	562
14	21381	-20084	-5050	12832	7142	-5426	-1750	-195	-1104	-1530	-1293	-705	-658	367	-54
15	10774	-19164	-9705	12378	6070	-4623	-2335	597	-1617	-1572	-2606	-753	-1142	529	-488
16	11629	-6102	-3960	2060	1886	-765	-169	-131	107	-677	-649	-537	-319	-266	-17
17	19799	5396	-1889	-3318	1739	-1899	-238	-265	354	-36	-293	224	-341	-154	-136
18	21328	3151	-4611	-495	3382	-4436	3133	678	-1375	-68	370	269	311	259	-192
19	17400	8461	-9000	-536	3179	-4245	1292	-55	-1892	478	161	260	128	538	100
20	12113	14247	-9578	2456	2999	-1512	554	548	-1203	1678	-142	782	516	1339	342
21	11007	3777	-2563	-840	832	605	-160	-43	-728	440	-424	-357	-29	-309	30
22	6615	-618	2893	-3276	-438	-735	-811	-657	115	-197	-919	-306	-106	-988	-247
23	57257	-16530	9437	3304	1431	798	2825	247	-258	1202	853	-776	118	1033	60
24	34747	-16930	5887	318	1701	-196	1800	-120	823	294	265	-416	306	246	148
25	17180	-2727	864	-116	2959	234	-638	322	1497	-488	-650	307	738	-560	-173
26	-23128	-20877	-8555	-2714	-9698	-6444	-3141	-3803	-3954	-1939	-1954	-2026	-1630	-426	-1121
27	-29500	-23812	-13037	-2654	-12008	-6640	-5339	-3252	-5019	-1626	-2459	-1392	-1150	-244	-769
28	-13046	-18206	-7821	-43	-8818	-4366	-3931	-1337	-3842	-233	-2294	7	-1266	764	-647
29	22337	-614	1586	-2358	2671	-609	249	-450	1207	-451	243	-217	408	-589	43
30	59971	-16578	5911	-1328	4237	-718	2554	-48	1862	65	967	-315	898	-138	198
31	68893	-15012	2646	1879	-12	923	1194	651	5	1242	243	-47	82	505	-382
32	-2438	-2110	495	-2674	907	-1273	-1586	131	740	-1142	-982	551	274	-914	-22

Table C-26: Fourier coefficients (10^{-5} mm) for the measured imperfections of specimen 4C120-900-2

Line	a_1	a_2	a_3	a_4	a_5	a_6	a_7	a_8	a_9	a_{10}	a_{11}	a_{12}	a_{13}	a_{14}	a_{15}
1	19323	-773	37	751	999	385	-1198	184	32	477	-793	105	-158	372	-82
2	74317	6349	1976	-1247	-410	-258	1484	124	116	-358	624	523	-65	-115	0
3	58619	-810	4898	-1766	2342	-383	2023	-649	1367	-414	698	-202	411	-227	279
4	18599	-4282	2250	344	1853	160	-64	-72	814	77	183	-232	250	145	149
5	-28977	23090	-6688	2422	-5495	715	-1378	-1192	-1582	-1403	-937	-875	-730	-714	-736
6	-37582	21519	-9191	1523	-6825	1689	-1340	-128	-1635	-249	-385	267	-418	-11	-60
7	-39671	16247	-7403	1690	-5665	3136	234	1760	-777	1326	715	1850	126	999	290
8	20071	808	2335	-470	3334	-176	-730	-491	1427	-114	-778	-648	629	50	-280
9	69156	16335	11182	1013	3773	1256	3067	497	2093	-385	1012	272	714	-190	466
10	86522	19724	8242	-1353	-723	588	2565	297	-482	-889	640	485	-317	-889	641
11	22595	2218	-1875	1711	2168	138	-2915	657	1352	645	-1612	-833	1147	705	-533
12	9639	-1841	2128	1737	1640	502	-167	93	1064	373	319	-431	500	109	603
13	-8905	10232	1339	-118	681	849	568	676	454	204	475	877	316	690	-8
14	-6849	10131	1767	-1295	127	397	38	-35	-379	28	-132	861	-253	534	-346
15	-10716	8859	1188	-1389	-838	521	156	144	-798	169	-968	1042	-883	519	-808
16	5594	-398	-1243	-671	3330	-217	-2342	-388	1676	653	-1242	-926	777	613	56
17	861	-4779	-4182	1774	-17	1150	-1080	502	968	-1000	-284	202	-151	-143	-398
18	-29210	-20936	-15151	9009	-913	-437	465	2153	-1062	1457	-429	1187	-607	1573	27
19	-20947	-24942	-17278	10201	-2985	-2609	278	228	-1714	968	-1283	844	-701	1193	-251
20	-21526	-17287	-14093	9409	-4509	-2573	-548	-484	-2856	1316	-2119	857	-1576	1460	-795
21	14534	-5178	320	2867	-34	-601	1468	-46	287	613	57	-393	162	-352	253
22	15381	-97	-563	3481	333	-138	-1203	226	-67	-239	-793	-483	-400	443	196
23	128125	-2684	5369	6660	1833	23	-155	2259	-364	35	-24	-242	86	306	194
24	99572	-10413	9430	7763	5327	-732	1400	-931	-772	-432	-354	-1056	-2	-300	459
25	26853	-8580	2615	761	2340	297	1632	-1646	-280	449	483	-591	587	-212	547
26	-14823	2163	-7917	8851	5315	-3935	-582	-2260	-703	-3232	-1308	-2828	-349	-1055	521
27	-32190	1326	-17134	11686	4626	-3148	-2118	541	-1342	-1656	-2623	-1211	-1340	249	-263
28	-24606	-5264	-14850	9197	5903	-1009	-1036	2202	-104	-260	-2024	12	-1281	752	-761
29	14617	-1263	-115	3164	3046	1013	59	1108	744	137	-163	180	182	262	473
30	26744	-20560	-10469	7098	9565	1813	-212	2978	1554	328	-323	91	-284	237	-118
31	53224	-27565	-4492	3266	6831	373	132	972	1072	119	265	-54	-140	-167	-309
32	24291	-5195	-3411	2024	-454	1173	-772	-1321	-999	998	-479	120	363	86	192

Table C-27: Fourier coefficients (10^{-5} mm) for the measured imperfections of specimen 4C120-300-1

Line	a_1	a_2	a_3	a_4	a_5	a_6	a_7	a_8	a_9	a_{10}	a_{11}	a_{12}	a_{13}	a_{14}	a_{15}
1	2033	-419	-1884	-198	3681	-355	-2069	451	1411	-390	-1363	730	425	-789	-568
2	-35549	-23109	4326	-1631	-2507	641	1726	-540	-792	323	674	-726	88	761	176
3	-13593	-18837	4233	-3004	1502	1043	241	-1034	836	464	414	47	14	168	-133
4	-3103	-2875	274	-3040	2903	-2	-1829	-271	1774	-945	-514	549	226	-1088	62
5	-7753	-3638	-6272	2271	-11592	-3820	2679	2818	-2275	551	-1488	-1490	1276	2568	-649
6	2690	-3453	-4993	1464	-10113	-4833	116	2195	-2262	54	-1565	-1735	181	1368	-625
7	21203	-3991	1936	1414	-5411	-3508	73	2376	-704	-533	-1161	-1584	-280	1615	164
8	12013	-3814	4690	-2403	2689	-109	685	-307	1003	-635	580	120	318	-552	293
9	59929	-21972	11636	-1909	4638	-56	2494	-516	1546	-53	698	-229	502	278	179
10	95515	-27651	11281	440	392	-542	1244	702	-595	546	154	305	-286	470	-270
11	4059	1175	2043	-1149	2716	-1117	-826	-208	480	-450	-464	41	87	-571	-68
12	8745	-2767	-3644	2597	-1421	2313	-428	-1022	-268	1221	-161	517	486	-45	631
13	8989	9066	-5206	12401	1199	3127	-4400	1288	-1073	-1186	-2640	-1922	-1299	710	904
14	26470	286	-4333	11468	5324	2403	-4253	2185	-288	-797	-2297	-1037	-927	763	414
15	25376	-8692	-5479	7397	8606	2301	-3004	2505	1790	-78	-2468	-220	-898	1443	444
16	-9124	-4297	-279	2636	1770	997	494	304	1095	-919	-121	-202	-127	-538	329
17	-17777	-3868	-3529	2435	-788	1848	-363	318	1060	-1415	-176	41	361	-294	-353
18	-25959	-2395	-19708	5108	-7866	2505	-2366	3487	-230	-1032	-2539	242	-1259	1969	776
19	-21467	-13394	-19826	5542	-9030	132	-465	2784	-39	-267	-2097	263	-728	1226	542
20	-20322	-15904	-16295	4982	-9167	-506	1006	2330	-540	1601	-2429	902	-243	2237	403
21	12332	-2375	-4125	3337	-1439	859	765	-7	-128	452	-430	307	-312	66	-202
22	-3017	-2266	-1167	2496	1232	-1159	-453	449	-825	-247	-1261	-858	-347	-32	149
23	66865	-1204	3537	3294	1963	674	-126	1112	116	-363	184	93	-139	-16	634
24	49242	386	4382	8159	4224	2416	261	-822	-71	-74	284	-34	213	-243	796
25	4994	-3181	-1273	80	1392	1921	307	-1437	-48	328	668	42	579	-536	590
26	-3571	2562	-9416	11294	965	-4991	-1071	2586	-3545	-2505	-3604	-3316	-541	1499	-1121
27	-12572	-3379	-13982	12978	6538	-3905	-2471	5057	-816	-1689	-2395	-2203	-1423	1612	-318
28	-9424	-6293	-10464	9075	9780	-2501	-1477	6038	2511	-921	-403	-999	-1953	2048	317
29	6080	-6243	-780	849	910	937	654	13	524	-138	-284	21	246	-579	208
30	38061	-22705	-10692	327	6298	1520	977	748	1817	97	-72	183	328	-284	353
31	78044	-18801	-6453	1502	2044	2001	-61	1303	474	535	147	638	-50	236	65
32	14243	-6183	-2417	2002	493	271	-24	-1052	-1052	1067	107	-264	481	-162	354

Table C-28: Fourier coefficients (10^{-5} mm) for the measured imperfections of specimen 4C120-300-2

Line	a_1	a_2	a_3	a_4	a_5	a_6	a_7	a_8	a_9	a_{10}	a_{11}	a_{12}	a_{13}	a_{14}	a_{15}
1	-2607	-2865	-911	-1240	-231	899	-1368	-479	75	441	-436	-461	-35	881	335
2	60329	23562	1914	-2713	92	447	1365	-242	-229	-1065	601	-490	390	-552	26
3	44644	21645	5665	506	3361	2277	1585	-849	1095	-479	462	-32	401	-359	-35
4	7140	4618	1828	458	2945	1925	439	55	802	387	23	130	104	-12	111
5	-38742	7382	-12341	3244	-7790	-1753	-1754	4117	-1412	-736	-309	-433	-245	2045	-101
6	-43043	1705	-15408	4556	-12421	-3183	-3842	3053	-4234	-126	-1362	-1539	-384	1077	-770
7	-15919	1242	-7369	6112	-7961	-3861	-1516	1388	-3620	246	-741	-2195	-744	1067	-768
8	-1125	8814	59	3782	1805	1865	-1561	1149	1709	-106	-645	505	283	-15	-411
9	-21027	42749	2530	2729	-1485	3373	617	1326	967	-699	106	371	-38	-459	-210
10	-23098	65987	3364	-4694	-4615	1226	3111	1586	-386	-400	573	464	-341	-77	486
11	1765	2053	277	-2185	1820	48	-1763	-422	1650	295	-997	-265	1159	592	-646
12	-3183	3411	-949	-4569	2602	3390	-140	-813	785	1839	-305	-891	581	1228	-247
13	15150	-20609	-5181	993	5149	-4547	-3296	2837	-683	901	148	-131	-1020	2318	-925
14	29094	-27647	-1669	-628	6998	-5220	-4617	2138	-337	883	-236	-225	-1778	1533	-716
15	32168	-21918	192	1031	6250	-2769	-3676	2088	-218	1611	-409	1117	-2191	1635	-511
16	3026	2469	752	-334	2226	392	767	-1192	656	430	-114	83	582	-120	-226
17	11087	2580	-791	400	257	-1055	-250	-338	500	-626	-19	158	-361	261	-283
18	12793	1144	-7711	-3955	10885	-2466	-1349	1098	-2535	2467	-259	-15	-1349	2177	-1559
19	10527	8830	-9769	-5389	12892	-1653	-1785	2174	-1613	2558	-411	-59	-1285	1728	-505
20	-2950	10326	-10310	-4671	8965	66	-2578	2828	-1509	2406	-1138	159	-1913	1905	-456
21	-3733	3769	227	-3920	1681	1266	1183	899	97	123	656	-162	208	-76	132
22	2209	4961	1927	-4264	333	2103	-28	-654	502	886	212	116	404	612	251
23	-311	-35670	804	-2192	-430	-2315	1259	1528	-471	-1532	262	791	-315	-854	423
24	7309	-29059	2754	-7553	3060	-1775	259	-694	494	161	1194	839	-296	-343	396
25	1884	-3746	928	-6495	3009	1629	221	-1547	817	1291	1048	-282	-4	326	726
26	-32868	-4002	-16226	7066	-13956	-4020	-3275	2275	-2652	-3027	-3412	-795	-1231	856	-924
27	-46984	-8834	-21661	7783	-17292	-2405	-4693	1693	-3055	-1695	-3335	-236	-1709	539	-483
28	-31463	-7622	-15921	6925	-9975	-1810	-3876	3008	-1486	160	-2209	-430	-1623	1211	-914
29	9051	-692	2033	-321	3100	276	283	-1170	366	670	282	223	336	158	71
30	44080	-13574	2975	-1995	3749	-1486	105	-1248	162	124	399	283	19	-148	154
31	50537	-16156	1041	-514	796	-1965	-38	-65	-162	-415	52	-161	-134	-391	116
32	3220	81	328	-5015	-116	2209	-119	-1576	164	1546	468	-679	189	651	583

Table C-29: Fourier coefficients (10^{-5} mm) for the measured imperfections of specimen 4C120-100-1

Line	a_1	a_2	a_3	a_4	a_5	a_6	a_7	a_8	a_9	a_{10}	a_{11}	a_{12}	a_{13}	a_{14}	a_{15}
1	10779	2194	1875	-2094	4471	2162	-381	-1449	1219	2081	-133	-1054	677	1110	-132
2	93603	-22290	2078	2160	-1604	-2325	1312	1082	-886	-974	306	710	-802	-881	538
3	65982	-22782	4977	-3522	1578	-2841	666	-1298	-7	-284	391	-376	-1111	-977	52
4	23297	-288	3398	-1753	2703	2077	515	-910	776	1614	267	-325	8	840	-28
5	-24975	-13837	-3945	-1276	-3375	-3509	-2016	-1078	-3010	-764	-1858	295	-583	-311	622
6	-45438	-10414	-11166	-1424	-6295	-2351	-5010	-728	-4816	-866	-2557	85	-434	-672	-189
7	-40116	-11676	-8731	-3474	-4197	-2308	-3694	-294	-3138	-779	-1936	-15	-579	-554	-304
8	38128	1628	7874	100	3323	1219	1514	-190	1294	501	621	-80	491	261	332
9	138518	-13414	12727	711	3799	-519	2160	-378	432	430	481	449	235	592	267
10	216001	-25326	12902	46	1260	-1954	1050	-304	-653	-1044	-178	68	-258	-348	-73
11	7669	4619	2733	-1412	2152	175	-31	8	79	932	-38	-91	257	201	-91
12	17579	1470	3286	-1480	3887	2964	21	-821	1372	2015	69	-549	695	952	-266
13	8758	-18151	1872	3387	436	-3335	-1811	704	161	1095	583	-640	-1160	538	-111
14	13041	-24122	2569	2913	16	-1843	-2015	1089	104	596	453	-592	-605	735	-205
15	16616	-23639	1962	41	265	-1220	-905	1038	87	537	599	-242	-380	885	194
16	11975	1623	3757	-1672	1877	220	78	-475	935	109	62	91	371	-29	-21
17	15636	3547	-1318	-3608	-589	-853	1285	-457	487	282	996	595	416	-29	192
18	-10513	19614	-10130	-4572	-3389	3365	209	-2030	-463	400	-25	-436	-225	1623	-535
19	-6549	25207	-8193	-3066	-3931	3011	1164	-1717	-414	-20	-20	438	61	539	-193
20	-6933	23525	-3382	-621	-2843	455	2467	-1936	-1037	-206	-824	368	731	-370	94
21	10916	2827	-84	-1039	-859	-1396	1108	131	1041	321	297	101	-80	-147	-100
22	14054	3956	815	452	2958	439	-205	-197	357	585	-658	159	168	326	-261
23	27361	-34981	825	-432	-2445	-1772	1710	511	-1016	-324	673	366	-1437	-300	282
24	23501	-22895	776	-2891	763	-1080	2590	56	201	465	535	-151	-112	272	192
25	7169	-2891	383	-2486	2967	754	271	-430	1303	642	-556	-172	618	-44	-753
26	-23095	-2411	-6096	4737	-7501	-1569	-4597	-449	-2376	-1306	-2730	61	17	1314	619
27	-30596	544	-8975	4775	-9939	-1724	-5051	1202	-2500	-1055	-3431	1189	-339	1427	-181
28	-28547	-1087	-8345	3188	-8495	-2090	-4114	959	-2197	-1898	-3560	380	-1125	807	-419
29	21547	-149	1330	-1590	1620	31	706	-691	539	608	212	248	313	18	-349
30	75403	-22921	570	-3324	2243	-1829	1580	-659	603	-512	1144	268	554	75	95
31	97767	-26635	-2106	-138	-1026	-1587	954	-23	-155	-380	294	174	-180	22	137
32	17059	2377	-87	-398	4160	1031	-1252	-689	1931	956	-1156	-210	1145	276	-643

Table C-30: Fourier coefficients (10^{-5} mm) for the measured imperfections of specimen 4C120-100-2

Line	a_1	a_2	a_3	a_4	a_5	a_6	a_7	a_8	a_9	a_{10}	a_{11}	a_{12}	a_{13}	a_{14}	a_{15}
1	21314	4708	-1030	-740	-539	-1208	405	1034	1169	-160	-393	-237	3	-505	-262
2	130319	34739	8380	-3017	2931	110	123	-2391	-1005	191	-290	-224	-413	-64	-498
3	76877	35113	2049	661	3093	1838	2457	-3747	-273	1173	844	634	-48	659	324
4	28694	-7226	-954	129	764	133	1408	1511	663	-27	233	120	-127	307	305
5	-31467	-1113	744	-809	-6153	-6775	-9920	2199	-180	881	-163	530	-3705	-1090	-664
6	-54699	-2336	-5579	-1899	-12155	-6748	-9045	-2929	-3133	785	-2648	-1406	-3009	-526	-276
7	-46684	1001	-4711	-348	-8243	-4582	-5143	-2062	-2415	-435	-1852	-515	-1771	-216	85
8	21621	4750	-2530	-3602	1180	717	1223	-486	824	-3	943	379	529	137	-187
9	73421	18421	-9750	-12516	758	20	3036	-965	742	-388	1248	747	447	-16	348
10	112469	21289	-12378	-6197	-586	-309	161	-543	-227	-435	194	-69	-357	3	-48
11	13185	1182	-3683	-3388	-737	-1192	68	-364	-216	16	123	353	290	179	11
12	16248	6817	1462	-869	1314	-1990	-647	390	638	477	-244	764	-557	-167	91
13	-22101	-4117	-7669	-4360	2568	-1368	-523	318	-400	-96	-342	762	-375	-339	-565
14	-22114	-2957	-7074	-4080	2259	-295	-107	676	-1471	-73	-592	874	-317	-261	-578
15	-14327	-1103	-3992	-1306	1969	79	1362	687	-2050	1145	-25	1026	-751	108	-882
16	17193	6482	1057	-1191	1040	-2259	-359	412	798	282	-23	633	-599	-33	97
17	27877	5136	825	1670	2065	-2491	-267	815	924	-2097	-846	330	438	-811	-774
18	-15182	6596	-5995	5200	-7830	2606	-4032	608	-1460	-28	-3065	459	-1650	-135	-571
19	-10805	5610	-6308	3748	-6537	2732	-4789	1275	-365	-235	-1752	381	-1219	-340	-378
20	-16392	7376	-8042	2548	-5890	3181	-4947	2027	-610	99	-1435	256	-1344	-354	-1110
21	32318	-5756	3496	882	1734	-1736	-577	-188	373	-1581	-852	-386	144	-592	-518
22	29941	710	-313	-434	1360	358	-642	15	659	110	-139	-439	305	111	-604
23	113031	-23323	5799	256	-2926	324	1959	-629	-859	678	611	-832	-569	760	48
24	89648	-17557	13547	-315	1185	-398	2215	-691	426	-226	-740	-309	46	-22	-336
25	37343	-3182	6536	594	4599	-578	881	517	1764	-764	-333	448	683	-463	173
26	-69124	-10444	-17157	-3211	-12924	-916	-5459	-1696	-3832	-1898	-2939	-459	-1525	-974	-2487
27	-83814	-1339	-23959	-542	-16316	-44	-8393	111	-6569	265	-4954	363	-2915	565	-1431
28	-56501	-16097	-16288	-1394	-9656	-496	-5959	-1136	-6023	236	-3505	48	-2286	-1162	660
29	20644	1565	4028	-2417	2654	-1398	903	131	1687	444	779	715	811	164	65
30	31585	-12182	4696	-3645	2524	-1759	2172	274	2030	1125	1539	1152	1313	739	323
31	13676	-15007	-4069	-864	-1171	-847	711	733	1362	2204	2167	2015	1835	1266	865
32	21792	1320	-2822	-1368	2098	-569	-2241	636	1328	-634	-1084	664	271	-777	-197

Table C-31: Fourier coefficients (10^{-5} mm) for the measured imperfections of specimen 4C64-900-1

Line	a_1	a_2	a_3	a_4	a_5	a_6	a_7	a_8	a_9	a_{10}	a_{11}	a_{12}	a_{13}	a_{14}	a_{15}
1	-48997	-25939	8323	-18496	-333	3733	-1163	-2412	1907	388	587	-896	828	-126	-912
2	33465	6123	23783	-4695	1499	3283	2215	-906	-1863	-356	-574	-472	-1813	-197	144
3	11549	2172	14167	-3645	-1173	1757	1211	-566	-1213	-227	-1086	-300	-418	-34	-344
4	9634	12774	6900	2410	-907	2278	1009	361	-138	45	140	471	207	-93	-6
5	-23642	-22096	-5913	-12588	869	-6878	-434	-4863	-1169	-3777	-179	-1548	225	-1247	6
6	-18242	-18711	-7239	-12496	50	-4259	-972	-3870	-2064	-2253	-310	-427	-80	-564	-349
7	-12419	-8259	-8776	-11261	-969	-1991	-1332	-2089	-1812	-1032	-760	7	-199	-539	-387
8	-15339	3005	5871	-326	-3626	-2665	-162	-742	59	378	-683	-1140	-771	297	144
9	-34186	-1316	3326	-7881	-7220	-2815	-715	-1130	-895	300	-869	-1124	-816	166	-383
10	-15757	3106	5761	-185	-3673	-2641	-237	-710	-7	426	-696	-1114	-838	293	125
11	-6366	-9000	4859	-15731	-873	1913	1687	-9219	-3280	-1817	-754	-3920	-2270	-2762	-1183
12	-32613	-20714	5584	-15708	766	6190	2613	-2863	2479	1491	1170	113	575	676	880
13	-15796	-23460	-6967	-1791	-724	-3906	-898	-2108	-1039	-1672	-322	-1441	-161	-806	321
14	-10610	-28560	-6399	500	-2086	-3888	-1336	-1216	-1904	-700	-512	-907	-517	-508	315
15	-11960	-22125	-9446	-775	-2205	-1035	-2874	12	-3037	537	-890	322	-577	1	532
16	-14229	-18255	694	-16066	-1258	1983	2272	-8361	-4502	-3381	-853	-4891	-2641	-4190	-1962
17	-26026	-8235	2608	3008	-1777	-5116	2967	33	-430	-1751	768	-1996	781	-1875	702
18	-10376	24060	-7516	2360	-1440	446	-464	1205	-1631	377	-619	316	-408	178	405
19	-32021	38502	-12947	5179	-2351	3744	-1600	3604	-2847	3186	-922	1700	-1296	1046	-595
20	-33652	39206	-10071	5619	-350	3305	-1184	2648	-2196	3228	-1307	1775	-1258	1087	-403
21	3360	-8601	16183	3462	-1278	-2320	5194	-112	1309	-2557	1646	-311	767	-583	1081
22	-21808	-25162	5044	-15244	1231	3628	-1284	-4085	604	772	877	-195	741	102	526
23	62581	6026	25955	-3966	3486	1327	2779	700	-219	-83	46	-1312	-1096	-1048	176
24	37420	7626	18753	-482	3710	1962	1820	826	274	848	89	-243	-130	-4	327
25	16522	12242	10992	2239	2295	3718	1115	1078	118	919	643	425	-66	331	230
26	-41354	-3444	-3282	-4447	-5021	-1689	-1551	-2791	-816	-2168	-496	-542	542	-487	566
27	-39933	-3689	-2696	-3809	-7693	-927	-3799	-2487	-1949	-1663	-786	-119	113	-109	495
28	-33540	1045	-5550	-3758	-5985	-634	-3957	-1343	-1017	-1069	-321	551	660	349	917
29	-26120	-3858	4221	-3899	-4953	-4448	-1272	-2185	-1204	-1369	-1018	-1644	-1353	-994	-312
30	-68173	-24657	-2849	-13187	-11347	-7016	-4670	-5289	-2922	-2708	-1912	-2308	-2135	-1179	-1472
31	-54940	-16892	4769	-8648	-6468	171	-910	327	385	1512	1019	1145	196	1307	429
32	7855	-10697	10075	-11358	301	556	4162	-7882	-2904	-1819	-809	-3686	-1897	-1742	-535

Table C-32: Fourier coefficients (10^{-5} mm) for the measured imperfections of specimen 4C64-900-2

Line	a_1	a_2	a_3	a_4	a_5	a_6	a_7	a_8	a_9	a_{10}	a_{11}	a_{12}	a_{13}	a_{14}	a_{15}
1	-48997	-25939	8323	-18496	-333	3733	-1163	-2412	1907	388	587	-896	828	-126	-912
2	33465	6123	23783	-4695	1499	3283	2215	-906	-1863	-356	-574	-472	-1813	-197	144
3	11549	2172	14167	-3645	-1173	1757	1211	-566	-1213	-227	-1086	-300	-418	-34	-344
4	9634	12774	6900	2410	-907	2278	1009	361	-138	45	140	471	207	-93	-6
5	-23642	-22096	-5913	-12588	869	-6878	-434	-4863	-1169	-3777	-179	-1548	225	-1247	6
6	-18242	-18711	-7239	-12496	50	-4259	-972	-3870	-2064	-2253	-310	-427	-80	-564	-349
7	-12419	-8259	-8776	-11261	-969	-1991	-1332	-2089	-1812	-1032	-760	7	-199	-539	-387
8	-15339	3005	5871	-326	-3626	-2665	-162	-742	59	378	-683	-1140	-771	297	144
9	-34186	-1316	3326	-7881	-7220	-2815	-715	-1130	-895	300	-869	-1124	-816	166	-383
10	-15757	3106	5761	-185	-3673	-2641	-237	-710	-7	426	-696	-1114	-838	293	125
11	-6366	-9000	4859	-15731	-873	1913	1687	-9219	-3280	-1817	-754	-3920	-2270	-2762	-1183
12	-32613	-20714	5584	-15708	766	6190	2613	-2863	2479	1491	1170	113	575	676	880
13	-15796	-23460	-6967	-1791	-724	-3906	-898	-2108	-1039	-1672	-322	-1441	-161	-806	321
14	-10610	-28560	-6399	500	-2086	-3888	-1336	-1216	-1904	-700	-512	-907	-517	-508	315
15	-11960	-22125	-9446	-775	-2205	-1035	-2874	12	-3037	537	-890	322	-577	1	532
16	-14229	-18255	694	-16066	-1258	1983	2272	-8361	-4502	-3381	-853	-4891	-2641	-4190	-1962
17	-26026	-8235	2608	3008	-1777	-5116	2967	33	-430	-1751	768	-1996	781	-1875	702
18	-10376	24060	-7516	2360	-1440	446	-464	1205	-1631	377	-619	316	-408	178	405
19	-32021	38502	-12947	5179	-2351	3744	-1600	3604	-2847	3186	-922	1700	-1296	1046	-595
20	-33652	39206	-10071	5619	-350	3305	-1184	2648	-2196	3228	-1307	1775	-1258	1087	-403
21	3360	-8601	16183	3462	-1278	-2320	5194	-112	1309	-2557	1646	-311	767	-583	1081
22	-21808	-25162	5044	-15244	1231	3628	-1284	-4085	604	772	877	-195	741	102	526
23	62581	6026	25955	-3966	3486	1327	2779	700	-219	-83	46	-1312	-1096	-1048	176
24	37420	7626	18753	-482	3710	1962	1820	826	274	848	89	-243	-130	-4	327
25	16522	12242	10992	2239	2295	3718	1115	1078	118	919	643	425	-66	331	230
26	-41354	-3444	-3282	-4447	-5021	-1689	-1551	-2791	-816	-2168	-496	-542	542	-487	566
27	-39933	-3689	-2696	-3809	-7693	-927	-3799	-2487	-1949	-1663	-786	-119	113	-109	495
28	-33540	1045	-5550	-3758	-5985	-634	-3957	-1343	-1017	-1069	-321	551	660	349	917
29	-26120	-3858	4221	-3899	-4953	-4448	-1272	-2185	-1204	-1369	-1018	-1644	-1353	-994	-312
30	-68173	-24657	-2849	-13187	-11347	-7016	-4670	-5289	-2922	-2708	-1912	-2308	-2135	-1179	-1472
31	-54940	-16892	4769	-8648	-6468	171	-910	327	385	1512	1019	1145	196	1307	429
32	7855	-10697	10075	-11358	301	556	4162	-7882	-2904	-1819	-809	-3686	-1897	-1742	-535

Table C-33: Fourier coefficients (10^{-5} mm) for the measured imperfections of specimen 4C64-300-1

Line	a_1	a_2	a_3	a_4	a_5	a_6	a_7	a_8	a_9	a_{10}	a_{11}	a_{12}	a_{13}	a_{14}	a_{15}
1	18982	-6774	12468	3819	1857	-4441	4321	3566	2097	-1749	2073	-514	1069	-721	-279
2	57401	-54089	26905	1814	4806	-819	2888	-396	66	127	-436	847	-1019	89	642
3	16186	-37719	12348	-2972	1531	-2377	1815	-1927	500	-405	736	-678	309	-679	168
4	-2128	-25742	5581	-3951	-1207	-907	-207	-1920	478	-1568	1066	-1154	627	-772	119
5	-29064	38821	-8778	11325	1623	8805	-743	4800	-3230	3658	-4188	-96	-1512	-56	-510
6	-24433	34299	-7978	11055	1923	12503	-406	6118	-3519	4415	-3785	1321	-2001	312	-996
7	-15627	25999	-7427	10432	1355	11544	531	6092	-1175	3232	-2108	2051	-1144	1088	-125
8	31665	-8101	13248	-2153	4385	-2519	1712	87	567	-270	393	-349	62	-433	231
9	35604	1640	16808	4888	5090	-544	1836	2516	-214	579	127	808	-452	39	-615
10	31665	-8101	13248	-2153	4385	-2519	1712	87	567	-270	393	-349	62	-433	231
11	-2609	-13251	-877	1914	1846	-2880	5079	1317	-167	-2606	1282	-1310	688	-1761	1096
12	-28429	-12133	15841	1458	6128	-3664	3065	2404	383	-1742	2244	-144	976	48	536
13	-18939	37048	-11082	1619	-8396	4777	5205	3249	-1156	983	-1467	1496	668	-255	-892
14	-10505	34913	-12347	1603	-5784	8474	4124	4195	-1398	1669	-985	2238	-220	268	-963
15	1252	21139	-8634	833	-1895	6616	1820	3908	-766	1272	-1211	2315	-1501	391	-1021
16	-118	5690	1416	2142	910	-7698	985	-108	995	-2474	1526	-637	564	-1654	641
17	11757	-7255	11311	-15838	-989	3390	3771	-7475	-4269	-3340	396	-4217	-2945	-2978	-1400
18	-7221	-23185	-3273	-6682	-1109	-4	1593	-1986	-1303	-1178	-1244	-451	1749	-1356	-430
19	-11935	-26247	1847	-7453	-743	-1354	285	-2459	-831	-1212	-1632	171	351	-683	-129
20	-20881	-28154	-2041	-9563	-673	-1786	-1520	-2861	-736	-1964	-2164	-121	-879	-1354	-520
21	-31549	-10835	2612	-21077	-3576	16	2834	-2920	827	1952	-372	-811	-133	173	-747
22	-24226	-25772	573	-16804	3841	3567	-1474	-1308	1670	308	461	-767	1034	-802	-310
23	43116	8690	21499	-4727	6003	1242	3064	-2293	-760	-567	-357	-648	-1175	518	-383
24	28321	3061	15136	-3426	4550	624	2178	-1884	-52	-567	-20	-257	-582	141	-595
25	27288	7509	11415	1916	3249	2191	1223	-222	139	-185	10	235	-254	252	29
26	-45936	1245	-18335	5769	-4515	71	-342	1503	-2477	-739	-755	-1691	566	-1086	-868
27	-23951	1529	-10722	12600	-5664	3936	-337	2496	-3443	376	-1737	-966	-46	-906	-1441
28	-8538	5847	-9308	12678	-4691	5056	-347	2116	-2927	1697	-1788	-1217	179	-807	-2189
29	3812	1105	8257	-5328	-1461	-2433	-940	-821	298	-88	-255	-657	-209	-216	-77
30	-11064	-14074	5088	-10208	-5292	-3108	-2279	-1854	-974	-226	-631	-1137	-843	-493	-434
31	-10905	-15370	3306	-10789	-4739	577	-1277	1069	479	1965	1132	1441	713	1127	858
32	21583	-8400	9460	-11478	2305	4107	4210	-7147	-3898	-1047	-693	-2943	-2446	-2079	-1141

Table C-34: Fourier coefficients (10⁻⁵ mm) for the measured imperfections of specimen 4C64-300-2

Line	a_1	a_2	a_3	a_4	a_5	a_6	a_7	a_8	a_9	a_{10}	a_{11}	a_{12}	a_{13}	a_{14}	a_{15}
1	27809	-13583	17469	7915	15	-4595	3524	2282	1608	-2882	1697	-1292	1173	-1072	-119
2	86937	-58518	29018	2362	5053	112	2823	-715	475	180	-601	1356	-848	120	250
3	15228	-39295	12442	-3208	3066	-1659	1266	-2287	-145	-1403	-398	65	-154	-871	-60
4	-20700	-21731	2901	-5358	3076	-985	1226	-2090	771	-1620	773	-250	280	-743	267
5	-10638	39885	-7168	3531	-4546	4993	-1011	3402	259	447	-3763	2863	-560	646	-37
6	-5744	35362	-12021	1962	-5952	4971	726	3443	-1912	949	-2443	2426	-485	666	-836
7	-8299	21501	-12032	2282	-4721	2050	2726	1055	-1428	533	-1247	651	975	444	-841
8	13686	-16302	5624	-2494	-363	-3842	-74	-1475	212	-340	268	-685	-139	-525	55
9	46997	-31612	9981	-2096	652	-4480	1040	-1537	242	-1245	231	-878	100	176	503
10	13991	-16245	5665	-2415	-313	-3812	-86	-1457	192	-322	275	-661	-143	-517	45
11	-5980	-12709	3017	2706	1682	-5003	3120	879	821	-2784	594	-1855	1561	-2076	1014
12	24945	-13989	15229	5692	4826	-9368	2557	2790	2336	-2943	2754	-1761	1644	-339	1445
13	-31985	26243	-16493	-128	-7079	2285	4883	3072	-535	-115	-1080	1845	1383	1055	-403
14	-26638	25605	-19200	-1087	-8624	3984	3825	3193	-2219	-271	-973	1724	843	936	-724
15	-4822	19137	-11355	175	-5260	2255	2087	2161	-1794	-1111	-1412	609	213	1522	-309
16	-32277	698	-1581	2828	-1515	-9164	68	-448	497	-2965	830	-1400	1231	-1710	1109
17	11493	-10249	13526	-9455	1741	3527	2775	-7333	-3067	-2927	-1114	-4230	-1877	-2721	-1034
18	-20531	-22299	-1688	-12892	-1417	-3991	352	-1777	798	-3346	-353	-259	1076	-819	28
19	-27124	-21938	3152	-12467	-1534	-5471	202	-1703	489	-3353	-536	-525	909	-168	315
20	-38196	-22214	-344	-11729	-2767	-6027	-707	-1448	-368	-3383	-1181	-772	669	-96	290
21	-37239	-12078	4959	-19858	-1077	3246	3310	2218	2568	1341	560	723	1515	573	197
22	-22130	-19134	10524	-17692	3413	2690	-767	-1056	1096	998	912	-553	1400	-279	447
23	20421	16742	24894	-5886	7059	1531	2462	-2421	-200	-780	-593	-762	-601	-138	-602
24	3429	9502	15422	-4644	5842	300	780	-2643	352	-914	243	-495	-711	-856	41
25	7800	15083	9115	1604	5390	1976	1030	-557	1088	-133	302	181	-37	-168	29
26	-13241	-8688	-7292	-4670	-6208	-2690	-1378	887	-1896	-1813	-3545	-380	125	391	-832
27	1099	-4601	-1474	-2369	-2996	153	-2398	2215	-549	-2002	-2741	641	-789	453	-7
28	-7238	2513	-4325	-894	-870	3412	-3258	3936	209	-1272	-2396	2028	-1794	565	258
29	-8722	-1934	10031	170	-1979	-1914	-233	-986	518	-498	-356	-1276	-548	-363	-38
30	-34851	-18559	5839	-2610	-3740	-3573	-1379	-2478	-242	-697	-528	-1588	-832	-648	152
31	-47307	-24216	3631	-3719	-3123	1090	-973	324	1170	1526	748	1045	679	1711	888
32	3742	-19108	7401	-9567	2757	-696	2319	-6618	-3078	-2550	-840	-3681	-1854	-2265	-1002

Table C-35: Fourier coefficients (10^{-5} mm) for the measured imperfections of specimen 4C64-100-1

Line	a_1	a_2	a_3	a_4	a_5	a_6	a_7	a_8	a_9	a_{10}	a_{11}	a_{12}	a_{13}	a_{14}	a_{15}
1	45780	-3892	14134	6675	3117	-6046	4627	1466	-18	-1122	2027	-653	1056	-216	1331
2	85010	-51717	32656	-2428	4747	-2587	2285	-236	1160	-411	241	1040	215	-698	32
3	33560	-32850	16883	-5461	2648	-3467	1295	-1654	-446	-1626	180	-794	243	-833	-318
4	4795	-22385	5076	-7973	3343	-2944	-224	-1539	-784	-2630	365	-1790	813	-908	-423
5	-64638	30882	-22821	12376	-6769	1797	-1120	4789	-1402	90	-2706	773	-1961	-185	681
6	-47321	24026	-30467	16870	-7510	-41	-1029	8488	-1831	-2639	-2146	1410	-1487	-801	152
7	-23681	17518	-21905	14362	-5438	253	-1517	7735	-1576	-2309	-1469	921	-1280	327	389
8	20842	-9732	7982	-1985	814	-1963	1232	-2376	-131	-732	451	-700	120	-793	-282
9	18790	-18841	14590	-1868	1069	-2293	1551	-2620	-177	-1493	422	-624	-545	-500	-323
10	20842	-9732	7982	-1985	814	-1963	1232	-2376	-131	-732	451	-700	120	-793	-282
11	-4084	-13083	-3837	3188	240	-8415	3440	1195	1459	-2484	735	-1457	1580	-1669	1493
12	12558	12733	4850	4442	1630	-5848	7286	-235	1585	-2413	2144	-654	1312	-520	1152
13	-29517	20596	-10692	4590	-1491	674	3690	3341	-874	2982	385	2470	-594	1520	-137
14	-5586	21243	-10698	2947	-1938	1651	5184	1726	-849	2625	-87	1417	-87	624	-706
15	15646	18355	-3878	1792	793	-471	4681	1529	93	494	-1526	-423	-180	892	-962
16	-16468	-2027	-4594	4780	-530	-2579	3195	1794	-792	-2038	696	412	640	-825	736
17	20097	-5178	205	-16162	643	1130	203	-7449	-4814	-2523	-33	-3217	-2933	-2124	-1066
18	6917	-35089	3008	-8951	-92	-2256	1124	99	-2757	-271	52	453	-670	-660	-3
19	5154	-36097	5996	-6826	514	-5910	1847	-2458	-1012	-238	-1289	-970	-46	-147	-428
20	-2488	-28566	3556	-9384	332	-6038	2472	-5359	443	-1516	-2272	-2860	32	-889	-756
21	-54394	-30076	-2125	-21874	-114	6381	1041	-5187	676	1380	723	-753	751	-18	406
22	-29246	-17368	-6666	-21379	-3193	5528	1605	-5564	997	519	562	109	-25	59	519
23	74132	24192	30096	-10466	4290	-210	142	-1505	-179	-1049	-964	-1451	-863	-1380	-749
24	42012	18431	20434	-5871	3417	672	-361	33	-46	-496	-446	73	-263	-511	-519
25	24915	12290	10064	2112	2843	67	1857	2042	-1016	358	1329	458	141	1204	167
26	-29143	-9369	-8711	-6534	85	1294	-701	-1572	755	-1865	-885	-1428	178	-1358	-2371
27	-9709	-16197	-10600	-3760	-1781	341	-3058	1882	-837	-548	-780	-437	-1062	-502	-438
28	-7615	-8822	-9375	-2904	-4798	1721	-4280	2516	-1732	795	-1553	-786	-1573	-285	-271
29	7828	102	8630	-3625	646	-1987	1208	-488	667	-540	-12	-556	-105	151	696
30	-19736	-11606	7726	-6171	-3579	-1323	-947	-2131	-1024	-809	-722	-197	-1086	-306	266
31	-31239	-13293	11202	-5681	-2779	1960	-360	353	689	1690	925	1324	738	1310	803
32	28009	-11919	1057	-15654	25	3655	2257	-7874	-3179	-1930	-1238	-4531	-1536	-2718	-767

Table C-36: Fourier coefficients (10^{-5} mm) for the measured imperfections of specimen 4C64-100-2

Line	a_1	a_2	a_3	a_4	a_5	a_6	a_7	a_8	a_9	a_{10}	a_{11}	a_{12}	a_{13}	a_{14}	a_{15}
1	-2107	-22718	6123	-20369	-4815	-1521	1529	-2752	1696	988	758	-425	-115	-453	562
2	54798	692	30561	-1417	6205	3928	2466	-1745	-163	-333	420	-1359	-266	-510	-515
3	27181	-345	20604	-2797	4057	4021	1992	-275	-417	-17	380	-1074	266	-287	-467
4	16143	14074	14077	961	2944	4999	1402	1589	338	1788	575	195	275	174	235
5	-41702	-16818	-13775	-9100	-1742	-12152	-408	-6111	980	-4977	2277	1009	-2716	-623	-1241
6	-14039	-21358	-3613	-10543	747	-13392	-115	-5313	-611	-1834	1736	1143	-2200	989	-2050
7	-1165	-24550	-1072	-11150	2190	-12102	-1561	-4585	-1526	-674	956	798	-1692	1872	-2223
8	-13576	8169	6784	241	-2298	-1279	-845	266	279	-460	-513	-1049	-440	-698	49
9	-48128	6263	3671	-5665	-5689	480	2	-1348	-255	-105	-875	-1005	-213	-426	96
10	-13144	7898	6980	194	-2172	-1354	-781	198	358	-491	-445	-1089	-410	-747	57
11	-14203	-9666	9542	-14083	-4610	1083	2505	-5293	-1891	-2662	349	-4260	-2126	-2544	-1336
12	-48450	-30177	-6528	-22703	-916	478	-37	-4462	-62	1486	620	-161	437	-236	-723
13	-15137	-24240	-4684	-9156	-2719	-6486	-1016	-4682	229	-1787	-2142	-2298	416	-1522	-1285
14	8388	-23598	-355	-9846	-6004	-3950	-1356	-3702	916	-1039	-2187	-1370	283	-1066	-892
15	15404	-23282	-764	-9158	-4511	-10	-2707	-3716	495	-971	-3017	-1706	-479	-1016	-1199
16	354	-901	12091	-19200	-1657	-1580	1145	-6761	-3499	-2323	-1348	-5797	-1794	-2992	-1551
17	-37614	6692	21100	-9149	1045	2616	6993	-2997	1192	1185	2483	-60	1174	-335	143
18	-5269	-9956	-10242	4008	-4240	-8167	1962	-3597	-903	-1000	-2731	-1629	-60	-1494	-1882
19	-5831	-7764	-14938	6902	-6490	-8967	3752	-3758	-951	-1222	-1774	-1391	551	-2009	-851
20	-9156	-1770	-8926	7325	-6522	-4030	435	-4196	-150	-544	-2866	-966	-680	-2804	-1184
21	-8668	1363	-9425	-808	-1178	4969	999	-1252	1953	2029	-212	1805	1327	751	1209
22	13608	-19381	13535	289	1726	-5041	1634	1283	575	-1701	1876	-1230	901	-1093	736
23	46378	-48390	34589	4744	1458	47	2790	-1098	988	-221	-831	963	-692	144	-507
24	3751	-36336	21614	-147	952	176	2576	-2320	1727	-2554	-23	-687	-347	-1177	45
25	-20598	-22414	12285	-3244	-217	2455	-22	-1314	1558	-2596	1087	-971	326	-1116	448
26	-39177	32640	-27596	-1213	-12606	-189	-3744	2717	775	1760	-1766	2151	-2141	2024	-2091
27	-40121	37077	-30757	-2656	-15887	2954	-4398	4174	771	1765	-1439	1493	-2758	1987	-2699
28	-19079	24676	-19555	-1868	-12546	1022	-3488	4190	2072	376	-3000	-266	-2667	1420	-2907
29	-598	-15001	4090	-2592	515	-1490	1457	-2126	160	119	676	281	535	-395	49
30	-2564	-28591	9994	-2383	647	-2309	2627	-2546	-45	-886	945	-606	502	-857	77
31	6820	-42067	16193	-1330	2669	-2317	5383	-1709	1612	-1081	1643	-894	628	-604	650
32	-22333	2152	2331	358	-1911	-7843	-1620	62	2120	-1668	751	-1013	519	-1539	609

Appendix D   Experimental and Numerical Results

This appendix includes the experimental data of all built-up sections tested. The load vs. axial shortening and load vs. transducer displacement graphs are presented for each specimen. The sign convention for displacements and the arrangement of transducers around each built-up cross-section are included in the graphs, where the detailed description can be found in Section 4.7.2. Finally, the experimental data are compared with the results of the FE simulations explained in Chapter 5.
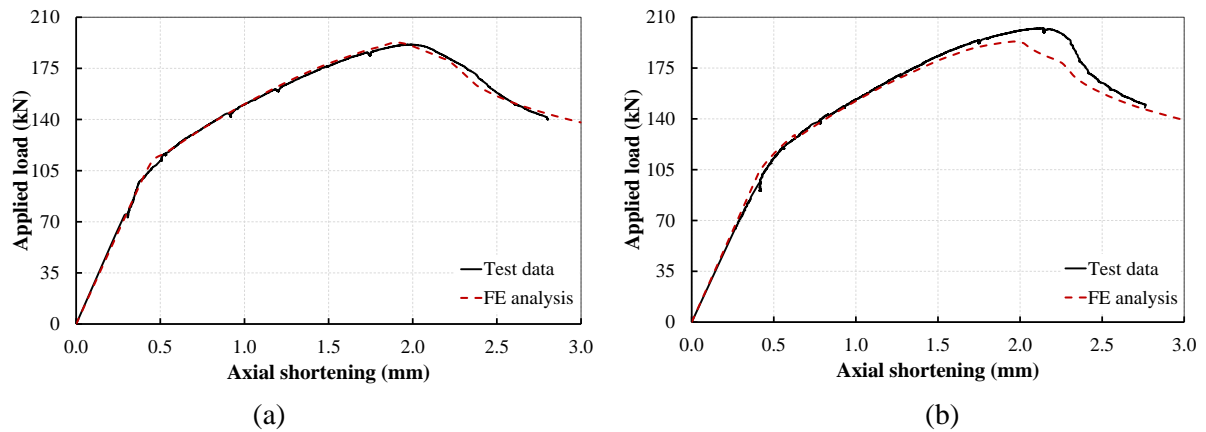
Figure D-1: Comparison between numerical predictions and experimental results of load vs. axial shortening curve of built-up I-sections with *s*=900 mm: (a) 2C120-900-1, (b) 2C120-900-2

Figure D-2: Comparison between numerical predictions and experimental results of transducers data of built-up I-sections with *s*=900 mm: (a) 2C120-900-1, (b) 2C120-900-2

(a)

(b)

Figure D-3: Comparison between numerical predictions and experimental results of load vs. axial shortening curve of built-up I-sections with *s*=300 mm: (a) 2C120-300-1, (b) 2C120-300-2
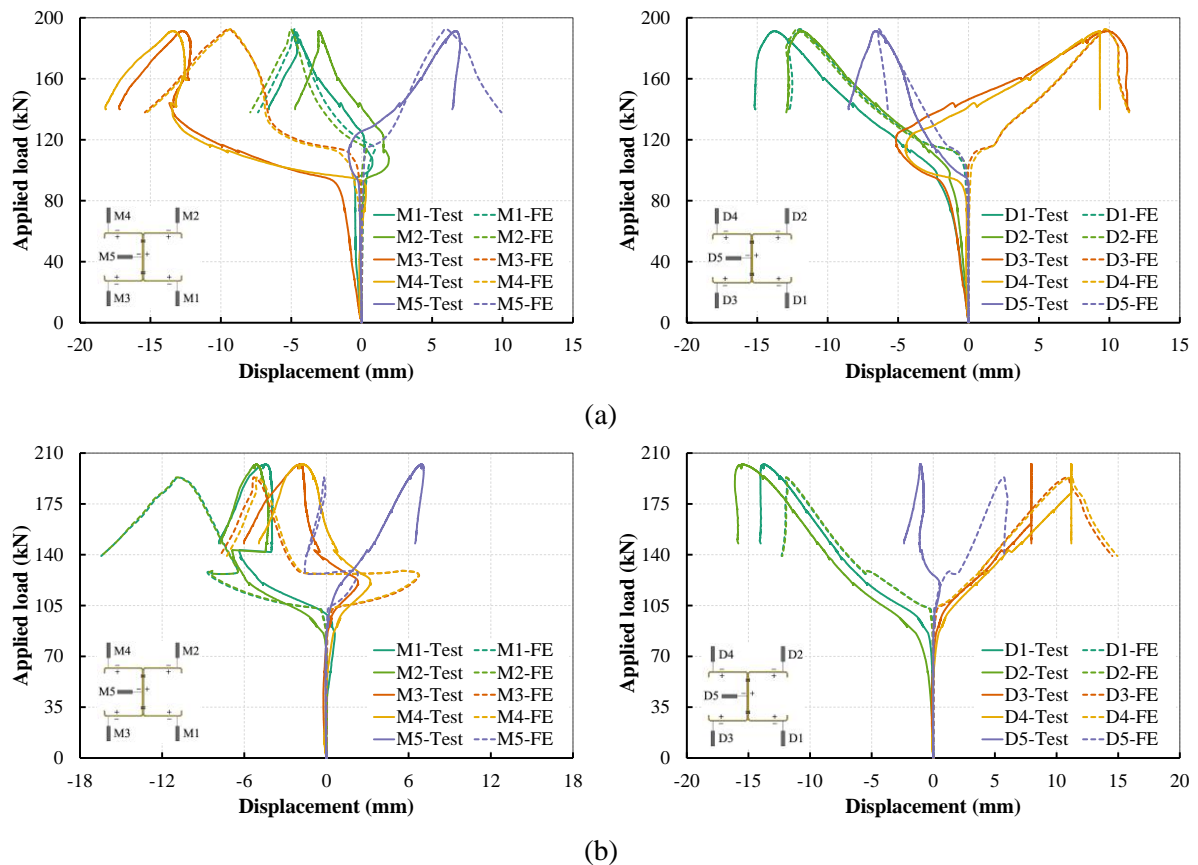

(a)

(b)

Figure D-4: Comparison between numerical predictions and experimental results of transducers data of built-up I-sections with *s*=300 mm: (a) 2C120-300-1, (b) 2C120-300-2

(a)   (b)

Figure D-5: Comparison between numerical predictions and experimental results of load vs. axial shortening curve of built-up I-sections with *s*=150 mm: (a) 2C120-150-1, (b) 2C120-150-2

(a)

(b)

Figure D-6: Comparison between numerical predictions and experimental results of transducers data of built-up I-sections with *s*=150 mm: (a) 2C120-150-1, (b) 2C120-150-2

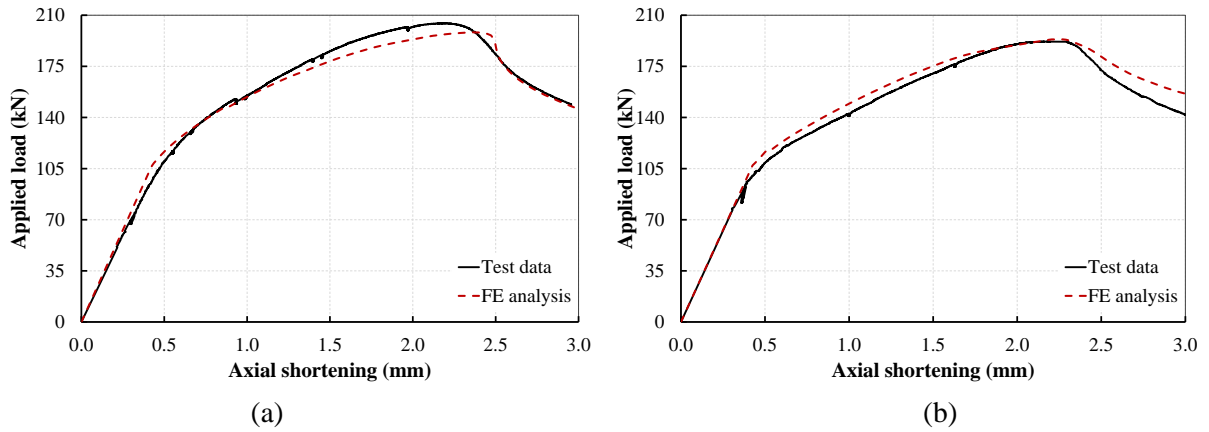(a)   (b)

Figure D-7: Comparison between numerical predictions and experimental results of load vs. axial shortening curve of built-up I-sections with *s*=100 mm: (a) 2C120-100-1, (b) 2C120-100-2
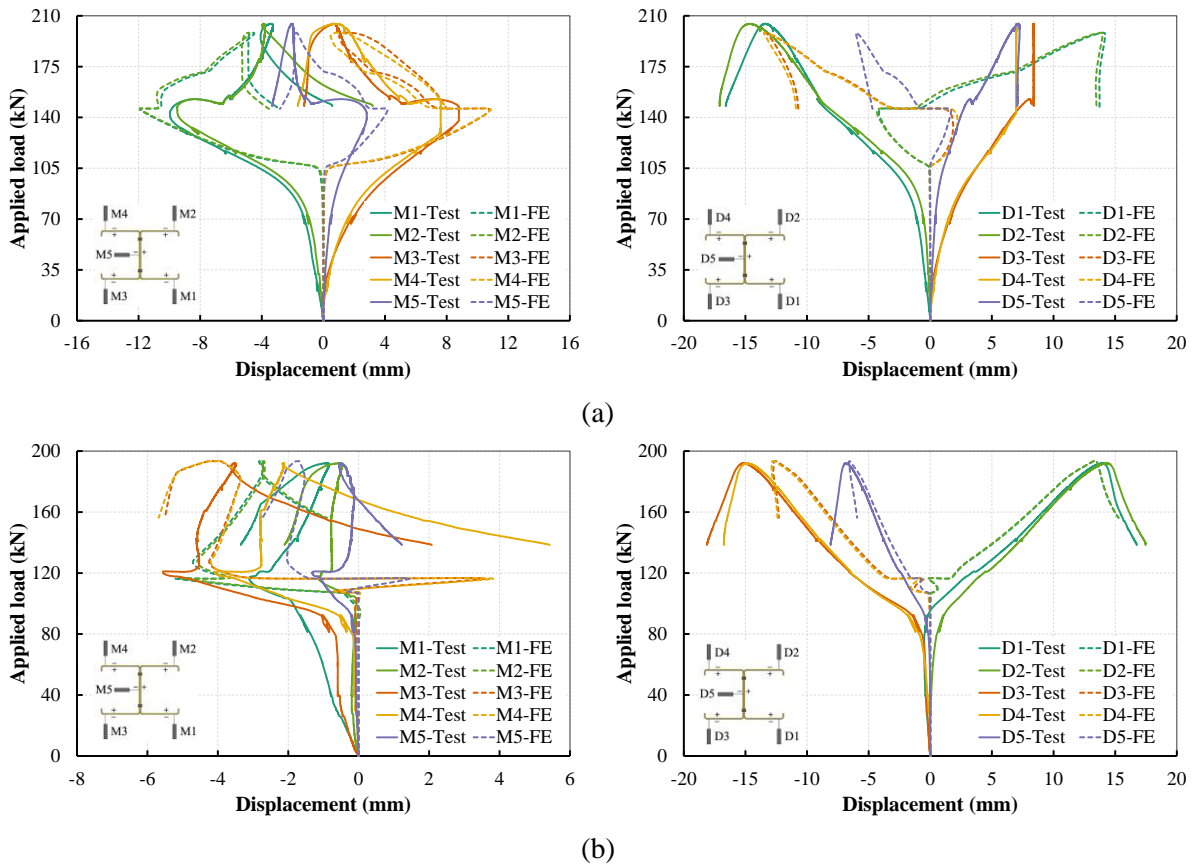

(a)

(b)

Figure D-8: Comparison between numerical predictions and experimental results of transducers data of built-up I-sections with *s*=100 mm: (a) 2C120-100-1, (b) 2C120-100-2
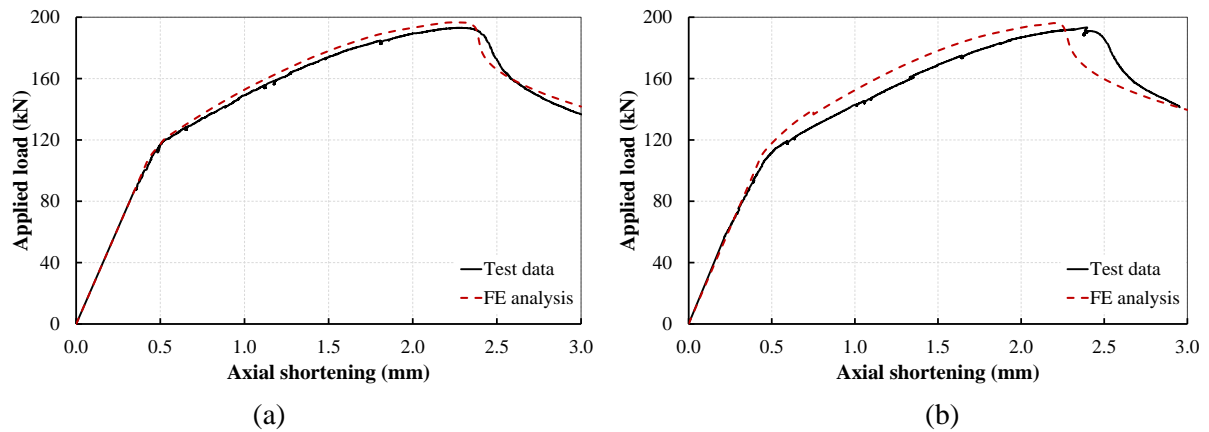
(a)

(b)

Figure D-9: Comparison between numerical predictions and experimental results of load vs. axial shortening curve of built-up 3C-sections with *s*=900 mm: (a) 3C120-900-1, (b) 3C120-900-2

(a)

(b)

Figure D-10: Comparison between numerical predictions and experimental results of transducers data of built-up 3C-sections with *s*=900 mm: (a) 3C120-900-1, (b) 3C120-900-2

(a)

(b)

Figure D-11: Comparison between numerical predictions and experimental results of load vs. axial shortening curve of built-up 3C-sections with *s*=300 mm: (a) 3C120-300-1, (b) 3C120-300-2
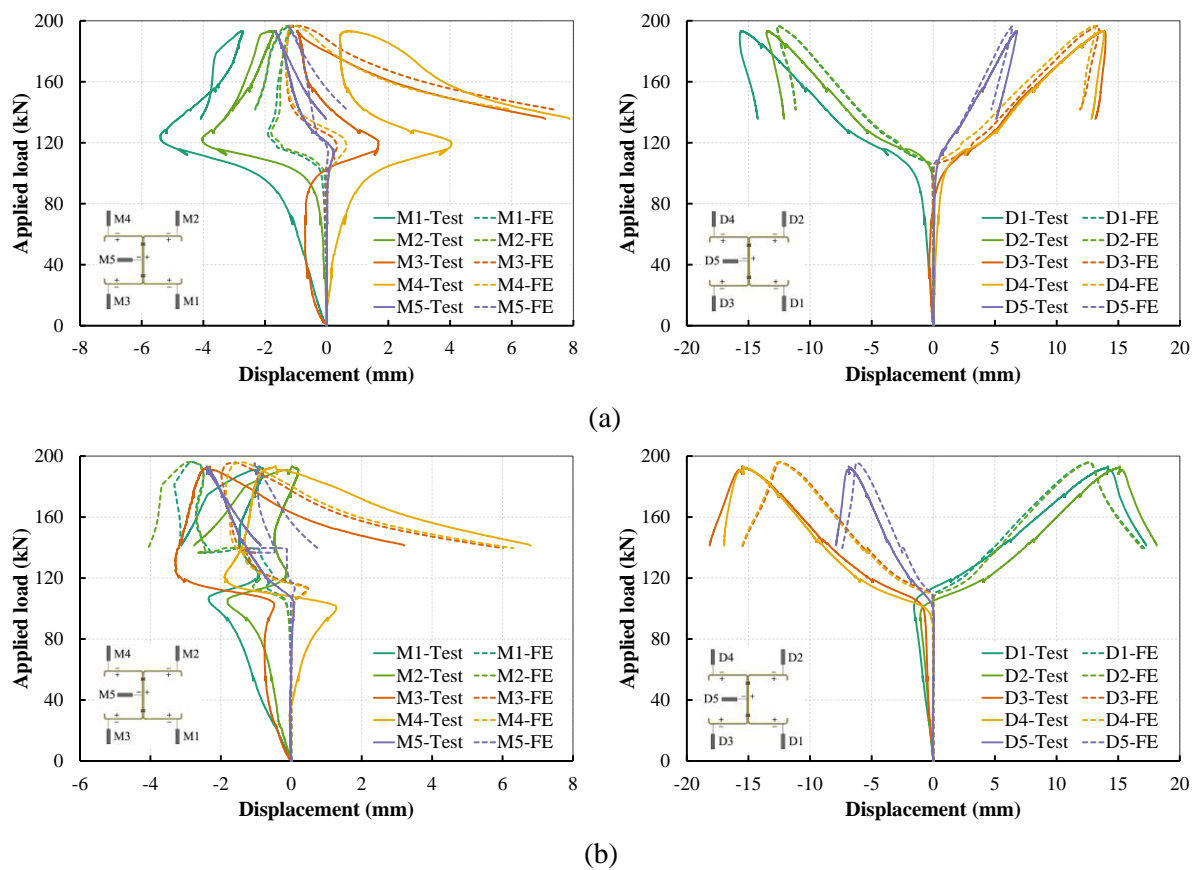

(a)

(b)

Figure D-12: Comparison between numerical predictions and experimental results of transducers data of built-up 3C-sections with *s*=300 mm: (a) 3C120-300-1, (b) 3C120-300-2
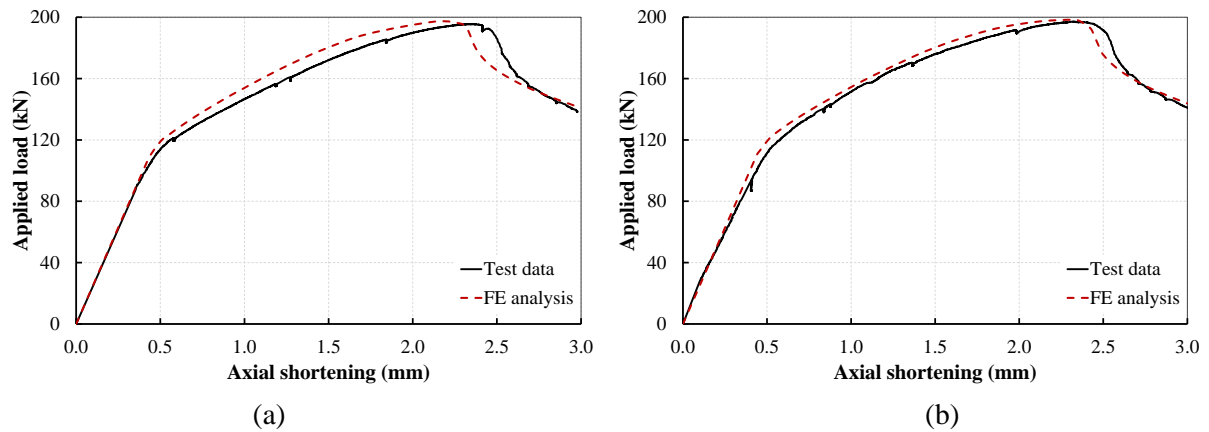
(a)   (b)

Figure D-13: Comparison between numerical predictions and experimental results of load vs. axial shortening curve of built-up 3C-sections with *s*=100 mm: (a) 3C120-100-1, (b) 3C120-100-2

(a)

(b)

Figure D-14: Comparison between numerical predictions and experimental results of transducers data of built-up 3C-sections with *s*=100 mm: (a) 3C120-100-1, (b) 3C120-100-2

(a)

(b)

Figure D-15: Comparison between numerical predictions and experimental results of load vs. axial shortening curve of built-up 4C-sections with *s*=900 mm: (a) 4C120-900-1, (b) 4C120-900-2
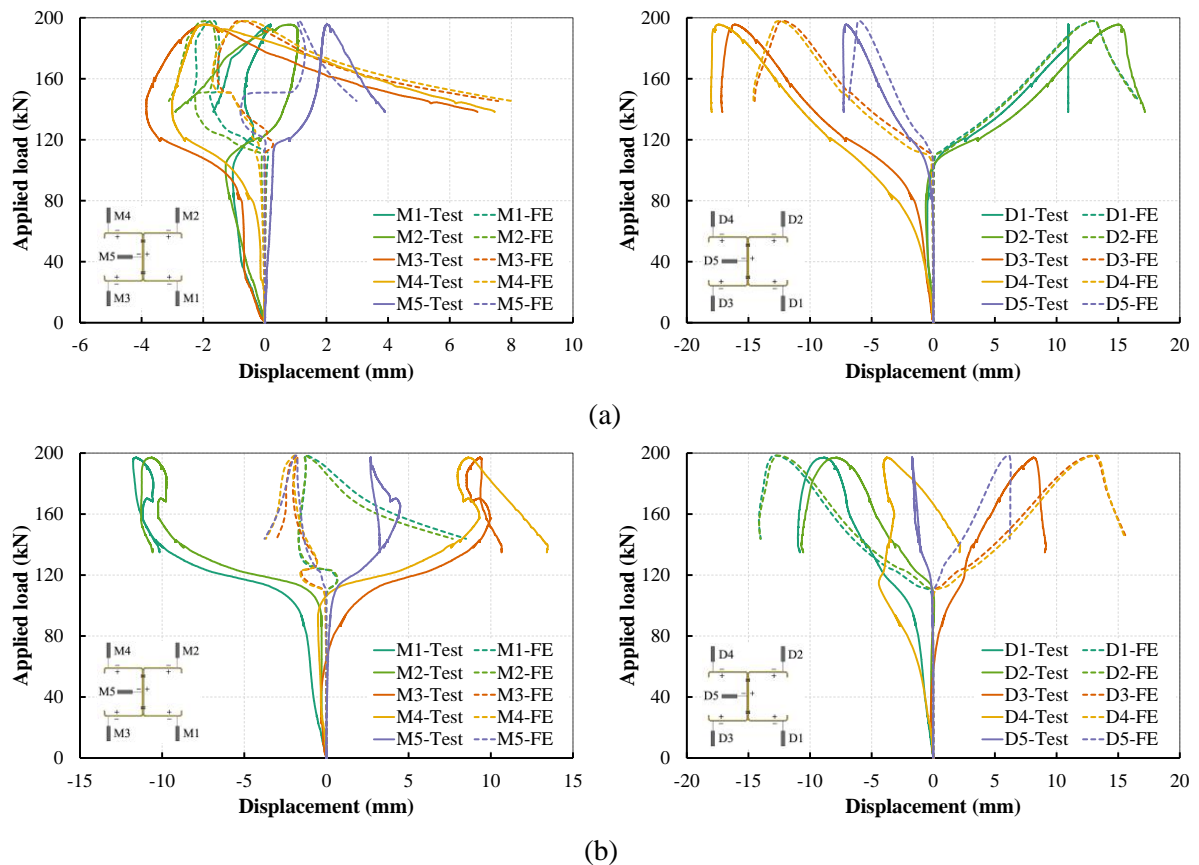

(a)

(b)

Figure D-16: Comparison between numerical predictions and experimental results of transducers data of built-up 4C-sections with *s*=900 mm: (a) 4C120-900-1, (b) 4C120-900-2

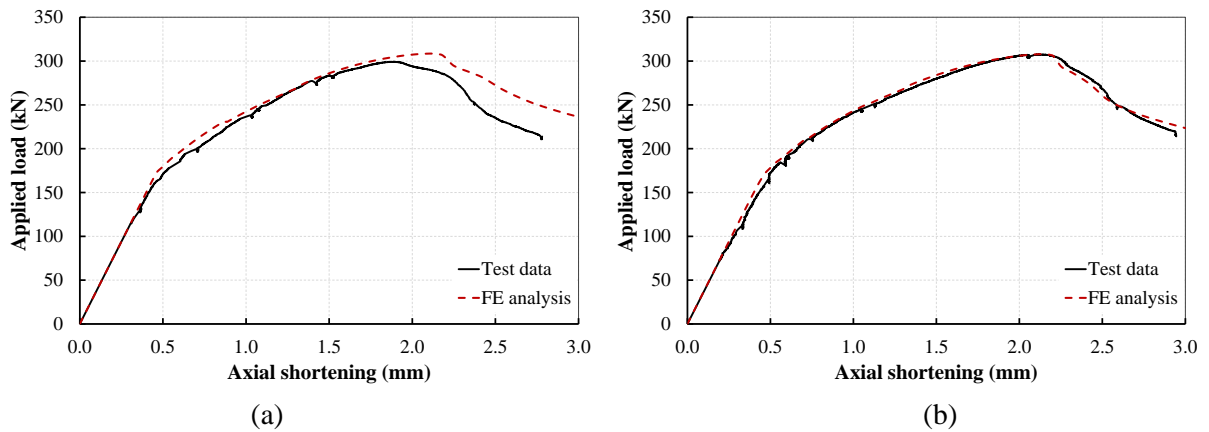(a)   (b)

Figure D-17: Comparison between numerical predictions and experimental results of load vs. axial
shortening curve of built-up 4C-sections with *s*=300 mm: (a) 4C120-300-1, (b) 4C120-300-2
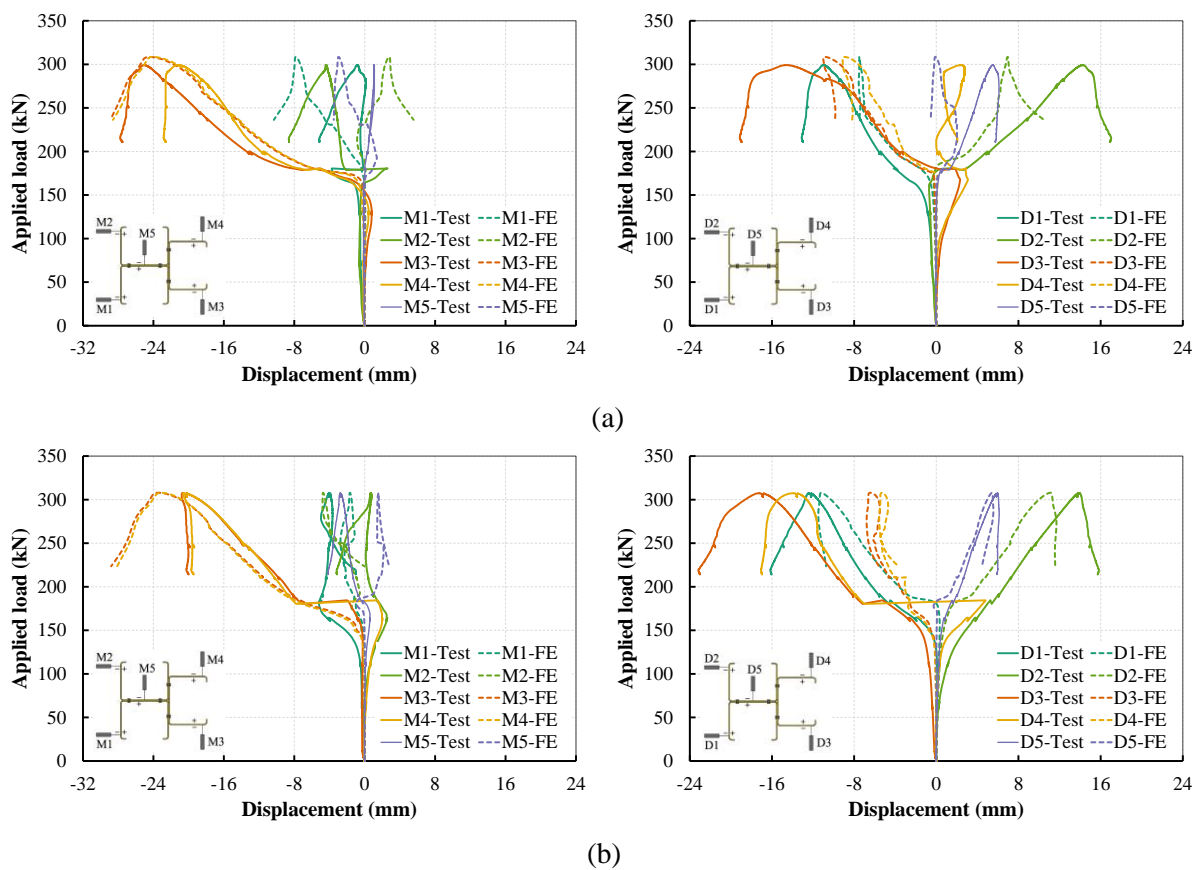

(a)

(b)

Figure D-18: Comparison between numerical predictions and experimental results of transducers data
of built-up 4C-sections with *s*=300 mm: (a) 4C120-300-1, (b) 4C120-300-2

(a)

(b)

Figure D-19: Comparison between numerical predictions and experimental results of load vs. axial shortening curve of built-up 4C-sections with *s*=100 mm: (a) 4C120-100-1, (b) 4C120-100-2

(a)

(b)
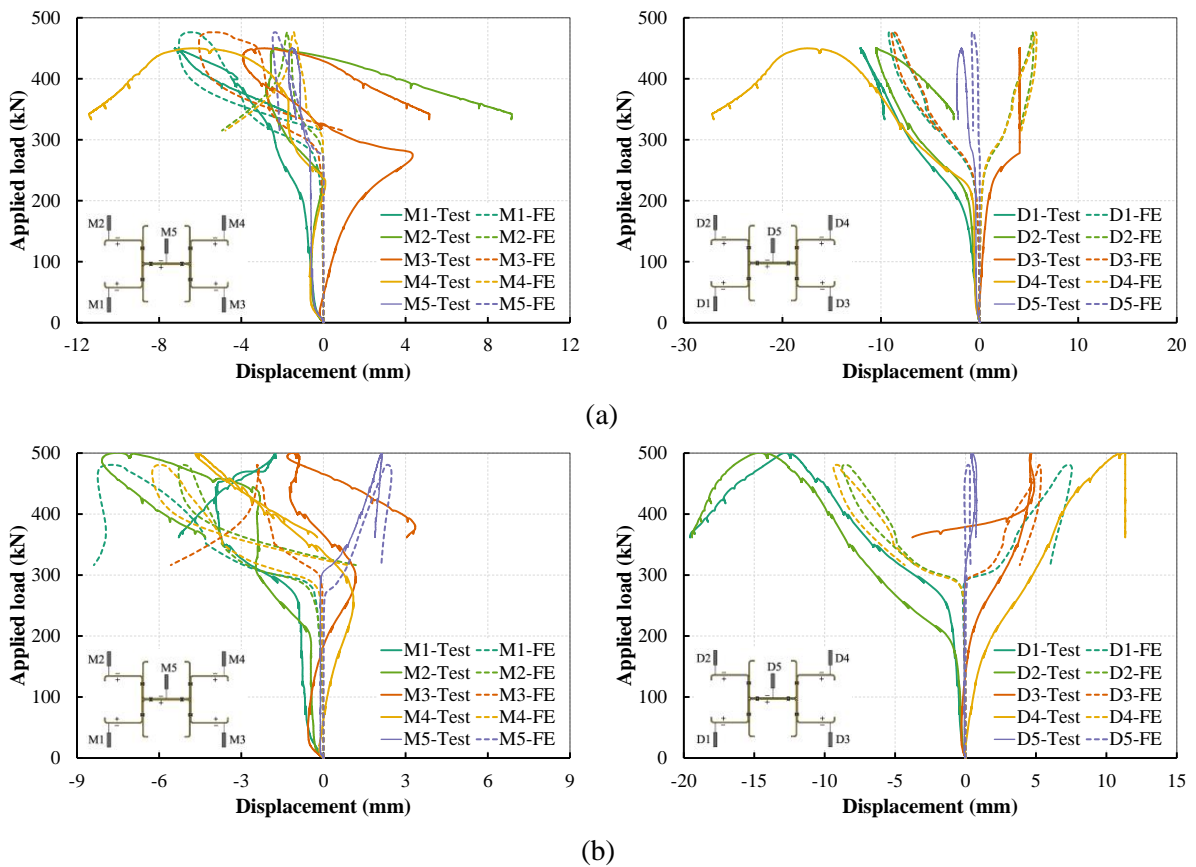
Figure D-20: Comparison between numerical predictions and experimental results of transducers data of built-up 4C-sections with *s*=100 mm: (a) 4C120-100-1, (b) 4C120-100-2
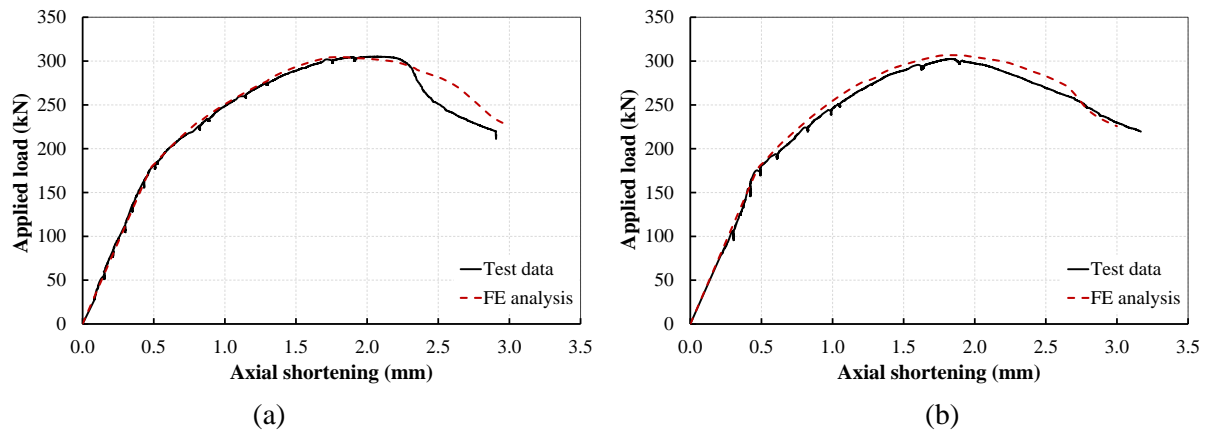
(a)

(b)
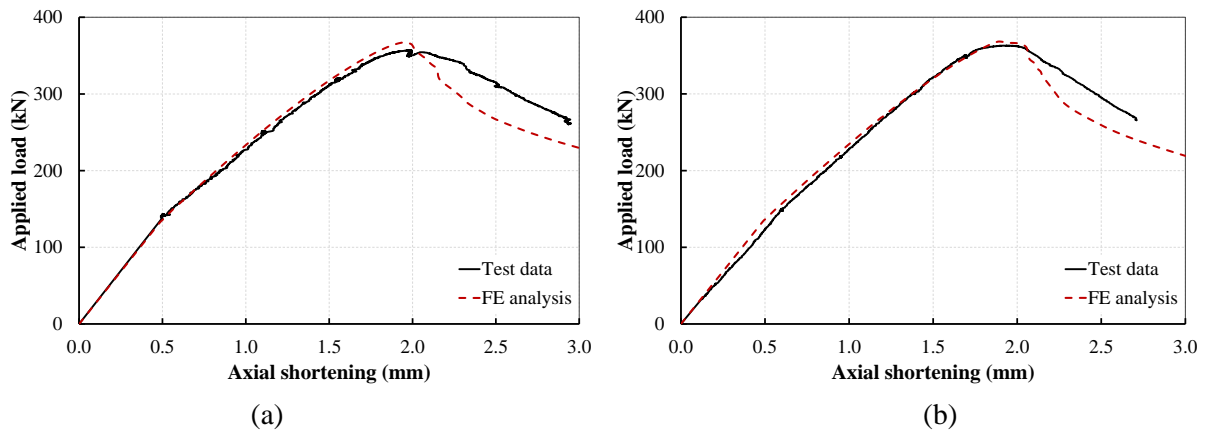
Figure D-21: Comparison between numerical predictions and experimental results of load vs. axial shortening curve of built-up 3C-sections with *s*=900 mm: (a) 3C64-900-1, (b) 3C64-900-2
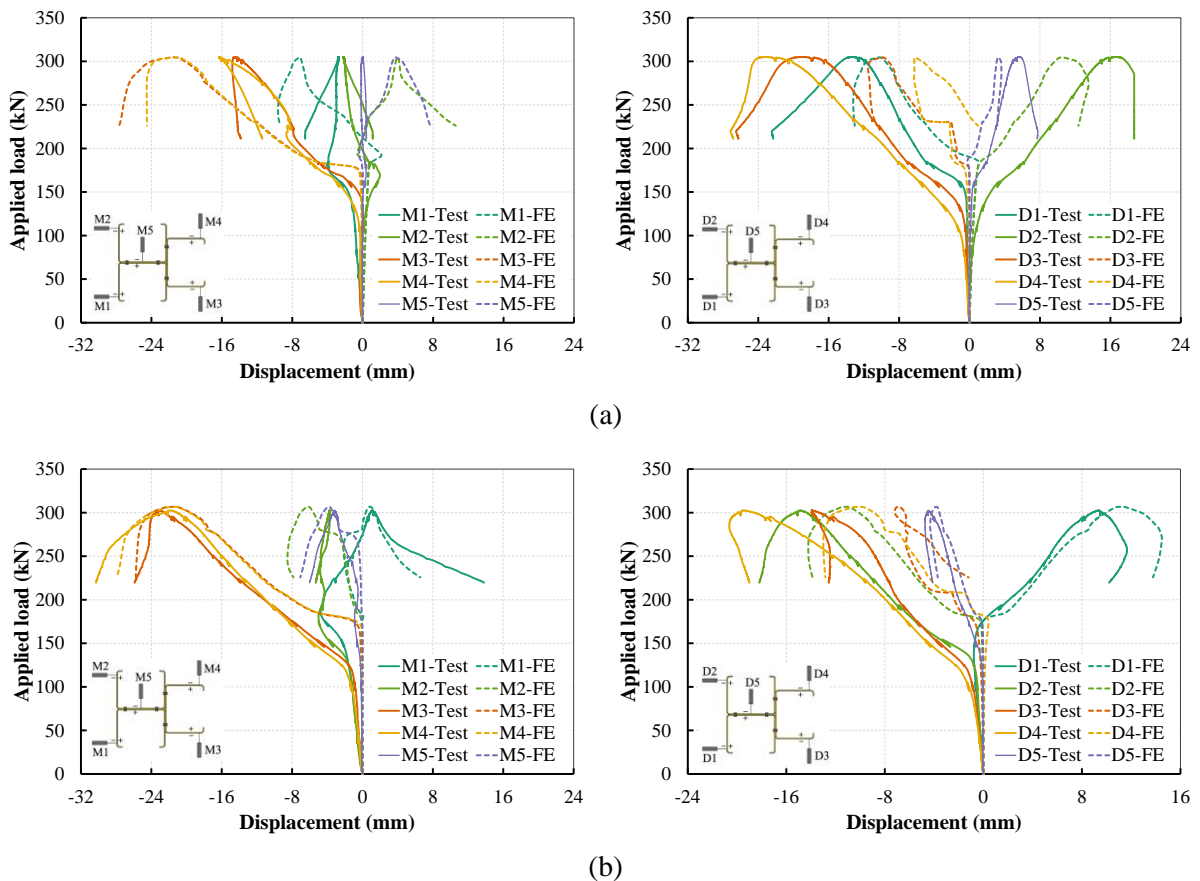

(a)

(b)
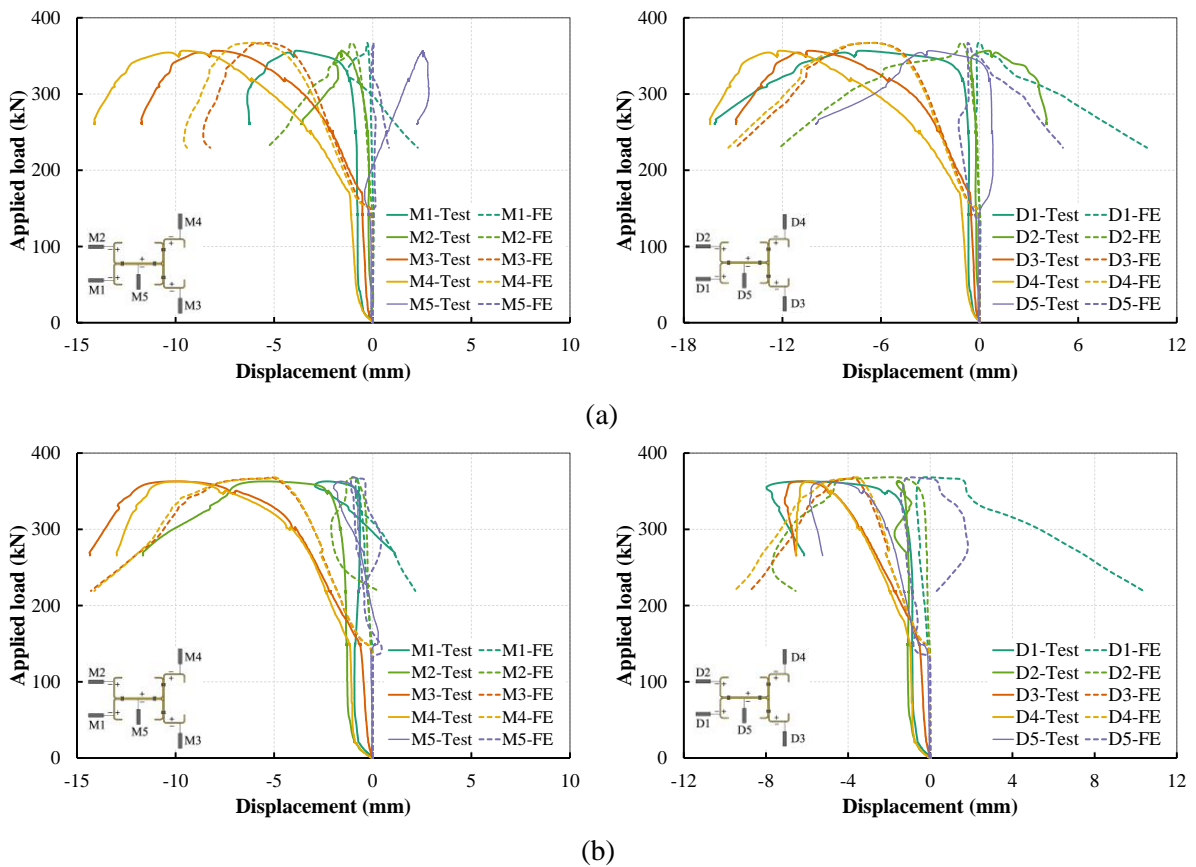
Figure D-22: Comparison between numerical predictions and experimental results of transducers data of built-up 3C-sections with *s*=900 mm: (a) 3C64-900-1, (b) 3C64-900-2
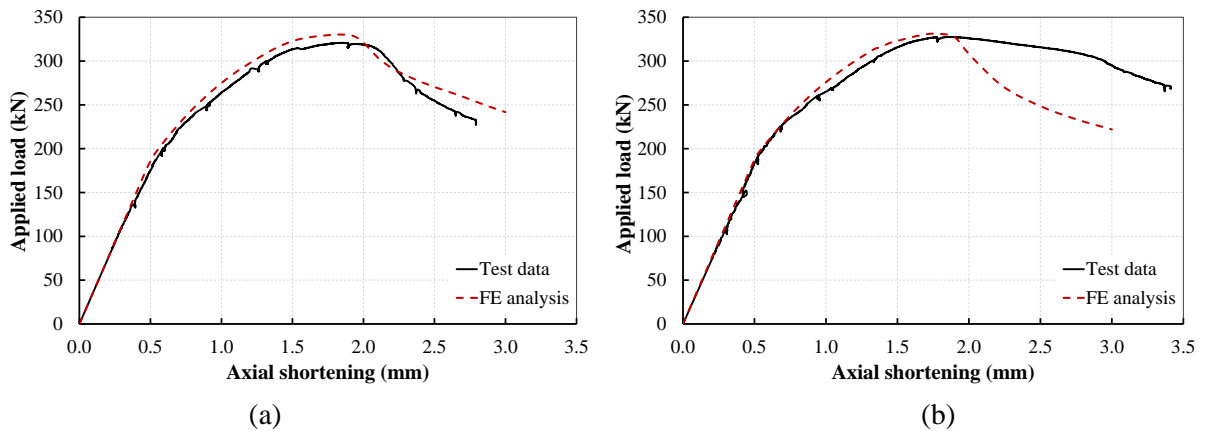
(a)   (b)
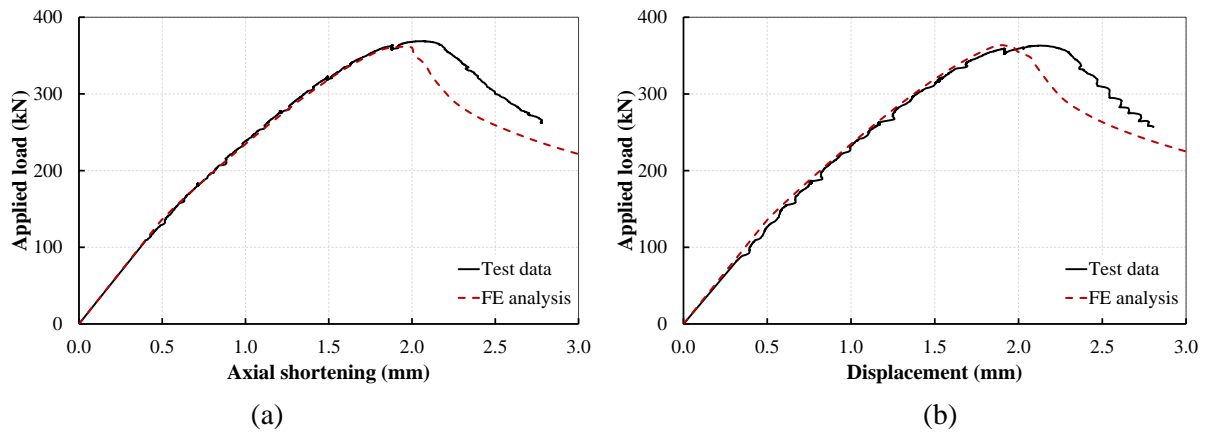
Figure D-23: Comparison between numerical predictions and experimental results of load vs. axial shortening curve of built-up 3C-sections with *s*=300 mm: (a) 3C64-300-1, (b) 3C64-300-2

(a)

(b)
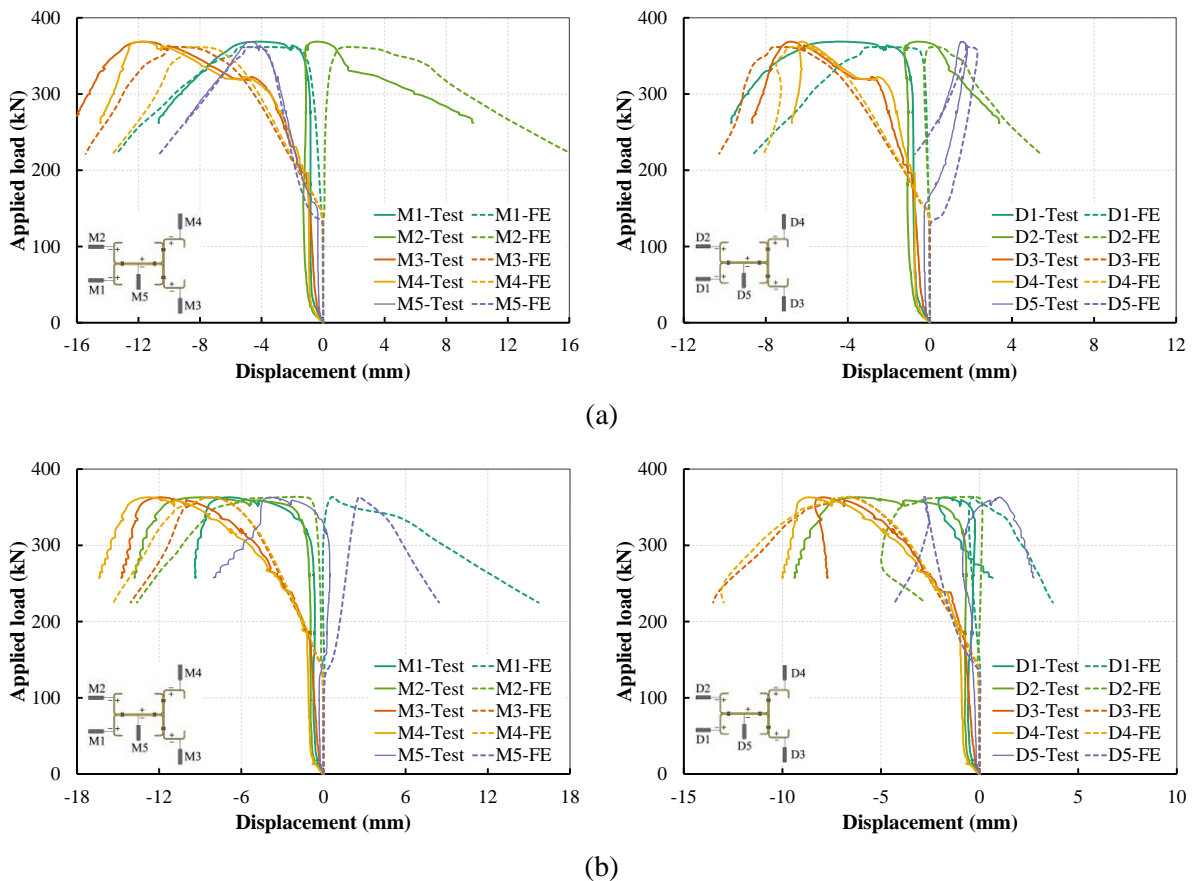
Figure D-24: Comparison between numerical predictions and experimental results of transducers data of built-up 3C-sections with *s*=300 mm: (a) 3C64-300-1, (b) 3C64-300-2

(a)

(b)
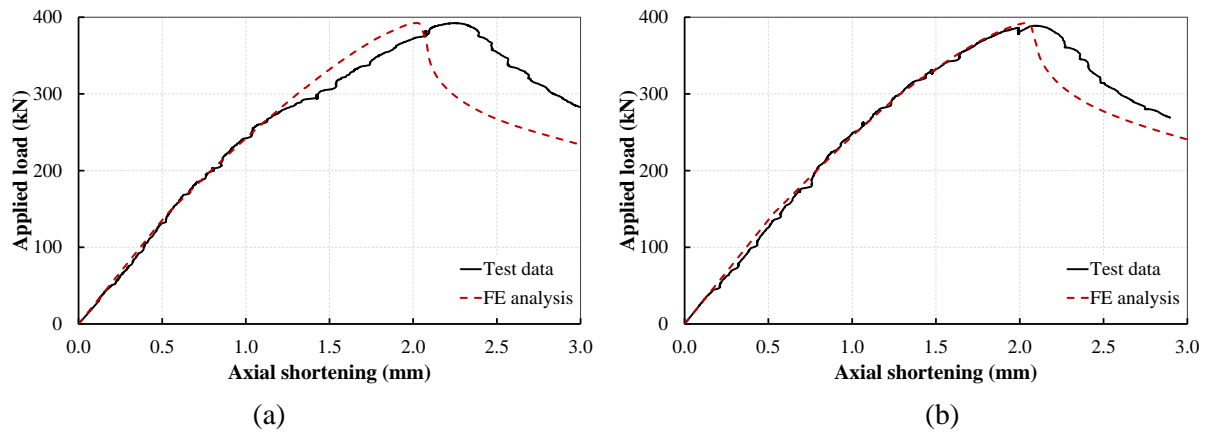
Figure D-25: Comparison between numerical predictions and experimental results of load vs. axial shortening curve of built-up 3C-sections with *s*=100 mm: (a) 3C64-100-1, (b) 3C64-100-2
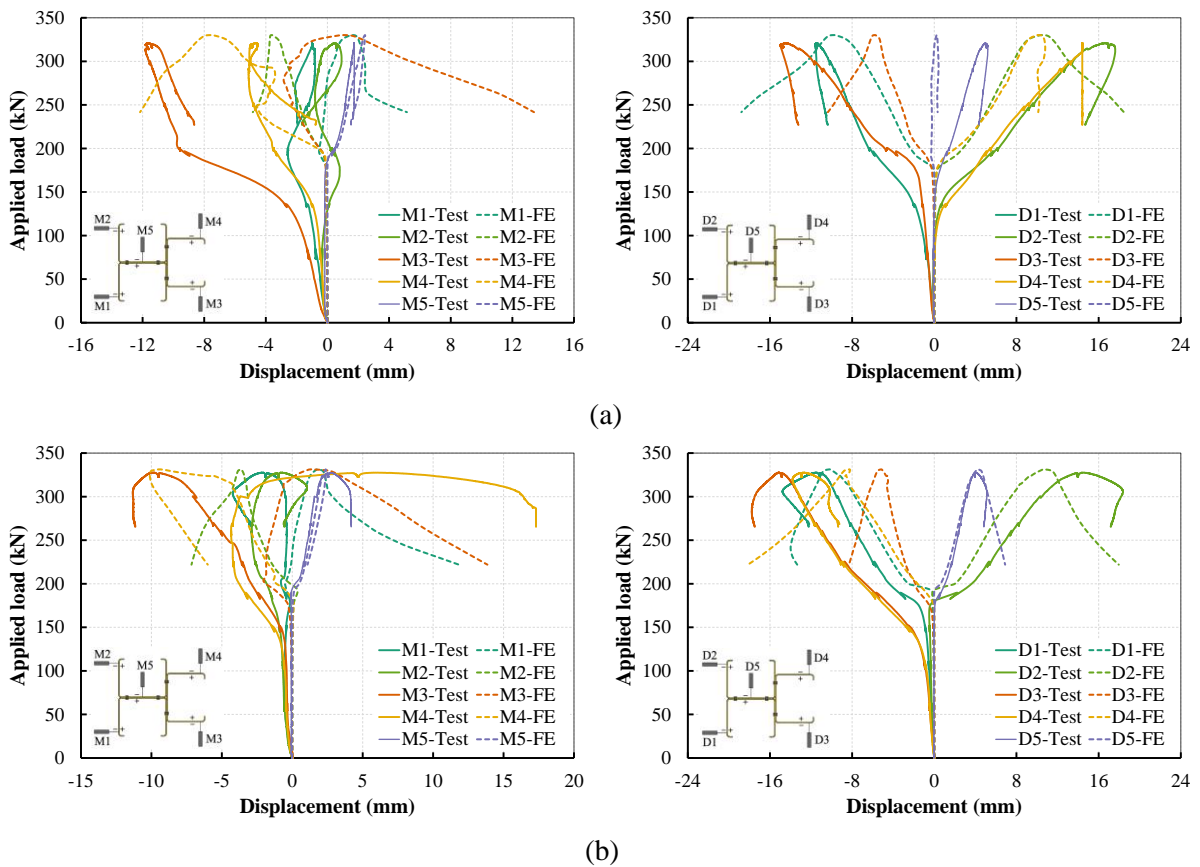

(a)

(b)
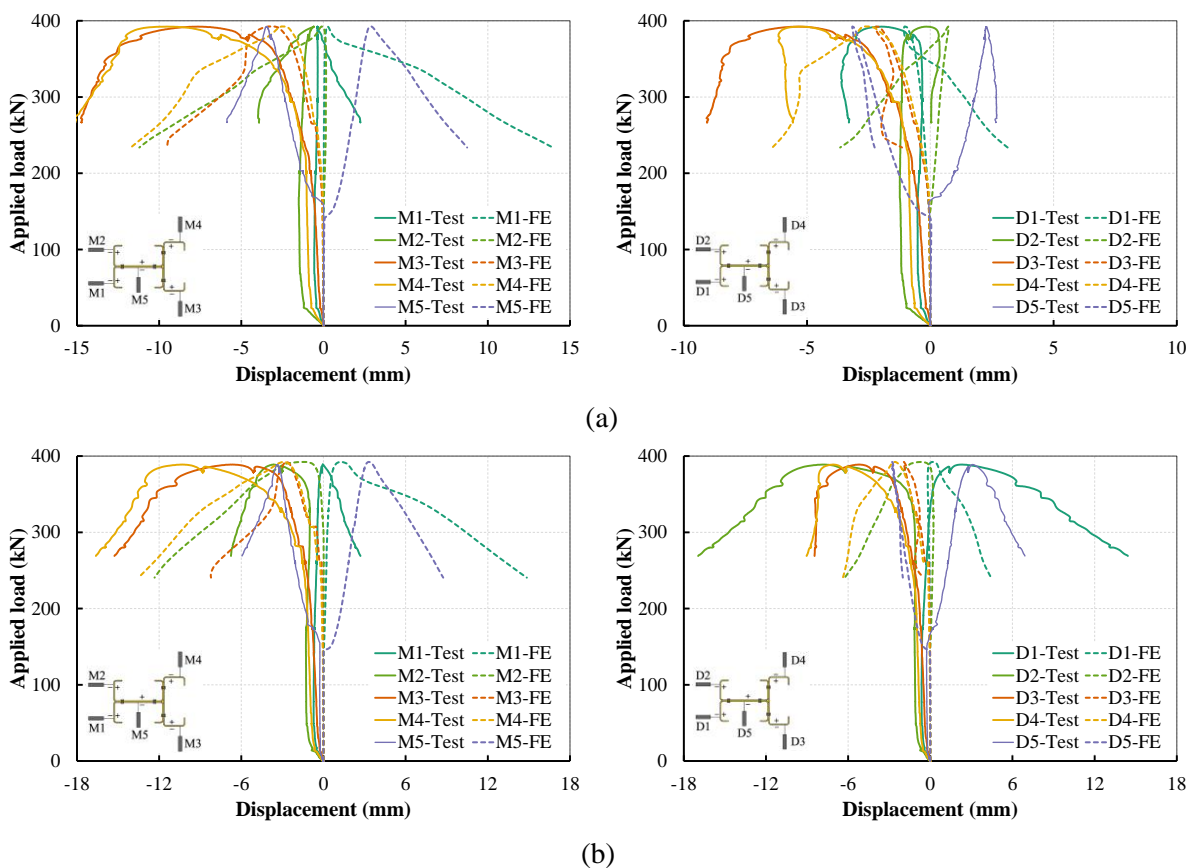
Figure D-26: Comparison between numerical predictions and experimental results of transducers data of built-up 3C-sections with *s*=100 mm: (a) 3C64-100-1, (b) 3C64-100-2
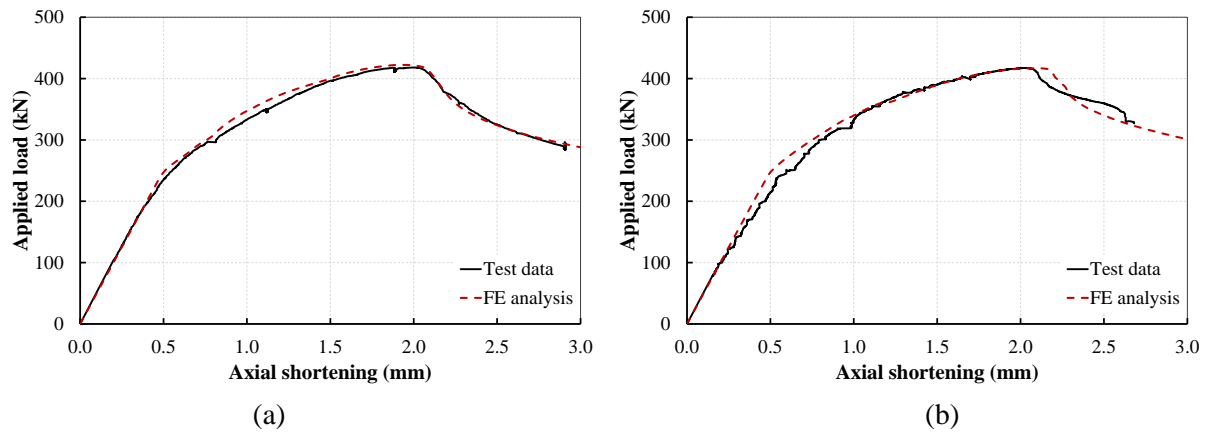
(a)　　　　　　　　　　　　　　　　(b)
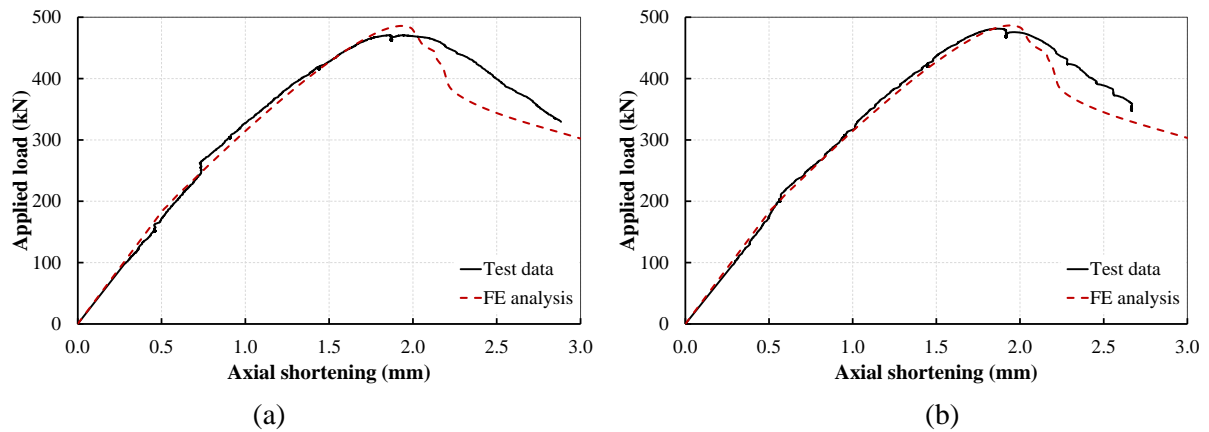
Figure D-27: Comparison between numerical predictions and experimental results of load vs. axial shortening curve of built-up 4C-sections with *s*=900 mm: (a) 4C64-900-1, (b) 4C64-900-2

(a)

(b)
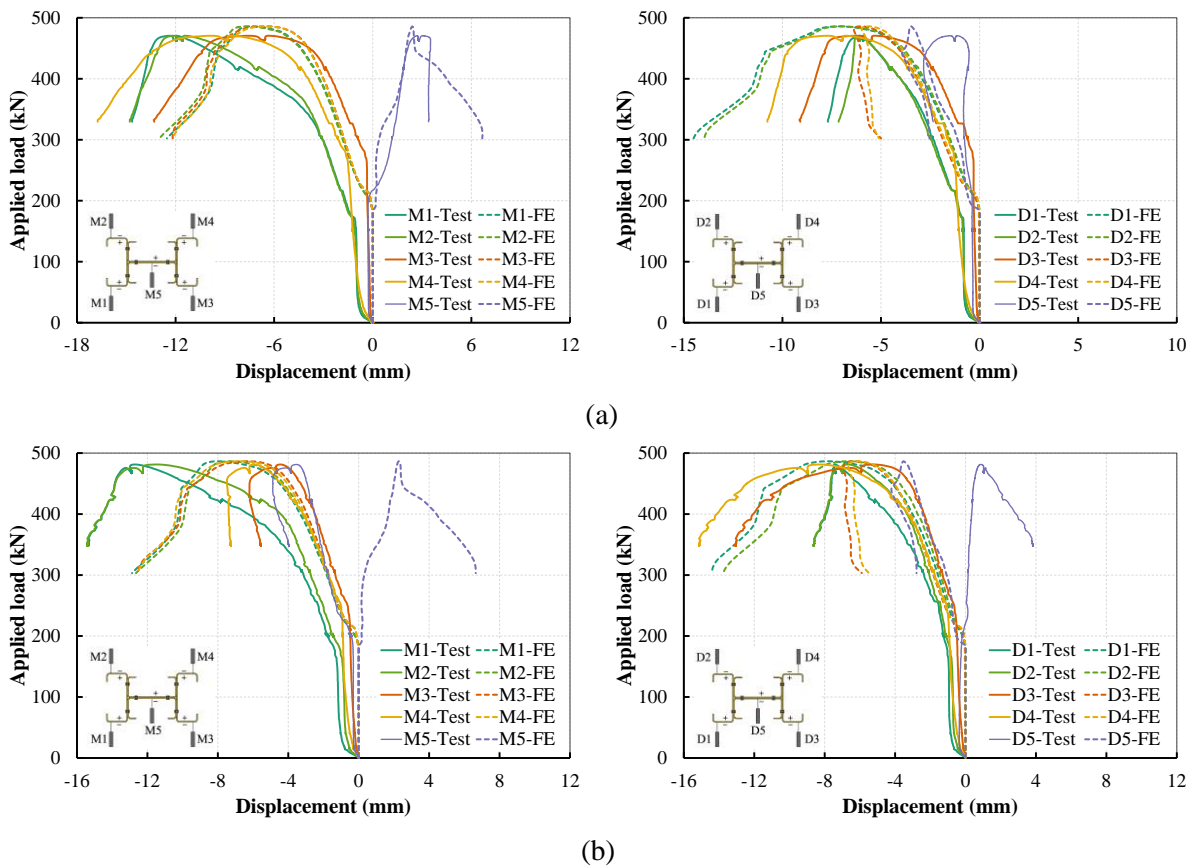
Figure D-28: Comparison between numerical predictions and experimental results of transducers data of built-up 4C-sections with *s*=900 mm: (a) 4C64-900-1, (b) 4C64-900-2

(a)

(b)
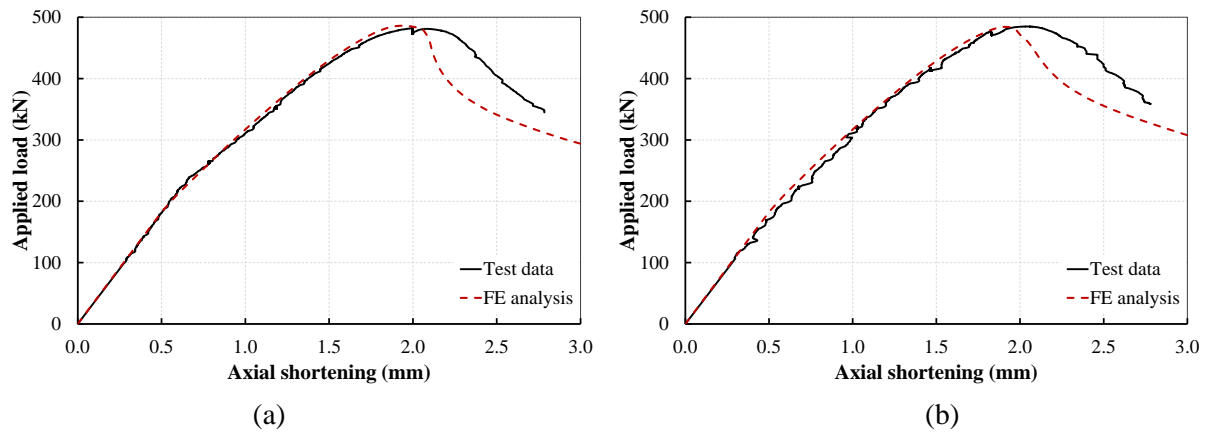
Figure D-29: Comparison between numerical predictions and experimental results of load vs. axial shortening curve of built-up 4C-sections with *s*=300 mm: (a) 4C64-300-1, (b) 4C64-300-2
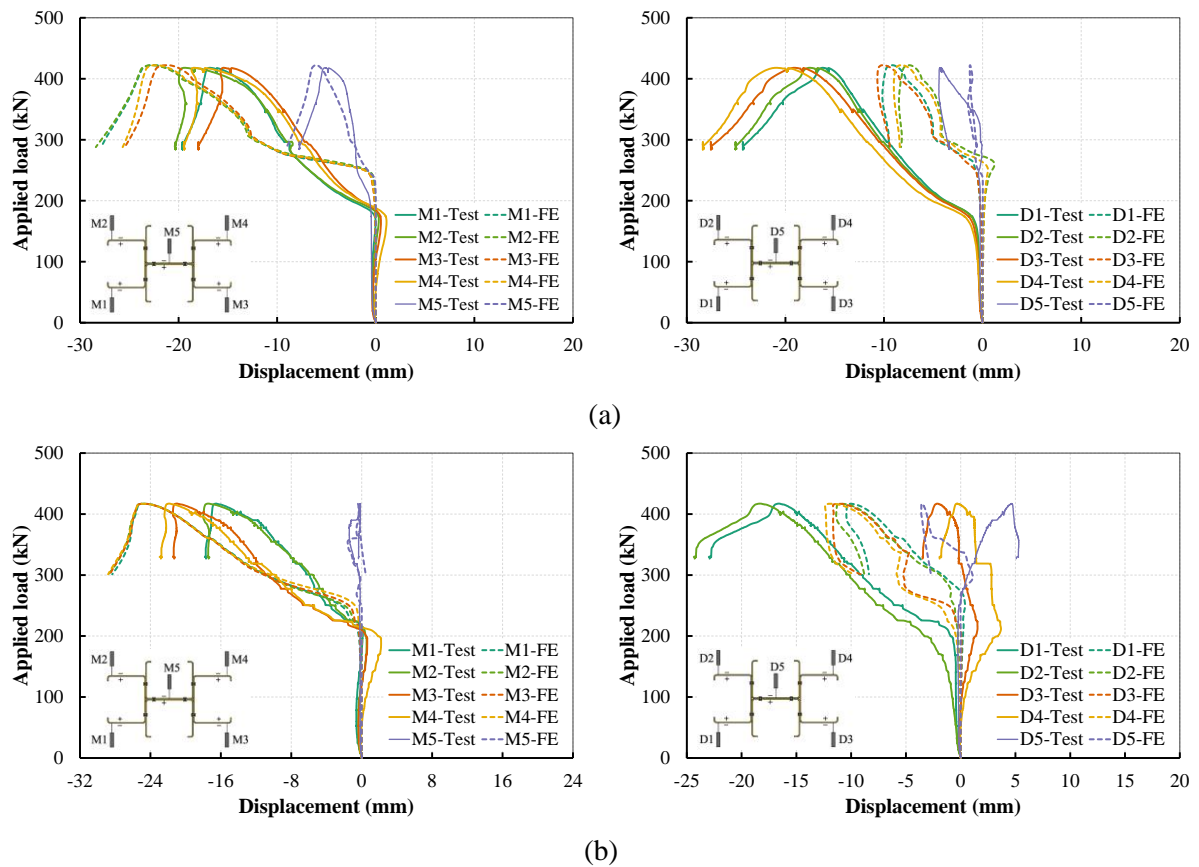

(a)

(b)
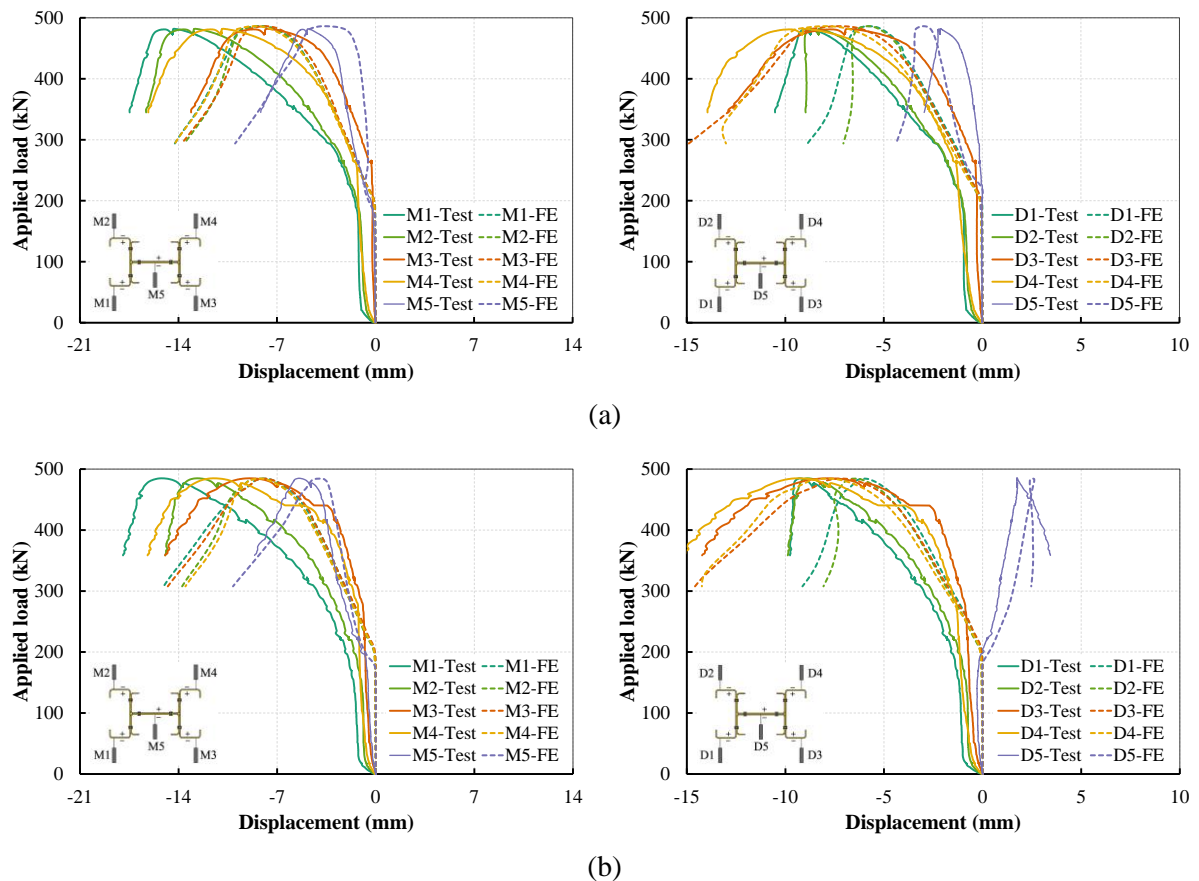
Figure D-30: Comparison between numerical predictions and experimental results of transducers data of built-up 4C-sections with *s*=300 mm: (a) 4C64-300-1, (b) 4C64-300-2
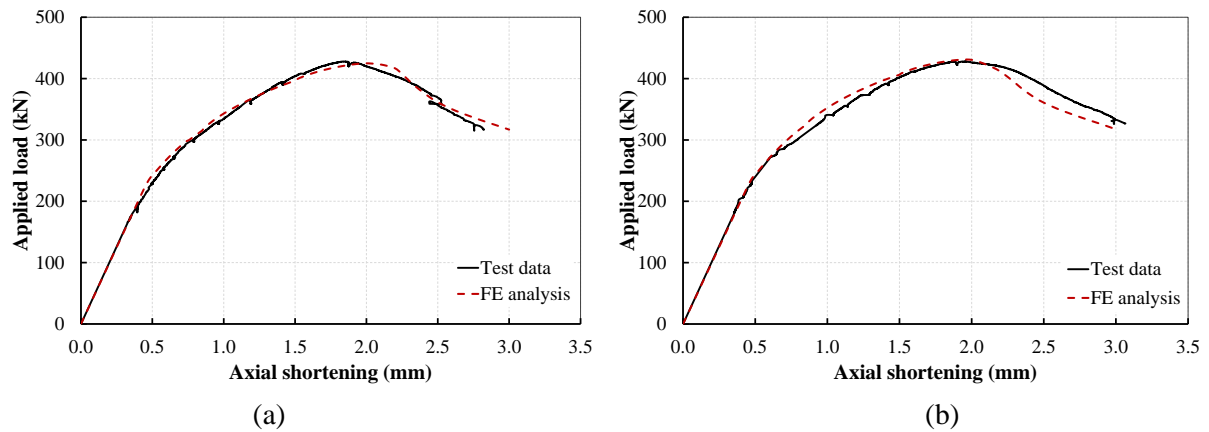
(a)   (b)
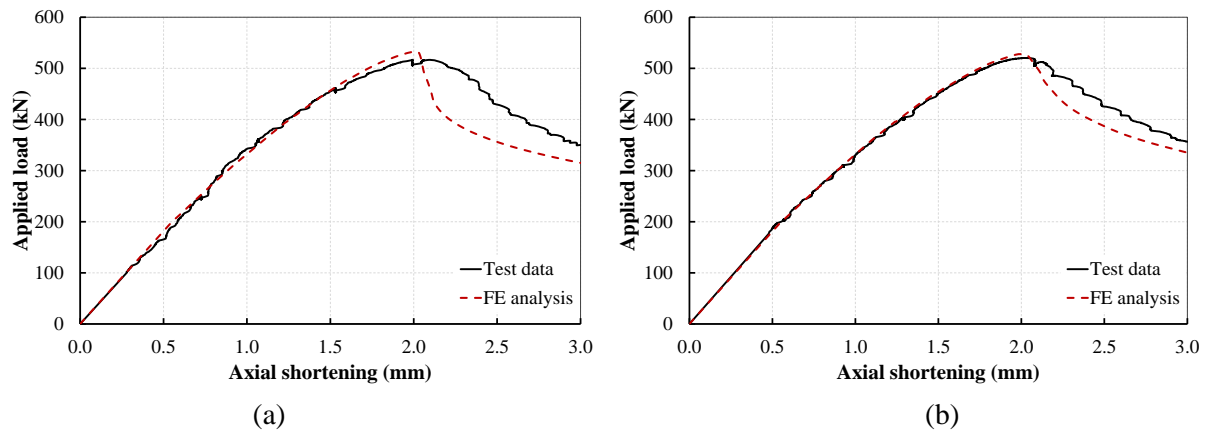
Figure D-31: Comparison between numerical predictions and experimental results of load vs. axial shortening curve of built-up 4C-sections with *s*=100 mm: (a) 4C64-100-1, (b) 4C64-100-2
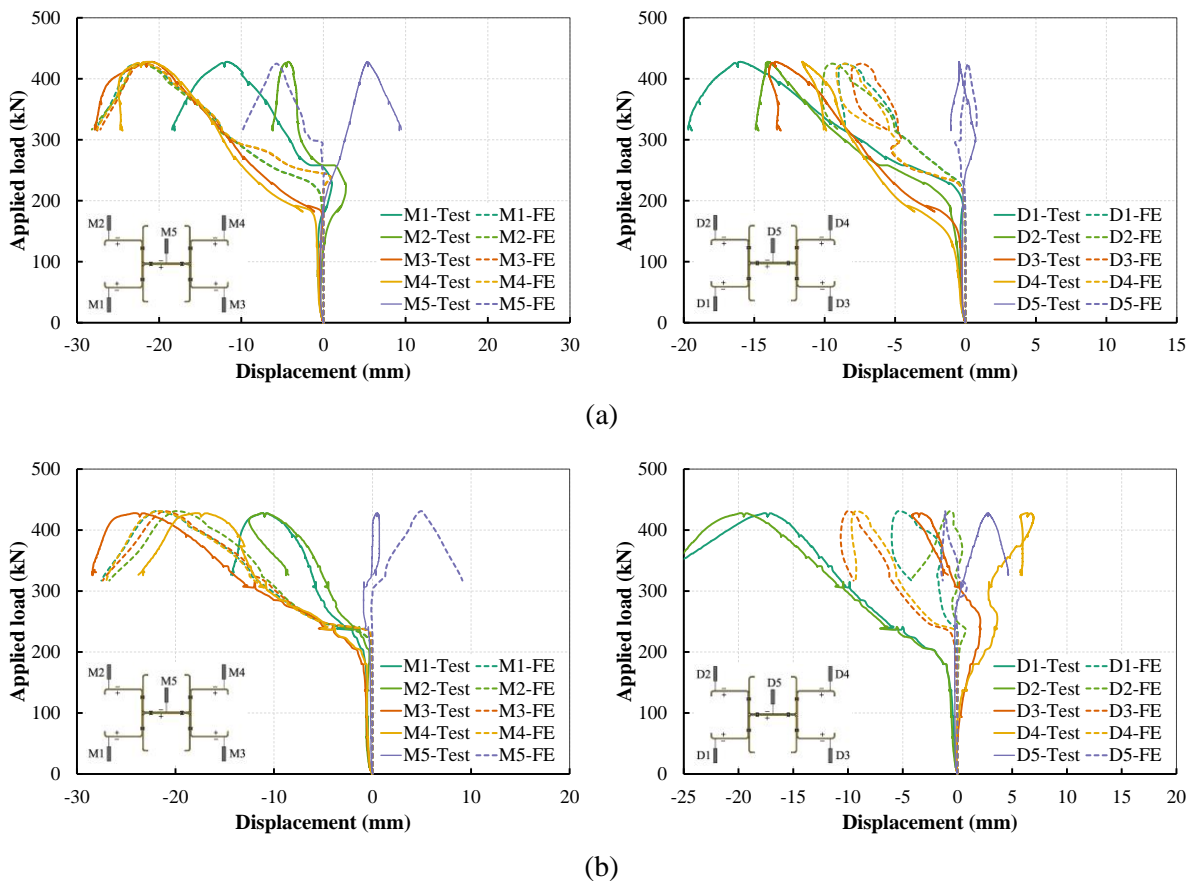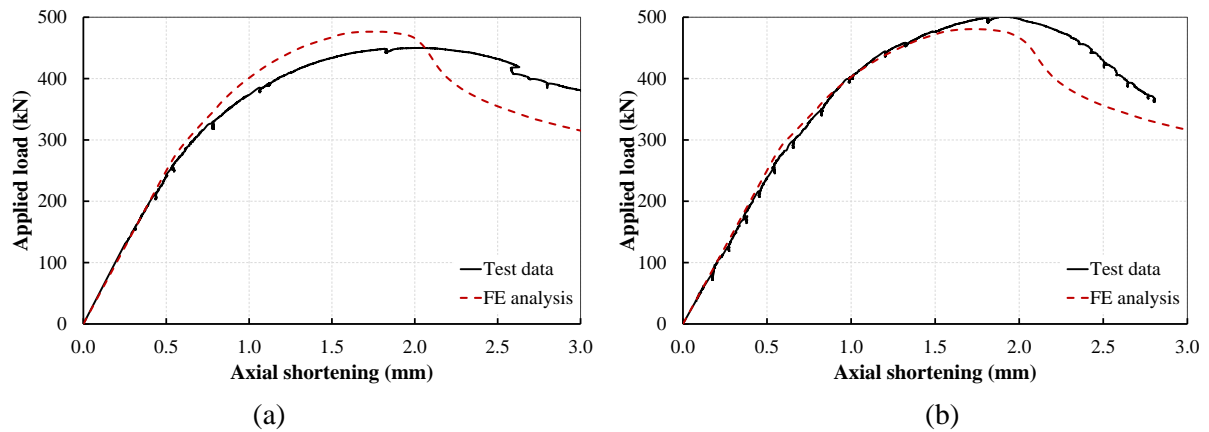

(a)

(b)
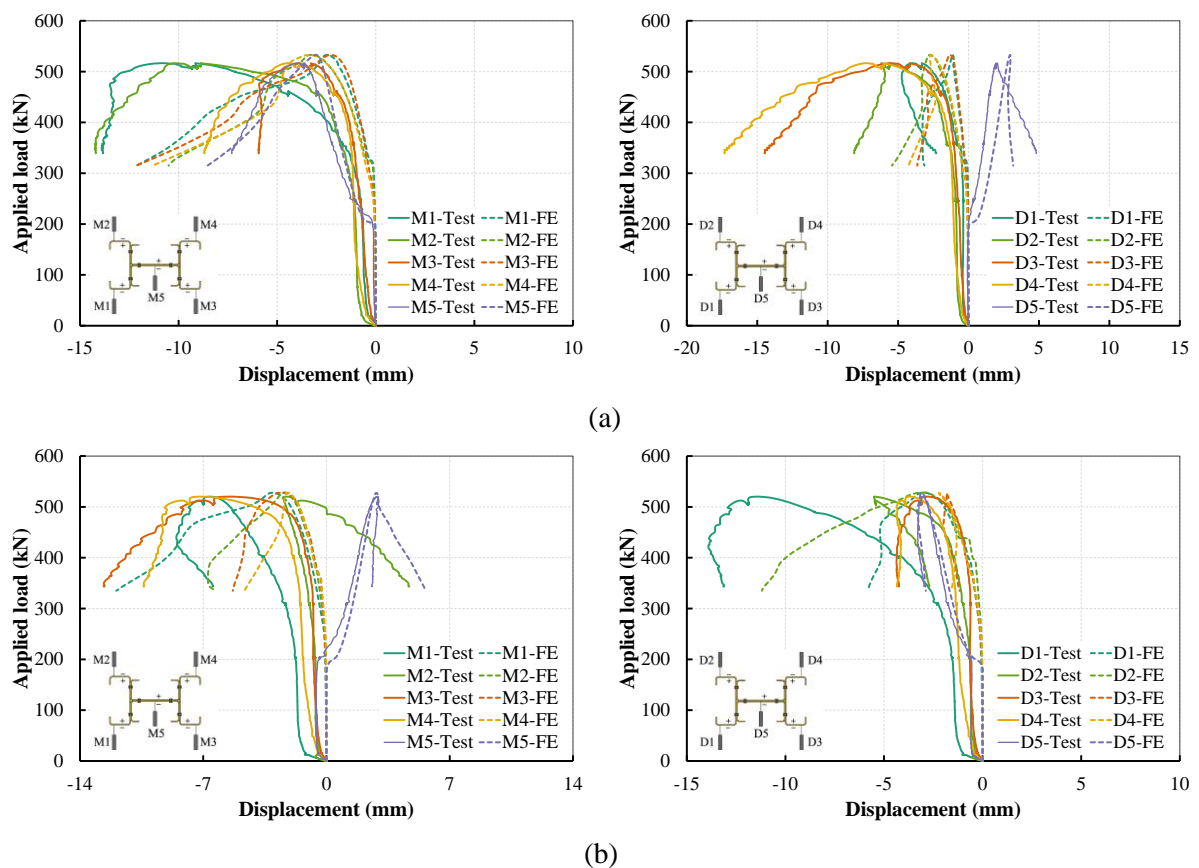
Figure D-32: Comparison between numerical predictions and experimental results of transducers data of built-up 4C-sections with *s*=100 mm: (a) 4C64-100-1, (b) 4C64-100-2

Appendix E   Parametric Study Results

Appendix E contains the parametric study results on the sectional buckling of built-up columns, the details of which are outlined in Section 5.4. The results of the elastic buckling analyses using the Compound Strip Method (CSM) and predictions for the ultimate load of the sections based on different design methods, as explained in Chapter 6, are also presented for all the specimens studied.

Table E-1: Summary of the design parameters and the ultimate load predictions for the built-up I-sections of set-L

Section	CSM			P_u (kN)			
	f_{crl} (MPa)	f_{crd} (MPa)	λ_l	FE	DSM	EWM (AS4600)	EWM (Eurocode)
2C100-40-1.2-1	167.2	307.9	1.78	152.4	139.1	155.2	129.8
2C100-40-1.2-2	167.4	307.9	1.78	152.8	139.2	155.2	129.8
2C100-40-1.2-4	172.8	328.0	1.75	153.3	140.7	155.2	131.8
2C100-40-1.2-5	173.5	331.7	1.75	153.8	140.9	155.2	132.2
2C100-40-1.2-8	178.4	347.6	1.73	161.4	142.3	155.2	133.6
2C100-40-1.2-16	192.2	377.8	1.66	166.4	146.2	155.2	136.1
2C100-40-1.9-1	421.9	608.4	1.12	306.4	311.3	340.3	294.8
2C100-40-1.9-2	422.1	608.4	1.12	311.8	311.3	340.3	294.8
2C100-40-1.9-4	426.3	617.5	1.12	312.1	312.4	340.3	295.5
2C100-40-1.9-5	427.9	619.0	1.11	312.5	312.8	340.3	295.6
2C100-40-1.9-8	430.6	629.0	1.11	327.7	313.4	340.3	296.3
2C100-40-1.9-16	440.4	649.7	1.10	345.0	315.8	340.3	297.6
2C200-80-1.5-1	63.0	126.0	2.90	240.2	240.2	256.5	200.4
2C200-80-1.5-2	63.4	126.0	2.89	241.0	240.9	256.5	200.4
2C200-80-1.5-4	64.2	130.9	2.88	242.2	241.9	256.5	201.2
2C200-80-1.5-5	64.4	132.0	2.87	242.3	242.2	256.5	201.3
2C200-80-1.5-8	65.4	136.0	2.85	250.2	243.6	256.5	201.9
2C200-80-1.5-16	68.2	144.7	2.79	250.8	247.4	256.5	203.2
2C200-80-1.9-1	101.3	182.5	2.29	384.3	364.6	385.1	319.4
2C200-80-1.9-2	101.4	182.5	2.29	386.2	364.9	385.1	319.4
2C200-80-1.9-4	102.3	185.9	2.28	386.9	366.0	385.1	320.1
2C200-80-1.9-5	102.8	186.6	2.27	391.3	366.6	385.1	320.2
2C200-80-1.9-8	103.4	189.7	2.27	404.7	367.4	385.1	320.8
2C200-80-1.9-16	105.6	196.6	2.24	409.8	370.3	385.1	322.0
2C300-120-1.9-1	44.6	103.9	3.45	395.4	404.5	434.3	325.5
2C300-120-1.9-2	44.6	104.1	3.45	396.0	404.8	434.3	325.5
2C300-120-1.9-4	45.0	105.9	3.44	396.6	406.1	434.3	326.0
2C300-120-1.9-5	45.2	106.4	3.43	396.9	406.7	434.3	326.2
2C300-120-1.9-8	45.5	108.2	3.42	402.4	407.7	434.3	326.7
2C300-120-1.9-16	46.4	112.4	3.38	408.4	410.9	434.3	327.9
2C300-120-2.4-1	71.3	156.0	2.73	650.0	615.2	663.5	525.0
2C300-120-2.4-2	71.4	156.0	2.73	652.5	615.4	663.5	525.0
2C300-120-2.4-4	71.7	157.5	2.72	653.2	616.4	663.5	525.5
2C300-120-2.4-5	71.9	157.8	2.72	653.2	617.0	663.5	525.7
2C300-120-2.4-8	72.1	159.3	2.71	670.9	617.6	663.5	526.2
2C300-120-2.4-16	72.9	162.6	2.70	674.3	620.1	663.5	527.4

Table E-2: Summary of the design parameters and the ultimate load predictions for the built-up 3C-sections of set-L

Section	CSM			P_u (kN)			
	f_{crl} (MPa)	f_{crd} (MPa)	λ_l	FE	DSM	EWM (AS4600)	EWM (Eurocode)
3C100-40-1.2-1	167.2	315.0	1.78	225.6	208.6	232.7	195.8
3C100-40-1.2-2	167.4	315.0	1.78	234.5	208.7	232.7	195.8
3C100-40-1.2-4	170.2	399.8	1.77	238.9	210.0	232.7	206.7
3C100-40-1.2-5	171.1	405.8	1.76	246.5	210.4	232.7	207.3
3C100-40-1.2-8	173.6	422.7	1.75	254.0	211.5	232.7	209.0
3C100-40-1.2-16	179.3	453.4	1.72	272.3	213.9	232.7	211.9
3C100-40-1.9-1	421.9	613.8	1.12	453.8	466.9	510.4	442.8
3C100-40-1.9-2	422.1	613.8	1.12	478.7	467.0	510.4	442.8
3C100-40-1.9-4	424.6	766.8	1.12	483.9	468.0	510.4	456.5
3C100-40-1.9-5	425.7	774.4	1.12	487.0	468.4	510.4	457.0
3C100-40-1.9-8	432.9	792.8	1.11	510.1	471.0	510.4	458.4
3C100-40-1.9-16	437.7	821.3	1.10	540.8	472.8	510.4	460.4
3C200-80-1.5-1	62.9	133.0	2.91	366.6	360.2	384.8	302.2
3C200-80-1.5-2	63.1	133.0	2.90	385.5	360.5	384.8	302.2
3C200-80-1.5-4	63.6	159.9	2.89	388.9	361.7	384.8	308.0
3C200-80-1.5-5	63.9	161.4	2.88	390.7	362.2	384.8	308.3
3C200-80-1.5-8	64.4	165.9	2.87	409.8	363.4	384.8	309.2
3C200-80-1.5-16	65.8	175.3	2.84	428.1	366.1	384.8	311.1
3C200-80-1.9-1	101.3	189.4	2.29	581.4	546.9	577.6	481.1
3C200-80-1.9-2	101.4	189.4	2.29	611.8	547.2	577.6	481.1
3C200-80-1.9-4	101.9	231.0	2.28	618.4	548.3	577.6	492.1
3C200-80-1.9-5	102.3	232.4	2.28	622.1	548.9	577.6	492.4
3C200-80-1.9-8	102.8	236.3	2.27	643.7	550.0	577.6	493.4
3C200-80-1.9-16	104.1	244.1	2.26	680.9	552.5	577.6	495.3
3C300-120-1.9-1	44.6	109.6	3.45	608.4	606.8	651.5	490.6
3C300-120-1.9-2	44.6	119.5	3.45	631.9	607.2	651.5	494.8
3C300-120-1.9-4	44.9	128.7	3.44	640.4	608.3	651.5	498.4
3C300-120-1.9-5	45.0	129.6	3.44	651.4	609.0	651.5	498.8
3C300-120-1.9-8	45.2	131.8	3.43	667.5	610.2	651.5	499.6
3C300-120-1.9-16	45.8	136.6	3.41	690.6	613.1	651.5	501.5
3C300-120-2.4-1	71.3	161.4	2.73	1013.3	922.8	995.3	790.4
3C300-120-2.4-2	71.4	175.4	2.73	1044.1	923.1	995.3	797.8
3C300-120-2.4-4	71.7	193.0	2.72	1048.2	924.4	995.3	806.7
3C300-120-2.4-5	71.8	194.0	2.72	1065.3	925.2	995.3	807.1
3C300-120-2.4-8	72.1	196.1	2.71	1095.2	926.4	995.3	808.2
3C300-120-2.4-16	72.7	200.4	2.70	1135.4	929.3	995.3	810.3

Table E-3: Summary of the design parameters and the ultimate load predictions for the built-up 4C-sections of set-L

Section	CSM			P_u (kN)			
	f_{crl} (MPa)	f_{crd} (MPa)	λ_l	FE	DSM	EWM (AS4600)	EWM (Eurocode)
4C100-40-1.2-1	167.2	331.5	1.78	300.5	278.2	310.3	264.3
4C100-40-1.2-2	167.4	331.5	1.78	313.2	278.3	310.3	264.3
4C100-40-1.2-4	170.5	535.6	1.77	321.4	280.1	310.3	291.1
4C100-40-1.2-5	171.5	538.4	1.76	329.9	280.7	310.3	291.4
4C100-40-1.2-8	174.8	544.1	1.74	345.1	282.6	310.3	291.9
4C100-40-1.2-16	181.3	549.1	1.71	381.3	286.3	310.3	292.4
4C100-40-1.9-1	421.9	621.8	1.12	607.6	622.6	680.5	591.6
4C100-40-1.9-2	422.1	621.8	1.12	641.9	622.7	680.5	591.6
4C100-40-1.9-4	425.5	1021.4	1.12	652.1	624.4	680.5	629.2
4C100-40-1.9-5	426.9	1035.1	1.12	652.6	625.1	680.5	630.1
4C100-40-1.9-8	430.4	1064.3	1.11	700.9	626.8	680.5	631.9
4C100-40-1.9-16	437.5	1091.7	1.10	740.3	630.3	680.5	633.6
4C200-80-1.5-1	62.9	143.4	2.91	496.3	480.3	513.0	406.0
4C200-80-1.5-2	63.1	143.4	2.90	535.0	480.6	513.0	406.0
4C200-80-1.5-4	63.8	213.5	2.89	539.7	482.7	513.0	424.2
4C200-80-1.5-5	64.1	215.0	2.88	540.8	483.5	513.0	424.5
4C200-80-1.5-8	64.9	216.5	2.86	568.5	485.8	513.0	424.9
4C200-80-1.5-16	66.5	217.8	2.83	598.3	490.2	513.0	425.2
4C200-80-1.9-1	101.3	197.4	2.29	783.3	729.2	770.2	644.3
4C200-80-1.9-2	101.4	197.4	2.29	837.2	729.7	770.2	644.3
4C200-80-1.9-4	102.2	302.8	2.28	849.4	731.7	770.2	682.7
4C200-80-1.9-5	102.6	304.1	2.28	881.3	732.7	770.2	683.4
4C200-80-1.9-8	104.3	306.9	2.26	890.1	737.2	770.2	685.0
4C200-80-1.9-16	106.0	309.4	2.24	950.7	741.5	770.2	686.4
4C300-120-1.9-1	44.6	117.3	3.45	840.2	809.0	868.7	658.5
4C300-120-1.9-2	44.6	144.0	3.45	896.1	809.6	868.7	672.4
4C300-120-1.9-4	45.0	168.8	3.44	907.4	811.9	868.7	684.1
4C300-120-1.9-5	45.2	170.4	3.43	908.2	813.1	868.7	684.8
4C300-120-1.9-8	45.5	174.2	3.42	926.7	815.6	868.7	686.5
4C300-120-1.9-16	46.3	181.7	3.39	985.4	820.7	868.7	689.9
4C300-120-2.4-1	71.3	168.5	2.73	1365.7	1230.4	1327.0	1058.9
4C300-120-2.4-2	71.4	204.2	2.73	1439.0	1230.8	1327.0	1082.8
4C300-120-2.4-4	71.8	256.4	2.72	1448.9	1233.7	1327.0	1093.3
4C300-120-2.4-5	72.1	258.7	2.71	1476.1	1235.3	1327.0	1096.4
4C300-120-2.4-8	72.5	263.5	2.71	1515.0	1238.1	1327.0	1102.4
4C300-120-2.4-16	73.5	271.2	2.69	1574.4	1243.9	1327.0	1112.0

Table E-4: Summary of the design parameters and the ultimate load predictions for the built-up I-sections of set-D

Section	CSM			P_u (kN)			
	f_{crl} (MPa)	f_{crd} (MPa)	λ_d	FE	DSM	EWM (AS4600)	EWM (Eurocode)
2C100-80-1.2-1	145.7	141.4	1.94	127.6	137.5	149.0	89.4
2C100-80-1.2-2	145.7	141.5	1.94	128.6	137.5	149.0	89.4
2C100-80-1.2-4	145.7	142.2	1.93	128.7	137.9	149.0	89.4
2C100-80-1.2-5	145.7	143.8	1.92	128.8	138.7	149.0	89.4
2C100-80-1.2-8	145.7	145.5	1.91	130.2	139.5	149.0	89.4
2C100-80-1.2-16	153.2	154.3	1.86	133.9	143.9	149.0	89.4
2C100-80-1.9-1	356.2	342.5	1.25	316.9	337.9	326.0	213.0
2C100-80-1.9-2	356.2	344.5	1.24	322.5	338.8	326.0	213.0
2C100-80-1.9-4	356.2	345.0	1.24	323.3	339.0	326.0	213.0
2C100-80-1.9-5	356.2	345.7	1.24	324.8	339.3	326.0	213.0
2C100-80-1.9-8	356.3	348.4	1.23	332.2	340.5	326.0	213.0
2C100-80-1.9-16	364.6	354.3	1.22	349.9	343.1	326.0	213.0
2C100-80-2.4-1	572.9	577.1	0.96	524.6	543.7	503.9	438.3
2C100-80-2.4-2	572.9	577.8	0.96	530.3	543.9	503.9	438.3
2C100-80-2.4-4	572.9	578.2	0.96	531.0	544.1	503.9	438.3
2C100-80-2.4-5	572.9	578.7	0.96	543.0	544.3	503.9	438.3
2C100-80-2.4-8	572.9	579.2	0.96	545.6	544.4	503.9	438.3
2C100-80-2.4-16	577.7	584.5	0.95	552.5	546.4	503.9	438.3
2C200-160-1.5-1	53.6	48.0	3.33	190.9	186.9	217.9	144.1
2C200-160-1.5-2	53.6	48.5	3.31	191.7	188.2	217.9	144.1
2C200-160-1.5-4	53.6	48.6	3.30	192.6	188.4	217.9	144.1
2C200-160-1.5-5	53.6	48.9	3.30	192.7	189.0	217.9	144.1
2C200-160-1.5-8	54.1	49.5	3.28	193.3	190.2	217.9	144.1
2C200-160-1.5-16	56.2	50.9	3.23	199.2	193.3	217.9	144.1
2C200-160-1.9-1	86.2	84.1	2.51	309.4	325.8	346.1	228.1
2C200-160-1.9-2	86.2	84.5	2.51	310.9	326.5	346.1	228.1
2C200-160-1.9-4	86.2	84.6	2.51	311.2	326.8	346.1	228.1
2C200-160-1.9-5	86.2	85.0	2.50	311.7	327.7	346.1	228.1
2C200-160-1.9-8	86.7	85.6	2.49	318.4	328.8	346.1	228.1
2C200-160-1.9-16	88.5	87.0	2.47	325.9	331.8	346.1	228.1
2C300-210-1.9-1	39.8	38.6	3.71	303.6	289.5	341.4	232.8
2C300-210-1.9-2	39.8	38.8	3.70	304.1	290.6	341.4	232.8
2C300-210-1.9-4	39.8	38.9	3.70	304.1	290.9	341.4	232.8
2C300-210-1.9-5	39.8	39.1	3.68	304.4	291.8	341.4	232.8
2C300-210-1.9-8	40.0	39.4	3.67	306.7	293.1	341.4	232.8
2C300-210-1.9-16	41.0	40.3	3.63	311.7	296.6	341.4	232.8
2C300-210-2.4-1	63.2	59.8	2.98	479.7	468.9	528.3	367.2
2C300-210-2.4-2	63.2	60.1	2.97	481.2	470.1	528.3	367.2
2C300-210-2.4-4	63.2	60.1	2.97	481.9	470.3	528.3	367.2
2C300-210-2.4-5	63.2	60.3	2.97	481.9	470.9	528.3	367.2
2C300-210-2.4-8	63.4	60.5	2.96	486.5	472.0	528.3	367.2
2C300-210-2.4-16	64.2	61.2	2.95	497.3	475.0	528.3	367.2

Table E-5: Summary of the design parameters and the ultimate load predictions for the built-up 3C-sections of set-D

Section	CSM			P_u (kN)			
	f_{crl} (MPa)	f_{crd} (MPa)	λ_d	FE	DSM	EWM (AS4600)	EWM (Eurocode)
3C100-80-1.2-1	147.8	141.4	1.94	197.4	206.3	223.4	134.1
3C100-80-1.2-2	147.8	141.5	1.94	206.2	206.3	223.4	134.1
3C100-80-1.2-4	147.8	142.2	1.93	209.6	206.8	223.4	134.1
3C100-80-1.2-5	147.8	142.4	1.93	215.0	207.0	223.4	134.1
3C100-80-1.2-8	147.8	142.8	1.93	225.3	207.3	223.4	134.1
3C100-80-1.2-16	161.8	155.7	1.85	239.5	216.9	223.4	134.1
3C100-80-1.9-1	357.5	342.4	1.25	499.3	506.7	489.0	319.6
3C100-80-1.9-2	357.5	350.8	1.23	529.4	512.4	489.0	319.6
3C100-80-1.9-4	357.5	351.2	1.23	535.6	512.7	489.0	319.6
3C100-80-1.9-5	357.5	358.4	1.22	548.1	517.4	489.0	319.6
3C100-80-1.9-8	360.3	360.8	1.21	557.7	519.0	489.0	319.6
3C100-80-1.9-16	385.2	385.8	1.17	580.7	534.8	489.0	319.6
3C100-80-2.4-1	573.7	576.9	0.96	817.4	815.4	755.9	739.4
3C100-80-2.4-2	573.7	578.6	0.96	841.2	816.3	755.9	739.4
3C100-80-2.4-4	573.7	578.9	0.96	865.0	816.5	755.9	739.4
3C100-80-2.4-5	573.7	584.4	0.95	880.1	819.5	755.9	739.4
3C100-80-2.4-8	573.7	586.2	0.95	882.4	820.5	755.9	739.4
3C100-80-2.4-16	607.2	612.9	0.93	921.1	834.4	755.9	739.4
3C200-160-1.5-1	55.4	48.0	3.33	300.2	280.4	326.8	216.1
3C200-160-1.5-2	55.4	49.9	3.26	305.7	286.6	326.8	216.1
3C200-160-1.5-4	55.4	50.1	3.26	308.5	287.3	326.8	216.1
3C200-160-1.5-5	55.4	51.9	3.20	310.1	293.0	326.8	216.1
3C200-160-1.5-8	57.4	56.1	3.08	330.8	306.0	326.8	216.1
3C200-160-1.5-16	60.2	58.0	3.03	353.6	311.7	326.8	216.1
3C200-160-1.9-1	87.9	84.1	2.51	487.7	488.6	519.1	342.2
3C200-160-1.9-2	87.9	85.1	2.50	497.0	491.7	519.1	342.2
3C200-160-1.9-4	87.9	85.2	2.50	502.2	492.2	519.1	342.2
3C200-160-1.9-5	87.9	87.0	2.47	517.1	497.6	519.1	342.2
3C200-160-1.9-8	90.9	90.1	2.43	532.1	507.4	519.1	342.2
3C200-160-1.9-16	94.4	94.0	2.38	588.7	519.2	519.1	342.2
3C300-210-1.9-1	40.6	38.6	3.71	481.5	434.1	512.1	349.1
3C300-210-1.9-2	40.6	39.3	3.68	493.2	438.8	512.1	349.1
3C300-210-1.9-4	40.6	39.6	3.66	509.2	440.7	512.1	349.1
3C300-210-1.9-5	40.6	40.7	3.61	517.6	447.5	512.1	349.1
3C300-210-1.9-8	42.1	42.2	3.55	532.9	456.9	512.1	349.1
3C300-210-1.9-16	43.2	43.1	3.51	559.7	462.6	512.1	349.1
3C300-210-2.4-1	64.0	59.8	2.98	763.8	703.3	792.4	550.8
3C300-210-2.4-2	64.0	61.8	2.93	785.7	716.1	792.4	550.8
3C300-210-2.4-4	64.0	62.3	2.92	797.4	719.4	792.4	550.8
3C300-210-2.4-5	64.0	64.1	2.88	797.8	731.0	792.4	550.8
3C300-210-2.4-8	66.7	67.2	2.81	857.9	750.3	792.4	550.8
3C300-210-2.4-16	67.7	68.4	2.79	903.7	757.8	792.4	550.8

Table E-6: Summary of the design parameters and the ultimate load predictions for the built-up 4C-sections of set-D

Section	CSM			P_u (kN)			
	f_{crl} (MPa)	f_{crd} (MPa)	λ_d	FE	DSM	EWM (AS4600)	EWM (Eurocode)
4C100-80-1.2-1	151.0	141.5	1.94	277.8	275.1	297.9	178.8
4C100-80-1.2-2	151.0	141.5	1.94	287.9	275.1	297.9	178.8
4C100-80-1.2-4	151.0	142.2	1.93	296.8	275.8	297.9	178.8
4C100-80-1.2-5	151.0	143.7	1.92	304.3	277.4	297.9	178.8
4C100-80-1.2-8	151.0	142.8	1.93	319.8	276.4	297.9	178.8
4C100-80-1.2-16	174.7	166.1	1.79	352.8	299.0	297.9	178.8
4C100-80-1.9-1	359.8	342.4	1.25	680.7	675.7	652.0	426.1
4C100-80-1.9-2	359.8	351.1	1.23	715.7	683.5	652.0	426.1
4C100-80-1.9-4	359.8	351.6	1.23	740.2	683.9	652.0	426.1
4C100-80-1.9-5	359.8	353.4	1.23	747.8	685.5	652.0	426.1
4C100-80-1.9-8	362.6	358.5	1.22	774.7	689.9	652.0	426.1
4C100-80-1.9-16	415.1	413.2	1.13	828.6	734.9	652.0	426.1
4C100-80-2.4-1	575.5	576.9	0.96	1104.7	1087.3	1007.8	808.3
4C100-80-2.4-2	575.5	579.0	0.96	1136.0	1088.7	1007.8	808.3
4C100-80-2.4-4	575.5	579.5	0.96	1158.8	1089.1	1007.8	808.3
4C100-80-2.4-5	575.5	585.9	0.95	1183.8	1093.7	1007.8	808.3
4C100-80-2.4-8	575.5	586.8	0.95	1204.9	1094.3	1007.8	808.3
4C100-80-2.4-16	644.3	646.6	0.91	1248.4	1134.8	1007.8	808.3
4C200-160-1.5-1	57.7	48.0	3.33	423.3	373.8	435.7	288.2
4C200-160-1.5-2	57.7	49.8	3.27	432.8	381.6	435.7	288.2
4C200-160-1.5-4	57.7	49.9	3.26	442.0	382.3	435.7	288.2
4C200-160-1.5-5	57.7	51.5	3.21	448.4	389.2	435.7	288.2
4C200-160-1.5-8	59.9	56.5	3.07	474.5	409.9	435.7	288.2
4C200-160-1.5-16	65.4	58.8	3.00	522.3	419.1	435.7	288.2
4C200-160-1.9-1	89.9	84.1	2.51	681.5	651.5	692.2	456.3
4C200-160-1.9-2	89.9	85.1	2.50	711.1	655.8	692.2	456.3
4C200-160-1.9-4	89.9	85.3	2.50	732.2	656.4	692.2	456.3
4C200-160-1.9-5	89.9	87.0	2.47	740.5	663.5	692.2	456.3
4C200-160-1.9-8	93.6	91.0	2.42	791.3	679.9	692.2	456.3
4C200-160-1.9-16	102.5	101.8	2.28	863.1	722.6	692.2	456.3
4C300-210-1.9-1	41.5	38.6	3.71	686.6	578.9	682.7	465.5
4C300-210-1.9-2	41.5	39.3	3.68	701.1	584.8	682.7	465.5
4C300-210-1.9-4	41.5	39.5	3.67	729.3	587.0	682.7	465.5
4C300-210-1.9-5	41.5	40.2	3.63	735.9	592.7	682.7	465.5
4C300-210-1.9-8	44.3	43.7	3.49	784.7	621.2	682.7	465.5
4C300-210-1.9-16	45.6	45.6	3.41	845.8	636.2	682.7	465.5
4C300-210-2.4-1	64.8	59.8	2.98	1079.2	937.7	1056.5	734.4
4C300-210-2.4-2	64.8	61.6	2.94	1103.3	953.4	1056.5	734.4
4C300-210-2.4-4	64.8	62.0	2.93	1141.4	957.1	1056.5	734.4
4C300-210-2.4-5	64.8	64.1	2.88	1144.3	974.5	1056.5	734.4
4C300-210-2.4-8	69.9	69.5	2.76	1196.8	1019.5	1056.5	734.4
4C300-210-2.4-16	71.5	72.3	2.71	1348.4	1041.6	1056.5	734.4

Appendix F   Design Examples

This appendix includes sample calculations for the capacity prediction of built-up test specimens based on the current direct strength design equations and the modified design equations proposed in Section 6.5. The results of the elastic buckling analyses using the Compound Strip Method (PC-approach) are used for the calculations based on the modified design equations, whereas the results of non-composite approach are employed for the calculations based on the codified recommendations. Further details on the elastic buckling analysis of built-up sections can be found in Section 6.3.
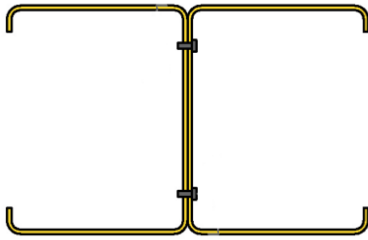
Specimen: 2C120-300-1

Ultimate capacity: $P_u^{exp} = 202.2$ kN

Measured geometry and material properties:

$A = 1182.54$ mm^2

E (Flat) $= 212.894$ GPa

E (Corner) $= 190.911$ GPa

$f_y = 570.25$ MPa

Strength predictions based on the Direct Strength Method (DSM)

Current design equations

Elastic buckling analysis results obtained using the FSM (Non-composite):

$f_{crl} = 93.7$ MPa, $L_{crl} = 140$ mm

$f_{crd} = 86.0$ MPa, $L_{crd} = 600$ mm

$$\frac{P_{ni}}{P_{mi}} = \begin{cases} 1 & \forall \lambda_i \le \lambda_{i.\lim}, \\ \left(a_i - \dfrac{b_i}{\lambda_i^{c_i}} \right) \dfrac{1}{\lambda_i^{c_i}} & \forall \lambda_i > \lambda_{i.\lim}, \end{cases}$$

Local (Table 6-1)	$a_l = 1.00$	
	$b_l = 0.15$	
	$c_l = 0.80$	
Eq. (6-35)	$\lambda_{l.\lim} = 0.776$	
$\lambda_l = \sqrt{f_y / f_{crl}}$	$\lambda_l = 2.47$	
Eq. (6-34)	$P_{nl} = 303.6$ kN	

Distortional (Table 6-1)	$a_d = 1.00$	
	$b_d = 0.25$	
	$c_d = 1.20$	
Eq. (6-35)	$\lambda_{d.\lim} = 0.561$	
$\lambda_d = \sqrt{f_y / f_{crd}}$	$\lambda_d = 2.57$	
Eq. (6-34)	$P_{nd} = 199.4$ kN	

$P_u^{design} = \min(P_{nl}, \underline{P_{nd}}) = 199.4$ kN

$P_u^{exp} / P_u^{design} = 1.01$

Modified design equations

Elastic buckling analysis results obtained using the CSM (Partially-composite):

$f_{crl} = 94.7$ MPa, $L_{crl} = 140$ mm
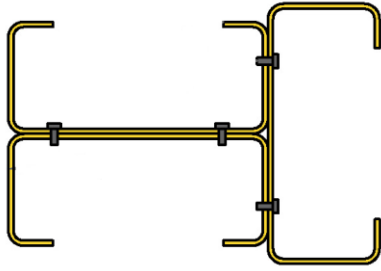
$f_{crd} = 92.2$ MPa, $L_{crd} = 600$ mm

$s/L_{crl} = \min(1.0, 300/140) = 1.0$

$1 - n_{rl} = 1.0$

$s/L_{crd} = \min(1.0, 300/600) = 0.5$

$1 - n_{rd} = 1.0$

Local	$a_l = 1.00$	
Eq. (6.77)	$b_{lr} = 0.15$	
Eq. (6.78)	$c_{lr} = 0.80$	
Eq. (6.76)	$\lambda_{l.\lim} = 0.776$	
$\lambda_l = \sqrt{f_y / f_{crl}}$	$\lambda_l = 2.45$	
Eq. (6.75)	$P_{nl} = 304.9$ kN	

Distortional	$a_d = 1.00$	
Eq. (6.73)	$b_{dr} = 0.22$	
Eq. (6.74)	$c_{dr} = 1.20$	
Eq. (6.72)	$\lambda_{d.\lim} = 0.724$	
$\lambda_d = \sqrt{f_y / f_{crd}}$	$\lambda_d = 2.49$	
Eq. (6.71)	$P_{nd} = 209.5$ kN	

$P_u^{design} = \min(P_{nl}, \underline{P_{nd}}) = 209.5$ kN

$P_u^{exp} / P_u^{design} = 0.97$

Specimen: 3C64-100-2

Ultimate capacity: $P_u^{exp} = 381.0$ kN

Measured geometry and material properties:

$A = 1317.76$ mm^2

E (Flat) $= 211.833$ GPa

E (Corner) $= 203.826$ GPa

$f_y = 537.4$ MPa

Strength predictions based on the Direct Strength Method (DSM)

Current design equations

Modified design equations

Elastic buckling analysis results obtained using the FSM (Non-composite):

$f_{crl} = 105.1$ MPa, $L_{crl} = 120$ mm

$f_{crd} = 194.4$ MPa, $L_{crd} = 600$ mm

Elastic buckling analysis results obtained using the CSM (Partially-composite):

$f_{crl} = 107.3$ MPa, $L_{crl} = 120$ mm
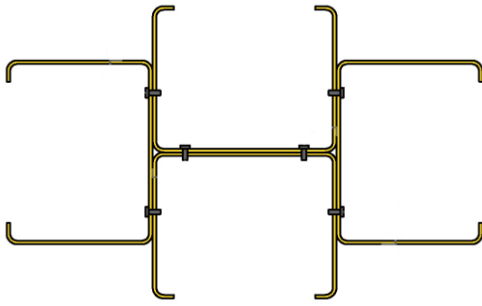
$f_{crd} = 265.0$ MPa, $L_{crd} = 600$ mm

$$\frac{P_{ni}}{P_{mi}} = \begin{cases} 1 & \forall \lambda_i \le \lambda_{i.\lim}, \\ \left(a_i - \dfrac{b_i}{\lambda_i^{c_i}} \right) \dfrac{1}{\lambda_i^{c_i}} & \forall \lambda_i > \lambda_{i.\lim}, \end{cases}$$

$s/L_{crl} = \min(1.0, 100/120) = 0.83$

$1 - n_{rl} = 0.67$

$s/L_{crd} = \min(1.0, 100/600) = 0.17$

$1 - n_{rd} = 0.67$

Local (Table 6-1)		**Local**	
	$a_l = 1.00$		$a_l = 1.00$
	$b_l = 0.15$	Eq. (6.77)	$b_{lr} = 0.13$
	$c_l = 0.80$	Eq. (6.78)	$c_{lr} = 0.73$
Eq. (6-35)	$\lambda_{l.\lim} = 0.776$	Eq. (6.76)	$\lambda_{l.\lim} = 0.806$
$\lambda_l = \sqrt{f_y / f_{crl}}$	$\lambda_l = 2.26$	$\lambda_l = \sqrt{f_y / f_{crl}}$	$\lambda_l = 2.24$
Eq. (6-34)	$P_{nl} = 339.9$ kN	Eq. (6.75)	$P_{nl} = 364.7$ kN

Distortional (Table 6-1)		**Distortional**	
	$a_d = 1.00$		$a_d = 1.00$
	$b_d = 0.25$	Eq. (6.73)	$b_{dr} = 0.19$
	$c_d = 1.20$	Eq. (6.74)	$c_{dr} = 1.09$
Eq. (6-35)	$\lambda_{d.\lim} = 0.561$	Eq. (6.72)	$\lambda_{d.\lim} = 0.765$
$\lambda_d = \sqrt{f_y / f_{crd}}$	$\lambda_d = 1.66$	$\lambda_d = \sqrt{f_y / f_{crd}}$	$\lambda_d = 1.43$
Eq. (6-34)	$P_{nd} = 332.5$ kN	Eq. (6.71)	$P_{nd} = 419.3$ kN

$P_u^{design} = \min(P_{nl}, \underline{P_{nd}}) = 332.5$ kN

$P_u^{design} = \min(\underline{P_{nl}}, P_{nd}) = 364.7$ kN

$P_u^{exp} / P_u^{design} = 1.15$

$P_u^{exp} / P_u^{design} = 1.04$

Specimen: 4C120-100-2

Ultimate capacity: $P_u{}^{exp} = 492.1$ kN

Measured geometry and material properties:

$A = 2359.84$ mm^2

E (Flat) $= 212.894$ GPa

E (Corner) $= 190.911$ GPa

$f_y = 570.25$ MPa

Strength predictions based on the Direct Strength Method (DSM)

Current design equations	*Modified design equations*
Elastic buckling analysis results obtained using the FSM (Non-composite):	Elastic buckling analysis results obtained using the CSM (Partially-composite):
$f_{crl} = 94.3$ MPa, $L_{crl} = 140$ mm	$f_{crl} = 106.4$ MPa, $L_{crl} = 140$ mm
$f_{crd} = 88.0$ MPa, $L_{crd} = 600$ mm	$f_{crd} = 102.2$ MPa, $L_{crd} = 600$ mm

---

$$\frac{P_{ni}}{P_{mi}} = \begin{cases} 1 & \forall \lambda_i \le \lambda_{i.\lim}, \\ \left(a_i - \dfrac{b_i}{\lambda_i^{c_i}}\right)\dfrac{1}{\lambda_i^{c_i}} & \forall \lambda_i > \lambda_{i.\lim}, \end{cases}$$

$s/L_{crl} = \min (1.0, 100/140) = 0.71$

$1 - n_{rl} = 0.5$

$s/L_{crd} = \min (1.0, 100/600) = 0.17$

$1 - n_{rd} = 0.5$

Local (Table 6-1)	$a_l = 1.00$	**Local**	$a_l = 1.00$
	$b_l = 0.15$	Eq. (6.77)	$b_{lr} = 0.11$
	$c_l = 0.80$	Eq. (6.78)	$c_{lr} = 0.69$
Eq. (6-35)	$\lambda_{l.\lim} = 0.776$	Eq. (6.76)	$\lambda_{l.\lim} = 0.817$
$\lambda_l = \sqrt{f_y / f_{crl}}$	$\lambda_l = 2.46$	$\lambda_l = \sqrt{f_y / f_{crl}}$	$\lambda_l = 2.32$
Eq. (6-34)	$P_{nl} = 607.2$ kN	Eq. (6.75)	$P_{nl} = 704.8$ kN

Distortional (Table 6-1)	$a_d = 1.00$	**Distortional**	$a_d = 1.00$
	$b_d = 0.25$	Eq. (6.73)	$b_{dr} = 0.19$
	$c_d = 1.20$	Eq. (6.74)	$c_{dr} = 1.04$
Eq. (6-35)	$\lambda_{d.\lim} = 0.561$	Eq. (6.72)	$\lambda_{d.\lim} = 0.759$
$\lambda_d = \sqrt{f_y / f_{crd}}$	$\lambda_d = 2.54$	$\lambda_d = \sqrt{f_y / f_{crd}}$	$\lambda_d = 2.36$
Eq. (6-34)	$P_{nd} = 402.9$ kN	Eq. (6.71)	$P_{nd} = 509.5$ kN

$P_u{}^{design} = \min(P_{nl}, \underline{P_{nd}}) = 402.9$ kN | $P_u{}^{design} = \min(P_{nl}, \underline{P_{nd}}) = 509.5$ kN

$P_u{}^{exp} / P_u{}^{design} = 1.22$ | $P_u{}^{exp} / P_u{}^{design} = 0.97$